Trends in Mathematics

B. Rushi Kumar
R. Sivaraj
B. S. R. V. Prasad
M. Nalliah
A. Subramanyam Reddy
Editors

Applied Mathematics and Scientific Computing

International Conference on Advances in Mathematical Sciences, Vellore, India, December 2017 - Volume II

Birkhäuser

Trends in Mathematics

Trends in Mathematics is a series devoted to the publications of volumes arising from conferences and lecture series focusing on a particular topic from any area of mathematics. Its aim is to make current developments available to the community as rapidly as possible without compromise to quality and to archive these for reference. Proposals for volumes can be submitted using the Online Book Project Submission Form at our website www.birkhauser-science.com.

Material submitted for publication must be screened and prepared as follows:

All contributions should undergo a reviewing process similar to that carried out by journals and be checked for correct use of language which, as a rule, is English. Articles without proofs, or which do not contain any significantly new results, should be rejected. High quality survey papers, however, are welcome.

We expect the organizers to deliver manuscripts in a form that is essentially ready for direct reproduction. Any version of TEX is acceptable, but the entire collection of files must be in one particular dialect of TEX and unified according to simple instructions available from Birkhäuser.

Furthermore, in order to guarantee the timely appearance of the proceedings it is essential that the final version of the entire material be submitted no later than one year after the conference.

More information about this series at http://www.springer.com/series/4961

B. Rushi Kumar • R. Sivaraj • B. S. R. V. Prasad
M. Nalliah • A. Subramanyam Reddy
Editors

Applied Mathematics and Scientific Computing

International Conference on Advances in Mathematical Sciences, Vellore, India, December 2017 - Volume II

Birkhäuser

Editors
B. Rushi Kumar
Department of Mathematics
School of Advanced Sciences
Vellore Institute of Technology
Vellore, Tamil Nadu, India

R. Sivaraj
Department of Mathematics
School of Advanced Sciences
Vellore Institute of Technology
Vellore, Tamil Nadu, India

B. S. R. V. Prasad
Department of Mathematics
School of Advanced Sciences
Vellore Institute of Technology
Vellore, Tamil Nadu, India

M. Nalliah
Department of Mathematics
School of Advanced Sciences
Vellore Institute of Technology
Vellore, Tamil Nadu, India

A. Subramanyam Reddy
Department of Mathematics
School of Advanced Sciences
Vellore Institute of Technology
Vellore, Tamil Nadu, India

ISSN 2297-0215 ISSN 2297-024X (electronic)
Trends in Mathematics
ISBN 978-3-030-01122-2 ISBN 978-3-030-01123-9 (eBook)
https://doi.org/10.1007/978-3-030-01123-9

Library of Congress Control Number: 2018966596

This book is published under the imprint Birkhäuser, www.birkhauser-science.com by the registered company Springer Nature Switzerland AG
The registered company address is: Gewerbestrasse 11, 6330 Cham, Switzerland

Preface

The Department of Mathematics, School of Advanced Sciences, Vellore Institute of Technology (Deemed to be University), Vellore, Tamil Nadu, India, organized the International Conference on Advances in Mathematical Sciences—2017 (ICAMS 2017) in association with the Society for Industrial and Applied Mathematics VIT Chapter from December 1, 2017, to December 3, 2017. The major objective of ICAMS 2017 was to promote scientific and educational activities toward the advancement of common man's life by improving the theory and practice of various disciplines of Mathematics. This prestigious conference was partially financially supported by the Council of Scientific and Industrial Research (CSIR), India. The Department of Mathematics has 90 qualified faculty members and 30 research scholars, and all were delicately involved in organizing ICAMS 2017 grandly. In addition, 30 leading researchers from around the world served as an advisory committee for this conference. Overall, more than 450 participants (professors/scholars/students) enriched their knowledge in the wings of Mathematics.

There were 9 eminent speakers from overseas and 33 experts from various states of India who delivered the keynote address and invited talks in this conference. Many leading scientists and researchers worldwide submitted their quality research articles to ICAMS. Moreover, 305 original research articles were shortlisted for ICAMS 2017 oral presentations that were authored by dynamic researchers from 25 states in India and 20 countries around the world. We hope that ICAMS will further stimulate research in Mathematics, share research interest and information, and create a forum of collaboration and build a trust relationship. We feel honored and privileged to serve the best of recent developments in the field of Mathematics to the reader.

A basic premise of this book is that quality assurance is effectively achieved through the selection of quality research articles by a scientific committee consisting of more than 100 reviewers from all over the world. This book comprises the contribution of several dynamic researchers in 62 chapters. Each chapter identifies the existing challenges in the areas of Differential Equations, Fluid Dynamics, and Graph Theory and emphasizes the importance of establishing new methods and algorithms to address the challenges. Each chapter presents a research problem, the

technique suitable for solving the problem with sufficient mathematical background, and discussions on the obtained results with physical interruptions to understand the domain of applicability. This book also provides a comprehensive literature survey which reveals the challenges, outcomes, and developments of higher level mathematics in this decade. The theoretical coverage of this book is relatively at a higher level to meet the global orientation of mathematics and its applications in science and engineering.

The target audience of this book is postgraduate students, researchers, and industrialists. This book promotes a vision of pure and applied mathematics as integral to modern science and engineering. Each chapter contains important information emphasizing core Mathematics, intended for the professional who already possesses a basic understanding. In this book, theoretically oriented readers will find an overview of Mathematics and its applications. Industrialists will find a variety of techniques with sufficient discussion in terms of physical point of view to adapt for solving the particular application based on mathematical models. The reader can make use of the literature survey of this book to identify the current trends in Mathematics. It is our hope and expectation that this book will provide an effective learning experience and referenced resource for all young mathematicians.

As Editors, we would like to express our sincere thanks to all the administrative authorities of Vellore Institute of Technology, Vellore, for their motivation and support. We also extend our profound thanks to all faculty members and research scholars of the Department of Mathematics and all staff members of our institute. We especially thank all the members of the organizing committee of ICAMS 2017 who worked as a team by investing their time to make the conference a great success. We thank the national funding agency, Council of Scientific and Industrial Research (CSIR), Government of India, for the financial support they contributed toward the successful completion of this international conference. We express our sincere gratitude to all the referees for spending their valuable time to review the manuscripts, which led to substantial improvements and selection of the research papers for publication. The organizing committee is grateful to Mr. Christopher Tominich, Editor at Birkhäuser/Springer, for his continuous encouragement and support toward the publication of this book.

Vellore, India — B. Rushi Kumar
Vellore, India — R. Sivaraj
Vellore, India — B. S. R. V. Prasad
Vellore, India — M. Nalliah
Vellore, India — A. Subramanyam Reddy

Contents

Part V Differential Equations

Numerical Solution to Singularly Perturbed Differential Equation of Reaction-Diffusion Type in MAGDM Problems 3
P. John Robinson, M. Indhumathi, and M. Manjumari

Application of Integrodifferential Equations Using Sumudu Transform in Intuitionistic Trapezoidal Fuzzy MAGDM Problems 13
P. John Robinson and S. Jeeva

Existence of Meromorphic Solution of Riccati-Abel Differential Equation 21
P. G. Siddheshwar and A. Tanuja

Expansion of Function with Uncertain Parameters in Higher Dimension 29
Priyanka Roy and Geetanjali Panda

Analytical Solutions of the Bloch Equation via Fractional Operators with Non-singular Kernels 37
A. S. V. Ravi Kanth and Neetu Garg

Solution of the Lorenz Model with Help from the Corresponding Ginzburg-Landau Model 47
P. G. Siddheshwar, S. Manjunath, and T. S. Sushma

Estimation of Upper Bounds for Initial Coefficients and Fekete-Szegö Inequality for a Subclass of Analytic Bi-univalent Functions 57
G. Saravanan and K. Muthunagai

An Adaptive Mesh Selection Strategy for Solving Singularly Perturbed Parabolic Partial Differential Equations with a Small Delay ... 67
Kamalesh Kumar, Trun Gupta, P. Pramod Chakravarthy, and R. Nageshwar Rao

Part VI Fluid Dynamics

Steady Finite-Amplitude Rayleigh-Bénard-Taylor Convection of Newtonian Nanoliquid in a High-Porosity Medium 79
P. G. Siddheshwar and T. N. Sakshath

MHD Three Dimensional Darcy-Forchheimer Flow of a Nanofluid with Nonlinear Thermal Radiation 87
Nainaru Tarakaramu, P. V. Satya Narayana, and B. Venkateswarlu

Effect of Electromagnetohydrodynamic on Chemically Reacting Nanofluid Flow over a Cone and Plate 99
H. Thameem Basha, I. L. Animasaun, O. D. Makinde, and R. Sivaraj

Effect of Non-linear Radiation on 3D Unsteady MHD Nanoliquid Flow over a Stretching Surface with Double Stratification 109
K. Jagan, S. Sivasankaran, M. Bhuvaneswari, and S. Rajan

Chemical Reaction and Nonuniform Heat Source/Sink Effects on Casson Fluid Flow over a Vertical Cone and Flat Plate Saturated with Porous Medium 117
P. Vijayalakshmi, S. Rao Gunakala, I. L. Animasaun, and R. Sivaraj

An Analytic Solution of the Unsteady Flow Between Two Coaxial Rotating Disks 129
Abhijit Das and Bikash Sahoo

Cross Diffusion Effects on MHD Convection of Casson-Williamson Fluid over a Stretching Surface with Radiation and Chemical Reaction 139
M. Bhuvaneswari, S. Sivasankaran, H. Niranjan, and S. Eswaramoorthi

Study of Steady, Two-Dimensional, Unicellular Convection in a Water-Copper Nanoliquid-Saturated Porous Enclosure Using Single-Phase Model 147
P. G. Siddheshwar and B. N. Veena

The Effects of Homo-/Heterogeneous Chemical Reactions on Williamson MHD Stagnation Point Slip Flow: A Numerical Study 157
T. Poornima, P. Sreenivasulu, N. Bhaskar Reddy, and S. Rao Gunakala

The Influence of Wall Properties on the Peristaltic Pumping of a Casson Fluid 167
P. Devaki, A. Kavitha, D. Venkateswarlu Naidu, and S. Sreenadh

Peristaltic Flow of a Jeffrey Fluid in Contact with a Newtonian Fluid in a Vertical Channel 181
R. Sivaiah, R. Hemadri Reddy, and R. Saravana

MHD and Cross Diffusion Effects on Peristaltic Flow of a Casson Nanofluid in a Duct 191
G. Sucharitha, P. Lakshminarayana, and N. Sandeep

Axisymmetric Vibration in a Submerged Piezoelectric Rod Coated with Thin Film 203
Rajendran Selvamani and Farzad Ebrahimi

Numerical Exploration of 3D Steady-State Flow Under the Effect of Thermal Radiation as Well as Heat Generation/Absorption over a Nonlinearly Stretching Sheet 213
R. Jayakar and B. Rushi Kumar

Radiated Slip Flow of Williamson Unsteady MHD Fluid over a Chemically Reacting Sheet with Variable Conductivity and Heat Source or Sink 225
Narsu Siva Kumar and B. Rushi Kumar

Approximate Analytical Solution of a HIV/AIDS Dynamic Model During Primary Infection 237
Ajoy Dutta and Praveen Kumar Gupta

Stratification and Cross Diffusion Effects on Magneto-Convection Stagnation-Point Flow in a Porous Medium with Chemical Reaction, Radiation, and Slip Effects 245
M. Bhuvaneswari, S. Sivasankaran, S. Karthikeyan, and S. Rajan

Natural Convection of Newtonian Liquids and Nanoliquids Confined in Low-Porosity Enclosures 255
P. G. Siddheshwar and K. M. Lakshmi

Study of Viscous Fluid Flow Past an Impervious Cylinder in Porous Region with Magnetic Field 265
D. V. Jayalakshmamma, P. A. Dinesh, N. Nalinakshi, and T. C. Sushma

Numerical Solution of Steady Powell-Eyring Fluid over a Stretching Cylinder with Binary Chemical Reaction and Arrhenius Activation Energy 275
Seethi Reddy Reddisekhar Reddy and P. Bala Anki Reddy

Effect of Homogeneous-Heterogeneous Reactions in MHD Stagnation Point Nanofluid Flow Toward a Cylinder with Nonuniform Heat Source or Sink 287
T. Sravan Kumar and B. Rushi Kumar

Effects of Thermal Radiation on Peristaltic Flow of Nanofluid in a Channel with Joule Heating and Hall Current 301
R. Latha and B. Rushi Kumar

Chemically Reactive 3D Nonlinear Magneto Hydrodynamic Rotating Flow of Nanofluids over a Deformable Surface with Joule Heating Through Porous Medium 313
E. Kumaresan and A. G. Vijaya Kumar

MHD Carreau Fluid Flow Past a Melting Surface with Cattaneo-Christov Heat Flux 325
K. Anantha Kumar, Janke V. Ramana Reddy, V. Sugunamma, and N. Sandeep

Effect of Porous Uneven Seabed on a Water-Wave Diffraction Problem 337
Manas Ranjan Sarangi and Smrutiranjan Mohapatra

Nonlinear Wave Propagation Through a Radiating van der Waals Fluid with Variable Density 347
Madhumita Gangopadhyay

Effect of Slip and Convective Heating on Unsteady MHD Chemically Reacting Flow Over a Porous Surface with Suction 357
A. Malarselvi, M. Bhuvaneswari, S. Sivasankaran, B. Ganga, and A. K. Abdul Hakeem

Solution of Wave Equations and Heat Equations Using HPM 367
Nahid Fatima and Sunita Daniel

Nonlinear Radiative Unsteady Flow of a Non-Newtonian Fluid Past a Stretching Surface 375
P. Krishna Jyothi, G. Sarojamma, K. Sreelakshmi, and K. Vajravelu

Heat Transfer Analysis in a Micropolar Fluid with Non-Linear Thermal Radiation and Second-Order Velocity Slip 385
R. Vijaya Lakshmi, G. Sarojamma, K. Sreelakshmi, and K. Vajravelu

Analytical Study on Heat Transfer Behavior of an Orthotropic Pin Fin with Contact Resistance 397
M. A. Vadivelu, C. Ramesh Kumar, and M. M. Rashidi

Numerical Investigation of Developing Laminar Convection in Vertical Double-Passage Annuli 407
Girish N, M. Sankar, and Younghae Do

Heat and Mass Transfer on MHD Rotating Flow of Second Grade Fluid Past an Infinite Vertical Plate Embedded in Uniform Porous Medium with Hall Effects 417
M. Veera Krishna, M. Gangadhar Reddy, and A. J. Chamkha

High-Power LED Luminous Flux Estimation Using a Mathematical Model Incorporating the Effects of Heatsink and Fins 429
A. Rammohan, C. Ramesh Kumar, and M. M. Rashidi

Soret and Dufour Effects on Hydromagnetic Marangoni Convection Boundary Layer Nanofluid Flow Past a Flat Plate 439
D. R. V. S. R. K. Sastry, Peri K. Kameswaran, Precious Sibanda, and Palani Sudhagar

Part VII Graph Theory

An Algorithm for the Inverse Distance-2 Dominating Set of a Graph 453
K. Ameenal Bibi, A. Lakshmi, and R. Jothilakshmi

γ-Chromatic Partition in Planar Graph Characterization 461
M. Yamuna and A. Elakkiya

Coding Through a Two Star and Super Mean Labeling 469
G. Uma Maheswari, G. Margaret Joan Jebarani, and V. Balaji

Computing Status Connectivity Indices and Its Coindices of Composite Graphs 479
K. Pattabiraman and A. Santhakumar

Laplacian Energy of Operations on Intuitionistic Fuzzy Graphs 489
E. Kartheek and S. Sharief Basha

Wiener Index of Hypertree 497
L. Nirmala Rani, K. Jennifer Rajkumari, and S. Roy

Location-2-Domination for Product of Graphs 507
G. Rajasekar, A. Venkatesan, and J. Ravi Sankar

Local Distance Pattern Distinguishing Sets in Graphs 517
R. Anantha Kumar

Construction of Minimum Power 3-Connected Subgraph with k Backbone Nodes in Wireless Sensor Networks 527
D. Pushparaj Shetty and M. Prasanna Lakshmi

Fuzzy Inference System Through Triangular and Hendecagonal Fuzzy Number 537
A. Felix, A. D. Dhivya, and T. Antony Alphonnse Ligori

Computation of Narayana Prime Cordial Labeling of Book Graphs 547
B. J. Balamurugan, K. Thirusangu, B. J. Murali, and J. Venkateswara Rao

Quotient-3 Cordial Labeling for Path Related Graphs: Part-II 555
P. Sumathi and A. Mahalakshmi

Relation Between k-DRD and Dominating Set 563
S. S. Kamath, A. Senthil Thilak, and Rashmi M

The b-Chromatic Number of Some Standard Graphs 573
A. Jeeva, R. Selvakumar, and M. Nalliah

***Encode-then-Encrypt*: A Novel Framework for Reliable and Secure Communication** 581
Rajrupa Singh, C. Pavan Kumar, and R. Selvakumar

New Bounds of Induced Acyclic Graphoidal Decomposition Number of a Graph 595
Mayamma Joseph and I. Sahul Hamid

Dominating Laplacian Energy in Products of Intuitionistic Fuzzy Graphs 603
R. Vijayaragavan, A. Kalimulla, and S. Sharief Basha

Power Domination Parameters in Honeycomb-Like Networks 613
J. Anitha and Indra Rajasingh

Improved Bound for Dilation of an Embedding onto Circulant Networks 623
R. Sundara Rajan, T. M. Rajalaxmi, Joe Ryan, and Mirka Miller

Volume I Contents

Part I Algebra

IT-2 Fuzzy Automata and IT-2 Fuzzy Languages 3
M. K. Dubey, P. Pal, and S. P. Tiwari

Level Sets of i_v_Fuzzy β-Subalgebras 13
P. Hemavathi and K. Palanivel

Interval-Valued Fuzzy Subalgebra and Fuzzy INK-Ideal in INK-Algebra 19
M. Kaviyarasu, K. Indhira, V. M. Chandrasekaran, and Jacob Kavikumar

On Dendrites Generated by Symmetric Polygonal Systems: The Case of Regular Polygons 27
Mary Samuel, Dmitry Mekhontsev, and Andrey Tetenov

Efficient Authentication Scheme Based on the Twisted Near-Ring Root Extraction Problem 37
V. Muthukumaran, D. Ezhilmaran, and G. S. G. N. Anjaneyulu

Dimensionality Reduction Technique to Solve E-Crime Motives 43
R. Aarthee and D. Ezhilmaran

Partially Ordered Gamma Near-Rings 49
T. Nagaiah

Novel Digital Signature Scheme with Multiple Private Keys on Non-commutative Division Semirings 57
G. S. G. N. Anjaneyulu and B. Davvaz

Cozero Divisor Graph of a Commutative Rough Semiring 67
B. Praba, A. Manimaran, V. M. Chandrasekaran, and B. Davvaz

Gorenstein FI-Flat Complexes and (Pre)envelopes 77
V. Biju

Bounds of Extreme Energy of an Intuitionistic Fuzzy Directed Graph 85
B. Praba, G. Deepa, V. M. Chandrasekaran, Krishnamoorthy Venkatesan, and K. Rajakumar

Part II Analysis

On Ultra Separation Axioms via $\alpha\omega$-Open Sets 97
M. Parimala, Cenap Ozel, and R. Udhayakumar

Common Fixed Point Theorems in 2-Metric Spaces Using Composition of mappings via A-Contractions 103
J. Suresh Goud, P. Rama Bhadra Murthy, Ch. Achi Reddy, and K. Madhusudhan Reddy

Coefficient Bounds for a Subclass of m-Fold Symmetric λ-Pseudo Bi-starlike Functions 111
Jay M. Jahangiri, G. Murugusundaramoorthy, K. Vijaya, and K. Uma

Laplacian and Effective Resistance Metric in Sierpinski Gasket Fractal 121
P. Uthayakumar and G. Jayalalitha

Some Properties of Certain Class of Uniformly Convex Functions Defined by Bessel Functions 131
V. Srinivas, P. Thirupathi Reddy, and H. Niranjan

A New Subclass of Uniformly Convex Functions Defined by Linear Operator 141
A. Narasimha Murthy, P. Thirupathi Reddy, and H. Niranjan

Coefficient Bounds of Bi-univalent Functions Using Faber Polynomial ... 151
T. Janani and S. Yalcin

Convexity of Polynomials Using Positivity of Trigonometric Sums 161
Priyanka Sangal and A. Swaminathan

Local Countable Iterated Function Systems 169
A. Gowrisankar and D. Easwaramoorthy

On Intuitionistic Fuzzy $\mathscr{C}$-Ends 177
T. Yogalakshmi and Oscar Castillo

Generalized Absolute Riesz Summability of Orthogonal Series 185
K. Kalaivani and C. Monica

Holder's Inequalities for Analytic Functions Defined by Ruscheweyh-Type q-Difference Operator 195
N. Mustafa, K. Vijaya, K. Thilagavathi, and K. Uma

Fuzzy Cut Set-Based Filter for Fixed-Value Impulse Noise Reduction 205
P. S. Eliahim Jeevaraj, P. Shanmugavadivu, and D. Easwaramoorthy

On (p, q)-Quantum Calculus Involving Quasi-Subordination 215
S. Kavitha, Nak Eun Cho, and G. Murugusundaramoorthy

Part III Operations Research

Sensitivity Analysis for Spanning Tree 227
K. Kavitha and D. Anuradha

On Solving Bi-objective Fuzzy Transportation Problem 233
V. E. Sobana and D. Anuradha

Nonlinear Programming Problem for an M-Design Multi-Skill Call Center with Impatience Based on Queueing Model Method 243
K. Banu Priya and P. Rajendran

Optimizing a Production Inventory Model with Exponential Demand Rate, Exponential Deterioration and Shortages 253
M. Dhivya Lakshmi and P. Pandian

Analysis of Batch Arrival Bulk Service Queueing System with Breakdown, Different Vacation Policies and Multiphase Repair 261
M. Thangaraj and P. Rajendran

An Improvement to One's BCM for the Balanced and Unbalanced Transshipment Problems by Using Fuzzy Numbers 271
Kirtiwant P. Ghadle, Priyanka A. Pathade, and Ahmed A. Hamoud

An Articulation Point-Based Approximation Algorithm for Minimum Vertex Cover Problem..... 281
Jayanth Kumar Thenepalle and Purusotham Singamsetty

On Bottleneck-Rough Cost Interval Integer Transportation Problems.... 291
A. Akilbasha, G. Natarajan, and P. Pandian

Direct Solving Method of Fully Fuzzy Linear Programming Problems with Equality Constraints Having Positive Fuzzy Numbers..... 301
C. Muralidaran and B. Venkateswarlu

An Optimal Deterministic Two-Warehouse Inventory Model for Deteriorating Items 309
K. Rangarajan and K. Karthikeyan

Analysis on Time to Recruitment in a Three-Grade Marketing Organization Having Classified Sources of Depletion of Two Types with an Extended Threshold and Shortage in Manpower Forms Geometric Process 315
S. Poornima and B. Esther Clara

Neutrosophic Assignment Problem via BnB Algorithm 323
S. Krishna Prabha and S. Vimala

Part IV Statistics

An Approach to Segment the Hippocampus from $T2$-Weighted MRI of Human Head Scans for the Diagnosis of Alzheimer's Disease Using Fuzzy C-Means Clustering 333
T. Genish, K. Prathapchandran and S. P. Gayathri

Analysis of $M^{[X]}/G_k/1$ Retrial Queueing Model and Standby 343
J. Radha, K. Indhira and V. M. Chandrasekaran

μ-Statistically Convergent Multiple Sequences in Probabilistic Normed Spaces 353
Rupam Haloi and Mausumi Sen

A Retrial Queuing Model with Unreliable Server in K Policy 361
M. Seenivasan and M. Indumathi

Two-Level Control Policy of an Unreliable Queueing System with Queue Size-Dependent Vacation and Vacation Disruption 373
S. P. Niranjan, V. M. Chandrasekaran, and K. Indhira

Analysis of M/G/1 Priority Retrial G-Queue with Bernoulli Working Vacations 383
P. Rajadurai, M. Sundararaman, Sherif I. Ammar, and D. Narasimhan

Time to Recruitment for Organisations having n Types of Policy Decisions with Lag Period for Non-identical Wastages 393
Manju Ramalingam and B. Esther Clara

A Novice's Application of Soft Expert Set: A Case Study on Students' Course Registration 407
Selva Rani B and Ananda Kumar S

Dynamics of Stochastic SIRS Model 415
R. Rajaji

Steady-State Analysis of Unreliable Preemptive Priority Retrial Queue with Feedback and Two-Phase Service Under Bernoulli Vacation 425
S. Yuvarani and M. C. Saravanarajan

An Unreliable Optional Stage $M^X/G/1$ Retrial Queue with Immediate Feedbacks and at most J Vacations 437
M. Varalakshmi, P. Rajadurai, M. C. Saravanarajan, and V. M. Chandrasekaran

Weibull Estimates in Reliability: An Order Statistics Approach 447
V. Sujatha, S. Prasanna Devi, V. Dharanidharan, and Krishnamoorthy Venkatesan

Intuitionistic Fuzzy ANOVA and Its Application Using Different Techniques 457
D. Kalpanapriya and M. M. Unnissa

A Resolution to Stock Prices Prediction by Developing ANN-Based Models Using PCA 469
Jitendra Kumar Jaiswal and Raja Das

A Novel Method of Solving a Quadratic Programming Problem Under Stochastic Conditions 479
S. Sathish and S. K. Khadar Babu

Part V
Differential Equations

Numerical Solution to Singularly Perturbed Differential Equation of Reaction-Diffusion Type in MAGDM Problems

P. John Robinson, M. Indhumathi, and M. Manjumari

Abstract In multiple attribute group decision-making (MAGDM) problems, weights of decision-makers play a vital role. In this paper, we present a new approach for finding the weights for decision-making process based on singular perturbation problem in which decision-makers' weights are completely unknown. The attribute weights are derived using the exact and numerical solution for reaction-diffusion type problem. For the decision-making process, we utilize a class of ordered weighted averaging (OWA) operator, and the newly calculated decision-maker weights are used in the computations of identifying the best alternative from the available alternatives. The feasibility of the proposed method is displayed through a numerical illustration, and comparison is made with existing ranking methods.

Keywords MAGDM · Intuitionistic fuzzy sets · Singular perturbation problem · Numerical methods · Ordered weighted averaging (OWA) operator

1 Introduction

MAGDM problems play an important role in our day-to-day life. To handle the vagueness and uncertainty in real-life problems, Zadeh [27] proposed the idea of fuzzy set, which handles imprecision through the concept of membership function. Using the concept of membership function, Atanassov [1, 2] developed the idea of intuitionistic fuzzy set (IFS). This IFS contains both a membership function and a non-membership function and also the hesitancy degree. Yager and Filev [23] introduced the induced OWA (IOWA) operator which is nothing but an extension of OWA operator. Using OWA operator, one can order the weight either in ascending or in descending order depending upon the data values, but for IOWA one can

P. J. Robinson · M. Indhumathi (✉) · M. Manjumari
Department of Mathematics, Bishop Heber College, Trichy, Tamilnadu, India
e-mail: robijohn@bhc.edu.in

B. Rushi Kumar et al. (eds.), *Applied Mathematics and Scientific Computing*,
Trends in Mathematics, https://doi.org/10.1007/978-3-030-01123-9_1

use the same technique of OWA where the only difference is that the weight can be ordered through the order-inducing variables. Li and Ye [8], Liu and Li [10], Yu and Li [25], Li and Wan [9] and Yu et al. [26] proposed novel methods for solving various decision problems. Robinson and Amirtharaj [19] and Robinson and Jeeva [20, 21] proposed methods for intuitionistic fuzzy decision problems based on correlation coefficients and utilized them in MAGDM problems for ranking the alternatives. Numerical methods are used to solve various differential equations arising in many real-life problems. Ross et al. [22] proposed a better method for analysing the singular perturbation problems using numerical methods. Miller et al. [15] have devoted their work on singular perturbation problems (SPPs) in two dimensions. Matthews et al. [14] examined a system of two coupled singularly perturbed ordinary differential equation of reaction-diffusion type problems using the Dirichlet boundary conditions. Malley [13] and Nayfeh [17] gave general introduction to SPPs. Paramasivam et al. [18] presented a linear second-order SPP with piecewise-uniform Shishkin mesh which is used to construct the numerical methods for the same. The idea of score function which can be used to measure the similarity degree between vague sets was proposed by Chen [3]. For vague sets/IFSs, Li et al. [12], Li and Xu [11] and Hung and Yang [6] proposed a degree of similarity measures and their applications. The cosine similarity measure for IFS was proposed by Ye [24]. For behaviour analysis problem, Hong and Kim [5] proposed a measure of similarity between the elements of vague sets. Using the concept of medians of intervals, Li and Chuntian [7] presented a degree of similarity measure between IFSs. Mitchell [16] proposed a modification method of Li and Chuntian [7] method. A novel degree of similarity measure under intuitionistic fuzzy sets was presented by Chen and Randyanto [4]. In this paper, the decision-maker weights are derived from boundary value problems through singular perturbation problems, where the weights are determined, normalized and utilized in decision-making problems. In the MAGDM problem proposed in this paper, the operators I-IFOWA and IFWA are used for aggregating the IFS information. The feasibility of the proposed method is displayed through a numerical illustration, and comparison is made with different ranking methods found in the literature.

2 Preliminaries

As an introduction, some basic definitions and averaging aggregation operators of IFS are discussed.

Definition 1 (Intuitionistic Fuzzy Set [1, 2]) Let X be a set which is fixed. An IFS $\tilde{A}$ in X is an object having the form

$$\tilde{A} = \{(x, \mu_{\tilde{A}}(x), , \gamma_{\tilde{A}}(x)), x \in X\}$$

where $\mu_{\tilde{A}(x)} : X \longrightarrow [0,1]$ and $\gamma_{\tilde{A}(x)} : X \longrightarrow [0,1]$ define the degree of membership and degree of non-membership, respectively, of the element $x \in X$ to the set $\tilde{A}$, which is a subset of X, for every element $x \in X$, $0 \leq \mu_{\tilde{A}}(x) + \gamma_{\tilde{A}}(x) \leq 1$.

2.1 Different Classes of Aggregation Operators

Definition 2 Let $\tilde{\beta}_k = (\mu_k, \gamma_k)$, $1 \leq k \leq n$ be a compilation of IFS values. The intuitionistic fuzzy weighted averaging (IFWA) operator, $IFWA : \Omega^n \to \Omega$, is defined as

$$IFWA(\tilde{\beta}_1, \tilde{\beta}_2, \ldots, \tilde{\beta}_n) = \sum_{k=1}^{n} \tilde{\beta}_k \omega_k = \left(1 - \prod_{k=1}^{n}(1-\mu_k)^{\omega_k}, \prod_{k=1}^{n}(\gamma_k)^{\omega_k}\right),$$

where $\omega = (\omega_1, \omega_2, \ldots, \omega_n)^T$ is the weight vector of $\tilde{\beta}_k$ for all $1 \leq k \leq n$, such that $\omega_k > 0 \;\&\; \sum_{k=1}^{n} w_k = 1$.

Definition 3 Let $\tilde{\beta}_k = (\mu_k, \gamma_k)$, $1 \leq k \leq n$ be a compilation of IFS values. The intuitionistic fuzzy ordered weighted averaging (IFOWA) operator, $IFOWA : \Omega^n \to \Omega$, is defined as

$$IFOWA(\tilde{\beta}_1, \tilde{\beta}_2, \ldots, \tilde{\beta}_n) = \sum_{k=1}^{n} \tilde{\beta}_k w_k = \left(1 - \prod_{k=1}^{n}(1-\mu_{\beta k})^{w_k}, \prod_{k=1}^{n}(\gamma_{\beta k})^{w_k}\right),$$

where $\sigma(1), \sigma(2), \ldots, \sigma(n)$ is a permutation of $(1, 2, \ldots, n)$ such that $\tilde{\beta}_{\sigma(k-1)} \geq \tilde{\beta}_{\sigma(k)}$ for all $1 \leq k \leq n$. $w = (w_1, w_2, \ldots, w_n)^T$ be the weight vector of $\tilde{\beta}_j$ for all $\omega_k > 0 \;\&\; \sum_{k=1}^{n} w_k = 1$.

Definition 4 Let $\tilde{\beta}_k = (\mu_k, \gamma_k)$, $1 \leq k \leq n$ be a compilation of IFS values. An induced intuitionistic fuzzy ordered weighted averaging (I-IFOWA) operator, $I - IFOWA : \Omega^n \to \Omega$, is defined as

$$I - IFOWA_w\left((v_1, \tilde{\beta}_1), (v_2, \tilde{\beta}_2), \ldots, (v_n, \tilde{\beta}_n)\right) = \sum_{k=1}^{n} \tilde{g}_k w_k$$

$$= \left(1 - \prod_{k=1}^{n}(1-\tilde{\mu}_k)^{w_k}, \prod_{k=1}^{n}\tilde{\gamma}_k)^{w_k}\right),$$

where $w = (w_1, w_2, \ldots, w_n)^T$ is the associated weighting vector such that $w_k \in [0, 1]$, $\sum_{k=1}^{n} w_k = 1$, $1 \leq k \leq n$, $\tilde{g}_k = (\mu_k, \gamma_k)$ is the $\tilde{\beta}_k$ value of the I-IFOWA pair $(v_i, \tilde{\beta}_i)$ having the k^{th} largest v_i, $v_i \in [0, 1]$, $1 \leq i \leq n$ and v_i in $(v_i, \tilde{\beta}_i)$ is referred to as an the order-inducing variable and $\tilde{\beta}_i$, $\tilde{\beta}_i = (\mu_i, \gamma_i)$ are the intuitionistic fuzzy values.

Properties of I-IFOWA Operator

1. Commutativity. $I - IFOWA_w\left[(v_1, \tilde{\beta}_1), (v_2, \tilde{\beta}_2), \ldots, (v_n, \tilde{\beta}_n)\right] = I - IFOWA_w\left[(v_1, \tilde{\beta}'_1), (v_2, \tilde{\beta}'_2), \ldots, (v_n, \tilde{\beta}'_n)\right]$ where $\left[(v_1, \tilde{\beta}'_1), (v_2, \tilde{\beta}'_2), \ldots, (v_n, \tilde{\beta}'_n)\right]$ is any permutation of $\left[(v_1, \tilde{\beta}_1), (v_2, \tilde{\beta}_2), \ldots, (v_n, \tilde{\beta}_n)\right]$.
2. Idempotency. If $\tilde{\beta}_k = \tilde{\beta}$, where $\tilde{\beta}_k = (\mu_k, \gamma_k)$ and $\tilde{\beta} = (\mu, \gamma)$ for every k, $I - IFOWA_w\left[(v_1, \tilde{\beta}_1), (v_2, \tilde{\beta}_2), \ldots, (v_n, \tilde{\beta}_n)\right]$
3. Monotonicity. If $\tilde{\beta}_k \leq \tilde{\beta}$, for every k, $I - IFOWA_w\left[(v_1, \tilde{\beta}_1), (v_2, \tilde{\beta}_2), \ldots, (v_n, \tilde{\beta}_n)\right] \leq I - IFOWA_w\left[(v_1, \tilde{\beta}'_1), (v_2, \tilde{\beta}'_2), \ldots, (v_n, \tilde{\beta}'_n)\right]$

3 Singular Perturbation Problem

Singular perturbation problem plays a prominent role in the field of differential equations and in the real-life application. The applications of singular perturbation problem in various applied areas are as follows: fluid dynamics, plasma dynamics, aerodynamics, oceanography, diffraction theory and reaction-diffusion process. A differential equation in which the highest-order derivative and/or the lowest-order derivatives is multiplied by a small positive parameter ε is known as a singular perturbation problem. If the order of the differential equation when the perturbation parameter $\varepsilon = 0$ is reduced by two, then the system is called as reaction-diffusion type problems. For instance, in the following equation $-\varepsilon u''(x) + a(x)u(x) = g(x)$ with $u_\varepsilon(0) = u_0$; $u_\varepsilon(1) = u_1$; $0 < x < 1$, where $0 < \varepsilon \ll 1$, $a(x)$ and $g(x)$ are smooth functions and continuous on $[0, 1]$, the solution behaviour for this equation depends upon the behaviour of the $a(x)$ and $g(x)$.

3.1 Numerical Methods

For the above boundary value problem, the classical finite difference operator is constructed with a suitable piecewise-uniform mesh which is also useful in discretizing the problem. The details are given below:

$$-\varepsilon\delta^2 U(x_j) + a(x_j)U(x_j) = g(x_j) \text{ for all } x_j,\ j = 1, \ldots, N$$

where

$$\delta^2 U(x_j) = \frac{(D_+ - D_-)}{\overline{h}} U(x_j),\ \overline{h} = \frac{h_j + h_{j+1}}{2}$$

$$D_+ U(x_j) = \frac{U(x_{j+1}) - U(x_j)}{h_{j+1}};\ D_- U(x_j) = \frac{U(x_j) - U(x_{j-1})}{h_j}$$

4 Weight Determination for MAGDM Using Singular Perturbation Problem

Problem Proposed by the Decision-Maker

The decision-maker represents weighting vector in the form of the following singularly perturbed differential equation, $-\varepsilon u''(x) + 4u(x) = 0$ with $u(0) = 0$, $u(1) = 1; 0 < x < 1$.

The exact solution of the above problem is $u(x) = \left(\frac{e^{\frac{-2}{\sqrt{\varepsilon}}} - e^{\frac{-4}{\sqrt{\varepsilon}}}}{1 - e^{\frac{-4}{\sqrt{\varepsilon}}}}\right) e^{\frac{2x}{\sqrt{\varepsilon}}} + \left(\frac{1 - e^{\frac{-2}{\sqrt{\varepsilon}}}}{1 - e^{\frac{-4}{\sqrt{\varepsilon}}}}\right) e^{\frac{-2x}{\sqrt{\varepsilon}}}$.

And the numerical solution is calculated by using the above finite difference scheme by fixing $\varepsilon = 0.001$.

By normalizing the exact and numerical solution the weight vectors can be obtained and the results are given in Tables 1 and 2.

Table 1 Exact solution for $-\varepsilon u''(x) + 4u(x) = 0$

N	Average of exact solution	Normalization of exact solution
64	0.07155	0.41274
128	0.05547	0.31997
256	0.04634	0.26731

Exact and Numerical Solution of $-\varepsilon u''(x)+4u(x) = 0$ are displayed in Figs. 1 and 2

Table 2 Numerical solution for $-\varepsilon u''(x) + 4u(x) = 0$

N	Average of numerical solution	Normalization of numerical solution
64	0.07211	0.32953
128	0.05565	0.25430
256	0.04639	0.21200
512	0.04046	0.18492

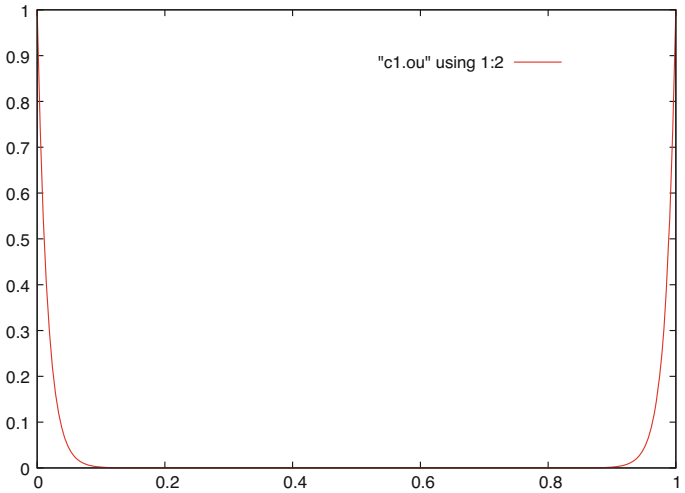

Fig. 1 Exact solution for $-\varepsilon u''(x) + 4u(x) = 0$

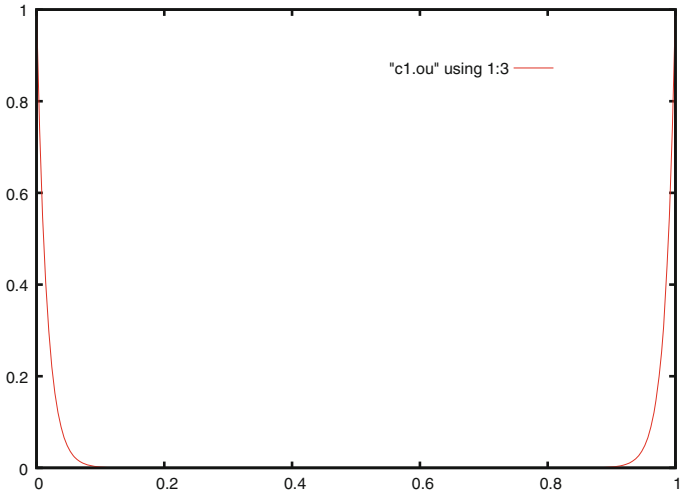

Fig. 2 Numerical solution for $-\varepsilon u''(x) + 4u(x) = 0$

5 Algorithm for MAGDM Problem Using I-IFOWA Operator and Similarity Measures of IFSs

The algorithm for MAGDM problem using I-IFOWA and IFWA operator is given below:

Step: 1 Use the I-IFOWA operator for the decision matrices $R_{(k)}$, to reduce k matrices into a single matrix:
$\tilde{s}_{ij}^{(k)} = I - IFOWA\left[(v_1, \tilde{s}_{ij}^{(1)}), (v_2, \tilde{s}_{ij}^{(2)},)(v_3, \tilde{s}_{ij}^{(3)},) \ldots, (v_n, \tilde{s}_{ij}^{(n)})\right], 1 \leq i \leq m, 1 \leq j \leq n.$

Step: 2 Use the IFWA operator, to find the aggregated IFS values of the alternatives A_i:
$\tilde{s}_i = (\mu_i, \gamma_i) = IFWA\left(\tilde{s}_i^{(1)}, \tilde{s}_i^{(2)}, \tilde{s}_i^{(3)}, \ldots, \tilde{s}_i^{(t)}\right), 1 \leq i \leq m.$

Step: 3 Use similarity measures to calculate the overall values $\tilde{s}_i$ and the positive ideal value $\tilde{s}^+$, where $\tilde{s}^+ = (1, 0)$.

Step: 4 Finally rank the alternatives and find the most desirable one.

6 Numerical Illustration

A company is interested to invest money in the best option to purchase laptops. The five possible types of laptops available in the market are named as A_1, A_2, A_3, A_4 and A_5. The following four attributes are p_1, the price of the laptop; p_2, portability of the laptop; p_3, battery life of laptop; and p_4, graphics quality of the laptop. The five possible alternatives A_i are to be evaluated using intuitionistic fuzzy numbers by the decision-makers whose weighting vector is obtained by normalizing the solution of singular perturbation problem given by decision-makers which is $\omega = (0.41274, 0.31997, 0.26731)^T$ and $w = (0.32953, 0.25430, 0.21200, 0.18492)^T$. The following decision matrices $R_{(k)}$ are listed below:

$$R_1 = \begin{pmatrix} (0.3, 0.4) & (0.2, 0.5) & (0.5, 0.2) & (0.6, 0.1) \\ (0.2, 0.6) & (0.1, 0.6) & (0.1, 0.6) & (0.4, 0.3) \\ (0.3, 0.5) & (0.3, 0.4) & (0.2, 0.4) & (0.2, 0.5) \\ (0.1, 0.7) & (0.2, 0.5) & (0.3, 0.2) & (0.5, 0.1) \\ (0.1, 0.5) & (0.2, 0.3) & (0.2, 0.6) & (0.2, 0.4) \end{pmatrix}$$

$$R_2 = \begin{pmatrix} (0.4, 0.5) & (0.2, 0.3) & (0.6, 0.3) & (0.7, 0.2) \\ (0.3, 0.7) & (0.2, 0.7) & (0.2, 0.7) & (0.5, 0.4) \\ (0.4, 0.4) & (0.4, 0.5) & (0.3, 0.5) & (0.3, 0.6) \\ (0.1, 0.8) & (0.3, 0.6) & (0.4, 0.3) & (0.2, 0.6) \\ (0.2, 0.6) & (0.3, 0.4) & (0.1, 0.7) & (0.3, 0.5) \end{pmatrix}$$

Table 3 Comparison of ranking methods in the literature

Similarty measure	Ranking the alternatives
Chen's method	$A_1 > A_3 > A_4 > A_5 > A_2$
Hong and Kim's method	$A_1 > A_3 > A_4 > A_5 > A_2$
Li and Xu's method	$A_1 > A_3 > A_4 > A_5 > A_2$
Li et.al.'s method	$A_1 > A_3 > A_4 > A_5 > A_2$
Li and Chuntian's method	$A_1 > A_3 > A_4 > A_5 > A_2$
Mitchell's method	$A_1 > A_3 > A_4 > A_5 > A_2$
Hung and Yang's (SHY_1) method	$A_1 > A_3 > A_4 > A_5 > A_2$
(SHY_2) method	$A_1 > A_3 > A_4 > A_5 > A_2$
(SHY_3) method	$A_1 > A_3 > A_4 > A_5 > A_2$
Ye's method	$A_1 > A_3 > A_4 > A_5 > A_2$
Chen and Randyanto's method	$A_1 > A_3 > A_4 > A_5 > A_2$

$$R_3 = \begin{pmatrix} (0.5, 0.4) & (0.4, 0.5) & (0.7, 0.2) & (0.8, 0.1) \\ (0.4, 0.6) & (0.3, 0.6) & (0.3, 0.6) & (0.6, 0.3) \\ (0.5, 0.6) & (0.5, 0.4) & (0.7, 0.1) & (0.4, 0.5) \\ (0.2, 0.7) & (0.4, 0.5) & (0.5, 0.2) & (0.7, 0.1) \\ (0.3, 0.5) & (0.4, 0.3) & (0.2, 0.6) & (0.6, 0.1) \end{pmatrix}$$

By using step 1 and step 2, we get the overall values as follows:

$s_1 = (0.47773, 0.30376)$,
$s_2 = (0.29737, 0.56485)$,
$s_3 = (0.37061, 0.42709)$,
$s_4 = (0.30405, 0.407773)$,
$s_5 = (0.24299, 0.44390)$.

Using step 3 we obtain the different similarity measures, and finally we get the best alternatives (Table 3).

Hence, from the above table, it can be clearly seen that the most desirable alternative is A_1.

7 Conclusion

In this work, we have given a new method for finding the weights for group decision-making process based on singular perturbation problem. The attribute weights for MAGDM are derived by using the solutions of singular perturbation problem under intuitionistic fuzzy set. In the process of determining weights, multi-criteria are explicitly considered. It can be seen from the comparison table that the choice of the best alternative made from different similarity measures is consistent.

References

1. Atanassov, K. : Intuitionistic fuzzy sets. Fuzzy Sets and Systems. (1986) https://doi.org/10.1016/0165-0114(89)90205-4
2. Atanassov, K. : More on intuitionistic fuzzy sets. Fuzzy Sets and Systems. (1989) https://doi.org/10.1016/0165-0114(89)90215-7
3. Chen, S. M. : Similarity measures between vague sets and between elements. IEEE Trans. Syst. Man Cybern. **27(1)**, 153–158 (1997)
4. Chen, S.M., Randyanto, Y. : A Novel Similarity Measure Between Intuitionistic Fuzzy Sets and its Applications. International Journal of Pattern Recognition and Artificial Intelligence. World Scientific Publishing Company. **27(7)**, 1350021–1350034 (34 pages) (2013)
5. Hong, D. H., Kim, C. : A note on similarity measures between vague sets and between elements. Inform. Sci. **115(1)**, 83–96 (1999)
6. Hung, W. L., Yang, M.S. : Similarity measures of intuitionistic fuzzy sets based on Hausdorff distance. Pattern Recogn. Lett. **25(14)**, 1603–1611 (2004)
7. Li, D-F., Chuntian, C. : New similarity measures of intuitionistic fuzzy sets and application to pattern recognitions. Pattern Recogn. Lett. **23(13)**, 221–225 (2002)
8. Li, D-F., Ye Y-F. : Interval-valued least square prenucleolus of interval-valued cooperative games and a simplified method. Operational Research. **18(1)**, 205–220 (2018)
9. Li, D-F., Wan, S-P. : Minimum Weighted Minkowski Distance Power Models for Intuitionistic Fuzzy Madm with Incomplete Weight Information. International Journal of Information Technology and Decision Making. **16(5)**, 1387–1408 (2017)
10. Liu, J-C., Li, D-F. : Correlations to TOPSIS-Based Nonlinear-Programming Methodology for Multiattribute Decision making With Interval-Valued Intuitionistic Fuzzy Sets. IEEE Trans. Fuzzy Systems. **26(1)**, 391 (2018)
11. Li, F., Xu, Z. Y. : Measures of similarity between vague sets. J. Software. **12(6)**, 922–927 (2001)
12. Li, L., Olson, D.L., Qin, Z. : Similarity measures between intuitionistic fuzzy (vague) sets: A comparative analysis. Pattern Recogn. Lett. **28(2)**, 278–285 (2007)
13. Malley, R. E. O. : Introduction to singular perturbations. Academic press New York (1974)
14. Matthews, S., O'Riordan, E., Shishkin, G.I. : A Numerical Method for a System of Singularly Perturbed Reaction-Diffusion Equations. Journal of Computational and Applied Mathematics. **145(1)**, 151–166 (2002)
15. Miller, J.J.H., O'Riordan, E., Shishkin, G.I. : Fitted numerical methods for singular perturbation problems. World scientific Publishing Co. Pvt. Ltd. (1996)
16. Mitchell, H. B. : On the Li, D-F., Chuntian similarity measure and its application to pattern recognition. Pattern Recogn. Lett. **24(16)**, 3101–3104 (2003)
17. Nayfeh, A.H. : Perturbation methods. John Wiley and sons Newyork (1973)
18. Paramasivam, M., Valarmathi, S., Miller, J.J.H.: Second Order Parameter-Uniform Convergence for a Finite Difference Method for a Singularly Perturbed Linear Reaction-Diffusion System. Math. Commun. **15(2)**, 587–612 (2010)
19. Robinson, J.P., Amirtharaj, E.C.H. : Contrasting Correlation Coefficient with Distance Measure in Interval Valued Intuitionistic Trapezoidal Fuzzy Numbers. International Journal of Fuzzy System Applications. **5(3)**, 42–76 (2016)
20. Robinson, J.P., Jeeva, S. : Mining Trapezoidal Intuitionistic Fuzzy Correlation Rules for Eigen Valued MAGDM Problems. International Journal of Control Theory and Applications. **9(7)**, 585–616 (2016)
21. Robinson, J.P., Jeeva, S. : Application of Jacobian & Sor Iteration process in Intuitionistic Fuzzy MAGDM Problems. Mathematical Sciences International Research Journal. **6(2)**, 130–134 (2017)
22. Ross, H.G., Stynes, M., Tobiska, L. : Numerical Methods for Singularly Perturbed Differential Equations. Springer-Verlag Newyork (1996)

23. Yager, R. R., Filev, D. P. : Induced ordered weighted averaging operators. IEEE Transactions on Systems, Man and Cybernetics. **29(1)**, 141–150 (1999)
24. Ye, J. : Cosine similarity measures for intuitionistic fuzzy sets and their applications. Math. Comput. Model. **53(1-2)**, 91–97 (2011)
25. Yu, G-F., Li, D-F. : Application of satisfactory degree to interval-valued intuitionistic fuzzy multi-attribute decision making. Journal of Intelligent and Fuzzy Systems. **32(1)**, 1019–1028 (2017)
26. Yu, G-F., Li., D-F., Qiu, J-M., Zheng X-X. : Some operators of intuitionistic uncertain 2-tuple linguistic variables and application to multi-attribute group decision making with heterogeneous relationship among attributes. Journal of Intelligent and Fuzzy Systems. **34(1)**, 599–611 (2018)
27. Zadeh, L. A. : Fuzzy Sets. Information and Control. **8(3)**, 338–356 (1965)

Application of Integrodifferential Equations Using Sumudu Transform in Intuitionistic Trapezoidal Fuzzy MAGDM Problems

P. John Robinson and S. Jeeva

Abstract Decision-making is a most powerful, well-organized, civic, and pecuniary effect. Power to produce logical and correct choices is the burden of any decision process imbued with uncertainty. In offices where the information or the data is of the form of intuitionistic trapezoidal fuzzy numbers, to construct the MAGDM problem, intuitionistic trapezoidal fuzzy weighted geometric (ITFWG) and intuitionistic trapezoidal fuzzy hybrid geometric (ITFHG) operators are applied. In this paper, a novel method of deriving the unknown decision-maker weights using Sumudu transform combined with integrodifferential equation is proposed, and the derived weights are used in computations for identifying the best alternative. A goodness of fit for this method is provided to show the effectiveness of the proposed approach.

1 Introduction

Multiple attribute group decision-making (MAGDM) is a method where decision-makers who act together penetrate through problems and select different types of actions and again select the solutions from it. Collective decisions are more effective than an individual decision since it requires lots of discussion, queries, and ideas. The major challenge is to give up the inaccuracy and to make it accurate. To deal with accuracy in qualitative, imprecise, and incomplete information in decision problems, Zadeh [37] proposed the fuzzy set theory. Intuitionistic fuzzy sets (IFSs) proposed by Attanassov [1] are a generalization of the concept of fuzzy sets. Attanassov and Gargov [2] expanded the IFSs by using interval value to express membership and nonmembership function of IFSs. Szmidt and Kacprzyk [25, 26]

P. J. Robinson · S. Jeeva (✉)
Department of Mathematics, Bishop Heber College, Trichy, Tamilnadu, India
e-mail: robijohn@bhc.edu.in

B. Rushi Kumar et al. (eds.), *Applied Mathematics and Scientific Computing*,
Trends in Mathematics, https://doi.org/10.1007/978-3-030-01123-9_2

computed several distance functions and similarity measures for IFSs which were applied in various decision problems. Li [9] and Wei [28, 29] contributed novel approaches to the study of fuzzy decision-making. Gerstenkorn and Manko [5] and Zeng and Li [33] investigated the correlation coefficient of IFS. Yu et al. [36], Li and Wan [11], Yu and Li [35], Liu and Li [12], and Li and Ye [10] proposed several methods in decision-making problem under different types of intuitionistic fuzzy sets. Robinson and Amirtharaj [13–22] defined correlation coefficient for different higher-order intuitionistic fuzzy sets and utilized in MAGDM problems. Robinson and Jeeva [23, 24] investigated and discussed the various decision-making algorithms under intuitionistic fuzzy environment using correlation coefficient as the ranking tool. Jeeva and Robinson [6] discussed the application of Sumudu transform method in intuitionistic fuzzy environment. Wu and Cao [30] developed the geometric aggregation operators in intuitionistic trapezoidal fuzzy numbers. Wang and Zhang [27], Yager [34], Xu and Yager [33], Xu and Chen [32], and Xu [31] discussed several aggregation operators like arithmetic and geometric operators with intuitionistic fuzzy uncertainty. In this work Sumudu transform combined with integrodifferential equations will be proposed for determining weights of decision-makers and used for decision-making problems. Hukuhara [7], Eltayeb and Kilicman [4], Khan and Razzaq [8], and Bulut et al. [3] discussed on solving fuzzy differential equations by fuzzy Sumudu transform. In this paper, Sumudu transform is used to obtain the result of the integrodifferential equation, and it is used to derive the decision-maker weights in MAGDM problems under intuitionistic trapezoidal fuzzy sets. A goodness for fit for this method is illustrated using numerical examples.

2 Preliminaries

Some basic concepts of fuzzy sets and arithmetic aggregation operators of intuitionistic trapezoidal fuzzy sets (ITFSs) are discussed in the following:

Definition 1 ([1] Intuitionistic Fuzzy Set) Let a set X be fixed. An IFS $\tilde{A}$ in X is an object having the form

$$\tilde{A} = \{(x, \mu_{\tilde{A}}(x), , \gamma_{\tilde{A}}(x)), x \in X\}$$

where $\mu_{\tilde{A}(x)} : X \longrightarrow [0, 1]$ and $\gamma_{\tilde{A}(x)} : X \longrightarrow [0, 1]$ define the degree of membership and degree of nonmembership, respectively, of the element $x \in X$ to the set $\tilde{A}$, which is a subset of X, for every element $x \in X$, $0 \leq \mu_{\tilde{A}}(x) + \gamma_{\tilde{A}}(x) \leq 1$.

Definition 2 ([30] Intuitionistic Trapezoidal Fuzzy Number) Let $\tilde{a}$ be an intuitionistic trapezoidal fuzzy number. Then its membership function and its nonmembership function are given as follows:

$$\mu_{\tilde{a}(x)} = \begin{cases} \frac{x-a}{b-a}\mu_{\tilde{a}}, & a \le x \le b \\ \mu_{\tilde{a}}, & b \le x \le c \\ \frac{d-c}{d-c}, & c \le x \le d \\ 0, & others. \end{cases},$$

where $0 \le \mu_{\tilde{a}} \le 1;\ 0 \le \gamma_{\tilde{a}} \le 1;\ a, b, c, d \in R.$

Definition 3 ([30]) Let $\tilde{a_1} = \left([a_1, b_1, c_1, d_1]; \mu_{\tilde{a_1}}, \gamma_{\tilde{a_1}}\right)$ and $\tilde{a_2} = ([a_2, b_2, c_2, d_2]; \mu_{\tilde{a_2}}, \gamma_{\tilde{a_2}})$ be two intuitionistic trapezoidal fuzzy numbers, and $\lambda \ge 0$. Then the normalized Hamming distance between $\tilde{a_1}$ and $\tilde{a_2}$ is defined as follows:

$$d(\tilde{a_1}, \tilde{a_2}) = \begin{pmatrix} |(1+\mu_{\tilde{a_1}})a_1 - (1+\mu_{\tilde{a_1}})a_2| + |(1+\mu_{\tilde{a_1}})a_1 - (1+\mu_{\tilde{a_1}})a_2| + \\ |(1+\mu_{\tilde{a_1}})a_1 - (1+\mu_{\tilde{a_1}})a_2| + |(1+\mu_{\tilde{a_1}})a_1 - (1+\mu_{\tilde{a_1}})a_2| \end{pmatrix}.$$

Definition 4 ([30]) Let $\tilde{a_i} = \left([a_i, b_i, c_i, d_i]; \mu_{\tilde{a_i}}, \gamma_{\tilde{a_i}}\right)$ be an intuitionistic trapezoidal fuzzy number and $\tilde{a}^+ = \left([a^+, b^+, c^+, d^+]; \mu^+, \gamma^+\right) = ([1, 1, 1, 1]; 1, 0)$ be the intuitionistic trapezoidal fuzzy-positive ideal solution. Then the distance between $\tilde{a_i}$ and $\tilde{a}^+$ is denoted as $d(\tilde{a_i}, \tilde{a}^+)$. If $d(\tilde{a_2}, \tilde{a}^+) < d(\tilde{a_1}, \tilde{a}^+)$, then $\tilde{a_1} > \tilde{a_2}$.

3 Aggregation Operators for Decision-Making

Definition 5 ([30]) Let $\tilde{a_k} = ([a_k, b_k, c_k, d_k]; \mu_k, \gamma_k)$, for all $1 \le k \le n$ be a compilation of ITFS values. An intuitionistic trapezoidal fuzzy weighted geometric (ITFWG) operator, $ITFWG : Q^n \to Q$, is defined as follows:

$$ITFWG(\tilde{a_1}, \tilde{a_2}, \ldots, \tilde{a_n}) = \prod_{k=1}^{n} \tilde{a_k}\omega_k$$

$$= \begin{pmatrix} \left[\prod_{k=1}^{n}(a_k)^{\omega_k}, \prod_{k=1}^{n}(b_k)^{\omega_k}, \prod_{k=1}^{n}(c_k)^{\omega_k}, \prod_{k=1}^{n}(d_k)^{\omega_k}\right]; \\ \prod_{k=1}^{n}(\mu_k)^{\omega_k}, 1 - \left(\prod_{k=1}^{n}(1-\gamma_k)^{\omega_k}\right) \end{pmatrix},$$

where $\omega = (\omega_1, \omega_2, \ldots, \omega_n)^T$ is the weight vector of $\tilde{a_k}$, $1 \le k \le n$ with $\omega_k \in [0, 1]$ and $\sum_{k=1}^{n} \omega_k = 1$.

Definition 6 ([30]) Let $\tilde{a_k} = ([a_k, b_k, c_k, d_k]; \mu_k, \gamma_k)$, for all $1 \le k \le n$ be a compilation of ITFS values. The intuitionistic trapezoidal fuzzy ordered weighted geometric (ITFOWG) operator, $ITFOWG : Q^n \to Q$, is defined as follows:

$$ITFOWG(\tilde{a_1}, \tilde{a_2}, \ldots, \tilde{a_n}) = \prod_{k=1}^{n} \tilde{a}_{\sigma(k)}\omega_k$$

$$= \begin{pmatrix} \left(\left[\prod_{k=1}^{n}(a_{\sigma(k)})^{\omega_k}, \prod_{k=1}^{n}(b_k)^{\omega_k}, \prod_{k=1}^{n}(c_{\sigma(k)})^{\omega_k}, \prod_{k=1}^{n}(d_{\sigma(k)})^{\omega_k}\right]; \right. \\ \left. \prod_{k=1}^{n}(\mu_{\sigma(k)})^{\omega_k}, 1 - \left(\prod_{k=1}^{n}(1-\gamma_{\sigma(k)})^{\omega_k}\right) \right) \end{pmatrix},$$

where $\omega = (\omega_1, \omega_2, \ldots, \omega_n)^T$ is the weight vector of $\tilde{a_k}$ for all $1 \leq k \leq n$, such that $\omega_k \in [0, 1]$ and $\sum_{k=1}^{n} \omega_k = 1$.

where $\sigma(1), \sigma(2), \ldots, \sigma(n)$, is a permutation of $(1, 2, \ldots, n)$ such that $\tilde{a}_{\sigma(k-1)} \geq \tilde{a}_{\sigma(k)}$ for all $1 \leq k \leq n$.

Definition 7 ([30]) Let $\tilde{a}_k = ([a_k, b_k, c_k, d_k]; \mu_k, \gamma_k)$, for all $1 \leq k \leq n$ be a compilation of ITFS values. The Intuitionistic trapezoidal fuzzy hybrid geometric (ITFHG) operator, $ITFHG : Q^n \to Q$, is defined as follows:

$$ITFHG(\tilde{a}_1, \tilde{a}_2, \ldots, \tilde{a}_n) = \prod_{k=1}^{n} \tilde{a}_{\sigma(k)\omega_k}$$

$$= \begin{pmatrix} \left[\prod_{k=1}^{n}(\dot{a}_{\sigma(k)})^{\omega_k}, \prod_{k=1}^{n}(\dot{b}_k)^{\omega_k}, \prod_{k=1}^{n}(\dot{c}_{\sigma(k)})^{\omega_k}, \prod_{k=1}^{n}(\dot{d}_{\sigma(k)})^{\omega_k}\right]; \\ \prod_{k=1}^{n}(\dot{\mu}_{\sigma(k)})^{\omega_k}, 1 - \left(\prod_{k=1}^{n}(1 - \dot{\gamma}_{\sigma(k)})^{\omega_k}\right) \end{pmatrix},$$

where $\tilde{a}_{\sigma(k)}$ is the kth largest of weighted intuitionistic trapezoidal fuzzy number $\tilde{a_k}$, $\omega = (\omega_1, \omega_2, \ldots, \omega_n)^T$ be the weight vector of $\tilde{a_k}$, $1 \leq k \leq n$ with $\omega_k \in [0, 1]$ and $\sum_{k=1}^{n} \omega_k = 1$.

4 Determining Expert Weights for MAGDM by Sumudu Transform

Definition 8 ([7]) Let A be the set of functions defined as follows:

$$A = \{f(x) | \exists M, \tau_1 \text{and /or } \tau_2 > 0, \ni |f(x)| < Me^{|x|/\tau_j}, \text{if } x \in (-1)^j \times [0, \infty)\},$$

where constant M must be finite, while τ_1 and τ_2 each may be finite and do not need to exist simultaneously. Using u to factor the variable t in the argument of the function f, Sumudu transform is defined as follows:

$$G(u) = S[f(x)] = \begin{cases} \int_0^\infty f(ut)e^{-t}dt & 0 \leq u < \tau_2 \\ \int_0^\infty f(ut)e^{-t}dt & -\tau_1 \leq u < \tau_0. \end{cases}$$

Here M is taken equal to 1, τ_2 is finite, and τ_1 is simply not needed. Both parts define the domain of f, and sign of variable t will remain unchanged.

Problem Proposed by Decision-Maker 1 The first decision-maker represents the weighting vector in the form of first-order integrodifferential equation $u' + 2u(x) + 5\int_0^x u(t)dt = 1$, with $u(0) = 0$. By using fuzzy Sumudu transform, we have $\frac{G(u)}{u} - \frac{u(0)}{u} + 2G(u) + 5uG(u) = 1$. Then we get the following results given in Table 1.

Table 1 Exact solution of $u' + 2u(x) + 5\int_0^x u(t)dt = 1$

t	$u(t) = \frac{1}{2}e^{-t}sin2t$	$w_i = \frac{u_i(t)}{\sum u_i(t)}$
0.2	0.318828772660741	0.181117907481532
0.4	0.480858167875714	0.273162376263091
0.6	0.511513895673254	0.290577056954165
0.8	0.449137371613558	0.255142659301212

Table 2 Exact solution of $u' - \int_0^x u(t)dt = 1$

t	$u(t) = sint$	$w_i = \frac{u_i(t)}{\sum u_i(t)}$
0.1	0.099833416646828	0.114124136689059
0.2	0.198669330795061	0.172346781593672
0.3	0.295520206661340	0.337822640876924
0.4	0.389418342308651	0.337822640876924
0.5	0.479425538604203	0.548053222434016
0.6	0.564642473395035	0.489830577529404

Problem Proposed by Decision-Maker 2 The second decision-maker represents the weighting vector in the form of first-order integrodifferential equation $u' - \int_0^x u(t)dt = 1$, with $u(0) = 0$. By using Fuzzy Sumudu transform, we have $\frac{G(u)}{u} - \frac{u(0)}{u} = 1 - uG(u)$. Then we get the following results given in Table 2.

5 Algorithm for MAGDM with Intuitionistic Trapezoidal Fuzzy Data

Step 1. Use the ITFWG operator for the decision matrix $\tilde{R}_{(k)}$, to derive the individual overall preference ITFS values,
$\tilde{r}_i^{(k)} = ITFWG\left(\tilde{r}_{i_1}^{(k)}, \tilde{r}_{i_2}^{(k)}, \tilde{r}_{i_3}^{(k)}, \ldots, \tilde{r}_{i_n}^{(k)}\right), 1 \le i \le m, 1 \le k \le t.$

Step 2. Use the ITFHG operator to derive the collective overall preference ITFS values of the alternatives X_i.
$\tilde{r}_i = (\mu_i, \gamma_i) = ITFHG\left(\tilde{r}_i^{(1)}, \tilde{r}_i^{(2)}, \tilde{r}_i^{(3)}, \ldots, \tilde{r}_i^{(t)}\right), 1 \le i \le m.$

Step 3. Calculate the distance between collective overall values $\tilde{r}_i = (\mu_i, \gamma_i)$ and intuitionistic trapezoidal fuzzy positive ideal solution using the distance formula given in Definition 3.

Step 4. Rank all the alternatives $X_i, 1 \le i \le m$ and select in accordance with $d(\tilde{c}_i, \tilde{c}^+)$. The smaller $d(\tilde{c}_i, \tilde{c}^+)$, the better alternatives X_i.

6 Numerical Illustration

A car company is prudent to pick the most suitable green supplier for one of the key components in its manufacturing process. Later pre-evaluation, five suppliers have remained as options for further evaluation. Four measures are seen as u1,

product of quality; u2, capability of technology; u3, control of pollution; and u4, managing the environment. This fellowship owns a group of decision-makers from five consultancy sectors: d1 is from the production sector; d2 is from the purchasing sector; d3 is from the quality inspection sector; d4 is from financial sector; and d5 is from the technology section. The five possible alternatives X_i are to be assessed using intuitionistic trapezoidal fuzzy numbers by the two decision-makers whose weighting vector is obtained by normalizing the solution of integrodifferential equations. The weight vector proposed by the first decision-maker is given by:

$w = (0.181117907481532, 0.273162376263091, 0.290577056954165, 0.255142659301212)^T$. The weights proposed by the second decision-maker are given by:

$\gamma = (0.114124136689059, 0.337822640876924, 0.548053222434016)^T$, and $\omega = (0.172346781593672, 0.337822640876924, 0.489830577529404)^T$. The decision matrices are listed in the following as:

$$R_1 = \begin{pmatrix} ([0.5, 0.6, 0.7, 0.8]; 0.5, 0.4) & ([0.1, 0.2, 0.3, 0.4]; 0.6, 0.3) & ([0.5, 0.6, 0.8, 0.9]; 0.3, 0.6) & ([0.4, 0.5, 0.6, 0.7]; 0.2, 0.7) \\ ([0.6, 0.7, 0.8, 0.9]; 0.7, 0.3) & ([0.5, 0.6, 0.7, 0.8]; 0.7, 0.2) & ([0.4, 0.5, 0.7, 0.8]; 0.7, 0.2) & ([0.5, 0.6, 0.7, 0.9]0.4, 0.5) \\ ([0.1, 0.2, 0.4, 0.5]; 0.6, 0.4) & ([0.2, 0.3, 0.5, 0.6]; 0.5, 0.4) & ([0.5, 0.6, 0.7, 0.8]; 0.5, 0.3) & ([0.3, 0.5, 0.7, 0.9]; 0.2, 0.3) \\ ([0.3, 0.4, 0.5, 0.6]; 0.8, 0.1) & ([0.1, 0.3, 0.4, 0.5]; 0.6, 0.3) & ([0.1, 0.3, 0.5, 0.7]; 0.3, 0.4) & ([0.6, 0.7, 0.8, 0.9]; 0.2, 0.6) \\ ([0.2, 0.3, 0.4, 0.5]; 0.6, 0.2) & ([0.3, 0.4, 0.5, 0.6]; 0.4, 0.3) & ([0.2, 0.3, 0.4, 0.5]; 0.7, 0.1) & ([0.5, 0.6, 0.7, 0.8]; 0.1, 0.3) \end{pmatrix}$$

$$R_2 = \begin{pmatrix} ([0.4, 0.5, 0.6, 0.7]; 0.4, 0.3) & ([0.1, 0.2, 0.3, 0.4]; 0.5, 0.2) & ([0.4, 0.5, 0.7, 0.8]; 0.2, 0.5) & ([0.3, 0.4, 0.5, 0.6]; 0.1, 0.6) \\ ([0.5, 0.6, 0.7, 0.8]; 0.6, 0.3) & ([0.4, 0.5, 0.6, 0.7]; 0.6, 0.1) & ([0.3, 0.4, 0.6, 0.7]; 0.6, 0.1) & ([0.4, 0.5, 0.6, 0.8]; 0.3, 0.4) \\ ([0.1, 0.2, 0.3, 0.4]; 0.5, 0.3) & ([0.1, 0.2, 0.4, 0.5]; 0.4, 0.3) & ([0.4, 0.5, 0.6, 0.7]; 0.4, 0.2) & ([0.2, 0.4, 0.6, 0.8]; 0.5, 0.2) \\ ([0.2, 0.3, 0.4, 0.5]; 0.7, 0.1) & ([01, 0.2, 0.3, 0.5]; 0.5, 0.2) & ([0.1, 0.2, 0.4, 0.6]; 0.2, 0.3) & ([0.5, 0.6, 0.7, 0.8]; 0.1, 0.5) \\ ([0.1, 0.2, 0.3, 0.4]; 0.5, 0.1) & ([0.2, 0.3, 0.4, 0.5]; 0.3, 0.2) & ([0.1, 0.2, 0.3, 0.4]; 0.6, 0.2) & ([0.4, 0.5, 0.6, 0.7]; 0.4, 0.2) \end{pmatrix}$$

$$R_3 = \begin{pmatrix} ([0.6, 0.7, 0.8, 0.9]; 0.4, 0.5) & ([0.2, 0.3, 0.4, 0.5]; 0.5, 0.4) & ([0.6, 0.7, 0.9, 1.0]; 0.2, 0.7) & ([0.5, 0.6, 0.7, 0.8]; 0.1, 0.8) \\ ([0.7, 0.8, 0.9, 1.0]; 0.6, 0.4) & ([0.6, 0.7, 0.8, 0.9]; 0.6, 0.3) & ([0.5, 0.6, 0.8, 0.9]; 0.6, 0.3) & ([0.6, 0.7, 0.8, 1.0]; 0.3, 0.6) \\ ([0.2, 0.3, 0.5, 0.6]; 0.5, 0.5) & ([0.3, 0.4, 0.6, 0.7]; 0.4, 0.5) & ([0.6, 0.7, 0.8, 0.9]; 0.4, 0.4) & ([0.4, 0.6, 0.8, 1.0]; 0.5, 0.4) \\ ([0.4, 0.5, 0.6, 0.7]; 0.7, 0.2) & ([0.2, 0.4, 0.5, 0.6]; 0.5, 0.4) & ([0.2, 0.4, 0.6, 0.8]; 0.2, 0.5) & ([0.7, 0.8, 0.9, 1.0]; 0.1, 0.7) \\ ([0.3, 0.4, 0.5, 0.6]; 0.5, 0.3) & ([0.4, 0.5, 0.6, 0.7]; 0.3, 0.4) & ([0.3, 0.4, 0.5, 0.6]; 0.6, 0.2) & ([0.6, 0.7, 0.8, 0.9]; 0.4, 0.4) \end{pmatrix}$$

Using the above decision-making algorithm, we get

$d(\tilde{c_1}, c^+) = 0.846730050473296$; $d(\tilde{c_2}, c^+) = 0.649502411930568$; $d(\tilde{c_3}, c^+) = 0.821819637954159$;
$d(\tilde{c_4}, c^+) = 0.845319573215105$; $d(\tilde{c_5}, c^+) = 0.785377576460831$.

Rank all the alternatives X_i, $(i = 1, 2, 3, 4, 5)$.

$X_2 < X_5 < X_3 < X_4 < X_1$.

Since the distance function is used to rank the alternative based on positive ideal solution, the minimum the distance, the better the rank. Hence, X_2 is the best alternative.

7 Conclusion

Intuitionistic trapezoidal fuzzy set has been an effective and feasible tool for addressing those uncertain MAGDM problems with the information of all the alternatives on attributes expressed with intuitionistic trapezoidal fuzzy numbers.

The attribute weight determining and normalizing methods for integrodifferential equations using Sumudu transform is introduced and analyzed. Hamming distance measure is applied to find the lengths of each alternative from positive ideal solution for the relative similarity of each option. It is clear that the rank of alternatives obtained by applying weights to MAGDM problem is consistent.

References

1. Atanassov, K.: Intuitionistic fuzzy sets. *Fuzzy Sets and Systems*. **20(1)**, 87–96 (1986) https://doi.org/10.1016/S0165-0114(86)80034-3
2. Atanassov, k., Gargov, G.: Interval-valued intuitionistic fuzzy sets. *Fuzzy Sets and Systems*. **31**, 343–349 (1989)
3. Bulut, H., Baskonus, H.M., Belgacem, F.B.M.: The analytical solution of some fractional ordinary differential equations by the Sumudu transform method. *A.Appl.Anal. Article ID 203875*, 1–6 (2013)
4. Eltayeb, H., Kilicman, A.: A note on the Sumudu transform and differential equations. *Applied Mathematical Sciences*. **4(22)** , 1089–1098 (2010)
5. Gerstenkorn, T., Manko, J.: Correlation of intuitionistic fuzzy sets. *Fuzzy Sets and Systems*. **44**, 39–43 (1991)
6. Jeeva, S., Robinson, J.P., Application of Sumudu Transform in Intuitionistic Fuzzy MAGDM Problems. *International Journal of Pure and Applied Mathematics*. **119(11)**, 109–117, (2017)
7. Hukuhara, M.: Integration des applications measurable don't la value rest un compact convexe. *Funkcial. Ekvac*. **10**, 205–229 (1967)
8. Khan, N.A., Razzaq, O.A.: On the solution of fuzzy differential equations by Fuzzy Sumudu Transform. *Nonlinear Engineering*. **4(1)**, 49–60 (2015)
9. Li, D.F.: Multi attribute decision-making models and methods using intuitionistic fuzzy sets. *Journal of Computer and System Sciences*, **70**, 73–85 (2005)
10. Li, D-F., Ye Y-F.: Interval-valued least square prenucleolus of interval-valued cooperative games and a simplified method. *Operational Research*. **18(1)**, 205–220 (2018)
11. Li, D-F., Wan, S-P.: Minimum Weighted Minkowski Distance Power Models for Intuitionistic Fuzzy Madm with Incomplete Weight Information, *International Journal of Information Technology and Decision Making*. **16(5)**, 1387–1408 (2017)
12. Liu, J-C., Li, D-F.: Correlations to TOPSIS-Based Nonlinear-Programming Methodology for Multiattribute Decision making With Interval-Valued Intuitionistic Fuzzy Sets. *IEEE Trans. Fuzzy Systems*. **26(1)**, 391 (2018)
13. Robinson, J.P., Amirtharaj, E.C.H.: A short primer on the correlation coefficient of Vague sets. *International Journal of Fuzzy System Applications*. **1(12)**, 55–69 (2011a) https://doi.org/10.4018/ijfsa.2011040105
14. Robinson, J.P., Amirtharaj, E.C.H., Extended TOPSIS with correlation coefficient of Triangular Intuitionistic fuzzy sets for Multiple Attribute Group Decision Making. *International Journal of Decision Support System Technology*. **3(3)**, 15–40 (2011b) https://doi.org/10.4018/jdsst.2011070102
15. Robinson, J.P., Amirtharaj, E.C.H.: Vague Correlation coefficient of Interval Vague sets. *International Journal of fuzzy System Applications*. **2(1)**, 18–34 (2012a)
16. Robinson, J.P., Amirtharaj, E.C.H.: A search for the Correlation coefficient of Triangular and Trapezoidal intuitionistic Fuzzy sets for Multiple Attribute Group Decision Making. *Communications in computer and Information Sciences-283, Springer-Verlag*. 333–342 (2012b)
17. Robinson, J.P., Amirtharaj, E.C.H.: A Strategic TOPSIS algorithm with correlation coefficient of interval vague sets. *International Journal of Computing Algorithm*. **2**, 314–33 (2013)

18. Robinson, J.P., Amirtharaj, E.C.H.: MADM Problems with Correlation Coefficient of Trapezoidal Fuzzy Intuitionistic Fuzzy Sets. *Advances in Decision Sciences*. **2014**, 1–10 (2014a)
19. Robinson, J.P., Amirtharaj, E.C.H.: MAGDM-Miner: A New Algorithm for Mining Trapezoidal Intuitionistic Fuzzy Correlation Rules, *International Journal of Decision Support System Technology*. **6(1)**, 34–58 (2014b)
20. Robinson, J.P., Amirtharaj, E.C.H.: Efficient Multiple Attribute Group Decision Making Models with Correlation Coefficient of Vague sets. *International Journal of Operations Research and Information Systems*. **5(3)**, 27–51 (2014c)
21. Robinson, J.P., Amirtharaj, E.C.H.: MAGDM Problems with Correlation coefficient of Triangular Fuzzy IFS. *International Journal of Fuzzy Applications*. **4(1)**, 1–32 (2015) https://doi.org/10.4018/IJFSA.2015010101
22. Robinson, J.P., Amirtharaj, E.C.H.: Multiple Attribute Group Decision Analysis for Intuitionistic Triangular and Trapezoidal Fuzzy Numbers. *International Journal of Fuzzy System Applications*. **5(3)**, 42–76 (2016) https://doi.org/10.4018/IJFSA.2016070104
23. Robinson, J.P., Jeeva, S.: Mining Trapezoidal Intuitionistic Fuzzy Correlation Rules for Eigen Valued Magdm Problems. *International Journal of Control Theory and Applications*. **9(7)**, 585–616 (2016)
24. Robinson, J.P., Jeeva, S.: Application of Jacobian & Sor Iteration process in Intuitionistic Fuzzy MAGDM Problems. *Mathematical Sciences International Research Journal*. **6(2)**, 130–134 (2017)
25. Szmidt, E., Kacprzyk, J.: Distances between intuitionistic fuzzy sets. *Fuzzy Sets and Systems*. **114**, 505–518 (2000)
26. Szmidt, E., Kacprzyk, J.: Using intuitionistic fuzzy sets in group decision making. *Control and Cybernetics*. **31**, 1037–1053 (2002)
27. Wang, J.Q., Zhang, Z.: Multi-criteria decision-making method with incomplete certain information based on intuitionistic fuzzy number, *Control Decision*. **24**, 226–230 (2009)
28. Wei, G.: Some induced geometric aggregation operators with intuitionistic fuzzy information and their application to group decision making. *Applied Soft Computing*. **10(2)**, 423–431 (2010a)
29. Wei, G.: Some arithmetic aggregation operators with intuitionistic trapezoidal fuzzy numbers and their application to group decision making. *Journal of Computers*. **5(3)**, 345–351 (2010b). https://doi.org/10.4304/jcp.5.3.345-351
30. Wu, J., Cao, Q-W.: Same families of geometric aggregation operators with intuitionistic trapezoidal fuzzy numbers, *Applied Mathematical Modelling*. **37**, 318–327 (2013) https://doi.org/10.1016/j.apm.2012.03.001.
31. Xu, Z.S.: Dynamic Intuitionistic fuzzy multi-attribute decision making, International Journal of Approximate Reasoning, **48(1)**, 246–262 (2008).
32. Xu, Z.S., Chen, J.: On geometric aggregation over interval-valued intuitionistic fuzzy information. in: *Fourth International Conference on Fuzzy Systems and Knowledge Discovery (FSKD 2007)*. **2**, 466–471 (2007)
33. Xu, Z.S., Yager, R.R.: Some geometric aggregation operators based on Intuitionistic Fuzzy sets. *International Journal of General Systems*, **35**, 417–433 (2006).
34. Yager, R.R.: On ordered weighted averaging aggregation operators in multi-criteria decision making. *IEEE Transactions on Systems, Man, and Cybernetics*. **18**, 183–190 (1988)
35. Yu, G-F., Li, D-F.: Application of satisfactory degree to interval-valued intuitionistic fuzzy multi-attribute decision making. *Journal of Intelligent and Fuzzy Systems*. **32(1)**, 1019–1028 (2017)
36. Yu, G-F., Li., D-F., Qiu, J-M., Zheng X-X.: Some operators of intuitionistic uncertain 2-tuple linguistic variables and application to multi-attribute group decision making with heterogeneous relationship among attributes. *Journal of Intelligent and Fuzzy Systems*. **34(1)**, 599–611 (2018)
37. Zadeh, L. A.: Fuzzy Sets. *Information and Control*. **8(3)**, 338–356 (1965) https://doi.org/10.1016/S0019-9958(65)90241-X

Existence of Meromorphic Solution of Riccati-Abel Differential Equation

P. G. Siddheshwar and A. Tanuja

Abstract We present meromorphic solution of the Riccati-Abel differential equation by considering the corresponding complex differential equation. Riccati-Abel differential equation is one of the most widely used equations of mathematical physics. A result from Nevanlinna theory that helps us in obtaining such a solution concerns sharing one value of meromorphic function and its first derivative.

1 Introduction

In this article, we use some basic results and symbols of Nevanlinna theory like characteristic function $T(r, F)$, proximity function $m(r, F)$, counting function $N(r, F)$, reduced counting function $\overline{N}(r, F)$, and the first and second main theorems (see [1–3]). It is difficult to prove that there is no meromorphic solution or to find all meromorphic solutions of a nonlinear complex differential equation if such solution exists. Thus, Nevanlinna theory plays a prominent role in obtaining entire or meromorphic solutions of complex differential equations.

We obtain meromorphic solution of Riccati-Abel differential equation which is defined as an equation between the first-order derivative and the cubic polynomial. The Riccati-Abel differential equation which arises in the modeling of real-world problems such as oceanic circulation, cosmology, cancer therapy, and fluid mechanics has the form

$$\frac{dF}{dz} = a_0 + a_1 F + a_2 F^2 + a_3 F^3, \tag{1}$$

where a_0, a_1, a_2 *and* a_3 denote small functions of F that are non-zero.

P. G. Siddheshwar
Department of Mathematics, Bangalore University, Bangalore, India
e-mail: pgsiddheshwar@bub.ernet.in

A. Tanuja (✉)
Department of Mathematics, Siddaganga Institute of Technology, Tumkur, India
e-mail: tanujaa@sit.ac.in

B. Rushi Kumar et al. (eds.), *Applied Mathematics and Scientific Computing*,
Trends in Mathematics, https://doi.org/10.1007/978-3-030-01123-9_3

2 Useful Results

Result 1 Suppose F is a meromorphic function, then $\frac{dF}{dz}$ is not a constant. Therefore,

$$T(r,F) \leq N\left(r,\frac{1}{F-1}\right)+\overline{N}\left(r,\frac{1}{\frac{dF}{dz}-1}\right)+\overline{N}(r,F)-N_0\left(r,\frac{1}{\frac{d^2F}{dz^2}}\right)+S(r,F),$$

where $N_0\left(r,\frac{1}{\frac{d^2F}{dz^2}}\right)$ represents counting function of the zeros of $\frac{d^2F}{dz^2}$ that are not zeros of $\frac{dF}{dz}$ and these zeros are counted according to their multiplicity. This result is a consequence of one of the results in [5].

Result 2 Suppose F is a meromorphic function, then $\frac{dF}{dz}$ is not constant. Now we have either

$$\left(\frac{d^2F}{dz^2}\right)^3 = c_1\left(\frac{dF}{dz}-\mu\right)^4, \tag{2}$$

for some nonconstant c_1 or

$$N_{2)}(r,F) \leq \overline{N}_{(3}(r,F)+N_{2)}\left(r,\frac{1}{\frac{dF}{dz}-\mu}\right)+\overline{N}\left(r,\frac{1}{\frac{d^2F}{dz^2}}\right)+S(r,F), \tag{3}$$

where μ is a constant.

Proof Let

$$\psi = 2\frac{\frac{d^3F}{dz^3}}{\frac{d^2F}{dz^2}}-3\frac{\frac{d^2F}{dz^2}}{\frac{dF}{dz}-\mu}. \tag{4}$$

Let us take z_∞ to be a pole of F of order 2. We can then arrive at the following expression:

$$\psi(z) = O((z-z_\infty)^3),$$

which implies z_∞ is a zero of ψ of multiplicity 3. Thus, if Eq. (2) is not true, i.e., $\psi \not\equiv 0$, then

$$N_{2)}(r,F) \leq N(r,\frac{1}{\psi}) \leq T(r,\psi)+O(1). \tag{5}$$

Note that ψ can have poles of order 2 at zeros of $\frac{d^2F}{dz^2}$ or $\frac{dF}{dz} - \mu$ or multiple poles of F. Therefore, from Eq. (4) we get the following equation:

$$N(r, \psi) \leq \overline{N}_{(3}(r, F) + N_{2)}\left(r, \frac{1}{\frac{dF}{dz} - \mu}\right) + \overline{N}\left(r, \frac{1}{\frac{d^2F}{dz^2}}\right). \tag{6}$$

Again from Equ. (4), we can easily get

$$m(r, \psi) = S(r, F).$$

From Eqs. (5) and (6), and above Equation we obtain

$$N_{2)}(r, F) \leq \overline{N}_{(3}(r, F) + N_{2)}\left(r, \frac{1}{\frac{dF}{dz} - \mu}\right) + \overline{N}\left(r, \frac{1}{\frac{d^2F}{dz^2}}\right) + S(r, F).$$

Result 3 Suppose F is a nonconstant meromorphic function. Now either Eq. (3) holds or

$$F(z) = \frac{27}{2c_1[z + 3A_1]^2} + \mu z + A_2, \tag{7}$$

where $c_1 \neq 0$, A_1, A_2, μ are constants.

Proof Let F' be a constant so that F denotes a polynomial of degree at most 1. Now we have $N_{2)}(r, F) = S(r, F)$ such that Eq. (3) is true. Let us further assume F' is not a constant. In Result 2, we have Eq. (3), and if it does not hold, then we have Eq. (2) which can now be written as

$$\left(\frac{\frac{d^2F}{dz^2}}{\frac{dF}{dz} - \mu}\right)^3 = c_1\left(\frac{dF}{dz} - \mu\right). \tag{8}$$

On differentiating Eq. (8), we get

$$3\left(\frac{\frac{d^2F}{dz^2}}{\frac{dF}{dz} - \mu}\right)^2 \left(\frac{\frac{d^2F}{dz^2}}{\frac{dF}{dz} - \mu}\right)' = c_1\frac{d^2F}{dz^2}. \tag{9}$$

From Eqs. (8) and (9), we get

$$\left(\frac{\frac{d^2F}{dz^2}}{\frac{dF}{dz} - \mu}\right)^{-2} \left(\frac{\frac{d^2F}{dz^2}}{\frac{dF}{dz} - \mu}\right)' = \frac{1}{3}. \tag{10}$$

On integrating Eq. (10) once and combining the result with Eq. (8), we obtain

$$\frac{dF}{dz} - \mu = \frac{-27}{c_1(z+3A)^3}. \tag{11}$$

Now integrating Eq. (11) we can obtain Eq. (7).

We now proceed to obtain the meromorphic solution of the Riccati-Abel differential equation.

Theorem 1 *Suppose F is a nonconstant meromorphic function satisfying the Riccati-Abel differential equation of the form $\frac{dF}{dz} = a_0 + a_1F + a_2F^2 + a_3F^3$, where the non-zero a_i's (i=0,1,2,3) represents small functions of F. Let $\frac{dF}{dz} - 1$ and $\frac{dF}{dz} - F$ share the value 0 CM, and then we have F and $\frac{dF}{dz}$ share the value 1 CM, and F satisfies the equation*

$$F(z) = \frac{z + A_1}{1 - c_1e^{-z}}, \tag{12}$$

where A_1 and $c_1 \neq 0$ are constants.

Proof From the differential equation (1), we can easily get $N_{(3}(r, F) + m(r, F) = S(r, F)$ which in turn gives $T(r, F) = N_{2)}(r, F) + S(r, F)$. Therefore, $N_{2)}(r, F) \neq S(r, F)$, i.e., $N_{=2}(r, F) \neq S(r, F)$. Following [4] we can get Eq. (12). Substituting Eq. (12) in Eq. (1), we get

$$\left[\frac{z + A_1}{1 - c_1e^{-z}}\right]' = a_0 + a_1\left(\frac{z + A_1}{1 - c_1e^{-z}}\right) + a_2\left(\frac{z + A_1}{1 - c_1e^{-z}}\right)^2 + a_3\left(\frac{z + A_1}{1 - c_1e^{-z}}\right)^3. \tag{13}$$

If $a_0 \not\equiv 0$, now using Eq. (13) we get $T(r, e^{-z}) = S(r, e^{-z})$; this is not possible. Hence, we can conclude that $a_0 \equiv 0$. Substituting $a_0 \equiv 0$ in Eq. (13) and equating the coefficients of like powers of c_1e^{-z}, we can obtain $a_1(z)$, $a_2(z)$, *and* $a_3(z)$.

Theorem 2 *Suppose F is a nonconstant meromorphic function satisfying the Riccati-Abel differential equation $\frac{dF}{dz} = a_0 + a_1F + a_2F^2 + a_3F^3$, where a_i's are defined as earlier. Let F and $\frac{dF}{dz}$ share the value 1 IM; now we have either*

$$\frac{dF}{dz} - 1 = a_3(F - 1)\left[F^2 + \left(1 + \frac{a_2}{a_3}\right)F - 1\right], \tag{14}$$

or

$$\frac{dF}{dz} - 1 = a_3(F - 1)\left[F^2 + \left(1 + \frac{a_2}{a_3}\right)F + A_1 - z + 1\right], \tag{15}$$

where A_1 is a constant.

Proof Let z_3 be a zero of $\frac{dF}{dz} - 1$ and $a_j(z_3) \not\equiv 0, \infty (j = 0, 1, 2, 3)$ with F and $\frac{dF}{dz}$ sharing the value 1 IM along with z_3 being a zero of $F - 1$ of order 2. Now using Eq. (1), we can obtain

$$(a_0 + a_1 + a_2 + a_3)(z_3) \equiv 1. \tag{16}$$

If $a_0 + a_1 + a_2 + a_3 \not\equiv 1$, we obtain

$$\begin{aligned}\overline{N}\left(r, \frac{1}{\frac{dF}{dz} - 1}\right) = N\left(r, \frac{1}{F-1}\right) &\leq N\left(r, \frac{1}{a_0 + a_1 + a_2 + a_3 - 1}\right) + S(r, f), \\ &\leq T(r, a_0 + a_1 + a_2 + a_3) + S(r, F), \\ &\leq T(r, a_0) + T(r, a_1) + T(r, a_2) \\ &\quad + T(r, a_3) + S(r, F), \\ &= S(r, F). \end{aligned} \tag{17}$$

From Eq. (1), we now get

$$N_{(3}(r, F) + m(r, F) = S(r, F). \tag{18}$$

Combining Eqs. (17) and (18), and using Result 1, we get

$$\begin{aligned} T(r, F) &\leq N\left(r, \frac{1}{F-1}\right) + \overline{N}\left(r, \frac{1}{\frac{dF}{dz} - 1}\right) + \overline{N}(r, F) - N_0\left(r, \frac{1}{\frac{d^2F}{dz^2}}\right) + S(r, F), \\ &= \overline{N}_{(3}(r, F) + N_{2)}(r, F) - N_0\left(r, \frac{1}{\frac{d^2F}{dz^2}}\right) + S(r, F). \end{aligned}$$

Also we can get the following expression:

$$N_0\left(r, \frac{1}{\frac{d^2F}{dz^2}}\right) = S(r, F). \tag{19}$$

Using Eqs. (3) and (7), with $\mu = 1$, we get either

$$N_{2)}(r, F) \leq \overline{N}_{(3}(r, F) + N_{2)}\left(r, \frac{1}{\frac{dF}{dz} - 1}\right) + \overline{N}\left(r, \frac{1}{\frac{d^2F}{dz^2}}\right) + S(r, F), \tag{20}$$

or

$$F(z) = \frac{27}{2c_1[z + 3A_1]^2} + z + A_2, \tag{21}$$

where A_1, A_2, and $c_1 \neq 0$ are constants. From Eqs. (17), (18), and (20), we get

$$T(r, F) \leq \overline{N}\left(r, \frac{1}{\frac{d^2F}{dz^2}}\right) + S(r, F). \tag{22}$$

Equation (22) together with Eq. (19) yields the following result:

$$T(r, F) \leq \overline{N}_{(3}\left(r, \frac{1}{\frac{dF}{dz} - 1}\right) + S(r, F). \tag{23}$$

Equations (23) and (17) yield the condition $T(r, F) = S(r, F)$, and this is a contradiction. Therefore, Eq. (20) does not hold. From Eq. (21), we find that

$$F(z) - 1 = \frac{27 + 2c_1[z + 3A_1]^2[z + A_2 - 1]}{2c_1[z + 3A_1]^2} \tag{24}$$

and

$$\frac{dF}{dz} - 1 = \frac{-27}{c_1[z + 3A_1]^3}. \tag{25}$$

Now F and $\frac{dF}{dz}$ cannot share 1 IM; this is not possible. Therefore,

$$a_0 + a_1 + a_2 + a_3 \equiv 1. \tag{26}$$

Substituting Eq. (26) into the differential equation (1), we get

$$\frac{dF}{dz} - 1 = a_3(F - 1)\left[\left(\frac{a_1}{a_3} + \frac{a_2}{a_3} + 1\right) + \left(\frac{a_2}{a_3} + 1\right)F + F^2\right]. \tag{27}$$

If $1 + \frac{a_1}{a_3} + \frac{a_2}{a_3} = -1$ or $1 + \left(\frac{a_1}{a_3}\right)' + \left(\frac{a_2}{a_3}\right)' = 0$, then we, respectively, arrive at the conclusion (14) or (15). Otherwise, we infer that

$$N\left(r, \frac{1}{\left(\frac{a_1}{a_3} + \frac{a_2}{a_3} + 1\right) + \left(\frac{a_2}{a_3} + 1\right)F + F^2}\right) = S(r, F).$$

Suppose $\left(\frac{a_1}{a_3} + \frac{a_2}{a_3} + 1\right) + \left(\frac{a_2}{a_3} + 1\right)F + F^2$ has a zero of multiplicity l at z_0, say, such that $\frac{1}{a_3}\frac{\frac{dF}{dz} - 1}{F - 1}$ has a zero of multiplicity l at z_0. Now let us consider the following cases:

(i) $F(z_0) = \infty$ or
(ii) $\frac{dF(z_0)}{dz} = F(z_0) = F^2(z_0) = 1$ or
(iii) $a_3(z_0) = \infty$.

If $F(z_0) = \infty$, then a_3 has a pole of multiplicity $l+1$ at z_0, while if $\frac{dF(z_0)}{dz} = F^2(z_0) = F(z_0) = 3$, then $\frac{a_1}{a_3} + 2\frac{a_2}{a_3} + 3$ has a zero of multiplicity 3 at z_0, and $1 + \left(\frac{a_1}{a_3}\right)' + \left(\frac{a_2}{a_3}\right)'$ has a zero of multiplicity $\min\{l-1, l+1-t\}$ at z_0; here t represents the possible multiplicity of the pole of a_3 at z_0. From case (iii), a_3 will have a pole of multiplicity p at z_0. Hence we have

$$N\left(r, \frac{1}{\left(\frac{a_1}{a_3} + \frac{a_2}{a_3} + 1\right) + \left(\frac{a_2}{a_3} + 1\right)F + F^2}\right) \leq N(r, a_3) + N\left(r, \frac{1}{\frac{a_1}{a_3} + 2\frac{a_2}{a_3} + 3}\right) + N\left(r, \frac{1}{1 + \left(\frac{a_1}{a_3}\right)' + \left(\frac{a_2}{a_3}\right)'}\right), = S(r, F). \tag{28}$$

Equation (27) may now be written as

$$\frac{\left[\left(\frac{a_1}{a_3} + \frac{a_2}{a_3} + 1\right) + \left(\frac{a_2}{a_3} + 1\right)F + F^2\right]' - \left[1 + \left(\frac{a_1}{a_3}\right)' + \left(\frac{a_2}{a_3}\right)'\right]}{\left[\left(\frac{a_1}{a_3} + \frac{a_2}{a_3} +\right) + \left(\frac{a_2}{a_3} + 1\right)F + F^2\right]} = a_3(F-1). \tag{29}$$

From Eqs. (18) and (29), it follows that if $1 + \left(\frac{a_1}{a_3}\right)' + \left(\frac{a_2}{a_3}\right)' \neq 0$, then

$$m\left(r, \frac{1}{\left(\frac{a_1}{a_3} + \frac{a_2}{a_3} + 1\right) + \left(\frac{a_2}{a_3} + 1\right)F + F^2}\right) = S(r, F). \tag{30}$$

From Eqs. (28) and (30), we can obtain $T(r, F) = S(r, F)$ which is not possible. Thus, we have

$$1 + \left(\frac{a_1}{a_3}\right)' + \left(\frac{a_2}{a_3}\right)' \equiv 0. \tag{31}$$

By integrating Eq. (31) w.r.t. "z", we have

$$\frac{a_1}{a_3} + \frac{a_2}{a_3} = A_1 - z. \tag{32}$$

From Eqs. (27) and (32), we arrive at Eq. (15).

3 Conclusion

Riccati-Abel differential equation is known as one of the unsolvable nonlinear differential equations. In this article, we use Nevanlinna theory to obtain meromorphic solution of Riccati-Abel differential equation with sharing one counting multiplicity or ignoring multiplicity. Our results show that complex method provides a powerful mathematical tool for solving nonlinear differential equation.

References

1. W. Hayman: Meromorphic Functions, Clarendon Press, Oxford (1964)
2. I. Laine: Nevanlinna Theory and Complex Differential Equations, Walter de Gruyter, Berlin (1993)
3. K. S. Charak: Value distribution theory of meromorphic functions, Mathematics Newsletter, **18**, 1–20 (2009)
4. A. H. H. Al-Khaladi: Meromorphic functions that share one value and the solution of Riccati differential equation, Arab J. Math, **2**, 129–137 (2013)
5. C. C. Yang, H. X. Yi, *Uniqueness theory of meromorphic functions,* Kluwer, Dordrecht (2004)

Expansion of Function with Uncertain Parameters in Higher Dimension

Priyanka Roy and Geetanjali Panda

Abstract This article considers uncertain parameters of a function as closed intervals. Expansion of these types of function in a single dimension is studied. μ-monotonic property of this function in higher dimension is introduced, and higher-order expansion in $\mathbf{R}^n$ is developed using μ-monotonic property.

1 Introduction and Motivation

Interval analysis has been introduced as an alternative approach to studying uncertainty theory from nonstatistical viewpoint, and its application has been increased in recent years in control, dynamic economy, climate modeling, optimization theory, etc. An interval function $\breve{F}$ can be treated as the image extension of a real-valued function or a function whose arguments are intervals. Calculus of interval functions is studied by many researchers in the light of calculus of set-valued functions as discussed in [1, 4, 8, 9] etc. Most of these works are limited up to the existence of derivative using gH difference. Using these concepts, few developments in the area of calculus of interval functions are discussed in [2, 3, 5, 6, 11, 12]. Markov [10] has introduced a nonstandard subtraction $\ominus_M$ in the set of intervals based on which calculus of interval function in a single variable is studied. Rall [11] developed interval version of mean value theorem and Taylor's theorem for the interval functions which map from the set of intervals to the interval space using interval inclusion property and Gateaux-type derivative. Stefanini [12] proposed generalization of Hukuhara difference and studied the connection of gH derivatives with several existing derivatives of interval functions. In the literature of interval analysis, expansion of interval function has not been studied so far.

P. Roy (✉) · G. Panda
Department of Mathematics, Indian Institute of Technology Kharagpur, Kharagpur, West Bengal, India
e-mail: proy180192@maths.iitkgp.ernet.in; geetanjali@maths.iitkgp.ernet.in

B. Rushi Kumar et al. (eds.), *Applied Mathematics and Scientific Computing*, Trends in Mathematics, https://doi.org/10.1007/978-3-030-01123-9_4

In this article, an attempt is made to proceed one step further to study the expansion of interval functions. In the present contribution, Markov difference is accepted due to its computational comfortability. Some notations and preliminaries on interval analysis are discussed in Sect. 2. μ-monotonicity of interval function in $\mathbf{R}$ has already developed in the existing theory of interval analysis. In Sect. 3, μ-monotonicity of interval function in $\mathbf{R}^n$ is introduced, and using this concept, differentiability in $\mathbf{R}^n$ is revisited. Using this new concept, expansion of interval functions in one dimension and higher dimension is developed.

2 Some Notations and Preliminaries

Throughout this article $K(\mathbf{R})$ denote the set of all compact intervals on $\mathbf{R}$. $\breve{\alpha} \in K(\mathbf{R})$ is the closed interval of the form $[\underline{\alpha}, \overline{\alpha}]$ where $\underline{\alpha} \leq \overline{\alpha}$. Spread of $\breve{\alpha}$ is denoted by $\mu(\breve{\alpha})$, where $\mu(\breve{\alpha}) = \overline{\alpha} - \underline{\alpha}$. For two points α_1 and α_2, (not necessarily $\alpha_1 \leq \alpha_2$), $\breve{\alpha}$ can be written as $\breve{\alpha} = [\alpha_1 \vee \alpha_2]$. Any real number r can be expressed as a degenerate interval denoted by $\breve{r}$, $\breve{r} = [r, r]$ or $r.\breve{I}$, where $\breve{I} = [1, 1]$. $\breve{0} = [0, 0] = 0.\breve{I}$ denotes the null interval.

The usual arithmetic operation has been used in this article except the interval subtraction. Additive inverse in $\langle K(\mathbf{R}), \oplus, \odot \rangle$ may not exist, that is, $\breve{\alpha} \ominus \breve{\alpha}$ is not necessarily $\breve{0}$ according to this approach. The nonstandard subtraction due to [10], denoted by $\ominus_M$, provides additive inverse, which is

$$\breve{\alpha} \ominus_M \breve{\beta} = \begin{cases} \left[\underline{\alpha} - \underline{\beta}, \overline{\alpha} - \overline{\beta}\right], & \text{if } \mu(\breve{\alpha} \geq \mu(\breve{\beta}) \\ \left[\overline{\alpha} - \overline{\beta}, \underline{\alpha} - \underline{\beta}\right], & \text{if } \mu(\breve{\alpha}) < \mu(\breve{\beta}) \end{cases} \tag{1}$$

The following properties of $\ominus_M$ due to [10] and [7] are used throughout the paper:

(i) $\breve{\alpha} \ominus_M \breve{\alpha} = \breve{0}$
(ii) $\ominus_M \breve{\alpha} = (-1)\breve{a}$
(iii) $\breve{\alpha} \oplus (-1)\breve{\beta} = \breve{\alpha} \ominus_M \breve{\beta}$ if and only if $\mu(\breve{\alpha})\mu(\breve{\beta}) = 0$
(iv) $\breve{\alpha} \ominus_M \left(\ominus_M \breve{\beta}\right) = \breve{\alpha} \oplus \breve{\beta}$ if and only if $\mu(\breve{\alpha})\mu(\breve{\beta}) = 0$

From the above properties, the following results can be derived easily:

(v) $\breve{\alpha} \ominus_M \left(\ominus_M (-1)\breve{\beta}\right) = \breve{\alpha} \ominus_M \breve{\beta}$.

(vi) $\breve{\alpha} \ominus_M (\ominus_M \breve{\alpha}) = \begin{cases} 2\breve{\alpha}, & \text{if } \mu(\breve{a}) = 0 \\ [\underline{\alpha} + \overline{\alpha}, \underline{\alpha} + \overline{\alpha}] & \text{otherwise} \end{cases}$

In $K(\mathbf{R})$, the norm $(\|.\|)$ of an interval $\breve{\alpha}$ [10] is defined as $\|\breve{\alpha}\| = \max\left\{|\underline{\alpha}|, |\overline{\alpha}|\right\}$.

3 Calculus of Interval Function in Higher Dimension

μ-Monotonic property of an interval function plays an important role while developing calculus of interval function in the higher dimension. In the light of μ-monotonic property of interval function in a single variable from [10], we first focus on μ-monotonic property in the higher dimension.

3.1 μ-Monotonic Property of $\breve{F}$

Consider $\breve{F} : \mathbf{R}^n \to K(\mathbf{R})$, $\breve{F}(x) = [\underline{F}(x), \overline{F}(x)]$, $\Lambda_n = \{1, 2, \cdots, n\}$, $(x : ih_i) = (x_1, x_2, \ldots, x_i + h, \ldots x_n)$. Denote $\mu_{\breve{F}}(x) = \overline{F}(x) - \underline{F}(x)$.

Definition 1 $\breve{F}$ is called μ-increasing in $\mathbf{R}^n$ with respect to ith component if and only if

$$\mu_{\breve{F}}(x) \leq \mu_{\breve{F}}(x : ih_i) \ \ whenever \ \ x_i \leq x_i + h_i, \forall x, (x : ih_i) \in \mathbf{R}^n \tag{2}$$

By reverting the inequality, μ-decreasing property of $\breve{F}$ with respect to ith component can be defined. $\breve{F}$ is μ-monotonic with respect to x_i if it is either μ-increasing or μ-decreasing with respect to ith component.

3.2 Differentiability of $\breve{F}$

Definition 2 For a n variable interval function $\breve{F} : \mathbf{R}^n \to K(\mathbf{R})$ if $\lim_{h_i \to 0} \frac{1}{h_i} \left(\breve{F}(x : ih) \ominus_M \breve{F}(x) \right)$ exists, then the partial derivative of $\breve{F}$ with respect to x_i exists, and the limiting value is denoted by $\frac{\partial \breve{F}(x)}{\partial x_i}$.

Remark 1 Existence of partial derivative of $\breve{F}$ at a point may not guarantee the existence of partial derivatives of the lower and upper bound functions at that point. Consider $\breve{F}(x_1, x_2) = \breve{a}x_1 \oplus \breve{b}x_2^2$ for $\breve{a}, \breve{b} \in K(\mathbf{R})$, $where\ \mu(\breve{a}) > 0$. $\frac{\partial \breve{F}(0,0)}{\partial x_1} = \breve{a}$, where as $\frac{\partial \underline{F}(0,0)}{\partial x_1}$ and $\frac{\partial \overline{F}(0,0)}{\partial x_1}$ do not exist.

Definition 3 $\breve{F} : \mathbf{R}^n \to K(\mathbf{R})$ is differentiable at x if $\underline{F}$ and $\overline{F}$ are differentiable.

Following these basic ideas, higher-order partial derivatives of an interval function can be defined.

$$\frac{\partial^2 \breve{F}}{\partial x_j \partial x_i} = \lim_{h_j \to 0} \frac{1}{h_j} \left(\frac{\partial \breve{F}(x : jh)}{\partial x_i} \ominus_M \frac{\partial \breve{F}(x)}{\partial x_i} \right) = \left[\frac{\partial^2 \underline{F}}{\partial x_j \partial x_i} \vee \frac{\partial^2 \overline{F}}{\partial x_j \partial x_i} \right]$$

4 Expansion of Interval Functions

4.1 Expansion of Interval Function in R

Proposition 1 *If $g : \boldsymbol{R} \to \boldsymbol{R}$ is first-order differentiable and $\breve{F} : \Omega \subseteq \boldsymbol{R} \to K(\boldsymbol{R})$ is differentiable, then $(g\breve{F})$ is differentiable, and $(g\breve{F})' = g'\breve{F} \oplus g\breve{F}'$.*

Proof of this result follows directly from Definition 2 in [10].

Theorem 1 *Let $\breve{F} : \boldsymbol{R} \to K(\boldsymbol{R})$ be such that $\breve{F}', \breve{F}'', \cdots, \breve{F}^s$ exist and μ-monotonic in $nbd(\eta)$, $\eta \in \boldsymbol{R}$. Then for any $x \in nbd(\eta)$, $x \neq \eta$,*

$$\breve{F}(x) \ominus_M \left[\breve{F}(\eta) \ominus_M \left(\ominus_M (x-\eta)\breve{F}'(\eta)\right) \ominus_M \left(\ominus_M \frac{(x-\eta)^2}{2!}\breve{F}''(a)\right) \ominus_M \cdots \right.$$
$$\left. \ominus_M \left(\ominus_M \frac{(x-\eta)^{s-1}}{(s-1)!}\breve{F}^{s-1}(\eta)\right)\right]$$
$$\subset \cup_{\vartheta\in[0,1]} \frac{(x-\eta)^s(1-\vartheta)^{s-1}}{(s-1)!}\breve{F}^s(\eta+\vartheta(x-\eta)) \tag{3}$$

Proof Consider an interval function $\breve{\Phi} : \Delta \to K(\mathbf{R})$ as

$$\breve{\Phi}(\tau) = \breve{F}(\tau) \ominus_M \left(\ominus_M (x-\tau)\breve{F}'(\tau)\right) \ominus_M \left(\ominus_M \frac{(x-\tau)^2}{2!}\breve{F}''(\tau)\right) \ominus_M$$
$$\cdots \ominus_M \left(\ominus_M \frac{(x-\tau)^{s-1}}{(s-1)!}\breve{F}^{s-1}(\tau)\right) \tag{4}$$

for $\Delta = [\eta, x]$ or $[x, \eta]$.

Since $\breve{F}, \breve{F}', \cdots, \breve{F}^{s-1}, \breve{F}^s$ exist in $nbd(\eta)$, so differentiability of $\breve{\Phi}$ in $nbd(\eta)$ follows from Theorem 7 in [10]. Since $\breve{F}, \breve{F}', \cdots, \breve{F}^{s-1}, \breve{F}^s$ all are μ-monotonic in $nbd(\eta)$, each of them will be either μ-increasing or μ-decreasing in $nbd(\eta)$.

Denote $\eta_i(\tau) = \frac{(x-\tau)^i}{i!}$.

Case 1

(i) Suppose $\breve{F}, \breve{F}', \breve{F}'', \ldots, \breve{F}^{s-1}, \breve{F}^s$ are all μ-increasing in Ω. Then $(\eta_i(\tau))\breve{F}^j(\tau)$ and $(\eta_i'(\tau))\breve{F}^j(\tau)$ are μ-increasing for all $i, j \in \Lambda_s$.

From Proposition 1 and Theorem 7 in [10],

$$\breve{\Phi}'(\tau) = \breve{F}'(\tau) \ominus_M \left(\ominus_M (-1)\breve{F}'(\tau)\right) \ominus_M \left(\ominus_M (x-\tau)\breve{F}''(\tau)\right) \ominus_M$$
$$\left(\ominus_M (-1)(x-\tau)\breve{F}''(\tau)\right) \ominus_M \left(\ominus_M \frac{(x-\tau)^2}{2!}\breve{F}'''(\tau)\right) \ominus_M$$
$$\left(\ominus_M (-1)\frac{(x-\tau)^2}{2}\breve{F}'''(\tau)\right) \ominus_M \cdots \ominus_M \left(\ominus_M \frac{(x-\tau)^{s-1}}{(s-1)!}\breve{F}^s(\tau)\right) \tag{5}$$

For $j = 1, 2, \cdots, s-1$,

$$\ominus_M \left(\ominus_M \frac{(x-\tau)^{j-1}}{(j-1)!} \breve{F}^j(\tau) \right) \ominus_M \left(\ominus_M (-1) \frac{(x-\tau)^{j-1}}{(j-1)!} \breve{F}^j(\tau) \right) = \breve{0}$$

holds, which follows from property (i) of $\ominus_M$.

For $j = s$, $\ominus_M \left(\ominus_M \frac{(x-\tau)^{s-1}}{(s-1)!} \breve{F}^s(\tau) \right) = \frac{(x-\tau)^{s-1}}{(s-1)!} \breve{F}^s(\tau)$ holds from the property (v) of $\ominus_M$. Hence the expressions for $\breve{\Phi}'(\tau)$ can be simplified further as

$$\breve{\Phi}'(\tau) = \frac{(x-\tau)^{s-1}}{(s-1)!} \breve{F}^s(\tau) \tag{6}$$

From Theorem 9 in [10],

$$\begin{aligned} &\breve{\Phi}(x) \ominus_M \breve{\Phi}(\eta) \subset (x-\eta) \cup_{\tau \in \Delta} \breve{\Phi}'(\tau) \\ &= \cup_{\vartheta \in [0,1]} \frac{(1-\vartheta)^{s-1}(x-\eta)^s}{(s-1)!} \breve{F}^s(\eta + \vartheta(x-\eta)) \end{aligned} \tag{7}$$

That is,

$$\begin{aligned} \breve{F}(x) \ominus_M \Bigg[\breve{F}(\eta) \ominus_M \left(\ominus_M (x-\eta) \breve{F}'(\eta) \right) \ominus_M \left(\ominus_M \frac{(x-\eta)^2}{2!} \breve{F}''(a) \right) \ominus_M \cdots \\ \ominus_M \left(\ominus_M \frac{(x-\eta)^{s-1}}{(s-1)!} \breve{F}^{s-1}(\eta) \right) \Bigg] \subset \\ \cup_{\vartheta \in [0,1]} \frac{(x-\eta)^s (1-\vartheta)^{s-1}}{(s-1)!} \breve{F}^s(\eta + \vartheta(x-\eta)) \end{aligned}$$

(ii) If $\breve{F}, \breve{F}', \breve{F}'', \ldots, \breve{F}^{s-1}, \breve{F}^s$ are μ-decreasing, using Theorem 7 from [10], it can be verified that the expression of Φ' will be same to (6). So (3) holds in this case.

Case 2 Suppose $\breve{F}, \breve{F}', \breve{F}'', \ldots, \breve{F}^{s-1}, \breve{F}^s$ are differently μ-monotonic.

For instance, suppose even order successive derivatives are μ-increasing and odd order successive derivatives are μ-decreasing .

Then μ-monotonicity of $\eta_i(\tau)\breve{F}^j(\tau)$ or $\eta_i'(\tau)\breve{F}^j(\tau)$ will depend on μ-monotonicity of corresponding $\breve{F}^j(\tau)$ where $i, j \in \Lambda_n$.

Using Proposition 1 and Theorem 7 in [10] in (4), the following relation holds:

$$\begin{aligned} \breve{\Phi}'(\tau) = [\breve{F}'(\tau) \ominus_M \left\{ \ominus_M (-1) \breve{F}'(\tau) \right\}] \oplus [\ominus_M \left\{ \ominus_M (x-\tau) \breve{F}''(\tau) \right\} \ominus_M \\ \left\{ \ominus_M (-1)(x-\tau) \breve{F}''(\tau) \right\}] \oplus [\ominus_M \left\{ \ominus_M \frac{(x-\tau)^2}{2!} \breve{F}'''(\tau) \right\} \ominus_M \\ \left\{ \ominus_M (-1) \frac{(x-\tau)^2}{2} \breve{F}'''(\tau) \right\}] \oplus \cdots \oplus [\ominus_M \left\{ \ominus_M \frac{(x-\tau)^{s-1}}{(s-1)!} \breve{F}^s(\tau) \right\}] \end{aligned} \tag{8}$$

Using property (i) and (v) of $\ominus_M$, (8) reduces to $\breve{\Phi}'(\tau) = \frac{(x-\tau)^{s-1}}{(s-1)!}\breve{F}^s(\tau)$, which is similar to the expression of $\breve{\Phi}'(\tau)$ in (6). Therefore (3) can be derived proceeding in similar way as in Case-1. If the role of μ-monotonicity for odd and even $\breve{F}^j$ are changed, then $\breve{\Phi}'$ will remain unchanged as in (6).

Moreover, if μ-monotonicity of $\breve{F}^j$ is not consistently changed (some consecutive $\breve{F}^j$s' are μ-increasing, and some consecutive $\breve{F}^j$s' are μ-decreasing), then using (5) and (8), it can be verified that the expression of $\breve{\Phi}'(\tau)$ will be same as (6), hence the theorem.

Corollary 1 *Suppose there exists $k > 0$ and $M > 0$, such that for s sufficiently large, $\| \breve{F}^{(s)}(x) \| < kM^s \ \forall\ x \in nbd(\eta)$. Then $(\frac{(x-\eta)^s(1-\vartheta)^{s-1}}{(s-1)!}) \cup_{\vartheta\in[0,1]} \breve{F}^s(\eta + \vartheta(x-\eta)) \to \breve{0}$ as $s \to \infty$.*

Proof $\| (\frac{(x-\eta)^s(1-\vartheta)^{s-1}}{(s-1)!})\breve{F}^s(\xi) \| \leqslant \frac{|x-\eta|^s(1-\vartheta)^{s-1}}{(s-1)!}kM^s$ holds for any $\xi \in nbd(a)$.

$$\lim_{n\to\infty} \frac{M^{s-1}|x-\eta|^{s-1}}{(s-1)!} = 0 \text{ and } \lim_{n\to\infty}(1-\vartheta)^{s-1} = \begin{cases} 0 & \vartheta \neq 0 \\ 1 & \vartheta = 0 \end{cases}.$$

This implies $(\frac{(x-\eta)^s(1-\vartheta)^{s-1}}{(s-1)!})\breve{F}^s(\xi) \to \breve{0}$ as $n \to \infty$ for each $\xi \in nbd(\eta)$ and hence $(\frac{(x-\eta)^s(1-\vartheta)^{s-1}}{(s-1)!}) \cup_{\vartheta\in[0,1]} \breve{F}^s(\eta + \vartheta(x-\eta)) \to \breve{0}$ as $s \to \infty$.

4.2 Expansion of Interval Function in R^n

Theorem 2 *Let $\breve{F} : \boldsymbol{R}^n \to K(\boldsymbol{R})$ be $s-1$ times differentiable. $\breve{F}$ and all the partial derivatives of $\breve{F}$ up to order s are component-wise μ-monotonic in $nbd(\eta)$ for some $\eta \in \mathbb{R}^n$. Then*

$$\breve{F}(x) \ominus_M \left\{ \breve{F}(\eta) \ominus_M \left(\ominus_M \sum_{i=1}^{n} \frac{\partial \breve{F}(\eta)}{\partial x_i}(x_i - \eta_i) \right) \ominus_M \right.$$

$$\left(\ominus_M \frac{1}{2!} \sum_{i,j=1}^{n} \frac{\partial^2 \breve{F}(\eta)}{\partial x_i \partial x_j}(x_i - \eta_i)(x_j - \eta_j) \right) \ominus_M \cdots$$

$$\left. \ominus_M \left(\ominus_M \frac{1}{(s-1)!} \sum_{i_1,i_2,\ldots,i_s=1}^{n} \frac{\partial^{s-1} \breve{F}(\eta)}{\partial x_{i1} \ldots \partial x i_{s-1}}(x_{i1} - \eta_{i1}) \ldots (x_{is-1} - \eta_{is-1}) \right) \right\}$$

$$\subset \cup_{\xi\in L.S\{\eta,x\}} \sum_{i_1,i_2,\ldots,i_s=1}^{n} \frac{1}{(s-1)!} \frac{\partial^s \breve{F}(c)}{\partial x_{i1} \ldots \partial x_{is}}(x_{i1} - \eta_{i1}) \ldots (x_{is} - \eta_{is}), \tag{9}$$

where $L.S\{\eta, x\}$ denotes the segment of line joining η and x.

Proof Suppose $\breve{\Phi}(\tau) = \breve{F}(\eta + \tau(x-\eta)) = \breve{F}(\nu(\tau))$, where $\nu(\tau) = \eta + \tau(x-\eta)$ From Theorem 8 in [10], $\breve{\Phi}'(\tau) = (x-\eta)'\nabla\breve{F}(\nu(\tau))$, $\breve{\Phi}''(\tau) = (x-\eta)'\nabla^2(\breve{F}(\nu(\tau))(x-\eta)$.

By induction, $\breve{\Phi}^{(s)}(\tau) = \sum_{i_1,i_2,\cdots,i_s=1}^{n} \frac{\partial^s \breve{F}(\tau)}{\partial x_{i1}\partial x_{i2}\cdots\partial x_{is}}(x_{i1}-\eta_{i1})\cdots(x_{is}-\eta_{is})$

From the assumptions of the theorem, $\breve{\Phi}$ is (s-1)times differentiable and $\breve{\Phi}, \breve{\Phi}', \cdots, \breve{\Phi}^{(s)}$ are μ-monotonic. From Theorem 9 in [10], for $\tau, \vartheta \in [0,1]$,

$$\begin{aligned}\breve{\Phi}(\tau) \ominus_M \left\{\breve{\Phi}(0) \ominus_M \left(\ominus_M \tau\breve{\Phi}'(0)\right) \ominus_M \left(\ominus_M \frac{\tau^2}{2!}\breve{\Phi}''(0)\right) \ominus_M \right.\\ \left. \cdots \ominus_M \left(\ominus_M \frac{\tau^{(s-1)}}{(s-1)!}\breve{\Phi}^{(s-1)}(0)\right)\right\} \subset \cup_{\vartheta\in[0,1]} \frac{\tau^s}{(s-1)!}\breve{\Phi}^{(s)}(\vartheta),\end{aligned} \tag{10}$$

In particular for t = 1,

$$\begin{aligned}\breve{\Phi}(1) \ominus_M \left\{\breve{\Phi}(0) \ominus_M \left(\ominus_M \breve{\Phi}'(0)\right) \ominus_M \left(\ominus_M \frac{1}{2!}\breve{\Phi}''(0)\right) \ominus_M \right.\\ \left. \cdots \ominus_M \left(\ominus_M \frac{1}{(s-1)!}\breve{\Phi}^{(s-1)}(0)\right)\right\} \subset \cup_{\vartheta\in[0,1]} \frac{1}{(s-1)!}\breve{\Phi}^{(s)}(\vartheta).\end{aligned} \tag{11}$$

$\breve{\Phi}(1) = \breve{F}(x), \breve{\Phi}(0) = \breve{F}(\eta), \breve{\Phi}'(0) = \sum_{i=1}^{n} \frac{\partial \breve{F}(\eta)}{\partial x_i}(x_i-\eta_i), \breve{\Phi}''(0) = \sum_{i,j=1}^{n} \frac{\partial^2 \breve{F}(\eta)}{\partial x_i \partial x_j}(x_i-\eta_i)(x_j-\eta_j)$, etc..

(9) follows after substituting these values in (11).

Corollary 2 *Suppose there exist $k > 0$ and $M > 0$, such that for sufficiently large n, $\| \frac{\partial^s \breve{F}(\xi)}{\partial x_{i1}\ldots\partial x_{is}} \| < kM^s \ \forall\, \xi \in L.S\{\eta, x\}$. Then*

$$\cup \sum_{i_1,i_2,\ldots,i_s=1}^{n} \left(\frac{1}{(s-1)!}\right) \frac{\partial^s \breve{F}(\xi)}{\partial x_{i1}\ldots\partial x_{is}}(x_{i1}-\eta_{i1})\ldots(x_{is}-\eta_{is}) \to \breve{0} \ \ as \ \ s \to \infty$$

Proof For any $\xi \in L.S\{\eta, x\}$, $\| \frac{\partial^s \breve{F}(\xi)}{\partial x_{i1}\ldots\partial x_{is}} \| = \max\left\{ | \frac{\partial^s \underline{F}(\xi)}{\partial x_{i1}\ldots\partial x_{is}} |, | \frac{\partial^s \overline{F}(\xi)}{\partial x_{i1}\ldots\partial x_{is}} | \right\}$.

Rest of the part is similar to the proof of Corollary 1.

The following result is derived from (9) and Corollary 2.

$$\begin{aligned}\breve{F}(x) \approx \breve{F}(\eta) \ominus_M \left(\ominus_M \sum_{i=1}^{n} \frac{\partial \breve{F}(\eta)}{\partial x_i}(x_i-\eta_i)\right) \ominus_M \\ \left(\ominus_M \frac{1}{2!} \sum_{i,j=1}^{n} \frac{\partial^2 \breve{F}(\eta)}{\partial x_i \partial x_j}(x_i-\eta_i)(x_j-\eta_j)\right) \ominus_M \cdots \\ \ominus_M \left(\ominus_M \frac{1}{(s-1)!} \sum_{i_1,i_2,\ldots,i_s=1}^{n} \frac{\partial^{s-1} \breve{F}(\eta)}{\partial x_{i1}\ldots\partial x i_{s-1}}(x_{i1}-\eta_{i1})\ldots(x_{is-1}-\eta_{is-1})\right)\end{aligned} \tag{12}$$

Remark 2 Expansion of interval function $\breve{F}(x)$ should not be misunderstood as the expansion of its lower and upper bound function. Suppose $\breve{F}(x) \approx \breve{G}(x)$, where $\breve{G}(x)$ is obtained by expanding $\breve{F}$ about a up to order n. If $\underline{F}(x) \approx h_1(x)$, $\overline{F}(x) \approx h_2(x)$, where $h_1(x)$ and $h_2(x)$ are the expansion of $\underline{F}(x)$ and $\overline{F}(x)$, respectively, of order n, then $\breve{G}(x)$ is not necessarily same as $[h_1(x), h_2(x)]$. Moreover due to μ monotonic property, existence of expansion of $\breve{F}(x)$ may not imply the existence of expansion of $h_1(x)$ and $h_2(x)$.

5 Conclusion and Future Scope

This article has focused on the expansion of interval function in $\mathbf{R}^n$. This expansion can provide a powerful tool for developing solution of system of equation, solving least mean square problems with interval parameters, which can be treated as future applications of the present contribution.

References

1. Artstein, Z.: A calculus for set-valued maps and set-valued evolution equations. Set-Valued Anal. **3**(3), 213–261 (1995)
2. Bede, B., Stefanini, L.: Generalized differentiability of fuzzy-valued functions. Fuzzy Sets and Systems. **230**, 119–141 (2013)
3. Bhurjee, A.K., Panda, G.: Efficient solution of interval optimization problem. Math Meth Oper Res. **76**(3), 273–288 (2012)
4. Chalco-Cano, Y., Román-Flores, H., Jiménez-Gamero, M.D.: Generalized derivative and π-derivative for set-valued functions. Information Sciences. **181**(11), 2177–2188 (2011)
5. Chalco-Cano, Y., Rufián-Lizana, A., Román-Flores, H., Jiménez-Gamero, M.D.: Calculus for interval-valued functions using generalized hukuhara derivative and applications. Fuzzy Sets and Systems. **219**, 49–67 (2013)
6. Costa, T., Chalco-Cano, Y., Lodwick, W.A., Silva, G.N.: Generalized interval vector spaces and interval optimization. Information Sciences **311**, 74–85 (2015)
7. Dimitrova, N., Markov, S., Popova, E.: Extended interval arithmetics: new results and applications. In Atanassova, L.; Herzberger, J. (eds.) Computer Arithmetics and Enclosure Methods pp. 225–232. Elsevier Sci. Publishers B. V. (1992)
8. Li, S., Meng, K., Penot, J.P.: Calculus rules for derivatives of multimaps. Set-Valued Var. Anal.**17**(1), 21–39 (2009)
9. Malinowski, M.T.: On set differential equations in banach spaces–a second type hukuhara differentiability approach. Appl Math Comput. **219**(1), 289–305 (2012)
10. Markov, S.: Calculus for interval functions of a real variable. Computing. **22**(4), 325–337 (1979)
11. Rall, L.B.: Mean value and taylor forms in interval analysis. SIAM J Math Anal. **14**(2), 223–238 (1983)
12. Stefanini, L., Bede, B.: Generalized hukuhara differentiability of interval-valued functions and interval differential equations. Nonlinear Anal Theory Meth Appl. **71**(3), 1311–1328 (2009)

Analytical Solutions of the Bloch Equation via Fractional Operators with Non-singular Kernels

A. S. V. Ravi Kanth and Neetu Garg

Abstract This article deals with the fractional Bloch equation by using Caputo-Fabrizio fractional derivative and Atangana-Baleanu fractional derivative with non-singular kernels. Bloch equation is extensively used in chemistry, physics, magnetic resonance imaging (MRI) and nuclear magnetic resonance (NMR). The nuclear magnetization $M = (M_x, M_y, M_z)$ is derived analytically, and its behaviour is discussed via plots for different fractional orders. A comparative study of the analytical solutions with Caputo-Fabrizio, Atangana-Baleanu and Caputo fractional derivatives is presented. Equilibrium stage is achieved faster via Atangana-Baleanu fractional derivative than other fractional derivatives.

1 Introduction

Fractional calculus is the study of derivatives and integrals of non-integer order which provides us an excellent opportunity to understand memory and hereditary properties of the complex systems. Thus its applications are growing numerously in mathematical biology [3, 14] in electric circuits [1], in medicine [6] and in many other areas.

For fractional generalization of a physical model, an appropriate definition is essential. In literature, many definitions of fractional derivative are introduced, namely, the Riemann-Liouville derivative, Caputo derivative, conformal derivative, etc. (see [7–9, 12]). The Riemann-Liouville derivative involves fractional initial conditions which do not have any physical significance, while the Caputo derivatives involves integer order initial conditions. Both Riemann-Liouville and Caputo derivatives involves singular kernels. Recently Caputo-Fabrizio [5] proposed a fractional derivative in the form of exponential kernel, and Atangana-Baleanu [4] introduced a fractional derivative with kernel in the form of generalized

A. S. V. Ravi Kanth (✉) · N. Garg
Department of Mathematics, National Institute of Technology Kurukshetra, Kurukshetra, Haryana, India
e-mail: asvravikanth@nitkkr.ac.in

B. Rushi Kumar et al. (eds.), *Applied Mathematics and Scientific Computing*, Trends in Mathematics, https://doi.org/10.1007/978-3-030-01123-9_5

Mittag-Leffler function. These derivatives can describe the heterogeneities which cannot be well portrayed by fractional models with singular kernel.

The classical Bloch equation is defined as [10]

$$\begin{aligned}\frac{dM_x(t)}{dt} &= w_0 M_y(t) - \frac{M_x(t)}{T_2},\\ \frac{dM_y(t)}{dt} &= -w_0 M_x(t) - \frac{M_y(t)}{T_2},\\ \frac{dM_z(t)}{dt} &= \frac{M_0 - M_z(t)}{T_1},\end{aligned} \tag{1}$$

with initial values $M_x(0) = M_z(0) = 0$ and $M_y(0) = 100$. $M_x(t)$, $M_y(t)$ and $M_z(t)$ represent the system magnetization components, M_0 equilibrium magnetization, T_1 the spin-lattice relaxation time taken in regrowth of the longitudinal component $M_z(t)$, T_2 the spin-spin relaxation time which denotes the signal decay in NMR and w_0 resonant frequency defined by Larmor relationship $w_0 = \gamma B_0$ (B_0 denotes static magnetic field in z-component). Fractional operators describe the dynamics and complexity of the systems more efficiently than the integer order models. Fractional Bloch equation have gained attention by many researchers (see [10, 11, 13, 15]). Magin et al. [10] presented the solution of the fractional Bloch equation analytically by using Caputo fractional derivative. The fractional Bloch equation is solved numerically by creating a Matlab function and Simulink model [11].

In the present work, the fractional Bloch equation is solved by using Caputo-Fabrizio fractional derivative and Atangana-Baleanu fractional derivative with non-singular kernels. The article is organized as follows. Various definitions of fractional derivative are discussed in Sect. 2. The fractional Bloch equation via Caputo-Fabrizio and Atangana-Baleanu fractional derivative are discussed in Sect. 3. In the Sect. 3.2, results and discussions are presented. The conclusion of our work is presented in the Sect. 4.

2 Basic Definitions

In this section, the definitions of Caputo, Caputo-Fabrizio and Atangana-Baleanu fractional derivatives are discussed.

Definition 1 Caputo fractional derivative (CFD) of $g(t)$ of order α (> 0) as defined in [12]

$${}_a^C D_t^\alpha g(t) = \frac{1}{\Gamma(n-\alpha)} \int_a^t \frac{g^{(n)}(\tau)}{(t-\tau)^{\alpha-n+1}} d\tau, \; n-1 < \alpha \leq n. \tag{2}$$

.

Definition 2 Assume that $g \in H^1(a,b)$, $b > a$, the Caputo-Fabrizio fractional derivative (CFFD) of $g(t)$ is defined as [5]

$$ {}^{CF}_{a}D^{\alpha}_{t} g(t) = \frac{M(\alpha)}{(1-\alpha)} \int_a^t e^{\frac{-\alpha(t-\tau)}{1-\alpha}} g'(\tau) d\tau, \ 0 \leq \alpha \leq 1, \tag{3} $$

where $M(\alpha)$, normalization constant, depends on α such that $M(0) = M(1) = 1$.

Definition 3 The Caputo-Fabrizio fractional integral of $g(t)$ is defined as [9]

$$ {}^{CF}I^{\alpha} g(t) = \frac{2(1-\alpha)}{(2-\alpha)M(\alpha)} g(t) + \frac{2\alpha}{(2-\alpha)M(\alpha)} \int_0^t g(\tau) d\tau. \tag{4} $$

This definition indicates that Caputo-Fabrizio fractional integral of $g(t)$ of order α is the average of $g(t)$ and its first order integral. Thus normalized function takes the form $M(\alpha) = \frac{2}{2-\alpha}$, $0 \leq \alpha \leq 1$. Thus CFFD of $g(t)$ is reformulated as [9]

$$ {}^{CF}_{a}D^{\alpha}_{t} g(t) = \frac{1}{(1-\alpha)} \int_a^t e^{\frac{-\alpha(t-\tau)}{1-\alpha}} g'(\tau) d\tau, \ 0 \leq \alpha \leq 1. \tag{5} $$

Definition 4 Assume that $g \in H^1(a,b)$, $b > a$, the Atangana-Baleanu fractional derivative in Caputo sense (ABFD) of $g(t)$ is given as [4]

$$ {}^{AB}_{a}D^{\alpha}_{t} g(t) = \frac{B(\alpha)}{(1-\alpha)} \int_a^t E_{\alpha} \left(\frac{-\alpha(t-\tau)^{\alpha}}{1-\alpha} \right) g'(\tau) d\tau, \ 0 \leq \alpha \leq 1, \tag{6} $$

where $B(\alpha)$ has the same properties as that of $M(\alpha)$.

3 Fractional Bloch Equation

3.1 Fractional Bloch Equation with Caputo-Fabrizio Fractional Derivative

We consider the fractional generalization of the Bloch equation (1) by introducing an auxiliary parameter σ into fractional operator to make it physically consistent [2, 10]:

$$ \frac{d}{dt} \rightarrow \frac{1}{\sigma^{1-\alpha}} \frac{d^{\alpha}}{dt^{\alpha}}, m-1 < \alpha \leq m, m = 1, 2, 3, \ldots \tag{7} $$

where σ has dimensions of seconds.

Thus, the fractional generalization of the Bloch equation (1) is obtained as

$$
\begin{aligned}
{}_0\mathrm{D}_t^{\alpha} M_x(t) &= \tilde{w_0} M_y(t) - \frac{M_x(t)}{\tilde{T_2}},\\
{}_0\mathrm{D}_t^{\alpha} M_y(t) &= -\tilde{w_0} M_x(t) - \frac{M_y(t)}{\tilde{T_2}},\\
{}_0\mathrm{D}_t^{\alpha} M_z(t) &= \frac{M_0 - M_z(t)}{\tilde{T_1}}, 0 < \alpha \leq 1,
\end{aligned} \tag{8}
$$

with initial values $M_x(0) = M_z(0) = 0$ and $M_y(t) = 100$. Here $\tilde{w_0} = w_0 \sigma^{1-\alpha}$, $\frac{1}{\tilde{T_1}} = \frac{\sigma^{1-\alpha}}{T_1}$, $\frac{1}{\tilde{T_2}} = \frac{\sigma^{1-\alpha}}{T_2}$ having units of $(sec)^{-\alpha}$.

To obtain both $M_x(t)$ and $M_y(t)$, we assume that

$$
M_*(t) = M_x(t) + i M_y(t), \tag{9}
$$

where $M_*(t)$ is the transverse magnetisation. Using $\lambda = \frac{1}{\tilde{T_2}} + i\tilde{w_0}$ and substituting Eq. (9) in the fractional system (8), we get

$$
\begin{aligned}
{}_0\mathrm{D}_t^{\alpha} M_*(t) &= -\lambda M_*(t),\\
{}_0\mathrm{D}_t^{\alpha} M_z(t) &= \frac{M_0 - M_z(t)}{\tilde{T_1}},
\end{aligned} \tag{10}
$$

with initial values

$$
\begin{aligned}
M_*(0) &= M_x(0) + i M_y(0),\\
M_z(0) &= 0.
\end{aligned} \tag{11}
$$

Using CFFD in (10), we get

$$
\begin{aligned}
\frac{1}{(1-\alpha)} \int_a^t e^{\frac{-\alpha(t-\tau)}{1-\alpha}} M_*'(\tau) d\tau &= -\lambda M_*(t),\\
\frac{1}{(1-\alpha)} \int_a^t e^{\frac{-\alpha(t-\tau)}{1-\alpha}} M_z'(\tau) d\tau &= \frac{M_0 - M_z(t)}{\tilde{T_1}}.
\end{aligned} \tag{12}
$$

By taking Laplace transform on both sides of (12) and using convolution theorem, we get

$$
\begin{aligned}
\frac{s\bar{M_*}(s) - M_*(0)}{s + \alpha(1-s)} &= -\lambda \bar{M_*}(s),\\
\frac{s\bar{M_z}(s) - M_z(0)}{s + \alpha(1-s)} &= -\frac{\bar{M_z}(s)}{\tilde{T_1}} + \frac{M_0}{\tilde{T_1} s}.
\end{aligned} \tag{13}
$$

By substituting (11) in (13) and applying inverse Laplace transform, we get the solution

$$M_x(t) + iM_y(t) = \frac{[M_x(0) + iM_y(0)]}{1+\lambda-\alpha\lambda} e^{\frac{-\alpha\lambda t}{1+\lambda-\alpha\lambda}},$$
$$M_z(t) = M_0\left[1 - \frac{\tilde{T}_1}{(\tilde{T}_1+1-\alpha)} e^{-\frac{\alpha t}{\tilde{T}_1+1-\alpha}}\right].$$

3.2 Fractional Bloch Equation with Atangana-Baleanu Fractional Derivative

Consider the fractional system (10) with ABFD (Caputo sense):

$$\frac{1}{(1-\alpha)}\int_a^t E_\alpha\left(\frac{-\alpha(t-\tau)^\alpha}{1-\alpha}\right) M_*'(\tau)d\tau = -\lambda M_*(t),$$
$$\frac{1}{(1-\alpha)}\int_a^t E_\alpha\left(\frac{-\alpha(t-\tau)^\alpha}{1-\alpha}\right) M_z'(\tau)d\tau = \frac{M_0 - M_z(t)}{\tilde{T}_1}. \tag{14}$$

By applying Laplace transform on both sides of (14), we get

$$\bar{M}_*(s) = \frac{s^{\alpha-1}M_*(0)}{s^\alpha(1+\lambda(1-\alpha))+\alpha\lambda},$$
$$\bar{M}_z(s) = M_0\left[\frac{1}{s} - \frac{s^{\alpha-1}\tilde{T}_1}{s^\alpha(\tilde{T}_1+1-\alpha)+\alpha}\right]. \tag{15}$$

The inverse Laplace transform of (15) gives us the solution

$$M_*(t) = \frac{M_*(0)}{1+\lambda-\alpha\lambda} E_\alpha\left(\frac{-\alpha\lambda t^\alpha}{1+\lambda-\alpha\lambda}\right),$$
$$M_z(t) = M_0\left[1 - \frac{\tilde{T}_1}{(\tilde{T}_1+1-\alpha)} E_\alpha\left(-\frac{\alpha t^\alpha}{\tilde{T}_1+1-\alpha}\right)\right].$$

4 Results and Discussions

In all the figures, we have assumed that $\tilde{w_0} = 1$, $\tilde{T_1} = 1(\text{s})^{\alpha}$, $\tilde{T_2} = 20(\text{ms})^{\alpha}$ and $M_0 = 100$.

Figure 1 portrays the plot of $M_x(t)$ for $\alpha = 0.9$ and 0.6 with initial value of $M_x(0) = 0$ by using fractional derivatives CFFD, ABFD and CFD. It is observed from the figure, as the fractional order α is decreasing, free induction decay curves take a much shorter relaxation time $\tilde{T_2}$.

Figure 2 depicts the plot of $M_y(t)$ for $\alpha = 0.9$ and 0.6 with initial value $M_y(0) = 100$ by using fractional derivatives CFFD, ABFD and CFD. It is observed from the figure that the solution corresponding to ABFD takes a much shorter spin-spin relaxation time with decreasing fractional order (α) in comparison with CFFD and CFD.

Figure 3 compares the behaviour of $M_z(t)$ corresponding to three fractional operators for $\alpha = 0.9$ and 0.6. From the figure, it is observed that $M_z(t)$ corresponding to CFFD achieves its equilibrium stage more quickly than ABFD and CFD with increasing time. We also observed that $M_x(t)$ and $M_z(t)$ increases, while $M_y(t)$ decays as the time increases.

Figure 4 demonstrates the dynamic relationship between the components $M_x(t)$ and $M_y(t)$ for $\alpha = 1, 0.9, 0.8$ and 0.7, respectively. A regular spiral is portrayed for $\alpha = 1$ and is noticed that it starts decaying at a faster rate with decreasing fractional order. The decay in the components by using ABFD is faster than that via CFFD and CFD. In Fig. 5, we have displayed the complete trajectory of magnetization in three dimension for $\alpha = 0.9$ and 1, respectively, with $M_x(0) = 0$, $M_y(0) = 100$ and $M_z(0) = 0$ converging to the equilibrium value M_0.

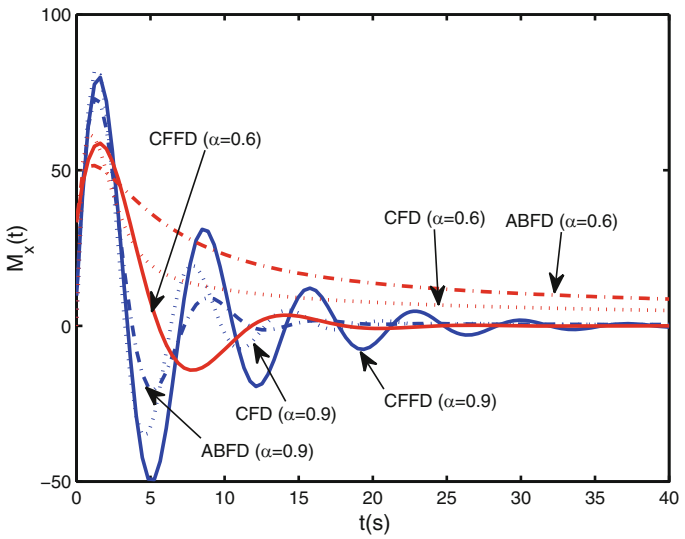

Fig. 1 $M_x(t)$ via CFFD, ABFD and CFD for $\tilde{T_2} = 20(\text{ms})^{\alpha}$, $\tilde{w_0} = 1$, $M_x(0) = 0$ and $\alpha = 0.9$ and 0.6

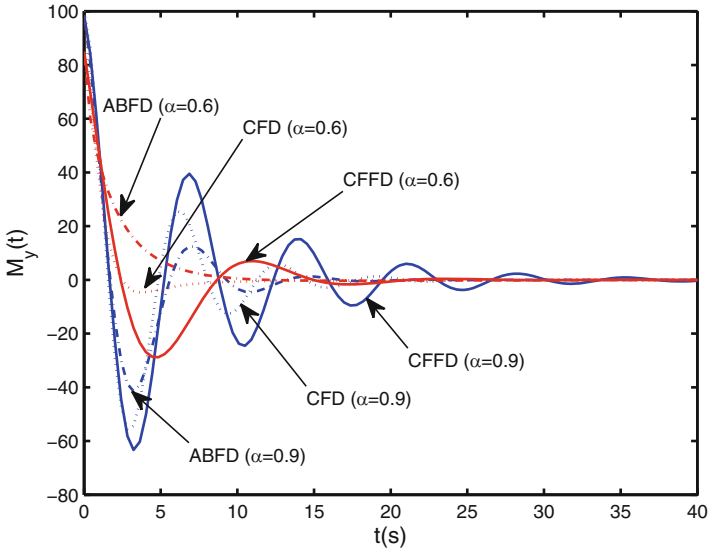

Fig. 2 $M_y(t)$ via CFFD, ABFD and CFD for $\tilde{T_2} = 20(\text{ms})^{\alpha}$, $\tilde{w_0} = 1$, $M_y(0) = 100$ and $\alpha = 0.9$ and 0.6

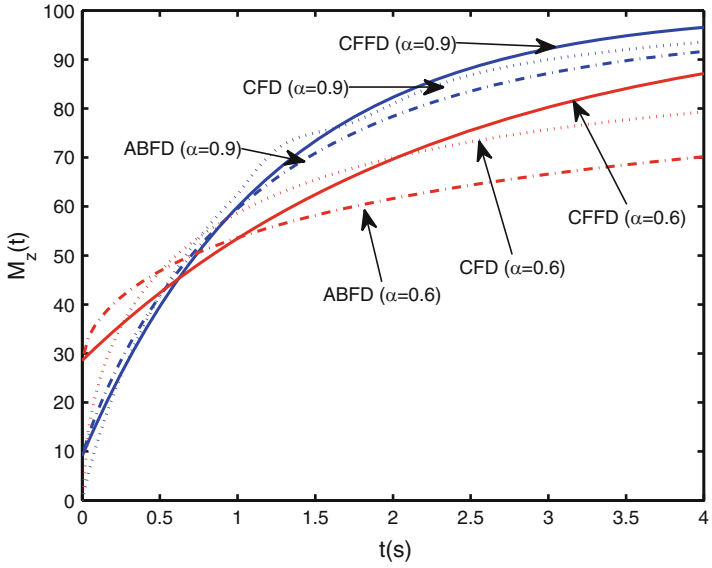

Fig. 3 $M_z(t)$ via CFFD, ABFD and CFD for $\tilde{T_1} = 1(\text{s})^{\alpha}$, $M_0 = 100$, $M_z(0) = 0$ and $\alpha = 0.9$ and 0.6

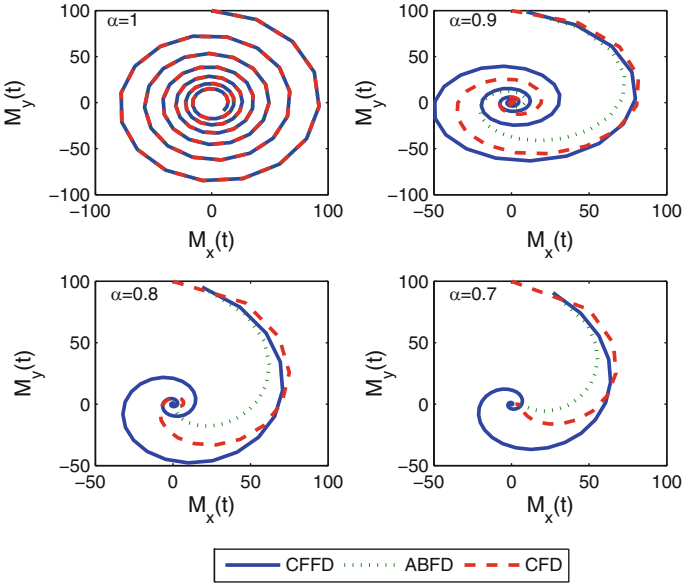

Fig. 4 $M_*(t)$ for $\alpha = 1, 0.9, 0.8$ and 0.7, respectively, with $\tilde{T}_2 = 20(\text{ms})^\alpha$, $\tilde{w_0} = 1$ with $M_x(0) = 0$ and $M_y(0) = 100$

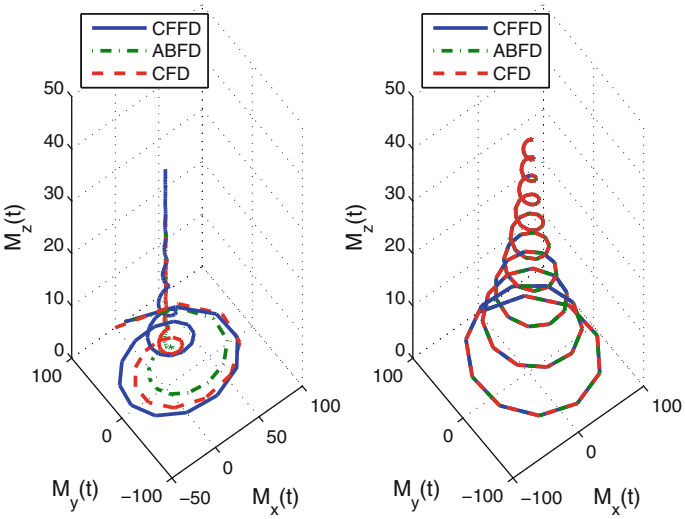

Fig. 5 Plot of the magnetization components for $\alpha = 0.9$ and 1, respectively, with $\tilde{T}_2 = 20(\text{ms})^\alpha$, $\tilde{T}_1 = 1(\text{s})^\alpha$ and $\tilde{w_0} = 1$

5 Conclusion

In this paper, the dynamics of fractional Bloch equation via CFFD and ABFD with non-singular kernels was studied. Fractional Bloch equation via ABFD and CFFD allows the description of the memory with non-singularity and behaves much better in comparison with CFD with singular kernel. The analytical solutions of the model using the CFFD and ABFD are derived for different fractional orders α. It is observed that the solution of corresponding classical equation is recovered as a particular case. We conclude that solution continuously varies according to the fractional order of the equation.

Acknowledgements The second author acknowledges the University Grants Commission of India for providing financial support for the above research (Sr.No. 2061440951, reference no.22/06/14(i)EU-V). The authors would like to thank the anonymous reviewers for their valuable suggestions and comments.

References

1. Aguilar, J.F.G., Martinez, H.Y. et al.: Analytical and numerical solutions of electrical circuits described by fractional derivatives. Appl. Math. Model. **40**, 9079–9094 (2016)
2. Aguilar, J.F.G., Martinez, H.Y. et al.: Modeling of a mass-spring-damper system by fractional derivatives with and without a singular kernel. Entropy. **17**, 6289–6303 (2015)
3. Almeida, R., Bastosa N.R.O., Monteiro M.T.T.: Modeling some real phenomena by fractional differential equations. Math. Meth. Appl. Sci. **39**, 4846–4855 (2016)
4. Atangana, A., Baleanu, D.: New fractional derivatives with nonlocal and non-singular kernel: theory and application to heat transfer model. Thermal. Sci. **20**, 763–769 (2016)
5. Caputo, M., Fabrizio, M.: A new definition of fractional derivative without singular kernel. Progr. Fract. Differ. Appl. **2**, 73–85 (2015)
6. Diethelm, K.: A fractional calculus based model for the simulation of an outbreak of dengue fever. Nonlinear. Dyn. **71**, 613–619 (2013)
7. Khalil, R., Al Horani, M., Yousef, A., Sababheh, M.: A new definition of fractional Derivative. J. comput. Appl. Math. **264**, 65–70 (2014)
8. Kilbas, A.A., Srivastava, H.M., Trujillo, J.J.: Theory and Applications of Fractional Differential Equations. Elsevier SanDiego (2006)
9. Losada, J., Nieto, J.J.: Properties of a new fractional derivative without singular kernel. Progr. Fract. Differ. Appl. **1**(2), 87–92 (2015)
10. Magin, R., Feng, X., Baleanu, D.: Solving the fractional order Bloch equation. Wiley. Inter. Sci. **34**A(1), 16–23 (2009)
11. Petras, I.: Modelling and numerical analysis of fractional order Bloch equations. Comput. Math. Appl. **6**, 341–356 (2011)
12. Podlubny, I.: Fractional Differential equations. Academic press San Diego (1999)
13. Singh, H.: Operational matrix approach for approximate solution of fractional model of Bloch equation. J. King. Saud. Univ-Sci. **29**(2), 235–240 (2017)
14. Varalta, N., Gomes A.V., Camargo R.F.: A prelude to the fractional calculus applied to tumor dynamic. Tema. **15**(2), 211–221 (2014)
15. Yu, Q., Liu, F., Turner, I., Burrage, K.: Numerical simulation of fractional Bloch Equations. J. Comput. Appl. Math. **255**, 635–651 (2014)

Solution of the Lorenz Model with Help from the Corresponding Ginzburg-Landau Model

P. G. Siddheshwar, S. Manjunath, and T. S. Sushma

Abstract Centre manifold theory, a useful tool in the study of dynamical systems, plays a crucial role in analysing the stability of the system. In the paper the three-dimensional manifold arising in the study of Rayleigh-Bénard-Brinkman convection in enclosures is reduced to a unidimensional manifold using a transformation dictated by the centre manifold theorem. Such a reduction is possible since the Lorenz model is autonomous. The advantage in this procedure is that the intractable Lorenz model gets reduced to a tractable Ginzburg-Landau equation and hence facilitates an analytical study of heat transport.

Keywords Rayleigh-Bénard-Brinkman convection · Center manifold · Enclosure

1 Introduction

The evolution of dynamical systems is studied in recent years. New techniques with better ideas for analysing these dynamical systems have emerged. The geometric concept of manifold theory is in use for solving the dynamical systems from a very long period. One such vigorous geometric tool is the centre manifold theory. The treatment of the theory for reducing a higher dimensional system to its corresponding smaller dimensions is in practice nowadays. Known by its name reduction principle, the centre manifold performs reduction of the higher dimensional dynamical systems to lower dimensions without disturbing the stability and behaviour of the original large dimensional system. This is described in detail in books [1, 3, 10, 15–17].

P. G. Siddheshwar (✉)
Department of Mathematics, Bangalore University, Bangalore, India
e-mail: pgsiddheshwar@bub.ernet.in

S. Manjunath · T. S. Sushma
Department of Mathematics, B. N. M. Institute of Technology, Bangalore, India

B. Rushi Kumar et al. (eds.), *Applied Mathematics and Scientific Computing*,
Trends in Mathematics, https://doi.org/10.1007/978-3-030-01123-9_6

The parameters encountered in the governing equations of the problem when varied may bring a qualitative change in the structure of the solutions or may give new solutions or even may change the stability of the solution. These changes are referred to as bifurcations. Centre manifold theory serves as the best device to retain the qualitative behaviour of the system around the critical points in bifurcation problems [1, 5].

This important concept of centre manifold was probably introduced by Pliss [12] and was developed by many others [1, 4, 6–10, 12]. The stability, existence and smoothness of the stable, centre-stable, centre-unstable and unstable manifolds also were given by Kelly [7, 8]. The problem of laminar mixed convection flow using centre manifold theory has been derived in the paper by Guillet et al. [4]. A brief description of the properties of centre manifold, viz. existence, uniqueness, smoothness, differentiability and analyticity, is discussed in the paper by Sijbrand [14]. The main applications of centre manifold in differential equations was given by Carr [1]. Be it a partial differential equation or an ordinary differential equation, integral equation, singular perturbations or functional differential equation, applications of the centre manifold theory is now widespread.

The present paper presents the derivation of the Ginzburg-Landau equation from the third-order Lorenz model for Rayleigh-Bénard convection in a porous enclosure using centre manifold technique. Extensive literature on Rayleigh-Bénard convection can be found [2, 11, 13].

2 Nomenclature

Latin symbols

A, B, C	Amplitudes of convection
A_r	Aspect ratio
G_{Ra}	Linear operator
H	Applied magnetic field
K	Quadratic operator
M	Ratio of specific heats
$M^{'}$	Hartmann number
p	Fluid pressure
Pr	Prandtl number
Ra	Rayleigh number
X, Z	Non-dimensional horizontal and vertical coordinates

Greek symbols

χ	Thermal diffusivity
μ	Dynamic viscosity
μ_1	Magnetic permeability
ν	Kinematic viscosity
ϕ	Porosity
Ψ	Non-dimensional stream function
ρ	Fluid density
Θ	Dimensionless temperature
σ	Electrical conductivity of the fluid

Subscripts

c	Critical
0	Reference

3 Mathematical Formulation

We consider a laminar free convection flow of an electrically conducting incompressible viscous fluid in an enclosure filled with porous medium of breadth b and height h. The lateral walls are kept insulated and heated from below. The isothermal boundaries are assumed to be stress-free. The velocity field is two-dimensional (Fig. 1).

The dimensionless governing equations are

$$\frac{1}{Pr}\frac{\partial}{\partial\tau}(\nabla_A^2\Psi)-\frac{A_r}{Pr}\frac{\partial(\Psi,\nabla_A^2\Psi)}{\partial(X,Z)}=a\wedge\nabla_A^4\Psi-aM'^2A_r^2\nabla_A^2\Psi-a^2RaA_r^4\frac{\partial\Theta}{\partial X}, \quad (1)$$

$$M\frac{\partial\Theta}{\partial\tau}=-A_r\frac{\partial\Psi}{\partial X}+A_r\frac{\partial(\Psi,\Theta)}{\partial(X,Z)}+aM\nabla_A^2\Theta, \quad (2)$$

where the constants

$$A_r=\frac{h}{b},\ a=\frac{\chi}{\chi_{bl}},\ M'=\mu_1H_0L\sqrt{\frac{\sigma}{\mu_f}},\ Pr=\frac{\mu}{\rho_0\chi},\ Ra=\frac{\rho_0\beta\Delta Tgb^3}{\mu\chi}$$

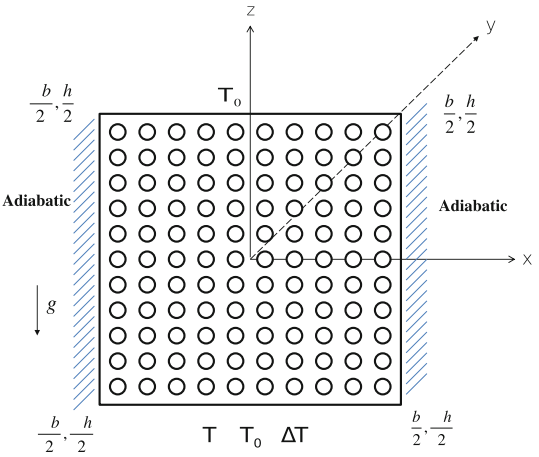

Fig. 1 Schematic representation of system under study

and

$$\nabla^2 = \frac{1}{h^2}\nabla_A^2.$$

4 Boundary Conditions

We consider the stress-free, isothermal, horizontal boundaries and stress-free, adiabatic, vertical boundaries as follows:

$$\left.\begin{aligned} \Psi = \frac{\partial^2 \Psi}{\partial Z^2} = \Theta = 0 \ \ at \ \ Z = \pm\frac{1}{2} \ \ and \ \ -\frac{1}{2} < X < \frac{1}{2}. \\ \Psi = \frac{\partial^2 \Psi}{\partial X^2} = \frac{\partial \Theta}{\partial X} = 0 \ \ at \ \ X = \pm\frac{1}{2} \ \ and \ \ -\frac{1}{2} < Z < \frac{1}{2}. \end{aligned}\right\} \tag{3}$$

5 Linear Stability Analysis

We perform linear stability analysis to find when convection sets in, and so assume

$$\left.\begin{aligned} \Psi(X, Z) = A_1 \sin\pi\left(X + \frac{1}{2}\right)\sin\pi\left(Z + \frac{1}{2}\right), \\ \Theta(X, Z) = B_1 \cos\pi\left(X + \frac{1}{2}\right)\sin\pi\left(Z + \frac{1}{2}\right), \end{aligned}\right\} \tag{4}$$

Equation (4) substituted into the dimensionless equations (1) and (2) gives us the critical Rayleigh number in the form

$$Ra_c = \frac{M\delta^4(\wedge\delta^2 + M'^2 A_r^2)}{\pi^2 A_r^5}, \tag{5}$$

where $\delta^2 = \pi^2(1 + A_r^2)$.

6 Lorenz Model

The following minimal representation of Fourier series is chosen to satisfy the boundary conditions (3).

$$\left.\begin{aligned} \Psi(X, Z, \tau) &= -\frac{\sqrt{2}M\delta^2}{\pi^2 A_r} A_1(\tau) \sin\pi\left(X + \frac{1}{2}\right) \sin\pi\left(Z + \frac{1}{2}\right), \\ \Theta(X, Z, \tau) &= \frac{\sqrt{2}}{\pi r} B_1(\tau) \cos\pi\left(X + \frac{1}{2}\right) \sin\pi\left(Z + \frac{1}{2}\right) - \frac{1}{\pi r} B_2(\tau) \sin 2\pi\left(Z + \frac{1}{2}\right). \end{aligned}\right\} \tag{6}$$

Substituting Eq. (6) into Eqs. (1) and (2), we obtain the following non-linear set of amplitude equations:

$$\left.\begin{aligned} \frac{dA_1}{dt_1} &= cPr(B_1 - A_1), \\ \frac{dB_1}{dt_1} &= A_1 - B_1 - A_1 B_2, \\ \frac{dB_2}{dt_1} &= -bB_2 + A_1 B_1, \end{aligned}\right\} \tag{7}$$

where

$$c = \frac{\wedge\delta^2 + M'^2 A_r^2}{\delta^2}, \quad r = \frac{Ra}{Ra_c}, \quad b = \frac{4\pi^2}{\delta^2}.$$

System (7) is the analytically intractable Lorenz model of the problem.

$$\frac{dS}{dt_1} = G_{Ra} S + K(S), \tag{8}$$

with

$$t_1 = \delta^2 \tau, \quad S = \begin{bmatrix} A_1 \\ B_1 \\ B_2 \end{bmatrix}, \tag{9}$$

and the operators G_{Ra} and K(S) are respectively given by

$$G_{Ra} = \begin{bmatrix} -cPr & cPr & 0 \\ r & -1 & 0 \\ 0 & 0 & -b \end{bmatrix}, \quad K(S) = \begin{bmatrix} 0 \\ \pi^2 \alpha A_1 B_2 \\ -\dfrac{\pi^2 \alpha}{2} A_1 B_1 \end{bmatrix}. \tag{10}$$

Introducing

$$\epsilon = Ra - Ra_c, \tag{11}$$

we write

$$G_{Ra} = G_{Ra}(Ra_c) + \tilde{G}(\epsilon), \tag{12}$$

where the term $G_{Ra}(Ra_c)$ is given by

$$G_{Ra}(Ra_c) = \begin{bmatrix} -cPr & cPr & 0 \\ r & -1 & 0 \\ 0 & 0 & -b \end{bmatrix} \tag{13}$$

and

$$\tilde{G}(\epsilon) = \begin{bmatrix} 0 & 0 & 0 \\ \epsilon & 0 & 0 \\ 0 & 0 & 0 \end{bmatrix}. \tag{14}$$

Thus

$$\frac{dS}{dt_1} = G_{Ra}(Ra_c) S + \tilde{a}(S, \epsilon). \tag{15}$$

The eigenvalues of $G_{Ra}(Ra_c)$ are $\lambda_1 = 0,\ \lambda_2 = -(1 + cPr) and\ \lambda_3 = -b$ and the corresponding eigenvectors as columns of a matrix are

$$E = \begin{bmatrix} 1 & -cPr & 0 \\ 1 & 1 & 0 \\ 0 & 0 & 1 \end{bmatrix}. \tag{16}$$

We now do the linear change of coordinates by applying the transformation

$$Y = E^{-1}S, \tag{17}$$

where

$$Y = \begin{bmatrix} U \\ V \\ W \end{bmatrix}. \tag{18}$$

Thus we get a diagonal matrix $L(Ra_c)$ from $G_{Ra}(Ra_c)$ in the form

$$L(Ra_c) = \begin{bmatrix} 0 & 0 & 0 \\ 0 & -(1+cPr) & 0 \\ 0 & 0 & -b \end{bmatrix}. \tag{19}$$

System (8) on using Eqs. (16), (17), (18) and (19) can be written as

$$\frac{dY}{dt_1} = L(Ra_c)Y + \tilde{n}(Y, \epsilon). \tag{20}$$

where $\tilde{n}(Y, \epsilon) = E^{-1}\tilde{a}(SY, \epsilon)$.

7 Reduction of the System Using Centre Manifold

$$\left.\begin{aligned} \frac{dU}{dt_1} &= \frac{cPr}{(1+cPr)}\left(\epsilon U - cPr\epsilon V - UW + cPrVW\right), \\ \frac{d}{dt_1}\begin{bmatrix} V \\ W \end{bmatrix} &= \begin{bmatrix} -(1+cPr) & 0 \\ 0 & -b \end{bmatrix}\begin{bmatrix} V \\ W \end{bmatrix} + \begin{bmatrix} \frac{1}{(1+cPr)}\left(\epsilon U - cPr\epsilon V - UW + cPrVW\right) \\ U^2 + (1-cPr)UV - cPrV^2 \end{bmatrix}. \end{aligned}\right\} \tag{21}$$

System (21) is a three-dimensional dynamical system which we aim to reduce to a single-dimensional system. The study is local, and hence the concentration lies only on the behaviour around the critical point. Thus the non-linear part on the right-hand side of system (21) as well as its first derivative will be equal to zero. In general, if $[V\ W]^T = [f_1(U)\ f_2(U)]^T$ where f(U) and its first order derivative become zero, then

$$\begin{bmatrix} V \\ W \end{bmatrix} = \begin{bmatrix} f_1(U) \\ f_2(U) \end{bmatrix}, \tag{22}$$

will be the centre manifold for the system. Now

$$\begin{bmatrix} V \\ W \end{bmatrix}' = \begin{bmatrix} f_1'(U) \\ f_2'(U) \end{bmatrix} U'. \tag{23}$$

The above Eq. (23) is the condition that the centre manifold has to satisfy. We approximate the functions V,W in terms of U using series expansion for $f_1'(U)$, $f_1'(U)$. So approximating V and W as follows:

$$\left.\begin{aligned} V &= a_1 U^2 + a_2 U\epsilon + a_3 U\epsilon^2 + O \parallel (U,\epsilon) \parallel^3, \\ W &= b_1 U^2 + b_2 U\epsilon + b_3 U\epsilon^2 + O \parallel (U,\epsilon) \parallel^3 . \end{aligned}\right\} \tag{24}$$

Equating the coefficient of U^2 and $U\epsilon$ and ensuring that the condition (23) is satisfied fetches us the constants

$$a_1 = 0,\ b_1 = \frac{1}{b},\ a_2 = \frac{1}{(1+Pr)^2},\ b_2 = 0.$$

Substituting the constants a_1, b_1, a_2, b_2 into Eq. (24) and again back-substituting them in first equation of system (21) gives the flow on the centre manifold

$$\frac{dU}{dt_1} = \frac{Pr}{(1+Pr)}\left[U\epsilon - \frac{1}{b}U^3\right]. \tag{25}$$

The above Eq. (25) is the *cubic, real Ginzburg-Landau* equation that is analytically tractable.

8 Results

Rayleigh-Bénard convection of Newtonian liquid in an enclosure filled with porous medium is studied using centre manifold theorem. The analytically intractable three-dimensional Lorenz model is reduced to analytically tractable one-dimensional Ginzburg-Landau equation. The analytical solution of the cubic Ginzburg-Landau equation for U is pretty straightforward. The quantities V and W can then be determined from Eq. (24). By considering S = EY, we can get the analytical solution of the Lorenz model using which the classical phase-space and phase-plane plots can be obtained.

References

1. Carr, J.: Applications of Center Manifold Theory. Applied Mathematical Sciences. Springer-Verlag New York(1982)
2. Gelfgat, A.Y.: Different modes of Rayleigh-Bénard instability in two and three-dimensional rectangular enclosures. J. Comp. Phy. **156**, 300–324(1999)
3. Guckenheimer, J. Holmes, P. J.: Non-linear oscillations, dynamical systems, and bifurcations of vector fields. Springer Science and Business Media(2013)
4. Guillet, C. Mare, T. Nguyen, C. T.: Application of a non-linear local analysis method for the problem of mixed convection instability. Int. J. Non Linear Mech. **42**, 981–988(2007)
5. Haragus, M. Iooss, G.: Local bifurcations, center manifolds, and normal forms in infinite-dimensional dynamical systems. Springer Science and Business Media(2010)
6. Henry, D.: Geometric theory of semi-linear parabolic equations. Springer-Verlag New York(1981)
7. Kelley, A.: Stability of the center-stable manifold. J. Math. Anal. Appl. **18**, 336–344(1967)
8. Kelley, A.: The stable, center-stable, center, center-unstable, unstable manifolds. J. Differential Equations **3**, 546–570(1967)
9. Knobloch, H. W. Aulbach, B.: The role of center manifolds in ordinary differential equations. Equadiff **5**, 179–189(1982)
10. Perko, L.: Differential Equations and Dynamical systems. Springer Science and business media(2013)
11. Platten, J. K. Marcoux, M. Mojtabi, A.: The Rayleigh-Bénard problem in extremely confined geometries with and without the Soret effect. Comptes Rendus Mecanique **335**, 638–654(2007)
12. Pliss, V. A.: A reduction principle in the theory of stability of motion. Izv. Akad. Nauk S.S.S.R. Mat. Ser. **6**, 1297–1324(1964)
13. Siddheshwar, P. G. Meenakshi, N.: Amplitude equation and heat transport for Rayleigh-Bénard convection in Newtonian liquids with nanoparticles. Int. J. Appl. and Comp. Math. **2**, 1–22(2015)
14. Sijbrand, J.: Properties of center manifolds. Trans. Amer. Math. Soc. **289**, 431–469(1985)
15. Scarpellini, B.: Center manifolds of infinite dimensions: Main results and applications. Z. Angew. Math. Phys. **42**, 1–32(1991)
16. Vanderbauwhede, A. Iooss, G.: Center manifold theory in infinite dimensions. Springer(1992)
17. Wiggins, S.: Introduction to Applied Nonlinear Dynamical systems and chaos. Springer-Verlag NewYork(1990)

Estimation of Upper Bounds for Initial Coefficients and Fekete-Szegö Inequality for a Subclass of Analytic Bi-univalent Functions

G. Saravanan and K. Muthunagai

Abstract In this article we have introduced a class $\tilde{\mathscr{R}}_{\Sigma}(\eta, q, \varsigma)$, $\eta \in \mathbb{C} - \{0\}$ of bi-univalent functions defined by symmetric q-derivative operator. We have estimated the upper bounds for the initial coefficients and Fekete- Szegö inequality by making use of Chebyshev polynomials.

Keywords Bi-univalent · Chebyshev polynomials · Symmetric q-derivative operator

2010 Mathematics Subject Classification 30C45, 30C15, 30C45

1 Introduction

Let A be the class of all normalized functions of the form

$$f(z) = z + \sum_{n=2}^{\infty} a_n z^n \tag{1}$$

which are analytic in the unit disk U. A holomorphic, injective function on U is said to be univalent on U. Let S, the subclass of A, be the class of all univalent functions on U.

G. Saravanan (✉)
School of Advanced Sciences, VIT Chennai, Chennai, Tamil Nadu, India

Department of Mathematics, Patrician College of Arts and Science, Chennai, Tamil Nadu, India
e-mail: saravanang.2015@vit.ac.in

K. Muthunagai
School of Advanced Sciences, VIT Chennai, Chennai, Tamil Nadu, India
e-mail: muthunagai@vit.ac.in

B. Rushi Kumar et al. (eds.), *Applied Mathematics and Scientific Computing*,
Trends in Mathematics, https://doi.org/10.1007/978-3-030-01123-9_7

A function $f(z) \in A$ is said to be bi-univalent in U, if $f(z) \in S$ and its inverse has an analytic continuation to $|w| < 1$. The class of all bi-univalent functions is denoted by Σ. There is a rich literature on the estimates of the initial coefficients of bi-univalent functions (see [5, 7, 8, 10, 12, 19–21]). However not much is known about the estimates of higher coefficients.

For $f(z)$and $g(z)$ analytic in U, we say that $f(z)$ is subordinate to $g(z)$, written $f(z) \prec g(z)$, if there exists a Schwarz function $w(z)$ with $w(0) = 0$ and $|w(z)| < 1$ in U such that $f(z) = g(w(z))$. That is if the range of one holomorphic function is contained in that of the second and these functions agree at a single point, then a sharp comparison of these two functions can be made.

The problem of finding sharp bounds for the linear functional $|a_3 - \zeta a_2^2|$ of any compact family of functions is popularly known as Fekete-Szegö problem. This coefficient functional on the normalized analytic functions in the unit disk represents various geometric quantities. For example, for $\zeta = 1$, the functional represents Schwarzian derivative, which plays a significant role in the theory of univalent functions, conformal mapping, and hypergeometric functions.

Usually to approximation of map projection, method of least squares is used. Determination of polynomial coefficients requires solutions of complicated system of equations. It is possible to avoid such problem using orthogonal Chebyshev polynomials. Though there are four kinds of Chebyshev polynomials, only the first and second kinds $T_n(x)$ and $U_n(x)$ are dealt by majority of the researchers. See for example, Doha [6] and Mason [14]. In the case of a real variable ς on $(-1,1)$, they are defined by

$$T_n(\varsigma) = cos\, n\theta,$$

$$U_n(\varsigma) = \frac{sin(n+1)\theta}{sin\theta},$$

where the subscript n denotes the polynomial degree and $x = cos\,\theta$.

Geometric function theory provides a platform to have a multiple dimensional view on the different subclasses of analytic functions with the help of q-calculus which is an effective tool of investigation. For example, the theory of q-calculus is used to describe the extension of the theory of univalent functions. For basic definitions, applications, terminologies, geometric properties, and approximation, one can refer [1, 3, 4, 9, 11, 13, 15, 17, 18].

Let us suppose $0 < q < 1$ throughout this paper.

Definition 1 The symmetric q-derivative $\widetilde{\mathfrak{D}}_q f$ of a function f given by (1) is defined as follows:

$$(\widetilde{\mathfrak{D}}_q f)(z) = \frac{f(qz) - f(q^{-1}z)}{(q - q^{-1})z}, \quad if\ z \neq 0,$$

and $(\widetilde{\mathfrak{D}}_q f)(0) = f'(0)$ provided $f'(0)$ exists.

we have

$$(\widetilde{\mathfrak{D}}_q f)(z) = 1 + \sum_{n=2}^{\infty} \widetilde{[n]}_q a_n z^{n-1},$$

where the symbol $\widetilde{[n]}_q$ denotes the number

$$\widetilde{[n]}_q = \frac{q^n - q^{-n}}{q - q^{-1}}.$$

Let P be the class of functions with positive real part consisting of all the analytic functions $p : U \to \mathbb{C}$ satisfying $p(0) = 1$ and $Re(p(z)) > 0$. The class P is called the class of Caratheodory functions. The following result will be required for proving our results.

Lemma 1 ([16]) *If the function $p \in P$ is defined by*

$$p(z) = 1 + p_1 z + p_2 z^2 + p_3 z^3 + \cdots .$$

then

$$|p_n| \leq 2 \qquad (n \in \mathbb{N} = \{1, 2, 3, \cdots\})$$

2 Main Results

Definition 2 Let $f \in \Sigma$. Then $f \in \tilde{\mathscr{R}}_{\Sigma}(\eta, q, \varsigma), \eta \in \mathbb{C} - \{0\}$ if

$$1 + \frac{1}{\eta}\left((\widetilde{\mathfrak{D}}_q f)(z) - 1\right) \prec \mathscr{R}(z, \varsigma) := \frac{1}{1 - 2\varsigma z + z^2}, \qquad \left(\frac{1}{2} < \varsigma < 1, z \in U\right)$$

and

$$1 + \frac{1}{\eta}\left((\widetilde{\mathfrak{D}}_q g)(w) - 1\right) \prec \mathscr{R}(w, \varsigma) := \frac{1}{1 - 2\varsigma w + w^2}, \qquad \left(\frac{1}{2} < \varsigma < 1, w \in U\right)$$

where $g = f^{-1}$.

We note that

$$\lim_{q \to 1^-} \tilde{\mathscr{R}}_{\Sigma}(\eta, q, \varsigma)$$

$$= \left\{ f \in \Sigma : \begin{array}{l} \lim_{q \to 1^-} \left(1 + \frac{1}{\eta}\left((\widetilde{\mathfrak{D}}_q f)(z) - 1\right)\right) > 0, \ z \in U \\ \lim_{q \to 1^-} \left(1 + \frac{1}{\eta}\left((\widetilde{\mathfrak{D}}_q g)(w) - 1\right)\right) > 0, \ w \in U \end{array} \right\} = \mathscr{R}_{\Sigma}(\eta, \varsigma).$$

The class $\mathscr{R}_{\Sigma}(\eta, \varsigma)$ is defined as follows:

Definition 3 Let $f \in \Sigma$. Then $f \in \mathscr{R}_{\Sigma}(\eta, \varsigma)$, $\eta \in \mathbb{C} - \{0\}$ if

$$1 + \frac{1}{\eta}\left(f'(z) - 1\right) \prec \mathscr{R}(z, \varsigma) := \frac{1}{1 - 2\varsigma z + z^2}, \qquad \left(\frac{1}{2} < \varsigma < 1, z \in U\right)$$

and

$$1 + \frac{1}{\eta}\left(g'(w) - 1\right) \prec \mathscr{R}(w, \varsigma) := \frac{1}{1 - 2\varsigma w + w^2}, \qquad \left(\frac{1}{2} < \varsigma < 1, w \in U\right)$$

where $g = f^{-1}$.

If $\varsigma = cos\alpha, \alpha \in \left(\frac{-\pi}{3}, \frac{\pi}{3}\right)$. Then

$$\mathscr{R}(z, \varsigma) = \frac{1}{1 - 2\varsigma z + z^2} = 1 + \sum_{n=1}^{\infty} \frac{sin(n+1)\alpha}{sin\alpha} z^n \qquad (z \in U)$$

Thus

$$\mathscr{R}(z, \varsigma) = 1 + 2cos\alpha z + (3cos^2\alpha - sin^2\alpha)z^2 + \cdots \qquad (z \in U).$$

The second kind of Chebyshev polynomials are given by

$$\mathscr{R}(z, \varsigma) = 1 + U_1(\varsigma)z + U_2(\varsigma)z^2 + \cdots \qquad (z \in U, \varsigma \in (-1, 1)),$$

where $U_{n-1} = \frac{sin(n\, arccos\varsigma)}{\sqrt{1-\varsigma^2}}$ $(n \in \mathbb{N})$.

We also have

$$U_n(\varsigma) = 2\varsigma U_{n-1}(\varsigma) - U_{n-2}(\varsigma),$$

and

$$U_1(\varsigma) = 2\varsigma, \qquad U_2(\varsigma) = 4\varsigma^2 - 1, \qquad U_3(\varsigma) = 8\varsigma^3 - 4\varsigma, \cdots \tag{2}$$

The generating function of the first kind of Chebyshev polynomials $T_n(\varsigma), \varsigma \in (-1, 1)$, is of the form

$$\sum_{n=0}^{\infty} T_n(\varsigma) z^n = \frac{1 - \varsigma z}{1 - 2\varsigma z + z^2} \qquad (z \in U)$$

2.1 Coefficient Bounds for $\tilde{\mathscr{R}}_{\Sigma}(\eta, q, \varsigma)$

Theorem 1 *Let f given by (1) be in the class $\tilde{\mathscr{R}}_{\Sigma}(\eta, q, \varsigma)$. Then*

$$|a_2| \leq \frac{2\varsigma\sqrt{2\varsigma}\,|\eta|}{\sqrt{4\left(|\eta|[\widetilde{3}]_q - [\widetilde{2}]_q^2\right)\varsigma^2 + 2[\widetilde{2}]_q^2\varsigma + [\widetilde{2}]_q^2}}$$

and

$$|a_3| \leq |\eta|\left\{\frac{2\varsigma}{[\widetilde{3}]_q} + \frac{4|\eta|\varsigma^2}{[\widetilde{2}]_q^2}\right\}$$

Proof Let $f \in \tilde{\mathscr{R}}_{\Sigma}(\eta, q, \varsigma)$ and g be the analytic extension of f^{-1} to U. Then there exist functions u and v, analytic in U with $u(0) = v(0) = 0$, $|u(z)| < 1$, $|v(w)| < 1$, $z, w \in U$ such that

$$1 + \frac{1}{\eta}\left((\widetilde{\mathfrak{D}}_q f)(z) - 1\right) = \mathscr{R}(u(z), \varsigma), \tag{3}$$

$$1 + \frac{1}{\eta}\left((\widetilde{\mathfrak{D}}_q g)(w) - 1\right) = \mathscr{R}(v(w), \varsigma). \tag{4}$$

Next, define the functions $p, q \in P$ by

$$p(z) = \frac{1 + u(z)}{1 - u(z)} = 1 + p_1 z + p_2 z^2 + \cdots$$

$$q(w) = \frac{1 + v(w)}{1 - v(w)} = 1 + q_1 w + q_2 w^2 + \cdots$$

From the equations mentioned above, one can derive

$$u(z) = \frac{p(z) - 1}{p(z) + 1} = \frac{1}{2}p_1 z + \frac{1}{2}\left(p_2 - \frac{1}{2}p_1^2\right)z^2 + \cdots \tag{5}$$

$$v(w) = \frac{q(w) - 1}{q(w) + 1} = \frac{1}{2}q_1 w + \frac{1}{2}\left(q_2 - \frac{1}{2}q_1^2\right)w^2 + \cdots \tag{6}$$

Combining (3), (4), (5) and (6)

$$1 + \frac{1}{\eta}\left((\widetilde{\mathfrak{D}}_q f)(z) - 1\right) = 1 + \frac{1}{2}U_1(\varsigma)p_1 z + \left(\frac{1}{4}U_2(\varsigma)p_1^2 + \frac{1}{2}U_1(\varsigma)\left(p_2 - \frac{1}{2}p_1^2\right)\right)z^2 + \cdots \tag{7}$$

$$1+\frac{1}{\eta}\left((\widetilde{\mathfrak{D}}_q g)(w)-1\right)=1+\frac{1}{2}U_1(\varsigma)q_1 w + \left(\frac{1}{4}U_2(\varsigma)q_1^2+\frac{1}{2}U_1(\varsigma)\left(q_2-\frac{1}{2}q_1^2\right)\right)w^2+\cdots \tag{8}$$

It follows from (7) and (8) that

$$\frac{\widetilde{[2]}_q a_2}{\eta}=\frac{U_1(\varsigma)p_1}{2} \tag{9}$$

$$\frac{\widetilde{[3]}_q a_3}{\eta}=\frac{U_1(\varsigma)}{2}\left(p_2-\frac{p_1^2}{2}\right)+\frac{U_2(\varsigma)}{4}p_1^2 \tag{10}$$

$$\frac{-\widetilde{[2]}_q a_2}{\eta}=\frac{U_1(\varsigma)q_1}{2} \tag{11}$$

and

$$\frac{\widetilde{[3]}_q}{\eta}(2a_2^2-a_3)=\frac{U_1(\varsigma)}{2}\left(q_2-\frac{q_1^2}{2}\right)+\frac{U_2(\varsigma)}{4}q_1^2, \tag{12}$$

From (9) and (11) we obtain

$$p_1=-q_1. \tag{13}$$

$$\frac{2\widetilde{[2]}_q^2 a_2^2}{\eta^2}=\frac{U_1^2(\varsigma)}{4}(p_1^2+q_1^2). \tag{14}$$

If we add (10) and (12)

$$\frac{2\widetilde{[2]}_q a_2^2}{\eta}=\frac{U_1(\varsigma)}{2}(p_2+q_2)+\frac{U_2(\varsigma)-U_1(\varsigma)}{4}(p_1^2+q_1^2). \tag{15}$$

Using (14) in (15)

$$2\left[\frac{\widetilde{[3]}_q}{\eta}-\frac{1}{\eta^2}\left[\frac{U_2(\varsigma)-U_1(\varsigma)}{U_1^2(\varsigma)}\right]\widetilde{[2]}_q^2\right]a_2^2=\frac{U_1(\varsigma)}{2}(p_2+q_2). \tag{16}$$

From Lemma 1, (2) and (16)

$$|a_2|\leq\frac{2\varsigma\sqrt{2\varsigma}\,|\eta|}{\sqrt{4\left(|\eta|\widetilde{[3]}_q-\widetilde{[2]}_q^2\right)\varsigma^2+2\widetilde{[2]}_q^2\varsigma+\widetilde{[2]}_q^2}}$$

Next, if we subtract (12) from (10) we get

$$\frac{2[\widetilde{3}]_q}{\eta}(a_3 - a_2^2) = \frac{U_1(\varsigma)}{2}(p_2 - q_2) + \frac{U_2(\varsigma) - U_1(\varsigma)}{4}(p_1^2 - q_1^2). \tag{17}$$

Equations (13), (14) and (17) yield

$$a_3 = \frac{\eta U_1(\varsigma)}{4[\widetilde{3}]_q}(p_2 - q_2) + \frac{\eta^2 U_1^2(\varsigma)(p_1^2 + q_1^2)}{8[\widetilde{2}]_q^2}.$$

By Lemma 1

$$|a_3| \leq |\eta| \left\{ \frac{2\varsigma}{[\widetilde{3}]_q} + \frac{4|\eta|\varsigma^2}{[\widetilde{2}]_q^2} \right\}$$

Remark 1 With the condition $\eta = 1$, theorem 1 reduces to the results of Altinkaya and Yalcin [2].

Theorem 2 *Let f given by (1) be in the class $\mathscr{R}_{\Sigma}(\eta, \varsigma)$. Then*

$$|a_2| \leq \frac{\varsigma\sqrt{2\varsigma}\ |\eta|}{\sqrt{1 + 2\varsigma + (3|\eta| - 4)\,\varsigma^2}}.$$

and

$$|a_3| \leq |\eta| \left\{ |\eta|\varsigma^2 + \frac{2\varsigma}{3} \right\}$$

2.2 Fekete-Szegö Inequality for $\tilde{\mathscr{R}}_{\Sigma}(\eta, q, \varsigma)$

Theorem 3 *Let f given by (1) be in the class $\tilde{\mathscr{R}}_{\Sigma}(\eta, q, \varsigma)$ and $\zeta \in \mathbb{R}$. Then*

$$|a_3 - \zeta a_2^2|$$

$$\leq \begin{cases} \dfrac{2\varsigma\eta}{[\widetilde{3}]_q} & for \quad |\zeta - 1| \leq \dfrac{4[\eta[\widetilde{3}]_q - [\widetilde{2}]_q^2]\varsigma^2 + 2[\widetilde{2}]_q^2\varsigma + [\widetilde{2}]_q^2}{4\eta[\widetilde{3}]_q\varsigma^2} \\ \dfrac{8\eta^2|1 - \zeta|\varsigma^3}{4[\eta[\widetilde{3}]_q - [\widetilde{2}]_q^2]\varsigma^2 + 2[\widetilde{2}]_q^2\varsigma + [\widetilde{2}]_q^2} & for \quad |\zeta - 1| \geq \dfrac{4[\eta[\widetilde{3}]_q - [\widetilde{2}]_q^2]\varsigma^2 + 2[\widetilde{2}]_q^2\varsigma + [\widetilde{2}]_q^2}{4\eta[\widetilde{3}]_q\varsigma^2} \end{cases}$$

Proof From (16) and (17)

$$a_3 - \zeta a_2^2 = (1-\zeta)\left[\frac{\eta^2 U_1^3(\varsigma)(p_2+q_2)}{4\left[\eta[\widetilde{3}]_q U_1^2(\varsigma) - (U_2(\varsigma)-U_1(\varsigma))[\widetilde{2}]_q^2\right]}\right] + \frac{\eta U_1(\varsigma)}{4[\widetilde{3}]_q}(p_2-q_2)$$

$$= U_1(\varsigma)\left[\left(s(\zeta) + \frac{\eta}{4[\widetilde{3}]_q}\right)p_2 + \left(s(\zeta) - \frac{\eta}{4[\widetilde{3}]_q}\right)q_2\right]$$

where

$$s(\zeta) = \frac{\eta^2 U_1(\varsigma)(1-\zeta)}{4\left[\eta[\widetilde{3}]_q U_1^2(\varsigma) - (U_2(\varsigma)-U_1(\varsigma))[\widetilde{2}]_q^2\right]}$$

So, we conclude that

$$|a_3 - \zeta a_2^2| \leq \begin{cases} \dfrac{2\varsigma\eta}{[\widetilde{3}]_q}, & 0 \leq |s(\zeta)| \leq \dfrac{\eta}{4[\widetilde{3}]_q} \\ \\ 8\varsigma|s(\zeta)|, & |s(\zeta)| \geq \dfrac{\eta}{4[\widetilde{3}]_q} \end{cases}$$

Remark 2 For $\eta = 1$ results are same as the results of Altinkaya and Yalcin [2].

Theorem 4 *Let f given by (1) be in the class $\mathscr{R}_{\Sigma}(\eta, \varsigma)$ and $\zeta \in \mathbb{R}$. Then*

$$|a_3 - \zeta a_2^2| \leq \begin{cases} \dfrac{2\varsigma\eta}{3}, & 0 \leq |1-\zeta| \leq \dfrac{(3\eta-4)\varsigma^2 + 2\varsigma + 1}{3\eta\varsigma^2} \\ \\ \dfrac{2|1-\zeta|\varsigma^3}{(3\eta-4)\varsigma^2 + 2\varsigma + 1}, & |1-\zeta| \geq \dfrac{(3\eta-4)\varsigma^2 + 2\varsigma + 1}{3\eta\varsigma^2} \end{cases}$$

References

1. Aldweby, H., Darus, M.: A subclass of harmonic univalent functions associated with q-analogue of Dziok- Srivastava operator. ISRN Math. Anal. (2013) doi:382312, 6 pages.
2. Altinkaya, Ş., Yalçn, S.: Estimates on coefficients of a general subclass of bi-univalent functions associated with symmetric q- derivative operator by means of the chebyshev polynomials. Asia Pacific Journal of Mathematices. **4**, no. 2, 90–99 (2017).
3. Aydoğan, M., Kahramaner, Y., Polatoğlu, Y.: Close-to-Convex Functions Defined by Fractional Operator. Appl. Math. Sci. **7**, 2769–2775 (2013).
4. Brahim, K. L., Sidomou, Y.: On some symmetric q-special functions. Le Mat. **68**, 107–122 (2013).

5. Brannan, D. A., Clunie, J. G.: Aspects of Contemporary Complex Analysis. Academic Press London and New York (1980).
6. Doha, E. H.: The first and second kind Chebyshev cofficients of the moments of the general-order derivative of an infinitely differentiable function. Int. J. Comput. Math. **51**, 21–35 (1994).
7. El-Ashwah, R. M.: Subclasses of bi-univalent functions defined by convolution. Journal of the Egyptian Mathematical Society. **22**, 348–351 (2014).
8. Frasin, B. A., Aouf, M. K.: New subclasses of bi-univalent functions. Applied Mathematics Letters. **24**, 1569–1573 (2011).
9. Gasper, G., Rahman, M.: Basic Hypergeometric Series. Cambridge Univ. Press Cambridge MA (1990).
10. Hayami, T., Owa, S.: Coefficient bounds for bi-univalent functions. Panamerican Mathematical Journal. **22**, 15–26 (2012).
11. Jackson, F. H.: On q-functions and a certain difference operator. Trans. Royal Soc. Edinburgh. **46**, 253–281 (1908).
12. Lewin, M.: On a Coefficient problem for bi-univalent functions. Proc. Amer. Math.Soc. **18**, 63–68 (1967).
13. Mohammed, A., Darus, M.: A generalized operator involving the q-hypergeometric function. Mat. Vesnik, **65**, 454–465 (2013).
14. Mason, J. C.: Chebyshev polynomials approximations for the L-membrane eigenvalue problem. SIAM J. Appl. Math. **15**, 172–186 (1967).
15. Polatoğlu, Y.: Growth and distortion theorems for generalized q-starlike functions. Adv. Math., Sci. J. **5**, 7–12 (2016).
16. Pommerenke, C.: Univalent Functions. Vandenhoeck & Ruprecht, G*ö*ttingen (1975).
17. Purohit, S. D., Raina, R. K.: Fractional q -calculus and certain subclass of univalent analytic functions. Mathematica. **55**, 62–74 (2013).
18. *Ö*zkan Ucar, H. E.: Cofficient inequalties for q-starlike functions. Appl. Math. Comp. **276**, 122–126 (2016).
19. Vijaya, R., Sudharsan, T. V., Sivasubramanian, S.: Coefficient Estimates for Certain Subclasses of Biunivalent Functions Defined by Convolution. International Journal of Analysis. (2016) doi: 6958098, 5 pages.
20. Xu, Q. H., Gui, Y. C., Srivastava, H. M.: Coefficient estimates for a certain subclass of analytic and bi-univalent functions. Applied Mathematics Letters. **25**, no. 6, 990–994 (2012).
21. Xu, Q. H., Xiao, H. G., Srivastava, H. M.: A certain general subclass of analytic and bi-univalent functions and associated coefficient estimate problems. Applied Mathematics and Computation. **218**, no. 23, 11461–11465 (2012).

An Adaptive Mesh Selection Strategy for Solving Singularly Perturbed Parabolic Partial Differential Equations with a Small Delay

Kamalesh Kumar, Trun Gupta, P. Pramod Chakravarthy, and R. Nageshwar Rao

Abstract In this paper, an adaptive mesh has been generated using the concept of entropy function for solving convection-diffusion singularly perturbed parabolic partial differential equations with a small delay. Similar problems are associated with a furnace used to process a metal sheet in control theory. The beauty of the method is, unlike the popular adaptive meshes (Bakhvalov and Shishkin), prior information of the width and position of the layers are not required. The method is independent of perturbation parameter ε and gives us an oscillation-free solution, without any user-introduced parameters. The applicability of the proposed method is illustrated by means of two examples.

1 Introduction

In the last few decades, there has been a growing interest in the study of delay differential equations due to their occurrence in a wide variety of application fields such as biosciences, control theory, economics, material science, medicine, robotics, etc. [1]. Singularly perturbed delay partial differential equations provide more realistic models in many areas of science and engineering that display time lag or aftereffect.

Numerical solution of singularly perturbed partial differential equations has been an active field of research from the last three decades, and an extensive literature has been developed [2, 3], but theory and numerical solution of singularly perturbed partial differential equations with delay are still at the initial stage. Lange and Miura

K. Kumar · T. Gupta · P. Pramod Chakravarthy
Department of Mathematics, Visvesvaraya National Institute of Technology, Nagpur, India
e-mail: kamleshkumar@students.vnit.ac.in,trun.mth@students.vnit.ac.in; ppchakravarthy@mth.vnit.ac.in

R. Nageshwar Rao (✉)
Vellore Institute of Technology, Vellore, Tamilnadu, India
e-mail: nraoragi@vit.ac.in

B. Rushi Kumar et al. (eds.), *Applied Mathematics and Scientific Computing*, Trends in Mathematics, https://doi.org/10.1007/978-3-030-01123-9_8

[4] studied the asymptotic analysis of singularly perturbed boundary value problems for differential-difference equations. The study of the problem considered in this paper was started by Ansari et al. [5], where they discussed finite difference scheme for singularly perturbed partial differential equations on a layer-adapted mesh. Natesan et al. [6, 7] had given finite difference schemes on Shishkin meshes for large delay in time. Sharma and Bansal [8, 9] developed parameter-uniform numerical schemes with general shift arguments. Chakravarthy and Rao [10] had given fitted Numerov method for singularly perturbed delay partial differential equations on uniform mesh.

It is noticeable that the standard central difference scheme on a uniform mesh, when applied on a singularly perturbed partial differential equation, would lead to oscillatory solution, which means that more points are required in the boundary layer region. As such the layer-adaptive meshes developed by Bakhvalov [11], Gartland [12], and others and special piecewise-uniform meshes developed by Shishkin [13] are serving the purpose. Though the Shishkin meshes are widely used due to their simplicity, the major drawback is the requirement of prior information of the location of the layer regions. To overcome this drawback, we proposed an adaptive mesh using the concept of entropy function for solving singularly perturbed delay parabolic partial differential equations. The method is independent of perturbation parameter ε and gives us an oscillation-free solution, without any user-introduced parameters.

The paper is organized as follows: In Sect. 2, we state the problem. In Sect. 3, the numerical scheme is presented. Section 4 deals with adaptive mesh algorithm, and we use central difference scheme for solving singularly perturbed delay parabolic partial differential equation. In Sect. 5, two examples have been solved to demonstrate the applicability and efficiency of the proposed method. Section 6 ends with brief conclusions.

2 Statement of the Problem

Let $\Omega = (0, 1)$, $D = \Omega \times (0, T]$, and $\Gamma = \Gamma_l \cup \Gamma_b \cup \Gamma_r$, where $\Gamma_l = \{(0, t) : 0 \leq t \leq T\}$ and $\Gamma_r = \{(1, t) : 0 \leq t \leq T\}$ are the left and the right sides of the domain D and $\Gamma_b = [0, 1] \times [-\delta, 0]$.

In this paper, we consider a class of singularly perturbed delay parabolic partial differential equation of the form

$$L_\varepsilon u(x,t) \equiv \frac{\partial u}{\partial t} - \varepsilon \frac{\partial^2 u}{\partial x^2} + a(x,t)u + b(x,t)\frac{\partial u}{\partial x} + c(x,t)u(x,t-\delta) = f(x,t),\ (x,t) \in D, \tag{1}$$

with the initial data

$$u(x,t) = \phi_b(x,t), \quad (x,t) \in \Gamma_b, \tag{2}$$

and the boundary conditions

$$u(0,t) = \phi_l(t), \text{ on } \Gamma_l, \text{ and } u(1,t) = \phi_r(t), \text{ on } \Gamma_r, \tag{3}$$

where $0 < \varepsilon \ll 1$ is the singular perturbation parameter, $\delta > 0$ represents the delay parameter, and $a(x,t), b(x,t), c(x,t), f(x,t)$ on $\overline{D}$ and $\phi_b(x,t), \phi_l(t), \phi_r(t)$ on Γ are assumed to be smooth and bounded function that satisfy the conditions $a(x,t) + c(x,t) \geq 0$, $b(x,t) \leq \beta < 0$ on $\overline{D}$. Under the above conditions, IBVP (1) exhibits boundary layer along $x = 0$. The existence and uniqueness of a solution of (1) can be established under the assumption that the data are Holder continuous and also satisfy appropriate compatibility conditions at the corner points $(0,0)$, $(1,0)$, $(0,-\delta)$, and $(1,-\delta)$ and then the required compatibility conditions are

$$\phi_b(0,0) = \phi_l(0), \quad \phi_b(1,0) = \phi_r(0), \tag{4}$$

$$\begin{aligned} &\frac{d\phi_l(0)}{dt} - \varepsilon \frac{\partial^2 \phi_b(0,0)}{\partial x^2} + a(0,0)\phi_b(0,0) + b(0,0)\frac{\partial \phi_b(0,0)}{\partial x} + \\ &\qquad c(0,0)\phi_b(0,-\delta) = f(0,0) \text{ and} \\ &\frac{d\phi_r(0)}{dt} - \varepsilon \frac{\partial^2 \phi_b(1,0)}{\partial x^2} + a(1,0)\phi_b(1,0) + b(1,0)\frac{\partial \phi_b(1,0)}{\partial x} + \\ &\qquad c(1,0)\phi_b(1,-\delta) = f(1,0). \end{aligned} \tag{5}$$

Under the above assumptions and conditions, problem (1) with the conditions (2)–(3) has a unique solution [14].

3 Numerical Scheme

When the delay parameter δ is smaller than perturbation parameter ε, the use of Taylor's series for the delay term is valid [15]. Using Taylor's series expansion to approximate the delayed argument, we get

$$u(x,t-\delta) \approx u(x,t) - \delta u_t(x,t) + O(\delta^2). \tag{6}$$

Substituting (6) in Eq. (1), we get

$$(1-\delta c(x,t))\frac{\partial u}{\partial t} - \varepsilon \frac{\partial^2 u}{\partial x^2} + (a(x,t)+c(x,t))u(x,t) + b(x,t)\frac{\partial u}{\partial x} = f(x,t). \tag{7}$$

Let the time interval $[0, T]$ be partitioned into N equal parts with constant step size Δt. We choose the step size Δt in such a way that the delay parameter $\delta = s\Delta t$, where s is some positive integer.

Let $0 = t_0, t_1, \ldots, t_N = T$ be the mesh points such that $t_j = j\frac{T}{N} = j\Delta t,\ j = 0, 1, \ldots, N$. Applying backward Euler formula for time derivative in Eq. (7), we obtain a system of ordinary differential equations at each time step as

$$(1 - \delta c(x))\frac{U^j(x) - U^{j-1}(x)}{\Delta t} - \varepsilon\frac{\partial^2 U^j(x)}{\partial x^2} + (a(x) + c(x))U^j(x) + b(x)\frac{\partial U^j(x)}{\partial x} = f(x),$$

where $U^j = U(x, t_j) \simeq u(x, t_j), a(x) = a(x, t_j), b(x) = b(x, t_j), c(x) = c(x, t_j)$, and $f(x) = f(x, t_j),\ j = 1, 2, \ldots, N$. The above equation can be rewritten as

$$-\varepsilon\frac{d^2U^j}{dx^2} + b(x, t_j)\frac{dU^j}{dx} + P(x, t_j)U^j = Q(x, t_j), \tag{8}$$

where $P(x, t_j) = \left(a(x, t_j) + c(x, t_j) + \frac{1-\delta c(x,t_j)}{\Delta t}\right)$ and $Q(x, t_j) = \left(f(x, t_j) + \frac{1-\delta c(x,t_j)}{\Delta t}U^{j-1}\right)$.

The boundary conditions (2–3) can be written as

$$\begin{aligned} &U(x, 0) = \phi_b(x, 0), \quad x \in [0, 1], \\ &U(0, t_j) = \phi_l(t_j),\ U(1, t_j) = \phi_r(t_j), \quad j = 1, 2, \ldots, N. \end{aligned} \tag{9}$$

We solve (8) along with the conditions (9) using central difference scheme with a minimum number of mesh points on uniform mesh in space direction. The presence of the singular perturbation parameter ε leads to occurrences of wild oscillation in the numerical solution. In order to avoid such oscillations, a large number of mesh points are required in layer region, when ε is very small. To overcome this, we generated a variable mesh using entropy function. The strategy for generating an adaptive mesh is given in the following section.

4 Adaptive Mesh Algorithm

We now rewrite Eq. (8) as

$-\varepsilon\frac{d^2U}{dx^2} + b(x)\frac{dU}{dx} + P(x)U = Q(x)$ where $U = U^j = U(x, t_j) \simeq u(x, t_j)$.

Now, we define the entropy production equation by multiplying with an appropriate test function. From the theory of scalar conservation law, we know that U^2 is always an appropriate entropy variable, and therefore $2U(x)$ is a suitable multiplying test function [16]. On multiplying with the test function, we obtain

$$\left(-\varepsilon\frac{d^2U}{dx^2}+b(x)\frac{dU}{dx}+P(x)U\right)\times 2U(x)=Q(x)\times 2U(x). \tag{10}$$

After simplifying, Eq. (10) can be written as

$$-\varepsilon Z''+bZ'+2PZ+2\varepsilon(U')^2=2UQ,\quad \text{where } Z=U^2.$$

The above equation can be rewritten as

$$-\varepsilon Z''+bZ'-2UQ=-2PZ-2\varepsilon(U')^2. \tag{11}$$

The right-hand side of Eq. (11) is considered as our entropy function and is always negative for all values $x \in [0, 1]$. As we know that, if we solve Eq. (8) by using central difference method, we get oscillations inside and near the boundary layer region. If we calculate the discrete analogue of the left-hand side part in (11) using the same central difference operator by taking $Z_i = U_i^2$, where U_i is the central difference computed solution of Eq. (8), we observe that the left-hand side is negative whenever the solution is smooth enough and positive where we have boundary layers. If we write the right-hand side part of (11) at the mesh point (x_i, t_j), as

$$-2P_{i,j}(U_{i,j}.U_{i-1,j})-2\varepsilon\left(\frac{U_{i,j}-U_{i-1,j}}{x_i-x_{i-1}}\right)\left(\frac{U_{i+1,j}-U_{i,j}}{x_{i+1}-x_i}\right), \tag{12}$$

we get the positive value whenever the oscillations occur.

To generate the adaptive mesh, first we calculate entropy function with a minimum number of initial uniform mesh points in space direction. Since the value of entropy function is always negative, but due to oscillation behavior of the solution at some mesh points, it will be positive. We find out the location of the mesh point, where the entropy is maximum and positive. We add mesh points, one to the left and other to the right side of the mesh point where entropy is maximum and positive. Now, we compute the solution with newly generated mesh points (nonuniform mesh) using central difference method and check whether the entropy is positive or negative throughout the interval. If the entropy is positive, we repeat the process of adding mesh points. We repeat this process till we get entropy negative throughout the interval.

We discretize the Eqs. (8)–(9) using central difference scheme on nonuniform mesh as follows:

$$L^N U_{i,j}=-\varepsilon\delta^2U_{i,j}+b_{i,j}D^0U_{i,j}+P_{i,j}U_{i,j}=Q_{i,j}, \tag{13}$$

with the boundary conditions

$$U_{i,0}=\phi_{b,i,0},\quad U_{0,j}=\phi_{l,j},\quad U_{1,j}=\phi_{r,j}, \tag{14}$$

$$\text{where } D^+U_{i,j} = \frac{U_{i+1,j} - U_{i,j}}{x_{i+1} - x_i}, \quad D^-U_{i,j} = \frac{U_{i,j} - U_{i-1,j}}{x_i - x_{i-1}},$$

$$D^0U_{i,j} = \frac{U_{i+1,j} - U_{i-1,j}}{x_{i+1} - x_{i-1}}, \quad \delta^2 u(x_i) = \frac{2(D^+U_{i,j} - D^-U_{i,j})}{x_{i+1} - x_{i-1}}.$$

We solved the system of Eq. (13) with the boundary conditions (14) by Gauss elimination method with partial pivoting.

5 Numerical Results

To demonstrate the applicability of the method presented above, we consider two test problems. Since the exact solution is not known, we use the following double mesh principle to compute the maximum point-wise errors:

$$E_{\varepsilon,\delta}^{M,N} = \max_{0 \le i \le N} \mid U^{M,N}(x_i, t_j) - U^{2M,2N}(x_{2i}, t_{2j}) \mid,$$

where $U^{M,N}(x_i, t_j)$ is the solution obtained on a mesh containing $M + 1$ points in spatial direction and $N + 1$ points in temporal direction.

The numerical rate of convergence is calculated using [17] the formula

$$R_{\varepsilon,\delta}^{M,N} = \frac{\log \mid E_{\varepsilon,\delta}^{M,N} - E_{\varepsilon,\delta}^{2M,2N} \mid}{\log 2}.$$

Example 1 $\dfrac{\partial u}{\partial t} - \varepsilon \dfrac{\partial^2 u}{\partial x^2} - \dfrac{\partial u}{\partial x} = -2e^{-1}u(x, t-\delta), \quad (x,t) \in (0,1) \times (0,2]$, with the initial data $u(x,t) = e^{-(t+x/\sqrt{\varepsilon})}$, $(x,t) \in [0,1] \times [-\delta, 0]$, and the boundary conditions $u(0,t) = e^{-t}$ and $u(1,t) = e^{-(t+1/\sqrt{\varepsilon})}$, $t \in (0,2]$.

Example 2 $\dfrac{\partial u}{\partial t} - \varepsilon \dfrac{\partial^2 u}{\partial x^2} - \dfrac{\partial u}{\partial x} + \dfrac{(1+x^2)}{2}u = t^3 - u(x, t-\delta), \quad (x,t) \in (0,1) \times (0,2]$, with the initial data $u(x,t) = 0$, $(x,t) \in [0,1] \times [-\delta, 0]$ and the boundary conditions $u(0,t) = 0$ and $u(1,t) = 0, t \in (0,2]$.

The numerical solution for these examples are plotted in Figs. 1, 2, 3, 4, 5, and 6. The maximum point-wise errors and rate of convergence for these examples for different values of perturbation parameter ε are presented in Tables 1 and 2.

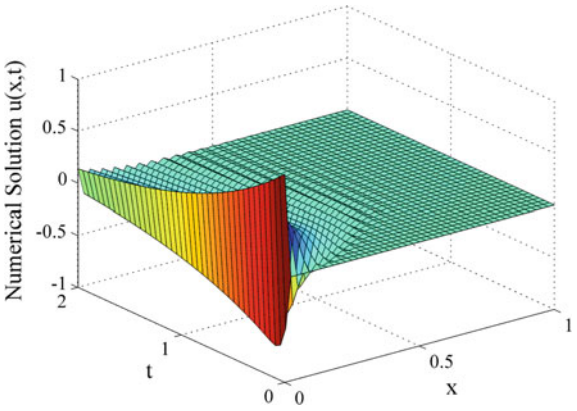

Fig. 1 Numerical solution of Example 1 with the central finite difference scheme on uniform mesh for $\varepsilon = 2^{-10}$, $\delta = 0.02\varepsilon$, M=44, and N=40

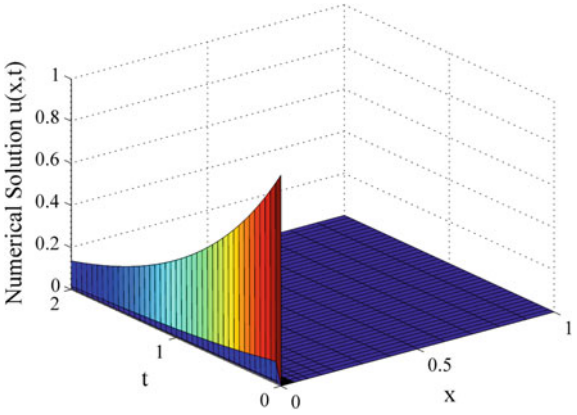

Fig. 2 Surface plot of the solution of Example 1, using adaptive mesh for $\varepsilon = 2^{-10}$, $\delta = 0.02\varepsilon$, $M = 10$(initially), $M^* = 44$, and N=40

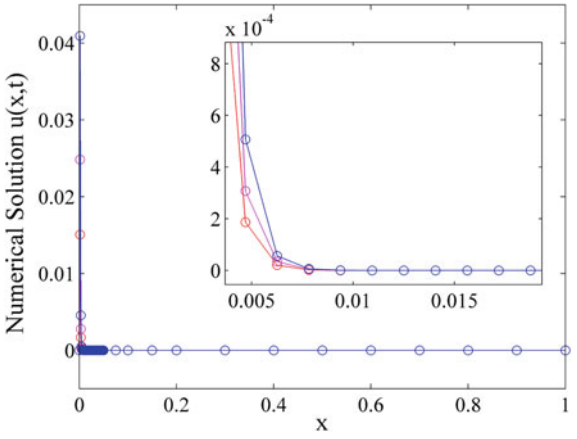

Fig. 3 Numerical solution of Example 1 using adaptive mesh for different time levels for $\varepsilon = 2^{-10}$, $\delta = 0.02\varepsilon$, $M = 10$(initially), $M^* = 44$, and N=40

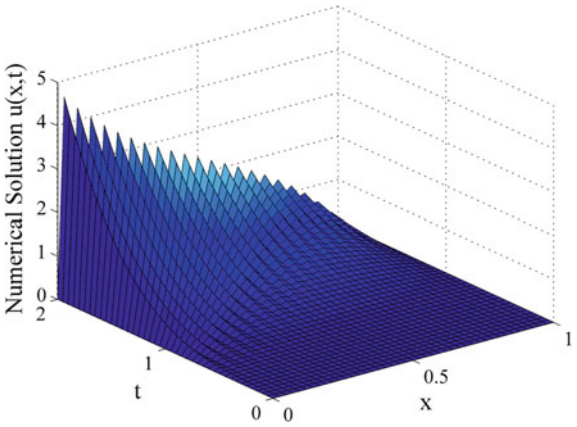

Fig. 4 Numerical solution of Example 2 with the central finite difference scheme on uniform mesh for $\varepsilon = 2^{-20}$, $\delta = 0.05\varepsilon$, M=42, and N=40

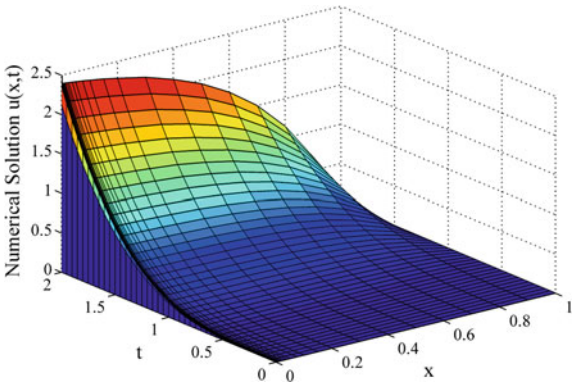

Fig. 5 Surface plot of the solution of Example 2, using adaptive mesh for $\varepsilon = 2^{-20}$, $\delta = 0.05\varepsilon$, $M = 10$(initially), $M^* = 42$, and N=40

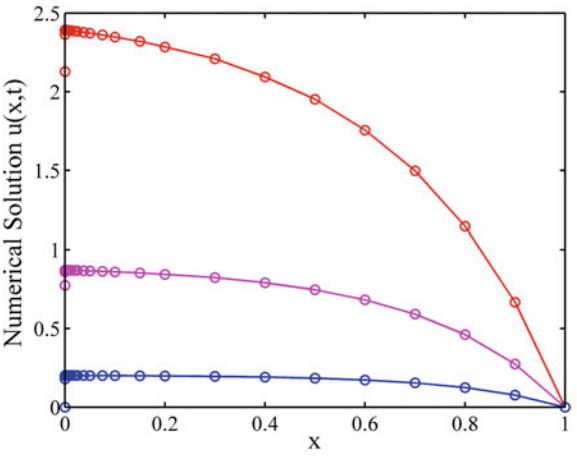

Fig. 6 Numerical solution of Example 2 using adaptive mesh for different time levels for $\varepsilon = 2^{-20}$, $\delta = 0.05\varepsilon$, $M = 10$(initially), $M^* = 42$, and N=40

Table 1 Maximum absolute error for Example 1 for different values of ε with $\delta = 0.02\varepsilon$, M=10, and N=40

ε	Generated mesh (M^*)	Max. error	Rate of convergence ($R^{M^*,N}$)
2^{-7}	80	0.0637	2.1557
2^{-8}	70	0.0652	2.1838
2^{-9}	42	0.0656	2.1628
2^{-10}	44	0.0669	2.1705
2^{-11}	46	0.0680	2.1815
2^{-12}	48	0.0685	2.1870
2^{-13}	80	0.0688	2.1898
2^{-14}	82	0.0689	2.1912
2^{-15}	84	0.0690	2.1919
2^{-16}	86	0.0690	2.1923

Table 2 Maximum absolute error for Example 2 for different values of ε with $\delta = 0.05\varepsilon$, M=10, and N=40

ε	Generated mesh (M^*)	Max. error	Rate of convergence ($R^{M^*,N}$)
2^{-7}	16	0.1620	2.1520
2^{-8}	18	0.1655	2.1665
2^{-9}	20	0.1673	2.1739
2^{-10}	22	0.1682	2.1776
2^{-11}	24	0.1687	2.1795
2^{-12}	26	0.1689	2.1804
2^{-13}	28	0.1691	2.1809
2^{-14}	30	0.1691	2.1812
2^{-15}	32	0.1691	2.1813
2^{-16}	34	0.1692	2.1813

6 Conclusions

In this paper, an adaptive mesh has been generated using the concept of entropy function for solving convection-diffusion singularly perturbed parabolic partial differential equations with small delay. The method is based on central finite difference scheme on nonuniform mesh. It has been found that our algorithm gives oscillation-liberated solution with a minimum number of mesh points. The efficiency of the method is tested with two numerical examples. From the results, it can be observed that the method converges uniformly with respect to the perturbation parameter ε and convergence quadratically. From the numerical results, it is concluded that our adaptive mesh offers a significant advantage over Bakhvalov and Shishkin meshes.

References

1. Wu, J.: Theory and Applications of Partial Functional Differential Equations. Springer, NewYork (1996)
2. Friedman, A: Partial Differential Equations of Parabolic Type. Prentice-hall, Englewood Cliffs (1964)
3. Roos, H.G., Stynes, M., Tobiska, L.: Numerical Methods for Singularly Perturbed Differential Equations. Springer-Verlag, Berlin (2008)
4. Lange, C.G., Miura,R.M.: Singular perturbation analysis of boundary-value problems for differential-difference equations. SIAM J. Appl. Math. **42**, 502–531 (1982)
5. Ansari, A.R., Bakr, S.A., Shishkin,G.I.: A parameter-robust finite difference method for singularly perturbed delay parabolic partial differential equations. J. Comput. Appl. Math. **205**, 552–566 (2007)
6. Das,A., Natesan,S.: Second-order uniformly convergent numerical method for singularly perturbed delay parabolic partial differential equations. Internat. J. Comput. Math. **95(3)**, 490–510 (2018)
7. Gowrisankar, S., Natesan, S.: ε–Uniformly convergent numerical scheme for singularly perturbed delay parabolic partial differential equations. Internat. J. Comput. Math. **94(3)**, 902–921 (2017)
8. Bansal, K., Sharma,K.K.: Parameter uniform numerical scheme for time dependent singularly perturbed convection-diffusion-reaction problems with general shift arguments. Numer. Algor. **75(1)**, 113–145 (2017)
9. Bansal, K., Rai, P., Sharma,K.K.: Numerical treatment for the class of time dependent singularly perturbed parabolic problems with general shift arguments. Diff. Equ. and Dyn. Sys. **25(2)**, 327–346(2017)
10. Nageshwar Rao, R., Chakravarthy, P. P.: A fitted numerov method for singularly perturbed parabolic partial differential equations with a small negative shift arising in control theory, Numer. Math. Theor. Meth. Appl. **7(1)**, 23–40 (2014)
11. Bakhvalov, N.S.: On the optimization of the methods for solving boundary value problems in the presence of boundary layers, Zh. Vychisl. Mater. Fiz. **9**, 841–859 (1969)
12. Gartland, E.C.: Graded-mesh difference schemes for singularly perturbed two-point boundary value problems. Math. Comput. **51(184)**, 631–657 (1988)
13. Miller, J. J. H., Riordan, E.O., Shishkin, I.G.: Fitted numerical methods for singular perturbation problems. Word Scientific, Singapore (1996)
14. Protter, M.H., Weinberger, H.F.: Maximum Principles in Differential Equations. Prentice Hall, Englewood Cliffs, NJ (1967)
15. Tian, H.: Numerical treatment of singularly perturbed delay differential equations. Ph.D. thesis, University of Manchester (2000)
16. Kumar, V., Srinivasan,B.: An adaptive mesh strategy for singularly perturbed convection diffusion problems. Appl. Math. Model. **39**, 2081–2091 (2015)
17. Doolan, E. R., Miller, J. J. H., Schilders, W. H. A.: Uniform numerical methods for problems with initial and boundary layers. Boole Press, Dublin (1980)

Part VI
Fluid Dynamics

Steady Finite-Amplitude Rayleigh-Bénard-Taylor Convection of Newtonian Nanoliquid in a High-Porosity Medium

P. G. Siddheshwar and T. N. Sakshath

Abstract Two-dimensional, steady, finite-amplitude Rayleigh-Bénard-Taylor convection of a Newtonian nanoliquid-saturated porous medium is studied using rigid-rigid isothermal boundary condition. The nanoliquid is assumed to conform to a single-phase description and occupies a loosely packed porous medium. Critical Rayleigh number and Nusselt number as functions of various parameters are analyzed, and this is depicted graphically. A non-zero Taylor number demands a higher temperature difference between the horizontal boundaries compared to that of a zero Taylor number case in order to initiate instability in the system and thus inhibits advection of heat. The isothermal boundaries of the rigid-rigid type do not allow as much heat to pass through as that by the free-free type, and hence we see a reduced heat transfer situation in the former case.

Keywords Nanoliquid · Rayleigh-Bénard convection · Rotation · Porous medium · Linear · Non-linear · Stability · Single-phase

Nomenclature

Greek and Latin symbols

α	Thermal diffusivity of the nanoliquid-saturated medium	A,B,C,D,E	Amplitudes of convection
β	Thermal expansion coefficient of the nanoliquid- saturated medium	C_p	Specific heat at constant pressure of nanoliquid-saturated medium
χ	Nanoparticle volume fraction	g=(0,0,-g)	Acceleration due to gravity
ΔT	Temperature difference	K	Permeability of the medium

P. G. Siddheshwar (✉) · T. N. Sakshath
Department of Mathematics, Bangalore University, Bangalore, India
e-mail: pgsiddheshwar@bub.ernet.in; sakshathtn@bub.ernet.in

B. Rushi Kumar et al. (eds.), *Applied Mathematics and Scientific Computing*,
Trends in Mathematics, https://doi.org/10.1007/978-3-030-01123-9_9

Λ	Brinkman number	k	Thermal conductivity of the nanoliquid-saturated medium
μ	Dynamic viscosity of the nanoliquid	M	Ratio of specific heats
μ'	Dynamic viscosity of the nanoliquid-saturated medium	Nu	Nusselt number of the nanoliquid-saturated medium
ν	Wave number	p	Pressure
Ω	Angular velocity	$\overrightarrow{\mathbf{q}} = u\hat{i} + v\hat{j} + w\hat{k}$	velocity vector
ϕ	Porosity	Ra	Rayleigh number of the nanoliquid-saturated medium
ψ	Dimensional stream function	Ta	Taylor number
ρ	Density of the nanoliquid-saturated medium	x,X	Dimensional and dimensionless horizontal coordinates
σ^2	Porous parameter	z,Z	Dimensional and dimensionless vertical coordinates
Θ	Non-dimensional temperature	h	Distance between the plates

Subscripts and Superscripts

0	Reference value	np	Nanoparticle
1	Liquid property in porous medium	s	Solid
b	Basic state	$'$	Perturbed quantity
c	Critical	FF	Free-free boundaries
l	Base liquid	RR	Rigid-rigid boundaries
nl	Nanoliquid		

1 Introduction

The practical importance of Rayleigh-Bénard convection in a clear fluid and in a porous medium is now well known [5, 10]. The effect of rotation is known to have a significant impact on the flow in a porous medium. The effect of rotation on the onset of convection and heat transfer using a local thermal equilibrium (LTE)

model is investigated in many works including those of Riahi [11] and Vadasz [15]. Subsequently a number of researchers have also studied various aspects of the problem both experimentally and theoretically [2, 8] in a clear fluid. The thermal instabilities of a fluid contained in a rotating system were studied by Busse [4]. Desaive et al. [7] studied the onset of stationary convection in a rotating porous layer.

Several works considering stability analysis in nanoliquid-saturated rotating porous layer have been reported [1, 3, 13, 14]. The thermal instability in a nanoliquid-saturated rotating porous layer was studied by Bhadauria and Agarwal [3] by considering the effect of thermophoresis and Brownian motion. Similar study considering an anisotropic porous layer was carried out by Agarwal et al. [1]. Linear and nonlinear realm of Rayleigh-Bénard-Taylor convection in a Newtonian nanoliquid and nanoliquid-saturated high-porosity medium was conducted by Siddheshwar and Sakshath [13, 14].

The following unconsidered aspects are investigated in the problem:

1. The onset of Rayleigh-Bénard-Taylor convection and quantification of heat transport in nanoliquid-saturated medium using rigid-rigid isothermal boundaries.
2. The results on Rayleigh-Bénard-Taylor convection of Newtonian base liquids
3. Regulation of the residence time of heat in the system using nanoparticles and porous matrix

2 Mathematical Formulation

The schematics of the physical system and the coordinate system are illustrated in Fig. 1. The system is rotated with constant angular velocity $\overrightarrow{\Omega}$.

The dimensionless forms of governing equations for the problem are:

$$a_1 \nabla^4 \Psi - a_1^2 Ra \frac{\partial \Theta}{\partial X} - a_1 \sigma^2 (\nabla^2 \Psi) + a_1 \sqrt{Ta} \frac{\partial V}{\partial Z} = 0, \tag{1}$$

$$-\frac{\partial \Psi}{\partial X} + a_1 M \nabla^2 \Theta + \frac{\partial (\Psi, \Theta)}{\partial (X, Z)} = 0, \tag{2}$$

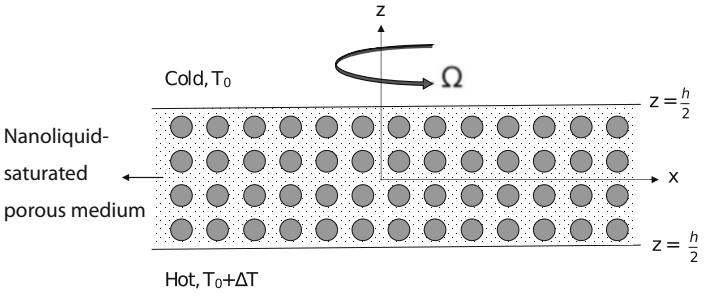

Fig. 1 Schematic representation of Rayleigh-Bénard-Taylor convection of Newtonian nanoliquid

$$\Lambda\nabla^2 V - \sigma^2 V - \sqrt{Ta}\frac{\partial \Psi}{\partial Z} + \frac{1}{Pr\phi}\frac{1}{a_1}\frac{\partial(\Psi, V)}{\partial(X, Z)} = 0, \tag{3}$$

where V is the y-component of velocity which varies along x and z directions:

$$a_1 = \frac{\alpha}{\alpha_1}(\text{thermal diffusivity ratio}),\ \Lambda = \frac{\mu'}{\mu}(\text{ratio of viscosities}),$$

$$\sigma^2 = \frac{h^2}{K}(\text{porous parameter}),\ Ra = \frac{(\rho\beta)h^3 g\Delta T}{\mu\,\alpha}(\text{effective Rayleigh number}),$$

$$Ta = \left(\frac{2\rho\Omega h^2}{\phi\mu}\right)^2(\text{modified Taylor number}),\ Pr = \frac{\mu}{\rho\alpha}(\text{Prandtl number}).$$

In the next section, we make a linear stability analysis and study the onset of convection.

2.1 *Linear Stability Analysis for Marginal Stationary Convection for Isothermal Rigid-Rigid Boundaries*

The isothermal rigid-rigid boundaries satisfy:

$$\Psi = \frac{\partial \Psi}{\partial Z} = \Theta = V = 0\ at\ Z = \pm\frac{1}{2}. \tag{4}$$

The normal mode solution for solving eigen boundary value problem is:

$$\left.\begin{aligned} \Psi &= A\ sin(\nu X)\ (C_f)_e(Z), \\ \Theta &= B\ cos(\nu X)\sin\left[\pi\left(Z+\frac{1}{2}\right)\right], \\ V &= D\ sin(\nu X)\ sin\left[2\pi\left(Z+\frac{1}{2}\right)\right], \end{aligned}\right\}, \tag{5}$$

where A, B, and D are the amplitudes, ν is the wave number, $(C_f)_e(Z)$ is the Chandrasekhar function (even solution) [5, 6, 9], and μ_1=4.73004074. Substituting Eq. (5) in the nondimensional form of the governing Eqs. (1)–(3) and following the standard orthogonalization procedure, the critical value of nanoliquid Rayleigh number for stationary onset can be arrived at in the form:

$$\begin{aligned} Ra_c^{RR} = {} & \frac{M\delta_c^2\left(F_1\Lambda\left(\mu_1^4+\nu_c^4\right)+F_2\mu_1^2\left(2\Lambda\nu_c^2+\sigma^2\right)+F_1\nu_c^2\sigma^2\right)}{2F_3^2\nu_c^2} \\ & + \frac{M\delta_c^2 F_4^2 \mathrm{Ta}}{\pi^2 F_3^2\nu_c^2\left(\Lambda\nu_c^2+4\pi^2\Lambda+\sigma^2\right)},\ (\delta_c^2 = \nu_c^2+\pi^2), \end{aligned} \tag{6}$$

$$\text{where } F_1 = \frac{1}{1+\cos(\mu_1)} - \frac{\tan\left(\frac{\mu_1}{2}\right)}{\mu_1} + \frac{1}{1+\cosh(\mu_1)} - \frac{\tanh\left(\frac{\mu_1}{2}\right)}{\mu_1}, \tag{7}$$

$$F_2 = \frac{1}{1+\cos(\mu_1)} + \frac{\tan\left(\frac{\mu_1}{2}\right)}{\mu_1} - \frac{1}{1+\cosh(\mu_1)} - \frac{\tanh\left(\frac{\mu_1}{2}\right)}{\mu_1}, \tag{8}$$

$$F_3 = \frac{4\pi\mu_1^2}{\pi^4 - \mu_1^4},\ F_4 = \frac{4\pi^2\mu_1 \tan\left(\frac{\mu_1}{2}\right)}{4\pi^2 - \mu_1^2} + \frac{4\pi^2\mu_1 \tanh\left(\frac{\mu_1}{2}\right)}{4\pi^2 + \mu_1^2}. \tag{9}$$

The nonlinear analysis will now be used to study the heat transport.

2.2 Weakly Nonlinear Stability Analysis

The truncated representation for making a weakly nonlinear analysis for rigid-rigid, isothermal boundaries is:

$$\left.\begin{aligned} \Psi &= A\ sin(v_c X)\ (C_f)_e(Z), \\ \Theta &= B\ cos(v_c X)\ sin\left[\pi\left(Z+\frac{1}{2}\right)\right] - C\ sin\left[2\pi\left(Z+\frac{1}{2}\right)\right], \\ V &= D\ sin(v_c X)\ sin\left[2\pi\left(Z+\frac{1}{2}\right)\right] + E\ sin(2v_c X) sin\left[\pi\left(Z+\frac{1}{2}\right)\right]. \end{aligned}\right\} \tag{10}$$

Substituting Eq. (10) into Eqs. (1)–(3) and using the orthogonality condition with the eigen functions on the resulting equations, we get a system of four algebraic equations whose solutions are:

$$A^2 = \frac{8M^2\pi^2\delta_c^2 a_1^2 r}{v_c^2 F_5^2}\left[1 - \frac{1}{r}\right],\ B = \frac{2v_c F_3}{M a_1 \delta_c^2 r} A, \tag{11}$$

$$C = \frac{F_3 F_5 v_c^2}{4M^2\pi^2 a_1^2 \delta_c^2 r} A^2 = \frac{2F_3}{F_5}\left[1 - \frac{1}{r}\right],\ D = \frac{2F_4\sqrt{\mathrm{Ta}}}{\pi\Lambda\left(v_c^2 + 4\pi^2\right) + \pi\sigma^2} A,$$

where $r = \dfrac{Ra}{Ra_c^{RR}}$ is the scaled Rayleigh number, F_1, F_2, F_3, *and* F_4 are given by Eqs. (7)–(9) (12)

$$\text{and } F_5 = \frac{16\pi^2\mu_1^2\left(\mu_1^4 + 39\pi^4\right)}{\mu_1^8 - 82\pi^4\mu_1^4 + 81\pi^8}. \tag{13}$$

We next calculate the Nusselt number.

2.3 Nusselt Number

The amount of heat transport by Taylor-Bénard convection for rigid-rigid isothermal boundary can be written down in terms of a Nusselt number, Nu, given by:

$$Nu = 1 + \frac{\text{Heat transport by advection}}{\text{Heat transport by molecular diffusion}}.$$

The Nusselt number for rigid-rigid, isothermal boundaries is given by:

$$Nu^{RR} = 1 + 2\left(\frac{2\pi F_3}{F_5}\right)\frac{k}{k_1}\left[1 - \frac{1}{r}\right], \tag{14}$$

where $F_3 and F_5$ are given by Eqs. (9) and (13) and r is given by (12).

In the succeeding section, the results obtained are discussed and made some conclusions.

3 Results and Discussion

The thermophysical properties of ethylene glycol [12] as the base liquid, copper [12] as the nanoparticle, and 30% glass fiber-reinforced polycarbonate porous material [16] are considered. The thermophysical properties of ethylene glycol-copper-saturated porous medium is calculated, and the same is tabulated in Tables 1 and 2.

The linear and nonlinear realms of two-dimensional Rayleigh-Bénard-Taylor convection of a Newtonian nanoliquid in a high-porosity medium are investigated. Figure 2a demonstrates the fact that increasing the rotation rate decreases the heat transport. This is because the creation of the y-component V uses up some energy and thereby leads to delayed onset.

We also infer Ra_c increases with increase in Λ, and this result is depicted in Fig. 2b. Increase in the value of Λ signifies decrease in the value of permeability (or porosity), and this means less space is available for the nanoliquid to flow. Hence

Table 1 Thermophysical properties of 30% glass fiber-reinforced polycarbonate porous material at 300 K [16]

ρ_s [kg m^{-3}]	$(C_p)_s$ [J/kg K]	k_s [W/m K]	α_s [m^2 s^{-1} $\times$ 10^7]	ϕ
1430	1130	0.24	1.4852	0.88

Table 2 Thermophysical properties of ethylene glycol-copper-saturated porous medium at 300 K for volume fraction, $\chi = 0.06$. and $\phi = 0.88$

ρ [kg/m^3]	C_p [J/kg K]	k [W/m K]	β [K^{-1} $\times$ 10^5]	μ' [kg/m s]	α [m^2 s^{-1} $\times$ 10^7]	(ρC_p) [J/m^3 K $\times$10^{-6}]	$(\rho\beta)$ [kg/m^3 K]
1565.09	1662.34	0.29294	39.17174	0.02522673	1.12545	2.60172	0.613073

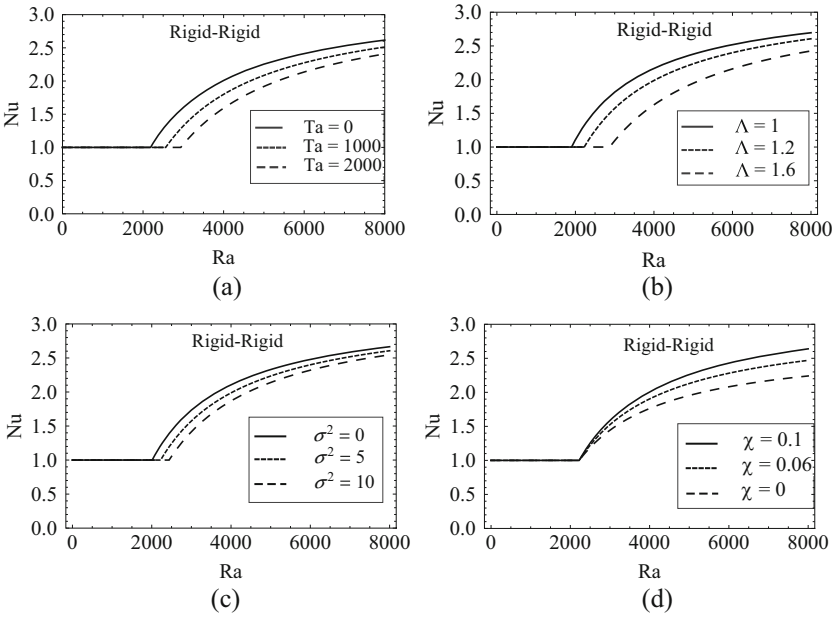

Fig. 2 Variation of Nusselt number, Nu with Rayleigh number, Ra for different values of (**a**) Taylor number, Ta, for Brinkman number, Λ=1.2, porous parameter, σ^2=5, volume fraction, χ=0.06 and porosity, ϕ=0.88. (**b**) Λ, for σ^2=5, χ=0.06, Ta=100 and ϕ=0.88. (**c**) σ^2, for Λ=1.2, χ=0.06, Ta=100 and ϕ=0.88. (**d**) χ, for Λ=1.2, σ^2=5, Ta=100 and ϕ=0.88

this results in delayed onset. The Nusselt number decreases with increase in Λ which is also depicted in Fig. 2b. The reason behind this is similar to the one explained in the context of Ra_c.

The increase in the value of Ra_c with increase in σ^2 is shown in Fig. 2c. The porous medium is a bad conductor of heat compared to the nanoliquid, and this implies larger Ra_c, thereby slowing down of the flow and delayed onset. The Nusselt number decreasing with increasing value of σ^2 is also depicted in Fig. 2c. The reason behind this is similar to the one explained in the context of Ra_c.

From Fig. 2d, it is clear that Ra_c decreases as χ increases as is to be expected. This implies that advanced onset of convection with increase in χ leads to an enhanced heat transport situation.

4 Conclusion

1. The critical values of Ra and Nu of the nanoliquid-saturated porous medium in free-free [13] and rigid-rigid boundaries vary as shown below:
   $Ra_c^{FF} < Ra_c^{RR}$, $Nu^{FF} > Nu^{RR}$.

2. Regulation of the residence time of heat energy can be made by considering ethylene glycol as the base liquid, copper as the nanoparticle, and glass fiber-reinforced polycarbonate porous material.
3. The effect of increasing Λ, σ^2, and Ta on the onset of convection leads to a "stabilized system," and χ has the opposite effect.

Acknowledgements One of the authors (TNS) would like to thank the Department of Backward Classes Welfare, Government of Karnataka, for providing fellowship to carry out his research work. The authors would like to thank Bangalore University for their support.

References

1. Agarwal, S., Bhadauria, B. S., Siddheshwar, P. G.: Thermal instability of a nanofluid saturating a rotating anisotropic porous medium. Spec. Topics Rev. Porous Med. **2(1)**, 53–64 (2011).
2. Balasubramanian, S., Ecke, R. E.: Experimental study of Rayleigh-Bénard convection in the presence of rotation. Int. J. Mater. Mech. Manuf. **1**, 148–152 (2013).
3. Bhadauria, B. S., Agarwal, S.: Natural convection in a nanofluid saturated rotating porous layer: A nonlinear study. Transp. Porous Med. **87**, 585–602 (2011).
4. Busse, F. H.: Thermal Convection in rotating systems. Proc. US Natl. Congr. Appl. Mech. Amer. Soc. Mech. Eng. 299–305 (1982).
5. Chandrasekhar, S.: Hydrodynamic and Hydromagnetic Stability. Clarendon Press, London (1961).
6. Chandrasekhar, S., Reid, W. H.: On the expansion of functions which satisfy four boundary conditions. Proc. Natl. Acad. Sci. U. S. A. **43**, 521–527 (1957).
7. Desaive, T., Hennenberg, M., Lebon, G.: Thermal instability of a rotating saturated porous medium heated from below and submitted to rotation. The Eur. Phys. J. B. **29**, 641–647 (2002).
8. Lopez, J. M., Marques, F.: Centrifugal effects in rotating convection: nonlinear dynamics. J. Fluid Mech. **628**, 269–297 (2009).
9. Nagata, M.: Bifurcations at the Eckhaus points in two-dimensional Rayleigh-Bénard convection. Phys. Rev. E. **52**, 6141–6145 (1995).
10. Nield, D. A., Bejan, A.: Convection in Porous Media. Third Edition, Springer Science and Business Media, New York (2006).
11. Riahi, D. H.: The effect of Coriolis force on nonlinear convection in a porous medium. Int. J. Math. Math. Sci. **17(3)**, 515–536 (1994).
12. Siddheshwar, P. G., Meenakshi, N.: Amplitude equation and heat transport for Rayleigh-Bénard convection in Newtonian liquids with nanoparticles. Int. J. Appl. Comput. Math. **2**, 1–22 (2015).
13. Siddheshwar, P. G., Sakshath, T. N.: Rayleigh-Bénard convection of Newtonian nanoliquids in a saturated, rotating high porous medium. Math. Sci. Int. Res. J. **6(1)**, 35–38 (2017).
14. Siddheshwar, P. G., Sakshath, T. N.: Rayleigh-Bénard-Taylor convection of Newtonian nanoliquid. WASET. Int. J. Mech. Aero. Ind. Mech. Manuf. Eng. **11(6)**, 1131–1135 (2017).
15. Vadasz, P.: Coriolis effect on gravity-driven convection in a rotating porous layer heated from below. J. Fluid Mech. 376, 351–375 (1998).
16. https://www.matbase.com/material-categories/natural-and-synthetic-composites/polymer-matrix-composites-pmc/reinforced-polymers/material-properties-of-polycarbonate-30-percent-glass-fiber-reinforced-pc-gf30.html.

MHD Three Dimensional Darcy-Forchheimer Flow of a Nanofluid with Nonlinear Thermal Radiation

Nainaru Tarakaramu, P. V. Satya Narayana, and B. Venkateswarlu

Abstract The numerical analysis of 3D magnetohydrodynamic Darcy-Forchheimer nanofluid flow with nonlinear thermal radiation is explored. Utilizing suitable similarity transformations, the governing PDEs are transformed into nonlinear ODEs. The resulting equations are then solved numerically by the most robust shooting technique with RK method of fourth order. The effect of various parameters like radiation, temperature ratio, Forchheimer and porosity parameters on $\theta(\eta)$ and $\phi(\eta)$, skin friction coefficient, and rate of heat transfer is discussed graphically. It is observed that the heat transfer rate reduces and skin friction coefficient increases for the rise of F_r and λ.

Keywords MHD · Nanofluid · Nonlinear thermal radiation · Darcy-Forchheimer porous medium

1 Introduction

The nanofluid technology is one of the effective fields which is used in industrial as well as engineering applications. Nanofluids are dilute suspensions of fibers and particles of nanosize submerged in liquids, and these nanoliquids change the thermal performance. The thermal conductivity is the most important in various physical implications because the thermal conductivity of the solids is higher than liquids. Choi [1] studied the enhancement of heat transfer based on the thermal conductivity of nanofluids. Theoretical and experimental reviews on nanofluids were presented by Wang and Mujumdar [2, 3], and Ahn and Kim [4]. Cai et

N. Tarakaramu · P. V. Satya Narayana (✉)
Department of Mathematics, School of Advanced Sciences, Vellore Institute of Technology, Vellore, India
e-mail: nainaru.tarakaramu@vit.ac.in; psatya@vit.ac.in

B. Venkateswarlu
Department of Mathematics, Madanapalli Institute of Technology & Science, Madanapalli, Andhra Pradesh, India

B. Rushi Kumar et al. (eds.), *Applied Mathematics and Scientific Computing*, Trends in Mathematics, https://doi.org/10.1007/978-3-030-01123-9_10

Nomenclature	
a, b constants	Sc Schmidt number= $\frac{\upsilon}{D_B}$
u, v, w Velocity components along x, y, respectively	α Ratio parameter (b/a)
K Permeable of porous medium	C_w Variable concentration $(Kg\,m^{-3})$
M Magnetic field=$\frac{\sigma B_0^2}{\rho_f a}$	D_T Thermophoresis diffusion $(m^2\,.s^{-1})$
T_∞ Ambient fluid temperature	K^* Mean absorption coefficient
h_f Heat transfer coefficient	T_f Temperature of hot fluid
N_t Thermophoresis parameter=$\frac{(\rho C)_p D_\infty C_\infty}{(\rho C)_f \upsilon}$	Greek symbols
Nu_x Nusselt number	υ Kinematic viscosity $= \frac{\mu}{\rho_f}$
N_b Brownian motion coefficient $=\frac{(\rho C)_p D_T (T_f - T_\infty)}{(\rho C)_f \upsilon T_\infty}$	C_∞ Uniform ambient concentration $(Kg\,m^{-3})$
C Nanoparticle volume fraction	θ Dimensionless temperature
C_f Skin friction coefficient	$(\rho c)_p$ Heat capacity of the nanoparticle material $\left(Jm^3K\right)$
F_r Inertia coefficient of porous medium $F_r = \frac{C_b}{(K)^{1/2}}$	ϕ Dimensionless concentration
α_m Thermal diffusion=$\frac{k}{(\rho C)_f}$	F Forchheimer
T Fluid temperature (K)	η Similarity variable
λ Porosity parameter=$\frac{\upsilon}{aK}$	ν Kinematic viscosity $(m^2.s^{-1})$
R_d Radiation parameter $\frac{16\sigma^* T_\infty^3}{3(\rho C)_f \alpha_m K^*}$	σ Electrical conductivity $(m^2\,s^{-1})$
Pr Prandtl number=$\frac{\upsilon}{\alpha_m}$	μ Dynamic viscosity of nanofluid $(Ns.m^{-2})$
Re_x and Re_y Reynolds number=$\frac{U_w x}{\upsilon}$ and $\frac{V_w y}{\upsilon}$	σ^* Boltzmann constant $(wm^{-2}K^{-4})$
D_B Brownian diffusion	ρ Fluid density $(Kg.m^{-3})$
γ Biot number=$\frac{h_f}{k_f}\left(\frac{\upsilon_f}{c}\right)^{1/2}$	ρ_f Fluid density
f Dimensionless stream function	μ Dynamic viscosity $(Pa.s^{-1})$
$f^{'}$ Dimensionless velocity	ρ_{nf} Density of nanofluid $(kg.m^{-3})$
C_p Specific heat constant kJ/kgK	Subscripts
B_0 Dimensionless magnetic field	w Wall mass transfer velocity $(m\,s^{-1})$
	∞ Condition at free stream

al. [5] developed the nanofluids and nanoparticles based on fractal approaches. Kakac and Pramuanjaroenkij [6] analyzed the heat transfer enhancement in thermal conductivity due to nanoparticle decomposition. Das [7] studied the influence of heat transfer characteristics of a nanofluid in a rotating system. Later, Narayana et al. [8, 9] examined the heat transfer of a nanofluid flow past a vertical porous plate with different heat and mass transfer effects.

The Darcy-Forchheimer model [10, 11] has many applications in engineering and thermal insulation materials like nuclear waste disposal, petroleum resources, energy storage units, solar receivers, heat exchanger, beds of fossil fuels, and so on. The influence of heterogeneous-homogeneous reactions on Darcy-Forchheimer flow is analyzed numerically by Khan et al. [12], Muhammad et al. [13] and Hayat et al.

[14, 15]. Mahammad et al. [16] presented magnetohydrodynamic flow on non-Darcy porous medium. The authors [17, 18] developed 3D flow on rotational channel in the presence of porous stretching wall. The effect of MHD on different non Newtonian fluid flow was studied numerically by Yousif et al. [19], Satya Narayana et al. [20], and Tarakaramu and Satya Narayana [21].

The objective of present paper is to study the numerical analysis of 3D MHD Darcy-Forchheimer flow of nanofluid over a stretching surface with nonlinear thermal radiation. The governing equations are solved numerically by RK method with the help of shooting scheme. Numerical results are plotted and analyzed for various values of emerging flow parameters.

2 Mathematical Analysis

Assume the steady 3D magnetohydrodynamic flow over stretching surface filled with porous space and the space characterized by Darcy-Forchheimer relation with nonlinear thermal radiation. Choose a Cartesian coordinate system (x, y, z) in which $x-$ and $y-$axes are along the stretchable surface in the direction of the flow and $z-$axis is normal to it. The physical model and coordinate system are shown in Fig. 1. The stretching velocities $U_w(x) = ax$ and $V_w(y) = by$ are along in the directions of x and y. Apply the effect of a constant magnetic field B_0 in the direction of z and perpendicular to the surface (i.e., xy-plane). The surface of the sheet is subjected to the convective boundary conditions. The continuity, momentum, energy, and spice concentration equations in the presence of thermal radiation and magnetic field over a stretching surface can be expressed as

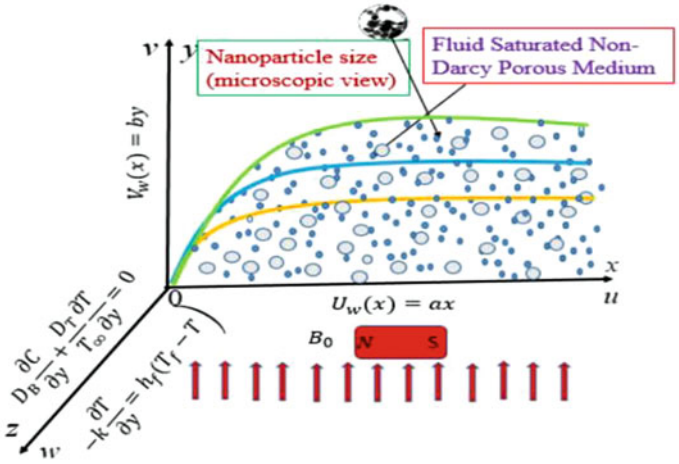

Fig. 1 Flow configuration and coordinate system

$$\frac{\partial u}{\partial x}+\frac{\partial v}{\partial y}+\frac{\partial w}{\partial z}=0 \tag{1}$$

$$u\frac{\partial u}{\partial x}+v\frac{\partial u}{\partial y}+w\frac{\partial u}{\partial z}=\upsilon\left(\frac{\partial^2 u}{\partial z^2}\right)-\frac{\upsilon}{K}u-Fu^2-\frac{\sigma B_0^2}{\rho}u \tag{2}$$

$$u\frac{\partial v}{\partial x}+v\frac{\partial v}{\partial y}+w\frac{\partial v}{\partial z}=\upsilon\left(\frac{\partial^2 v}{\partial z^2}\right)-\frac{\upsilon}{K}v-Fv^2-\frac{\sigma B_0^2}{\rho}v \tag{3}$$

$$u\frac{\partial T}{\partial x}+v\frac{\partial T}{\partial y}+w\frac{\partial T}{\partial z}=\alpha_m\frac{\partial^2 T}{\partial z^2}-\frac{1}{(\rho C)_f}\frac{\partial q_r}{\partial z}+\frac{(\rho C)_p}{(\rho C)_f}\left(D_B\frac{\partial T}{\partial z}\frac{\partial C}{\partial z}+\frac{D_T}{T_\infty}\left(\frac{\partial T}{\partial z}\right)^2\right) \tag{4}$$

$$u\frac{\partial C}{\partial x}+v\frac{\partial C}{\partial y}+w\frac{\partial C}{\partial z}=D_B\frac{\partial^2 C}{\partial z^2}+\frac{D_T}{T_\infty}\left(\frac{\partial^2 T}{\partial z^2}\right) \tag{5}$$

The relevant boundary conditions are

$u=ax, \quad v=by, \quad w=0,$

$-k_f\frac{\partial T}{\partial y}=h_f(T_f-T), \quad D_B\left(\frac{\partial C}{\partial z}\right)+\frac{D_T}{T_\infty}\left(\frac{\partial T}{\partial z}\right)=0 \quad at \quad z=0$

$u\to 0, \quad v\to 0, \quad T\to T_\infty, \quad C\to C_\infty \quad as \quad z\to\infty$

The radiative heat flux q_r according to the Ref. [22] is

$$q_r=-\frac{4\sigma^*}{3K^*}\frac{\partial T^4}{\partial z} \tag{6}$$

Differentiating Eq. (6) with respect to z, we get

$\frac{\partial q_r}{\partial z}=-\frac{16\sigma^*}{3K^*}\frac{\partial}{\partial z}\left(T^3\frac{\partial T}{\partial z}\right)$

Substituting above equation in Eq. (4), we get

$$u\frac{\partial T}{\partial x}+v\frac{\partial T}{\partial y}+w\frac{\partial T}{\partial z}=\alpha_m\frac{\partial^2 T}{\partial z^2}+\frac{1}{(\rho C)_f}\left(\frac{16\sigma^*}{3K^*}\frac{\partial}{\partial z}\left(T^3\frac{\partial T}{\partial z}\right)\right)+\frac{(\rho C)_p}{(\rho C)_f}\left(D_B\frac{\partial T}{\partial z}\frac{\partial C}{\partial z}+\frac{D_T}{T_\infty}\left(\frac{\partial T}{\partial z}\right)^2\right) \tag{7}$$

The similarity transformations are

$u=axf'(\eta), \quad v=ayg(\eta), \quad w=-\sqrt{a\upsilon}(f+g)$

$\phi(\eta)=\frac{C-C_\infty}{C_\infty}, \quad \eta=\sqrt{\frac{a}{\upsilon_f}}z$

In view of above similarity transformations, the Eqs. (2)–(4) and (7) become

$$f'''+f'(f+g)'-\left(f'\right)^2(1+F_r)-f'(M+\lambda)=0 \tag{8}$$

$$g'''+g'(f+g)'-\left(g'\right)^2(1+F_r)-g'(M+\lambda)=0 \tag{9}$$

$$\left(\frac{1+R_d(\theta(\theta_w-1)+1)^3}{\Pr}\right)\theta''+N_b\phi'\theta'+N_t\theta'^2+\theta'(f+g)=0 \tag{10}$$

$$\phi''+Sc\phi'(f+g)+\theta''\left(\frac{N_t}{N_b}\right)=0 \tag{11}$$

Corresponding boundary conditions are

$f=0,\quad f'=1,\quad g=0,\quad g'=\alpha,\quad \theta'=-\gamma(1-\theta),$
$N_b\phi+N_t\theta'=0,\qquad at\quad \eta=0$
$f'\to 0,\quad g'\to 0,\quad \theta\to 0,\quad \phi\to 0,\qquad as\quad \eta\to\infty$

Moreover the skin friction coefficient and Nusselt number are below:

$\sqrt{(Re_x)}C_{fx}=-f''(0)$
$\sqrt{(Re_x)}C_{fy}=-\alpha^{3/2}g''(0)$
$\frac{1}{\sqrt{(Re_x)}}Nu_x=-\left(1+R_d(\theta(\theta_w-1)+1)^3\right)\theta'(0)$

3 Results and Discussion

Equations (8)–(11) are solved numerically by RK method along with eminent shooting procedure. The influence of various parameters on $\theta(\eta)$ and $\phi(\eta)$ profiles is elucidated with the help of graphical illustration from Figs. 2, 3, 4, 5, 6, 7, 8, 9, 10, 11, and 12.

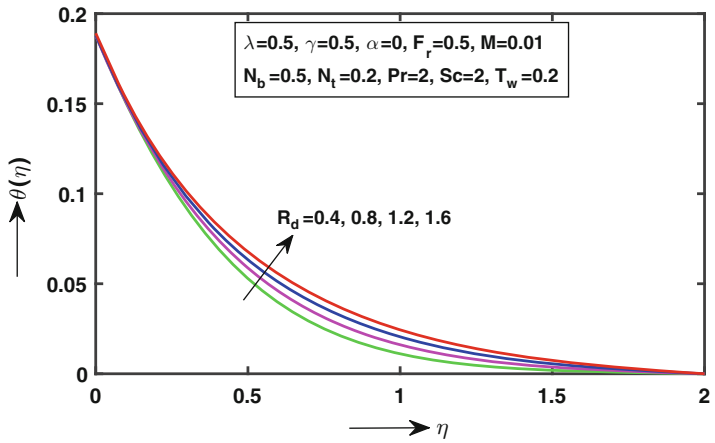

Fig. 2 Influence of R_d on $\theta(\eta)$

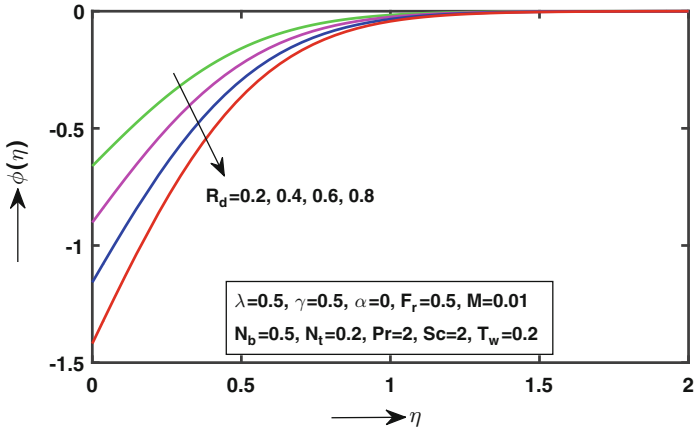

Fig. 3 Influence of R_d on $\phi(\eta)$

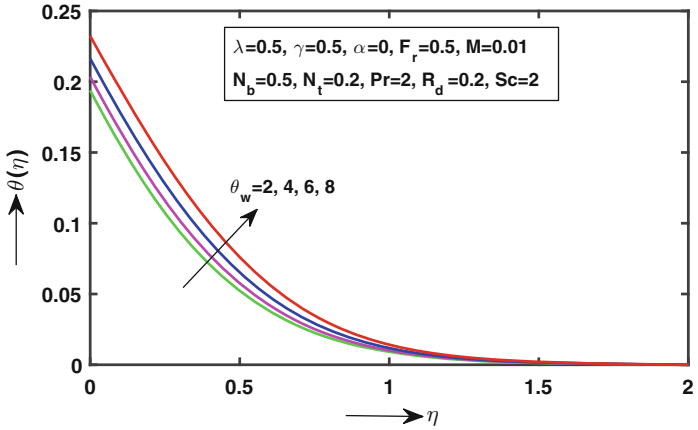

Fig. 4 Influence of θ_w on $\theta(\eta)$

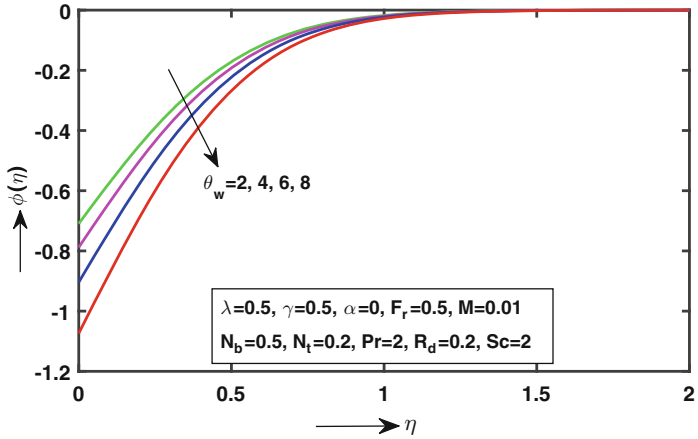

Fig. 5 Influence of θ_w $\phi(\eta)$

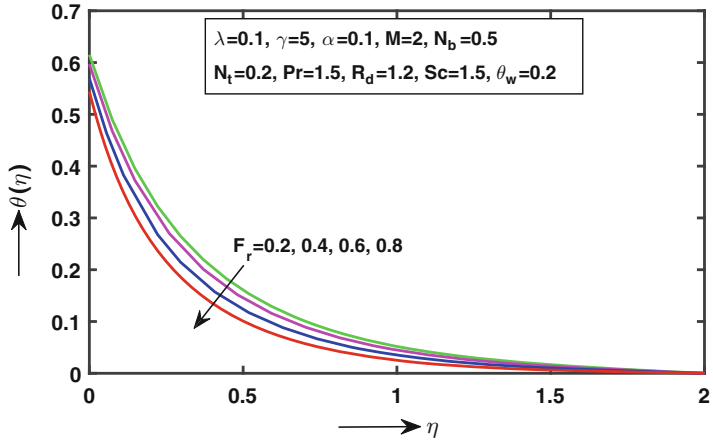

Fig. 6 Influence of F_r $\theta(\eta)$

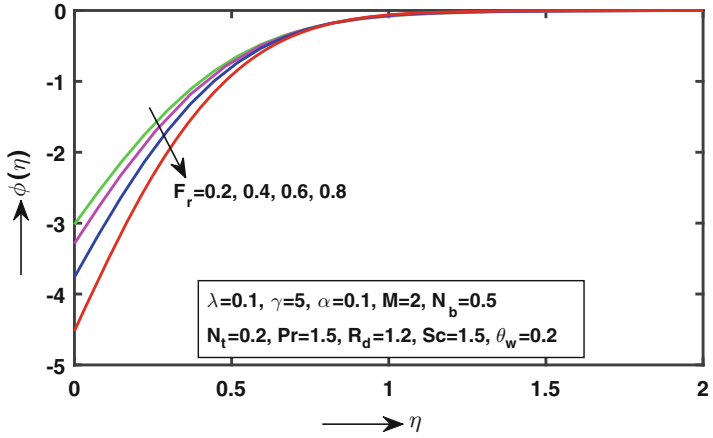

Fig. 7 Influence of F_r on $\phi(\eta)$

The effect of R_d on $\theta(\eta)$ and $\phi(\eta)$ is illustrated in Figs. 2 and 3. It is noted that the increasing values of R_d correspond to results in an enhancement of the fluid temperature and lead to decrease in concentration. Physically, thermal radiation is inversely proportional to the thermal diffusivity.

Figures 4 and 5 depict the $\theta(\eta)$ and $\phi(\eta)$ profiles for various values of temperature ratio parameter θ_w. It is pointed out that the temperature increases for distinct values of θ_w, while opposite effect occurs in concentration.

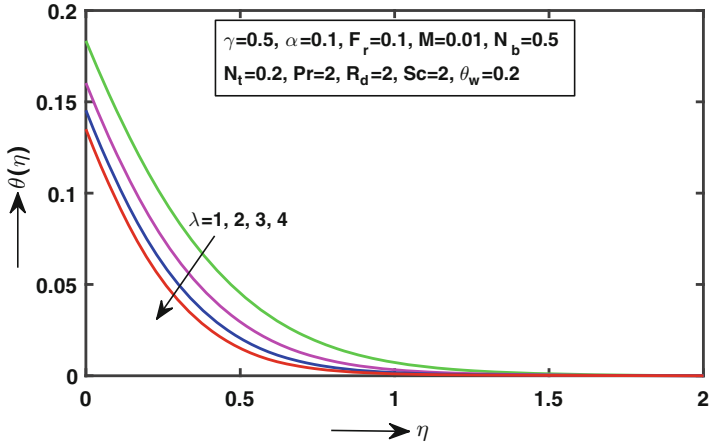

Fig. 8 Influence of λ on $\theta(\eta)$

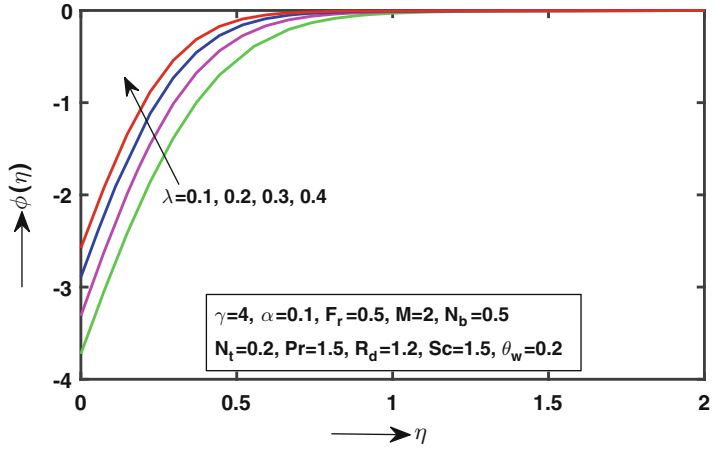

Fig. 9 Influence of λ on $\phi(\eta)$

The variations of temperature and concentration fields with distinct values of inertia coefficient F_r are shown in Figs. 6 and 7. Increasing values of inertia coefficient F_r leads to diminish both the temperature and concentration fields. This is due to the fact that F_r is inversely proportional to permeability porous medium in fluid motion.

Figures 8 and 9 are plotted to examine how the fluid temperature and concentration profiles are affected with the variation in porosity parameter λ. It is clear that the fluid temperature diminishes with rising values of λ; however the reverse trend

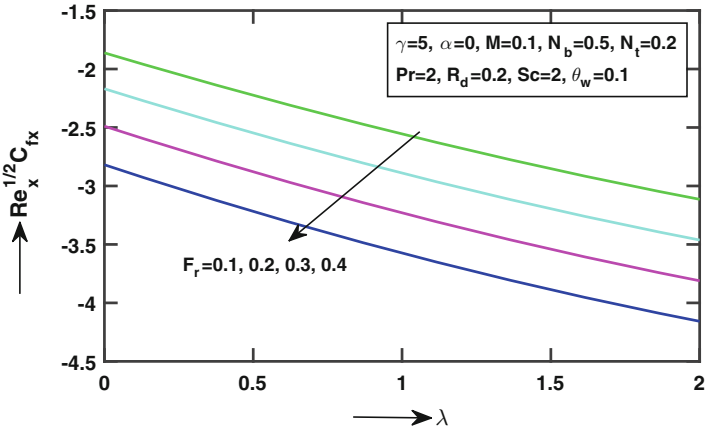

Fig. 10 Influence of F_r via λ on $Re_x^{1/2}C_{fx}$

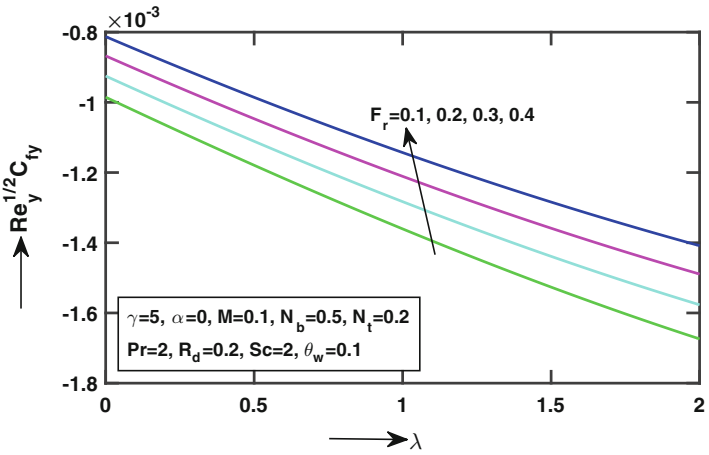

Fig. 11 Influence of F_r via λ on $Re_y^{1/2}C_{fy}$

is observed in the case of concentration. Physically, the strong drag force applied on high speed of porous flow of nanoparticles yields to the weak temperature and high concentration.

Figures 10, 11, and 12 depict the influence of F_r on skin friction coefficients and $Re_x^{-1/2}Nu_x$. It is observed that skin friction coefficient along the x-axis and rate of heat transfer decreased with the rise of F_r values; on the other hand F_r shows opposite trend in case of skin friction coefficient along the y-axis.

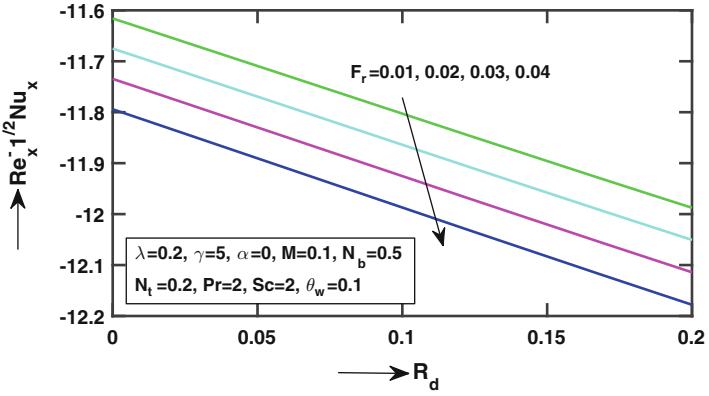

Fig. 12 Influence of F_r via R_d on $Re_x^{-1/2}Nu_x$

4 Conclusion

Three-dimensional MHD Darcy-Forchheimer nanofluid flow over stretching surface with nonlinear thermal radiation and convective condition is investigated in the present work. The present work finds the application in the field of engineering and geophysical such as groundwater, porous pipes, blood flow via arteries or lungs, insulation of granule and fiber, grain storage, casting solidification, vessels of gas-cooled reactors, machines of high-power density, petroleum reservoirs, porous bearings, and gas-cleaning filtration.
The most important conclusions of this study are as follows:

1. The temperature profile increases with increasing values of R_d and θ_w, while it decreases with raising values of F_r and λ.
2. An increasing value of R_d , θ_w, and F_r leads to dwindle in concentration whereas increase with rising values of λ.
3. Both the directions of skin friction coefficient dwindle for distinct ascending large values of λ.

References

1. Choi, S.U.S.: Enhancing thermal conductivity of fluids with nanoparticles, USA ASME, FED 231/MD **66**, 99–105 (1995).
2. Wang, X., Mujumdar, A. S.: A review on nanofluids part-I: Theoretical and numerical investigations. Braz. J. Chem. Eng. **24**, 613–530 (2008).
3. Wang, X., Mujumdar, A. S.: A review on nanofluids part-II: Experiments and applications. Braz. J. Chem. Eng. **24**, 613–530 (2008).
4. Ahn, H. S., Kim, M. H.: A review on critical heat flux enhancement with nanofluids and surface modification. J. Heat Transfer **134**, 1–14 (2012).

5. JCai, J., Hu, X. B., Xiao, B., Zhou, Y., Wei, W.: Recent developments on fractal based approaches to nanofluids and nanoparticle aggregation. Int. J. Heat Mass Transfer **105**, 623–637 (2017).
6. Kakac, S., Pramuanjaroenkij, A.: Review convective heat transfer enhancement with nanofluids. Int. J. Heat Mass Transfer **52**, 3187–96 (2009).
7. Das, K.: Flow and heat transfer characteristics of nanofluids in a rotating frame, Alexandria Eng. J. 1–9 (2014) http://dxdoi.org/10.1016/j.aej.2014.04.003.
8. Satya Narayana, P. V., Akshit, S. M., Ghori, J. P., Venkateswarlu, B.: Thermal radiation effects on an unsteady MHD nanofluid flow over a stretching sheet with non-uniform heat source/sink. J. Nanofluids, **8**, 1–5 (2017).
9. Satya Narayana, P. V.: Lie group analysis for the flow and heat transfer of a nanofluid over a stretching sheet with viscous dissipation, J. Nanofluids, **6**, 1181–1187 (2017).
10. Darcy, H.: Les Fontaines Publiques De La Ville De Dijon, Victor Dalmont, Paris, 1856.
11. Forchheimer, P.: Wasserbewegung durch boden, Zeitschrift, Ver D. Ing. **45**, 1782–1788 (1901).
12. Khan, I.M., Hayat, T., Alsaedi, A.: Numerical analysis for Darcy-Forchheimer flow in presence of heterogeneous-homogeneous reactions. Results Phys. **7**(7), 2644–2650 (2017).
13. Muhammad, T., Alsaedi, A., Hayat, T., Ali Shehzad, S.: A revised model for Darcy-Forchhiemer three-dimensional flow of nanofluid subject to convective boundary condition. Results Phys. **7**, 2791–2797 (2017).
14. Hayat, T., Shah, F., Alsaedi, A., Hussain, Z.: Outcome of homogeneous and heterogeneous reactions in Darcy-Forchheimer flow with nonlinear thermal radiator and convection condition. Results Phys. **7**, 2497–2505 (2017).
15. Hayat, T., Shah, F., Alsaedi, A., Ijaz Khan, M.: Development of homogeneous/heterogeneous reaction in flow based through non-Darcy Forchheimer medium. J. Theoretical Comp. Chemistry, **16**, 5, 1–21 (2017).
16. Mahammad, T., Alsaedi, A., Ali Shehzad, S., Hayat, T.: A revised model for Darcy-Forchhiemer flow of Maxwell nanofluid subject to convective boundary condition. Chi. J. Phys., **55**(9), 63–976 (2017).
17. Durga Prasad, P. Varma, S. V. K. Kiran Kumar, R. V. M. S. S.: MHD free convection and heat transfer enhancement of nanofluids through a porous medium in the presence of variable heat flux. J. Nanofluids, **6**, 1–9 (2017).
18. Gupta, S., Sharma, K.: Numerical simulation for magnetohydrodynamic three dimensional flow of Casson nanofluid with convective boundary conditions and thermal radiation. Eng. Comp. 1–32 (2017).
19. Yousif, M. A., Mahmood, B. A., Rashidi, M. M.: Using differential transform method and Pade approximation for solving MHD three-dimensional Casson fluid flow past a porous linearly stretching sheet. J. Math. Computer Sci., **17**, 169–178 (2017).
20. Satya Narayana, P. V., Tarakaramu, N., Akshit, M.S., Jatin, Ghori, P.: MHD flow and heat transfer of an eyring - powell fluid over a linear stretching sheet with viscous dissipation - a numerical study, Frontiers Heat Mass Transfer, **9**(9), 1–5 (2.017).
21. Tarakaramu, N., Satya Narayan, P. V.: Unsteady MHD nanofluid flow over a stretching sheet with chemical reaction, IOP Conf. Series: Mater. Science Eng., **263**, 1–8 (2017) https://doi.org/10.1088/1757-899X/263/6/062030.
22. Brewster, M. Q.: Thermal Radiative Transfer Properties, Wiley, New York, (1972).

Effect of Electromagnetohydrodynamic on Chemically Reacting Nanofluid Flow over a Cone and Plate

H. Thameem Basha, I. L. Animasaun, O. D. Makinde, and R. Sivaraj

Abstract The intention of this communication is to explore the significance of electromagnetohydrodynamic (EMHD) on the fluid transport properties of a chemically reacting nanofluid with two types of geometries. Simulations have been done to investigate the controlling equations by utilizing Crank-Nicolson scheme. Influence of embedded parameters such as Hartman number, heat source/sink, Brownian diffusion, chemical reaction, and thermophoretic diffusivity is graphically presented. Tables demonstrate the significant impact of sundry parameters on skin friction factor and heat and mass transfer rates. It is observed that the electrical field parameter has high influences on the fluid flow and heat transfer characteristics.

Keywords Non-uniform heat source/sink · Thermophoretic diffusivity · EMHD · Thermal radiation · Chemical reaction

1 Introduction

Nowadays, the use and analysis of the magnetohydrodynamics (MHD) in power industries, medical equipment, biomedical treatment, and thermal systems have gained considerable attention such as magnetic resonance imaging (MRI) equipment, cooling of nuclear reactors, transportation of biological materials, blood

H. Thameem Basha · R. Sivaraj (✉)
Department of Mathematics, School of Advanced Sciences, Vellore Institute of Technology, Vellore, Tamilnadu, India
e-mail: thameembasha.h@vit.ac.in; sivaraj.r@vit.ac.in

I. L. Animasaun
Department of Mathematical Sciences, Federal University of Technology, Akure, Ondo State, Nigeria
e-mail: makinded@sun.ac.za

O. D. Makinde
Faculty of Military Science, Stellenbosch University, Saldanha, South Africa
e-mail: ilanimasaun@futa.edu.ng

B. Rushi Kumar et al. (eds.), *Applied Mathematics and Scientific Computing*, Trends in Mathematics, https://doi.org/10.1007/978-3-030-01123-9_11

pump devices, magnetic compass in airplanes, drug delivery, hyperthermia, and high-temperature plasma. Makinde et al. [1] utilized the Buongiorno model for analyzing the heat and mass transport mechanism of nanofluid under the influence of Lorentz force. Kandasamy et al. [2] analyzed hydromagnetic flow over a vertical surface with solar radiation. The influence of Lorentz force in nanofluid flow subject to Navier slip condition was examined by Khan et al. [3]. Khan and Makinde [4] scrutinized the influence of convective heating in hydromagnetic nanofluid flow over a flat plate. Hayat et al. [5] investigated the MHD peristaltic transport past a symmetric channel. Nadeem et al. [6] simulated 2D Maxwell fluid flow in an extending surface under the influence of a magnetic field. Mabood et al. [7] used RK Fehlberg method to study water-based nanofluid flow in an extending surface with applied magnetic field. Farooq et al. [8] examined the role of different parameters on Brownian motion and thermophoretic diffusivity of MHD viscoelastic nanofluid. Sheikholeslami et al. [9] examined the flow of hydromagnetic nanofluid with radiative heat flux over two types of plates. Rashad et al. [10] investigated the flow of Cu water-based nanofluid in a lid-driven cavity. Srinivas et al. [11] employed the 2D Buongiorno model to examine the heat and mass transfer behavior of hydromagnetic nanofluid in a porous duct. Bondareva et al. [12] reported the influence of Lorentz force on nanofluid flow in a trapezoidal cavity. Sheremet et al. [13] employed the Cu nanoparticle to upsurge the heat transfer in a wavy porous cavity in the presence of Lorentz force. The prime idea of this investigation is to explore the influence of EMHD on chemically reacting nanofluid flow in two different geometries. The Crank-Nicolson scheme has been applied to examine the controlling equations. Such consideration is significant in drug targeting and cancer therapy research. The impacts of diverse pertinent parameters are studied, and the outcomes are indicated graphs and tables.

2 Mathematical Formulation

We examine the two-dimensional (x, y) nanofluid flow over two different geometries (cone and plate) as demonstrated in Fig. 1. In a coordinated system, x and y are the surface of the geometries and normal to the geometries, respectively. The

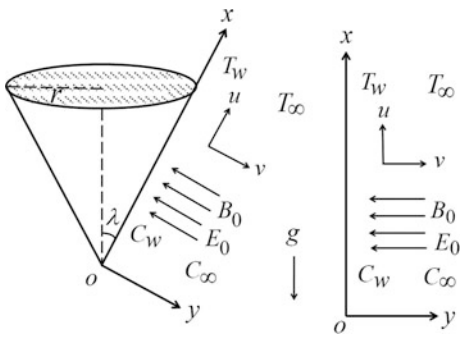

Fig. 1 Geometry of the problem

transverse magnetic field of strength B_0 and electrical field E_0 are implemented in the y-direction. It is assumed that the neighboring (wall) fluid temperature (T_w) and concentration (C_w) are stationary, which are higher than the ambient fluid temperature ($T_w > T_\infty$) and concentration ($C_w > C_\infty$), respectively. The governing equations for the present flow problem are [14–17]

$$\frac{\partial (r^\omega u)}{\partial x} + \frac{\partial (r^\omega v)}{\partial y} = 0 \tag{1}$$

$$\rho_f \left(\frac{\partial u}{\partial t^*} + u\frac{\partial u}{\partial x} + v\frac{\partial u}{\partial y} \right) = \mu \left(\frac{\partial^2 u}{\partial y^2} \right) + \sigma B_0 \left(E_0 - B_0 u \right) + g\left[(1 - C_\infty)\, \rho_f \beta \left(T - T_\infty \right) - \left(\rho_p - \rho_f \right) \left(C - C_\infty \right) \right] cos\lambda \tag{2}$$

$$\left(\rho C_p \right)_p \left(\frac{\partial T}{\partial t^*} + u\frac{\partial T}{\partial x} + v\frac{\partial T}{\partial y} \right) = k \left(\frac{\partial^2 T}{\partial y^2} \right) + \left(\rho C_p \right)_f \left[D_B \frac{\partial C}{\partial y}\frac{\partial T}{\partial y} + \frac{D_T}{T_\infty} \left(\frac{\partial T}{\partial y} \right)^2 \right] + q''' - \frac{\partial q_r}{\partial y} \tag{3}$$

$$\frac{\partial C}{\partial t^*} + u\frac{\partial C}{\partial x} + v\frac{\partial C}{\partial y} = D_B \frac{\partial^2 C}{\partial y^2} + \frac{D_T}{T_\infty}\frac{\partial^2 T}{\partial y^2} - K_r (C - C_\infty) \tag{4}$$

q_r is the radiative heat flux, E_0 is the electrical field, D_B and D_T are the Brownian and thermophoretic diffusivity of a nanoparticle, and K_r is the dimensional chemical reaction parameter.

The transport properties during primary assumptions ($t^* \leq 0$) are

$$u = 0, \quad v = 0, \quad T = T_\infty, \quad C = C_\infty \quad \text{for all} \quad x, y \tag{5}$$

The transport properties at the limits of the geometry at any time ($t^* > 0$) are

$$\begin{aligned} &u = 0, \quad v = 0, \quad T = T_w, \quad C = C_w \quad \text{at} \quad y = 0 \\ &u = 0, \quad T = T_\infty, \quad C = C_\infty \quad \text{at} \quad x = 0 \\ &u \to 0, \quad T \to T_\infty, \quad C \to C_\infty \quad \text{as} \quad y \to \infty \end{aligned} \tag{6}$$

when $\omega = 1$ corresponds to flow over a vertical cone and $\omega = \lambda = 0$ corresponds to flow over a vertical flat plate.

In the energy equation, q''' is considered as

$$q''' = \frac{(Gr)^{1/2}}{L^2} \left(\frac{\gamma_1 L}{\nu\, (Gr)^{1/2}} \left(T_w - T_\infty \right) u + \gamma_2 \left(T - T_\infty \right) \right) \tag{7}$$

Here, $\gamma_1 > 0$ and $\gamma_2 > 0$ indicate the internal heat generation, while $\gamma_1 < 0$ and $\gamma_2 < 0$ indicate the internal heat absorption.

Radiative heat flux in terms of σ^* and k^* are considered as

$$q_r = -\frac{4}{3}\frac{\sigma^*}{k^*}\frac{\partial T^4}{\partial y} = -\frac{16}{3}\frac{\sigma^*}{k^*}T^3\frac{\partial T}{\partial y} \tag{8}$$

where σ^* is the Stefan-Boltzmann constant and k^* is the mean absorption coefficient.

The dimensionless variables are considered as

$$X = \frac{x}{L}, \quad Y = \frac{y}{L}(Gr)^{1/4}, \quad R = \frac{r}{L}, \quad r = xsin(\lambda), \quad U = \frac{uL}{\nu}(Gr)^{-1/2},$$
$$V = \frac{\nu L}{\nu}(Gr)^{-1/4}, \quad t = \frac{\nu t^*}{L^2}(Gr)^{1/2}, \quad \theta = \frac{T - T_\infty}{T_w - T_\infty}, \quad \phi = \frac{C - C_\infty}{C_w - C_\infty} \tag{9}$$

The governing Eqs. (1)−(4) are dimensionalized by means of Eq. (9) and stated below

$$\frac{\partial(R^\omega U)}{\partial X} + \frac{\partial(R^\omega V)}{\partial Y} = 0 \tag{10}$$

$$\frac{\partial U}{\partial t} + U\frac{\partial U}{\partial X} + V\frac{\partial U}{\partial Y} = \frac{\partial^2 U}{\partial Y^2} + M(E_1 - U) + [\theta - N_R\phi]\,cos\lambda \tag{11}$$

$$\frac{\partial \theta}{\partial t} + U\frac{\partial \theta}{\partial X} + V\frac{\partial \theta}{\partial Y} = \frac{1}{P_r}\left(1 + \frac{4}{3}R_d\right)\left(\frac{\partial^2 \theta}{\partial Y^2}\right) + N_B\frac{\partial \phi}{\partial Y}\frac{\partial \theta}{\partial Y}$$
$$+N_T\left(\frac{\partial \theta}{\partial y}\right)^2 + \frac{1}{P_r}(\gamma_1 U + \gamma_2\theta) \tag{12}$$

$$\frac{\partial \phi}{\partial t} + U\frac{\partial \phi}{\partial X} + V\frac{\partial \phi}{\partial Y} = \frac{1}{S_c}\left[\frac{\partial^2 \phi}{\partial Y^2} + \frac{N_T}{N_B}\frac{\partial^2 \theta}{\partial Y^2}\right] - K_R\phi \tag{13}$$

The dimensionless form of the conditions stated in Eqs. (5) and (6) are

$$\begin{aligned}
&t \le 0 : U = 0, \quad V = 0, \quad \theta = 0, \quad \phi = 0 \quad \text{for all} \quad X, Y \\
&t > 0 : U = 0, \quad V = 0, \quad \theta = 1, \quad \phi = 1 \quad \text{at} \quad Y = 0 \\
&\qquad U = 0, \quad \theta = 0, \quad \phi = 0 \quad \text{at} \quad X = 0 \\
&\qquad U \to 0, \quad \theta \to 0, \quad \phi \to 0 \quad \text{as} \quad Y \to \infty
\end{aligned} \tag{14}$$

Gr is the Grashof number, M is the Hartmann number, N_R is the buoyancy ratio parameter, R_d is the thermal radiation parameter, N_B is the Brownian diffusivity, N_T is the thermophoretic diffusivity, K_R is the dimensionless chemical reaction parameter, Sc is the Schmidt number, E_1 is the electrical field parameter, and τ is the ratio between the base fluid and nanoparticle heat capacity that are, respectively, as follows:

$$Gr = \frac{g\beta\,(T_w - T_\infty)\,(1 - C_\infty)\,L^3}{\nu^2}, M = \frac{\sigma B_0^2 L^2}{\nu (Gr)^{1/2} \rho_f}, \alpha = \frac{k}{\left(\rho C_p\right)_p}, P_r = \frac{\nu}{\alpha}$$

$$K_R = \frac{K_r\,(C_w - C_\infty)\,L^2}{\nu\,(Gr)^{1/2}}, Sc = \frac{\nu}{D_B}, E_1 = \frac{E_0 L}{B_0 \nu (Gr)^{1/2}},$$

$$R_d = \frac{4\sigma^* T_\infty^3}{k^* k}, \tau = \frac{\left(\rho C_p\right)_f}{\left(\rho C_p\right)_p}$$

$$N_B = \frac{\tau D_B\,(C_w - C_\infty)}{\nu}, N_T = \frac{\tau D_T\,(T_w - T_\infty)}{\nu},$$

$$N_R = \frac{\left(\rho_p - \rho_f\right)(C_w - C_\infty)}{\beta \rho_f\,(T_w - T_\infty)\,(1 - C_\infty)} \tag{15}$$

The local skin friction factor (Sf_x), Nusselt number (Nu_x), and Sherwood number (Sh_x) are

$$Sf_x = Gr^{3/4}\left(\frac{\partial U}{\partial Y}\right)_{Y=0}, \quad Nu_x = -XGr^{1/4}\left(\frac{\partial \theta}{\partial Y}\right)_{Y=0},$$

$$Sh_x = -XGr^{1/4}\left(\frac{\partial \phi}{\partial Y}\right)_{Y=0} \tag{16}$$

The mean skin friction ($\overline{Sf}$), rate of heat transfer coefficient ($\overline{Nu}$) , and rate of mass transfer coefficient ($\overline{Sh}$) can be written as

$$\overline{Sf} = Gr^{3/4}\int_0^1 \left(\frac{\partial U}{\partial Y}\right)_{Y=0} dX, \qquad \overline{Nu} = -Gr^{1/4}\int_0^1 \left(\frac{\left(\frac{\partial \theta}{\partial Y}\right)_{Y=0}}{\theta_{Y=0}}\right) dX,$$

$$\overline{Sh} = -Gr^{1/4}\int_0^1 \left(\frac{\left(\frac{\partial \phi}{\partial Y}\right)_{Y=0}}{\phi_{Y=0}}\right) dX \tag{17}$$

3 Results and Discussion

The required section is aimed at addressing outcomes of pertinent parameters on velocity (U), temperature (θ) and concentration (ϕ), skin friction, and heat and mass transfer rates for various sundry parameters. Calculations are made for diverse values of M = 0.40, 0.70, 1.0, and 1.2; E_1 = 0.20, 0.40, 0.60, and 0.80; N_B = 0.10, 0.30, 0.50, and 0.70; and N_T = 0.10, 0.30, 0.50, and 0.70. The discretized governing equations are solved by Crank-Nicolson scheme, and the outputs are portrayed in

Table 1 Effect of M, N_B, N_T, and E_1 on $\overline{Sf}$, $\overline{Nu}$ and $\overline{Sh}$

Physical Parameters	Values	$\overline{Sf}\,(Gr^{-3/4})$		$\overline{Nu}\,(Gr^{-1/4})$		$\overline{Sh}\,(Gr^{-1/4})$	
		Plate	Cone	Plate	Cone	Plate	Cone
M	0.10	0.73192	0.45203	0.41495	0.33173	0.54968	0.52260
	0.40	0.75092	0.48620	0.42218	0.34778	0.55413	0.52903
	0.70	0.76743	0.51571	0.42648	0.35836	0.55641	0.53303
	1.0	0.77771	0.53371	0.42847	0.36374	0.55732	0.53498
N_B	0.10	0.73192	0.45203	0.41495	0.33173	0.54968	0.52260
	0.30	0.74738	0.45981	0.37102	0.29265	0.64775	0.58648
	0.50	0.75902	0.46580	0.32807	0.25521	0.67013	0.60096
	0.70	0.76981	0.47138	0.28811	0.22068	0.68149	0.60824
N_T	0.10	0.73192	0.45203	0.41495	0.33173	0.54968	0.52260
	0.30	0.72952	0.45165	0.37842	0.30087	0.38630	0.44010
	0.50	0.72866	0.45207	0.34525	0.27279	0.30992	0.43264
	0.70	0.72915	0.45320	0.31514	0.24724	0.30456	0.48704
E_1	0.20	0.66547	0.37809	0.37862	0.27508	0.52749	0.49970
	0.40	0.73192	0.45203	0.41495	0.33173	0.54968	0.52260
	0.60	0.79807	0.52619	0.44479	0.37458	0.56740	0.54199
	0.80	0.86379	0.59937	0.47057	0.40958	0.58289	0.55914

Table 2 Comparison table

Parameters		$\overline{Nu}\,(Gr^{-1/4})$			$\overline{Sh}\,(Gr^{-1/4})$		
N_B	N_T	Hayth et al. [18]	Sreedevi et al. [19]	Present Study	Hayth et al. [18]	Sreedevi et al. [19]	Present Study
0.30	0.20	0.3842	0.3842	0.3843	0.2336	0.2335	0.2336
0.40	0.25	0.3697	0.3698	0.3696	0.1983	0.1983	0.1982
0.50	0.30	0.3556	0.3556	0.3550	0.1643	0.1644	0.1633

graphs and tables. Table 1 characterizes the average skin friction factor, average Nusselt number, and average Sherwood number for various pertinent parameters. Table 2 demonstrates the perfection of the obtained results of this present analysis by means of a comprehensive comparative study on N_B and N_T with the reported data of Hayat et al. [18] and Sreedevi et al. [19]. Variation of U and θ profiles for diverse values of M is plotted in Fig. 2a, b. The large values of M reduce the fluid U since a resistive force occurs which decelerates motion of the fluid and hence enhances the heat transfer in the thermal boundary layer. Influence of active parameter E_1 on U and θ is portrayed in Fig. 2c, d. From the physical point of view, E_1 promotes the resistive force, which usually declines the frictional resistance. According to this fact, U enhances; however, the reverse situation is observed for θ. Figure 3a, b reveals the effect of N_B on θ and ϕ. The larger values of N_B yield higher random motion of nanoparticle. It means that the θ boundary layer thickness increases and ensures the decay in ϕ boundary layer thickness. Figure 3c, d is demonstrated to investigate the influence of N_T on heat and mass transfer mechanisms. Physically,

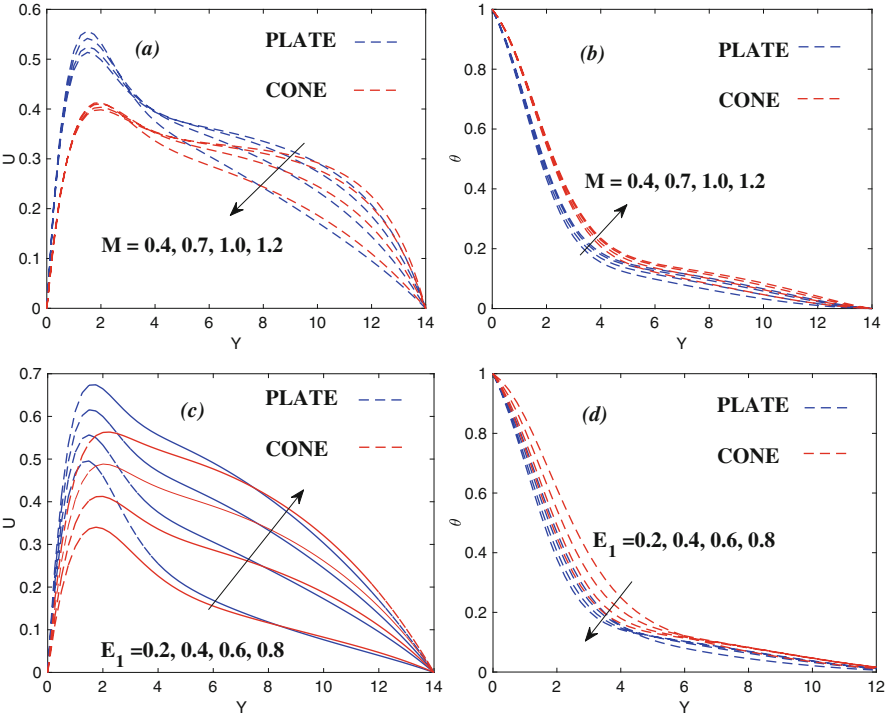

Fig. 2 U and θ for diverse values of M and E_1

as N_T increases, the motion of nanoparticles from hot wall to the cold ambient space will be promoted and hence enhance the heat transfer of nanoparticles. Likewise the motion of nanoparticles from high concentration to low concentration will be promoted and hence enhance the mass transfer of nanoparticles.

4 The Conclusions

A numerical study is performed for analyzing the chemically reacting nanofluid flow with electrohydromagnetic and nonuniform heat sources/sinks over two types of geometries. The key findings are enhancement in θ is observed for larger magnetic number. U boosts for larger E_1, whereas reverse behavior is found in θ. The effect of N_B and N_T on θ is similar and is opposite behavior in ϕ.

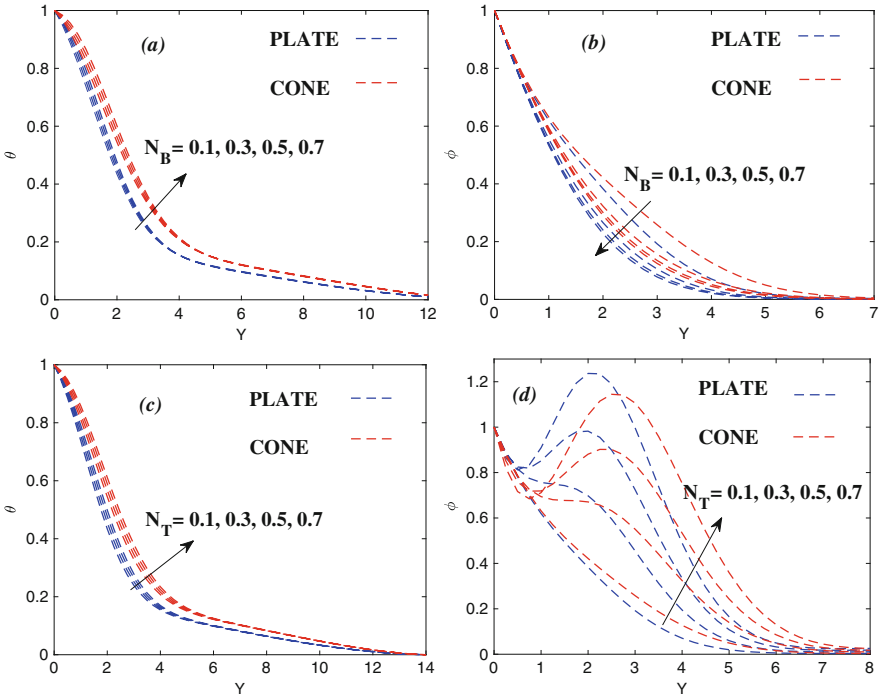

Fig. 3 θ and ϕ for diverse values of N_B and N_T

References

1. O.D. Makinde , W.A.Khan , Z.H.Khan 2013 Buoyancy effects on MHD stagnation point flow and heat transfer of a nanofluid past a convectively heated stretching/shrinking sheet, International Journal of Heat and Mass Transfer, 62:526–533.
2. R. Kandasamy , I.Muhaimi, R. Mohamad 2013 Thermophoresis and Brownian motion effects on MHD boundary-layer flow of a nanofluid in the presence of thermal stratifi cation due to solar radiation, International JournalofMechanicalSciences, 70:146–154.
3. W.A. Khan , O.D. Makinde , Z.H. Khan 2014 MHD boundary layer flow of a nanofluid containing gyrotactic microorganisms past a vertical plate with Navier slip, International Journal of Heat and Mass Transfer 74:285–291.
4. W.A. Khan, O.D. Makinde 2014 MHD nanofluid bioconvection due to gyrotactic microorganisms over a convectively heat stretching sheet, International Journal of Thermal Sciences, 81:118–124.
5. T. Hayat, M. Waqas, M. I. Khan, A. Alsaedi 2016 Analysis of thixotropic nanomaterial in a doubly stratified medium considering magnetic field effects, International Journal of Heat and Mass Transfer 102:1123–1129.
6. S. Nadeem , R.U. Haq, Z.H. Khan 2014 Numerical study of MHD boundary layer flow of a Maxwell fluid past a stretching sheet in the presence of nanoparticles, Journal of the Taiwan Institute of Chemical Engineers 45:121–126.
7. F. Mabood , W.A. Khan , A.I.M .Ismail 2015 MHD boundary layer flow and heat transfer of nanofluids over a nonlinear stretching sheet: A numerical study, Journal of Magnetism and Magnetic Materials 374:569–576.

8. M. Farooq , M.I. Khan, M.Waqas , T.Hayat , A. Alsaedi , M. Imran Khan 2016 MHD stagnation point flow of viscoelastic nanofluid with non-linear radiation effects, Journal of Molecular Liquids 221:1097–1103.
9. M. Sheikholeslami, D.D. Ganji, M.M. Rashidi 2016 Magnetic field effect on unsteady nanofluid flow and heat transfer using Buongiorno model, Journal of Magnetism and Magnetic Materials 416:164–173.
10. A.M. Rashad, M.A. Ismael, A.J. Chamkha, M.A. Mansour 2016 MHD mixed convection of localized heat source/sink in a nanofluid-filled lid-driven square cavity with partial slip, Journal of the Taiwan Institute of Chemical Engineers 68:173–186.
11. S. Srinivas, A.V.lakshmi, A.S. Reddy, T.R.R. Mohan, MHD flow of a nanofluid in an expanding or Contracting porous pipe with chemical reaction and heat source/sink, Propulsion and Power Research 2016;5(2):134–148
12. Bondareva, N.S., Sheremet, M. A., Pop, I., 2015 Magnetic field effect on the unsteady natural convection in a right-angle trapezoidal cavity filled with a nanofluid, International Journal of Numerical Methods for Heat & Fluid Flow, http://dx.doi.org/10.1108/HFF-07-2014-0236
13. M.A. Sheremet, H.F. Oztop, I. Pop K, A. Salem 2016 MHD free convection in a wavy open porous tall cavity filled with nanofluids under an effect of corner heater, International Journal of Heat and Mass Transfer 103:955–964.
14. D. Mythili, R. Sivaraj 2016 Influence of higher order chemical reaction and non-uniform heat source/sink on Casson fluid flow over a vertical cone and flat plate, Journal of Molecular Liquids 216:466–475.
15. R. Sivaraj, B.R. Kumar 2013 Viscoelastic fluid flow over a moving vertical cone and flat plate with variable electric conductivity, International Journal of Heat and Mass Transfer 61: 119–128.
16. B.R. Kumar, R. Sivaraj 2013 Heat and mass transfer in MHD viscoelastic fluid flow over a vertical cone and flat plate with variable viscosity, International Journal of Heat and Mass Transfer 56:370–379.
17. D. Mythili, R. Sivaraj, M. M. Rashidi and Z. Yang 2015 Casson fluid flow over a vertical cone and flat plate with non-uniform heat source/sink and high order chemical reaction, Journal of Naval Architecture and Marine Engineering, http://dx.doi.org/10.3329/jname.v12i2.25269.
18. T. Hayat, M. Imtiaz, A. Alsaedi 2015 Partial slip effects in flow over nonlinear stretching surface, Appl. Math. Mech. -Engl. Ed., https://doi.org/10.1007/s10483-015-1999-7.
19. P. Sreedevi , P.S. Reddy ,A.J. Chamkha 2017 Heat and mass transfer analysis of nanofluid over linear and non-linear stretching surfaces with thermal radiation and chemical reaction, Powder Technology 315:194–204.

Effect of Non-linear Radiation on 3D Unsteady MHD Nanoliquid Flow over a Stretching Surface with Double Stratification

K. Jagan, S. Sivasankaran, M. Bhuvaneswari, and S. Rajan

Abstract The key goal of the article is to examine the non-linear thermal radiation and double stratification effects on 3D MHD convective stream of nanoliquid over a non-linear stretchable surface in a porous medium. Using suitable transformations, the governing systems are converted into ODEs and are solved by using homotopy analysis method (HAM). While increasing thermal and solutal stratification parameter, the temperature decreases. The temperature enhances by raising the values of non-linear thermal radiation. The skin friction coefficient along x- and y-axis, local Nusselt number and Sherwood number are plotted for important parameter involved in the study, and the results are discussed in detail.

Keywords Nanofluid · Stratification · Non-linear thermal radiation · Porous medium · MHD

1 Introduction

The importance of convective stream and thermal transport of nanoliquid is discussed in [1–4]. Hayat et al. [5] studied the non-linear thermal radiation effect on three-dimensional magnetohydrodynamic flow of viscoelastic nanoliquid. Das et al. [6] and Madhu et al. [7] analysed about the influence of thermal radiation on unsteady stream of nanoliquid and Maxwell nanoliquid over a stretching surface. Hayat et al. [8] investigated about the unsteady magnetohydrodynamic flow of nanoliquid with double stratification. The impact of double stratification on mass

K. Jagan
Department of Mathematics, Nandha Engineering College, Erode, Tamil Nadu, India

S. Sivasankaran (✉) · M. Bhuvaneswari
Department of Mathematics, King Abdulaziz University, Jeddah, Saudi Arabia
e-mail: smsivanandam@kau.edu.sa

S. Rajan
Department of Mathematics, Erode Arts and Science College, Erode, Tamil Nadu, India

B. Rushi Kumar et al. (eds.), *Applied Mathematics and Scientific Computing*,
Trends in Mathematics, https://doi.org/10.1007/978-3-030-01123-9_12

and heat transport in unsteady MHD nanoliquid stream over a horizontal surface was studied by Mutuku et al. [9]. In this paper, the examination is made on three-dimensional unsteady MHD convective stream of nanoliquid over a stretchable sheet in a porous medium in the existence of dual stratification and non-linear thermal radiation.

2 Mathematical Formulation

The three-dimensional unsteady electrically conducting nanoliquid flow towards a stretchable sheet in the existence of the applied magnetic field of a constant strength B_0 is considered. At $t = 0$, the velocity components is taken as $v_1 = a_1 x$ and $v_2 = b_1 y$ where v_1 and v_2 are the velocity components along x- and y-axis and a_1 and b_1 are positive constants. Due to the existence of nanoparticles, the thermophoresis and Brownian motion are taken into account. The radiative heat flux is taken as $q_r = -\frac{4\sigma^*}{3k^*}\frac{\partial T^4}{\partial z}$. The ambient temperature and concentration are assumed as $T_\infty = T_0 + d_1 x$ and $C_\infty = C_0 + d_3 x$. The fluid temperature and concentration are considered as $T_w = T_0 + d_2 x$ and $C_w = C_0 + d_4 x$ where d_1, d_2, d_3 and d_4 are dimensional constants. The thermal and concentration stratification effects are considered into account. The governing systems for the analysis can be derived as follows:

$$\frac{\partial v_1}{\partial x} + \frac{\partial v_2}{\partial y} + \frac{\partial v_3}{\partial z} = 0, \tag{1}$$

$$\frac{\partial v_1}{\partial t} + v_1\frac{\partial v_1}{\partial x} + v_2\frac{\partial v_1}{\partial y} + v_3\frac{\partial v_1}{\partial z} = \nu\frac{\partial^2 v_1}{\partial z^2} - \frac{\sigma B_0^2}{\rho}v_1 - \frac{\nu\varphi}{k}v_1, \tag{2}$$

$$\frac{\partial v_2}{\partial t} + v_1\frac{\partial v_2}{\partial x} + v_2\frac{\partial v_2}{\partial y} + v_3\frac{\partial v_2}{\partial z} = \nu\frac{\partial^2 v_2}{\partial z^2} - \frac{\sigma B_0^2}{\rho}v_2 - \frac{\nu\varphi}{k}v_2, \tag{3}$$

$$\frac{\partial T}{\partial t} + v_1\frac{\partial T}{\partial x} + v_2\frac{\partial T}{\partial y} + v_3\frac{\partial T}{\partial z} = \alpha\frac{\partial^2 T}{\partial z^2} + \tau D_B\left(\frac{\partial T}{\partial z}\frac{\partial C}{\partial z}\right) + \frac{\tau D_T}{T_\infty}\left(\frac{\partial T}{\partial z}\right)^2 - \frac{1}{\rho c_p}\frac{\partial q_r}{\partial z}, \tag{4}$$

$$\frac{\partial C}{\partial t} + v_1\frac{\partial C}{\partial x} + v_2\frac{\partial C}{\partial y} + v_3\frac{\partial C}{\partial z} = D_B\frac{\partial^2 C}{\partial z^2} + \frac{D_T}{T_\infty}\frac{\partial^2 T}{\partial z^2}, \tag{5}$$

and the boundary conditions are

$$\begin{aligned} &v_1 = 0,\ v_2 = 0,\ v_3 = 0,\ T = T_\infty,\ C = C_\infty;\ t < 0,\\ &v_1 = v_{1,w} = a_1 x,\ v_2 = v_{2,w} = b_1 y,\ v_3 = 0,\ T = T_w,\ C = C_w,\ z = 0;\ t \geq 0,\\ &v_1 \to 0,\ v_2 \to 0,\ T \to T_\infty,\ C \to C_\infty,\ as\ z \to \infty;\ t \geq 0. \end{aligned} \tag{6}$$

where v_3 is velocity component along z-axis and α, ν, σ, φ, k_1, D_B and D_T are thermal diffusivity, kinematic viscosity, electrical conductivity, porosity, permeability of the porous medium, Brownian motion and thermophoresis coefficient, respectively. The similarity transformations are

$$\eta = z\sqrt{\frac{a_1}{\nu\xi}},\ \xi = 1 - e^{-\tau},\ \tau = a_1 t,\ \ v_1 = a_1 x f',\ v_2 = a_1 y g',$$

$$v_3 = -\sqrt{a_1\,\nu\,\xi}\,(f+g),\, \theta(\eta) = \frac{T - T_\infty}{T_w - T_\infty},\ \phi(\eta) = \frac{C - C_\infty}{C_w - C_\infty}. \tag{7}$$

where prime denotes the derivative with respect to η.

Substituting (7) in (1), (1) is satisfied identically. Substituting (7) in (2) to (6), we get

$$f''' + (\xi - 1)\left[\xi\frac{\partial f'}{\partial \xi} - \frac{\eta}{2}f''\right] - \xi\left[f'^2 - f''(f+g)\right] - \xi\ \left[f'\left(\lambda + M^2\right)\right] = 0, \tag{8}$$

$$g''' + (\xi - 1)\left[\xi\frac{\partial g'}{\partial \xi} - \frac{\eta}{2}g''\right] - \xi\left[g'^2 - g''(f+g)\right] - \xi\ \left[g'\left(\lambda + M^2\right)\right] = 0, \tag{9}$$

$$\left(1 + \frac{4}{3}Rd\right)\theta'' + \frac{4}{3}Rd\left[\theta_w^3\left(3\theta^2\theta'^2 + \theta^3\theta''\right) + 3\theta_w^2\left(2\theta\theta'^2 + \theta^2\theta''\right)\right.$$
$$\left. + 3\theta_w\left(\theta'^2 + \theta\theta''\right)\right] + PrNb\,\theta'\phi' + PrNt\theta'^2 + Pr\,(\xi - 1)\left[\xi\frac{\partial\theta}{\partial\xi} - \frac{\eta}{2}\theta'\right]$$
$$+ Pr\,\xi\left[\theta'(f+g) - f'\theta - S_T f'\right] = 0, \tag{10}$$

$$\phi'' + Sc(\xi - 1)\left[\xi\frac{\partial\phi}{\partial\xi} - \frac{\eta}{2}\phi'\right] + Sc\,\xi\left[\phi'(f+g) - f'\phi - S_P f'\right]$$
$$+ \frac{Nt}{Nb}\theta'' = 0, \tag{11}$$

$$f(\xi,0) = g(\xi,0) = 0,\ f'(\xi,0) = 1,\ \theta(\xi,0) = 1 - S_T,\ \phi(\xi,0) = 1 - S_P,$$

$$g'(\xi,0) = c,\ f'(\xi,\infty) = 0,\ g'(\xi,\infty) = 0,\ \theta(\xi,\infty) = 0,\ \phi(\xi,\infty) = 0. \tag{12}$$

where Pr, M, Sc, c, λ, Nb, Nt, Rd, θ_w, S_T and S_P are Prandtl number, local Hartman number, Schmidt number, stretching ratio, local porosity, Brownian motion, thermophoresis, thermal radiation, temperature ratio, thermal stratification and solutal stratification parameters that are defined as

$$Pr = \frac{\alpha}{\nu},\ M^2 = \frac{\sigma B_0^2}{a_1 \rho},\ Sc = \frac{\nu}{D},\ c = \frac{b_1}{a_1},\ \lambda = \frac{\nu\varphi}{a_1 k_1},\ Nb = \frac{\tau D_B\,(C_w - C_\infty)}{\nu},$$
$$Nt = \frac{\tau D_T\,(T_w - T_\infty)}{\nu T_\infty},\ Rd = \frac{4\sigma^* T_\infty^3}{kk^*},\ \theta_w = \frac{T_w - T_0}{T_\infty},$$
$$S_T = \frac{d_1}{d_2},\ S_P = \frac{d_3}{d_4}. \tag{13}$$

The local skin friction coefficient along x- and y-directions and local Nusselt number are defined as follows.

$$\xi^{\frac{1}{2}} Re_x^{1/2} C_{f_x} = -f''(\xi, 0)\,. \tag{14}$$

$$\xi^{\frac{1}{2}} Re_y^{1/2} C_{f_y} = -g''(\xi, 0)\,. \tag{15}$$

$$\xi^{\frac{1}{2}} Re_x^{-1/2} Nu = -\left(1 + \frac{4}{3} Rd\,(\theta_w)^3\right)\theta'(\xi, 0)\,. \tag{16}$$

$$\xi^{\frac{1}{2}} Re_x^{-1/2} Sh = -\phi'(\xi, 0)\,. \tag{17}$$

where $Re_x = \frac{v_{1,w} x}{\nu}$ and $Re_y = \frac{v_{2,w} y}{\nu}$ are local Reynolds numbers.

3 Solution Procedure

The Eqs. (8) to (12) are solved using HAM by choosing the initial approximation and auxiliary linear operators as

$$f_0(\xi, \eta) = 1 - exp(-\eta), \quad g_0(\xi, \eta) = c\,[1 - exp(-\eta)],$$
$$\theta_0(\xi, \eta) = (1 - S_T)\,exp(-\eta), \quad \phi_0(\xi, \eta) = (1 - S_P)\,exp(-\eta). \tag{18}$$
$$L_f(f) = \frac{d^3 f}{d\eta^3} - \frac{df}{d\eta}, \quad L_g(g) = \frac{d^3 g}{d\eta^3} - \frac{dg}{d\eta},$$
$$L_\theta(\theta) = \frac{d^2\theta}{d\eta^2} - \theta, \quad L_\phi(\phi) = \frac{d^2\phi}{d\eta^2} - \phi. \tag{19}$$

which satisfies the property

$$L_f[A_1 + A_2\,exp(-\eta) + A_3\,exp(\eta)] = 0. \tag{20}$$
$$L_g[A_4 + A_5\,exp(-\eta) + A_6\,exp(\eta)] = 0. \tag{21}$$

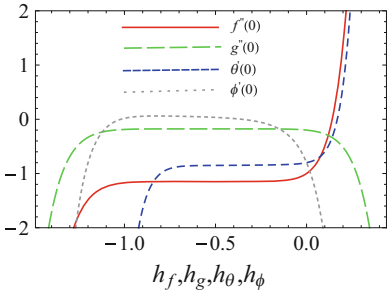

Fig. 1 h-curve for $f''(\xi, 0)$, $g''(\xi, 0)$, $\theta'(\xi, 0)$ and $\phi'(\xi, 0)$

$$L_\theta[A_7\, exp\,(-\eta) + A_8\, exp\,(\eta)] = 0. \tag{22}$$

$$L_\phi[A_9\, exp\,(-\eta) + A_{10}\, exp\,(\eta)] = 0. \tag{23}$$

where $A_1, A_2, \ldots, A_{10}$ are the arbitrary constants.

The resulting equations contain the auxiliary parameters h_f, h_g, h_θ and h_ϕ. The h-curve is plotted for $c = \lambda = M = Nb = Nt = S_T = S_P = 0.2$, $Pr = 1.5$, $Rd = 0.3$, $Sc = 0.5$, $\theta_w = 0.1$ and $\xi = 1$. From Fig. 1, it is clear that the admissible range of h_f, h_g, h_θ and h_ϕ are $-1.0 \leq h_f \leq -0.1, -1.1 \leq h_g \leq 0.0, -0.7 \leq h_\theta \leq -0.1$ and $-1.0 \leq h_\phi \leq -0.3$.

4 Results and Discussion

The discussions are prepared for several combinations of relevant factors involved in the study. It is discovered from Fig. 2 that while increasing the value of the porosity parameter λ, Hartmann number M and unsteady parameter ξ, the velocity profiles along x- and y-directions decrease. From Fig. 3, it is clear that the temperature enhances by increasing the non-linear thermal radiation parameter Rd, but it decreases with increase in unsteady parameter ξ and thermal stratification parameter S_T. The nanoparticles' volume fraction profile drops by raising the values of the solutal stratification parameter S_P. The skin friction along x- and y-directions enhances while growing the porosity parameter and Hartmann number; see Fig. 4. In Fig. 5, it is witnessed that the local Nusselt number diminishes when raising the values of the porosity parameter, Hartmann number and non-linear thermal radiation parameter Rd. The local Sherwood number diminishes by raising the solutal stratification parameter S_P values.

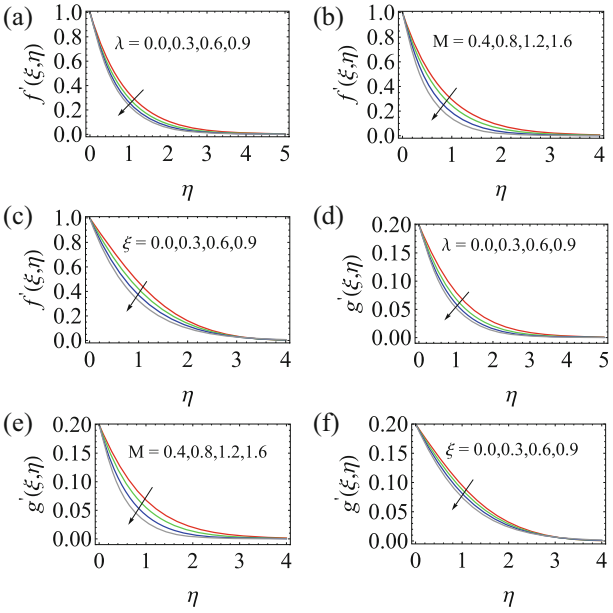

Fig. 2 Influence of λ M, ξ on $f'(\xi, \eta)$ and $g'(\xi, \eta)$, (**a**) $S_T = 0.2$, $S_P = 0.2$, $Rd = 0.3$, $\theta_w = 0.1$, $M = 0.2$, $c = 0.2$, $Nb = 0.2$, $Nt = 0.2$, $\xi = 1$. (**b**) $l = 0.2$, $S_T = 0.2$, $S_P = 0.2$, $Rd = 0.3$, $\theta_w = 0.1$, $c = 0.2$, $Nb = 0.2$, $Nt = 0.2$, $\xi = 1$. (**c**) $l = 0.2$, $S_T = 0.2$, $S_P = 0.2$, $Rd = 0.3$, $\theta_w = 0.1$, $M = 0.2$, $c = 0.2$, $Nb = 0.2$, $Nt = 0.2$. (**d**) $S_T = 0.2$, $S_P = 0.2$, $Rd = 0.3$, $\theta_w = 0.1$, $M = 0.2$, $c = 0.2$, $Nb = 0.2$, $Nt = 0.2$, $\xi = 1$. (**e**) $l = 0.2$, $S_T = 0.2$, $S_P = 0.2$, $Rd = 0.3$, $\theta_w = 0.1$, $c = 0.2$, $Nb = 0.2$, $Nt = 0.2$, $\xi = 1$. (**f**) $l = 0.2$, $S_T = 0.2$, $S_P = 0.2$, $Rd = 0.3$, $\theta_w = 0.1$, $M = 0.2$, $c = 0.2$, $Nb = 0.2$, $Nt = 0.2$

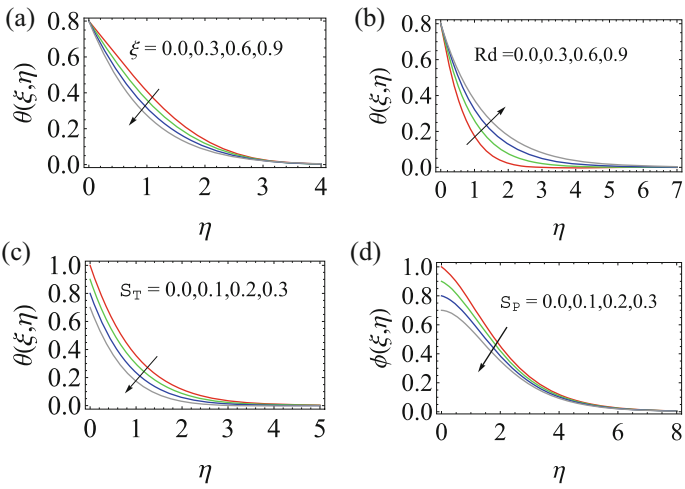

Fig. 3 Influence of ξ Rd, S_T on temperature and S_P on concentration, (**a**) $\lambda = 0.2$, $S_T = 0.2$, $S_P = 0.2$, $Rd = 0.3$, $\theta_w = 0.1$, $M = 0.2$, $c = 0.2$, $Nb = 0.2$, $Nt = 0.2$. (**b**) $\lambda = 0.2$, $S_T = 0.2$, $S_P = 0.2$, $\theta_w = 0.1$, $M = 0.2$, $c = 0.2$, $Nb = 0.2$, $Nt = 0.2$, $\xi = 1$. (**c**) $\lambda = 0.2$, $S_P = 0.2$, $Rd = 0.3$, $\theta_w = 0.1$, $M = 0.2$, $c = 0.2$, $Nb = 0.2$, $Nt = 0.2$, $\xi = 1$. (**d**) $\lambda = 0.2$, $S_T = 0.2$, $Rd = 0.3$, $\theta_w = 0.1$, $M = 0.2$, $c = 0.2$, $Nb = 0.2$, $Nt = 0.2$, $\xi = 1$

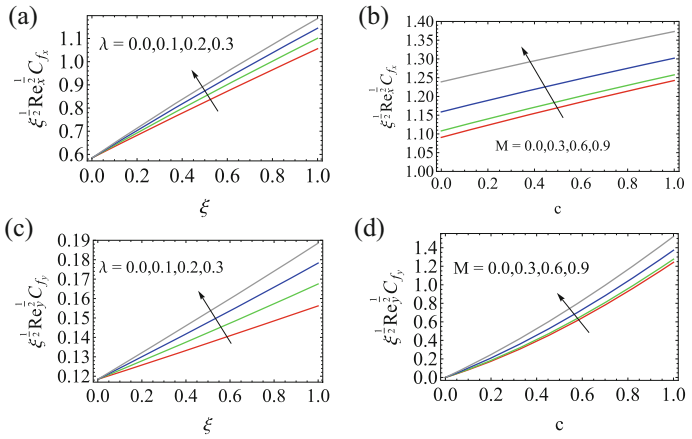

Fig. 4 Influence of λ and M on $\xi^{\frac{1}{2}} Re_x^{1/2} C_f$, (**a**) $S_T = 0.2$, $S_P = 0.2$, $Rd = 0.3$, $\theta_w = 0.1$, $M = 0.2$, $c = 0.2$, $Nb = 0.2$, $Nt = 0.2$. (**b**) $l = 0.2$, $S_T = 0.2$, $S_P = 0.2$, $Rd = 0.3$, $\theta_w = 0.1$, $Nb = 0.2$, $Nt = 0.2$, $\xi = 1$. (**c**) $S_T = 0.2$, $S_P = 0.2$, $Rd = 0.3$, $\theta_w = 0.1$, $M = 0.2$, $c = 0.2$, $Nb = 0.2$, $Nt = 0.2$. (**d**) $S_T = 0.2$, $S_P = 0.2$, $Rd = 0.3$, $\theta_w = 0.1$, $Nb = 0.2$, $Nt = 0.2$

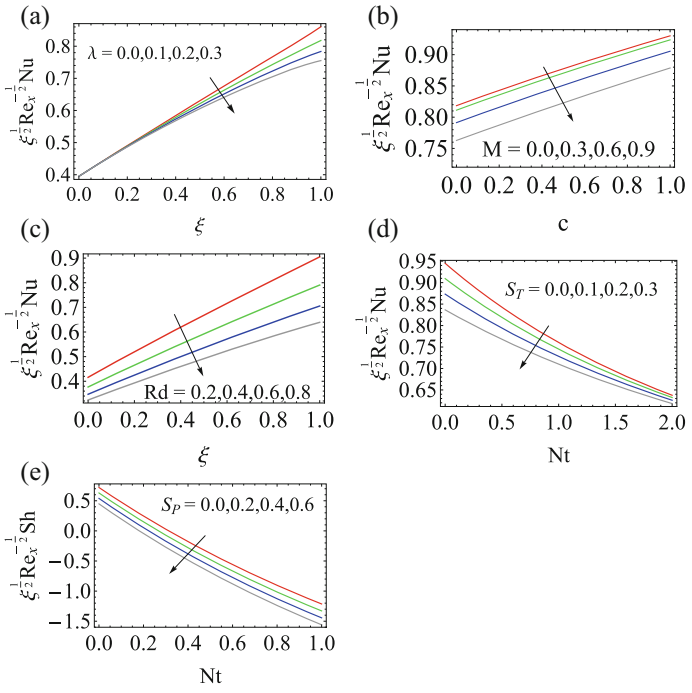

Fig. 5 Influence of λ, M, Rd, S_T on $\xi^{\frac{1}{2}} Re_x^{-1/2} Nu$ and S_P on $\xi^{\frac{1}{2}} Re_x^{-1/2} Sh$, (**a**) $S_T = 0.2$, $S_P = 0.2$, $Rd = 0.3$, $\theta_w = 0.1$, $M = 0.2$, $c = 0.2$, $Nb = 0.2$, $Nt = 0.2$. (**b**) $l = 0.2$, $S_T = 0.2$, $S_P = 0.2$, $Rd = 0.3$, $\theta_w = 0.1$, $Nb = 0.2$, $Nt = 0.2$, $\xi = 1$. (**c**) $l = 0.2$, $S_T = 0.2$, $S_P = 0.2$, $\theta_w = 0.1$, $M = 0.2$, $c = 0.2$, $Nb = 0.2$, $Nt = 0.2$. (**d**) $l = 0.2$, $S_P = 0.2$, $Rd = 0.3$, $\theta_w = 0.1$, $M = 0.2$, $c = 0.2$, $Nb = 0.2$, $\xi = 1$. (**e**) $l = 0.2$, $S_T = 0.2$, $Rd = 0.3$, $\theta_w = 0.1$, $M = 0.2$, $c = 0.2$, $Nb = 0.2$, $\xi = 1$

5 Conclusion

The study of unsteady three-dimensional MHD convective nanoliquid stream over a non-linear stretchable sheet with non-linear thermal radiation and thermal and solutal stratification in a porous medium is examined. The thermal boundary layer thickness enhances while raising the non-linear thermal radiation parameter which results in diminish on energy transfer rate. The thickness of momentum boundary layer and local Nusselt number diminishes, whereas the thickness of temperature boundary layer and skin friction enhances while growing porosity and Hartman number. While raising thermal stratification, the momentum boundary layer thickness and local Nusselt number diminish. The nanoparticles' volume fraction profile and local Sherwood number diminish with increase in solutal stratification.

References

1. Kasmani, R.Md., Sivasankaran, S., Siri, Z.: Effect of Chemical Reaction on Convective Heat Transfer of Boundary Layer Flow in Nanofluid over a Wedge with Heat Generation/Absorption and Suction. J. Applied Fluid Mech. **9(1)**, 379–388 (2016)
2. Sivasankaran, S., Aasaithambi, T., Rajan, S.: Numerical analysis on convection heat transfer using different nanofluids in a cavity with linearly varying wall temperature. Maejo Int. J. Sci. Tech. **4(3)**, 468–482 (2010)
3. Sivasankaran, S., Pan, K.L.:Natural Convection of Nanofluids in a Cavity with Non-uniform Temperature Distributions on Side Walls. Numerical Heat Transfer A **65**, 247–268 (2014)
4. Reddy, J.V.R., Sugunamma, V., Sandeep, N.: Thermophoresis and Brownian motion effects on unsteady MHD nanofluid flow over a slendering stretching surface with slip effects. Alexandria Engineering Journal, (2017) http://dx.doi.org/10.1016/j.aej.2017.02.014
5. Hayat, T., Muhammad, T., Alsaedi, A., Alhuthali, M.S.: Magnetohydrodynamic three dimensional flow of viscoelastic nanofluid in the presence of nonlinear thermal radiation. J. Magn. Magn. Mater. **385**, 222–229 (2015)
6. Das, K., Duari, P.R., Kundu, P.K.: Nanofluid flow over an unsteady stretching surface in presence of thermal radiation. Alexandria Engineering Journal **53**, 737–745 (2014)
7. Madhu, M., Kishan, N., Chamkha, A.J.: Unsteady flow of a Maxwell nanofluid over a stretching surface in the presence of magnetohydrodynamic and thermal radiation effects. Propulsion and Power Research **6(1)**, 31–40 (2017)
8. Hayat, T., Imtiaz, M., Alsaedi, A.: Unsteady flow of nanofluid with double stratification and magnetohydrodynamics. Int. J. Heat Mass Transfer **92**, 100–109 (2016)
9. Mutuku, W.N., Makinde, O.D.: Double stratification effects on heat and mass transfer in unsteady MHD nanofluid flow over a flat surface. Mutuku and Makinde Asia Pac. J. Comput. Engin. (2017) https://doi.org/10.1186/s40540-017-0021-2

Chemical Reaction and Nonuniform Heat Source/Sink Effects on Casson Fluid Flow over a Vertical Cone and Flat Plate Saturated with Porous Medium

P. Vijayalakshmi, S. Rao Gunakala, I. L. Animasaun, and R. Sivaraj

Abstract The intention of this communication is to explore the characteristics of electromagnetohydrodynamics on the fluid transport properties of a chemically reacting Casson fluid with two types of geometries. Formulations consist of salient features of radiative heat transfer, Lorentz force, and chemical reaction. This model is constituted with governing equations which are solved numerically by an efficient finite difference scheme of Crank-Nicolson type. Impact of pertinent parameters like Casson fluid, electrical field, Hartmann number, and chemical reaction is observed through graphs. The outcomes of surface shear stress, rate of heat, and mass transfers are presented through tables. Results enable us to state that larger electrical field decelerates the Casson fluid flow. Influence of the magnetic field on mean surface shear stress is more significant in the flow on a plate than that of cone.

1 Introduction

MHD flow problems have been analyzed in distinct areas like measurement of moving blood, generating of power, nuclear production, and generators. These are technical strategy also adopting electromagnetic methods. The non-Newtonian fluids have incorporated a lot of aspects due to their distinct utilization in manufactory

P. Vijayalakshmi · R. Sivaraj (✉)
Department of Mathematics, School of Advanced Sciences, Vellore Institute of Technology, Vellore, Tamilnadu, India
e-mail: vijayalakshmi.p2016@vitstudent.ac.in; sivaraj.r@vit.ac.in

S. Rao Gunakala
Department of Mathematics and Statistics, The University of the West Indies, St. Augustine, Trinidad and Tobago
e-mail: sreedhara.rao@sta.uwi.edu

I. L. Animasaun
Department of Mathematical Sciences, Federal University of Technology, Akure, Ondo State, Nigeria
e-mail: ilanimasaun@futa.edu.ng

B. Rushi Kumar et al. (eds.), *Applied Mathematics and Scientific Computing*, Trends in Mathematics, https://doi.org/10.1007/978-3-030-01123-9_13

and engineering. The non-Newtonian fluids enhance the deportation of coal oil from petroleum production. In past few decades, the study of hydromagnetics over a cone and plate has attracted many researchers attention. In food industries and engineering, the hydromagnetic flow of Casson fluid has been an interesting area of research. The Casson fluid miniature can be preferred to correct the rheological details for manifold constituents like jelly, ketchup, and mishmash. Ketchup is a shear-thinning fluid. Shear thinning means that the fluid viscosity decreases with increasing shear stress. In other words, fluid motion is initially difficult at slow rates of deformation but will flow more freely at high rates. It is fascinating to indicate that the Casson fluid miniature can be selected for blood flow of human beings investigations as a result of blood has abundant elements like red corpuscles, fibrinogen, and protein. Sharma et al. [1] described the effects of heat source/sink on magnetohydrodynamic assorted change of possession stagnation point flow ahead a perpendicular stretching sheet in the existence of extrinsic Hartmann number. Kumar and Sivaraj [2] analyzed the Walters' B-liquid flow throughout the extend of a flat plat and a vertical cone sopped with porosity in the existence of Dufour and Soret effects. Kong et al. [3] determined the oversees performs together accumulate the electromagnetic radiation signals that the antenna acquire and analyzed the passion of the electromagnetic radiation signal. Mathematical investigations of Casson fluid which accomplished a topmost convective surface of paraboloid of innovation to nonlinear radiation and viscous dissipation were presented in Reddy et al. [4]. Hayat et al. [5] committed to the flow change of possession of viscous fluid by a bowed elongated sheet. Zhang et al. [6] examined the effect of thermal radiation on magnetohydrodynamics natural convection in two-dimensional and three-dimensional cavity. Some current absorbing write off connected with the flow, chemical reaction, and heat and mass transfer typical features of Casson fluids can be found in Ahmed et al. [7]. Gupta et al. [8] investigated the Brownian motion and dispersion of thermophoresis in non-Newtonian nanofluid and concluded a bent on stretching surface accompanying effects of thermal radiation and chemical reaction. Siddiqa et al. [9] concerned with the problem at fixed intervals MHD natural deportation boundary layer flow of emitting micropolar fluid beside a perpendicular surface. The radiative heat transfer flow of a reactive hydromagnetic fluid inside a chamber permeated with non-Darcy saturated porous medium with convective wall cooling is investigated by Hassan et al. [10]. Wang and Zhao [11] represented basic scheme for the eventuality of thermal radiation in anisotropic porous medium. Malik and Nayak [12] presented the heat transfer characteristics of MHD nanofluid flow in an enclosure saturated porous medium. In this paper, the predominant idea is to examine the chemically reacting Casson flow over a cone and plate in the presence of electromagnetohydrodynamics and nonuniform heat source/sink. The Crank-Nicolson scheme has been applied to solve the controlling equations. The impacts of diverse pertinent parameters are studied, and the outcomes are indicated through graphs and tables.

2 Mathematical Formulation

Two-dimensional Casson fluid flow of an incompressible and EMHD is deliberated with two distinct geometries saturated with porous medium as exhibits in Fig. 1. In the system of Cartesian coordinates, x-axis represents the surface of the vertical cone and flat plate. The y-axis represents normal to the surface. At fixed temperature T_w and fixed concentration C_w, the wall is maintained at y = 0 which is greater than the medium temperature T_∞ and medium concentration C_∞, respectively. Then electrical field E_0 and the transverse Hartmann number of strength B_0 are implemented in the y-direction. The porous is pretended to be uniform. The Casson fluid flow characterizes the nonuniform heat source/sink, chemical reaction and thermal radiation effects. The set of governing equations is modeled based on previously reported studies [13–17].

$$\frac{\partial\left(r^h u\right)}{\partial x}+\frac{\partial\left(r^h v\right)}{\partial y}=0 \tag{1}$$

$$\rho\left(\frac{\partial u}{\partial t}+u\frac{\partial u}{\partial x}+v\frac{\partial u}{\partial y}\right)=\left(1+\frac{1}{\beta}\right)\mu\frac{\partial^2 u}{\partial y^2}-\frac{\mu}{K}u-\sigma B_0\left(B_0 u-E_0\right)$$
$$+g\rho\cos\lambda\left(\beta_T\left(T-T_\infty\right)+\beta_C\left(C-C_\infty\right)\right) \tag{2}$$

$$\rho C_P\left(\frac{\partial T}{\partial t}+u\frac{\partial T}{\partial x}+v\frac{\partial T}{\partial y}\right)=k\frac{\partial^2 T}{\partial y^2}+q'''-\frac{\partial q_r}{\partial y} \tag{3}$$

$$\frac{\partial C}{\partial t^*}+u\frac{\partial C}{\partial x}+v\frac{\partial C}{\partial y}=D\frac{\partial^2 C}{\partial y^2}-k_R\left(C-C_\infty\right) \tag{4}$$

Here q_r , E_0 , β, K, and k_R represent the radiative heat flux, electrical field, Casson fluid, porosity, and dimensional chemical reaction parameter, respectively.

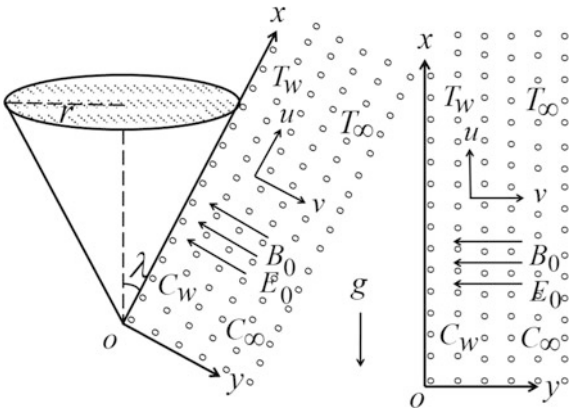

Fig. 1 Physical view

The transport properties during primary assumption ($t^* \leq 0$) are

$$u = 0, \quad v = 0, \quad T = T_\infty, \quad C = C_\infty \quad \text{for all} \quad x, y \tag{5}$$

The transport properties at the limits of the geometries at any time ($t^* > 0$) are

$$\begin{aligned} &u = 0, \quad v = 0, \quad T = T_w, \quad C = C_w \quad \text{at} \quad y = 0 \\ &u = 0, \quad T = T_\infty, \quad C = C_\infty \quad \text{at} \quad x = 0 \\ &u \to 0, \quad T \to T_\infty, \quad C \to C_\infty \quad \text{as} \quad y \to \infty \end{aligned} \tag{6}$$

when $h = 1$ corresponds to flow over a vertical cone and $h = \alpha = 0$ corresponds to flow over a vertical flat plate.

The nonuniform heat generator/absorber q''' is defined as

$$q''' = \frac{(Gr)^{1/2}}{L^2}\left(\frac{\gamma_1 L}{\upsilon (Gr)^{1/2}}(T_w - T_\infty)\, u + \gamma_2 (T - T_\infty)\right) \tag{7}$$

By employing the Rosseland resemblance for radiative heat flux

$$q_r = -\frac{4}{3}\frac{\sigma_s}{k_e}\frac{\partial T^4}{\partial y} = -\frac{16}{3}\frac{\sigma_s}{k_e}T^3\frac{\partial T}{\partial y} \tag{8}$$

The dimensionless variables are defined as

$$\begin{aligned} &X = \frac{x}{L}, \quad Y = \frac{y}{L}(Gr_T)^{1/4}, \quad R = \frac{r}{L}, \quad r = xsin(\lambda), \quad U = \frac{uL}{\upsilon}(Gr_T)^{-1/2}, \\ &V = \frac{vL}{\upsilon}(Gr_T)^{-1/4}, \quad t = \frac{\upsilon t^*}{L^2}(Gr_T)^{1/2}, \quad \theta = \frac{T - T_\infty}{T_w - T_\infty}, \quad \phi = \frac{C - C_\infty}{C_w - C_\infty}, \end{aligned} \tag{9}$$

The governing Eqs. (1)−(4) are dimensionalized by means of Eq. (9) and stated below

$$\frac{\partial \left(R^h U\right)}{\partial X} + \frac{\partial \left(R^h V\right)}{\partial Y} = 0 \tag{10}$$

$$\frac{\partial U}{\partial t} + U\frac{\partial U}{\partial X} + V\frac{\partial U}{\partial Y} = \left(1 + \frac{1}{\beta}\right)\frac{\partial^2 U}{\partial Y^2} - \left(\frac{1}{K} + M\right)U + ME_1 + \cos\lambda\,(\theta + N\phi) \tag{11}$$

$$\frac{\partial \theta}{\partial t} + U\frac{\partial \theta}{\partial X} + V\frac{\partial \theta}{\partial Y} = \frac{1}{\Pr}\left(1 + \frac{4}{3}Rd\right)\frac{\partial^2 \theta}{\partial Y^2} + \frac{1}{\Pr}(AU + B\theta) \tag{12}$$

$$\frac{\partial \phi}{\partial t} + U\frac{\partial \phi}{\partial X} + V\frac{\partial \phi}{\partial Y} = \frac{1}{Sc}\frac{\partial^2 \phi}{\partial Y^2} - K_R\phi \tag{13}$$

The dimensionless form of the conditions stated in Eqs. (5) and (6) are

$$\begin{aligned} &t \le 0 : U = 0, \quad V = 0, \quad \theta = 0, \quad \phi = 0 \quad \text{for all} \quad X, Y \\ &t > 0 : U = 0, \quad V = 0, \quad \theta = 1, \quad \phi = 1 \quad \text{at} \quad Y = 0 \\ &\qquad U = 0, \quad \theta = 0, \quad \phi = 0 \quad \text{at} \quad X = 0 \\ &\qquad U \to 0, \quad \theta \to 0, \quad \phi \to 0 \quad \text{at} \quad Y \to \infty \end{aligned} \tag{14}$$

Grashof number(Gr), Hartmann number(M), Casson fluid parameter(β), thermal radiation parameter (q_r), electrical field (E), porosity (K), dimensionless chemical reaction parameter (K_R), and skin-friction number (Sc) are, respectively, as follows:

$$\begin{aligned} &Gr_T = \frac{g\beta_T(T_w - T_\infty)L^3}{\upsilon^2}, \quad N = \frac{\beta_C\,(C_W - C_\infty)}{\beta_T\,(T_W - T_\infty)}, \quad M = \frac{\sigma B_0^2 L^2}{\upsilon(Gr)^{1/2}\rho}, \\ &Pr = \frac{\mu C_P}{k}, \\ &E = \frac{E_0 L}{B_0\upsilon(Gr)^{1/2}}, \quad q_r = \frac{16\sigma_s T_\infty^3}{k_e k_0}, \quad Sc = \frac{\upsilon}{D}, K_R = \frac{k_R(C_W - C_\infty)L^2}{\upsilon(Gr)^{1/2}} \end{aligned} \tag{15}$$

The local skin-friction factor (Sf_x), Nusselt number (Nu_x), and Sherwood numbers (Sh_x) can be represented as

$$\begin{aligned} &Sf_x = -\left[1 + \frac{1}{\beta}\right]\left(\frac{\partial U}{\partial Y}\right)_{Y=0}, \quad Nu_x = -X\left(\frac{\partial \theta}{\partial Y}\right)_{Y=0}, \\ &Sh_x = -X\left(\frac{\partial \phi}{\partial Y}\right)_{Y=0} \end{aligned} \tag{16}$$

The mean skin-friction ($\overline{Sf}$), rate of heat transfer coefficient ($\overline{Nu}$), and rate of mass transfer coefficient ($\overline{Sh}$) can be represented as

$$\begin{aligned} &\overline{Sf} = -\left[1 + \frac{1}{\beta}\right]\int_0^1 \left(\frac{\partial U}{\partial Y}\right)_{Y=0} dX, \qquad \overline{Nu} = -\left(\frac{\left(\frac{\partial \theta}{\partial Y}\right)_{Y=0}}{\theta_{Y=0}}\right) dX, \\ &\overline{Sh} = -\left(\frac{\left(\frac{\partial \phi}{\partial Y}\right)_{Y=0}}{\phi_{Y=0}}\right) dX \end{aligned} \tag{17}$$

3 Results and Discussion

The set of nonlinear equations (10) to (13) are solved by using the Crank-Nicolson scheme with boundary conditions (14). Crank-Nicolson scheme has been utilized dramatically by many investigators [13–17]. Such a system of equations is derived and explained by Hans Petter Langtangen et al.[18]. This section addresses the characteristics of temperature, velocity, and concentration distributions as well as Nusselt number, Sherwood number, and skin-friction variations of pertinent parameters. The table constitutes the average skin friction, average Nusselt number, and average Sherwood number for distinct parameters. Computations are formed for distinct values of $E = 0.1, 0.3, 0.5, 0.7$; $M = 0, 1, 2, 3$; $\beta = 1.0, 1.5, 2.0, 2.5$; and $K_R = 0, 1, 2, 3$. Variation of velocity (U) and temperature (θ) drawing of outline across the electrical field is displayed in Figs. 2 and 3. In the presence of an electrical field, a Lorentz force occurs, which causes the velocity increases and temperature decreases. Figures 4 and 5 represent the magnetic field; it creates the resistive force that is called Lorentz force it exhibits velocity decrease and temperature increase. Domination of rapid parameters β on velocity and skin friction (Sf_x) is illustrated in Figs. 6 and 7. Figure 7 annotates that greater values of β have the disposition to slow down the fluid flow. It is prepared for that β increases furnished to diminishing the yield stress which raise the value of plastic dynamic viscosity. An increase in radiation enhances the boundary layer. A raise in chemical reaction parameter decreases the concentration whereas increases the Sherwood number profiles as portrayed in Figs. 8 and 9. Table 1 illustrates the influence of β, E, M, and K_R on average skin friction, average Nusselt number and average Sherwood number.

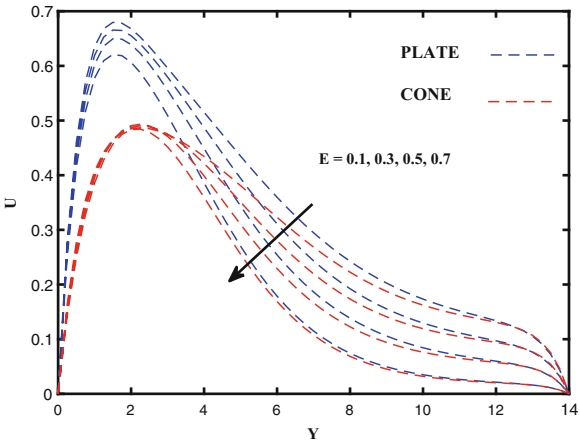

Fig. 2 U for various values of E

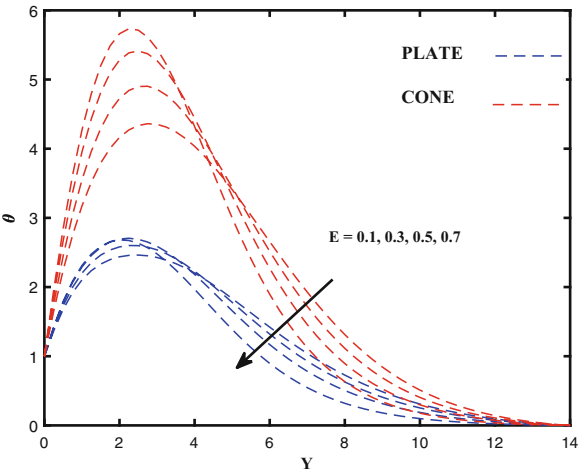

Fig. 3 θ for various values of E

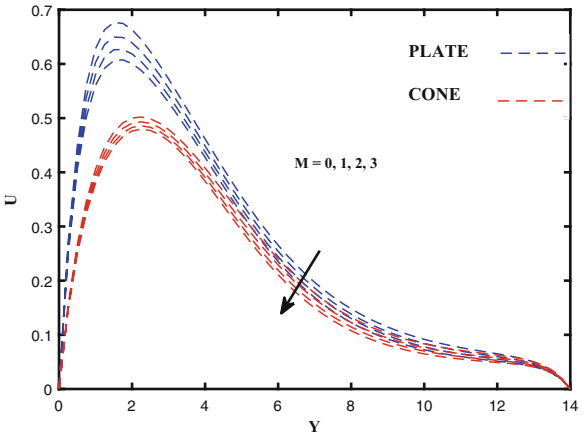

Fig. 4 U for various values of M

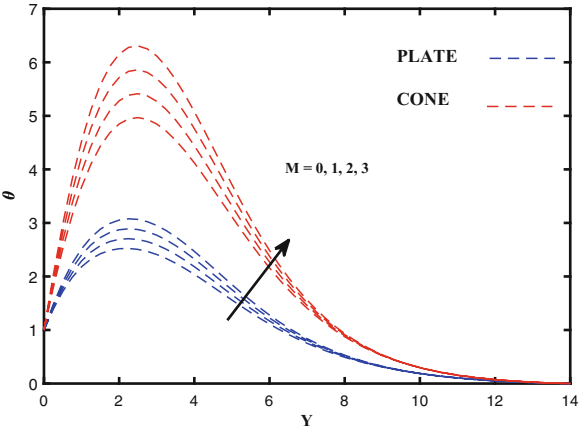

Fig. 5 θ for various values of M

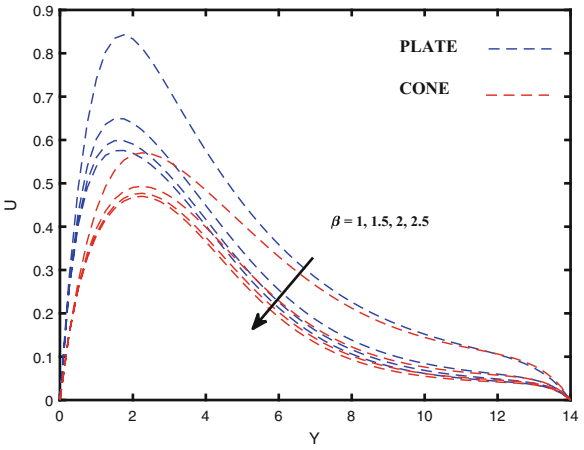

Fig. 6 U for various values of β

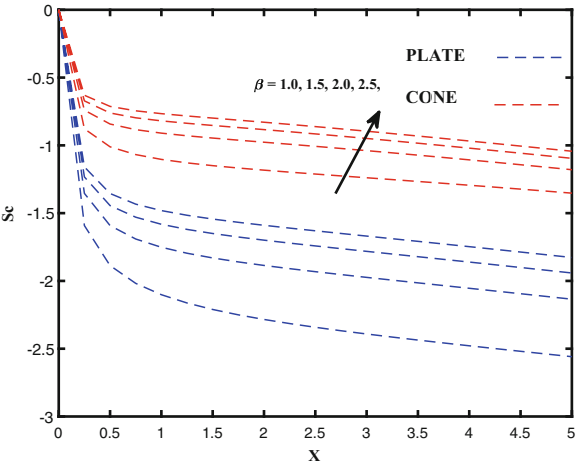

Fig. 7 Sf_x for various values of β

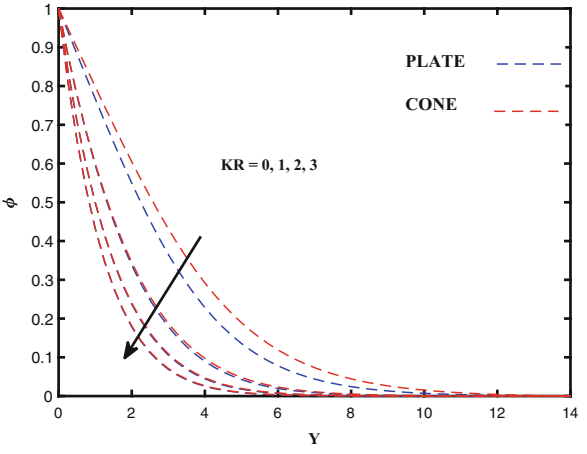

Fig. 8 ϕ for various values of K_R

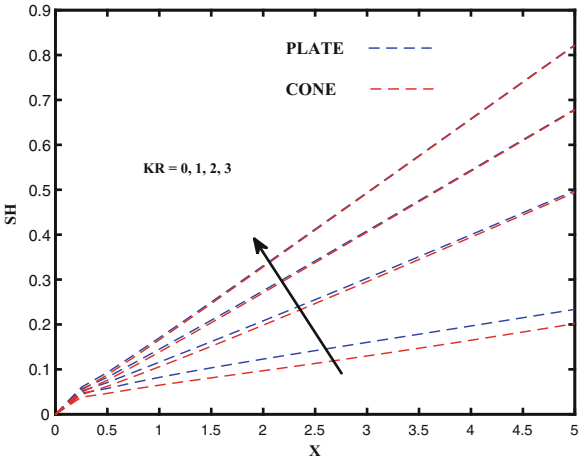

Fig. 9 Sh_x for various values of K_R

Table 1 Effect of β, E, M, and K_R on $\overline{Sf_x}$, $\overline{Nu_x}$, and $\overline{Sh_x}$

Physical parameters	Values	$\overline{Sf_x}$		$\overline{Nu_x}$		$\overline{Sh_x}$	
		Plate	Cone	Plate	Cone	Plate	Cone
β	1.0	1.11987	0.58609	−0.24907	−0.69043	0.57463	0.53420
	1.5	1.11571	0.59146	−0.50400	−1.30899	0.55609	0.52389
	2.0	1.12118	0.59973	−0.64902	−1.66993	0.55004	0.52096
	2.5	1.12625	0.60583	−0.74050	−1.89651	0.54707	0.51956
E	0.1	1.06322	0.54484	−0.53559	−1.54897	0.55027	0.51919
	0.3	1.11517	0.59146	−0.50400	−1.30899	0.55609	0.52389
	0.5	1.16566	0.63818	−0.44307	−1.07145	0.56087	0.52808
	0.7	1.21578	0.68687	−0.38402	−0.88146	0.56545	0.53243
M	0.0	1.14404	0.60535	−0.45009	−1.17690	0.55947	0.52575
	1.0	1.11571	0.59146	−0.50400	−1.30899	0.55609	0.52389
	2.0	1.08960	0.57884	−0.55902	−1.44462	0.55306	0.52224
	3.0	1.06543	0.56729	−0.61510	−1.58331	0.55031	0.52078
K_R	0.0	1.15206	0.60713	−0.40332	−1.07713	0.34715	0.28109
	1.0	1.11571	0.59146	−0.50400	−1.30899	0.55609	0.52389
	2.0	1.09034	0.58101	−0.57905	−1.44323	0.71507	0.69308
	3.0	1.07046	0.57263	−0.63583	−1.53071	0.84669	0.82948

4 The Conclusions

A numerical study is executed for hydromagnetic Casson fluid flow with chemical reaction and nonuniform heat source/sink over two types of geometries. The following findings can be drawn. Intensification in temperature is observed for larger magnetic number. Skin-friction factor boosts for larger β, whereas the trend is reversed in velocity distribution. The magnitude of decrease in temperature and velocity is more significant when the fluid flow over plate compare with the fluid

flow over cone. Casson fluid velocity increases with viscosity variation, moving plate velocity, and heat source. Temperature is decreasing with thermal radiation and heat sink.

References

1. P.R. Sharma, S. Sinha, R.S. Yadav, A. N. Filippov , MHD mixed convective stagnation point flow along a vertical stretching sheet with heat source / sink, International Journal of Heat and Mass Transfer 117 (2018) 780–786.
2. B. R. Kumar, R. Sivaraj, MHD viscoelastic fluid non-Darcy flow over a vertical cone and a flat plate, International Communications in Heat and Mass Transfer 40 (2013) 1–6.
3. B. Kong, E. Wang, Z. Li, Y. Niu, Time-varying characteristics of electromagnetic radiation during the coal-heating process, International Journal of Heat and Mass Transfer 108 (2017) 434–442.
4. J. V. R. Reddy, V. Sugunamma, N. Sandeep, Enhanced heat transfer in the flow of dissipative non-Newtonian Casson fluid flow over a convectively heated upper surface of a paraboloid of revolution, Journal of Molecular Liquids 229 (2017) 380–388.
5. T. Hayat, M. Rashid, M. Imtiaz, A. Alsaedi, MHD convective flow due to a curved surface with thermal radiation and chemical reaction, Journal of Molecular Liquids 225 (2017) 482–489.
6. J. Zhang, B. Li, H. Dong, X. Luo, H. Lin, Analysis of magnetohydrodynamics (MHD) natural convection in 2D cavity and 3D cavity with thermal radiation effects, International Journal of Heat and Mass Transfer 112 (2017) 216–223.
7. S. Ahmed, J. Zueco, L. M. Lopez-Gonzalez, Effects of chemical reaction, heat and mass transfer and viscous dissipation over a MHD flow in a vertical porous wall using perturbation method, International Journal of Heat and Mass Transfer 104 (2017) 409–418.
8. S. Gupta, D. Kumar, J. Singh, MHD mixed convective stagnation point flow and heat transfer of an incompressible nanofluid over an inclined stretching sheet with chemical reaction and radiation, International Journal of Heat and Mass Transfer 118 (2018) 378–387.
9. S. Siddiqa, A. Faryad, N. Begum, M.A. Hossain, R. S. R. Gorla, Periodic magnetohydrodynamic natural convection flow of a micropolar fluid with radiation, International Journal of Thermal Sciences 111 (2017) 215–222.
10. A.R. Hassan, R. Maritz, J.A. Gbadeyan, A reactive hydromagnetic heat generating fluid flow with thermal radiation within porous channel with symmetrical convective cooling, International Journal of Thermal Sciences 122 (2017) 248–256.
11. B.X. Wang, C.Y. Zhao, Effect of anisotropy on thermal radiation transport in porous ceramics, International Journal of Thermal Sciences 111 (2017) 301–309.
12. S. Malik, A.K. Nayak, MHD convection and entropy generation of nanofluid in a porous enclosure with sinusoidal heating, International Journal of Heat and Mass Transfer 111 (2017) 329–345.
13. D. Mythili, R. Sivaraj, Influence of higher order chemical reaction and non-uniform heat source/sink on casson fluid flow over a vertical cone and flat plate, Journal of Molecular Liquids 216 (2016) 466–475.
14. R. Sivaraj, B. R. Kumar, J. Prakash, MHD mixed convective flow of viscoelastic and viscous fluids in a vertical porous channel, An International Journal of Applications and Applied Mathematics 7 (June 2012) 99–116.
15. B. R. Kumar, R. Sivaraj, A. J. Benazir, Chemically reacting MHD free convective flow over a vertical cone with variable electric conductivity, International Journal of Pure and Applied Mathematics 101 (2015) 821–828.

16. D. Mythili, R. Sivaraj, M. M. Rashidi, Z. Yang, Casson fluid flow over a vertical cone with non-uniform heat source/sink and higher order chemical reaction, Journal of Naval Architecture and Marine Engineering 12 (2) (2015).
17. R. Sivaraj, B. R. Kumar, Viscoelastiic fluid flow over a moving vertical cone and flat plate with variable electric conductivity, International Journal of Heat and Mass Transfer 61 (2013) 119–128.
18. H. P. Langtangen, S. Linge, Finite difference computing with PDE's A modern software approach, 2016.

An Analytic Solution of the Unsteady Flow Between Two Coaxial Rotating Disks

Abhijit Das and Bikash Sahoo

Abstract In this study, analytical solutions are obtained for the unsteady flow of a viscous, incompressible fluid between two coaxial rotating disks of infinite dimensions, using the homotopy analysis method (HAM). Using similar variables, we first simplify the exact Navier–Stokes equation to highly coupled nonlinear partial differential equations. Upon application of the HAM these equations are replaced by a system of linear and uncoupled ordinary differential equations and solutions effective throughout the entire temporal and spatial domains are obtained. The nature of the flow fields is discussed under the influence of the same or opposite direction of rotation, Reynolds number, etc. Physically interesting quantities, such as radial and tangential shear stresses, are also obtained, and are valid throughout the temporal domain. To the best of our knowledge, no such series solution is available in the literature for the problem under consideration.

Keywords Rotating disk · unsteady flow · Reynolds number · HAM

1 Introduction

The study of flows related to rotating disks is of significant importance in the field of fluid dynamics because of its industrial and technical applications in rotating machinery, such as centrifugal pumps, turbines, or computer storage devices or rheometers, or oceanography. More specifically, internal air-cooling systems are usually modeled via disks rotating at different speeds, such as in gas or marine

A. Das (✉)
Department of Mathematics, ASET, Amity University Gwalior, Gwalior, India
e-mail: adas@gwa.amity.edu

B. Sahoo
Department of Mathematics, National Institute of Technology Rourkela, Rourkela, India
e-mail: bikashsahoo@nitrkl.ac.in

B. Rushi Kumar et al. (eds.), *Applied Mathematics and Scientific Computing*,
Trends in Mathematics, https://doi.org/10.1007/978-3-030-01123-9_14

turbines, counter rotating disks and rotor–stator systems. Moreover, it is possible to find similarity solutions to the Navier–Stokes equations in some idealized infinite configurations. In 1951, Batchelor [1] first considered the two-disk problem, generalizing the solutions given by Kármán [6] and Bodewadt [2] for a single disk, and surmised the general characteristics of the flow between two disks, but did not provide any explicit solution. Later, in 1953, Stewartson [10] revisited the same problem experimentally (for small or large Reynolds numbers) and his results were in agreement with those of Batchelor on co-rotating disks. However, when the direction of rotation was reversed, he found that there is no core rotation as was mentioned in [1]. This Batchelor–Stewartson controversy was settled in the study [13], showing that both Batchelor's and Stewartson's solutions can be obtained from the similarity solutions. Among recent studies, Das [3] produced analytical solutions for Batchelor's problem using the homotopy analysis method (HAM). Turkyilmazoglu [11] extended this problem to the case in which the disk's surfaces are allowed to stretch radially at a constant rate and produced numerical solutions, discussing the effects of surface stretching on the velocity and temperature fields.

An unsteady counterpart of Batchelor's problem has been studied by many researchers such as Pearson [9], who solved the problem numerically, considering the disk's angular velocity to be time-dependent and assuming a similar radius dependence to that used in [1, 6] for the steady flow; the problem was extended to study the heat transfer process by Ibrahim [4] following similar assumptions made by Hazma and Macdonald [5] regarding the disk's angular velocities and the gap between them.

The present investigation deals with the unsteady version of Batchelor's problem. Similarity solutions effective throughout the entire temporal and spatial domains are obtained using the efficient HAM introduced by Liao [7, 8] and to the best of author's knowledge no such analytical solutions exist in the literature. The HAM is different from all other analytic techniques owing to the presence of the convergence control parameter, $\hbar$, which helps to adjust and control the convergence of the solution series whenever necessary. Moreover, the similarity transformations used in this study enable us to treat the similarity variable for time (ζ) as a parameter, which greatly simplifies solving for the higher order terms of the solution series.

The remainder of the chapter is organized as follows. Fundamental equations are derived in Sect. 2. The HAM is applied to the governing system of coupled and nonlinear partial differential equations (PDEs) and the results obtained are discussed in Sect. 3. Finally, in Sect. 4, the conclusions are drawn.

2 Fundamental Equations

Let us consider the time-dependent flow of a viscous, incompressible fluid between two coaxial rotating disks, lying in the planes $z = 0$ and $z = d$. Let the lower and upper disks be started impulsively (at $t = 0$) into rotation with angular velocities

Ω_1 and Ω_2 respectively. Let the velocity components along (r, θ, z) be (u, v, w) respectively. Next, following [12], we consider the similarity variables:

$$u = r\Omega_1 \frac{\partial H(\eta,\zeta)}{\partial \eta}, \quad v = r\Omega_1 G(\eta,\zeta), \quad w = -2d\Omega_1\sqrt{\zeta}H(\eta,\zeta),$$
$$\eta = \frac{z}{d\sqrt{\zeta}}, \quad \zeta = 1 - e^{-\tau}, \quad \tau = \Omega_1 t \tag{1}$$

and the equations governing the flow become:

$$\frac{\partial^4 H}{\partial \eta^4} - Re(1-\zeta)\left(\zeta\frac{\partial^2 H}{\partial\zeta\partial\eta^2} - \frac{\eta}{2}\frac{\partial^3 H}{\partial\eta^3} - \frac{1}{2}\frac{\partial^2 H}{\partial\eta^2}\right) + 2Re\zeta\left(G\frac{\partial G}{\partial\eta} + H\frac{\partial^3 H}{\partial\eta^3}\right) = 0 \tag{2}$$

$$\frac{\partial^2 G}{\partial \eta^2} - Re(1-\zeta)\left(\zeta\frac{\partial G}{\partial\zeta} - \frac{\eta}{2}\frac{\partial G}{\partial\eta}\right) - 2Re\zeta\left(G\frac{\partial H}{\partial\eta} - H\frac{\partial G}{\partial\eta}\right) = 0 \tag{3}$$

with the following boundary conditions:

$$H(0,\zeta) = 0, \quad G(0,\zeta) = 1, \quad \frac{\partial H(0,\zeta)}{\partial\eta} = 0 \tag{4}$$

$$H(1,\zeta) = 0, \quad G(1,\zeta) = \Omega, \quad \frac{\partial H(1,\zeta)}{\partial\eta} = 0 \tag{5}$$

where, $Re = \frac{\rho d^2\Omega_1}{\mu}$ is the Reynolds number, $\Omega = \frac{\Omega_2}{\Omega_1}$ is the rotation rate.

The shear stresses of the lower disk (τ_r and τ_θ) can be calculated as:

$$\tau_r = \mu\left.\frac{\partial u}{\partial z}\right|_{(0,\zeta)} = \left.\frac{\mu r\Omega_1}{d\sqrt{\zeta}}\frac{\partial^2 H}{\partial\eta^2}\right|_{(0,\zeta)} \tag{6}$$

$$\tau_\theta = \mu\left.\frac{\partial v}{\partial z}\right|_{(0,\zeta)} = \left.\frac{\mu r\Omega_1}{d\sqrt{\zeta}}\frac{\partial G}{\partial\eta}\right|_{(0,\zeta)} \tag{7}$$

When $\zeta = 0$ (initial unsteady flow), corresponding to $\tau = 0$, we have from (2) and (3):

$$\frac{\partial^4 H}{\partial\eta^4} + Re\left(\frac{\eta}{2}\frac{\partial^3 H}{\partial\eta^3} - \frac{1}{2}\frac{\partial^2 H}{\partial\eta^2}\right) = 0 \tag{8}$$

$$\frac{\partial^2 G}{\partial\eta^2} + \frac{Re\eta}{2}\frac{\partial G}{\partial\eta} = 0 \tag{9}$$

and the relevant boundary conditions are:

$$H(0,0)=0, \quad G(0,0)=1, \quad \left.\frac{\partial H}{\partial \eta}\right|_{(0,0)}=0 \tag{10}$$

$$H(1,0)=0, \quad G(1,0)=\Omega, \quad \left.\frac{\partial H}{\partial \eta}\right|_{(1,0)}=0 \tag{11}$$

Solutions for Eqs. (8)–(11) are:

$$H(\eta,0)=0, \quad G(\eta,0)=1+\frac{(\Omega-1)}{Erf[\frac{\sqrt{Re}}{2}]}Erf[\frac{\sqrt{R}x}{2}] \tag{12}$$

where $Erf[x]$ is the error function defined by:

$$Erf[x]=\frac{2}{\sqrt{\pi}}\int_0^x e^{-s^2}ds \tag{13}$$

The steady-state equations corresponding to $\zeta = 1$ ($\tau \to \infty$) have been dealt with and discussed in detail by many researchers [3].

3 Solution of the HAM and Analysis of Results

It is to be noted that $H(\eta,\zeta)$, $G(\eta,\zeta)$ will contain power terms of η and ζ as these variables appear explicitly in Eqs. (2) and (3). Therefore, considering the boundary conditions (4)–(5), we chose the set of base functions $\{\eta^i\zeta^j | i \geq 0, j \geq 0\}$ and the initial guesses as:

$$H_0(\eta,\zeta)=0 \tag{14}$$

$$G_0(\eta,\zeta)=1+(\Omega-1)\eta \tag{15}$$

Also, we select

$$\mathscr{L}_H(f)=\frac{\partial^4 f}{\partial \eta^4} \tag{16}$$

$$\mathscr{L}_G(f)=\frac{\partial^2 f}{\partial \eta^2} \tag{17}$$

as the linear operators so that

$$\mathscr{L}_H(c_1+c_2\eta+c_3\eta^2+c_4\eta^3)=0 \tag{18}$$

$$\mathscr{L}_G(c_5+c_6\eta)=0 \tag{19}$$

where c_i, $i = 1-6$ are arbitrary constants.

Now, the zero-order deformation equations are constructed as follows

$$(1-\mathscr{Q})\mathscr{L}_H[\hat{\mathscr{H}}(\eta,\zeta;\mathscr{Q})-H_0(\eta,\zeta)]=\mathscr{Q}\hbar N_H[\hat{\mathscr{H}}(\eta,\zeta;\mathscr{Q}),\hat{\mathscr{G}}(\eta,\zeta;\mathscr{Q})] \tag{20}$$

$$(1-\mathscr{Q})\mathscr{L}_G[\hat{\mathscr{G}}(\eta,\zeta;\mathscr{Q})-G_0(\eta,\zeta)]=\mathscr{Q}\hbar N_G[\hat{\mathscr{H}}(\eta,\zeta;\mathscr{Q}),\hat{\mathscr{G}}(\eta,\zeta;\mathscr{Q})] \tag{21}$$

and the relevant boundary conditions are

$$\hat{\mathscr{H}}(0,\zeta;\mathscr{Q})=0,\quad \hat{\mathscr{G}}(0,\zeta;\mathscr{Q})=1,\quad \left.\frac{\partial\hat{\mathscr{H}}(\eta,\zeta;\mathscr{Q})}{\partial\eta}\right|_{\eta=0}=0 \tag{22}$$

$$\hat{\mathscr{H}}(1,\zeta;\mathscr{Q})=0,\quad \hat{\mathscr{G}}(1,\zeta;\mathscr{Q})=\Omega,\quad \left.\frac{\partial\hat{\mathscr{H}}(\eta,\zeta;\mathscr{Q})}{\partial\eta}\right|_{\eta=1}=0 \tag{23}$$

where, $\hbar$ is the auxiliary parameter and $\mathscr{Q}\in[0,1]$ is the embedding parameter. For $\mathscr{Q}=0$ and $\mathscr{Q}=1$, the above zero-order deformation equations (20), (21) have the solutions:

$$\hat{\mathscr{H}}(\eta,\zeta;0)=H_0(\eta,\zeta),\quad \hat{\mathscr{G}}(\eta,\zeta;0)=G_0(\eta,\zeta) \tag{24}$$

$$\hat{\mathscr{H}}(\eta,\zeta;1)=H(\eta,\zeta),\quad \hat{\mathscr{G}}(\eta,\zeta;1)=G(\eta,\zeta) \tag{25}$$

Thus, as $\mathscr{Q}$ varies from 0 to 1, $\hat{\mathscr{H}}(\eta,\zeta;\mathscr{Q}),\hat{\mathscr{G}}(\eta,\zeta;\mathscr{Q})$ deform continuously from the initial approximations to the solutions of the Eqs. (2) and (3). The nonlinear differential operators N_H and N_G are given by:

$$N_H[\hat{\mathscr{H}}(\eta,\zeta;\mathscr{Q}),\hat{\mathscr{G}}(\eta,\zeta;\mathscr{Q})]=\frac{\partial^4\hat{\mathscr{H}}}{\partial\eta^4}-Re(1-\zeta)\left(\zeta\frac{\partial^2\hat{\mathscr{H}}}{\partial\zeta\partial\eta^2}-\frac{\eta}{2}\frac{\partial^3\hat{\mathscr{H}}}{\partial\eta^3}-\frac{1}{2}\frac{\partial^2\hat{\mathscr{H}}}{\partial\eta^2}\right)$$
$$+2Re\zeta\left(\hat{\mathscr{G}}\frac{\partial\hat{\mathscr{G}}}{\partial\eta}+\hat{\mathscr{H}}\frac{\partial^3\hat{\mathscr{H}}}{\partial\eta^3}\right) \tag{26}$$

and

$$N_G[\hat{\mathscr{H}}(\eta,\zeta;\mathscr{Q}),\hat{\mathscr{G}}(\eta,\zeta;\mathscr{Q})]=\frac{\partial^2\hat{\mathscr{G}}}{\partial\eta^2}-Re(1-\zeta)\left(\zeta\frac{\partial\hat{\mathscr{G}}}{\partial\zeta}-\frac{\eta}{2}\frac{\partial\hat{\mathscr{G}}}{\partial\eta}\right)$$
$$-2Re\zeta\left(\hat{\mathscr{G}}\frac{\partial\hat{\mathscr{H}}}{\partial\eta}-\hat{\mathscr{H}}\frac{\partial\hat{\mathscr{G}}}{\partial\eta}\right) \tag{27}$$

respectively. Next, following Liao [8], the rth-order deformation equations are derived from (20), (21) as

$$\mathscr{L}_H[H_r(\eta,\zeta) - \chi_r H_{r-1}(\eta,\zeta)] = \hbar \mathscr{R}_r^H \tag{28}$$

$$\mathscr{L}_G[G_r(\eta,\zeta) - \chi_r G_{r-1}(\eta,\zeta)] = \hbar \mathscr{R}_r^G \tag{29}$$

with the boundary conditions:

$$H_r(0,\zeta) = 0, \quad G_r(0,\zeta) = 0, \quad \left.\frac{\partial H_r(\eta,\zeta)}{\partial \eta}\right|_{\eta=0} = 0 \tag{30}$$

$$H_r(1,\zeta) = 0, \quad G_r(1,\zeta) = 0, \quad \left.\frac{\partial H_r(\eta,\zeta)}{\partial \eta}\right|_{\eta=1} = 0 \tag{31}$$

where, $H_r(\eta,\zeta) = \frac{1}{r!}\left.\frac{\partial^r \hat{H}(\eta,\zeta;\mathscr{Q})}{\partial \mathscr{Q}^r}\right|_{\mathscr{Q}=0}$ and $G_r(\eta,\zeta) = \frac{1}{r!}\left.\frac{\partial^r \hat{G}(\eta,\zeta;\mathscr{Q})}{\partial \mathscr{Q}^r}\right|_{\mathscr{Q}=0}$. And

$$\mathscr{R}_r^H = \frac{\partial^4 H_{r-1}}{\partial \eta^4} - Re(1-\zeta)\left(\zeta\frac{\partial^2 H_{r-1}}{\partial\zeta\partial\eta^2} - \frac{\eta}{2}\frac{\partial^3 H_{r-1}}{\partial\eta^3} - \frac{1}{2}\frac{\partial^2 H_{r-1}}{\partial\eta^2}\right) + 2Re\zeta\sum_{n=0}^{r-1}\left(G_n\frac{\partial G_{r-1-n}}{\partial\eta} + H_n\frac{\partial^3 H_{r-1-n}}{\partial\eta^3}\right) \tag{32}$$

$$\mathscr{R}_r^G = \frac{\partial^2 G_{r-1}}{\partial \eta^2} - Re(1-\zeta)\left(\zeta\frac{\partial G_{r-1}}{\partial\zeta} - \frac{\eta}{2}\frac{\partial G_{r-1}}{\partial\eta}\right) - 2Re\zeta\sum_{n=0}^{r-1}\left(G_n\frac{\partial H_{r-1-n}}{\partial\eta} - H_n\frac{\partial G_{r-1-n}}{\partial\eta}\right) \tag{33}$$

and

$$\chi_r = \begin{cases} 1 & r > 1 \\ 0 & r \le 0 \end{cases} \tag{34}$$

It is to be noted that the Eqs. (28) and (29) are linear and uncoupled ordinary differential equations (ODEs) that can be solved respectively, in the order $r = 1, 2, 3, \ldots$, by using symbolic software such as Mathematica. Also note that the variable for time, ζ, is considered only as a parameter, and as a consequence it becomes easier solving for $H_r(\eta,\zeta)$ and $G_r(\eta,\zeta)$. The presence of the auxiliary parameter, also known as the convergence control parameter $\hbar$, provides us with a simple way of guaranteeing the convergence of the solution series. Liao [8] showed that a suitable value of $\hbar$ can be selected by plotting the $\hbar$-curves. One such curve is shown in Fig. 1 and it is clear that for $-1.5 \le \hbar \le -0.1$ we can obtain convergent

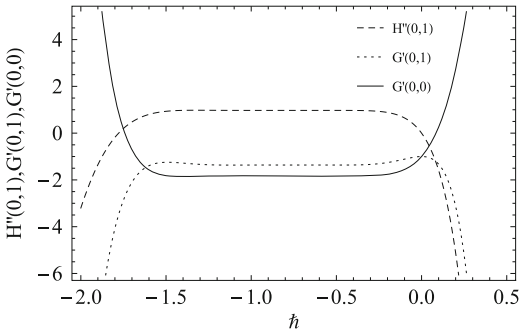

Fig. 1 $\hbar$-curves at 10th-order of homotopy approximations for $R = 10$, $\Omega = 0$

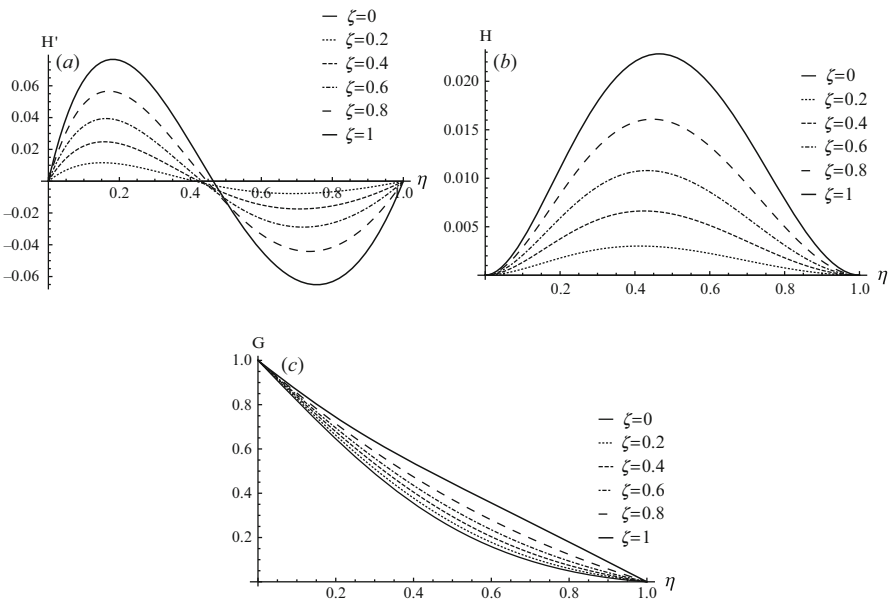

Fig. 2 The flow fields for $Re = 10$, $\Omega = 0$ obtained using 10th-order homotopy analysis method (HAM) approximations (**a**) radial, (**b**) axial, (**c**) tangential

solutions at $\zeta = 0$ and $\zeta = 1$. In a similar way, we have selected suitable values of $\hbar$ to guarantee a convergent solution series for any other values of $\zeta \in (0, 1)$, Re and Ω. The radial (H'), axial (H), and transverse (G) velocity profiles are shown in Figs. 2 and 3 for different values of Ω keeping $Re = 10$, fixed for $\zeta \in [0, 1]$, obtained using 10th-order HAM approximations. The rotor–stator case, i.e., when the upper disk is static and the lower disk is rotating ($\Omega = 0$), is shown in Fig. 2. The flow is radially outward over the rotating disk and inward toward the disk at rest for all ζ. The axial flow is from the stationary to the rotating one and the transverse component of velocity varies almost linearly, increasing from its initial unsteady value to the steady state as ζ increases from 0 to 1.

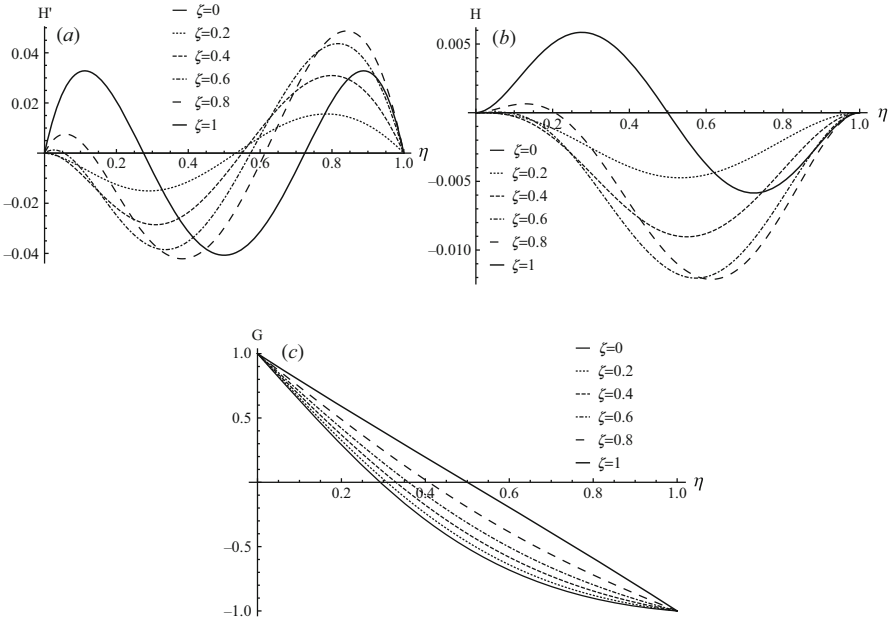

Fig. 3 The flow fields for $Re = 10$, $\Omega = -1$ obtained using 10th-order HAM approximations (**a**) radial, (**b**) axial, and (**c**) tangential

The case of counter rotation $\Omega = -1$ is presented in Fig. 3. It can be seen that for $\zeta = 0.2, 0.4, 0.6$, radial velocity is negative near to the disk placed at $z = 0$ and positive near to the other disk, but as ζ approaches 1 ($\zeta = 0.8, 1$), the flow region parts into three sections and there is a central core in which $\frac{\partial H}{\partial \eta}$ is negative. The value of H is negative for initial values of ζ, but changes its sign from positive (nearby the disk at $z = 0$) to negative (nearby the disk at $z = d$) for $\zeta = 0.8, 1$. Again, the tangential component of velocity is seen to increase as ζ increases.

In Tables 1 and 2, we report the values of $H''(0)$ and $-G'(0)$ for $\zeta \in [0, 1]$ and different Ω, keeping $Re = 1$ fixed. From Table 1 it is clear that, $H''(0)$ increases with increasing ζ, whereas Table 2 shows that $G'(0)$ decreases with increasing ζ, for all the values of the rotation rate shown. Moreover, good agreement of our results with those reported by [11] can be seen at $\zeta = 1$ from both the tables.

4 Conclusions

In this paper, an unsteady flow of a viscous incompressible fluid between two coaxial rotating disks of infinite dimension is considered and analytical solutions are produced by means of the HAM. Similarity variables reduce the governing differential equations to a set of fully uncoupled and nonlinear system of PDEs,

Table 1 10th-order HAM approximations for $H''(0)$ when $Re = 1$ for different ζ and Ω

	$\Omega = -0.3$		$\Omega = 0$		$\Omega = 0.5$	
ξ	HAM results	Ref. [11]	HAM results	Ref. [11]	HAM results	Ref. [11]
0.0	0		0		0	
0.1	0.0102057		0.00996622		0.00674617	
0.2	0.0204537		0.0199422		0.0134781	
0.3	0.0307441		0.0299271		0.0201944	
0.4	0.0410767		0.0399198		0.0268936	
0.5	0.0514515		0.0499192		0.0335741	
0.6	0.0618682		0.0599242		0.0402344	
0.7	0.0723267		0.0699335		0.0468726	
0.8	0.0828268		0.0799456		0.0534867	
0.9	0.0933683		0.0899591		0.0600747	
1.0	0.103951	0.10395088	0.0999722	0.09997221	0.0666342	0.6663419

Table 2 10th-order HAM approximations for $-G'(0)$ when $Re = 1$ for different ζ and Ω

	$\Omega = -0.3$		$\Omega = 0$		$\Omega = 0.5$	
ξ	HAM results	Ref. [11]	HAM results	Ref. [11]	HAM results	Ref. [11]
0.0	1.40912		1.08394		0.541969	
0.1	1.39921		1.07633		0.538168	
0.2	1.3892		1.06865		0.534346	
0.3	1.37908		1.06091		0.530499	
0.4	1.36885		1.05309		0.526626	
0.5	1.35848		1.0452		0.522723	
0.6	1.34799		1.03722		0.518787	
0.7	1.33734		1.02915		0.514813	
0.8	1.32655		1.02098		0.510797	
0.9	1.31558		1.01269		0.506732	
1.0	1.30442	1.30442355	1.00428	1.00427756	0.502614	0.50261351

which upon application of HAM are replaced by a sequence of linear ODEs. As a result, this complicated unsteady nonlinear problem could be solved with great ease. The velocity fields valid for all time are shown graphically under the influence of the parameters of interest, such as rotation rate and Reynolds number. Moreover, the quantities of physical interest, such as radial and tangential shear stresses $(H''(0), G'(0))$ are computed and tabulated. Unlike all other previous analytic solutions, solutions obtained in this study are valid for all time $\zeta \in [0, 1]$ corresponding to $\tau \in [0, \infty)$, in the entire spatial domain.

References

1. Batchelor, G.K.: Note on a class of solutions of the Navier-Stokes equations representing steady rotationally-symmetric flow. Quart. J. Mech. Appl. Math. **4**, 29–41 (1951)
2. Boedewadt, U.T.: Die Drehstr ́omung ́uber festem Grunde. ZAMM-J. Appl. Math. Mech. **20**, 241–253 (1940)
3. Das, A.: Analytical solution to the flow between two coaxial rotating disks using HAM. Procedia Engineering **127**, 377–382 (2015)
4. Ibrahim, F. N.: Unsteady flow between two rotating discs with heat transfer. J. of Phys. D: Appl. Phys. **24**, 1293 (1991)
5. Hamza, E. A., MacDonald, D. A.: A similar flow between two rotating disks. Q. Appl. Math. **41**, 495–511 (1984)
6. Kármán, T.V.: Über laminare und turbulente Reibung. ZAMM-J. Appl. Math. Mech. **1**, 233–252 (1921)
7. Liao, S.J.: Ph.D. Thesis, Shanghai Jiao Tong University, China (1992)
8. Liao, S.J.: Beyond perturbation: introduction to the homotopy analysis method. CRC press (2003)
9. Pearson, C.E.: Numerical solutions for the time-dependent viscous flow between two rotating coaxial disks. J. Fluid Mech. **21**, 623–633 (1965)
10. Stewartson, S.: On the flow between two coaxial rotating disks. Math. Proc. Cambridge Phil. Soc. **49**, 333–341 (1953)
11. Turkyilmazoglu, M.: Flow and heat simultaneously induced by two stretchable rotating disks. Physics of Fluids **28**, 043601 (2016)
12. Xu, H., Liao, S.J.: A series solution of the unsteady Von Kármán swirling viscous flows. Acta Appl. Math. **94**, 215–231 (2006)
13. Zandbergen, P.J., Dijkstra, D.: Von Kármán swirling flows. Annual review of fluid mechanics **19**, 465–491 (1987)

Cross Diffusion Effects on MHD Convection of Casson-Williamson Fluid over a Stretching Surface with Radiation and Chemical Reaction

M. Bhuvaneswari, S. Sivasankaran, H. Niranjan, and S. Eswaramoorthi

Abstract The thermal diffusion and diffusion-thermo effects on radiative mixed convective flow and heat transfer of Casson-Williamson fluid over a stretching surface are examined in the presence of uniform external magnetic field. The thermal radiation and chemical reaction effects are included in the study. This physical model is mathematically modelled by a set of nonlinear partial differential equations with boundary conditions. The governing system of equations is reformed into ordinary differential equations with the help of similarity variables, and then they are solved using homotopy analysis method. The concentration profile increases on increasing the dufour parameter, and the temperature profile increases on increasing the radiation parameter.

1 Introduction

The study of boundary layer flow of non-Newtonian fluids has anticipated significance in recent years because of its extensive applications in engineering discipline. Less number of studies on flow of non-Newtonian fluids is available due to more complex nature of such kind of flows which arise in the chemical processing industry, plastics processing industry, mining industry, lubrication, and biomedical flows [1–3]. Eswaramoorthi et al. [1] investigated the convective flow of viscoelastic fluid over a surface in the presence of radiation and chemical reaction. Rushi Kumar

M. Bhuvaneswari · S. Sivasankaran
Department of Mathematics, King Abdulaziz University, Jeddah, Saudi Arabia

H. Niranjan (✉)
Department of Mathematics, VIT University, Vellore, Tamil Nadu, India
e-mail: niranjan.hari@vit.ac.in

S. Eswaramoorthi
Department of Mathematics, Dr.N.G.P. Arts and Science College, Coimbatore, Tamil Nadu, India

B. Rushi Kumar et al. (eds.), *Applied Mathematics and Scientific Computing*,
Trends in Mathematics, https://doi.org/10.1007/978-3-030-01123-9_15

and Sivaraj [2] studied the magneto-convection of viscoelastic fluid over a flat plate and vertical cone with variable viscosity. In another study, they [3] examined the effect of variable electric conductivity.

The cross diffusion effects are investigated by several researchers [4–6]. Ruhaila et al. [4] explored the cross diffusion effects on the convective heat and mass transfer of a nanofluid past a moving wedge with suction. Niranjan et al. [5] numerically examined the soret and dufour effects on magneto-convection stagnation point flow with slip condition and radiation. The chemical reaction effect on convection heat transfer of nanofluid over a wedge in the presence of heat generation and suction was explored by Ruhaila et al. [7]. Sivasankaran et al. [8] studied the chemical reaction and slip effects on combined convection stagnation-point flow in a porous medium with thermal radiation.

In this paper, we extend the study of MHD convective flow of Casson fluid with chemical reaction and suction done by Shehzad et al. [9]. We include the thermal radiation and soret and dufour effects on convective flow of Casson-Williamson fluid over a stretching surface.

2 Mathematical Modelling

We consider the steady two-dimensional boundary layer flow of a Casson-Williamson fluid over a stretching surface. Assume that the surface is moving with velocity $u = U_w = cx$ where $c > 0$. The x-axis is taken parallel to the surface, and y-axis is perpendicular to the surface. A constant magnetic field is applied in y-direction and neglected the induced magnetic field because of the small effect of magnetic Reynolds number. Let T_w and C_w are the surface temperature and concentration which are greater than the free stream temperature T_∞ and concentration C_∞, respectively. Assume that the fluid has heat absorbing/generating, and the thermal radiation, first-order chemical reaction, and soret and dufour effects are considered. Under these assumptions, the governing boundary layer equations with Boussinesq's approximation are as follows:

$$\frac{\partial u}{\partial x} + \frac{\partial v}{\partial y} = 0, \tag{1}$$

$$u\frac{\partial u}{\partial x} + v\frac{\partial u}{\partial y} = \nu\left(1 + \frac{1}{\beta}\right)\frac{\partial^2 u}{\partial y^2} + \sqrt{2}\,\nu\Gamma\,\frac{\partial u}{\partial y}\,\frac{\partial^2 u}{\partial y^2} - \frac{\sigma B_0^2}{\rho}u, \tag{2}$$

$$u\frac{\partial T}{\partial x} + v\frac{\partial T}{\partial y} = \alpha_m\left(1 + \frac{16\sigma^* T_\infty^3}{3kk^*}\right)\frac{\partial^2 T}{\partial y^2} + \frac{D_e k_T}{c_s c_p}\frac{\partial^2 C}{\partial y^2} + \frac{Q}{\rho c_p}(T - T_\infty), \tag{3}$$

$$u\frac{\partial C}{\partial x} + v\frac{\partial C}{\partial y} = D_e\frac{\partial^2 C}{\partial y^2} + \frac{D_e k_T}{T_m}\frac{\partial^2 T}{\partial y^2} - k_1\left(C - C_\infty\right), \tag{4}$$

where u and v are the velocity components in x and y directions, ν is the kinematic viscosity, β the non-Newtonian Casson parameter, Γ is a time constant, σ is the electrical conductivity of the fluid, ρ is the density, α_m is the thermal diffusivity, σ^* is the Stefan-Boltzmann constant, k is the thermal conductivity, k^* is the mean absorption coefficient, D_e is the mass diffusivity, k_T is the thermal diffusion ratio, c_s is the free stream concentration, c_p is the specific heat, Q is the internal heat generation (>0) or absorption (<0) of the fluid, T_m is the mean fluid temperature, and k_1 is the coefficient of chemical reaction.

The boundary conditions of the above model are given by

$$u = U_w = ax,\ v = -V_w,\ T = T_w,\ C = C_w\ at\ y = 0$$

$$u \to 0,\ \frac{\partial u}{\partial z} \to 0,\ T \to T_\infty, C \to C_\infty\ \ as\ y \to\ \infty \tag{5}$$

Define the following similarity variables

$$\eta = \sqrt{\frac{a}{v}}y,\ u = axf'(\eta),\ v = -\sqrt{av}f(\eta),\ \theta = \frac{T - T_\infty}{T_w - T_\infty},\ \phi = \frac{C - C_\infty}{C_w - C_\infty} \tag{6}$$

Substituting Eq. (6) into the Eqs. (2–4), we get the following non-dimensional form

$$\left(1 + \frac{1}{\beta}\right)f''' + ff'' - f'^2 + \lambda f''f''' - Mf' = 0 \tag{7}$$

$$\left(1 + \frac{4}{3}Rd\right)\theta'' + Prf\theta' + PrDf\phi'' + PrHg\theta = 0 \tag{8}$$

$$\phi'' + Scf\phi' - ScCr\phi + ScSr\theta'' = 0 \tag{9}$$

the boundary conditions become,

$$f(0) = f_w,\ f'(0) = 1, f'(\infty) = 0,\ f''(\infty) = 0,\quad \theta(0) = 1\ ,$$

$$\theta(\infty) = 0, \phi'(0) = 1\ ,\ \phi(\infty) = 0 \tag{10}$$

where $\lambda = \Gamma x\sqrt{\frac{2c^2}{v}}$, $M = \frac{\sigma B_0^2}{\rho c}$, $Pr = \frac{v}{\alpha_m}$, $Rd = \frac{4\sigma^* T_\infty^3}{kk^*}$, $Df = \frac{D_e k_T}{vc_s c_p}\frac{(C_w - C_\infty)}{(T_w - T_\infty)}$, $Hg = \frac{Q}{c\rho c_p}$, $Sc = \frac{v}{D_e}$, $Sr = \frac{D_e k_T}{vT_m}\frac{(T_w - T_\infty)}{(C_w - C_\infty)}$, $Cr = \frac{k_1}{c}$, and $fw = \frac{V_w}{\sqrt{cv}}$ are the Williamson parameter, Magnetic field parameter, Prandtl number, thermal radiation parameter, dufour number, heat generation/absorption parameter, Schmidt number, Soret number, chemical reaction parameter, and suction/injection parameter.

The skin-friction coefficient, local Nusselt number, and the local Sherwood number are important physical parameters, and the reduced skin-friction coefficient, local Nusselt number, and local Sherwood number are given by

$$\frac{1}{2}C_f\sqrt{Re} = \left(1+\frac{1}{\beta}\right)f''(0) + \frac{\lambda}{2}f''^2(0) \tag{11}$$

$$Nu/\sqrt{Re} = -\left(1+\frac{4}{3}Rd\right)\theta'(0) \tag{12}$$

$$Sh/\sqrt{Re} = -\phi'(0) \tag{13}$$

3 HAM Solutions

The initial approximations of homotopy analysis solutions are chosen as $f_0 = f_w + 1 - e^{-\eta}$; $\theta_0 = e^{-\eta}$; $\phi_0 = e^{-\eta}$; the auxiliary linear operators L_f, L_θ, and L_ϕ are defined as $L_f = f''' - f'$; $L_\theta = \theta'' - \theta$; $L_\phi = \phi'' - \phi$ with satisfying $L_f\left[C_1 + C_2e^{\eta} + C_3e^{-\eta}\right] = 0$; $L_\theta\left[C_4e^{\eta} + C_5e^{-\eta}\right] = 0$; $L_\phi\left[C_6e^{\eta} + C_7e^{-\eta}\right] = 0$, where C_i, $(i = 1-7)$ denotes the arbitrary constants. The general solution of the Equations (7)–(9) is $f_m(\eta) = f^*{}_m(\eta) + C_1 + C_2e^{\eta} + C_3e^{-\eta}$, $\theta_m(\eta) = \theta^*{}_m(\eta) + C_4e^{\eta} + C_5e^{-\eta}$ and $\phi_m(\eta) = \phi^*{}_m(\eta) + C_6e^{\eta} + C_7e^{-\eta}$ where $f^*{}_m(\eta)$, $\theta^*{}_m(\eta)$ and $\phi_m(\eta)$ are the special solutions.The symbolic calculations are obtained by Mathematica.

These general solutions contain the auxiliary parameters h_f, h_θ, and h_ϕ. These parameters are adjusting and controlling the convergence of the final solutions. The h_f, h_θ, and h_ϕ curves are plotted in Fig. 1. From this figure, we found the range values of h_f, h_θ and h_ϕ are $-0.8 \le h_f \le -0.2$ and $-1.3 \le h_\theta, h_\phi \le -0.2$. It is observed from our computation results that the HAM solution convergence in the whole region of η when $h_f = h_\theta = h_\phi = -0.5$. The order of approximation for the converged solutions are given in Table 1.

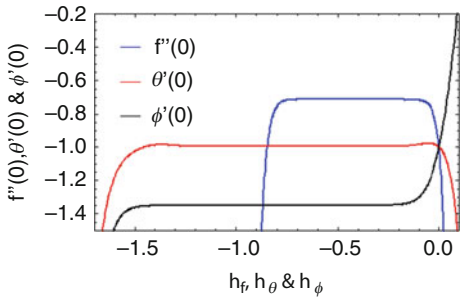

Fig. 1 h-curve of f'', θ', *and* ϕ'

Table 1 Order of approximations

Order	$-f''(0)$	$-\theta'(0)$	$-\phi'(0)$
1	0.73333	0.96333	1.13333
5	0.72562	0.98939	1.33811
10	0.72553	0.99719	1.34698
15	0.72553	0.99533	1.34771
20	0.72553	0.99533	1.34768
25	0.72553	0.99533	1.34768
30	0.72553	0.99533	1.34768
35	0.72553	0.99533	1.34768
40	0.72553	0.99533	1.34768

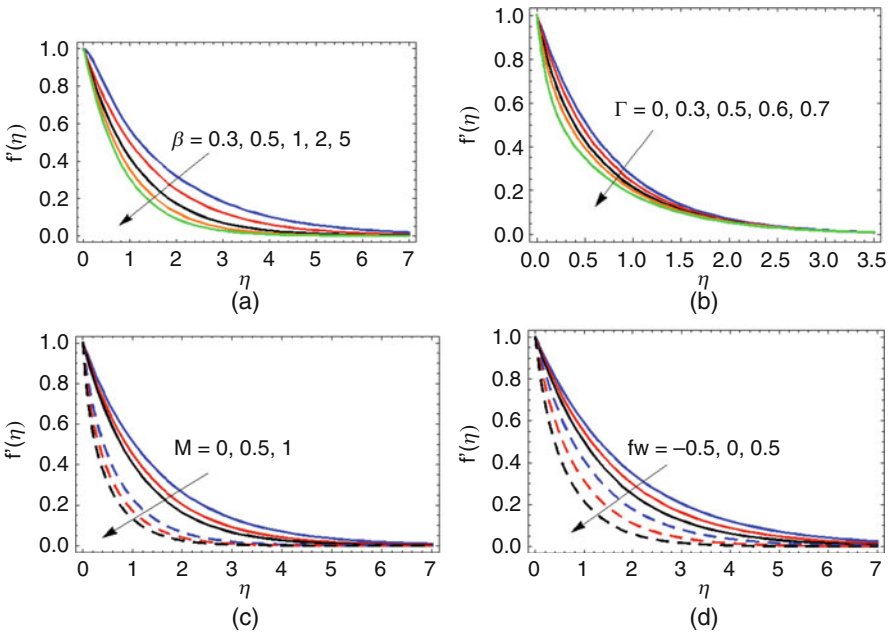

Fig. 2 Velocity profiles for different values of (**a**) β, (**b**) Γ, (**c**) M, (**d**) fw

4 Results and Discussion

The results are presented in different combinations of pertinent parameters involved in the study, ($h = -0.5$, $\beta = 0.5$, $\lambda = 0.5$, $fw = 0.5$, $Hg = -0.2$, $Rd = 0.2$, $M = 0.1$, $\mathrm{Cr} = 1$, $\mathrm{Pr} = 1.2$, $\mathrm{Sc} = 1$, $\mathrm{Df} = 0.1$, $\mathrm{Sr} = 0.3$). Figure 2 shows the velocity profiles for different values of β, Γ, M, fw. It is found that the velocity of the fluid diminishes by these parameters. The temperature profiles for different values of fw, Rd, Df, and Hg are plotted in Fig. 3. The thermal boundary layer thickness reduces with increasing the suction values. The thermal radiation, dufour, and heat generation effects boosted up the temperature inside the boundary

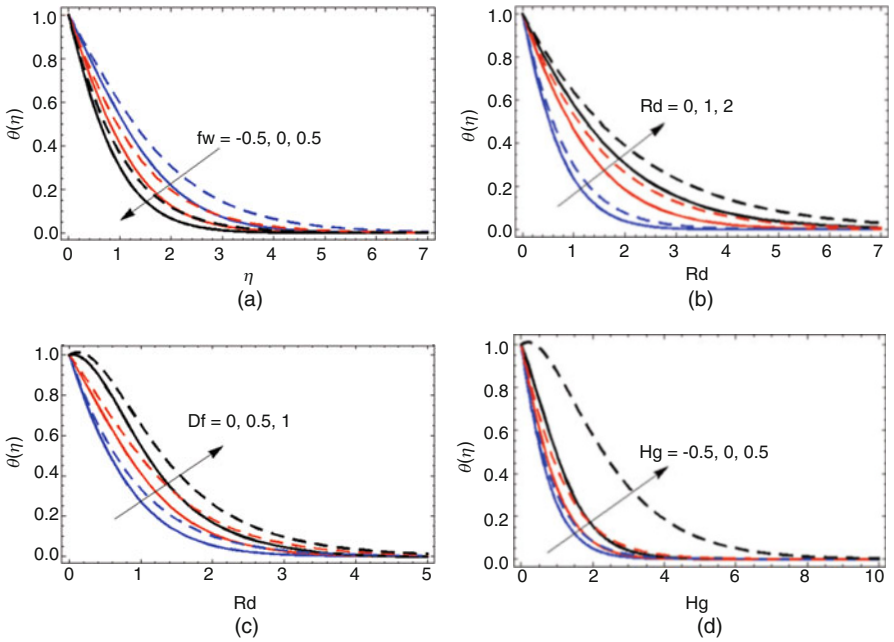

Fig. 3 Temperature profiles for different values of (**a**) fw, (**b**) Rd, (**c**) Df, (**d**) Hg

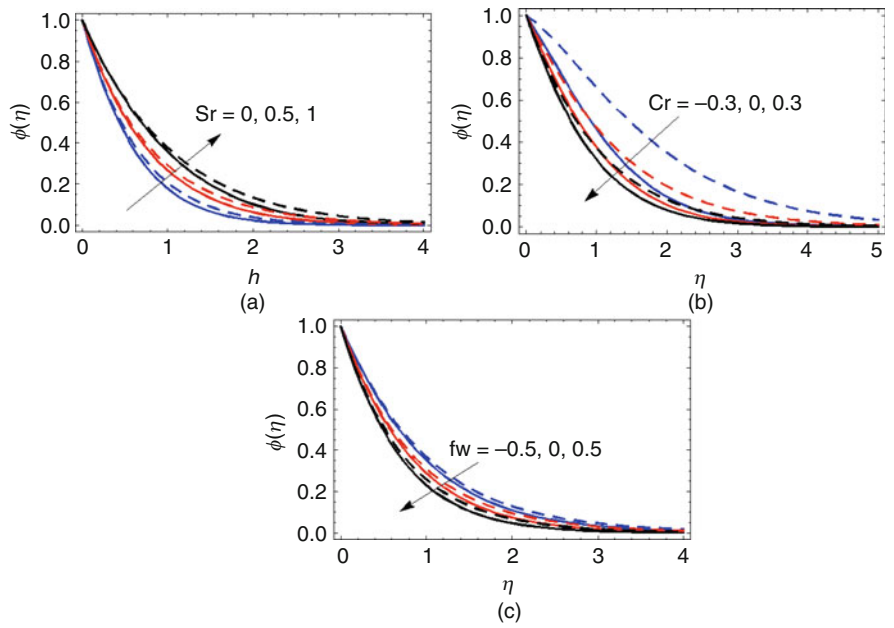

Fig. 4 Concentration profiles for different values of (**a**) Sr, (**b**) Cr, (**c**) fw

Table 2 Shows that the complete agreement between the comparison results exists. This gives confidence in the numerical results to be reported subsequently

β	M	fw	Present study	Ref. [6]
0.5	0.25	0.5	2.20256	2.20256
0.9	0.25	0.5	1.94558	1.94558
1.4	0.25	0.5	1.75799	1.75799
2.0	0.25	0.5	1.64194	1.64195
0.8	0	0.5	1.77069	1.77069
0.8	0.36	0.5	2.01706	2.01706
0.8	1.44	0.5	2.60637	2.60638
0.8	2.25	0.5	2.96569	2.96570
0.8	0.25	0	1.67705	1.67705
0.8	0.25	0.7	2.06318	2.06318
0.8	0.25	1.4	2.51728	2.51728
0.8	0.25	2	2.95256	2.95256

layer. Figure 4 depicted the effect on concentration profiles for different values of Sr, Cr, and fw. The soret effect enhances the thickness of the solutal boundary layer. However, concentration decreases when increasing the chemical reaction and suction parameters.

5 Conclusion

The soret and dufour effects on radiative mixed convective flow and heat transfer of Casson-Williamson fluid over a stretching surface are examined in the presence of uniform external magnetic field and first-order chemical reaction. The governing equations are solved by homotopy analysis method. It is concluded from the study that temperature (concentration) enhances with dufour (soret) parameter. Temperature enhances with increasing radiation parameter, and the thickness of the solutal boundary layer reduces with chemical reaction.

References

1. Eswaramoorthi, S., Bhuvaneswari, M., Sivasankaran, S., Rajan, S.: Soret and dufour effects on viscoelastic boundary layer flow over a stretching surface with convective boundary condition with radiation and chemical reaction. Scientia Iranica B Mech Engg. **23(6)**, 2575–2586 (2016)
2. Rushi Kumar, B., Sivaraj, R.: Heat and mass transfer in MHD viscoelastic fluid flow over a vertical cone and flat plate with variable viscosity. International Journal of Heat and Mass Transfer. **56(1–2)**, 370–379 (2013)
3. Sivaraj, R., Rushi Kumar, B.: Viscoelastic fluid flow over a moving vertical cone and flat plate with variable electric conductivity. International Journal of Heat and Mass Transfer. **6**, 19–128 (2013)

4. Ruhaila, Md., Sivasankaran, S., Bhuvaneswari, M., Hussein, A.K.: Analytical and numerical study on convection of nanofluid past a moving wedge with soret and dufour effects. International Journal of Numerical Methods for Heat & Fluid Flow. **27(10)**, 2333–2354 (2017)
5. Niranjan, H., Sivasankaran, S., Bhuvaneswari, M.: . Chemical reaction, soret and dufour effects on MHD mixed convection stagnation point flow with radiation and slip condition. Scientia Iranica B Mech Engg. **24(2)**, 698–706 (2017)
6. Karthikeyan, S., Bhuvaneswari, M., Sivasankaran, S., Rajan S.: Soret and dufour effects on MHD mixed convection heat and mass transfer of a stagnation point flow towards a vertical plate in a porous medium with chemical reaction, radiation and heat generation. J. Applied Fluid Mech. **9(3)**, 1447–1455 (2016)
7. Kasmani, R.M., Sivasankaran, S., Bhuvaneswari, M., Siri, Z.: Effect of chemical reaction on convective heat transfer of boundary layer flow in nanofluid over a wedge with heat generation absorption and suction. J. Applied Fluid Mech. **9(1)**, 379–388 (2016)
8. Sivasankaran, S., Niranjan, H., Bhuvaneswari, M.: Chemical reaction, radiation and slip effects on MHD mixed convection stagnation-point flow in a porous medium with convective boundary condition. Int. J. Numerical Methods for Heat & Fluid Flow. **27(2)**, 454–470 (2017)
9. Shehzad, S.A., Hayat, T., Qasim, M., Asghar, S.: Effects of mass transfer on MHD flow of casson fluid with chemical reaction and suction. Brazilian Journal of Chemical Engineering. **30(1)**, 187–195 (2013)

Study of Steady, Two-Dimensional, Unicellular Convection in a Water-Copper Nanoliquid-Saturated Porous Enclosure Using Single-Phase Model

P. G. Siddheshwar and B. N. Veena

Abstract In the present paper, we study Brinkman-Bénard convection in nanoliquid-saturated porous enclosure with vertical walls being adiabatic and horizontal walls being isothermal for two velocity boundary combinations, namely, free-free (FF) and rigid-rigid (RR). Brinkman model has been modified in the present study to account for added nanoparticles. Thermophysical properties of nanoliquid in a saturated porous medium as a function of corresponding properties of base liquid, nanoparticle and porous medium are modelled using phenomenological laws and mixture theory. An analytical study has been made of Brinkman-Bénard convection in a porous enclosure using single-phase model. The effect of nanoparticles is to advance onset of convection and enhance heat transfer, whereas porous medium facilitates delayed onset and retainment of heat energy in the system. The present study shows good agreement with those of previous works.

Keywords Porous enclosure · Free-free · Rigid-rigid and single-phase model

1 Introduction

Nanoliquid is a base liquid containing nano-sized particles (termed nanoparticles) with size ranging from 1 to 100 nm. These liquids are engineered colloidal suspensions of nanoparticles in a base liquid. Masuda et al. [4], Eastman et al. [6] and Das et al. [7] have reported remarkable enhancements in the thermal conductivity of nanoliquid with a very low volume fraction of nanoparticles. The word nanoliquid was first coined by Choi and Eastman [5]. Nanoliquids have many applications in heat transfer which includes microelectronics, fuel cells, pharmaceutical processes, hybrid powered engines, engine-cooling/vehicle thermal management, domestic

P. G. Siddheshwar (✉) · B. N. Veena
Department of Mathematics, Bangalore University, Bangalore, India
e-mail: pgsiddheshwar@bub.ernet.in; veenabn@bub.ernet.in

B. Rushi Kumar et al. (eds.), *Applied Mathematics and Scientific Computing*,
Trends in Mathematics, https://doi.org/10.1007/978-3-030-01123-9_16

refrigerator, chiller, heat exchanger, grinding and machining [13]. The study of heat transfer in nanoliquids is normally done with one of the three types of models, namely, single-phase model of Khanafer-Vafai-Lightstone [8, 12, 16], two-phase model of Buongiorno [10] and modified Buongiorno two-phase model [14]. Heat transfer in enclosures filled with nanoliquids has been studied by many authors [8, 15, 16], and review of literature shows that most of the enclosure problems have been solved numerically, and an analytical study would thus be a welcome effort.

The objectives of the present paper are to study:

- Boundary effects on onset of convection and heat transfer in an enclosure using single-phase model by considering water-copper as nanoliquid and 30% glass fibre reinforced polycarbonate as porous material.
- Unicellular convection and the range of aspect ratio, A, in which unicellular convection is valid.
- The effect of volume fraction, χ, Brinkman number, Λ, and porous parameter, σ^2 on the onset of instability and on heat transfer.

2 Formulation of the Problem

A nanoliquid-saturated porous enclosure of breadth b and height h is considered. The water-copper nanoliquid is assumed to be a Newtonian viscous liquid (water) with suspended copper nanoparticles. The porous medium is assumed to be homogeneous and isotropic, and nanoparticles are assumed to be spherical, of same size, and manufactured at the same temperature and other operating conditions. The upper and lower boundaries are maintained at constant temperatures T_0 and $T_0 + \Delta T$ ($\Delta T > 0$), respectively, and the vertical walls are insulated. We assume that the Oberbeck-Boussinesq approximation is valid. The flow configuration is as shown in Fig. 1.

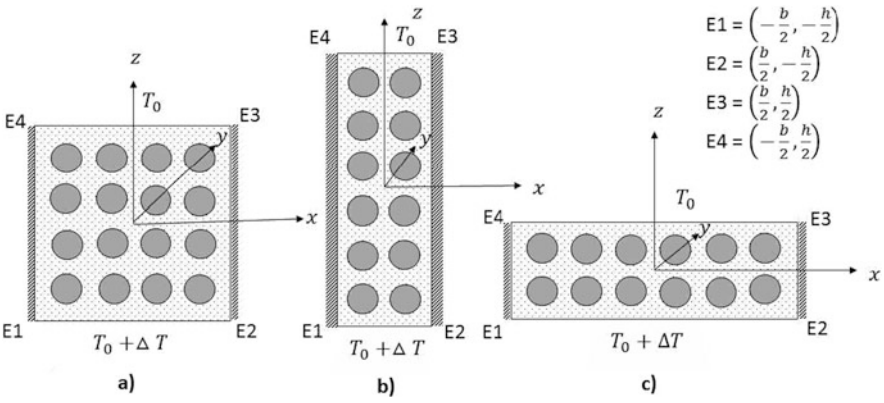

Fig. 1 Schematic representation of the flow configuration. (**a**) Square enclosure. (**b**) Tall enclosure. (**c**) Shallow enclosure

The non-dimensional form of equations for studying Brinkman-Bénard convection are given by:

$$a\Lambda\nabla_A^4\Psi - a\sigma^2 A^2\nabla_A^2\Psi - a^2 Ra_{ne}A^4\frac{\partial\Theta}{\partial X} = 0, \tag{1}$$

$$-A\frac{\partial\Psi}{\partial X} + a\,M\nabla_A^2\Theta + A\frac{\partial(\Psi,\Theta)}{\partial(X,Z)} = 0. \tag{2}$$

The non-dimensional parameters appearing in Eqs. (1) and (2) are:

$$a = \frac{\alpha_{ne}}{\alpha_{bl}},\quad \Lambda = \frac{\mu_{ne}}{\mu_{nl}},\quad \sigma^2 = \frac{b^2}{K},\quad A = \frac{h}{b},\quad Ra_{ne} = \frac{(\rho\beta)_{ne}g\Delta T b^3}{\phi^{2.5}\mu_{ne}\alpha_{ne}}. \tag{3}$$

The thermophysical properties of nanoliquid as a function of corresponding properties of base liquid and nanoparticles are modelled using either phenomenological laws [1, 3] or mixture theory, and the properties of nanoliquid-saturated porous medium are obtained from mixture theory [9] (see [16]). To solve Eqs. (1) and (2), we consider two sets of boundary conditions:

- **Case (i): Free-free isothermal horizontal boundaries and free-free adiabatic vertical boundaries**

$$\left.\begin{aligned}\Psi = \frac{\partial^2\Psi}{\partial Z^2} = \Theta = 0 \;\; at \;\; Z = -\frac{1}{2},\frac{1}{2} \;\; and \;\; \frac{-1}{2} < X < \frac{1}{2}\\ \Psi = \frac{\partial^2\Psi}{\partial X^2} = \frac{\partial\Theta}{\partial X} = 0 \;\; at \;\; X = -\frac{1}{2},\frac{1}{2} \;\; and \;\; \frac{-1}{2} < Z < \frac{1}{2}\end{aligned}\right\}. \tag{4}$$

- **Case (ii): Rigid-rigid isothermal horizontal boundaries and rigid-rigid adiabatic vertical boundaries**

$$\left.\begin{aligned}\Psi = \frac{\partial\Psi}{\partial Z} = \Theta = 0 \;\; at \;\; Z = -\frac{1}{2},\frac{1}{2} \;\; and \;\; \frac{-1}{2} < X < \frac{1}{2}\\ \Psi = \frac{\partial\Psi}{\partial X} = \frac{\partial\Theta}{\partial X} = 0 \;\; at \;\; X = -\frac{1}{2},\frac{1}{2} \;\; and \;\; \frac{-1}{2} < Z < \frac{1}{2}\end{aligned}\right\}. \tag{5}$$

3 Nonlinear Stability Analysis

Case (i) We consider minimal number of modes in the double Fourier series solution to describe the steady finite amplitude convection and the same is given by

$$\Psi(X,Z) = \frac{\sqrt{2}M\delta_A^2 a}{A\pi^2}U\sin\left(\pi X + \frac{\pi}{2}\right)\sin\left(\pi Z + \frac{\pi}{2}\right), \tag{6}$$

$$\Theta(X, Z) = \frac{1}{2} - Z + \frac{1}{r\pi}\left[-\sqrt{2}V\cos\left(\pi X + \frac{\pi}{2}\right)\sin\left(\pi Z + \frac{\pi}{2}\right) - W\sin(2\pi Z + \pi)\right], \tag{7}$$

where $r = \dfrac{Ra_{ne}^{FF}}{Ra_{ne_c}^{FF}}$ and $Ra_{ne_c}^{FF}$ represents critical Rayleigh number for free-free boundary combination given by:

$$Ra_{ne_c}^{FF} = \frac{M\delta_A^4}{\pi^2 A^3}\left[\frac{\Lambda\delta_A^2}{A^2} + \sigma^2\right]. \tag{8}$$

Substituting Eqs. (6) and (7) in Eqs. (1) and (2), we get nonlinear algebraic equations connecting the amplitudes in the form:

$$V - U = 0, \quad rU - UW - V = 0, \quad UV - b_1 W = 0, \tag{9}$$

where U, V and W are the amplitudes of convection, $b_1 = \frac{4\pi^2}{\delta_A^2}$ and $\delta_A^2 = \pi^2(A^2+1)$.

Estimation of Enhanced Heat Transport

The Nusselt number, Nu_{ne}, in a nanoliquid-saturated porous enclosure for the stationary mode of convection evaluated at the lower boundary $Z = -\frac{1}{2}$ is given by

$$Nu_{ne} = \frac{\left[-k_{be}\int_{-\frac{1}{2}}^{\frac{1}{2}}\frac{d\Theta_b}{dZ}dX\right]_{Z=-\frac{1}{2}} + \left[-k_{ne}\int_{-\frac{1}{2}}^{\frac{1}{2}}\frac{\partial\Theta}{\partial Z}dX\right]_{Z=-\frac{1}{2}}}{\left[-k_{be}\int_{-\frac{1}{2}}^{\frac{1}{2}}\frac{d\Theta_b}{dZ}dX\right]_{Z=-\frac{1}{2}}}, \tag{10}$$

where $\Theta = \dfrac{T - T_0}{\Delta T}$, $\Theta_b = \dfrac{T_b - T_0}{\Delta T}$.

On simplifying Eq. (10), we get Nusselt number expression for free-free boundaries as follows:

$$Nu_{ne} = 1 + 2\frac{k_{ne}}{k_{be}}\left[1 - \frac{1}{r}\right]. \tag{11}$$

Case (ii) The minimal number of modes in the double Fourier series solution to describe the steady finite amplitude convection in a nanoliquid is given by

$$\Psi(X, Z) = \frac{M\delta_A^2 a}{2\sqrt{2}AP_5}UC_{fe}(X)C_{fe}(Z), \tag{12}$$

$$\Theta(X,Z) = \frac{1}{2} - Z + \frac{P_2}{rP_5}\left[-\sqrt{2}V\cos\left(\pi X + \frac{\pi}{2}\right)\sin\left(\pi Z + \frac{\pi}{2}\right) - W\sin(2\pi Z + \pi)\right], \tag{13}$$

where $C_{fe}(X)$ and $C_{fe}(Z)$ are Chandrashekar even function [2], $r = \dfrac{Ra_{ne}^{RR}}{Ra_{ne_c}^{RR}}$, and $Ra_{ne_c}^{RR}$ represents critical Rayleigh number expression for rigid-rigid boundary combination given by:

$$Ra_{ne_c}^{RR} = \frac{M\delta_A^2}{4A^3P_2^2}\left[\frac{\Lambda P_3(1+A^4)}{A^2} + \Lambda P_4 - (1+A^2)P_1\sigma^2\right]. \tag{14}$$

The various quantities appearing in Eq. (14) are:

$$P_1 = \frac{1}{16}P_6P_7P_8, \quad P_2 = \frac{16\pi^3\mu_1^4}{(\pi^4-\mu_1^4)^2}, \quad \mu_1 = 4.73004074,$$

$$P_3 = \frac{\mu_1^2}{16}P_6P_7^2, \quad P_4 = \frac{\mu_1^2}{8}P_6P_8^2, \quad P_6 = \sec^4[\frac{\mu_1}{2}]\,\mathrm{sech}^4[\frac{\mu_1}{2}],$$

$$P_7 = 2\sin[\mu_1]\cosh^2[\frac{\mu_1}{2}] + 2\sinh[\mu_1]\cos^2[\frac{\mu_1}{2}] - \mu_1(2+\cos[\mu_1]+\cosh[\mu_1]),$$

$$P_8 = 2\sin[\mu_1]\cosh^2[\frac{\mu_1}{2}] - 2\sinh[\mu_1]\cos^2[\frac{\mu_1}{2}] - \mu_1(\cos[\mu_1]-\cosh[\mu_1]).$$

Substituting Eqs. (12) and (13) in Eqs. (1) and (2), we get the algebraic equations connecting the amplitudes in the form:

$$V - U = 0, \quad rU - UW - V = 0, \quad UV - b_1W = 0. \tag{15}$$

Note that Eq. (15) is essentially Eq. (9) but with a different scaling of quantities.

Estimation of Enhanced Heat Transport

Following the procedure of free-free boundaries we get the expression for Nusselt number for nanoliquid-saturated porous medium, Nu_{ne}, for rigid-rigid boundaries as follows:

$$Nu_{ne} = 1 + 2\frac{k_{ne}}{k_{be}}\frac{P_2}{P_5}\left[1 - \frac{1}{r}\right], \tag{16}$$

where

$$P_5 = \frac{32\pi^3\mu_1^4(39\pi^4+\mu_1^4)}{(\pi^4-\mu_1^4)^2(81\pi^4-\mu_1^4)},$$

and the other quantities are as defined earlier.

4 Results and Discussions

Brinkman-Bénard convection in a nanoliquid-saturated porous medium is investigated by considering water as base liquid, copper as nanoparticle and 30% glass fibre reinforced polycarbonate as porous material. Thermophysical properties of base liquid [12], nanoparticles [12] and porous medium [17] (see Table 1) are collected from literature. Thermophysical properties of nanoliquid-saturated porous medium are calculated by considering nanoparticles' volume fraction, χ=0.06, and porous medium with porosity, ϕ=0.88, at 300 K using phenomenological laws and mixture theory.

From the study of linear theory, we can rewrite Rayleigh number, Ra_{ne}, for free-free and rigid-rigid boundaries as follows:

$$Ra_{ne} = F\ Ra_{be},\ \ F = \frac{(\rho\beta)_{ne}}{(\rho\beta)_{be}}\frac{\mu_{be}}{\mu_{ne}}\frac{\alpha_{be}}{\alpha_{ne}}. \tag{17}$$

Hence $Ra_{ne} < Ra_{be}$. This shows us that the presence of nanoparticles in base liquid advances onset of convection.

From Fig. 2a it is observed that onset of convection is advanced with the increase in aspect ratio, A, and a sudden rise in the scaled Rayleigh number, r, is observed when value of A decreases below 0.85 which shows the invalidity of the result for unicellular assumption. The condition $A << 1$ refers to classical Rayleigh-Bénard convection problem. Hence we conclude that unicellular convection is possible in the range $0.85 < A < 1.2$. Further, from Fig. 2b, c, it is observed that onset of convection is delayed with increase in Brinkman number, Λ, and porous parameter,

Table 1 Thermophysical properties of porous material (30% glass fibre reinforced polycarbonate) at 300 K [17]

Quantity	Density [kgm^{-3}]	Thermal expansion coefficient [K^{-1} × 10^5]	Specific heat [J/kg-K]	Thermal conductivity [W/m-K]	Porosity
30% glass fibre reinforced polycarbonate	ρ_s=1430	β_s=3.5	$(C_p)_s$=1130	k_s=0.24	ϕ=0.88 [9]

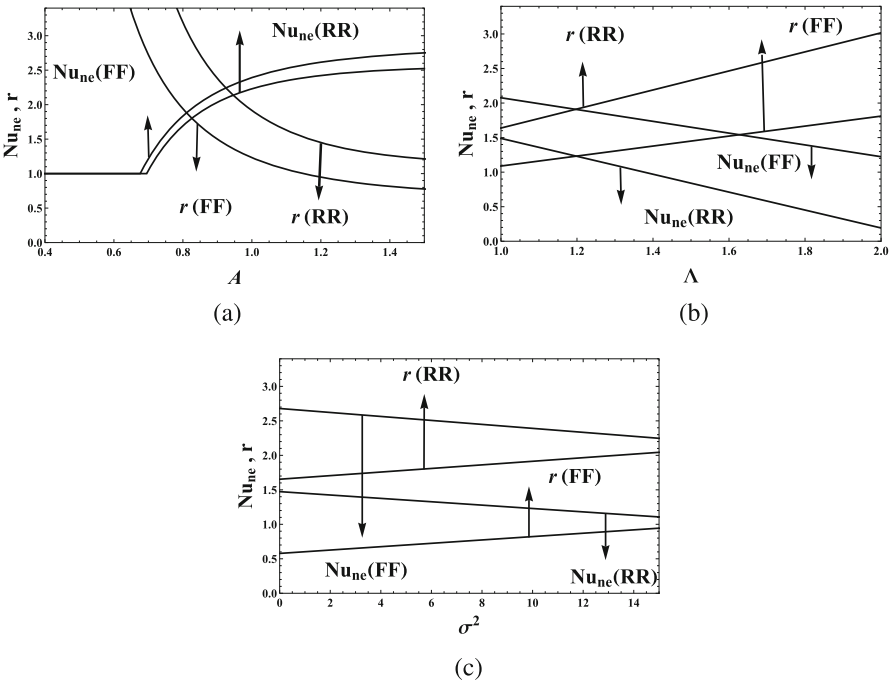

Fig. 2 Variation of Nusselt number for nanoliquid-saturated porous medium, Nu_{ne}, or scaled Rayleigh number, r, for different values of aspect ratio, A, Brinkman number, Λ and porous parameter, σ^2. (**a**) $\sigma^2 = 10$ and $\Lambda = 1.2$. (**b**) A = 1 and $\sigma^2 = 10$. (**c**) A = 1 and $\Lambda = 1.2$

σ^2, for free-free and rigid-rigid boundaries. Hence χ and A have destabilizing effect, whereas Λ and σ^2 have stabilizing effect on the onset of convection. Further, from Fig. 2a, it is observed that enhanced heat transfer is seen in enclosures with high-aspect ratio, compared to enclosures with low-aspect ratio in the case of both free-free and rigid-rigid boundaries. From Fig. 2b, c, it is observed that heat transfer decreases with increase in Λ and σ^2. From Fig. 2 it is further clear that free-free boundaries facilitates greater amount of heat transport compared to rigid-rigid boundaries.

Our results in a limiting case were compared with existing results. In the case of rigid-rigid boundary condition with $\chi = 0.08$ and Ra_{nl}^{RR}=5000 for water-copper nanoliquid occupying rectangular enclosures, our results tally with those of Elhajjar et al. [11] for aspect ratios 0.8687 and 0.8689, respectively.

Acknowledgements One of the authors (BNV) would like to thank the University Grants Commission, Government of India for awarding her the "National Fellowship for Higher Education" to carry out her research. The authors thank the Bangalore University for encouragement and support.

Nomenclature		β	thermal expansion coefficient
Latin Symbols		χ	volume fraction
a	ratio of thermal diffusivity	ΔT	temperature difference
A	aspect ratio	Λ	Brinkman number
C_p	specific heat	μ	dynamic viscosity
$\mathbf{g}$	acceleration due to gravity $(0, 0, -g)$	ϕ	porosity
k	thermal conductivity	Ψ	non-dimensional stream function
K	permeability	ρ	actual density
M	ratio of specific heat	Θ	non-dimensional temperature
Nu	Nusselt number		
r	scaled Rayleigh number	***Subscripts***	
Ra	Rayleigh number	b	basic state
T	temperature	be	base liquid-saturated porous medium
T_0	temperature at the lower boundary	c	critical
X	non-dimensional horizontal coordinate	ne	nanoliquid-saturated porous medium
Z	non-dimensional vertical coordinate	nl	nanoliquid
Greek Symbols		s	solid
α	thermal diffusivity		

References

1. Brinkman, H.C.: The viscosity of concentrated suspensions and solutions. J. Chem. Phys. **20**, 571–571 (1952)
2. Chandrasekhar, S.: Hydrodynamic and Hydromagnetic Stability. Oxford University Press-London (1961)
3. Hamilton, R.L., Crosser, O.K.: Thermal conductivity of heterogeneous two-component systems. Ind. Eng. Chem. Fund. **1**, 187–191 (1962)
4. Masuda, H., Ebata, A., Terama, K., Hishinuma, N.: Alteration of thermal conductivity and viscosity of liquid by dispersing ultra-fine particles dispersion of Al_2O_3, SiO_2 and TiO_2 ultra-fine particles. Netsu Bussei. **7**, 227–233 (1993)
5. Choi, S.U.S., Eastman, J.A.: Enhancing thermal conductivity of fluids with nanoparticles. D. A. Siginer and H. P. Wang (Eds.) Development and applications of Non-Newtonian Flows, ASME-Publications-Fed. **231**, 99–106 (1995)
6. Eastman, J.A., Choi, S.U.S., Li, S., Yu, W., Thompson, L.J.: Anomalously increased effective thermal conductivities of ethylene glycol-based nanofluids containing copper nanoparticles. Appl. Phys. Lett. **78**, 718–720 (2001)
7. Das, S.K., Putra, N., Thiesen, P., Roetzel, W.: Temperature dependence of thermal conductivity enhancement for nanofluids. J. Heat Transfer, ASME. **125**, 567–574 (2003)
8. Khanafer, K., Vafai, K., Lightstone, M.: Buoyancy-driven heat transfer enhancement in a two-dimensional enclosure utilizing nanofluids. Int. J. Heat Mass Transfer. **46**, 3639–3653 (2003)

9. Nield, D.A., Bejan, A.: Convection in Porous Media. Wiley-New York (2006)
10. Buongiorno, J.: Convective transport in nanofluids. J. Heat Transfer, ASME. **128**, 240–250 (2006)
11. Elhajjar, B., Bachir, G., Mojtabi, A., Fakih, C., Charrier-Mojtabi, M.C.: Modeling of Rayleigh-Bénard natural convection heat transfer in nanofluids. C. R. Mécanique. **338**, 350–354 (2010)
12. Siddheshwar, P.G., Meenakshi, N.: Amplitude equation and heat transport for Rayleigh-Bénard convection in Newtonian liquids with nanoparticles. Int. J. Appl. Comput. Math. **2**, 1–22 (2015)
13. Bianco, V., Manca, O., Nardini, S., Vafai, K.: Heat transfer enhancement with nanofluids. CRC Press-New York (2015)
14. Siddheshwar, P.G., Kanchana, C., Kakimoto, Y., Nakayama, A.: Steady finite-amplitude Rayleigh-Bénard convection in nanoliquids using two phase model: Theoretical answer to the phenomenon of enhanced heat transfer. J. Heat Transfer, ASME. **139**, 012402–012412 (2017)
15. Siddheshwar, P.G., Veena, B. N.: Unsteady Rayleigh-Bénard convection of nanoliquids in enclosures. World Academy of Science, Engineering and Technology, International Journal of Mechanical, Aerospace, Industrial, Mechatronic and Manufacturing Engineering. **11**, 1051–1060 (2017)
16. Siddheshwar, P.G., Veena, B. N.: A theoretical study of natural convection of water-based nanoliquids in low-porosity enclosures using single-phase model. J. Nanofluids. **7**, 1–12 (2018)
17. https://www.matbase.com/material-categories/natural-andsynthetic-composites/polymer-matrix-composites-pmc/reinforcedpolymers/material-properties-of-polycarbonate-30-percent-glass-fiberreinforced-pc-gf30.html.

The Effects of Homo-/Heterogeneous Chemical Reactions on Williamson MHD Stagnation Point Slip Flow: A Numerical Study

T. Poornima, P. Sreenivasulu, N. Bhaskar Reddy, and S. Rao Gunakala

Abstract The objective of the present paper is to examine numerically the chemical reaction and mass transfer effects on magnetohydrodynamic Williamson fluid past an exponentially stretching sheet. The basic flow field equations are transformed to coupled, nonlinear ordinary differential equations using suitable similarity variables and then solved using the Runge–Kutta–Fehlberg method. The effects of various material parameters on the flow field momentum and species in addition to wall shear stress are computed effectively and portrayed graphically. The diffusion rate is low for both homogeneous and heterogeneous reactions. Acceleration in the values of Williamson fluid parameters accelerates the friction.

1 Introduction

There is an increased need to model the behavior of rheological fluids because of their huge application in the technological and engineering process such as coating items with emulsions, polymer solutions, paints, etc., One of these is pseudoplastic fluids, which are non-Newtonian fluid exhibiting shear-thinning behaviors. The model was developed in 1929 by Williamson to examine pseudoplastic flows. Nadeem et al. [1] investigated the Williamson fluid flow past a stretching

T. Poornima (✉)
Department of Mathematics (SAS), VIT University, Vellore, India
e-mail: poornima.t@vit.ac.in

P. Sreenivasulu
Department of Mathematics, SVCET, Chittoor, Andhra Pradesh, India
e-mail: hod_sh@svew.edu.in

N. Bhaskar Reddy
Department of Mathematics, S.V. University, Tirupati, Andhra Pradesh, India

S. Rao Gunakala
Department of Mathematics and Statistics, The University of the West Indies, St. Augustine, Trinidad and Tobago
e-mail: sreedhara.rao@sta.uwi.edu

B. Rushi Kumar et al. (eds.), *Applied Mathematics and Scientific Computing*,
Trends in Mathematics, https://doi.org/10.1007/978-3-030-01123-9_17

sheet. Mabood et al. [2] analyzed the magnetohydrodynamic (MHD) effects on Williamson nanofluid considering radiation. Bing et al. [3] analyzed the influence of heat transfer on Williamson nanofluids along a stretching sheet taking into account thermal radiation.In the world of chemical engineering and in some other industrial processes, the reaction between the species with the help of a catalyst or occurring in different media is a reliable concept. If the reaction occurs in a uniform phase it is termed 'Homo,' whereas if the reaction occurs in different phases in the presence of a catalyst, 'Hetero' is coined. The rate of reaction is proportioned directly to the species concentration (first-order chemical reaction). Shehzad et al. [4] discussed and portrayed the impact of the chemical reaction on Casson fluid. The effects of a chemical reaction on a circular cylinder were studied by Poornima et al. [5]. With heat generation/absorption, Jena et al. [6] investigated the behavior of Jeffry fluid in porous media, taking into account the chemical reaction. In most of the problems, no slip is considered. In natural and engineering processes such as suspensions, emulsions, foams, etc., the slip phenomenon is observed. Recent application of a boundary slip is the polishing of internal cavities and artificial heart valves. Sheikh and Abbas [7] discussed the chemical reaction effects on Casson fluid toward a stretching/shrinking sheet with slip conditions. Ibrahim and Makinde [8] portrayed their ideas on the stagnation point of Casson nanofluid with a Navier slip thematically. Poornima et al. [9] analytically discussed the slip flow regime on Casson rheological fluid.

2 Basic Transport Equations

Consider a steady two-dimensional flow past an exponential stretching sheet on an MHD Williamson fluid with slip effects. The fluid is confined to $y > 0$. The wall is kept stretched exponentially with a stretching velocity $U_w = be^{\frac{x}{L}}$ and a stagnant velocity $U_e = ae^{\frac{x}{L}}, a, b > 0$. A variable magnetic field $B = B_0 e^{\frac{x}{2L}}$, is normally applied to the sheet. The interactions between the homo- and heterogeneous reactions are examined for this precise model using the given mathematical representation, which is as follows:

$$\begin{aligned} A + 2B &\longrightarrow 3B, rate = k_c cd^2 \\ A &\longrightarrow B, rate = k_s cd^2 \end{aligned} \tag{1}$$

with the species constant rates k_s, k_c and c,d are the concentrations of chemical species A and B. The schematic representation of the model is portrayed in Fig. 1. The boundary layer equations with the restricted conditions of the flow field is of the form:

$$\frac{\partial u}{\partial x} + \frac{\partial u}{\partial y} = 0 \tag{2}$$

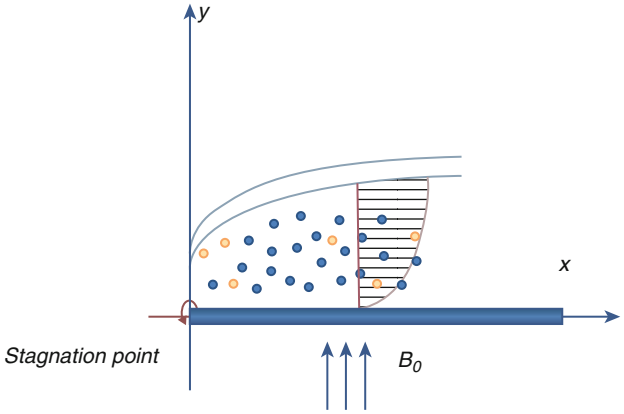

Fig. 1 Flow model representation

$$u\frac{\partial u}{\partial x}+v\frac{\partial u}{\partial y}=U_\infty\frac{dU_\infty}{dx}+\nu\frac{\partial^2 u}{\partial y^2}+\sqrt{2}\Gamma\nu\frac{\partial u}{\partial y}\frac{\partial^2 u}{\partial y^2}-\frac{\sigma B^2(u-U_\infty)}{\rho} \tag{3}$$

$$u\frac{\partial c}{\partial x}+v\frac{\partial c}{\partial y}=D_A\frac{\partial^2 c}{\partial y^2}-k_c c d^2 \tag{4}$$

$$u\frac{\partial d}{\partial x}+v\frac{\partial d}{\partial y}=D_B\frac{\partial^2 d}{\partial y^2}+k_c c d^2 \tag{5}$$

$$y=0:\quad u=U_w(x)+N\nu\left(\frac{\partial u}{\partial y}\right)+\frac{\Gamma}{\sqrt{2}}\left(\frac{\partial u}{\partial y}\right)^2, V=V_w,$$

$$D_A\frac{\partial c}{\partial y}=k_s c,\ D_B\frac{\partial d}{\partial y}=-k_s c$$

$$y\longrightarrow\infty:\quad u=U_e(x), V=0, c=c_0, d=0 \tag{6}$$

where u and v denote the velocity components in x and y directions, ν is the kinematic viscosity, D_A, D_B are the respective diffusion coefficients. N is the velocity slip, $V_w=-V_0e^{\frac{x}{2L}}$ the suction/blowing parameter, Γ the Williamson parameter.

Introducing the similarity variables:

$$\eta=y\sqrt{\frac{b}{2L\nu}}e^{\frac{x}{2L}}, g(\eta)=\frac{d}{c_0}, h(\eta)=\frac{d}{c_0}, \Omega=\Gamma\sqrt{\frac{b^3e^{\frac{3x}{L}}}{\nu L}},\ S=\frac{V_0}{\sqrt{\frac{b\nu}{2L}}}, \delta=\frac{a}{b},$$

$$M=\frac{2L\sigma B_0^2}{\rho b}, Sc=\frac{\nu}{D_A}, \varsigma=\frac{D_B}{D_A}, N_0=N\sqrt{\frac{\nu b}{2L}}, \kappa=\frac{k_c c_0^2 L}{d}, \kappa_s=\frac{k_s}{\sqrt{Re}\,D_A} \tag{7}$$

The flow field equation turns dimensionless and takes the following form:

$$f''' + ff'' + 2(\delta^2 - (f'^2)) + \Omega f'' f''' - M(f' - \delta) = 0 \tag{8}$$

$$g'' + Scfg' - \kappa gh^2 = 0 \tag{9}$$

$$h'' + Scfh' + \kappa gh^2 = 0 \tag{10}$$

The associated boundary conditions are as follows:

$$f'(0) = 1 + N_0\left(f''(0) + \Omega f''^2(0)\right), f = S, g'(0) = \kappa_s g(0), \varsigma h'(0) = -\kappa_s h(0)$$

$$f' \longrightarrow \delta, g \longrightarrow 1, h \longrightarrow 0 \; as \; \eta \longrightarrow \infty \tag{11}$$

Here, Ω is the Williamson parameter, δ the velocity ratio (stagnation) parameter, ς ratio of diffusion coefficients, N_0 the velocity slip parameter, κ the measure of strength of the homogeneous reaction, κ_s the measure of strength of the heterogeneous parameter. It is assumed here that $\varsigma = 1$, i.e., the diffusion coefficients, are equal. In most practical applications, the diffusion coefficients of chemical species are required to be of comparable size. Thus, the assumption leads to the relation: $g(\eta) + h(\eta) = 1$.

Hence, the species equations (9) and (10) reduce and give the final form

$$\phi'' + Scf\phi' - \kappa\phi\left(1 - \phi^2\right) = 0 \tag{12}$$

The respective boundary conditions are

$$\phi' = \kappa_s\phi \; at \; \eta = 0$$

$$\phi \longrightarrow 1 \; as \; \eta \longrightarrow \infty \tag{13}$$

Engineering quantities of our interest are calculated as

$$C_f = \frac{\tau_w}{\rho U_w^2(x)} \; where \; \tau_w = \mu\left[\left(\frac{\partial u}{\partial y}\right) + \frac{\Gamma}{\sqrt{2}}\left(\frac{\partial u}{\partial y}\right)^2\right]_{y=0}$$

$$\Rightarrow \sqrt{2Re}C_f = f''(0) + \frac{\Omega}{2}f''^2(0)$$

$$ShRe^{\frac{1}{2}}(x) = -\phi'(0) \tag{14}$$

3 Results and Discussion

To see in detail the effects of various material parameters found in the flow field on the fluid velocity, concentration in addition to the skin friction coefficient and Sherwood number is illustrated through graphs and tables. However, for want of space, here, we have shown the effects of few important parameters using graphs. The several physical parameters present are the fluid parameter (Williamson parameter) Ω, slip (N_0), the suction/injection (S), and the stretching parameter (δ).

Figure 2 represents the effect of the homogeneous chemical reaction parameter on solutal concentration. Species concentration decreases near the wall within the region $0 <= h(\eta) <= [0, 3]$, while the trend seems reversed in the region $\eta > 3$. This is due to the fact that reactions occurring near the plate diffuses species more effectively than in the ambient stream.

Figure 3 represents the effect of heterogeneous chemical reaction parameter on solutal concentration. If $\kappa_s = 0$, then $\phi = 1$, which implies that the absence of the reaction is almost linear. As κ_s increases, greater dispersion of species particles of the Williamson fluid occurs, thereby decreasing the solutal concentration. Interestingly, a reverse trend is observed after $\eta > 3$. Figure 4 portrays the influence of the Williamson parameter on the fluid concentration. As the fluid parameter increases, the solutal concentration decreases as the concentration boundary layer thickness reduces. It is seen that all the profiles coincide at the point $\eta = 3.0$ and reach a maximum of $\phi = 1.0$.

The velocity profiles versus the stretching parameter is shown in Fig. 5. As both stretching and stagnant velocity are equal, then the momentum of the fluid is linear. If $a < b$, then the profiles are under the case of $a = b$, i.e., the motion of the fluid descends near the plate and linear motionobserved as it approaches free stream.

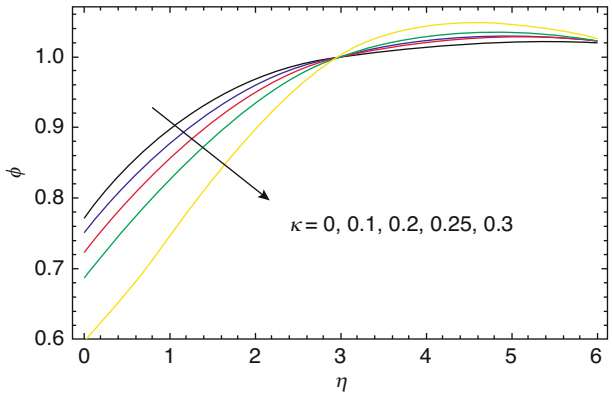

Fig. 2 Solutal profiles versus homogeneous chemical reaction parameter

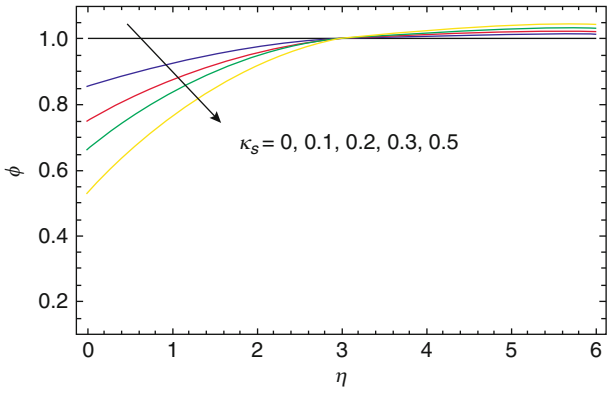

Fig. 3 Effect of κ_s on concentration

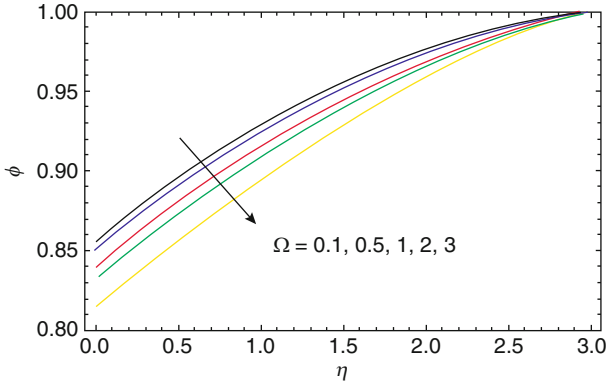

Fig. 4 Concentration profiles for different Williamson parameters

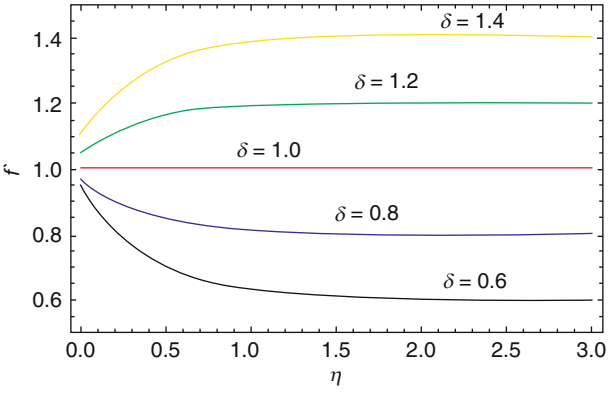

Fig. 5 Velocity profiles for various stretching parameters

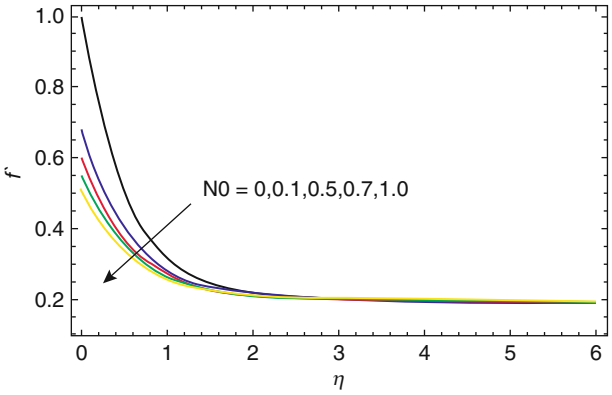

Fig. 6 Effect of slip on velocity

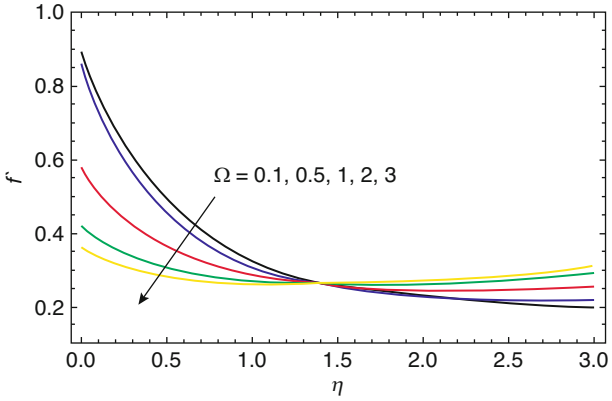

Fig. 7 Velocity profiles for different values of the Williamson parameter

Similarly, if $a > b$, then the profiles are over the linear profile $a = b$, i.e., the fluid momentum ascends and approaches linearly to the free stream. Figure 6 portrays the influence of partial slip on the motion of the fluid. Owing to the partial slip presence, near the plate, the fluid slips within the layers, thereby reducing fluid movement.

The influence of the Williamson fluid parameter on the translational velocity is portrayed in Fig. 7. Near the sheet surface, the profiles are descending and the profiles coincide at the point of inflection $\eta = 1.5$; later they ascend and reach the free stream.

Table 1 presents the effect of various pertinent parameters on the wall shear stress and Sherwood number. As Navier's slip increases, the skin friction coefficient increases and increases the rate of mass transfer. Homogeneous and heterogeneous reactions influence the fluid flow, particularly on the mass transfer. The transfer rate of species is lower if the homogeneous reaction takes place. Suppose if the reaction between the heterogeneous particles takes place, the diffusion rate decreases. The

Table 1 Computation of the skin friction coefficient and Sherwood number for various physical parameters

N_0	S	κ	κ_s	Ω	δ	C_f	$-\phi'(0)$
1.0						−0.26252	−1.9310
2.0						−0.1598	−1.5190
0.5	−0.1					−0.4413	−0.0380
	1.0					−0.4003	1.8499
		0.1				−0.3773	−0.1033
		0.5				−0.3773	−0.2075
			0.1			−0.3773	−1.8565
			0.5			−0.3773	0.1291
				0.1		−0.4094	−0.8290
				0.5		−0.3773	0.1291
					0.4	0.4873	0.0692
					0.6	0.3773	0.1291

ascending fluid parameter increases the friction at the wall and also increases the species transfer rate. For gases, the diffusion transfer rate is 0.1497 in the presence of a chemical reaction. In the case of water, the rate of species transfer is 0.055 with chemically reactive substances.

4 Conclusions

A computational analysis is carried out to study the effect of mass transfer with slip effects on MHD Williamson fluid flow taking the chemical reaction into account. Numerical computations are performed and the outcomes are: The slip parameter decreases the motion of the fluid. The Williamson parameter decreases the velocity near the wall and increases the profiles in the ambient flow. Species diffusion and its rate is low in cases of both homogeneous and heterogeneous reaction. Acceleration in the values of the Williamson fluid parameter accelerates the friction.

References

1. Nadeem, S., Hussain, S. T., and Changhoon, L. Flow of a Williamson fluid over a stretching sheet. Brazilian Journal of Chemical Engineering. **30(3)**,619–625 (2017).
2. Mabood, F., Ibrahim, M., Lorenzini, M., and Lorenzini, E. Radiation effects on Williamson nanofluid flow over a heated surface with magnetohydrodynamics. International Journal of Heat and Technology. **35(1)**,196–204 (2017).
3. Bing, K. Y., Hussanan, A., Mohamed M. K. A., Sarif, N. M., Ismail, Z., and Salleh, M. Z. Thermal radiation effect on MHD flow and heat transfer of Williamson nanofluids over a stretching sheet with Newtonian heating. AIP Conference Proceedings. (2017) https://doi.org/10.1063/1.4980885.

4. Shehzad, S. A., Hayat, T., Qasim, M., and Asghar, S. Effects of mass transfer on MHD flow of Casson fluid with chemical reaction and suction. Brazilian Journal of Chemical Engineering. **30(1)**, 187–195 (2013).
5. Poornima, T., Sreenivasulu, P., and Reddy, N. B. Chemical reaction effects on an unsteady MHD mixed convective and radiative boundary layer flow over a circular cylinder. Journal of Applied Fluid Mechanics. **9(6)**, 2877–2885 (2016).
6. Jena, S., Mishra, S. R., and Dash, G. C. Chemical reaction effect on MHD Jeffery fluid flow over a stretching sheet through porous media with heat generation/absorption. International Journal of Applied and Computational Mathematics. **3(2)**,1225–1238 (2017).
7. Sheikh, M. and Abbas, Z. Homogeneous–heterogeneous reactions in stagnation point flow of Casson fluid due to a stretching/shrinking sheet with uniform suction and slip effects. Ain Shams Engineering Journal. **8(3)**,467–474 (2017).
8. Ibrahim, W. and Makinde, O. D. Magnetohydrodynamic stagnation point flow and heat transfer of Casson nanofluid past a stretching sheet with slip and convective boundary condition. Journal of Aerospace Engineering. (2016) https://doi.org/10.1061/(ASCE)AS.1943-5525.0000529.
9. Poornima, T., Bhaskar Reddy, N., and Sreenivasulu, P. Slip flow of Casson rheological fluid under variable thermal conductivity with radiation. Heat Transfer Asian Research Journal. **44(8)**,718–737 (2015).

The Influence of Wall Properties on the Peristaltic Pumping of a Casson Fluid

P. Devaki, A. Kavitha, D. Venkateswarlu Naidu, and S. Sreenadh

Abstract Wall properties effect has been investigated on the peristaltic flow of Casson fluid in a channel by assuming long wavelength and low Reynolds number. The governing equations are solved analytically to find the expression for velocity and stream function. The effect of different parameters of wall and fluid properties on the velocity and stream function is discussed through graphs. The results obtained create interest among young researchers to concentrate on the wall effects of different types of Newtonian and non-Newtonian fluids in the presence of peristalsis.

1 Introduction

In general fluid flows from high pressure to low pressure in nature but there are certain physical situations where it is essential for the transport of fluid from low pressure to high pressure and this is not possible by normal flow technique. Such type of fluid transport takes place through the phenomenon of peristalsis. Peristalsis pumps fluids from one place to another in many physiological ducts of the human body. This effect of peristalsis has to be considered as an important effect whenever the study is based on the wall properties of the channel or tube.

Wall properties play a vital role in the study of blood flow in the ducts of living organisms. As the organs like arteries, capillaries and veins are elastic in nature,

P. Devaki (✉)
Department of Mathematics, School of Engineering and Technology, CMR University, Bangalore, India

A. Kavitha
VIT, Vellore, India
e-mail: kavitha@vit.ac.in

D. Venkateswarlu Naidu
Vemu Engineering College, Chittoor, India

S. Sreenadh
Sri Venkateswara University, Tirupati, India

B. Rushi Kumar et al. (eds.), *Applied Mathematics and Scientific Computing*, Trends in Mathematics, https://doi.org/10.1007/978-3-030-01123-9_18

this elasticity finds its impact on the flow of blood in the tube or channel. The blood can in general be considered as Newtonian or non-Newtonian fluid. The past investigations reveal the fact that the blood mostly behaves like a non-Newtonian fluid. There are many non-Newtonian fluid models among which the blood behaves like a Casson model at very less shear rates, suggested by Scott Blair [2]. Casson [3] says that at the yield stress of the blood is zero at low shear rates. The blood was considered as a two-fluid model by Srivastava and Srivastava [8] and they also involved the effect of peristalsis and the two fluids considered are Casson and Newtonian fluids. Vajravelu et al. [6, 7] assumed blood as Herschel–Bulkley fluid and they obtained many interesting results in the presence of peristaltic pumping of fluid in a channel and inclined tube, respectively.

The effect of yield stress and peristalsis on the flow of fluid in a tube with elasticity was studied by Vajravelu et al. [9]. As the Herschel-Bulkley fluid is the special case of Newtonian, Bingham and Power-law fluids. The same investigation was also concentrated for these fluids and results were given for all four different fluids. Micropolar fluid flow with peristaltic pumping under the effect of wall properties was investigated by Sankad and Radha Krishnamacharya [5] in a channel with inclination. Nadeem and Ijaz [4] studied on the elastic artery including the effect of stenosis overlap when the blood flows in a tube. Pseudo plastic features was involved by Akbar and Nadeem [1] with blood flow and investigated on the stenosis of the tube. Herschel–Bulkley fluid in a tube with elasticity under the influence of peristalsis was analysed. Vajravelu et al. [10] investigated on elastic tube by taking Casson model as the non-Newtonian model of blood along with peristalsis. The present paper deals with the Casson model under the effect of wall properties and peristalsis. The mathematical model was solved analytically and obtained velocity and stream function in terms of various elastic parameters.

2 Mathematical Modeling

A two dimensional channel wall effects of the Casson fluid is investigated including peristalsis. The peristaltic wave of the channel is given by

$$y = \eta(x, t) = d(x) + \varphi Sin\frac{2\pi}{\lambda}(X - ct)) \tag{1}$$

where $d(x) = d + mX, m \ll 1$

ϕ is the amplitude, λ is the wavelength, d is the mean half width of the channel and m' is the dimensional non-uniformity of the channel.

The equations governing the motion for the present problem are

$$\frac{\partial u}{\partial x} + \frac{\partial w}{\partial y} = 0 \tag{2}$$

$$\rho\left(\frac{\partial u}{\partial t}+u\frac{\partial u}{\partial x}+w\frac{\partial u}{\partial y}\right)=-\frac{\partial p}{\partial x}+\mu\left(\frac{\partial^2 u}{\partial x^2}\right)+\frac{\partial}{\partial y}\left(\tau_0^{1/2}+\left(-\mu\frac{\partial u}{\partial y}\right)^{1/2}\right)^2 \tag{3}$$

$$\rho\left(\frac{\partial w}{\partial t}+u\frac{\partial w}{\partial x}+w\frac{\partial w}{\partial y}\right)=-\frac{\partial p}{\partial y}+\mu\left(\frac{\partial^2 w}{\partial x^2}+\frac{\partial^2 w}{\partial y^2}\right) \tag{4}$$

where u, w are the components of velocity along x-axis, y-directions, respectively, ρ is the density, μ is the coefficient of velocity of the fluid, p is the pressure, d is the mean half width of the channel, Φ is the amplitude, λ is the wavelength, c is the phase speed of the wave and m' is the dimensional non-uniformity of the channel.

The governing equations of motion of the flexible wall may be expressed as

$$C^*(h)=p-p_0 \tag{5}$$

where C^* is an operator, which is used to represent the motion of stretched membrane with viscosity damping forces such that

$$C^*=-\tau\frac{\partial^2}{\partial x^2}+m_1\frac{\partial^2}{\partial t^2}+c_1\frac{\partial}{\partial t} \tag{6}$$

Here τ is the elastic tension in the membrane, m_1 is the mass per unit area, c_1 is the coefficient of viscous damping forces and p_0 is the pressure on the outside surface of the wall due to the tension in the muscles.

Continuity of stress at $y=\eta$ and using x-momentum equation yields

$$\frac{\partial C^*(h)}{\partial x}=-\frac{\partial p}{\partial x}=\mu\left(\frac{\partial^2 u}{\partial x^2}\right)+\frac{\partial}{\partial y}\left(\tau_0^{1/2}+\left(-\mu\frac{\partial u}{\partial y}\right)^{1/2}\right)^2-\rho\left(\frac{\partial u}{\partial t}+u\frac{\partial u}{\partial x}+w\frac{\partial u}{\partial y}\right) \tag{7}$$

$$u=0 \quad at \quad y=\eta=d+m'x+aSin\frac{2\pi}{\lambda}(X-ct) \tag{8}$$

For simplicity, we assume that $p_0=0$.

Introducing ζ such that $u=\frac{\partial\zeta}{\partial y}$ and $w=-\frac{\partial\zeta}{\partial x}$ and the following non-dimensional quantities:

$$x'=\frac{x}{\lambda},\ y'=\frac{y}{d},\ \zeta'=\frac{\zeta}{cd},\ t'=\frac{ct}{\lambda},\ h'=\frac{h}{\lambda},\ p'=\frac{d^2p}{c\lambda\mu},\ k'=\frac{k}{d^2},\ \tau_0'=\frac{d\tau_0}{c\mu}$$

The non-dimensional governing equations after dropping primes, we get

$$R\delta\left(\frac{\partial^2\zeta}{\partial t\partial y}+\frac{\partial\zeta}{\partial y}\frac{\partial^2\zeta}{\partial x\partial y}-\frac{\partial\zeta}{\partial x}\frac{\partial^2\zeta}{\partial y^2}\right)=-\frac{\partial p}{\partial x}+\delta^2\left(\frac{\partial^3\zeta}{\partial x^2\partial y}\right)+\frac{\partial}{\partial y}\left(\tau_0^{1/2}+\left(-\frac{\partial^2\zeta}{\partial y^2}\right)^{1/2}\right)^2 \tag{9}$$

$$R\delta\left(\frac{\partial^2\zeta}{\partial t\partial x}+\frac{\partial\zeta}{\partial y}\frac{\partial^2\zeta}{\partial x^2}-\frac{\partial\zeta}{\partial x}\frac{\partial^2\zeta}{\partial x\partial y}\right)=-\frac{\partial p}{\partial y}+\delta^4\left(\frac{\partial^3\zeta}{\partial x^3}\right)+\delta^2\left(\frac{\partial^3\zeta}{\partial x\partial y^2}\right) \tag{10}$$

$$\frac{\partial \zeta}{\partial y} = 0 \quad at \quad y = \eta = 1 + mx + \varepsilon Sin2\pi(x - t) \tag{11}$$

$$\delta^2 \left(\frac{\partial^3 \zeta}{\partial x^2 \partial y} \right) + \frac{\partial}{\partial y} \left(\tau_0^{1/2} + \left(-\frac{\partial^2 \zeta}{\partial y^2} \right)^{1/2} \right)^2 - R\delta \left(\frac{\partial^2 \zeta}{\partial t \partial y} + \frac{\partial \zeta}{\partial y} \frac{\partial^2 \zeta}{\partial x \partial y} - \frac{\partial \zeta}{\partial x} \frac{\partial^2 \zeta}{\partial y^2} \right) = \left(E_1 \frac{\partial^3}{\partial x^3} + E_2 \frac{\partial^3}{\partial x \partial t^2} + E_3 \frac{\partial^2}{\partial x \partial t} \right) \eta \tag{12}$$

Non-dimensional boundary conditions are

$$\zeta_p = 0 \ at \quad y = 0 \quad \zeta_{yy} = 0 \ at \ \ y = 0 \tag{13}$$

where $\varepsilon = \frac{\phi}{d}, \delta = \frac{d}{\lambda}$ are geometric parameters, $R = \frac{cd\rho}{\mu}$ is the Reynolds number, $E_1 = \frac{\tau d^3}{\lambda^3 \mu c}$, $E_2 = \frac{m_1 c d^3}{\lambda^3 \mu}$, $E_3 = \frac{cd^3}{\lambda^2 \mu}$ are the non-dimensional elastic parameters, $m = \frac{\lambda m'}{d}$ is the non-uniform parameter.

3 Solution of the Problem

Using the long wavelength and low Reynolds number approximations, one can find from Eqs. (9) to (12) that

$$0 = -\frac{\partial p}{\partial x} + \frac{\partial}{\partial y} \left(\tau_0^{1/2} + \left(-\frac{\partial^2 \zeta}{\partial y^2} \right)^{1/2} \right)^2 \tag{14}$$

$$0 = -\frac{\partial p}{\partial y} \tag{15}$$

Equation (15) shows that p is not a function of y. On differentiating Eq. (14) with respect to y, we get

$$\frac{\partial^2}{\partial y^2} \left(\tau_0^{1/2} + \left(-\frac{\partial^2 \zeta}{\partial y^2} \right)^{1/2} \right)^2 = 0 \tag{16}$$

From Eq. (12) we get

$$\frac{\partial}{\partial y} \left(\tau_0^{1/2} + \left(-\frac{\partial^2 \zeta}{\partial y^2} \right)^{1/2} \right)^2 = \left(E_1 \frac{\partial^3}{\partial x^3} + E_2 \frac{\partial^3}{\partial x \partial t^2} + E_3 \frac{\partial^2}{\partial x \partial t} \right) \eta \tag{17}$$

The closed-form solution for Eq. (16) using the boundary conditions (11), (13) and (17) can be obtained as

$$u = \frac{E}{2}(\eta^2 - y^2) - \frac{4}{3}(E\tau_0)^{1/2}(\eta^{3/2} - y^{3/2}) + \tau_0(\eta - y) \qquad y_0 \le y \le \eta \tag{18}$$

We find the upper limit of plug flow region using the boundary condition that $\varsigma_{yy} = 0$ at $y = 0$. It is given by

$$y_0 = \frac{\tau_0}{E} \tag{19}$$

Taking $y = y_0$ in Eq. (18) and using the relation (19), we get the velocity in the plug flow region as

$$u_p = E\left(\frac{\eta^2}{2} - \frac{4}{3}y_0^{1/2}\eta^{3/2} + y_0\eta - \frac{17}{6}y_0^2\right), \quad 0 \le y \le y_0 \tag{20}$$

By using Eqs. (18) and (20), we get

$$\zeta = \tau_0\left(\frac{(y - y_0)^2}{2} - \beta(y - y_0) - \eta(y - y_0)\right) - E\left(\frac{y^3 - 4y_0^3}{6} - \frac{\eta^2}{2} - \beta\eta y + y_0^2(\beta + \eta)\right) \tag{21}$$

$$\zeta_p = Ey\left(y_0^2 - \beta y_0 - \eta y_0 - \frac{1}{2}(y_0^2 - \eta^2 - 2\beta\eta)\right) \tag{22}$$

where

$$E = -8\varepsilon\pi\left[(E_1 + E_2)Cos2\pi(x - t) - \frac{E_3}{2\pi}Sin2\pi(x - t)\right] \tag{23}$$

4 Results and Discussions

Casson fluid with peristalsis is investigated under the effect of elastic properties of the wall. The velocity and stream functions were analysed by plotting graphs for different parameters of elastic wall by using Matlab software. The graphs are depicted from Figs. 1, 2, 3, 4, 5, 6, 7, 8, 9, 10, 11, 12, 13, 14, 15, 16, 17, 18, 19 and 20 for the following factors.

1. Non-uniform parameter m determines the non-uniformity of the channel.
2. The yield stress τ_0.
3. E_1, E_2 and E_3, flexible wall properties of the channel.

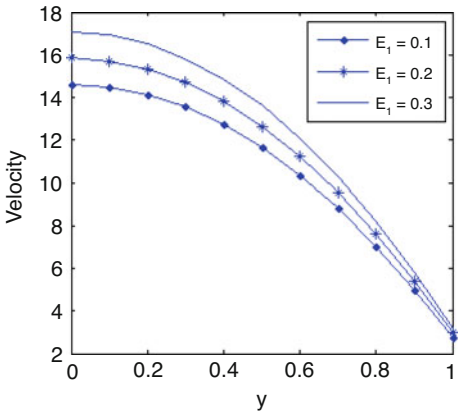

Fig. 1 E_1 on the velocity distribution

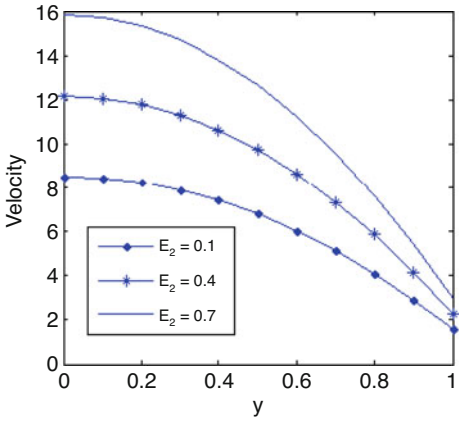

Fig. 2 E_2 on the velocity distribution

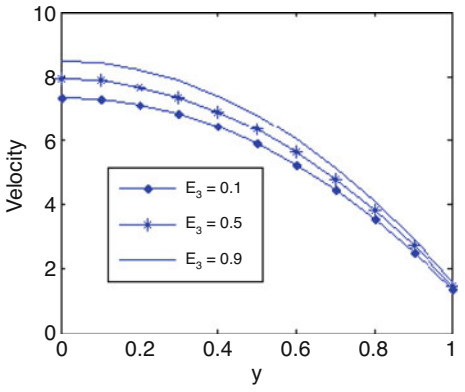

Fig. 3 E_2 on the velocity distribution

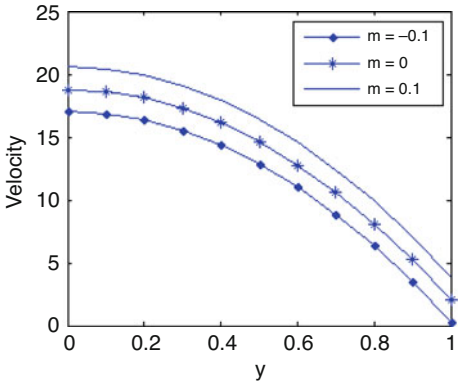

Fig. 4 m on the velocity distribution

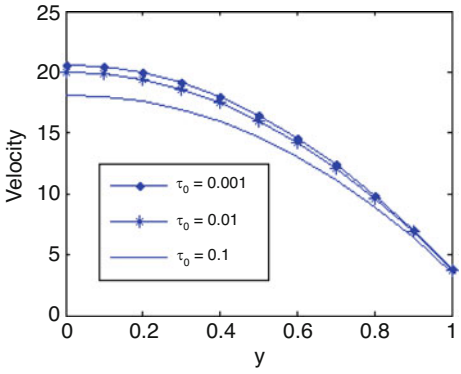

Fig. 5 Velocity distribution for different τ_0

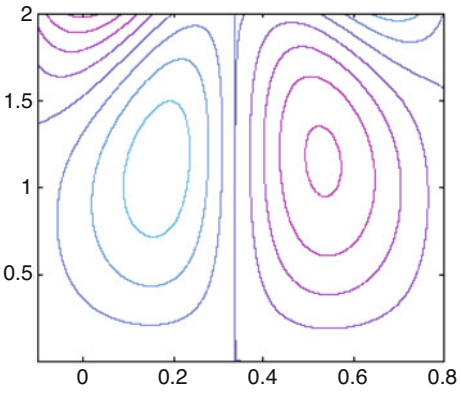

Fig. 6 Stream function if E_1=0.5

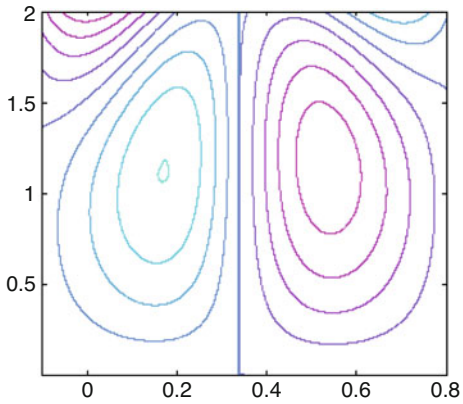

Fig. 7 Stream function if E_1=0.6

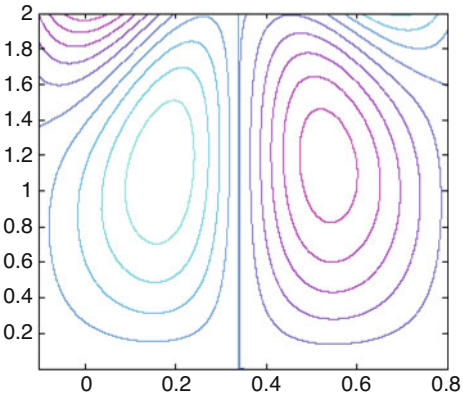

Fig. 8 Stream function if E_1=0.8

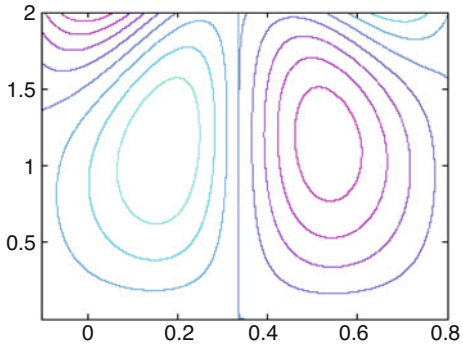

Fig. 9 Stream function if E_2=0.2

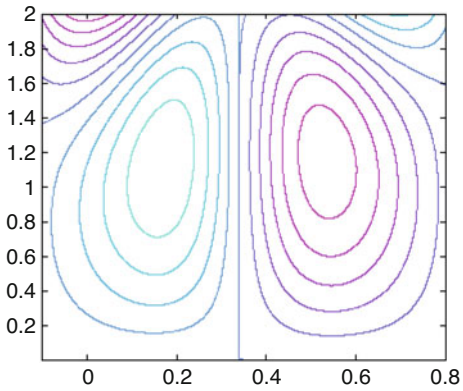

Fig. 10 Stream function if E_2=0.4

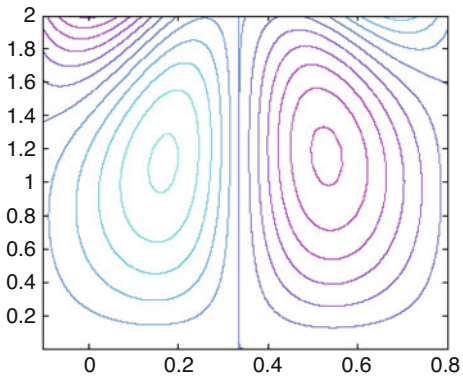

Fig. 11 Stream function if E_2=0.5

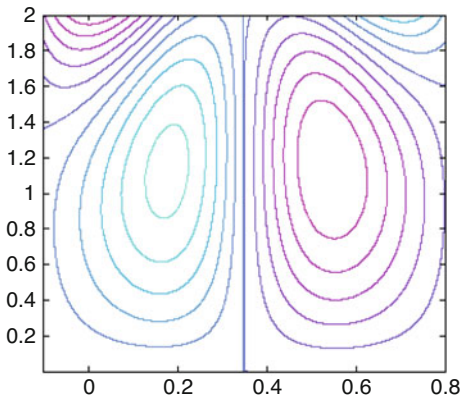

Fig. 12 Stream function if E_3=0.1

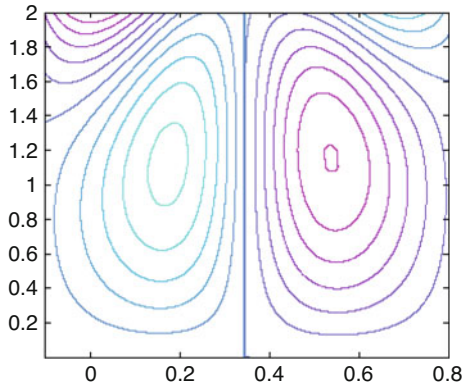

Fig. 13 Stream function if E_3=0.3

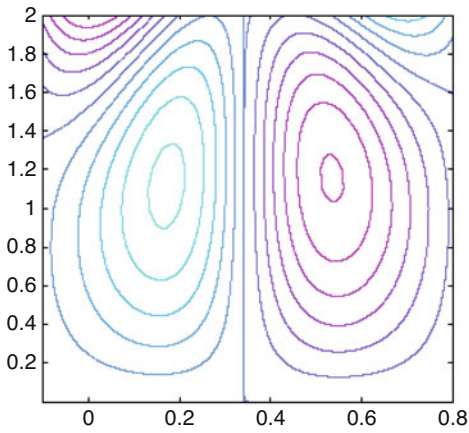

Fig. 14 Stream function if E_3=0.5

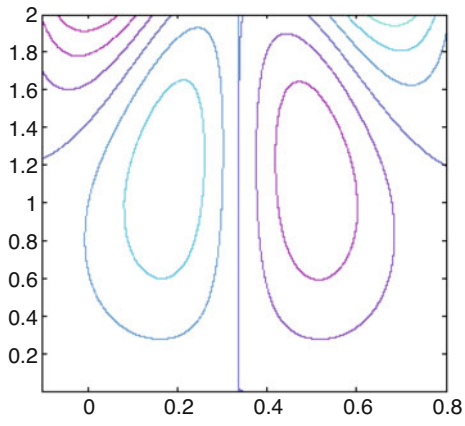

Fig. 15 Stream function if m=−0.1

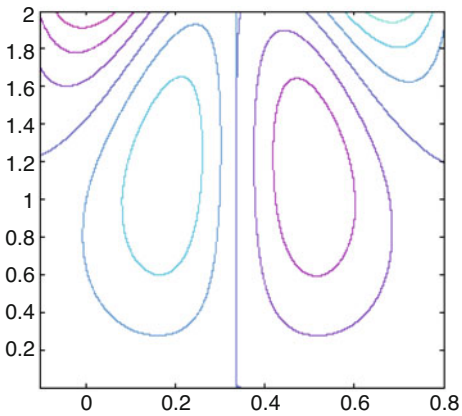

Fig. 16 Stream function if m=0

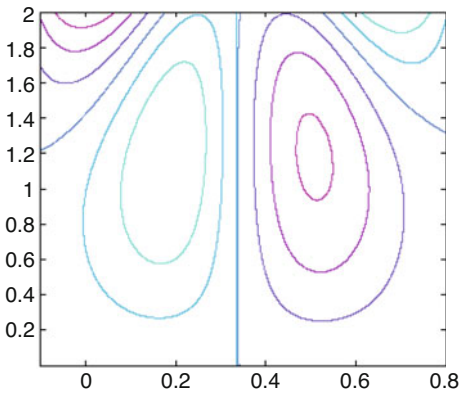

Fig. 17 Stream function if m=0.1

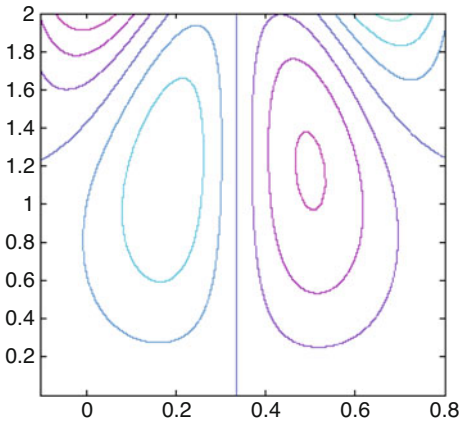

Fig. 18 Stream function if τ_0=0.001

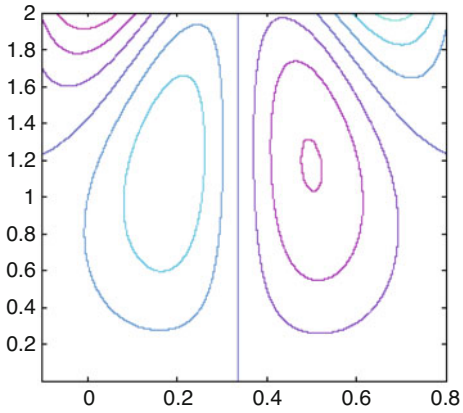

Fig. 19 Stream function if τ_0=0.01

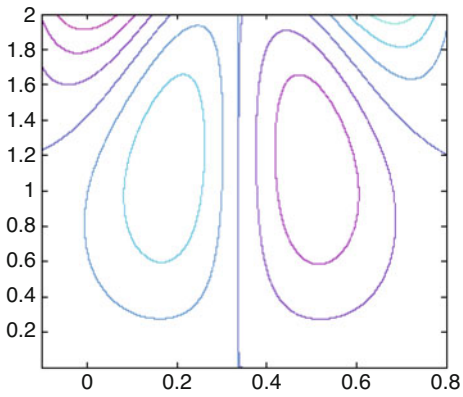

Fig. 20 Stream function if τ_0=0.1

Figures 1, 2 and 3 depict, respectively, the behaviours of the velocity u versus y with changes in elastic parameters, namely E_1, E_2 and E_3. The effect of an increase in E the rigidity parameter E_1 gives rise to an increase in the velocity u when the other elastic parameters. The same behaviour is observed for the other elastic parameters, namely E_1 and E_2. Figure 4 shows the variation of velocity u with y for different values of non-uniform parameter m [namely convergent channel $m < 0$, uniform channel $m = 0$ and divergent channel $m > 0$]. From the graphical representation, it is observed that the velocity u in the case of convergent channel is less than that in the uniform channel and this is less than the divergent channel. The variation of velocity u with y is calculated for different values of yield stress τ_0 and is depicted in Fig. 5. The numerical results are obtained for different values of yield stress τ_0 in the range 0–0.1. We note that, in cardiovascular system, the Casson fluid behaves like blood only when lies in between 0 and 0.1. For higher values, the Casson fluid behaves like industrial fluids possessing yield stress. It can be seen from Fig. 5 that the velocity depends on yield stress and it decreases with increasing yield stress τ_0.

4.1 Trapping Phenomenon

In the present study peristalsis is involved, so trapping of the fluid has to be concentrated. Figures 6, 7 and 8 show that for higher rigidity E_1, the size of the trapped bolus increases. From Figs. 9, 10 and 11 we observe that more trapped bolus appears with increase in stiffness parameter. Further as viscous damping force increases, the size of the trapped bolus also increases as seen in Figs. 12, 13 and 14. The size of the bolus increases on the left-hand side for convergent channel and decreases for divergent channel, and the size of the bolus is symmetric for uniform channel which is shown in Figs. 15, 16 and 17. Figs. 18, 19 and 20 depict the fact that as yield stress increases trapped bolus decreases.

References

1. Akbar, N. S., Nadeem, S.: Blood flow analysis in tapered stenosed arteries with pseudo plastic characteristics, Int. J. BioMath. **7(6)**, 1450065 (2014)
2. Scott Blair, G. W.: An equation for the flow of blood, plasma and serum through glass capillaries, Nature **183**, 613 (1959)
3. Casson, N.: Rheology of Disperse Systems, C. C. Mill, ed., Pergamon Press, London, (**1959**)
4. Nadeem, S., Ijaz, S.: Nanoparticles analysis on the blood flow through a tapered catheterized elastic artery with overlapping stenosis, Eur. Phys. J. Plus. **129**, 249 (2014)
5. Sankad, G.C., Radha Krishnamacharya, G.: Influence of Wall Properties on Peristaltic Transport of a Micropolar Fluid in an Inclined Channel, J. New Results Sci. **6(6)**, 62 (2014)
6. Vajravelu, K., Sreenadh, S., Ramesh Babu, V.: Peristaltic transport of a Herschel-Bulkley fluid in an inclined tube, Int. J. Nonlinear Mech. **40**, 83 (2005)
7. Vajravelu, K., Sreenadh, S., Ramesh Babu, V.: Peristaltic transport of a Herschel-Bulkley fluid in a channel, Appl. Math and Comput. **169**, 726 (2005)
8. Srivastava, L.M., Srivastava, V.P.: Peristaltic transport of blood Casson Model II J. Biomechanics **17**, 821 (1984)
9. Vajravelu, K., Sreenadh, S., Devaki, P., Prasad, K.V.: Mathematical model for a Herschel-Bulkley fluid flow in an Elastic tube, Central Eur. J. Phys. **9(5)**, 1357 (2011)
10. Vajravelu, K., Sreenadh, S., Devaki, P., Prasad, K.V.: Peristaltic transport of Casson fluid in an elastic tube, J. Appl. Fluid Mech. **9(4)**, 1897 (2016)

Peristaltic Flow of a Jeffrey Fluid in Contact with a Newtonian Fluid in a Vertical Channel

R. Sivaiah, R. Hemadri Reddy, and R. Saravana

Abstract The flow of a Jeffrey fluid is extended to include a Newtonian fluid through a vertical symmetric channel with peristalsis under the assumptions of long wavelength and small Reynolds number. The model is applicable to study the behavior in physiological systems. The velocity field, stream function, interface shape, pressure rise (drop), and frictional force at the wall over a cycle of wavelength are obtained, and the results are shown graphically. It is observed that the variation of interface shape yields the thinner peripheral region in the dilated region with increasing Jeffrey parameter λ_1 and thicker peripheral region in the dilated region for low viscosity ratio.

Keywords Jeffrey fluid · Newtonian fluid · interface · vertical channel

1 Introduction

Peristalsis is an inherent biological mechanism in human beings. In practical, the peristaltic pumps are modelled to pump the corrosive fluids to avoid the contact of walls of the pumping machinery. In order to understand the effect of fluid coating in the physiological systems such as esophagus and ureter, the study of peristaltic flow of single fluid is extended to two-fluid flow. The two-fluid flow natural phenomenon can be observed in many physiological systems such as swallowing of food bolus through esophagus, passage of urine through ureter, blood pumping in blood vessels, etc.

R. Sivaiah · R. Hemadri Reddy (✉)
Department of Mathematics, School of Advanced Sciences, VIT University, Vellore, Tamil Nadu, India
e-mail: rhreddy@vit.ac.in

R. Saravana
Department of Mathematics, Madanapalle Institute of Technology and Science, Madanapalle, Andhra Pradesh, India

B. Rushi Kumar et al. (eds.), *Applied Mathematics and Scientific Computing*, Trends in Mathematics, https://doi.org/10.1007/978-3-030-01123-9_19

The Jeffrey fluid model is the simple non-Newtonian fluid model proposed for biofluids. Hayat et al. [1] analyzed the peristaltic flow of a compressible Jeffrey fluid in a tube. Nadeem and Akbar [2] studied the peristaltic pumping of an incompressible viscosity varying Jeffrey fluid in an asymmetric channel. Kavitha et al. [3] presented the peristaltic transport of a Jeffrey fluid in a permeable channel with suction and injection. Saravana et al. [4] examined the wall properties effect on MHD peristaltic flow of a Jeffrey fluid through a porous nonuniform channel.

The peristaltic flow of two-fluid analysis has been reported by several authors [5–9]. All these authors have specified the interface shape. Very recently, Vajravelu et al. [10] addressed the peristaltic transport of a Jeffrey fluid in a core region and a Newtonian fluid in a peripheral region through a horizontal channel with heat transfer. Saravana et al. [11] investigated the peristaltic pumping of a Bingham fluid in a core region and a Jeffrey fluid in a peripheral region through a symmetric channel.

Motivated by the above studies, we propose to study the two-fluid peristaltic flow of a Jeffrey fluid with a Newtonian fluid in a vertical channel under the consideration of low Reynolds number and long wavelength. The velocity field, the stream function, shape of interface, the pressure rise (drop), and the frictional force per cycle of wavelength are obtained and are shown graphically.

2 Mathematical Formulation and Solution

We choose the peristaltic transport of two incompressible fluids of viscosities and occupy the core region by a Jeffrey fluid and peripheral region by a Newtonian fluid through a vertical channel. The half width of the channel is a.

The propagation of an infinite peristaltic wave is represented by

$$Y = H(X,\ t) = a + b\ \sin\frac{2\pi}{\lambda}(X - ct) \tag{1}$$

where λ indicates the wavelength and b and c represent the amplitude and the wave speed, respectively.

The subsequent deformation of the interface separating the core and peripheral layers is represented by and is shown in Fig. 1, which is unknown a priori.

2.1 Equations of the Motion

Following the considerations of two-fluid analysis of Kavitha et al. [9], the transformation from the laboratory frame to wave frame is as follows:

$$x = X - ct, y = Y, u(x, y) = U(X - ct, Y) - c, v(x, y) = V(X - ct, Y)$$
$$p(x) = P(X, t), \psi = \Psi - Y \tag{2}$$

where ψ and ψ indicate the stream functions in wave and laboratory frames, respectively. The non-dimensional quantities are as follows:

$$\bar{x} = \frac{x}{\lambda}, \bar{y} = \frac{y}{a}, \bar{h} = \frac{h}{a}, \bar{h}_1 = \frac{h_1}{a}, \bar{t} = \frac{ct}{\lambda}, v(x, y) = V(X - ct, Y)$$

$$\bar{\psi}^{(i)} = \frac{\psi^{(i)}}{ac}, \quad \bar{q} = \frac{q}{ac}, \bar{F} = \frac{Fa}{\mu_1 \lambda c}, \quad \bar{u}^{(i)} = \frac{u^{(i)}}{c} = \frac{\partial \psi^{(i)}}{\partial \bar{y}},$$

$$\bar{v}^{(i)} = \frac{v^{(i)}\lambda}{ac} = \frac{-\partial \psi^{(i)}}{\partial \bar{x}} \ (i = 1, 2), \bar{\mu} = \begin{cases} 1, & 0 \le \bar{y} \le \bar{h}_1 \\ \mu \left(= \frac{\mu_2}{\mu_1}\right), & \bar{h}_1 \le \bar{y} \le \bar{h} \end{cases} \tag{3}$$

where $\bar{u}^{(i)}$ and $\bar{v}^{(i)}$ (superscript $i = 1, 2$ represents the flow in core and peripheral layer) are the velocities along the and directions.

The equations governing the motion of two fluids in wave frame analysis under the consideration of long wave length and low Reynolds number assumptions are as follows (dropping the bars):

$$\frac{\partial}{\partial y}\left[\frac{1}{(1+\lambda_1)}\frac{\partial^2 \psi^{(1)}}{\partial y^2}\right] + \eta = \frac{\partial P}{\partial x} \tag{4}$$

$$0 = \frac{\partial p}{\partial y} \tag{5}$$

$$\text{and} \quad \frac{\partial^2}{\partial y^2}\left[\mu \frac{\partial^2 \psi^{(2)}}{\partial y^2}\right] = 0 \tag{6}$$

where η is the gravity parameter.

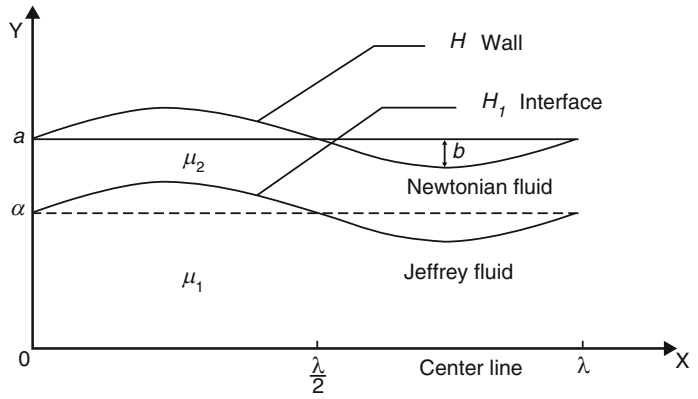

Fig. 1 Physical model

The non-dimensional boundary conditions associated with the flow in wave frame are

$$\psi^{(1)} = 0 \qquad at \qquad y = 0 \tag{7}$$

$$\psi^{(1)}_{yy} = 0 \qquad \text{at} \qquad \text{y} = 0 \tag{8}$$

$$\psi^{(2)} = q = constant \qquad at \qquad y = h \tag{9}$$

$$\psi^{(1)} = \psi^{(2)} = q_1 = constant \qquad at \qquad y = h_1 \tag{10}$$

$$\psi^{(2)}_{y} = -1 \qquad \text{at} \qquad \text{y} = \text{h} \tag{11}$$

where q and q_1 represent the total and the core fluxes across any cross section in the wave frame analysis. Further the shear stress and velocity are continuous across the interface. The peripheral layer flux is followed by $q_2 = q - q_1$. It indicates that the incompressibility of the fluids that q, q_1 and q_2 are independent of x.

The non-dimensional volume flow rate $\bar{Q}$ of one period $T\left(=\frac{\lambda}{c}\right)$ of the peristaltic wave is defined as

$$\bar{Q} = \frac{1}{T}\int_0^T \int_0^h (u+1)\, dy\, dt = q + 1 \tag{12}$$

2.2 Solution

By solving the Eqs. (4)–(6) with suitable boundary conditions (7)–(11), we get the stream function in the core region and peripheral layer as

$$\psi^{(1)} = -y + \left[\frac{3y\,(q+h)\,F_2 - \mu\,(1+\lambda_1)\,(q+h)\,y^3}{2F_3}\right] \quad for \;\; 0 \le y \le h_1 \tag{13}$$

$$\psi^{(2)} = -y + (q+h) + \left[\frac{9\,(q+h)\,h^2 y - 3\,(q+h)\,y^2 - 6\,(q+h)\,h^2}{6F_3}\right]$$

$$for \qquad h_1 \le y \le h \tag{14}$$

$F_j = h^j + (\mu(1+\lambda_1) - 1)h_1^j (j = 2, 3)$.

The axial pressure gradient obtained from (4) or (6) is as follows

$$\frac{dp}{dx} = \frac{-3\mu(q+h)}{F_3} + \eta \tag{15}$$

2.3 The Equation of the Interface

The interface is also a streamline as seen from the boundary condition (10). For a given geometry of the wave and the time-averaged flux $\bar{Q}$, the unknown interface $h_1(x)$ is solved from (14) using the boundary condition (10). Substituting (10) in (14), we get the algebraic equation governing the interface $h_1(x)$ as

$$2[(1+\lambda_1)\mu - 1]\,h_1^4 - [(q+h)\,[2\mu(1+\lambda_1) - 3] + 2(1-\mu(1+\lambda_1)q_1]\,h_1^3 - \left[h^3 + 3qh^2\right]h_1 + 2q_1h^3 = 0 \tag{16}$$

where q and q_1 are independent of x.

The condition $h_1 = \alpha$ at $x = 0$ in Eq. (16) produces q_1 as follows:

$$q_1 = \frac{\bar{Q}(2\mu(1+\lambda_1) - 3)\alpha^3 + (3\bar{Q} - 2)\alpha - 2(\mu(1+\lambda_1) - 1)\alpha^4}{2((1-(1+\lambda_1)\mu)\,\alpha^3 + 1)} \tag{17}$$

2.4 The Pumping Characteristics

By integrating Eq. (15) w. r. to x over one wavelength, we get the pressure rise (drop) over one cycle wave as follows:

$$\Delta p = -3\mu(\bar{Q} - 1)\,I_1 - 3\mu\,I_2 + \eta I_3 \tag{18}$$

where $I_1 = \int_0^1 \frac{dx}{F_3}$, $I_2 = \int_0^1 \frac{h}{F_3}dx$, $I_3 = \int_0^1 dx$

The dimensionless frictional force F at the channel wall across one wavelength is given by

$$F = \int_0^1 -h\,\frac{dp}{dx}\,dx \tag{19}$$

3 Results and Discussion

The shape of the wave interface for different Jeffrey parameter λ_1 with $\phi = 0.6$, $\mu = 0.1, \alpha = 0.8$, and $\bar{Q} = 0.1$ is shown in Fig. 2. We observe that the interface shape gives rise to thinner peripheral region in the dilated region with increasing λ_1. The shape of the interface for different μ with $\phi = 0.4$, $\lambda_1 = 0.1$, $\alpha = 0.5$, and

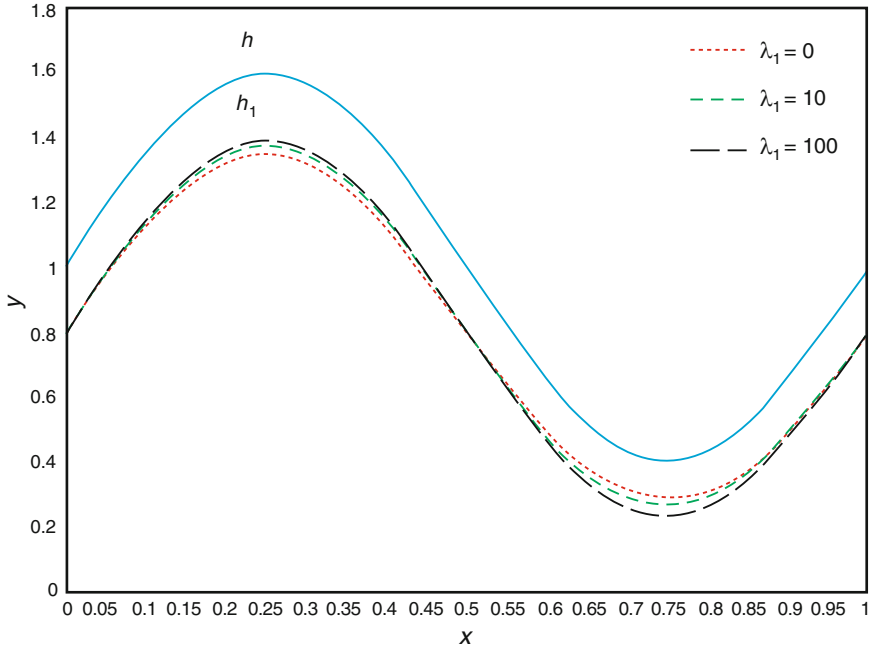

Fig. 2 Shape of interface for λ_1 with $\phi = 0.6$, $\mu = 0.1$, $\alpha = 0.8$ and $\bar{Q} = 0.1$

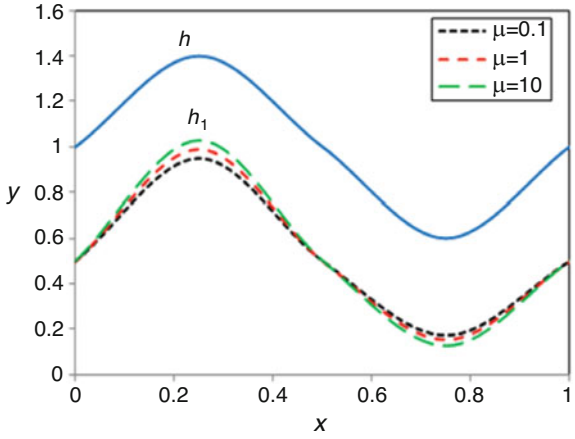

Fig. 3 shape of interface for μ with $\phi = 0.4$, $\lambda_1 = 0.1$, $\alpha = 0.5$ and $\bar{Q} = 0.1$

$\bar{Q} = 0.1$ is depicted in Fig. 3. The interface shape variation for low viscosity ratio gives rise to a thicker peripheral region in the dilated region.

The pressure rise with time-averaged flux is obtained from Eq. (18), and the plot for various values of a Jeffrey parameter λ_1 with $\phi = 0.6$, $\mu = 0.1$, $\alpha = 0.8$ and $\eta = 1$ is shown in Fig. 4. For $0 \leq \bar{Q} \leq 0.37$, we found that ΔP decreases with the increase of Jeffrey number λ_1 and increases in the rest of the region. The ΔP with

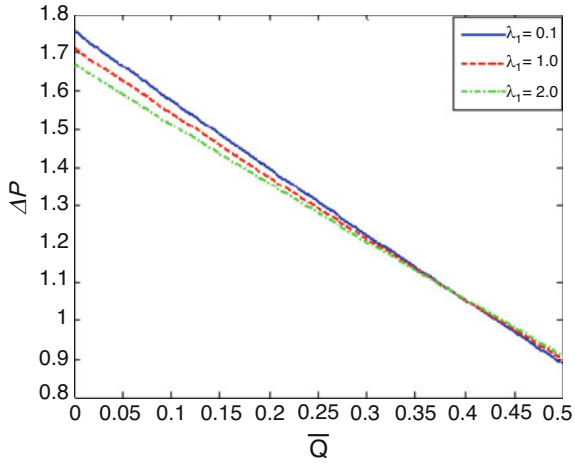

Fig. 4 ΔP vs $\bar{Q}$ for λ_1 with $\phi = 0.6, \mu = 0.1, \alpha = 0.8$ and $\eta = 1$

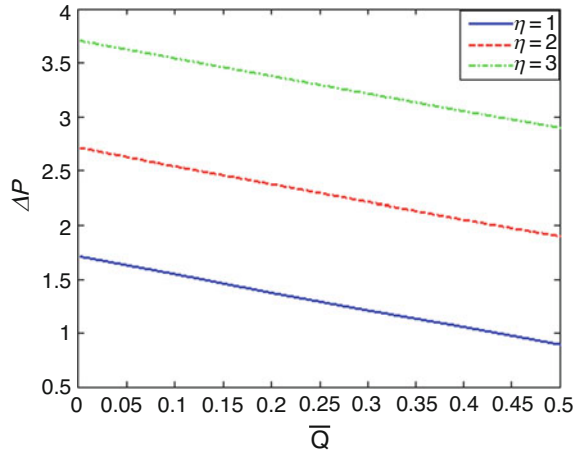

Fig. 5 ΔP vs $\bar{Q}$ for η with $\phi = 0.6, \mu = 0.1, \alpha = 0.8$ and $\lambda_1 = 1$

$\bar{Q}$ for various values of gravity parameter η with $\phi = 0.6, \mu = 0.1, \alpha = 0.8$ and $\lambda_1 = 1$ is shown in Fig. 5. From the plot, we find that ΔP increases with increasing gravity parameter η. The nature phenomenon of enhancement in the pressure rise exists with increasing the gravity parameter.

The frictional force F with $\bar{Q}$ is evaluated from Eq. (19), and the plot for various values of λ_1 with $\phi = 0.6, \mu = 0.1, \alpha = 0.8$, and $\eta = 1$ is depicted in Fig. 6. For $0 \leq \bar{Q} \leq 0.25$, we clearly see that F increases with the increase of λ_1 and decreases in the rest of the region. The variation of F with $\overline{Q}$ for the chosen values of η with $\phi = 0.6, \mu = 0.1, \alpha = 0.8$ and $\lambda_1 = 1$ is shown in Fig. 7. We observe that decreases with the increasing of η.

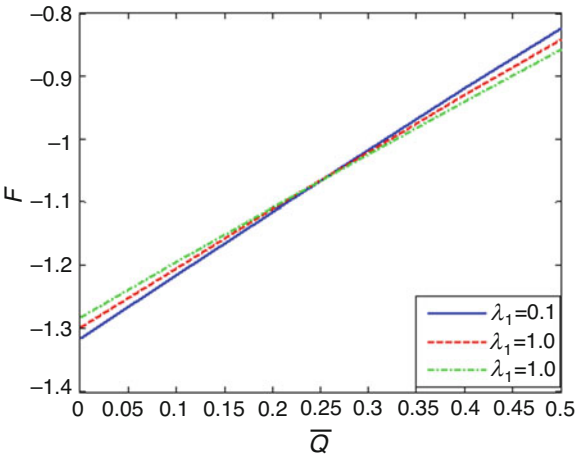

Fig. 6 F vs $\bar{Q}$ for λ_1 with $\phi = 0.6, \mu = 0.1, \alpha = 0.8$ and $\eta = 1$

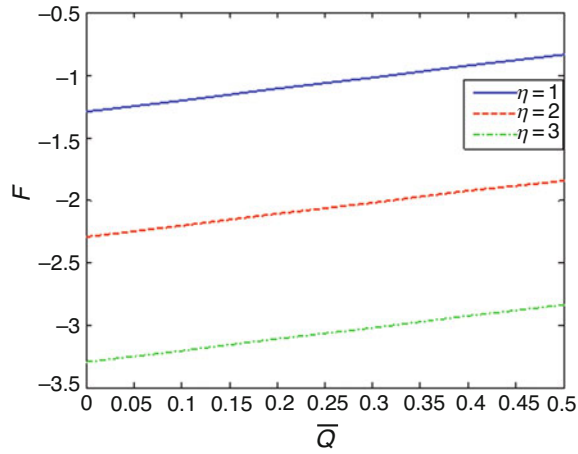

Fig. 7 F vs $\bar{Q}$ for η with $\phi = 0.6, \mu = 0.1, \alpha = 0.8$ and $\lambda_1 = 1$

4 Conclusion

In this paper, we study the peristaltic flow of a Jeffrey fluid in the core region and a Newtonian fluid in the peripheral region through a vertical symmetric channel under the consideration of long wavelength and low Reynolds number. The pressure rise variation with time-averaged flux and the interface shape is obtained. Some of the interesting findings in the analysis are as follows: (1) the interface shape variation yields the thinner peripheral region with increasing the Jeffrey fluid parameter; (2) the interface shape for low viscosity ratio yields the thicker peripheral layer in the dilated region; (3) for time-averaged flux, the pressure rise decreases with the increase of Jeffrey fluid parameter and enhances in the rest of the region; and (4) ΔP increases with the increase of viscosity ratio and decreases in the remaining region.

References

1. Hayat, T., Ali, N., Asghar, N.: An analysis of peristaltic transport for flow of a Jeffrey fluid. Acta Mechanica. **193**, 101–112(2007) https://doi.org/10.1007/s00707-007-0468-2.
2. Sohail Nadeem, Noreen Sher Akbar.: Peristaltic flow of a Jeffrey fluid with variable viscosity in an asymmetric channel. Z. Naturforsch. **64**, 713–722(2009)
3. Kavitha, A., Reddy, R.H., Srinivas, A. N. S., Sreenadh, S.,Saravana, R.: Peristaltic transport of a Jeffrey fluid in a porous channel with suction and injection. International Journal of Mechanical and Materials Engineering.**7**, 152–157(2012)
4. Saravana, R., Sreenadh, S., Venkataramana, S., Hemadri Reddy, R., Kavitha, A.: Influence of slip conditions, wall properties and heat transfer on MHD peristaltic transport of a Jeffrey fluid in a non-uniform porous channel. International Journal of Innovative Technology and Creative Engineering, **1**, 10–24(2011)
5. Brasseur, J.G., Corrsin, S., Lu, Nan Q.: The influence of a peripheral layer of different viscosity on peristaltic pumping with Newtonian fluids. J. Fluid Mech. **174**, 495–519(1987)
6. Ramachandra Rao, A., Usha, S.: Peristaltic transport of two immiscible viscous fluid in a circular tube. J.Fluid Mech. **298**, 271–285(1995)
7. Vajravelu, K., Sreenadh, S., Hemadri Reddy, R., Murugeshan, K.: Peristaltic transport of a Casson fluid in contact with a Newtonian fluid in a circular tube with permeable wall. International Journal of Fluid Mechanics Research. **36**, 244–254(2009)
8. Hari Prabakaran, P., Hemadri Reddy, R., Sreenadh, S., Saravana, R., Kavitha, A.: Peristaltic pumping of a Bingham fluid in contact with a Newtonian fluid in an inclined channel under long wave length approximation. Advances and Applications in Fluid Mechanics. **13**, 127–139(2013)
9. Kavitha, A., Hemadri Reddy, R., Saravana, R., Sreenadh, S.: Peristaltic transport of a Jeffrey fluid in contact with a Newtonian fluid in an inclined channel. Ain Shams Engineering Journal.**8**, 683–687(2017)
10. Vajravelu, K., Sreenadh, S., Saravana, R.: Influence of velocity slip and temperature jump conditions on the peristaltic flow of a Jeffrey fluid in contact with a Newtonian fluid. Applied Mathematics and Nonlinear Sciences.**2**, 429–442(2017)
11. Saravana R., Hariprabakaran P., Hemadri Reddy R., Sreenadh S.: Peristaltic Flow of a Bingham Fluid in Contact with a Jeffrey Fluid. Applications of Fluid Dynamics, Lecture Notes in Mechanical Engineering, (2018) Springer, Singapore. https://doi.org/10.1007/978-981-10-5329-0-37.

MHD and Cross Diffusion Effects on Peristaltic Flow of a Casson Nanofluid in a Duct

G. Sucharitha, P. Lakshminarayana, and N. Sandeep

Abstract The Soret and Dufour effects on the peristaltic transport of a conducting Casson nanofluid in a flexible channel are studied. The influence of dissipation and Joule heating are also discussed. The governing equations are simplified by using a long wave length and small Reynolds number approximations. The analytical solutions for stream function and axial velocity are obtained. Moreover, the Runge–Kutte-based shooting method is utilized to solve the coupled energy and concentration equations. The impact of important parameters on the flow is explained using graphs for both Newtonian and Casson fluid cases. It is observed that the Casson fluid has more velocity than the Newtonian fluid in the middle of the channel and the situation is reversed at the channel walls. Further, a higher temperature is noted for Casson fluid than for Newtonian fluid throughout the channel, whereas concentration shows the opposite behavior.

1 Introduction

Peristaltic transport problems with different fluids and geometries have been investigated by many authors because of the important and useful applications in engineering and medical sciences. Various types of peristaltic pumps are designed to transport sanitary and some industrial fluids. The study of peristalsis helps to improve the quality of biomedical instruments such as a blood pump machine, a heart–lung machine, and a dialysis machine. Latham [1], Fung and Yih [2],

G. Sucharitha
Department of Mathematics, Sreenivasa Institute of Technology and Management Studies, Chittoor, India

P. Lakshminarayana (✉)
Department of Mathematics, VIT, Vellore, India
e-mail: lakshminarayana.p@vit.ac.in

N. Sandeep
Department of Mathematics, Central University of Karnataka, Kalaburagi, India

B. Rushi Kumar et al. (eds.), *Applied Mathematics and Scientific Computing*, Trends in Mathematics, https://doi.org/10.1007/978-3-030-01123-9_20

Shapiro et al. [3] initiated the study of peristalsis. Further several authors [4–7] have presented their works on this topic. Most of the biofluids and industrial fluids behave like non-Newtonian fluid and the study of these fluids plays a vital role in fulfilling the present requirements in engineering and medical sciences. In view of these observations, many authors have considered the non-Newtonian fluid flow problems in channels and tubes [8–12, 20–23]. The study of conducting non-Newtonian fluid flows with heat transfer has important applications in industry and biosciences, such as the reduction of bleeding during surgery, cancer treatment, the design of biomagnetic devices, hypothermia, and laser therapy. Hayat et al. [13] analyzed the influence of heat transfer and an inclined magnetic field on the peristaltic motion of fourth-grade fluid with variable viscosity. Saleem et al. [14] analyzed the upper-convected Maxwell fluid flow using the Cattaneo–Christov heat flux model. Recently, the authors [15–18] have studied the influence of wall properties and heat transfer on the peristaltic flow of MHD non-Newtonian fluids. In the present chapter, we examined the impact of Joule heating and cross diffusion on MHD peristaltic flow of a Casson nanofluid in a channel. The expressions for the velocity and the stream function are obtained. Further, the Runge–Kutte (R-K)-based shooting method is applied to solve the energy and concentration equations. The effects of important parameters on the flow quantities are discussed in detail with the help of graphs.

2 Formulation of the Problem

We consider the peristaltic transport of a conducting Casson nanofluid in a two-dimensional channel of width. The fluid flow is produced by a peristaltic wave spreading along the flexible walls of the channel with a constant speed c (Fig. 1). The Joule heating and the Soret and Dufour effects on the flow are also considered. The geometry of the channel wall is given by:

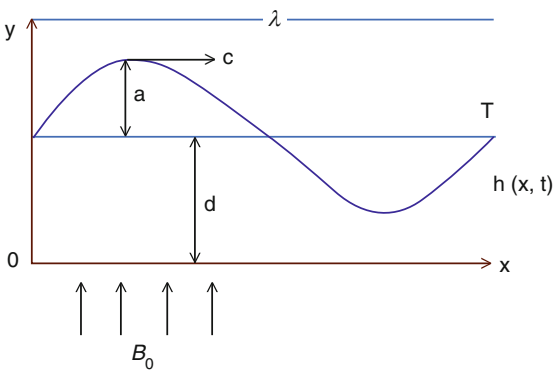

Fig. 1 Physical model

$$h'(x', t') = a\, Sin\frac{2\pi}{\lambda}\left(x' - ct'\right) + d, \tag{1}$$

According to the study by Akbar [10] and using a negligible Reynolds number and protracted wavelength assumptions, the nondimensional momentum equation for this study is obtained as:

$$\frac{\partial p}{\partial x} = \left(1 + \frac{1}{\beta}\right)\frac{\partial^3 \psi}{\partial y^3} - M^2\frac{\partial \psi}{\partial y}, \tag{2}$$

$$\frac{\partial p}{\partial y} = 0, \tag{3}$$

where we present the stream function as $u = \frac{\partial \psi}{\partial y}$, $V = -\frac{\partial \psi}{\partial x}$ and $\beta\left(= \mu_\beta \frac{\sqrt{2\pi c}}{p_y}\right)$ is the Casson fluid parameter, $M\left(= \sqrt{\frac{\sigma}{\mu}}\, B_0 d\right)$ is the magnetic parameter, λ is the wavelength, c is the wave speed, σ is the electrical conductivity, B_0 is the magnetic field, μ is the viscosity, t is the time, p is the pressure, x, y are the Cartesian coordinates, u, v are the fluid velocities in the x and y directions respectively, d is the mean width of the channel, and a is the amplitude.

Hayat et al. [19] studied the effects of slip and Joule heating on a mixed convective peristaltic flow by considering cross diffusion. In the view of this study, dimensionless energy and concentration equations for the present problem are presented as:

$$\begin{aligned}\frac{\partial^2 \theta}{\partial y^2} &+ Br\left[\left(\frac{\partial^2 \psi}{\partial y^2}\right)^2 + M^2\left(\frac{\partial \psi}{\partial y}\right)^2\right] \\ &+ \Pr\left[N_t\left(\frac{\partial \theta}{\partial y}\right)^2 + N_b\frac{\partial \theta}{\partial y}\frac{\partial \phi}{\partial y} + Du\frac{\partial^2 \phi}{\partial y^2}\right] = 0,\end{aligned} \tag{4}$$

$$\frac{\partial^2 \phi}{\partial y^2} + \left[Sr\, Sc + \frac{N_t}{N_b}\right]\frac{\partial^2 \theta}{\partial y^2} = 0, \tag{5}$$

corresponding dimension-less boundary conditions (Sucharitha et al. [17, 18]) are given by:

$$\psi = 0,\ \frac{\partial^2 \psi}{\partial y^2} = 0,\ \frac{\partial \theta}{\partial y} = 0,\ \frac{\partial \phi}{\partial y} = 0 \quad at \quad y = 0, \tag{6}$$

$$\frac{\partial \psi}{\partial y} = 0,\ \theta = 1,\ \phi = 1 \quad at \quad y = h, \tag{7}$$

$$\left(1+\frac{1}{\beta}\right)\frac{\partial^3 \psi}{\partial y^3} - M^2 \frac{\partial \psi}{\partial y} - \left(E_3 \frac{\partial^2 h}{\partial x \partial t} + E_1 \frac{\partial^3 h}{\partial x^3} + E_2 \frac{\partial^3 h}{\partial x \partial t^2}\right) = 0,\ at\ y = h, \tag{8}$$

where $h\ (=\ \varepsilon\ \sin 2\pi\ (x - t) + 1)$ is the wall deformation, $E_1\left(= \frac{-\tau d^3}{\lambda^3 \mu c}\right)$ is the wall tension parameter, $E_2\left(= \frac{m_1 c d^3}{\lambda^3 \mu}\right)$ is the wall mass description parameter, $E_3\left(= \frac{c d^3}{\lambda^2 \mu}\right)$ is the damping force parameter, $\varepsilon\left(= \frac{a}{d}\right)$ is the amplitude ratio, N_t is the thermophoresis parameter, N_b is the Brownian motion parameter, Sr is the Soret number, θ, ϕ are the nondimensional temperature and concentration respectively, $Br\ (= Ec\ \mathrm{Pr})$ is the Brinkman number, Du is the Dufour number, Ec is the Eckert number, Pr is the Prandtl number.

3 Exact Solution

On differentiation of Eq. (2) with respect to y we obtain:

$$\frac{\partial^4 \psi}{\partial y^4} - N^2 \frac{\partial^2 \psi}{\partial y^2} = 0, \tag{9}$$

The exact solution of the Eq. (9) by using the boundary conditions (6)–(8) is given by:

$$\psi = \frac{a_1 \sinh Ny}{N^3 \cosh Nh} - \frac{a_1 y}{N^2} \tag{10}$$

Corresponding axial velocity is:

$$u = \frac{a_1 \cosh Ny}{N^2 \cosh Nh} - \frac{a_1}{N^2} \tag{11}$$

where $N^2 = \frac{M^2}{\left(1+\frac{1}{\beta}\right)}$

$a_1 = 8\,\varepsilon\,\pi^3 \left[\frac{E_3}{2\pi}\ \sin\ 2\pi(x - t) - (E_1 + E_2)\ \cos\ 2\pi(x - t)\right]$

4 Numerical Solution

The energy and concentration equations (4) and (5) are coupled and nonlinear. Thus, these equations are solved numerically by employing the R-K-based shooting method with the help of the boundary equations (6)–(8). The Nusselt and Sherwood numbers at the wall are defined by:

$$Nu = -\left(\frac{d\theta}{dy}\right)_{at\ y=h}, \quad Sh = -\left(\frac{d\phi}{dy}\right)_{at\ y=h} \tag{12}$$

5 Results of the Problem

In this section, we have studied the effects of pertinent parameters on the flow quantities in both Newtonian and Casson fluid cases with the fixed values: $\varepsilon = 0.3, \beta = 2, M = 2, x = 0.2, t = 0.25, E_1 = 0.3, E_2 = 0.2, E_3 = 0.1, Nt = 0.5, Nb = 0.5, Br = 0.02, Sc = 0.6, Sr = 0.2, Pr = 7, Du = 0.2$. Figures 2, 3, and 4 are drawn to study the impact of MHD on the velocity, temperature, and concentration fields. We observed that the increase in M decreases the velocity in the middle of the channel as it enhances at the channel wall. We noted that the rise in M reduces the temperature whereas it improves the concentration. It shows the influence of the magnetic field on the flow. Also, it is perceived that velocity and thermal fields are maximal at the midway point of the channel, whereas the concentration field is minimal near the center of the channel. From Figs. 5, 6, 7,

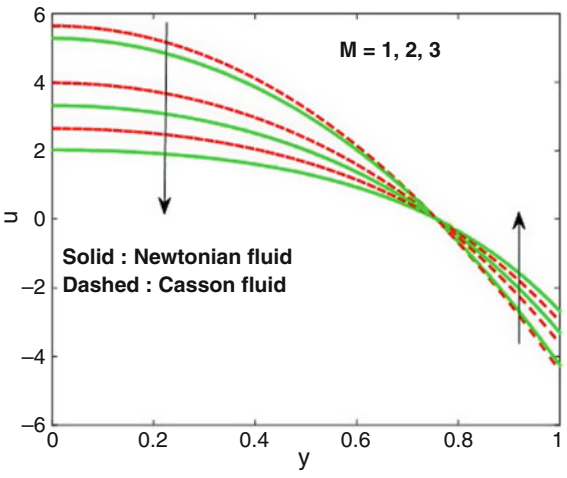

Fig. 2 Effect of M on velocity

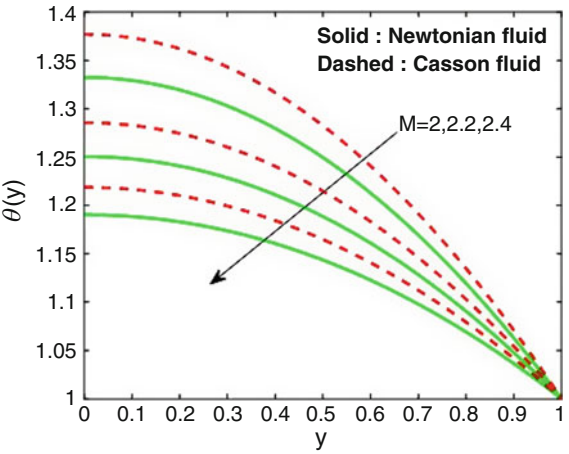

Fig. 3 Effect of M on temperature

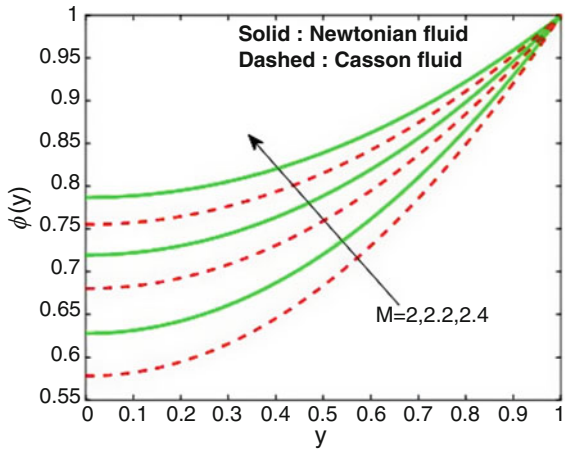

Fig. 4 Effect of M on concentration

and 8, we identified that the high values of the thermophoresis parameter boost the temperature and diminish the concentration. Moreover, reverse behavior is observed in the case of the Brownian motion parameter. Figures 9, 10, 11, and 12 show that

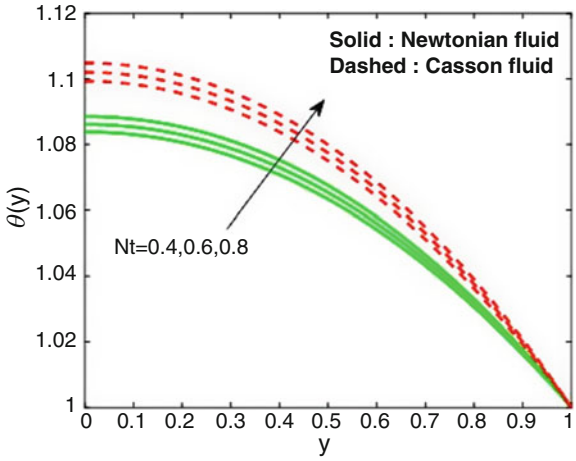

Fig. 5 Effect of Nt on temperature

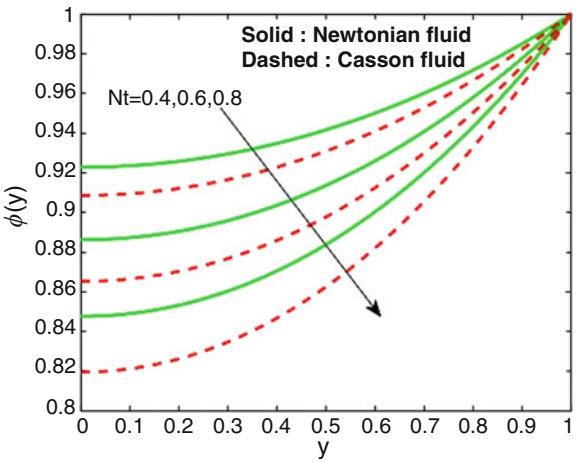

Fig. 6 Effect of Nt on concentration

the increment in the Soret number decreases both temperature and concentration fields. The high values of the Dufour number reduces the concentration, whereas it increases the thermal field. The influence of the Casson fluid parameters β and M on the formation of a circulating bolus by surrounding streamlines in the fluid flow is presented in Figs. 13 and 14. The increase in β and M reduces the size of the trapped bolus.

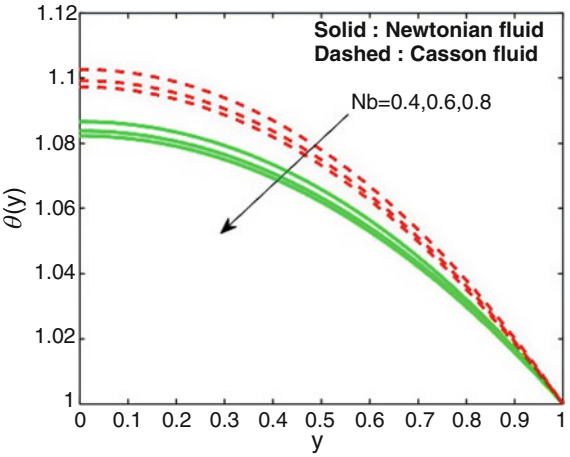

Fig. 7 Effect of *Nb* on temperature

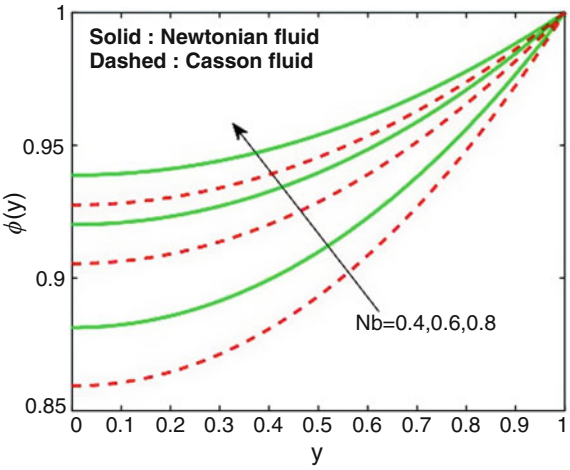

Fig. 8 Effect of *Nb* on concentration

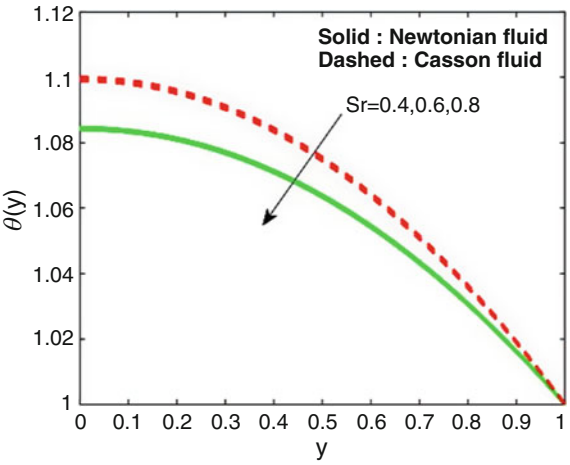

Fig. 9 Effect of *Sr* on temperature

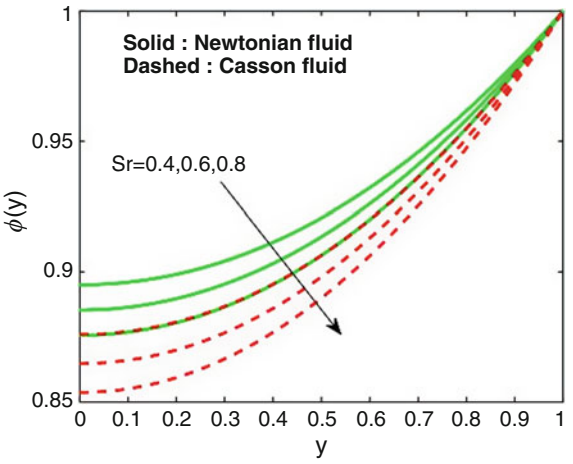

Fig. 10 Effect of *Sr* on concentration

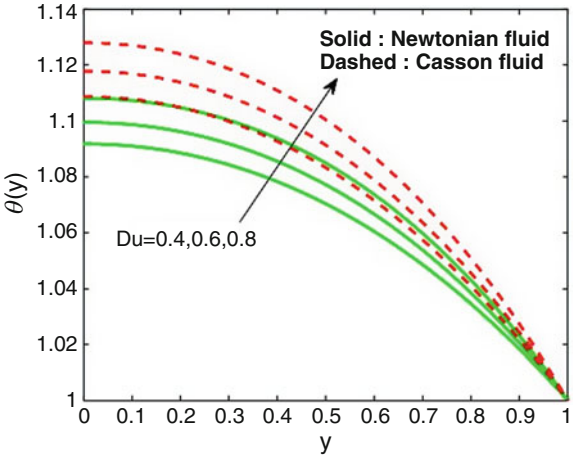

Fig. 11 Effect of *Du* on temperature

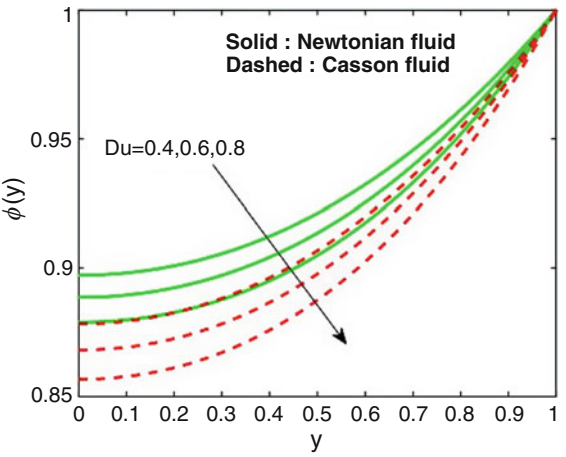

Fig. 12 Effect of *Du* on concentration

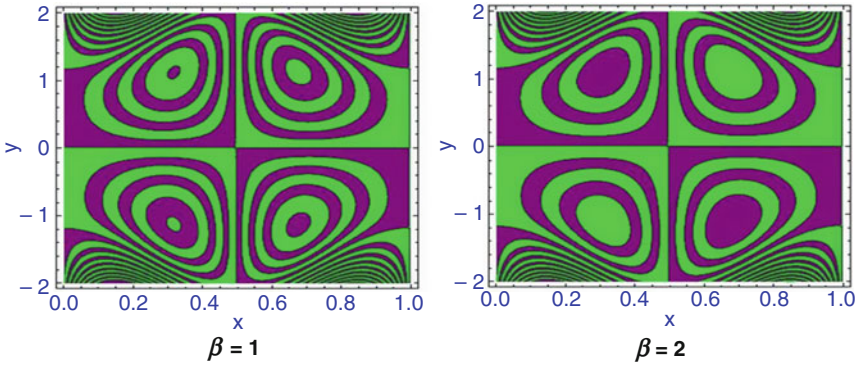

Fig. 13 Influence of β on trapping

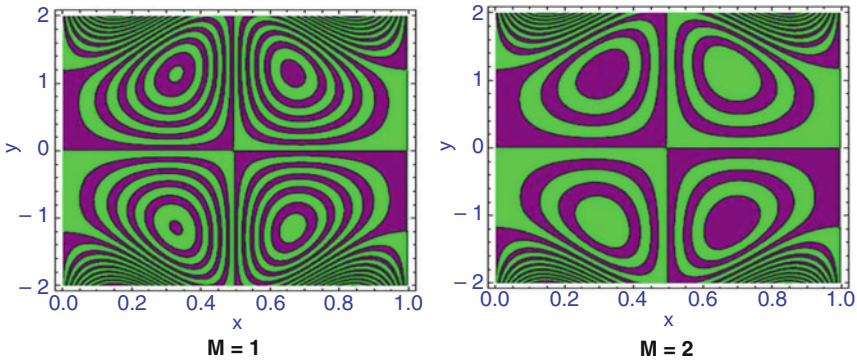

Fig. 14 Influence of M on trapping

References

1. Latham, T.W.: Fluid motions in a peristaltic pump. M.S. Thesis, Massachusetts Institute of Technology, Cambridge (1966)
2. Fung, Y.C., Yih, C.S.: Peristaltic transport. Trans. ASME, J. Appl. Mech. **35**, 669–675 (1968)
3. Shapiro, A.H., Jaffrin, M.Y., Weinberg, S.L.: Peristaltic pumping with long wavelengths at low Reynolds number. J. Fluid Mech. **37** (4), 799–825 (1969)
4. Usha, S., Ramachandra Rao, A.: Peristaltic transport of two-layered power-law fluids. J. Biomech. Eng. **119**, 483–488 (1997)
5. Srinivas, S., Kothandapani, M.: The influence of heat and mass transfer on MHD peristaltic flow through a porous space with compliant walls. Appl. Math. Comput. **213**, 197–208 (2009)

6. Lakshminarayana, P., Sreenadh, S., Sucharitha, G., Nandagopal, K.: Effect of slip and heat transfer on peristaltic transport of a Jeffrey fluid in a vertical asymmetric porous channel. Adv. Appl. Sci. Res. **6** (2), 107–118 (2015)
7. Vajravelu, K., Sreenadh, S., Lakshminarayana, P., Sucharitha, G., Rashidi, M. M.: Peristaltic flow of Phan-Thien-Tanner fluid in an asymmetric channel with porous medium. J. Appl. Fluid Mech. **9** (4), 1615–1625 (2016)
8. Vajravelu, K., Sreenadh, S., Lakshminarayana, P., Sucharitha, G.: The effect of heat transfer on the nonlinear peristaltic transport of a Jeffrey fluid through a finite vertical porous channel. Int. J. Biomath. **9** (2) 1650023 (25 pages) (2016)
9. Vajravelu, K., Sreenadh, S., Dhananjaya, S., Lakshminarayana, P.: Peristaltic flow and heat transfer of a conducting Phan-Thien-Tanner fluid in an asymmetric channel - application to chyme movement in small intestine. Int. J. of Appl. Mech. Eng. **21** (3), 713–736 (2016)
10. Akbar, N. S.: Influence of magnetic field on peristaltic flow of a Casson fluid in an asymmetric channel: Application in crude oil refinement. J. Magn. Magn. Mater. **378**, 463–468 (2015)
11. Nadeem, S., Ul Haq, R., Akbar, N. S., Khan, Z. H.: MHD three dimensional flow of Casson fluid past a porous linearly stretching sheet. Alex. Eng. J. **52**, 577–582 (2013)
12. Raju, C. S. K., Sandeep, N., Saleem, S.: Effects of induced magnetic field and homogeneous-heterogeneous reactions on stagnation flow of a Casson fluid. Eng. Sci. Technol. Int. J. **19** (2), 875–887 (2016)
13. Hayat, T. Ali Bhatti, Z., Ahmad, B., Alsadi, A.: Effects of variable viscosity and inclined magnetic field on peristaltic motion of fourth-grade fluid with heat transfer. Heat Trans. Res. **47** (5), 489–503 (2016)
14. Saleem, S., Awais, M., Nadeem, S., Sandeep, N., Mustafa, M. T.: Theoretical analysis of upper-convected Maxwell fluid flow with Cattaneo-Christov heat flux model. Chin. J. Phys. (2017) doi:org/10.1016/j.cjph.2017.04.005
15. Satyanarayana, K.V.V., Sreenadh, S., Sucharitha, G., Lakshminarayana, P.: The effect of wall properties on the convective peristaltic transport of a conducting Bingham fluid through porous medium. Ind. J. Sci. Tech. **9** (42), 1–9 (2016)
16. Sucharitha, G., Lakshminarayana, P., Sandeep, N.: Joule heating and wall flexibility effects on the peristaltic flow of magnetohydrodynamic nanofluid. Int. J. Mech. Sci. **131–132**, 52–62 (2017)
17. Lakshminarayansa, P., Sreenadh, S., Sucharitha, G.: The influence of slip, wall properties on the peristaltic transport of a conducting Bingham fluid with heat transfer. Proc. Eng. **127**, 1087–1094 (2015)
18. Sucharitha, G., Lakshminarayana, P., Sandeep, N.: Dual solutions of cross diffusion effects on MHD Peristaltic flow in a conduit. IOP Conference series, Material Science and Engineering **263**, 062026 (2017)
19. Hayat, T., Abbasi, F. M., Maryem, A., Monaquel, S.: Slip and Joule heating effects in mixed convection peristaltic transport of nanofluid with Soret and Dufour effects. J. Mol. Liq. **194**, 93–99 (2014)
20. Mehmood, R., Nadeem, S., Saleem, S., Akbar, N. S.: Flow and heat transfer analysis of a Jeffery nano fluid impinging obliquely over a stretched plate. J. Taiwan Inst. Chem. Eng. **74**, 49–58 (2017)
21. Nadeem, S., Khan, S., A. U., Saleem, S.: A comparative analysis on different nanofluid models for the oscillatory stagnation point flow. Eur. Phys. J. Plus **131**, 261 (2016)
22. Nadeem, S., Ahmed, Z., Saleem, S.: The effect of variable viscosities on micro-polar flow of two nanofluid. Z. Naturforsch A **71** (12), 1121–1129 (2016)
23. Lakshminarayana, P., Vajravelu, K., Sucharitha, G., Sreenadh, S.: Peristaltic slip flow of a Bingham fluid in an inclined porous conduit with Joule heating. Appl. Math. Nonlinear Sci. **3** (1), 41–54 (2018)

Axisymmetric Vibration in a Submerged Piezoelectric Rod Coated with Thin Film

Rajendran Selvamani and Farzad Ebrahimi

Abstract This paper is concerned with the axisymmetric elastic waves in a transversely isotropic submerged piezoelectric rod coated with thin film using a constitutive form of linear theory of elasticity and piezoelectric equations. The equations of motion along radial and axial directions are decoupled by using potential functions. The surface area of the rod is coated by a perfectly conducting material, and no slip boundary condition is employed along the solid-fluid interactions. The dispersion equation which contains the longitudinal and flexural modes is derived and is studied numerically. To observe the variations of mechanical and electric displacement in the coated piezoelectric rod, the authors compute the numerical values of the field variables for the ceramic $PZT-4$. The effects of fluid and coating environment on the variation of field variables are analyzed and presented graphically. This type of study is important in the modeling of underwater sensors for the navigation applications.

Keywords Axisymmetric waves in piezoelectric rod/glass fiber · Forced vibration · Bessel function · Actuators/sensors · Thin film

1 Introduction

The piezoelectric materials are the important structural components in devices like pressure transducers and accelerometers. Initially piezoelectric materials are used as resonators for ultrasound sources in sonar devices. The piezoelectric materials such as barium titanate ($BiTiO3$) are fabricated by the advancement of piezoelectricity in engineering field. Coated piezoelectric polymers are used in a variety of real-time

R. Selvamani (✉)
Department of Mathematics, Karunya University, Coimbatore, TamilNadu, India
e-mail: selvamani@karunya.edu

F. Ebrahimi
Department of Mechanical Engineering, Faculty of Engineering, Imam Khomeini International University, Qazvin, Iran

B. Rushi Kumar et al. (eds.), *Applied Mathematics and Scientific Computing*, Trends in Mathematics, https://doi.org/10.1007/978-3-030-01123-9_21

engineering applications and structural components for a large variety of model from transducers in acoustic, sensor, and actuator applications to microelectromechanical systems and nanoelectromechanical systems, image processing, and some industrial nondestructive testing instruments. The effect of fluid in the medium will attenuate the wave and energy transfer. Also, the thin film coating and fluid medium can highly influence the performance of the wave propagation.

The elastic wave pattern in solid material has been discussed elaborately by Graff [7] and Achenbach [1]in a more elucidated manner. Wave propagation in elongated cylinders and plates was analyzed based on linear theory of elastic and governing equation models by Meeker and Meitzler [9]. Tiersten [12] studied the modeling and development of piezoelectric plate under cylindrical structures using theory of linear elasticity. The author developed modeling for small vibrations of piezoelectric bodies by the linear theory of piezoelectricity through Maxwell's equations. In piezoelectricity the quasistatic electric field is coupled to the dynamic mechanical motion. Electroelastic governing equations of piezoelectric materials are presented by Parton and Kudryavtsev [13]. Paul and Venkatesan [14] introduced an elastic wave model in piezoelectric cylinders of noncircular cross section with infinite extent using Fourier expansion collocation method which is devised by Nagaya [11]. Ebenezer and Ramesh [6] have rightly analyzed the application of the Bessel series to study the axially polarized piezoelectric cylinders with arbitrary boundary conditions on the flat surfaces. Later Botta and Cerri [5] have extended the same approach further and compared their results with those in which the effect of variable electric potential was not considered. An investigation was made in radially polarized piezoelectric cylindrical transducers by Kim and Lee [8]. In that study, they validated their result with the outcomes from the experiment and quantitative analysis by the finite element method. Selvamani [15] has developed the modeling of elastic waves in a submerged piezoelectric circular fiber. It was inferred by him that the impact of fluids (inner and outer) along with the anisotropy of the material with thickness on the many considered wave characteristics is more significant and dominant in the flexural modes of vibration.

Sinha et al.[18] developed a two-part elaborative study on the axisymmetric waves in a cylindrical shell contact with fluid. In that study, the theoretical derivation of the wave modes is analyzed in part I, and the vibration modes in the absence of tension are studied theoretically and numerically in part II. Berliner and Solecki [3] investigated the wave motion in the transversely isotropic direction of fluid-loaded cylinder. In their study, part I explains the formulation of the problem which consists of both solid and outer fluid medium, and part II explains the computed numerical values.

The influence of rotation in axisymmetric elastic waves of a solid bar submerged in water was studied by Selvamani and Ponnusamy [16]. In that paper, they identified the rotational parameter having significance effect with vibrational modes. Free vibration in a generalized thermo-piezoelectric bar of circular cross section rotating with a linear angular velocity has been studied by Selvamani and Ponnusamy [17] using Bessel function solution. Wang [20] discussed the axisymmetric wave propagation in a cylinder coated with a piezoelectric layer. Research on its

application for time-delay devices has been investigated by Sun and Cheng [19]. A theoretical model of the coated structure is investigated by Minagawa [10] to predict attenuation characteristics for finding suitable modes for a guided-wave inspection. Barshinger [2] investigated the guided waves in pipes with viscoelastic coatings. He found that the presence of attenuative, viscoelastic coatings causes significant problems for developing a guided-wave, nondestructive inspection of coated pipes.

The axisymmetric elastic wave of coated piezoelectric rod submerged in inviscid fluid (water) is considered using a constitutive form of equations consisting of the theory of linear elasticity and electrostatic components. Velocity potentials updated based on equilibrium equations and are used to uncouple the governing equations. The surface area of the rod is coated by a perfectly conducting gold layer. The dispersion equation which consists of longitudinal and flexural modes of piezoelectric rod is calculated for the ceramic material $PZT-4$. The variation mechanical displacement and electric displacement are investigated and are given as dispersion curves.

2 Modeling of the Problem

A homogeneous transversely isotropic piezoelectric circular rod of infinite length coated by a thin film in the axisymmetric direction is considered for this problem. The governing equations of motion in the absence of body forces are given as

$$\frac{\partial}{\partial r}T_{rr}+\frac{\partial}{\partial z}T_{rz}+\frac{T_{rr}}{r}=\rho\frac{\partial^2 u_r}{\partial t^2},\quad \frac{\partial}{\partial r}T_{rz}+\frac{\partial}{\partial z}T_{zz}+\frac{T_{rz}}{r}=\rho\frac{\partial^2 u_z}{\partial t^2} \tag{1}$$

The Gauss electric conduction equation without free charge is

$$\frac{1}{r}\frac{\partial}{\partial r}(rD_r)+\frac{\partial D_z}{\partial r}=0 \tag{2}$$

The coupled form of stress equations is given as

$$\begin{aligned} &T_{rr}=c_{11}e_{rr}+c_{13}e_{zz}-e_{31}E_z,\quad T_{zz}=c_{13}e_{rr}+c_{33}e_{zz}-e_{33}E_z,\\ &T_{rz}=2c_{44}e_{rz}-e_{15}E_r\\ &D_r=e_{15}e_{rz}+\varepsilon_{11}E_r,\quad D_z=e_{31}(e_{rr}+e_{\theta\theta})+e_{33}e_{zz}+\varepsilon_{33}E_z \end{aligned} \tag{3}$$

where T_{rr} and T_{zz} are the normal stresses in the radial and thickness directions; T_{rz} is the shear stress element; e_{rr} and e_{zz} are the normal strains in the radial and thickness directions; e_{rz} is the shear strain element; u_r and u_z are the displacement components; c_{11}, c_{13}, c_{33}, and c_{44} are the elastic constants; e_{31}, e_{15}, and e_{33} are the piezoelectric constants; ε_{11} and ε_{33} are the dielectric constants; and ρ is the density of the material under consideration.

The strain displacement relations and the electric field vector E_i, $(i = r, z)$ with electric potential E are defined as

$$e_{rr} = u_{r,r}, e_{zz} = u_{z,z}, e_{rz} = u_{z,r} + u_{r,z}, \quad E_r = -\frac{\partial E}{\partial r} \text{ and } E_z = -\frac{\partial E}{\partial z} \tag{4}$$

The comma in the subscripts represents the differentiation with respect to the variables. Substituting Eqs. (3) and (4) in Eqs. (1) and (2) results in

$$\begin{gathered} c_{11}(u_{rr,r} + r^{-1}u_{r,r} - r^{-2}u_r) + c_{44}u_{r,zz} \\ +(c_{44} + c_{13})u_{z,rz} + (e_{31} + e_{15})V_{,rz} = \rho u_{r,tt} \\ c_{44}(u_{z,rr} + r^{-1}u_{z,r}) + r^{-1}(c_{44} + c_{13})(u_{r,z}) + (c_{44} + c_{13})u_{r,rz} + c_{33}u_{z,zz} \\ +e_{33}V_{,zz} + e_{15}(V_{,rr} + r^{-1}V_{,r}) = \rho u_{z,tt} \\ e_{15}(u_{z,rr} + r^{-1}u_{z,r}) + (e_{31} + e_{15})(u_{r,zr} + r^{-1}u_{r,z}) + e_{33}u_{z,zz} - \varepsilon_{33}V_{,zz} \\ -\varepsilon_{11}(V_{,rr} + r^{-1}V_{,r}) = 0. \end{gathered} \tag{5}$$

3 Solution Methodology

The time-harmonic elastic waves in piezoelectric material are obtained by assuming the displacement components in the following form which will also satisfy the equation of motion and boundary conditions (Paul and Venkatesan [11]): $u_r(r, z, t) = (\phi_{,r})e^{i(kz+\omega t)}$, $V(r, z, t) = iVe^{i(kz+\omega t)}$, $E_z(r, z, t) = E_{,z}e^{i(kz+\omega t)}$, $u_z(r, z, t) = (\frac{i}{a})We^{i(kz+\omega t)}$, $E_r(r, z, t) = -E_{,r}e^{i(kz+\omega t)}$ where $i = \sqrt{-1}$, k is the wave number, ω is the angular frequency, $\phi(r)$ and $W(r)$ are the displacement potentials, and the parameter a describes the geometric component of the rod and $V(r, \theta)$ is the electric potential. By applying the following nondimensional components $x = r/a$, $\vartheta = ka$, $\varpi^2 = \rho\omega^2a^2/c_{44}$, $\bar{c}_{11} = c_{11}/c_{44}$, $\bar{c}_{13} = c_{13}/c_{44}$, $\bar{c}_{33} = c_{33}/c_{44}$, $\bar{c}_{66} = c_{66}/c_{44}$, $\bar{\varepsilon}_{11} = \varepsilon_{11}c_{44}/e_{33}^2$, $\bar{e}_{31} = e_{31}/e_{33}$, and $\bar{e}_{15} = e_{15}/e_{33}$, Eq. (5) can be rewritten as

$$\begin{vmatrix} (\bar{c}_{11}\nabla^2 + (\varpi^2 - \vartheta^2)) & -\vartheta(1 + \bar{c}_{13}) & -\vartheta(\bar{e}_{31} + \bar{e}_{15}) \\ \vartheta(1 + \bar{c}_{13})\nabla^2 & (\nabla^2 + (\varpi^2 - \vartheta^2\bar{c}_{33})) & (\bar{e}_{15}\nabla^2 - \vartheta^2) \\ \vartheta(\bar{e}_{31} + \bar{e}_{15})\nabla^2 & (\bar{e}_{15}\nabla^2 - \vartheta^2) & (\vartheta^2\bar{\varepsilon}_{33} - \bar{\varepsilon}_{11}\nabla^2) \end{vmatrix} (\phi, W, V) = 0 \tag{6}$$

where $\nabla^2 = \frac{\partial^2}{\partial x^2} + x^{-1}\frac{\partial}{\partial x} + x^{-2}\frac{\partial^2}{\partial\theta^2}$. Evaluating the determinant given in Eq. (6), we obtain a partial differential equation of the form

$$(P\nabla^6 + Q\nabla^4 + R\nabla^2 + S)(\phi, W, V) = 0 \tag{7}$$

From Eq. (7), the following solutions are obtained:

$$\phi = \sum_{i=1}^{3} A_i J_n(\tau_i a x)\cos n\theta,\ W = \sum_{i=1}^{3} a_i A_i J_n(\tau_i a x)\cos n\theta,$$
$$V = \textstyle\sum_{i=1}^{3} b_i A_i J_n(\tau_i a x)\cos n\theta \tag{8}$$

Here $(\tau_i a)^2 > 0$ and $(i = 1, 2, 3)$ are the roots of the algebraic equation:

$$A(\tau a)^6 - B(\tau a)^4 + C(\tau a)^2 + D = 0 \tag{9}$$

In the above solutions, J_n represents Bessel function which will take the real or complex roots $(\tau_i a)^2$, $(i = 1, 2, 3)$, and I_n represents the modified Bessel function which will take imaginary roots. In case $(\alpha_4 a)^2 < 0$, J_n is replaced by I_n.

The constants a_i, b_i defined in the Eq. (8) is derived from the following equations:

$$(1 + \bar{c}_{13})\vartheta a_i + (\bar{e}_{31} + \bar{e}_{15})\vartheta b_i = -(\bar{c}_{11}(\tau_i a)^2 - \varpi^2 + \vartheta^2) \tag{10}$$

$$((\tau_i a)^2 - \varpi^2 + \vartheta^2 \bar{c}_{33})a_i + (\bar{e}_{15}(\tau_i a)^2 + \vartheta^2)b_i = -(\bar{c}_1 3 + 1)\vartheta(\tau_i a)^2 \tag{11}$$

4 Modeling and Solutions of the Fluid Medium

The radial movement and acoustic pressure equations of the inviscid fluid in polar form are taken from Berliner [3]:

$$p^f = -b^f(u^f_{,r} + r^{-1}(u^f) + w^f_{,z}) \text{ and } c_f^{-2}u^f_{,tt} = \Delta_{,r} \tag{12}$$

where b^f and ρ^f are the bulk modulus and density of the fluid, $c^f = \sqrt{b^f/\rho^f}$ is the acoustic phase velocity in the fluid, and (u^f, w^f) is the displacement vector, and assume the solution of (12) in the form

$$\varphi^f(r, \theta, z, t) = [\varphi^f(r)]e^{i\omega t}, \tag{13}$$

the wave propagation of the fluid medium is given by

$$\varphi^f = A_{33}H_n(\delta a x) \tag{14}$$

where $(\delta a)^2 = \Omega^2/\bar{\rho}^f\bar{b}^f - \vartheta^2$, in which $\bar{\rho}^f = \rho/\rho^f$, $\bar{b}^f = b^f/c_{44}$, H_n is the Hankel function. If $(\sigma a)^2 < 0$, then the Hankel function of the first kind is to be replaced by the modified Bessel function of the second kind K_n. From Eqs. (13), (12), and (14), the value of acoustic pressure is calculated as

$$p^f = A_{33}\Omega^2\bar{\rho}H_n(\delta a x)e^{i(\Omega T_a)} \tag{15}$$

5 Interfacial Boundary Conditions and Frequency Equations

The axisymmetric free vibration of the transversely isotropic piezoelectric rotating rod coated with a thin film is considered. For the coated surface, the boundary conditions can be written as

$$\sigma_{rj} = -\delta_{jb} 2\mu' h' \left[\left(\frac{3\lambda' + 2\mu'}{\lambda' + 2\mu'} \right) U_{a,ab} + U_{b,aa} \right] + 2h'\rho' \ddot{U}_j, \qquad V = 0 \qquad (16)$$

where λ', μ', ρ', and h' are Lame's constants, density, and thickness of the material coating, respectively; δ_{jb} is the Kronecker delta function with a; b takes the value of θ and z; and j takes r, θ and z. In order to get the axisymmetric waves, a and b can take only z. Then the transformed boundary conditions are as follows:

$$\sigma_{rr} + p^f = 2h'\rho'\ddot{U}, \quad \sigma_{rz} = -2h'\mu' G^2 W_{,zz} + 2h'\rho'\ddot{W}, \quad (u - u^f) = 0, \quad V = 0 \qquad (17)$$

at $r = a$ and where $G^2 = \frac{1+C'_{12}}{C'_{11}}$.

By using Eqs. (8) and (15) in Eq. (17), we can get the following linear equation:

$$[L]\{Z\} = \{0\} \qquad (18)$$

where $[L]$ is a 4×4 matrix of unknown wave amplitudes and $\{Z\}$ is a 4×1 column matrix with the amplitudes L_1, L_2, and L_3. To obtain the nontrivial solution of Eq. (18), the determinant of the coefficient of the amplitudes $\{Z\}$ will be equal to zero.

6 Numerical Results and Investigations

For the graphical illustration, the axisymmetric free vibration of the transversely isotropic piezoelectric rotating rod coated with a thin film is considered. Equation (18) is solved numerically for the mechanical and electrical displacements. The material chosen for the numerical calculation is $PZT - 4$ ceramics coated with gold material which is taken from Berlincourt et al. [4].

$c_{11} = 13.9 \times 10^{10} Nm^{-2}$, $c_{12} = 7.78 \times 10^{10} Nm^{-2}$, $c_{13} = 7.43 \times 10^{10} Nm^{-2}$,
$c_{33} = 11.5 \times 10^{10} Nm^{-2}$, $c_{44} = 2.56 \times 10^{10} Nm^{-2}$, $c_{66} = 3.09 \times 10^{10} Nm^{-2}$,
$e_{31} = -5.2 Cm^{-2}$, $e_{33} = 15.1 Cm^{-2}$, $e_{15} = 12.7 Cm^{-2}$,
$\varepsilon_{11} = 6.46 \times 10^{-9} C^2 N^{-1} m^{-2}$, $\varepsilon_{33} = 5.62 \times 10^{-9} C^2 N^{-1} m^{-2}$,
$\rho = 7500 Kgm^{-2}$, $\rho^f = 1000 Kgm^{-3}$.

For Gold material, $\rho' = 19.28 gcm^{-3}, \lambda' = 1.63 * 10^{10} Nm^{-2}, and \mu' = 0.42 * 10^{10} Nm^{-2}$

In the figures, FSM and $FASM$, respectively, denote the flexural symmetric mode and flexural antisymmetric mode. The numbers 1 and 2 represent the first and second mode, respectively.

The variation of mechanical displacement versus the dimensionless wave number for flexural modes of coated piezoelectric circular rod with and without fluid medium is considered in Figs. 1 and 2. Figure 1 shows the oscillation in the lower range of wave number and becomes linear propagation with respect to its higher wave number in different flexural modes of the rod with fluid environment. But in Fig. 2, there is a small energy transfer between the modes in the lower range of wave number which might happen due to the coating of the rod and the absence of fluid medium. The coating and fluid environment decrease the magnitude of the mechanical displacement in Figs. 1 and 2. Figures 3 and 4 exhibit the propagation of electric displacement with respect to the thickness of the coated layer. Whenever the thickness of the rod increases, the electric displacement is decreasing and again increasing and travels in the wave propagation. These trends of the curves admit the elastic properties of the solid due to the effect of fluid and coating of the material.

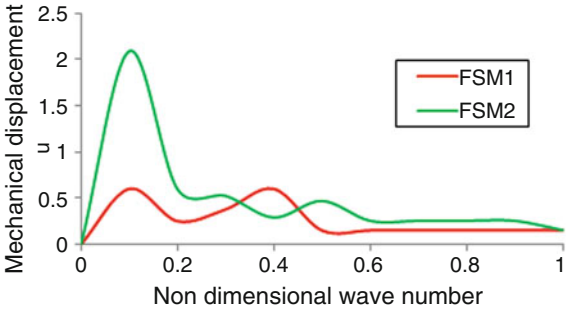

Fig. 1 Dispersion of mechanical displacement versus nondimensional wave number of coated piezoelectric rod with fluid

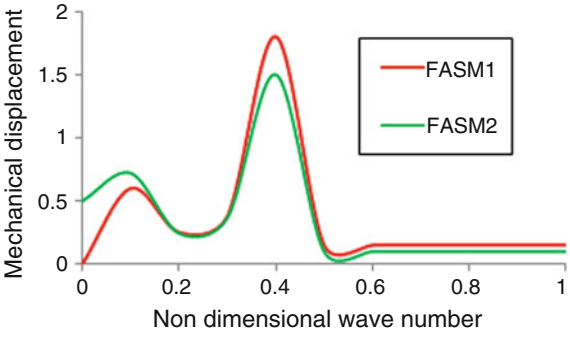

Fig. 2 Dispersion of mechanical displacement versus nondimensional wave number of coated piezoelectric rod without fluid

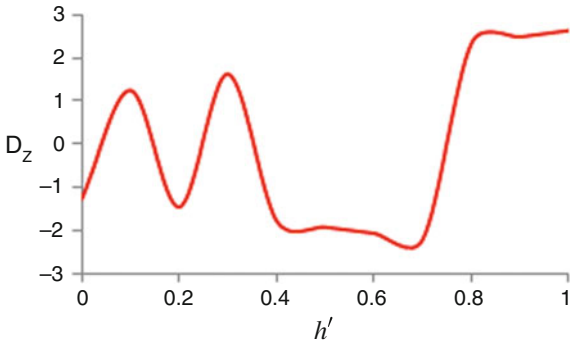

Fig. 3 Variation of electric displacement versus thickness of the coating material for piezoelectric rod with fluid

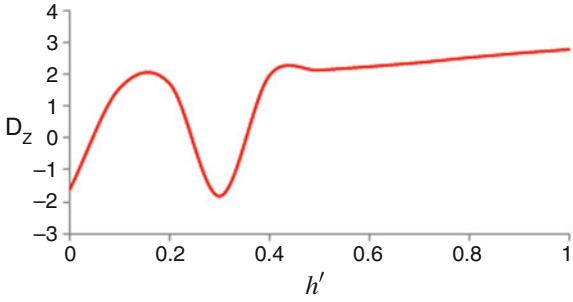

Fig. 4 Variation of electric displacement versus thickness of the coating material for piezoelectric rod without fluid

7 Conclusions

The modeling and analysis of axisymmetric elastic waves of a coated piezoelectric rod submerged in an infinite fluid (water) are considered in the context of constitutive equations consisting of the theory of linear elasticity and electrostatic components. Velocity potentials are updated based on equilibrium equations and are used to uncouple the governing equations. The surface area of the rod is coated by a perfectly conducting gold layer. The dispersion equation which consists of longitudinal and flexural modes of piezoelectric rod is calculated for the ceramic material $PZT - 4$. The computed mechanical and electric displacements are presented in the form of dispersion curves. From the graphical pattern, it is observed that the fluid and the coating of the piezoelectric rod highly influence the variations of the mechanical parameters in flexural symmetric and flexural antisymmetric modes.

References

1. Achenbach, J.D.: Wave motion in elastic solids. Amsterdam, North-Holland (1984).
2. Barshinger, J.N.: Guided waves in pipes with viscoelastic coatings. Ph.D. dissertation, The Pennsylvania State University, State College, PA (2001).

3. Berliner, J., Solecki, R.: Wave Propagation in a fluid-loaded transversely isotropic cylinder. Part I. Analytical formulation; Part II Numerical results, J. Acoust. Soc. Am. **99**, 1841–1853 (1996).
4. Berlin Court, D.A., Curran, D.R., Jaffe, H.: Piezoelectric and piezomagnetic materials and their function in transducers. Physical Acoustics, **1A** (W.P.Mason, editor), Academic Press, New York and London (1964).
5. Botta, F., Cerri, G.: Wave propagation in Reissner-Mindlin piezoelectric coupled cylinder with non-constant electric field through the thickness. Int. J. Solid and Struct. **44**, 6201–6219 (2007).
6. Ebenezer, D.D., Ramesh, R.: Analysis of axially polarized piezoelectric cylinders with arbitrary boundary conditions on the flat surfaces. J. Acoust. Soc. Am. **113(4)**, 1900–1908 (2003).
7. Graff, K.F.: Wave motion in elastic solids. Dover, Newyork (1991).
8. Kim, J.O., Lee, J.G.: Dynamic characteristics of piezoelectric cylindrical transducers with radial polarization. J. Sound Vib. **300**, 241–249 (2007).
9. Meeker, T.R., Meitzler, A.H.: Guided wave propagation in elongated cylinders and plates. Physical acoustics, New York Academic (1964).
10. Minagawa, S.: Propagation of harmonic waves in a layered elasto-piezoelectric composite. Mech.Mater. **19**, 165–170 (1995).
11. Nagaya, K.: Dispersion of elastic waves in bars with polygonal cross-section. J. Acoust. Soc. Am. **70**, 763–770 (1981).
12. Tiersten, H.F.: Linear piezoelectric plate vibrations, New York, Plenum (1969).
13. Parton, V.Z., Kudryavtsev, B.A.: Electromagnetoelasticity. Gordon and Breach, New York (1988).
14. Paul, H.S., Venkatesan, M.: Wave propagation in a piezoelectric ceramic cylinder of arbitrary cross section. J. Acoust. Soc. Am. **82(6)**, 2013–2020 (1987).
15. Selvamani, R.: Modeling of elastic waves in a fluid-loaded and immersed piezoelectric circular fiber, Int. J. Appl. Comput. Math. **3**, 3263–3277 (2017).
16. Selvamani, R., Ponnusamy, P.: Effect of rotation in an axisymmetric vibration of a transversely isotropic solid bar immersed in an inviscid fluid. Mater. Phys. Mechs. **15**, 97–106 (2012).
17. Selvamani, R., Ponnusamy, P.: Wave propagation in a generalized piezothermoelastic rotating bar of circular cross-section. Multidi. Model. Mater. Struct. **11(2)**, 216–237 (2015).
18. Sinha, K., Plona, J., Kostek, S., Chang, S.: Axisymmetric wave propagation in a fluid-loaded cylindrical shell. I: Theory; II Theory versus experiment. J. Acoust. Soc. Am. **92**, 1132–1155 (1992).
19. Sun, C.T., Cheng, N.C.: Piezoelectric waves on a layered cylinder. J. Appl. Phy. **45**, 4288–4294 (1974).
20. Wang, Q.: Axi-symmetric wave propagation in a cylinder coated with a piezoelectric layer. Int. J. Solid and Struct. **39**, 3023–3037 (2002).

Numerical Exploration of 3D Steady-State Flow Under the Effect of Thermal Radiation as Well as Heat Generation/Absorption over a Nonlinearly Stretching Sheet

R. Jayakar and B. Rushi Kumar

Abstract This paper aims at the study of numerical investigation into the three-dimensional steady-state flow of a nanofluid under the effect of thermal radiation as well as heat generation/absorption over a nonlinearly stretching sheet. The set of partial differential equations is transformed into ordinary differential equations by employing the suitable similarity transformations. The solution to the governing equation is obtained by using numerical techniques specifically the bvp4c function in MATLAB. A nonuniform velocity with power-law index is the boundary condition specified for solving the governing equation.

Keywords MHD · Stagnation point · Homogeneous-heterogeneous reactions · Nanofluid flow · Non-uniform heat source/sink

1 Introduction

Numerous investigators have been spurred to examine magnetohydrodynamic steady-state flow of nanofluid over solid surfaces, keeping in perspective to their captivating heat energy transfer and thermophysical properties in addition to the tremendous potential application. References [1–5] gave a numerical way to deal with MHD transport of nanofluid past a vertical stretching sheet considering exponential temperature-dependent viscosity and lightness effects; furthermore, thermal physical properties of water built nanofluid past a stretching sheet were

R. Jayakar
Department of Mathematics, Vellore Institute of Technology, Vellore, Tamil Nadu, India
e-mail: jayakar.r2012@vit.ac.in

B. Rushi Kumar (✉)
Department of Mathematics, School of Advanced Sciences, Vellore Institute of Technology, Vellore, Tamil Nadu, India
e-mail: rushikumar@vit.ac.in

B. Rushi Kumar et al. (eds.), *Applied Mathematics and Scientific Computing*, Trends in Mathematics, https://doi.org/10.1007/978-3-030-01123-9_22

investigated by Akbar et al. [6], Sheikholeslami and Bhatti [7], Akbar et al. [8], and Bhatti et al. [9]. Nanofluids are fluids that have nanoparticles such as metals along with numerous traditional base fluids such as kerosene, railway locomotive oil, triethylene dihydric alcohol and ethane, and so on. Through the most recent decade, numerous specialists have been pulled in light of a legitimate concern for doing research on nanofluids that are crucial in perspective of their huge designing applications that incorporate more secure surgery, coolants in PCs and atomic reactors, a few electronic gadgets for use in military segments, major fabricating ventures including materials and chemicals, polymer expulsion, vehicles and transformers, cooling of microelectronics, and nourishment and drink, empowering to chill or cool structures. In the current decades, heat transfer is one of the basic key highlights in the vitality advancement at the modern level and assembling procedure of any hardware. In spite of that reality, heat addition, starting with one place then to the next place during the assembling procedure, is completely in view of the heat execution of working fluid. In a few cases, water, motor oil, lubricants, and other basic working fluids have poor heat conductivity in contrast with the required conductivity at the modern level. Addition of modest particles inside the working liquid plays a vital role in enhancing the poor warm conductivity of base fluid. The above overview uncovers the fact that no one hitherto has explored yet the three-dimensional MHD flow of nanofluids over a permeable stretching sheet, observing heat radiation accompanied by heat generation and absorption with power-law index. In this way in the present examination, we pioneered the exploration of the effect of magnetic field, heat generation , heat radiation, and other physical parameters on the three-dimensional flow of a nanofluid over a permeable stretching sheet. In our view, the nanofluid volume fraction on the boundary will be more easily controlled, making our investigation totally unique and physically more practical. The governing equations have been numerically solved using Runge-Kutta method with shooting technique. Graphical representation for the various parameters including velocity, temperature, and concentration has been discussed in detail for the said boundary conditions.

2 Mathematical Analysis

Consider a steady three-dimensional electrically conducting magnetohydrodynamic nanofluid flow past a nonlinearly permeable stretching sheet. Assume that a uniform transverse magnetic field of strength B_0 is applied parallel to the z-axis as shown in Fig. 1. Also the induced magnetic and electric fields are assumed to be neglected. The sheet is maintained at constant temperature T_w. The mass flux of the nanoparticles near the surface is assumed to be zero. T_∞ and C_∞ denote the ambient values of temperature and nanoparticle volume fraction, respectively. The governing equations describing flow pattern are as follows:

$$\frac{\partial u}{\partial x} + \frac{\partial v}{\partial y} + \frac{\partial w}{\partial z} = 0 \tag{1}$$

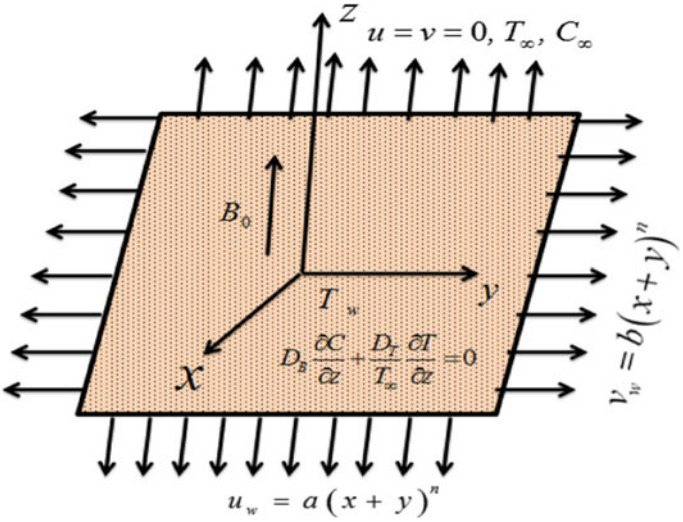

Fig. 1 Schematic interpretation of 3D MHD flow over a permeable stretching sheet

$$u\frac{\partial u}{\partial x} + v\frac{\partial u}{\partial y} + w\frac{\partial u}{\partial z} = \upsilon_f \frac{\partial^2 u}{\partial z^2} - \frac{\sigma B_0^2 u}{\rho_f} - \frac{\upsilon_f u}{K_p} \tag{2}$$

$$u\frac{\partial v}{\partial x} + v\frac{\partial v}{\partial y} + w\frac{\partial v}{\partial z} = \upsilon_f \frac{\partial^2 v}{\partial z^2} - \frac{\sigma B_0^2 v}{\rho_f} - \frac{\upsilon_f v}{K_p} \tag{3}$$

$$u\frac{\partial T}{\partial x} + v\frac{\partial T}{\partial y} + w\frac{\partial T}{\partial z} = \alpha\frac{\partial^2 T}{\partial z^2} + \tau\left[D_B\frac{\partial C}{\partial z}\frac{\partial T}{\partial z} + \frac{D_T}{T_\infty}\left(\frac{\partial T}{\partial z}\right)^2\right] \tag{4}$$

$$-\frac{1}{(\rho C_p)_f}\frac{\partial q_r}{\partial z} + \frac{Q_0}{(\rho C_p)_f}(T - T_\infty)$$

$$u\frac{\partial C}{\partial x} + v\frac{\partial C}{\partial y} + w\frac{\partial C}{\partial z} = D_B\frac{\partial^2 C}{\partial z^2} + \frac{D_T}{T_\infty}\frac{\partial^2 T}{\partial z^2} \tag{5}$$

with the boundary conditions

$$\begin{aligned} &u = u_w = a(x+y)^n,\ v = v_w = b(x+y)^n \quad \text{at } w = 0 \\ &T = T_w,\ D_B\frac{\partial C}{\partial z} + \frac{D_T}{T_\infty}\frac{\partial T}{\partial z} = 0 \quad \text{at } z = 0 \\ &u \to 0,\ v \to 0,\ T \to T_\infty,\ C \to C_\infty \quad \text{at } z \to \infty, \end{aligned} \tag{6}$$

where u, v and w are the velocity components in the x, y and z directions, respectively, ρ is the fluid density, p is the pressure, υ represents kinematic viscosity, σ is the electrical conductivity, B_0 is the magnetic field, and K_p is the porosity parameter. The radiative heat flux using Rosseland's approximation is given by

$$q_r = -\frac{4\sigma^*}{3k_1}\frac{\partial T^4}{\partial z} \tag{7}$$

Assume that the differences in the temperature within the flow are such that T^4 can be expressed as a linear combination of the temperature. Thus, expanding T^4 in a Taylor series about T_∞ and neglecting higher-order terms, we obtain

$$T^4 = 4T_\infty^3 T - 3T_\infty^4 \tag{8}$$

Thus,

$$\frac{\partial q_r}{\partial z} = \frac{-16\sigma^* T_\infty^3}{3k_1}\frac{\partial^2 T}{\partial z^2} \tag{9}$$

So, Eq. (4) becomes

$$u\frac{\partial T}{\partial x} + v\frac{\partial T}{\partial y} + w\frac{\partial T}{\partial z} = \alpha\frac{\partial^2 T}{\partial z^2} + \tau\left[D_B\frac{\partial C}{\partial z}\frac{\partial T}{\partial z} + \frac{D_T}{T_\infty}\left(\frac{\partial T}{\partial z}\right)^2\right]$$

$$+\frac{1}{(\rho C_p)_f}\frac{16\sigma^* T_\infty^3}{3k_1}\frac{\partial^2 T}{\partial z^2} + \frac{Q_0}{(\rho C_p)_f}(T - T_\infty) \tag{10}$$

by introducing the following nondimensional variables:

$$\eta = \sqrt{\frac{a}{\upsilon_f}}(x+y)^{n-1/2} z,\ u = a(x+y)^n f'(\eta),\ v = b(x+y)^n g'(\eta)$$

$$w = -\sqrt{a\upsilon_f}(x+y)^{n-1/2}\left(\frac{n+1}{2}(f+g) + \frac{n-1}{2}\eta\left(f'+g'\right)\right),$$

$$T = T_\infty + (T_w - T_\infty)\theta(\eta),\ C = C_\infty + C_\infty\phi(\eta), \tag{11}$$

and substituting Eq. (11) in (2), (3), (10), and (5) takes the form

$$g''' + \left(\frac{n+1}{2}\right)(f+g)g'' - n\left(f'+g'\right)g' - (M+K)g' = 0 \tag{12}$$

$$f''' + \left(\frac{n+1}{2}\right)(f+g)f'' - n\left(f'+g'\right)f' - (M+K)f' = 0 \tag{13}$$

$$\left(\frac{1+R}{\Pr}\right)\theta'' + Nb\phi'\theta' + Nt\theta'^2 + \frac{\theta'(n+1)(f+g)}{2} + Q\theta = 0 \quad (14)$$

$$\phi'' + \frac{n+1}{2}Sc(f+g)\phi' + \frac{Nt}{Nb}\theta'' = 0 \quad (15)$$

Subject to the transformed boundary conditions are as follows:

$$\begin{aligned} &f(0) = g(0) = 0,\ f'(0) = 1,\ g'(0) = \lambda,\ \theta(0) = 1, \\ &Nb\phi'(0) + Nt\theta'(0) = 0, \\ &f'(\infty) \to 0,\ g'(\infty) \to 0,\ \theta(\infty) \to 0,\ \phi(\infty) \to 0, \end{aligned} \quad (16)$$

Here M is the magnetic field parameter, K is the porosity parameter, Pr is the Prandtl number, Nb is the Brownian motion parameter, Nt is the thermophoresis parameter, λ is the ratio of the stretching rate along the y direction to the stretching rate along the x direction, and Sc is the Schmidt number. These parameters can be given as

$$\begin{aligned} &M = \sigma B_0^2/\rho a,\ K = 1/ak_0,\ \Pr = v/\alpha,\ Nb = \tau D_B C_\infty/v, \\ &Nt = \tau D_T (T_w - T_\infty)/v_f T_\infty,\ \lambda = b/a,\ Sc = v_f/D_B, \end{aligned} \quad (17)$$

The above equation reduces to the case of two-dimensional flow when $\lambda = 0$. At $\lambda = 1$, the differential system governing the axisymmetric flow of nanofluid due to nonlinearly stretching sheet is recovered. The dimensionless form of the skin-friction coefficient and the local Nusselt number is calculated by the following equation:

$$Nu\mathrm{Re}_x^{-1/2} = -\theta'(0)$$

where $\mathrm{Re}_x = u_w(x+y)/v_f$ and $\mathrm{Re}_y = v_w(x+y)/v_f$ are the local Reynolds numbers along the x and y directions, respectively. The component of velocity at far field condition can be expressed as

$$w(x, y, \infty) = -\sqrt{av_f(x+y)^{n-1}}\frac{n+1}{2}[f(\infty) + g(\infty)]$$

3 Results and Discussions

The array of governing equations is solved by using the numerical technique bvp4c MATLAB. For numerical effects, we have recognized $n = 1$, $Nt = Nb = 0.5$, $\lambda = 0.5$, $\Pr = 1$, $Sc = 20$, $k = 0.5$, $R = 0.5$, and $Q = 0.5$. These

values are kept as regular in whole investigation except the varied values as shown in the respective figures. The figures have been drawn using different physical parameters on the velocity, temperature, and concentration profiles for $n = 1$ and $n = 3$ cases. Figures 3, 7, and 10 demonstrate the velocity, temperature, and concentration profile for various values of magnetic parameter M. An expansion of the magnetic parameter depreciates the velocity while expanding the thermal and concentration profile. The magnetic parameter reduces the fluid velocity which in turn causes the momentum boundary layer to stretch. It is recognizing the way in which the transverse magnetic field, in interaction with conducting nanofluid, develops a retarding Lorentz force which slows down the fluid motion. We might

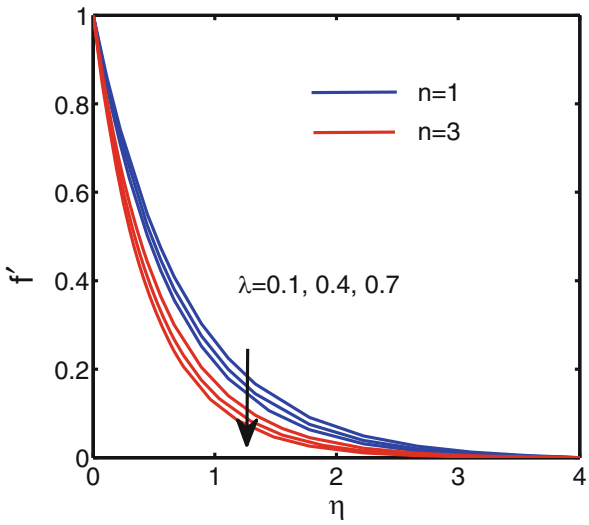

Fig. 2 Velocity for different λ

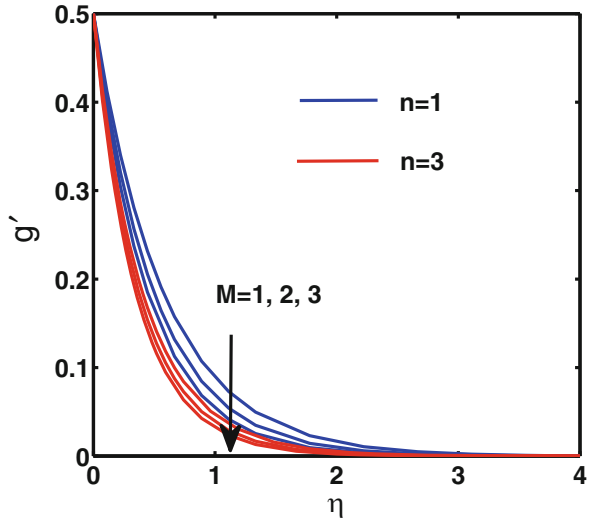

Fig. 3 Velocity for different M

want to comment here that unless and until the magnetic field was applied to the conducting fluid, it would not have been contradicted by Lorentz force so that the deceleration of fluid motion would not have been accomplished. It is indeed additionally fascinating to say that expansion in power-law index diminishes the velocity, temperature, and concentration boundary layers.

Figures 2, 4, and 8 reveal that enhancing the stretching rate ratio parameter reduces the velocity in x direction and temperature profile. But it helps to enhance the velocity in the y direction. Generally increasing the stretch in parameter tends to increase the pressure on the flow, and due to this reason, we have seen a decrease in temperature of the flow. From Fig. 5, we see that an increase in the

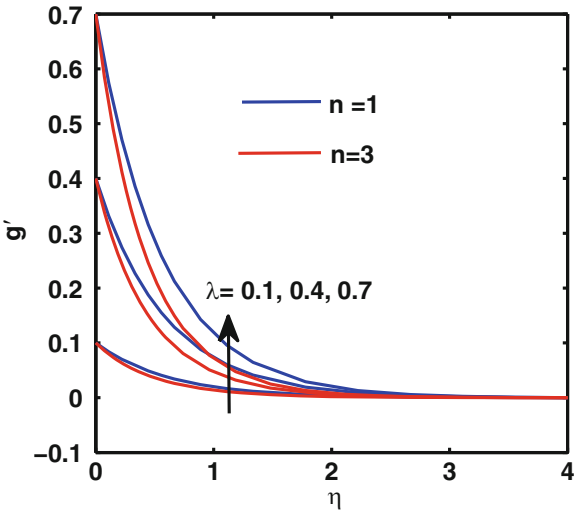

Fig. 4 Velocity for different λ

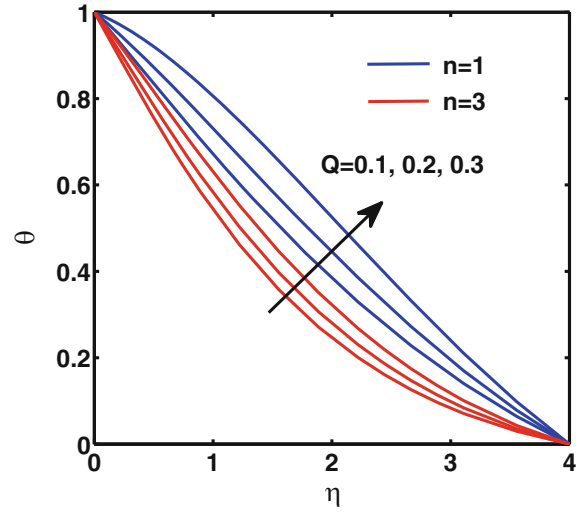

Fig. 5 Temperature for different Q

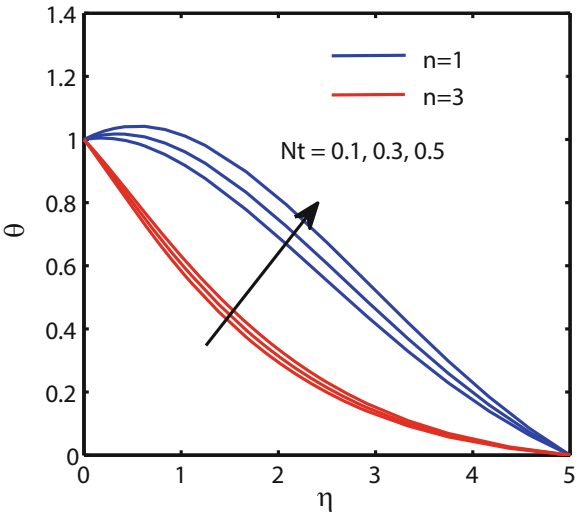

Fig. 6 Temperature for different Nt

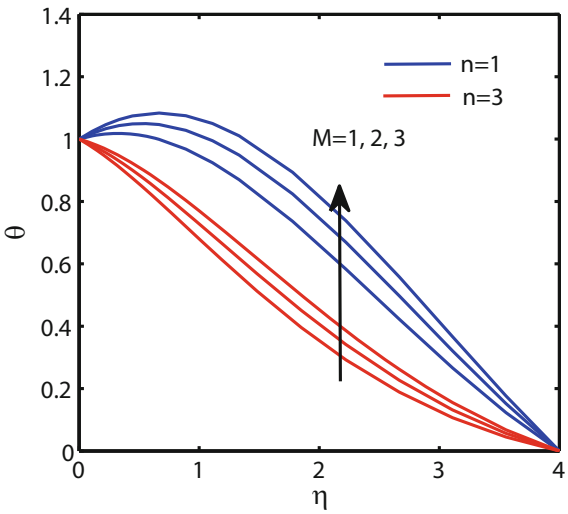

Fig. 7 Temperature for different M

nature of the heat source enhances the temperature. This is because the heat source can add more heat to the stretching sheet which extends its temperature, and in this way, the temperature of the fluid is enhanced. Additionally the temperature boundary layer also starts increasing by extending the nature of heat source. Fig. 11 noticed that the concentration for various values of heat sink. It is also noticed that the nature of the heat sink is quite opposite to the nature of heat source; i.e., the temperature diminishes by expanding the nature of the heat sink. This is in light of the fact that when the nature of the heat sink expands, more heat is expelled from the stretching sheet and also diminishes the thickness of temperature boundary layer. Thermophoresis is a phenomenon observed in mixtures

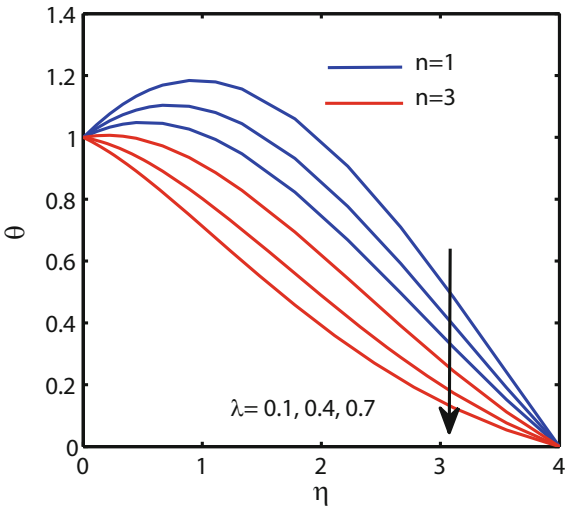

Fig. 8 Temperature for different λ

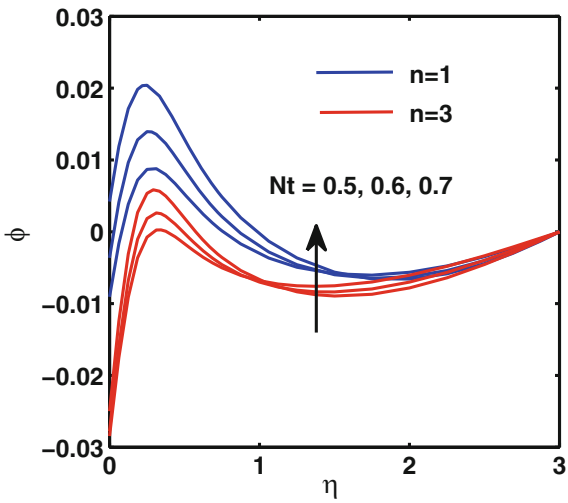

Fig. 9 Concentration for different Nt

of mobile particles where the different particle types exhibit different responses to the force of a temperature gradient. Figure 6 noticed the temperature for various Nt. It is noticed that an expansion in Nt expands the temperature of the fluid. At the point when Nt expands, the heat diffusivity of the nanoparticles will accelerate the temperature of the nanofluid. Figure 9 indicates the concentration for various values of Nt. It is obvious that the increase in the thermophoresis parameter Nt expands the boundary layer thickness of concentration. Due to this reason, the various nanoparticles have the various values of thermophoresis parameter Nt.

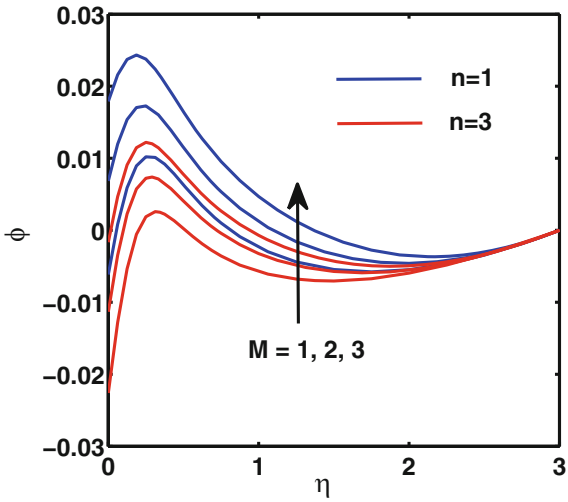

Fig. 10 Concentration for different M

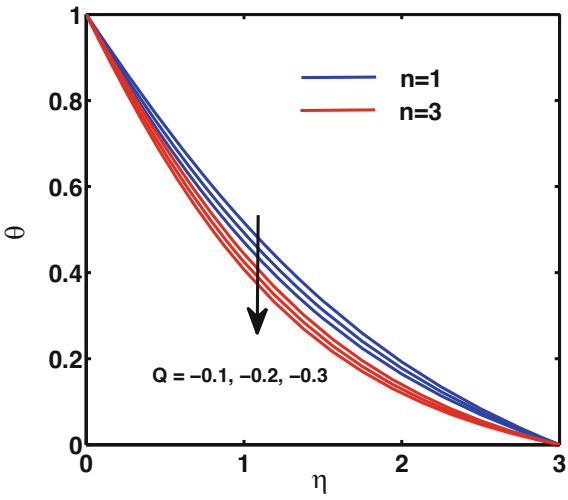

Fig. 11 Concentration for different Q

4 Conclusion

The imperative points of conclusion are as follows:

1. Expanded power of the cold fluid at the periphery of the stretching sheet with an expansion in λ diminishes the fluid temperature.
2. Additionally it is indeed fascinating to say that expansion in power-law index diminishes the velocity, temperature, and concentration boundary layers.

3. An expansion of the heat source improves the temperature. Due to this reason, the heat source can add more heat to the stretching sheet which expands its temperature along with the temperature of fluid upgrades. Moreover, the temperature boundary layer begins to increment by expanding the nature of the heat source.

References

1. Sheikholeslami, M. Hatami, M. Ganji, D.: Nanofluid flow and heat transfer in a rotating system in the presence of a magnetic field. J. Mol. liq. **190**, 112–120 (2014)
2. Akbar, N. S. Tripathi, D. Khan, Z. H. Bég, O. A.: A numerical study of magnetohydrodynamic transport of nanofluids over a vertical stretching sheet with exponential temperature-dependent viscosity and buoyancy effects. Chem. Phys. Letts. **661**, 20–30 (2016)
3. Nadeem, S. Haq, R. U. Khan, Z. H. : Heat transfer analysis of water-based nanofluid over an exponentially stretching sheet. Alexandria Eng. J. **53**, 219–224 (2014)
4. Hayat, T. Shafique, M. Tanveer, A. Alsaedi, A.: Magnetohydrodynamic effects on peristaltic flow of hyperbolic tangent nanofluid with slip conditions and Joule heating in an inclined channel. Int. J. Heat Mass Trans. **102**, 54–63 (2016)
5. Makinde, O. Animasaun, I.: Bioconvection in MHD nanofluid flow with nonlinear thermal radiation and quartic autocatalysis chemical reaction past an upper surface of a paraboloid of revolution. Int. J. Therm. Sci. **109**, 159–171 (2016)
6. Akbar, N. S. Huda, A. B. Tripathi, D.: Thermally developing MHD peristaltic transport of nanofluids with velocity and thermal slip effects. European Phys. J. Plus. **131**, 332 (2016)
7. Sheikholeslami, M. Bhatti, M.: Forced convection of nanofluid in presence of constant magnetic field considering shape effects of nanoparticles. Int. J. Heat Mass Trans. **111**, 1039–1049 (2017)
8. Akbar, N. S. Tripathi, D. Beg, O. A.: MHD convective heat transfer of nanofluids through a flexible tube with buoyancy: a study of nano-particle shape effects. Advanced Powder Tech. **28**, 453–462 (2017)
9. Bhatti, M. Zeeshan, A. Ellahi, R.: Simultaneous effects of coagulation and variable magnetic field on peristaltically induced motion of Jeffrey nanofluid containing gyrotactic microorganism, Microvascular Research. **110**, 32–42 (2017)

Radiated Slip Flow of Williamson Unsteady MHD Fluid over a Chemically Reacting Sheet with Variable Conductivity and Heat Source or Sink

Narsu Siva Kumar and B. Rushi Kumar

Abstract This study addresses the effects of unsteady MHD radiative slip flow of Williamson fluid due to the chemically reacting sheet with variable conductivity and heat source or sink. The boundary layer equations of the Williamson fluid model for heat and mass transfer are deliberated. The governing partial differential equations are transformed into a set of coupled ordinary differential equations of motion for Williamson fluid are modeled under the sheet and then solved numerically by the shooting technique with BVP4C package. The physical features of the model are presented and discussed in graphs and tables.

1 Introduction

In non-Newtonian fluids, the most generally encountered fluids are pseudoplastic fluids with lessening viscosity when considered shear strain. The concept of pseudoplastic fluids has a wide range of applications in engineering and industry in the extrusion of polymer sheets. Especially, recent paints are pseudoplastic materials.

The Navier-Stokes equations are inadequate to illustrate the physical properties of pseudoplastic fluids. The behavior of pseudoplastic fluids was insinuated to fill this gap such as Ellis model, Carreau model, and power law, but little attention has been paid to the Williamson fluid model. In 1929, Williamson [1] first introduced a model to study the pseudoplastic fluid flow. This model verifies both the minimal maximal viscosity (μ_∞ and μ_0) of the fluid wanted for pseudoplastic fluids. Later on, different channels were investigated due to Williamson fluid [2]. Lyubimov and

N. S. Kumar
Fluid Dynamics Division, School of Advanced Sciences, VIT University, Vellore, India
e-mail: narsusivakumar.c@ktr.srmuniv.ac.in

B. Rushi Kumar (✉)
Department of Mathematics, School of Advanced Sciences, Vellore Institute of Technology, Vellore, Tamil Nadu, India
e-mail: rushikumar@vit.ac.in

B. Rushi Kumar et al. (eds.), *Applied Mathematics and Scientific Computing*, Trends in Mathematics, https://doi.org/10.1007/978-3-030-01123-9_23

Perminov [4] investigated a thin layer of a Williamson fluid flow over an inclined surface due to the gravitational field. Khan et al. [3] investigated the Homotopy analysis of boundary layer flow of Williamson fluid by scaling transformation.

The fluid flow over a stretching surface has evolved the attention of several researchers in the presence of good applications in engineering processes, for example, manufacture of foods, polymer extrusion, crystal growing, and drawing of plastic films. The flow caused by a linear velocity due to the stretched surface has been broadly studied. To the best of our knowledge, the flow of heat transfer peculiarity over a nonlinear stretching sheet has been studied [5–8]. Babu et al. [9] demonstrated MHD non-Newtonian fluid flow over a slender sheet due to cross-diffusion effects. It is also observed that the Soret and Dufour effects on the Williamson fluid flow across variable thickness stretching sheet by viewing slip parameters. MHD boundary layer flow of Williamson fluid due to ohmic dissipation and thermal radiation was demonstrated by Hayat et al. [10]. In this paper momentum and thermal boundary layer thickness lessen with an increasing suction parameter. Hakeem et al. [11] have discussed the effect of partial slip on MHD boundary layer flow over stretching surface with temperature-dependent heat generation, thermal radiation, and wall mass transformation through a porous medium. Later on, three-dimensional MHD Williamson fluid flows over a nonlinear stretching surface were investigated by Malik et al. [12]. Zehra et al. [13] examined the flow of Williamson fluid in an inclined channel with pressure-dependent viscosity. A detailed observation of the literature displays that, to the best of author's cognition, nobody has discussed the radiated slip flow of Williamson unsteady MHD fluid over a chemically reacting sheet with variable conductivity and heat source/sink.

The governing partial differential equations are first transformed into ordinary ones, before being solved shooting approximation. We have extended the work of Vajravelu et al. [14] to study the effect of unsteady convective boundary layer flow of viscous fluid properties. It is worth mentioning that the velocity and temperature boundary layer thickness decrease with an increase in the unsteady parameter.

2 Mathematical Formulation

Consider an unsteady laminar two-dimensional boundary layer flow of incompressible electrically conducting Williamson fluid through a semi-infinite porous plate coinciding with plane $y = 0$. The effects of different physical parameters namely, thermophoresis parameter, Brownian motion parameter, magnetic field parameter, chemical reaction parameter, Williamson slip parameter, slip parameter and heat source parameter have been taken into account. The Cartesian coordinate system has chosen its origin located at the leading edge of the sheet with the positive $x-$axis extending along the sheet and is positive in the direction of the sheet to the fluid. We assume that for time $t < 0$, the fluid and heat flows are steady. The unsteady fluid and heat flow starts start at $t = 0$, and the sheet is being stretched with the velocity $U_w(x, t)$ along the $x-$axis keeping the origin fixed. The temperature of the

sheet $T_w(x,t)$ and the concentration of the sheet $C_w(x,t)$ are assumed to be a linear function of x. Under the aforesaid assumptions, the governing equations boundary layer equations can be expressed as

$$\frac{\partial u}{\partial x}+\frac{\partial u}{\partial y}=0. \tag{1}$$

$$\frac{\partial u}{\partial t}+u\frac{\partial u}{\partial x}+v\frac{\partial u}{\partial y} = \vartheta\frac{\partial^2 u}{\partial y^2}+\sqrt{2}\,\vartheta\,\Gamma\frac{\partial u}{\partial y}\frac{\partial^2 u}{\partial y^2}$$

$$\pm g\beta_T(T-T_\infty)\pm g\beta_C(C-C_\infty)-\frac{\sigma B_0^2}{\rho}u-\frac{\vartheta}{K_0}u \tag{2}$$

$$\rho C_p\left(\frac{\partial T}{\partial t}+u\frac{\partial T}{\partial x}+v\frac{\partial T}{\partial y}\right)$$

$$=\frac{\partial}{\partial y}\left(K(T)\frac{\partial T}{\partial y}\right)-Q(T-T_\infty)+\tau$$

$$\left[D_B\frac{\partial C}{\partial y}\frac{\partial T}{\partial y}+\frac{D_T}{T_\infty}\left(\frac{\partial T}{\partial y}\right)^2\right]-\frac{\partial q_r}{\partial y} \tag{3}$$

$$\frac{\partial C}{\partial t}+u\frac{\partial C}{\partial x}+v\frac{\partial C}{\partial y} = D_B\frac{\partial^2 C}{\partial y^2}-K_0(C-C_\infty)+\frac{D_T}{T_\infty}\frac{\partial^2 T}{\partial y^2} \tag{4}$$

Subject to the boundary conditions

$$\begin{gathered} u=U_w+l\frac{du}{dy},\ v=v_w(t),\ T=T_w\ at\ y=0 \\ u\to 0,\ T\to T_\infty,\ C\to C_\infty\ as\ y\to\infty \end{gathered} \tag{5}$$

where u and v are the velocity components in the x and y directions, respectively, g is the acceleration due to gravity, ϑ is the kinematic viscosity, β is the coefficient of thermal expansion, T is the fluid temperature, T_∞ is the ambient temperature, ρ is the density, C_p is the specific heat at constant pressure, $K(T)$ is the variable thermal conductivity, $v_w(t)=\frac{v_0}{\sqrt{1-ct}}$ is the suction/injection velocity, and q_r is the radiative heat flux. The third term in Eq. (2) is due to the buoyancy force. The "+" and "−" signs refer to the buoyancy assisting and buoyancy opposing flow conditions, respectively. Here we assumed that the thermal conductivity varies linearly with temperature [14] as

$$K(T)=K_\infty\left(1+\frac{\varepsilon}{\Delta T}(T-T_\infty)\right).$$

Here, $\Delta T = (T_w - T_\infty), T_w$, where ε is a small parameter called thermal conductivity parameter, T_w is the surface or wall temperature, and K_∞ is the thermal conductivity of the fluid far away from the sheet. The radiative heat flux can be expressed [15] as

$$q_r = -\frac{4\sigma^*}{3k^*}\frac{\partial T^4}{\partial y}.$$

Here, σ^* and k^* are Stephan-Boltzmann constant and mean absorption coefficient. We assume that $(T - T_\infty)$, i.e., the temperature difference within the flow is such that the term T^4 can be expressed as a linear function of temperature. So now, expanding T^4 by a Taylor series about T_∞ and ignoring higher order terms, we get

$$T^4 \approx 4T_\infty^3 T - T_\infty^4.$$

Following Ishak et al. [16], the stretching velocity is assumed as $U_w(x,t) = {ax}/{1 - ct}$, where a and c are constants (with $a \geq 0$ and $c \geq 0$ where $ct < 1$). We have a as the initial stretching rate $\frac{a}{1-ct}$ and it is increasing with time. We assume $T_w(x,t)$ and $C_w(x,t)$ are surface temperature and concentration of the stretching sheet to vary with distance x and inverse square law for its decrease with time in the following form: $T_w(x,t) = T_\infty + \frac{bx}{(1-ct)^2}$, $C_w(x,t) = C_\infty + \phi\frac{bx}{(1-ct)^2}$ Here b is a constant and has dimension temperature or length, with $b > 0$ (assisting flow), $b < 0$ (opposing flow), and $b = 0$ for the forced convection limit (absence of buoyancy force). These particular forms of $U_w(x,t)$, $T_w(x,t)$, and $C_w(x,t)$ have been preferred in order to obtain a new similarity transformation, which transforms the governing equations (PDEs) (1)–(4) into a set of coupled ordinary differentiable equations (ODEs), thereby facilitating the exploration of the effects of the controlling parameters.

Following dimensionless functions f, θ, and ϕ with the similarity variable ς (see Vajravelu et al. [14]):

$$\varsigma = \left(\frac{a}{\vartheta(1-ct)}\right)^{\frac{1}{2}} y,\ \psi = \left(\frac{\vartheta a}{(1-ct)}\right)^{\frac{1}{2}} x f(\varsigma),\ \theta(\varsigma) = \frac{(T - T_\infty)}{(T_w - T_\infty)},$$

$$\phi(\varsigma) = \frac{(C - C_\infty)}{(C_w - C_\infty)},\ \mathrm{A} = \frac{c}{a},\ \Lambda = \Gamma x\left(\frac{a^3}{\sqrt{1-ct}}\right)^{\frac{1}{2}},$$

$$Pr = \frac{\rho C_p}{K_\infty},\ f_w = -\frac{v_0}{\sqrt{\upsilon a}},$$

$$Nr = \frac{16T_\infty^3\sigma^*}{3k^*K_\infty},\ M = \frac{\sigma B_0^2}{\rho U_\infty},\ N_b = \frac{\tau D_B(C_w - C_\infty)}{\vartheta},$$

$$N_t = \frac{\tau D_T (T_w - T_\infty)}{T_\infty}\vartheta,$$

$$\lambda_T = \frac{g\beta_T b}{a^2},\ \lambda_C = \frac{g\beta b}{a^2} \tag{6}$$

where $\psi(x, y, t)$ a stream function is defined as $(u, v) = \left(\frac{\partial\psi}{\partial y}, -\frac{\partial\psi}{\partial x}\right)$ which identically satisfies the continuity equation (1). Substituting Eq. (6) in Eqs. (2)–(4), we obtain

$$f''' + ff'' - f'^2 - A\left(f' + \frac{1}{2}\varsigma f''\right) + \Lambda f'' f''' \pm \lambda_T\theta \pm \lambda_C\phi - (M + K)\, f' = 0 \tag{7}$$

$$\frac{1}{\mathrm{Pr}}\left(\theta'' + \varepsilon\theta'^2 + \varepsilon\theta\theta''\right) - Q_H\theta + \frac{Nr}{\mathrm{Pr}}\theta'' + f\theta' - \theta f' - \frac{A}{2}\varsigma\theta' - 2A\theta$$
$$+N_b\theta\phi' + N_t\theta'^2 = 0 \tag{8}$$

$$\frac{1}{Sc}\phi'' + \left(f\phi' - \phi f\right) - \frac{A}{2}\varsigma\phi' - 2A\phi - KrA\phi = 0 \tag{9}$$

Corresponding the following boundary conditions are

$$\begin{aligned} f'(0) = 1 + Lf''(0),\ f(0) = f_w,\ \theta(0) = 1,\ \phi(0) = 1\ at \\ f'(\infty) \to 0,\ \theta(\infty) \to 0\ \phi(\infty) \to 0 \end{aligned} \tag{10}$$

where primes denote differentiation with respect to ς. The physical quantities of interest are the local heat flux and local mass flux, which is defined as

$$C_f = \frac{\tau_w}{\rho U_w^2/2},\ Nu_x = \frac{xq_w}{K_\infty (T_w - T_\infty)},$$

where the skin friction τ_w and the heat transfer q_w from the sheet are given by

$$\tau_w = \mu\left(\frac{\partial u}{\partial y}\right)_{y=0}, q_w = -K_\infty\left(\frac{\partial T}{\partial y}\right)_{y=0}$$

3 Results and Discussion

The present investigation is extended out by determining the impact of pertinent parameters on fluid velocity, temperature, and concentration distribution presented in Figs. 1, 2, 3, 4, 5, 6, 7, and 8. The numerical values of some important physical

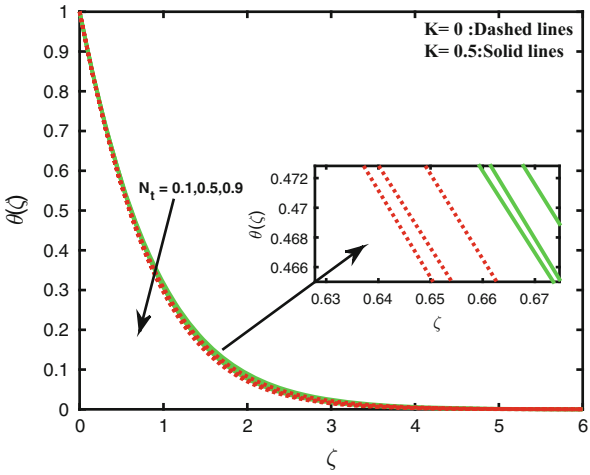

Fig. 1 Impact of N_t on $\theta(\varsigma)$

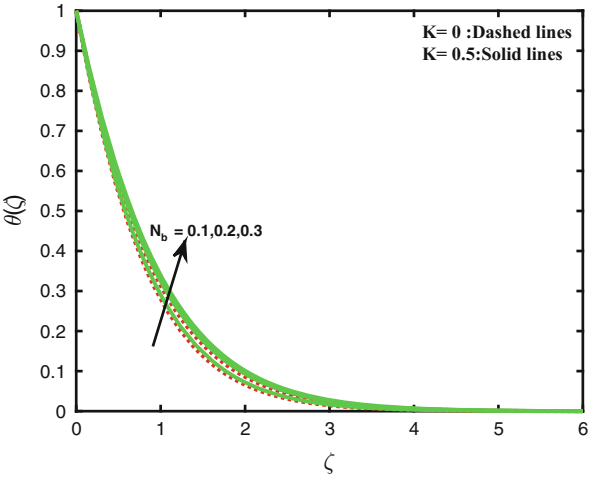

Fig. 2 Impact of N_b on $\theta(\varsigma)$

quantities are presented in Tables 1 and 2. For simplicity, the constants assumed for several parameters are K $= 0.5$, $Q_H = 0.5$, Pr $= 0.7$, $N_t = 1$, $N_b = 1$, $\Lambda = 0.2$, $A = 0.2$, $\varepsilon = 0.1$, M $= 2$, Kr $= 0.1$, Nr $= 0.2$, $\varsigma = 0.5$, L $= 0.3$. The effects of the thermophoresis parameter N_t on temperature profiles is presented in Fig. 1. It is noted that the rising of N_t enhances the thickness of thermal boundary layer. Figure 2 displays the effect of N_b (the Brownian motion parameter) on the temperature for both the cases of the absence and presence of porosity. The temperature increases for increasing values of Brownian motion parameter. The dimensionless temperature distribution for various values of the thermal radiation parameter Nr is shown in Fig. 3 for both the absence and presence of porosity. It reveals that the greater values of Nr enhance the thermal boundary layer thickness.

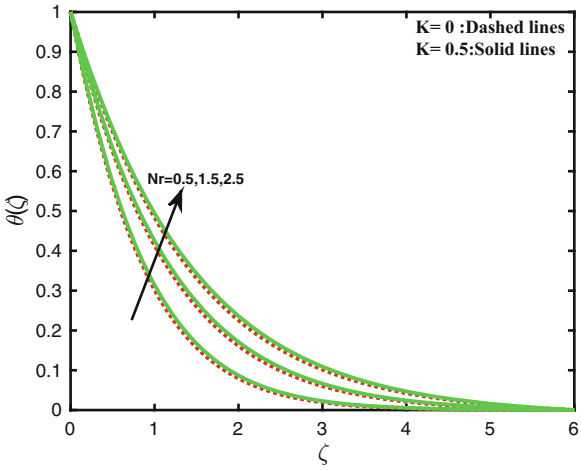

Fig. 3 Impact of Nr on $\theta(\varsigma)$

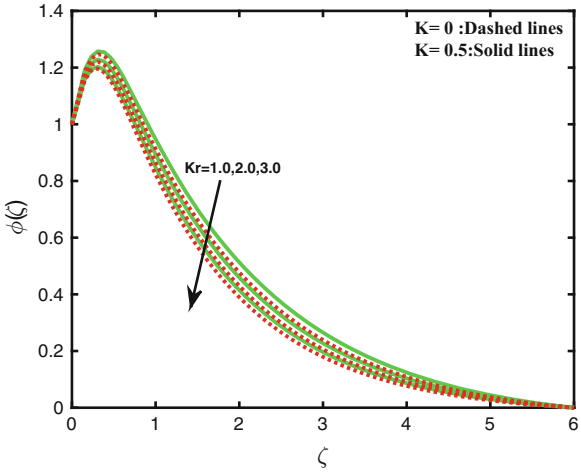

Fig. 4 Impact of Kr on $\phi(\varsigma)$

It is also observed that the presence of porosity is very high compared with the absence of porosity.

The effects of the chemical reaction parameter Kr on concentration fields are displayed in Fig. 4. The depreciation in the concentration field has been noted for both presence and absence of porosity. The influence of magnetic parameter M on velocity profiles is exhibited in Fig. 5 for both porosity parameters on the presence and absence, respectively. We observed the velocity depreciates for increasing values of the magnetic parameter. Figures 6 and 7 present the effects of the Williamson parameter Λ and the slip parameter L on velocity field for both the presence and absence of porosity parameter. The velocity field is improved with higher values of Λ and L. Due to this reason, we have a seen a hike in velocity field. Figure 8 demonstrates the effect of Q_H on temperature distribution of the flow. It is

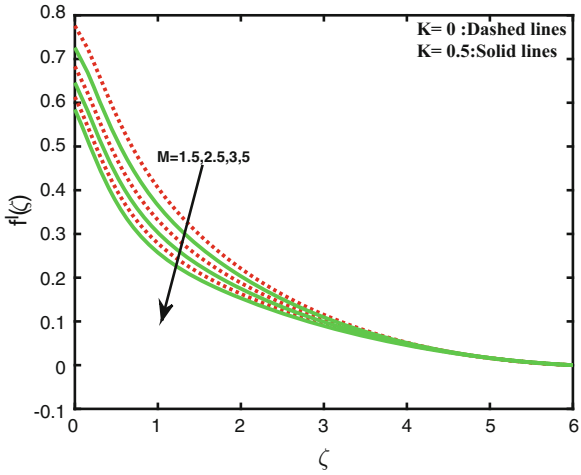

Fig. 5 Impact of M on $f'(\varsigma)$

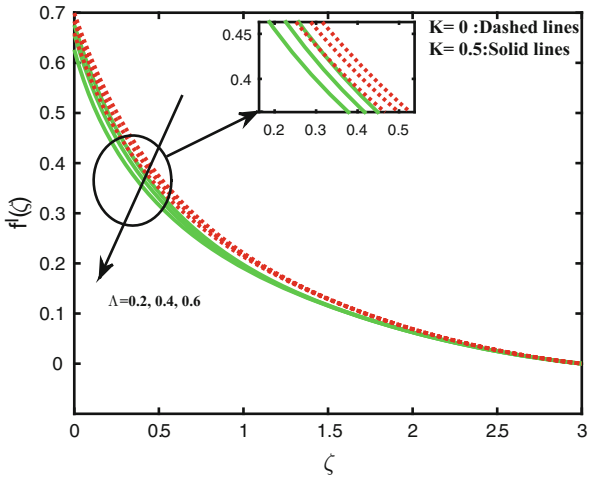

Fig. 6 Impact of Λ on $f'(\varsigma)$

seen that increasing values of the heat source parameter Q_H suppressed the thermal boundary layer thickness of the flow.

Tables 1 and 2 depict the effect of nondimensional parameters on friction factor coefficient, local Nusselt, and Sherwood numbers for both the cases (absence and presence of porosity). It is apparent from Table 1 (absence of porosity) that rising values of N_b, Nr, L intensifies and N_b, Kr, M, Q_H, Λ lessens the friction factor coefficient. Higher values of N_t, Nr, Kr, M, L, Λ lessen and N_t, Q_H improve the heat transfer rate. The rate of mass transfer has been decreased by increasing the values of N_t, Nr, M, Q_H, whereas it has been increased by increasing the values of N_b, Nr, Kr, L, Λ. The same strategy has been observed quantitatively in the presence of porosity, which is portrayed in Table 2.

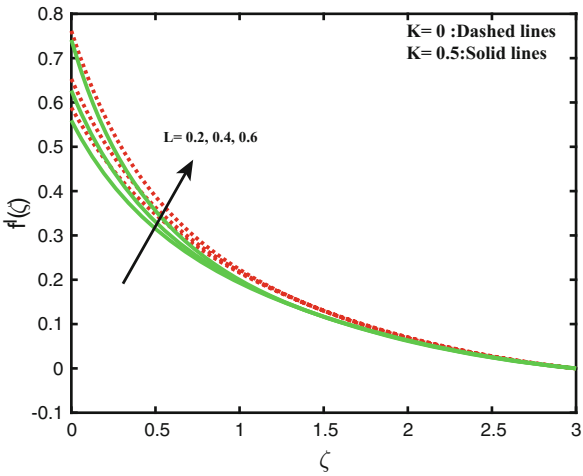

Fig. 7 Velocity profile for various L

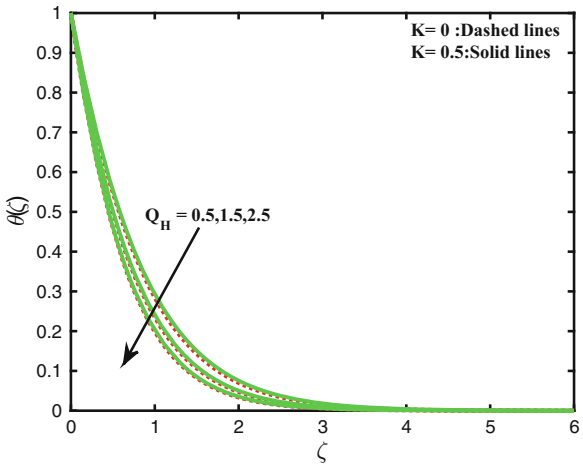

Fig. 8 Temperature profile for Q_H

4 Conclusions

The investigated problem explores the influences of various parameters on velocity, temperature, and concentration. The present analysis also elaborates the radiated slip flow of Williamson unsteady MHD fluid over a chemically reacting sheet with variable conductivity and heat source/sink. Some of the interesting conclusions are as follows:

Table 1 Values of skin friction, Nusselt and Sherwood number for various values N_t, N_b, Nr, Kr, M, Q_H, L, Λ when $K = 0$

N_t	N_b	Nr	Kr	M	Q_H	L	Λ	$f''(0)$	$-\theta'(0)$	$-\phi'(0)$
0.1								0.222699	0.245502	0.266937
0.5								0.454265	0.457273	0.249630
0.9								0.728861	0.474866	0.226946
	0.1							0.250135	0.464364	0.402339
	0.2							0.233904	0.458243	0.599029
	0.3							0.228544	0.455087	0.664762
		0.5						0.080354	2.605393	0.087209
		1.5						0.122236	1.221540	0.286496
		2.5						0.148632	0.893089	0.398128
			1.0					−0.173419	55.851104	−1.709512
			2.0					−0.182086	54.899934	−1.573263
			3.0					−0.189631	54.061307	−1.451098
				1.5				−0.223987	56.269999	−1.863575
				2.5				−0.316713	55.576415	−1.919693
				3.5				−0.386487	55.059958	−1.965386
					0.5			0.072783	2.753548	0.041842
					1.5			0.052473	3.192599	−0.090618
					2.5			0.037057	3.572928	−0.203450
						0.2		−1.192513	4.391221	−0.158618
						0.4		−0.867385	4.313113	−0.155426
						0.6		−0.685916	4.265128	−0.153488
							0.2	−1.002530	4.346763	−0.156795
							0.4	−1.056346	4.324802	−0.156747
							0.6	−1.135629	4.297181	−0.156295

- It is observed that an increase in Nr produces significant intensities in the thickness of the temperature boundary layer of the fluid.
- The momentum boundary layer diminishes with higher values of the magnetic parameter.
- Increasing values of Q_H suppressed the thermal boundary layer thickness of the flow.
- The temperature increases for increasing values of N_b and in the reverse phenomena of concentration respectively.

Table 2 Values of skin friction, Nusselt and Sherwood number for variou svalues N_t, N_b, Nr, Kr, M, Q_H, L, Λ when $K = 0.5$

N_t	N_b	Nr	Kr	M	Q_H	L	Λ	$f''(0)$	$-\theta'(0)$	$-\phi'(0)$
0.1								0.125439	0.440820	0.688181
0.5								0.146232	0.443727	0.437762
0.9								0.165843	0.446018	0.193734
	0.1							0.150523	0.450579	0.366330
	0.2							0.135659	0.444655	0.560123
	0.3							0.130761	0.441613	0.624939
		0.5						0.001676	2.541169	0.056138
		1.5						0.039081	1.188685	0.253994
		2.5						0.062225	0.868082	0.364298
			1.0					−0.104892	56.437691	−1.682630
			2.0					−0.114365	55.541383	−1.554807
			3.0					−0.122703	54.743334	−1.439173
				1.5				−0.273841	55.895873	−1.893058
				2.5				−0.353918	55.300798	−1.943722
				3.5				−0.415237	54.848704	−1.985003
					0.5			−0.005635	2.694255	0.008741
					1.5			−0.025128	3.144790	−0.128497
					2.5			−0.039849	3.532450	−0.244439
						0.2		−1.294271	4.344928	−0.162493
						0.4		−0.932662	4.263959	−0.158966
						0.6		0.733977	4.214626	−0.156833
							0.2	−1.082027	4.298730	−0.160472
							0.4	−1.146237	4.273752	−0.160180
							0.6	−1.245774	4.241481	−0.159360

References

1. Williamson, R.V.: The flow of pseudo plastic materials. nd. Eng. Chem. **21**, 1108–1111 (1929)
2. Nadeem, S.,Hussain,S.T.,Lee,C.: Flow of a Williamson fluid over a stretching sheet. Braz. J. Chem. Eng. **30**, 619–625 (2013)
3. Khan, N.A., Aziz,S., Khan,N.A.: MHD flow of Powell Eyring fluid over a rotating disk. J Taiwan Inst Chem Eng. **45**, 2859–2867 (2014)
4. Lyubimov D.V., Perminov,A.V.: Motion of a thin oblique layer of a pseudo plastic fluid. Journal of Engineering Physics and Thermophysics **4**, 920–924 (2002)
5. Rana,P., Bhargava,R.: Flow and heat transfer of a nanofluid over a nonlinearly stretching sheet: A numerical study. Commun Nonlinear Sci Numer Simulat. **17**, 212–226 (2012)
6. Mukhopadhyay,S.: Casson fluid flow and heat transfer over a nonlinearly stretching surface. Chin. Phys. B. **22**, 074701 (2013)
7. Alinejad,J.,Samarbakhsh,S.: Viscous Flow over Nonlinearly Stretching Sheet with Effects of Viscous Dissipation. Journal of Applied Mathematics, 587834, 1–10 (2012)

8. Zaimi,K., Ishak,A., Pop,I.: Boundary layer flow and heat transfer over a nonlinearly permeable stretching/ shrinking sheet in a nanofluid,Scientific Reports (2014) https://doi.org/10.1038/srep04404.
9. Jayachandra Babu, M., Sandeep, N.: MHD non-Newtonian fluid flow over a slendering stretching sheet in the presence of cross-diffusion effects. Alexandria Engineering Journal **55**, 2193–2201 (2016)
10. Hayat, T., Shafiq ,A., Alsaedi, A.: Hydromagnetic boundary layer flow of Williamson fluid in the presence of thermal radiation and Ohmic dissipation. Alexandria Engineering Journal **55**, 2229–2240.
11. Abdul Hakeem, A.K.., Kalaivanan,R., Vishnu Ganesh, N., Ganga,B.: Effect of partial slip on hydromagnetic flow over a porous stretching sheet with non-uniform heat source/sink, thermal radiation and wall mass transfer. Ain Shams Engineering Journal **5**, 913–922 (2014)
12. Malik,M. Y.,Bilal,S.,Salahuddin,T.,Ur Rehman, K.: Three-Dimensional Williamson Fluid Flow over a Linear Stretching Surface. Math. Sci. Lett. **6**, 53–61 (2017)
13. Zehra,I.,Yousaf, M. M.,Nadeem, S.: Numerical solutions of Williamson fluid with pressure dependent Viscosity. Results in Physics **5**, 20–25 (2015)
14. Vajravelu, K.,Prasad, K.V.,Chiu-On Ng.: Unsteady convective boundary layer flow of a viscous fluid at a vertical surface with variable fluid properties. Nonlinear Anal Real World Appl **14**, 455–464 (2013)
15. Brewster,M.Q.: Thermal Radiative Transfer Properties, John Wiley and Sons (1972)
16. Ishak,A.,Nazar, R. I. Pop.: Boundary layer flow and heat transfer over an unsteady stretching vertical surface. Meccanica **44**, 369–375 (2009)

Approximate Analytical Solution of a HIV/AIDS Dynamic Model During Primary Infection

Ajoy Dutta and Praveen Kumar Gupta

Abstract HIV/AIDS is a very challenging epidemic disease all over the world. In the present chapter, the homotopy analysis method (HAM) is functional for evaluating the estimated solution of the HIV dynamic model during primary infection. By using the HAM, we have adjusted and controlled the area of convergence of the infinite series solution with the help of auxiliary parameters. Numerical results for different cases obtained graphically show that series solutions are convergent and the residual errors curve shows that the HAM is very effective at gaining an accurate approximation.

1 Introduction

The infectious disease AIDS is not yet fully curable and is the cause of HIV. Various nonlinear models have been developed to explain HIV [6, 8–10]. A model with different classes was devised.

Here, the HAM is established for the model Srivastava et al. [14], where they consider three classes: $A(\eta)$, $B(\eta)$ *and* $C(\eta)$ are uninfected, infected CD4+ T cells and the virus respectively. According to Rong et al. [12] and Essunger and Perelson [1], some portion of $B(\eta)$ due to natural recovery of CD4+ T cells back to the uninfected class. The model is [14].

$$\left.\begin{aligned} \frac{dA}{dt} &= r - \alpha_1 AC - \beta_1 A + \alpha_2 B \\ \frac{dB}{dt} &= \alpha_1 AC - \alpha_2 B - \beta_2 B \\ \frac{dC}{dt} &= V\beta_3 B - \beta_4 C \end{aligned}\right\} \tag{1}$$

with

$$A(0) = A_0 > 0,\ B(0) = B_0 > 0,\ C(0) = C_0 > 0 \tag{2}$$

A. Dutta (✉) · P. K. Gupta
National Institute of Technology Silchar, Silchar, Assam, India
e-mail: ajoy@.rs.math.student.nits.ac.in; praveen@math.nits.ac.in

B. Rushi Kumar et al. (eds.), *Applied Mathematics and Scientific Computing*,
Trends in Mathematics, https://doi.org/10.1007/978-3-030-01123-9_24

Here, η represents the time, r is the inflow rate of $A(\eta)$, α_1 is the rate of infection of CD4+ T-cells becoming active, α_2 is the rate of infected cells transforming back to uninfected cells, β_1 is the removal rate of $A(\eta)$, $\beta_2(\geq \beta_2)$ is the removal rate of $B(\eta)$, β_3 is the lytic death rate for $Y(\eta)$, β_4 is the removal rate of $C(\eta)$, and V is the average number of viruses produced by $B(\eta)$.

In [14], the authors have discussed the stability and existence of the model (1). The literature shows that the HAM [2–5, 11, 13] is applied to various nonlinear problems to find approximate solution.

2 The HAM Solution of the HIV Model

First, we define the homotopy map:

$$H_A(\widehat{A}(\eta,\tau),\widehat{B}(\eta,\tau),\widehat{C}(\eta,\tau)) = (1-\tau)L_A[\widehat{A}(\eta,\tau)-A_0(\eta)] - \tau\hbar h_A(\eta)N_A[\widehat{A}(\eta,\tau),\widehat{B}(\eta,\tau),\widehat{C}(\eta,\tau)] \quad (3)$$

$$H_B(\widehat{A}(\eta,\tau),\widehat{B}(\eta,\tau),\widehat{C}(\eta,\tau)) = (1-\tau)L_B[\widehat{B}(\eta,\tau)-B_0(\eta)] - \tau\hbar h_B(\eta)N_B[\widehat{A}(\eta,\tau),\widehat{B}(\eta,\tau),\widehat{C}(\eta,\tau)] \quad (4)$$

$$H_C(\widehat{A}(\eta,\tau),\widehat{B}(\eta,\tau),\widehat{C}(\eta,\tau)) = (1-\tau)L_C[\widehat{Z}(\eta,\tau)-Z_0(\eta)] - \tau\hbar h_Z(\eta)N_C[\widehat{A}(\eta,\tau),\widehat{B}(\eta,\tau),\widehat{C}(\eta,\tau)] \quad (5)$$

where $\tau \in [0,1]$, $\hbar$ are embedding, auxiliary parameters and h_A, h_B and h_C are auxiliary functions. The nonlinear operators are defined as:

$$N_A(\widehat{A}(\eta,\tau),\widehat{B}(\eta,\tau),\widehat{C}(\eta,\tau)) = \frac{\partial\widehat{A}(\eta,\tau)}{\partial\eta} - r + \alpha_1\widehat{A}(\eta,\tau)\widehat{C}(\eta,\tau) + \beta_1\widehat{A}(\eta,\tau) - \alpha_2\widehat{B}(\eta,\tau) \quad (6)$$

$$N_B(\widehat{A}(\eta,\tau),\widehat{B}(\eta,\tau),\widehat{C}(\eta,\tau)) = \frac{\partial\widehat{B}(\eta,\tau)}{\partial\eta} - \alpha_1\widehat{A}(\eta,\tau)\widehat{C}(\eta,\tau) + \alpha_2\widehat{B}(\eta,\tau) + \beta_2\widehat{B}(\eta,\tau) \quad (7)$$

$$N_C(\widehat{A}(\eta,\tau),\widehat{B}(\eta,\tau),\widehat{C}(\eta,\tau)) = \frac{\partial\widehat{C}(\eta,\tau)}{\partial\eta} - V\beta_3\widehat{B}(\eta,\tau) + \beta_4\widehat{C}(\eta,\tau). \quad (8)$$

We take $\tau = 0$ and $\tau = 1$ in the homotopy map (3)–(5) and:

$$H_A(\widehat{A}(\eta,\tau),\widehat{B}(\eta,\tau),\widehat{C}(\eta,\tau)) = H_B(\widehat{A}(\eta,\tau),\widehat{B}(\eta,\tau),\widehat{C}(\eta,\tau)) = H_C(\widehat{A}(\eta,\tau),\widehat{B}(\eta,\tau),\widehat{C}(\eta,\tau)) = 0. \quad (9)$$

We can find:

$$(1-\tau)L_A[\widehat{A}(\eta,\tau) - A_0(\eta)] = \tau\hbar h_A(\eta)N_A[\widehat{A}(\eta,e),\widehat{B}(\eta,\tau),\widehat{C}(\eta,\tau)], \quad (10)$$

$$(1-\tau)L_B[\widehat{B}(\eta,\tau) - B_0(\eta)] = \tau\hbar h_B(\eta)N_B[\widehat{A}(\eta,\tau),\widehat{B}(\eta,\tau),\widehat{C}(\eta,\tau)], \quad (11)$$

$$(1-\tau)L_C[\widehat{C}(\eta,\tau) - Z_0(\eta)] = \tau\hbar h_C(\eta)N_C[\widehat{A}(\eta,\tau),\widehat{B}(\eta,\tau),\widehat{C}(\eta,\tau)]. \quad (12)$$

Applying the Taylor series with respect to τ yields:

$$\widehat{A}(\eta,\tau) = A_0(\eta) + \sum_{m=1}^{\infty} A_m(\eta)\tau^m, \widehat{B}(\eta,\tau) = B_0(\eta) + \sum_{m=1}^{\infty} B_m(\eta)\tau^m, \widehat{C}(\eta,\tau) = Z_0(\eta) + \sum_{m=1}^{\infty} Z_m(\eta)\tau^m, \quad (13)$$

where

$$A_m = \frac{1}{m!}\left[\frac{\partial^m \widehat{A}(\eta,\tau)}{\partial\tau^m}\right], B_m = \frac{1}{m!}\left[\frac{\partial^m \widehat{B}(\eta,\tau)}{\partial\tau^m}\right], C_m = \frac{1}{m!}\left[\frac{\partial^m \widehat{C}(\eta,\tau)}{\partial\tau^m}\right]. \quad (14)$$

After simplifying (10)–(12) we get:

$$L_A[A_m(\eta) - \chi_m A_{m-1}(\eta)] = \hbar h_A(\eta)R_{m,A}(\overrightarrow{A}_{m-1}, \overrightarrow{B}_{m-1}, \overrightarrow{C}_{m-1}) \quad (15)$$

$$L_B[B_m(\eta) - \chi_m B_{m-1}(\eta)] = \hbar h_B(\eta)R_{m,B}(\overrightarrow{A}_{m-1}, \overrightarrow{B}_{m-1}, \overrightarrow{C}_{m-1}) \quad (16)$$

$$L_C[C_m(\eta) - \chi_m C_{m-1}(\eta)] = \hbar h_B(\eta)R_{m,C}(\overrightarrow{A}_{m-1}, \overrightarrow{B}_{m-1}, \overrightarrow{C}_{m-1}) \quad (17)$$

with initial condition:

$$A_m(0) = 0, B_m(0) = 0, C_m(0) = 0, \quad (18)$$

where

$$R_{m,A}(\eta) = \frac{dA_{m-1}(\eta)}{d\eta} - (1-\lambda_m)r + \alpha_1\sum_{i=0}^{m-1} A_i(\eta)C_{m-1-i}(\eta) + \beta_1\sum_{i=0}^{m-1} A_i(\eta)A_{m-1-i}(\eta) - \alpha_2\sum_{i=0}^{m-1} B_i(\eta)B_{m-1-i}(\eta),$$

$$R_{m,B}(\eta) = \frac{dB_{m-1}(\eta)}{d\eta} - \alpha_1 \sum_{i=0}^{m-1} A_i(\eta) C_{m-1-i}(\eta) + \beta_2 \sum_{i=0}^{m-1} B_i(\eta) B_{m-1-i}(\eta) + \alpha_2 \sum_{i=0}^{m-1} B_i(\eta) B_{m-1-i}(\eta),$$

$$R_{m,C}(\eta) = \frac{dC_{m-1}(\eta)}{d\eta} - V\beta_3 \sum_{i=0}^{m-1} B_i(\eta) B_{m-1-i}(\eta) + \beta_4 \sum_{i=0}^{m-1} C_i(\eta) C_{m-1-i}(\eta).$$

Using $h_A(\eta) = h_B(\eta) = h_C(\eta) = 1$, the solution of the m-order deformation Eqs. (15)–(17) for $m \geq 1$ becomes:

$$A_m(\eta) = \lambda_m A_{m-1}(\eta) + \hbar \int_0^\eta R_{m,A}(s)ds, \tag{19}$$

$$B_m(\eta) = \lambda_m B_{m-1}(\eta) + \hbar \int_0^\eta R_{m,B}(s)ds, \tag{20}$$

$$C_m(\eta) = \lambda_m C_{m-1}(\eta) + \hbar \int_0^\eta R_{m,C}(s)ds. \tag{21}$$

In-depth study of the convergence of the HAM can be found in [3, 7].

3 Numerical Results

To demonstrate the capacity of the HAM, the values of the variables and parameters of the model (1) are given in following Table: $A(0) = 1000$, $B(0) = 0$ and $C(0) = 0.001$.

With the help of Mathematica software, we have drawn the following figure.

Table 1 List of parameters and their values

Parameter	Value	Data source
r	$10\,\text{mm}^{-3}\,\text{day}^{-1}$	[14]
α_1	$0.000024\,\text{mm}^{-3}\,\text{day}^{-1}$	[14]
α_2	$0.2\,\text{day}^{-1}$	[14]
β_1	$0.01\,\text{day}^{-1}$	[14]
β_2	$0.5\,\text{day}^{-1}$	[14]
β_3	$0.16\,\text{day}^{-1}$	[14]
β_4	$3.4\,\text{day}^{-1}$	[14]
V	1000	[14]

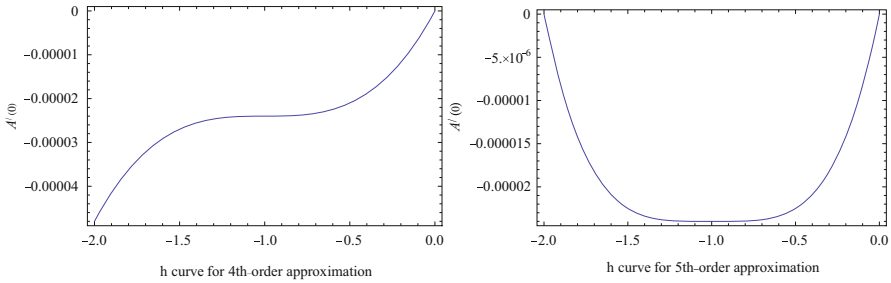

Fig. 1 The $\hbar$-curves of obtained by the (**a**) 4th-order and (**b**) 5th-order approximation of the HAM for $T'(0)$

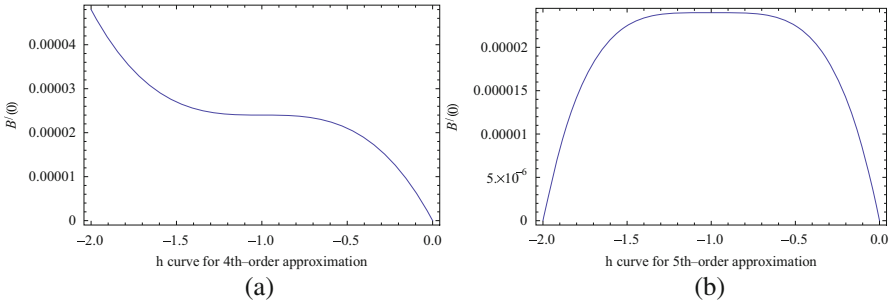

Fig. 2 The $\hbar$-curves of obtained by the (**a**) 4th-order and (**b**) 5th-order approximation of the HAM for $I'(0)$

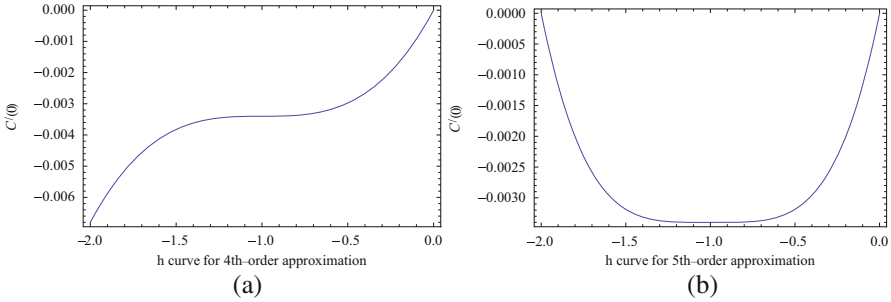

Fig. 3 The $\hbar$ curves obtained by the (**a**) 4th-order and (**b**) 5th-order approximation of the HAM for $V'(0)$

Figures 1a, b, 2a, b, and 3a, b are the $\hbar$ curves obtained by the 4th-order and 5th-order approximation of the HAM respectively.

From Figs. 1, 2, and 3 it was observed that the line segment of $\hbar$ curves is nearly parallel to the horizontal axis, and ensures that the series solutions obtained are convergent.

Table 2 The above values of $\hbar$ derive from Figs. 1, 2, and 3

$A(\eta)$	$-1.5 \leq \hbar \leq -0.5$
$B(\eta)$	$-1.5 \leq \hbar \leq -0.5$
$C(\eta)$	$-1.5 \leq \hbar \leq -0.5$

Table 3 The minimum values of $RA(\hbar_1^*)$, $RB(\hbar_1^*)$, $RC(\hbar_1^*)$

	$\hbar^*$	Minimum value
$RA(\hbar_1)$	-0.639467	8.06216×10^{-13}
$RB(\hbar_2)$	-0.643968	9.26825×10^{-13}
$RC(\hbar_3)$	-0.51468	1.0034×10^{-6}

Table 4 The residual errors for various values η

t	$ER_1(A, B, C; -0.639467)$	$ER_1(A, B, C; -0.643968)$	$ER_1(A, B, C; -0.51468)$
0	1.12472×10^{-6}	-1.08312×10^{-6}	0.000388654
0.1	-3.76069×10^{-7}	4.38038×10^{-7}	-0.000179256
0.2	-8.20159×10^{-7}	-4.60439×10^{-7}	-0.000580455
0.3	-5.70582×10^{-7}	8.97059×10^{-7}	-0.000848859
0.4	4.9731×10^{-8}	6.27566×10^{-7}	-0.00101581
0.5	7.5653×10^{-7}	-3.61895×10^{-8}	0.00111014
0.6	1.13028×10^{-6}	-7.99505×10^{-7}	0.00115823
0.7	1.47749×10^{-6}	-1.4058×10^{-6}	0.0011841
0.8	1.10376×10^{-6}	-1.30321×10^{-6}	-0.00120947
0.9	3.79016×10^{-6}	-2.590007×10^{-7}	-0.00125381
1	-1.83226×10^{-6}	1.61566×10^{-6}	0.00133441

For residual functions for the model (1) are

$$RA(\hbar_1) = \int_0^1 (ER_1(A, B, C, \hbar_1))^2 dt \tag{22}$$

$$RB(\hbar_2) = \int_0^1 (ER_2(A, B, C, \hbar_2))^2 dt \tag{23}$$

$$RC(\hbar_3) = \int_0^1 (ER_3(A, B, C, \hbar_3))^2 dt \tag{24}$$

The residual errors ER_1, ER_2, and ER_3 are shown in Fig. 4 for $\eta \in (0, 1)$ and for different $\hbar$. In Fig. 4, we can observe that the results acquired by applying the HAM provide an analytical solution with a high order of accuracy and with only a few iterations.

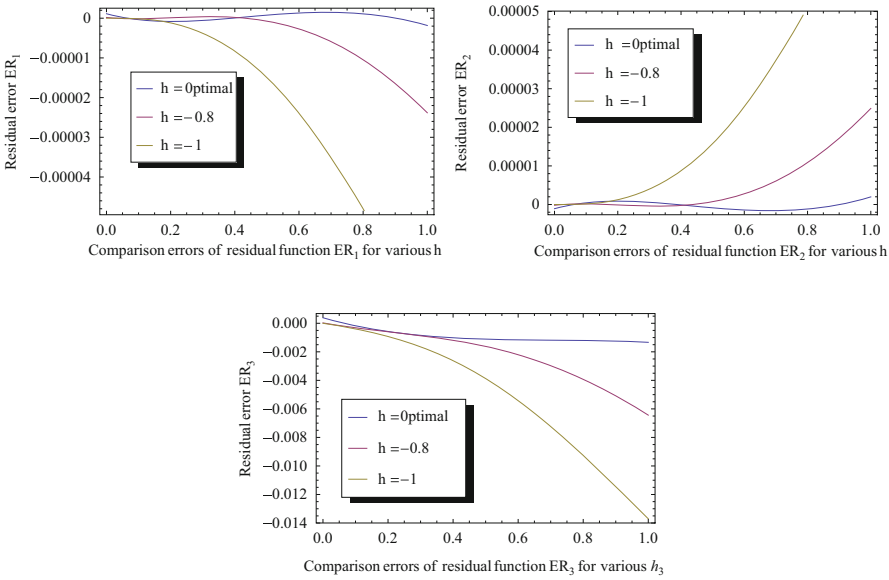

Fig. 4 Fourth-order residual error plot for various values of $\hbar$ and $\eta \in (0, 1)$

4 Conclusion

It is observed that the HAM has the intended result after solving a model for HIV and CD4+ T cells during primary infection. The HAM avoids the difficulties and huge amount of computational work of other numerical methods.

References

1. Essunger, P., Perelson, A. S.: Modeling HIV infection of CD4+ T cells subpopulations. J. Theoret. Biol. **170**, 367–391 (1994)
2. Liao, S. J.: The proposed homotopy analysis technique for the solution of nonlinear problems. PhD thesis, Shanghai Jiao Tong University (1992)
3. Liao, S. J.: A kind of approximate solution technique which does not depend upon small parameters (II): an application in fluid mechanics. Int. J. Non-Linear Mech. **32**, 815–822 (1997)
4. Liao, SJ.: An explicit, totally analytic approximation of Blasius viscous flow problems. Int. J. Non-Linear Mech. **34**, 759–778 (1999)
5. Liao, SJ.: Beyond perturbation: introduction to the homotopy analysis method. Boca Raton: Chapman & Hall/CRC Press (2003)
6. Nowak, M. A., May, R. M.: Virus dynamics. Oxford University Press (2000)
7. Odibat, M.: A study on the convergence of homotopy analysis method. Appl. Math. Comput. **217**, 782–789 (2010)
8. Perelson, A. S.: Modelling the interaction of the immune system with HIV, in: C. Castillo-Chavez (Ed.) Mathematical and statistical approaches to AIDS epidemiology. Springer, Berlin (1989)

9. Perelson, A. S., Nelson, P. W.: Mathematical analysis of HIV-1 dynamics in vivo. SIAM Rev. **41**, 3–44 (1999)
10. Perelson, A. S., Kirschner, D. E., De Bore, R.: Dynamics of HIV infection of CD4+ T cells. Math. Biosci **114**, 81–125 (1993)
11. Poincare, H.: Second complement analysis situs. Proc London Math Soc. **32**, 277–308 (1900)
12. Rong, L., Gilchrist, M. A., Feng, Z., Perelson, A. S.: Modeling within host HIV-1 dynamics and the evolution of drug resistance: Trade offs between viral enzyme function and drug susceptibility. J. Theoret. Biol. **247**, 804–818 (2007)
13. Sen, S.: Topology and geometry for physicists. Academic Press, Florida (2003)
14. Srivastava, P. K., Chandra, P.: Modeling the dynamics of HIV and CD4+ T cells during primary infection. Nonlinear analysis: real world applications. **11**, 612–618 (2008)

Stratification and Cross Diffusion Effects on Magneto-Convection Stagnation-Point Flow in a Porous Medium with Chemical Reaction, Radiation, and Slip Effects

M. Bhuvaneswari, S. Sivasankaran, S. Karthikeyan, and S. Rajan

Abstract The analysis on the changes due to mass and heat transfer in the presence of chemical reaction, thermal radiation, internal heat generation, and Dufour-Soret effects on an unsteady hydromagnetic combined convection stagnation-point flow toward a vertical plate embedded in a solutally and thermally stratified porous surrounding subjected to the slip conditions on velocity, thermal, and solutal fields is presented deliberately in this paper. Relations of similarity are inducted for the conversion of flow relations as ordinary differential equations and the solution is obtained upon the application of shooting method combined with Runge-Kutta algorithm. An analysis is presented upon the graphical depictions on the profiles of velocity of the liquid, its temperature, and its concentration with respect to some physical entities, and conclusions thereby are drawn.

Keywords: Stagnation-point; Porous medium; Thermal radiation; Stratification; Slip conditions; Chemical reaction.

1 Introduction

Transfer of mass and energy in MHD convection with chemical reaction and radiation occupies a pivotal place in haystack burning, fluidized bed catalysis, drying processes of porous solids, and temperature reduction of reactors in atomic power stations. The changes due to chemical reaction and radiation on different configurations of the problem have been researched by many authors. By employing Lie group analysis, Bhuvaneswari et al. [1] explored the convective double-diffusive flow of an incompressible liquid past an inclined semi-infinite surface

M. Bhuvaneswari · S. Sivasankaran (✉)
Department of Mathematics, King Abdulaziz University, Jeddah, Saudi Arabia
e-mail: smsivanandam@kau.edu.sa

S. Karthikeyan · S. Rajan
Department of Mathematics, Erode Arts and Science College, Erode, Tamil Nadu, India

B. Rushi Kumar et al. (eds.), *Applied Mathematics and Scientific Computing*,
Trends in Mathematics, https://doi.org/10.1007/978-3-030-01123-9_25

with first-order homogeneous chemical reaction. The effect of flow, mass, and heat transfer on hydromagnetic chemically reacting flow in a two-dimensional irregular channel subject to radiation and Dufour effect is investigated by Ruchi Kumar and Sivaraj [2].

In recent years, quite a large number of studies dealing with Dufour-Soret effects on mass and heat transfer of viscoelastic fluids have appeared. Dufour-Soret effects combined with chemical reaction and radiation on viscoelastic flow upon a stretched surface with convective boundary condition was the case dealt by Eswaramoorthi et al. [3]. Radiation, internal heat generation, and Dufour-Soret effects on MHD combined convection stagnation-point flow toward a vertical plate in a porous neighborhood with mass and heat transfer were examined by Karthikeyan et al. [4]. Aman et al. [5] have concentrated upon the action of hydromagnetic stagnation-point flow toward a shrinking/stretching sheet with boundary slip effect. Variations in temperature and concentration differences or existence of fluids having different densities are the causes for stratification. The analysis of free/combined convection in a stratified medium is a problem of fundamental interest because of its important applications in engineering. MHD combined convection from a vertical plate over a stratified porous surrounding with thermal dispersion was probed by Chamkha et al. [6]. Changes due to slip conditions are significant for fluids that show wall slip such as polymer solutions, foams, emulsions, etc. In many of the technological applications such as the polishing of internal cavities and artificial heart valves, fluids exhibiting slip are important. Slip effects in the flow of a nanofluid in a stretching cylinder with double stratification and radiation were analyzed by Hayat et al. [7]. Partial slip on steady stagnation-point flow of an incompressible liquid toward a shrinking sheet was considered by Bhattacharyya et al. [8]. Rohini et al. [9] have made a study on the action of suction and temperature slip upon the unsteady combined convection boundary layer flow near the stagnating point on a permeable vertical surface encompassed in a porous medium. By drawing motivation from the above works, we attempt this study to analyze the changes due to the stratification and slip on hydromagnetic stagnation-point flow in a porous medium with cross diffusion, chemical reaction, and radiation.

2 Flow Analysis

Steady-state two-dimensional hydromagnetic flow of an incompressible electrically conducting viscous liquid in the vicinity of a point of stagnation at the surface $y = 0$ with the flow region as $y > 0$ is considered. By setting the origin fixed, two forces of equal magnitude and opposite direction are employed along x-axis. The liquid arriving from y-axis make an impact on the wall at $y = 0$, and as a result, there are two streams leaving in upper and lower directions. In nearby surrounding of a stagnating point, flow velocity is taken as $U_\infty = nx$, where n is positive. A magnetic domain B_0, a constant, is employed in y direction. The electric field as well as the magnetic field is negligible because of polarization. The concentration and the

temperature of the liquid are C_∞ and T_∞ and that of the liquid at stretching wall are C_w and T_w, respectively. We assume that the plate gets heated due to convection by a hot liquid having T_f as temperature. Further, we assume that the electrical and viscous dissipation are negligibly small. The equations pertaining to this MHD stagnating-point flow of mass and energy transfer upon a hot vertical plate are

$$\frac{\partial u}{\partial x} + \frac{\partial v}{\partial y} = 0 \tag{1}$$

$$u\frac{\partial u}{\partial x} + v\frac{\partial u}{\partial y} = \nu\frac{\partial^2 u}{\partial y^2} + g\beta(T - T_\infty) + g\beta^*(C - C_\infty) - \left(\frac{\sigma_e B_0^2}{\rho} + \frac{v}{\tilde{K}}\right)(u - U_\infty) + U_\infty\frac{dU_\infty}{dx} \tag{2}$$

$$u\frac{\partial T}{\partial x} + v\frac{\partial T}{\partial y} = \alpha\frac{\partial^2 T}{\partial y^2} - \frac{\alpha}{k}\frac{\partial q_r}{\partial y} + \frac{D_m K_T}{c_s c_p}\frac{\partial^2 C}{\partial y^2} + Q(T - T_\infty) \tag{3}$$

$$u\frac{\partial C}{\partial x} + v\frac{\partial C}{\partial y} = D_m\frac{\partial^2 C}{\partial y^2} + \frac{D_m K_T}{T_m}\frac{\partial^2 T}{\partial y^2} - K_1 C \tag{4}$$

with

$$u = u_w + L\frac{\partial u}{\partial y},\ v = 0,\ T = T_w + K_1\frac{\partial T}{\partial y}, C = C_w + K_2\frac{\partial C}{\partial y} \text{ at } y = 0,$$
$$u \to 0,\ T \to T_\infty,\ C \to C_\infty, \text{ as } y \to \infty \tag{5}$$

where $u_w = \frac{u_0 x}{l}$, $T_w = T_0 + a\frac{x}{l}$, $C_w = C_0 + b\frac{x}{l}$, $T_\infty = T_0 + d\frac{x}{l}$, and $C_\infty = C_0 + e\frac{x}{l}$,

where L, K_1, and K_2 are, respectively, the slip factors with respect to velocity, thermal effect, and concentration; a, b, d, and e are the constants of dimensionality; and l is the reference length. Here, with usual notations, we take

$$q_r = -\frac{4\sigma^*}{3K'}\frac{\partial T^4}{\partial y} \tag{6}$$

On the assumption that the temperature variations are too minimal, we can take T^4 as

$$T^4 \cong 4T_\infty^3 T - 3T_\infty^4. \tag{7}$$

We incorporate the nondimensional expressions listed below.

$$Gr = \frac{g\beta(T_w - T_\infty)x^3}{v^2},\ Gc = \frac{g\beta(C_w - C_\infty)x^3}{v^2},\ S = \frac{Qv}{\alpha n},\ R_d = \frac{4\sigma^* T_\infty^3}{kK'},$$

$$Df = \frac{K_T D_m (C_w - C_\infty)}{c_p \alpha c_s (T_w - T_\infty)}, K = \frac{v}{n\widetilde{K}}, \ Pr = \frac{v}{\alpha}, \ Sc = \frac{v}{D_m}, \ M = \frac{B_0^2 \sigma_e}{\rho n},$$
$$v = \frac{\mu}{\rho}, \ Sr = \frac{K_T (T_w - T_\infty)}{T_m v (C_w - C_\infty)}, \ Cr = \frac{K_1}{n}, Re_x = \frac{U_\infty x}{v}, \ Ri_T = \frac{Gr}{Re_x^2}, \quad (8)$$
$$Ri_C = \frac{Gc}{Re_x^2}, \ S_T = \frac{d}{a}, \ d_T = K_1 \sqrt{\frac{U_0}{lv}}, \ Sc = \frac{e}{b}, \ d_C = K_2 \sqrt{\frac{U_0}{lv}}.$$

Here S_C, S_T, d, d_C, and d_T are, respectively, the parameters corresponding to solutal stratification, thermal stratification, velocity slip, solutal slip, and thermal slip. We now introduce the following similarity relations:

$$\eta = y\sqrt{\frac{n}{v}}, \ \psi = \sqrt{vn} x f(\eta), \ \theta = \frac{T - T_\infty}{T_w - T_0}, \ \phi = \frac{C - C_\infty}{C_w - C_0} \quad (9)$$

where $\psi(x, y)$ is the stream function defined by $u = \frac{\partial \psi}{\partial y}$ and $v = -\frac{\partial \psi}{\partial x}$ so as to satisfy Eq. (1) identically. Equations (2)–(5), on the application of Eqs. (7)–(9), yield the equivalent set of ordinary differential equations as

$$f''' + ff'' - f'^2 + \theta Ri_T + \phi Ri_C + (K + M)(1 - f') = -1 \quad (10)$$
$$(1 + 4Rd/3)\theta'' - S_T Prf' - Prf'\theta + Prf\theta' + S\theta + Df\phi'' = 0 \quad (11)$$
$$\phi'' - S_c Scf' - Scf'\phi + SrSc\theta'' + Scf\phi' - ScCr\phi = 0. \quad (12)$$

where K, Rd M, Cr, and S are, respectively, the parameters corresponding to porous surrounding permeability, thermal radiation, magnetic domain, chemical reaction, and internal heat generation. On the substitution of Eqs. (7)–(9), conditions in (5) are modified as

$$f' = 1 + df'', f = 0, \theta = 1 - S_T + d_T\theta', \phi = 1 - S_c + d_C\phi' \text{ at } \eta = 0$$
$$f' = 0, \theta = 0, \phi = 0 \text{ as } \eta \to \infty \quad (13)$$

Solutions of Eqs. (10)–(12) subject to (13) are attained by the application of shooting method combined with Runge-Kutta fourth-order algorithm. Localized Nusselt and Sherwood numbers and then the coefficient of skin-friction are given by

$$C_f = \frac{2\tau_w}{\rho U_\infty^2}, \quad Nu = \frac{xq_w}{k(T_w - T_\infty)}, \quad Sh = \frac{xq_m}{D_m(C_w - C_\infty)}. \quad (14)$$

where

$$\tau_w = \mu \left.\frac{\partial u}{\partial y}\right|_{y=0}, \ q_w = -k \left.\frac{\partial T}{\partial y}\right|_{y=0} = -\left.\frac{4\sigma^*}{3K'}\frac{\partial T^4}{\partial y}\right|_{y=0}, \ q_m = -D \left.\frac{\partial C}{\partial y}\right|_{y=0}. \quad (15)$$

The relations for localized Nusselt and Sherwood numbers and then the coefficient of skin-friction are derived as

$$C_f Re^{\frac{1}{2}} = f''(0), \quad Nu/Re^{\frac{1}{2}} = -\left(1 + \frac{4}{3}Rd\right)\theta'(0), \quad Sh/Re^{\frac{1}{2}} = -\phi'(0). \quad (16)$$

3 Results and Discussion

Throughout the numerical computations, we fix the values for the parameters as $Ri_T = 1$, $Ri_C = 1$, $K = 1$, $M = 1$, $Pr = 0.7$, $Sc = 0.5$, $a = 1$, $d = 0.5$, $S = 1.0$, $Df = 0.5$, $Rd = 0.5$, $Sr = 0.5$, $Cr = 0.5$, $d_T = 1.0$, $d_C = 1.0$, $S_T = 0.5$, $S_C = 0.5$ unless stated otherwise. It is seen in Fig. 1 that rising the velocity due to ascending values of d. Figure 2a–c indicates the changes due to radiation parameter on f', θ, and ϕ. From Fig. 2a–b, it is observed that a rise in radiation parameter initially tends to diminish the velocity and temperature, while the reverse trend occurs when $\eta > 1$. Figure 2c indicates that, for the accelerating values of radiation parameter, concentration picks up first and it declines after $\eta = 1$ and again it reverses when $\eta > 3$. From Fig. 3a–b, it is observed that the changes of ascending Dufour number raise the fluid temperature significantly. It is seen that the concentration lowers down and it rises again slightly as it reaches the free stream value.

Figure 4a–b represents the concentration profiles for Soret number and chemical reaction parameter, respectively. Rise in chemical reaction parameter reduces the concentration. However, the concentration lowers down near boundary and it rises again slightly as it reaches the free stream value as presented in Fig. 3b.

Figure 5a–b displays the rise in both temperature and velocity because of a rise in temperature slip parameter d_T. The changes due to concentration slip parameter d_C on velocity and concentration are depicted in Fig. 6a–b. Both the velocity and concentration become low with ascending values of d_C. It is noticed in Fig. 7a–b that

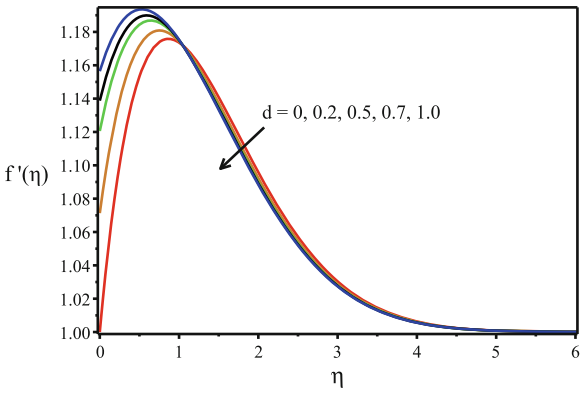

Fig. 1 Effect of d on velocity

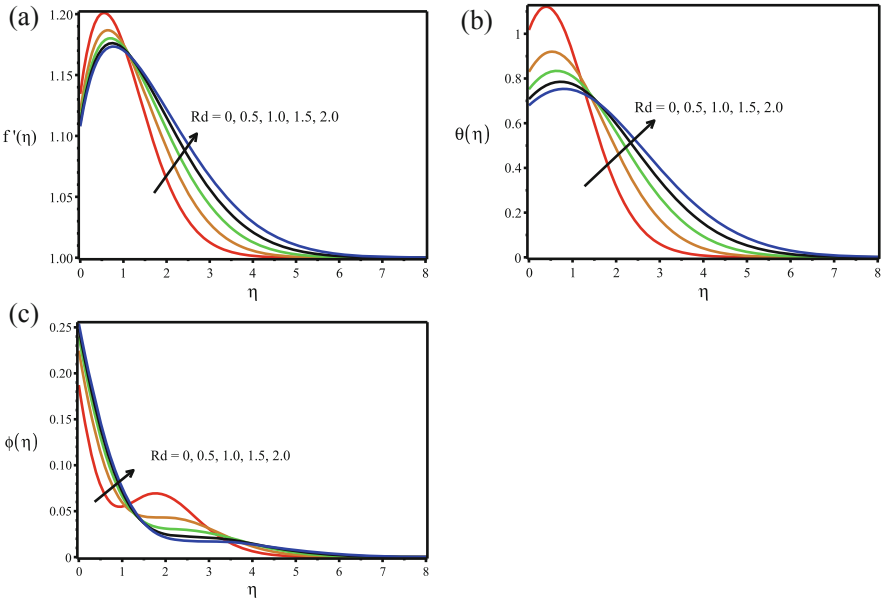

Fig. 2 Effect of Rd on velocity (**a**), temperature (**b**), and concentration (**c**)

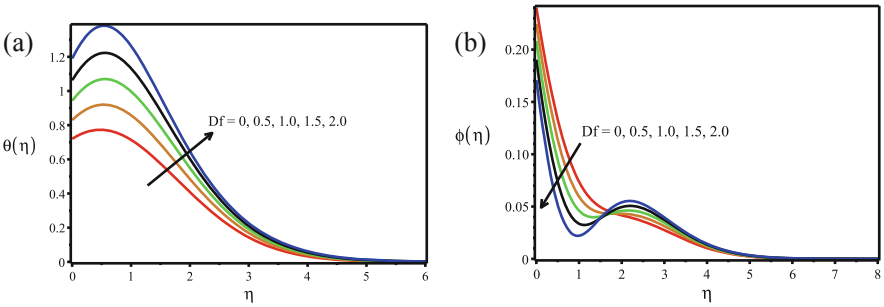

Fig. 3 Effect of Df on temperature (**a**), and concentration (**b**)

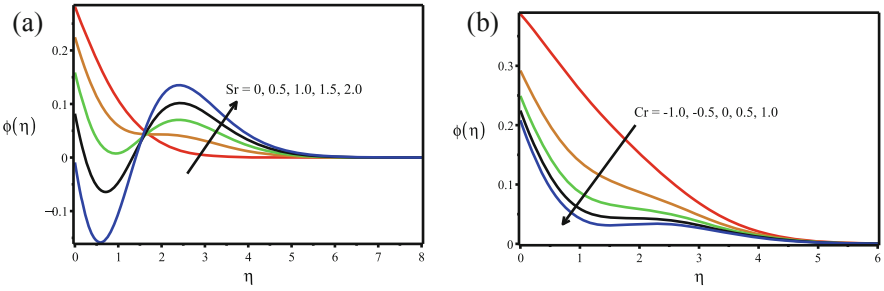

Fig. 4 Effect of Sr (**a**) and Cr (**b**) on concentration

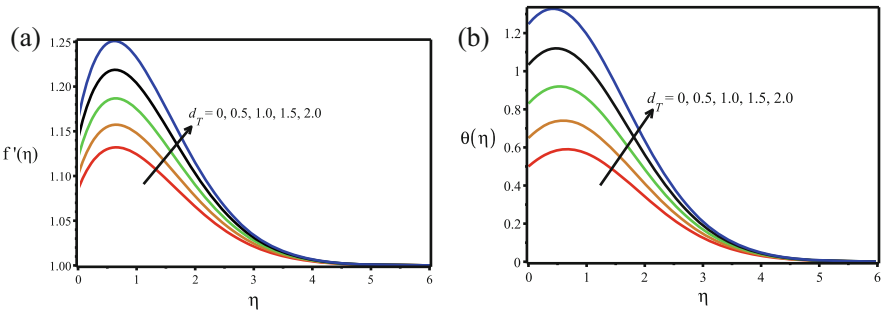

Fig. 5 Effect of d_T on velocity (**a**) and temperature (**b**)

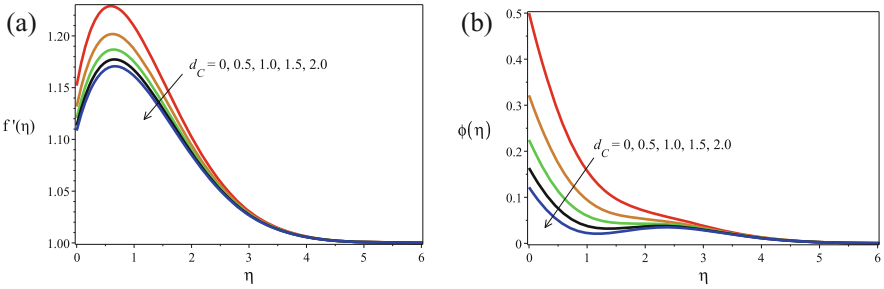

Fig. 6 Effect of d_C on velocity (**a**) and concentration (**b**)

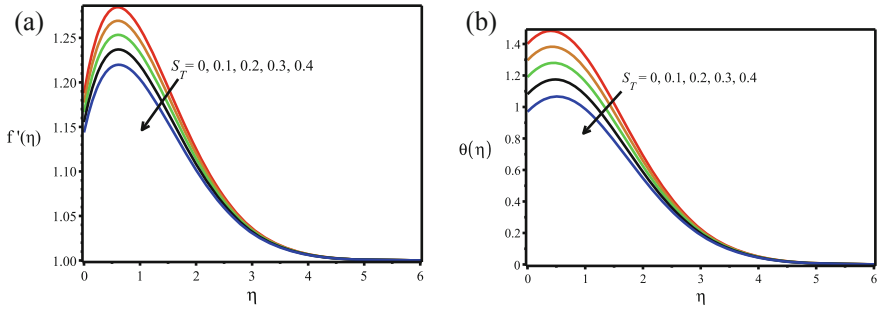

Fig. 7 Effect of S_T on velocity (**a**) and temperature (**b**)

a rise in thermal stratification parameter diminishes the temperature and velocity and thus shrinks thermal boundary layer thickness. Descending trends in the velocity and concentration profiles are observed due to the rise in solutal stratification parameter in Fig. 8a–b.

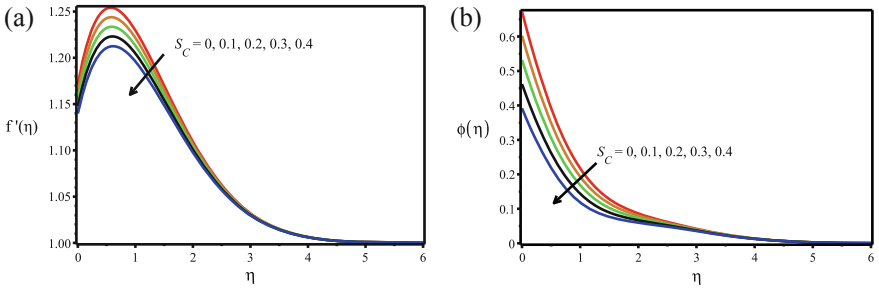

Fig. 8 Effect of S_C on velocity (**a**) and concentration (**b**)

4 Conclusion

The changes due to stratification and velocity, thermal, and solutal slip conditions on hydromagnetic combined convection stagnating-point flow upon a plate placed upright in a porous surrounding with mass and heat transfer in the influence of internal heat generation, radiation, and Dufour-Soret effects are deliberately analyzed in this paper. Shooting method with Runge-Kutta algorithm is applied for finding the solution. Conclusions of the study are as follows:

- Radiation parameter initially tends to diminish temperature and velocity profiles; but when $\eta > 1$, the reverse trend occurs.
- Ascending values of chemical reaction parameter leads to diminish the species concentration at the boundary layer.
- Both temperature and velocity enhance on rising the thermal slip parameter.
- A rise in thermal stratification parameter brings down the temperature and velocity and thus thermal boundary layer thickness slims down.

References

1. Bhuvaneswari, M., Sivasankaran, S., Kim, Y.J.: Lie group analysis of radiation natural convection flow over an inclined surface in a porous medium with internal heat generation, Journal of Porous Media, 15(12), 1155–1164 (2012).
2. Rushi Kumar, B., Sivaraj, R.: Radiation and Dufour effects on chemically reacting MHD mixed convective slip flow in an irregular channel, Elixir Thermal Engg., 39, 4675–4683 (2011).
3. Eswaramoorthi, S., Bhuvaneswari, M., Sivasankaran, S., Rajan, S.: Soret and Dufour effects on viscoelastic boundary layer flow over a stretching surface with convective boundary condition with radiation and chemical reaction, Scientia Iranica B, 23(6), 2575–2586 (2016).
4. Karthikeyan, S., Bhuvaneswari, M., Rajan, S., Sivasankaran, S.: Soret and Dufour effects on MHD mixed convection heat and mass transfer of a stagnation point flow towards a vertical plate in a porous medium with chemical reaction, radiation and heat generation, J. Appl. Fluid Mech., 9(3), 1447–1455 (2016).
5. Aman, F., Ishak, A., Pop, I.: Magnetohydrodynamic stagnation-point flow towards a stretching/shrinking sheet with slip effects, International Communications in Heat and Mass Transfer, 64, 1091–1100 (2013).

6. Chamkha, A.J., Khaled, A.R.A.: Hydromagnetic simultaneous heat and mass transfer by mixed convection from a vertical plate embedded in a stratified porous medium with thermal dispersion effects, Heat and Mass Transfer, 36, 63–70 (2000).
7. Hayat, T., Nassem, A., Khan, M.I., Farooq, M., Al-Saedi, A.: Magnetohydrodynamic (MHD) flow of nanofluid with double stratification and slip conditions, Physics and Chemistry of Liquids, 1–20 (2017).
8. Bhattacharyya, K., Mukhopadhyay, S., Layek, G.C.: Slip effects on boundary layer stagnation-point flow and heat transfer towards a shrinking sheet, International Journal of Heat and Mass Transfer, 54, 308–313 (2011).
9. Rohni, A.M., Ahmad, S., Pop, I., Merkin, J.H.: Unsteady mixed convection boundary layer flow with suction and temperature slip effects near the stagnation point on a vertical permeable surface embedded in a porous medium, Trans. Porous Med., 92, 1–14 (2012).

Natural Convection of Newtonian Liquids and Nanoliquids Confined in Low-Porosity Enclosures

P. G. Siddheshwar and K. M. Lakshmi

Abstract Natural convection of nanoliquids confined in a low-porosity enclosure when the lateral walls are subject to constant heat and mass fluxes is studied analytically using modified Buongiorno-Darcy model and Oseen-linearised approximation. For the study we considered water-copper nanoliquid and aluminium foam, glass balls as porous materials. The effective thermophysical properties are calculated using phenomenological laws and mixture theory. An analytical solution is obtained for boundary layer velocity and Nusselt number. The study shows that dilute concentration of high thermal conductivity nanoparticles significantly facilitates enhanced heat transport. The porous medium, however, diminishes heat transport when the thermal conductivity of the porous material, k_{pm}, is less compared to that of nanoparticles, k_{np}. When $k_{pm} \geq k_{np}$ then the presence of nanoparticles does not affect the heat transport.

1 Introduction

Natural convection heat transfer in a low-porosity medium due to the temperature difference between the vertical walls is frequently encountered in design of thermal insulation systems, geothermal reservoirs, grain storage, heat exchangers, electronics cooling, nuclear reactors, etc. In all these applications, the primary limitation of using Newtonian liquids as a medium for heat exchange is its low thermal conductivity. We can overcome this limitation by introducing nanoscaled engineered particles, i.e., nanoparticles of high thermal conductivity into the Newtonian liquids as this will significantly increase the effective thermal conductivity of the liquid system.

Natural convection in nanoliquids is generally studied using KVL single-phase model [6, 10, 15] and Buongiorno two-phase model [5, 8, 11–13, 17, 20, 22]. The

P. G. Siddheshwar (✉) · K. M. Lakshmi
Department of Mathematics, Bangalore University, Bangalore, India
e-mail: pgsiddheshwar@bub.ernet.in

B. Rushi Kumar et al. (eds.), *Applied Mathematics and Scientific Computing*,
Trends in Mathematics, https://doi.org/10.1007/978-3-030-01123-9_26

limitation of using KVL model is that this model does not account for important effects such as Brownian motion and thermophoresis. In the present paper, we have modelled the conservation equations for nanoliquid-saturated porous medium using modified Buongiorno-Darcy model (MBDM) with the effective thermophysical properties being modelled using phenomenological laws [4, 9] and traditional mixture theory. These are few works that consider natural convection due to heating of vertical walls in enclosures [1, 2, 7, 10, 19]. In many practical situations such as design of insulating systems, the fluid layer will be exposed to radiation heating. Our problem is the simulation of such situations. Many researchers have studied natural convection subjected to uniform heat and mass fluxes in Newtonian liquid-saturated porous medium [3, 14, 16, 18]. We extend the problem to a nanoliquid-saturated porous medium with actual thermophysical properties of water-copper nanoliquid and aluminium foam, glass balls porous materials being used.

Nomenclature

A	aspect ratio	R_1	thermal Rayleigh number
a	core temperature gradient	R_2	concentration Rayleigh number
b	core concentration gradient	T	effective temperature
C_p	effective specific heat capacity	t(x)	temperature profile
C	concentration of nanoparticles	u, v	velocity components
c(x)	concentration profile	x, y	spatial coordinates
D_B	Brownian diffusion coefficient	α	volume fraction ($0 \leq \alpha < 1$)
d_{np}	diameter of nanoparticles	β_1	thermal expansion coefficient
D_T	thermophoresis coefficient	β_2	solutal analog of β_1
g	acceleration due to gravity	χ	effective thermal diffusivity
H	height of the enclosure	ΔT	temperature difference
j”	mass flux	ΔC	concentration difference
k	effective thermal conductivity	μ	dynamic coeffecient of viscosity
K	permeability	ϕ	porosity ($0 < \phi \leq 1$)
K_B	Boltzmann constant	ρ_0	effective density
L	enclosure thickness		
Le	Lewis number		***Subscripts***
M	ratio of specific heats	*bl*	base liquid
N_A	modified diffusivity ratio	*c*	critical
N_T	Thermophoresis parameter	bl_{eff}	base liquid porous medium
n	buoyancy ratio	L, R	left and right boundary layer region
Nu	Nusselt number	*nl*	nanoliquid
P	dynamic pressure	*np*	nanoparticle
q	velocity of the nanoliquid	pm	porous material
q”	heat flux	0	at reference value

2 Mathematical Formulation

Two-dimensional rectangular enclosures are filled with nanoliquid-saturated low-porosity medium whose horizontal walls are insulated and impermeable to nanoparticles and base liquid, while the vertical walls are subjected to uniform heat and mass fluxes:

$$q'' = -k\left(\frac{\partial T}{\partial x}\right)_{x=0,L}, \tag{1}$$

$$j'' = -D_B\left(\frac{\partial C}{\partial x}\right)_{x=0,L}. \tag{2}$$

Since equal quantities of influx and outflux are given to the system, it allows the system to generate a static core region between the cells as shown in Fig. 1.

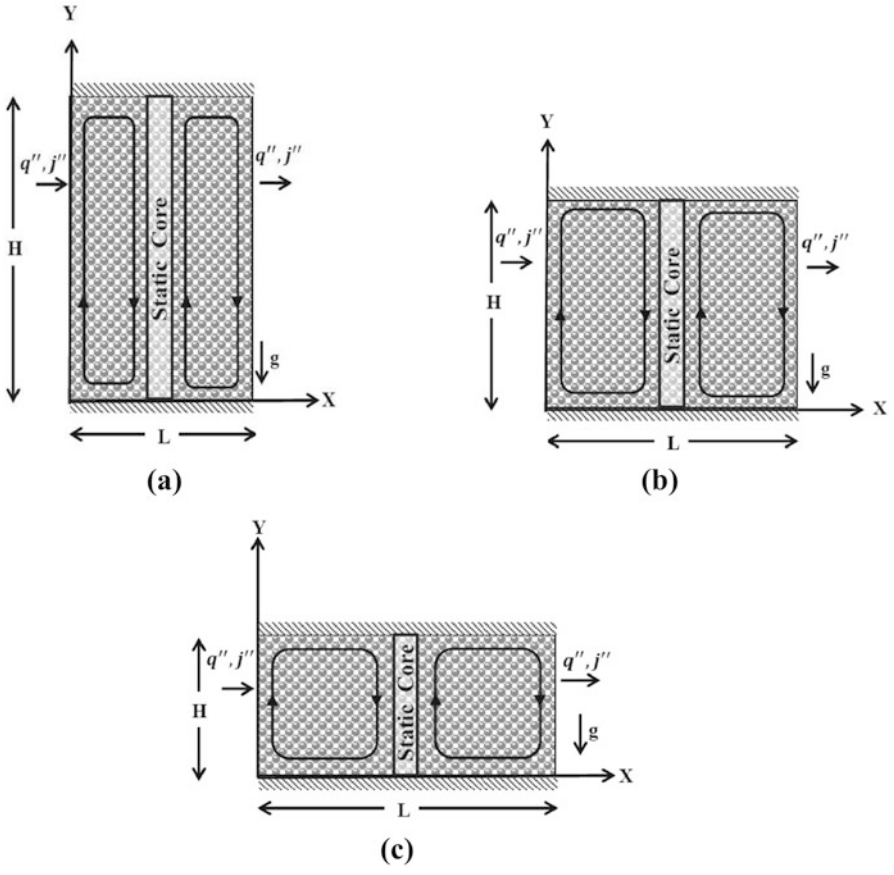

Fig. 1 Schematic representation of nanoliquid-saturated porous enclosures. (**a**) Tall. (**b**) Square. (**c**) Shallow

The modified Buongiorno-Darcy governing equations are:

$$\nabla \cdot \mathbf{q} = 0, \tag{3}$$

$$-\nabla P - \frac{\mu_{nl}}{K}\mathbf{q} + [\rho_0 - \rho_0\beta_1 (T - T_0) + \rho_0\beta_2 (C - C_0)]\,\mathbf{g} = 0, \tag{4}$$

$$(\mathbf{q} \cdot \nabla)\, T = M\, \chi\, \nabla^2 T, \tag{5}$$

$$(\mathbf{q} \cdot \nabla)\, C = D_B \nabla^2 C + \frac{D_T}{T_0}\nabla^2 T, \tag{6}$$

where

$$\nabla = \hat{i}\frac{\partial}{\partial x} + \hat{k}\frac{\partial}{\partial z}, \quad D_B = \frac{\phi\, K_B T}{3\pi\,\mu\, d_{np}}\,, \quad D_T = \frac{0.26\,\phi\, k}{2k + k_p}\frac{\mu}{\rho_0}C$$

and other nanoliquid properties are found from phenomenological laws and mixture theory [16].

Oseen-Linearisation Transformation and Boundary Layer Regime

The assumptions required in the study are:

1. constant boundary layer thickness which is y-independent,
2. u=0 and v=0 in the core,
3. linearly stratified temperature and concentration in the core
4. linearly increasing temperature and concentration along vertical walls.

According to Weber [21], Oseen-linearisation transformation is an analytical technique for a porous medium and it takes the form:

$$\left.\begin{aligned} T(x, y) &= t(x) + T_0 + ay \\ C(x, y) &= c(x) + C_0 + by \end{aligned}\right\}. \tag{7}$$

Here T_0 and C_0 represent the temperature and concentration found at the centre of the static core (x=L/2, y=0), and t(x), c(x) satisfy the following core-limiting condition:

$$\lim_{t\to\infty} (v,\ t,\ c) = 0. \tag{8}$$

Applying the transformation (7) in the governing equations (3)–(6), the boundary layer equations take the form:

$$v - \frac{(\rho_0\beta_1)gK}{\mu_{nl}}t + \frac{(\rho_0\beta_2)gK}{\mu_{nl}}c = 0, \tag{9}$$

$$av = M\chi t'', \tag{10}$$

$$bv = D_B \; c'' + \frac{D_T}{T_0} t''. \tag{11}$$

Eliminating t from the above equations and making use of core-limiting condition (8) and uniform heat flux condition (1), we get:

$$t(x) = \frac{q''}{k\gamma} e^{-\gamma x}, \quad \gamma^2 = \frac{gK}{\mu_{nl}} \frac{(\rho_0 \beta_1)}{M\chi} a(1+n), \quad n = -\frac{M\chi}{D_B} \frac{b(\rho_0 \beta_2)}{a(\rho_0 \beta_1)} \left[1 - \frac{a}{b} \frac{D_T}{T_0 M\chi} \right]. \tag{12}$$

Using (12), the concentration and velocity profiles can be obtained in the form:

$$c(x) = \frac{M\chi q'' b}{D_B k \gamma a} \left[1 - \frac{a}{b} \frac{D_T}{T_0 M\chi} \right] e^{-\gamma x}, \quad v(x) = \frac{M\chi\gamma q''}{ak} e^{-\gamma x}. \tag{13}$$

Invoking the mass flux condition (2) into the c(x) gives us the following important result connecting core temperature and concentration gradients:

$$\frac{a}{b} = \frac{M\chi \; q''}{[kj'' + D_T / T_0 \; q'']} \tag{14}$$

The unknowns a and b appearing in Eqs. (12) and (13) can be found from the condition that the net flow of enthalpy through the porous layer at all points of y must be balanced by vertical thermal diffusion downward through the static core, i.e.,

$$\int_0^\infty \rho_0 C_p v_L \; T_L dx + \int_0^\infty \rho_0 C_p v_R T_R dx\_ = \int_0^L k \frac{\partial T}{\partial y} dx. \tag{15}$$

Similarly equivalent mass transfer condition with impermeable horizontal walls is

$$\int_0^\infty v_L \; C_L dx + \int_0^\infty v_R C_R dx\_ = \int_0^L D_B \frac{\partial C}{\partial y} dx, \tag{16}$$

In Eqs. (15) and (16), the quantities T_L, C_L, v_L and T_R, C_R, v_R are the temperature, concentration and velocity profiles at the left and right of the static core, respectively. The quantity x_ is the x-coordinate measured from right lateral wall to the static core.

Solving Eqs. (15) and (16) for a and b, we get:

$$a = \frac{q''}{k} \sqrt{\frac{M}{\gamma L}}, \quad b = \frac{j''}{D_B} \frac{1}{\sqrt{\gamma L}} \sqrt{1 + \frac{D_T}{T_0 k} \frac{q''}{j''}}. \tag{17}$$

The heat and mass transports in the system can be found using the Nusselt and Sherwood numbers and the analytical expression for the same is given by

$$Nu = \frac{k}{k_{bl_{eff}}} \frac{1}{2} R_1^{2/5} (1+n)^{2/5} \left(\frac{H}{L}\right)^{-4/5} M^{-1/5}, \tag{18}$$

$$Sh = \frac{1}{2} R_1^{2/5} (1+n)^{2/5} \left(\frac{H}{L}\right)^{-4/5} M^{-1/5} \left(1 + \frac{1}{N_T}\right), \tag{19}$$

where

$$R_1 = \frac{\rho_0 \beta_1 g K H^2 q''}{k \mu_{nl} \chi}.$$

3 Results and Discussion

Natural convection in a nanoliquid-saturated low-porosity medium is studied analytically. The thermophysical properties of nanoliquid and nanoliquid-saturated porous medium are taken from various sources [15–17]. From the tabulated values from various papers, the following inequalities are found to hold good:

$$\rho_0 \beta_1 < (\rho_0 \beta_1)_{ble}, \quad \mu_{nl} > \mu_{bl}, \quad k > k_{ble}, \quad \chi_{ble} < \chi. \tag{20}$$

On rewriting the definition of Darcy-Rayleigh number, we have

$$R_1 = F \; R_{1_{ble}}, \quad F = \frac{\mu_{bl} k_{ble} \chi_{ble} (\rho_0 \beta_1)}{\mu_{nl} \; k \; \chi \; (\rho_0 \beta_1)_{ble}} < 1 \Rightarrow R_1 < R_{1_{ble}}. \tag{21}$$

This clearly explains the advanced onset of convection in nanoliquid-saturated porous medium compared to base liquid-saturated porous medium.

In Table 1 we have tabulated the values of Nusselt number for different values of volume fraction in both aluminium foam and glass balls' porous medium. We observe the heat transport enhancement in the presence of water-copper-saturated glass balls' porous medium, whereas in the case of water-saturated glass balls' porous medium (in the absence of copper nanoparticles), the heat transport is

Table 1 Contribution of nanoparticles on thermal conductivity of nanoliquid-saturated porous medium

Porous materials	k_{ble}	k	$\frac{k}{k_{ble}}$
Aluminium foam	102.8065	102.865	1.00057
Glass balls	000.8315	000.8899	1.0702

diminished. However, in the case of water-copper-saturated aluminium foam porous medium, the presence of nanoparticles does not affect the heat transport at all. To find the reason for this situation, we consider the definition of Nusselt number as in Eq. (18). From this equation, we observe that the contribution of nanoparticles on heat transfer comes from the term $\frac{k}{k_{bleff}}$. On looking at the tabulated values of $\frac{k}{k_{bleff}}$ in Table 1 of water-copper-saturated aluminium foam porous medium case, we observe the following.

The addition of dilute concentration of nanoparticles increases the effective thermal conductivity of the system in both the types of porous medium. But the contribution of nanoparticles on heat transport is very less in the case of aluminium foam saturated by water-copper compared to that in the case of glass balls' porous medium. Thus we conclude that the participation of nanoparticles in heat transport is only in case of a porous medium that has low thermal conductivity. When the thermal conductivity of the porous medium is very high or near to the thermal conductivity of nanoparticles, then the heat transport rates in both base liquid-saturated porous medium and nanoliquid-saturated porous medium are the same (Table 2).

Table 2 Values of Nusselt number for R_1=30, M=0.775028(Glass Balls), M=0.615132(Aluminium foam) and n=2 for different values of volume fraction, α, in the case of a square enclosure

Volume fraction	Glass balls	Aluminium foam
0	3.18513	3.16999
0.02	3.25587	3.16987
0.04	3.32954	3.16965
0.06	3.40632	3.16945

Table 3 Values of Nusselt number for R_1=30, α=0.06, M=0.775028(Glass balls), M=0.615132(Aluminium foam) and n=2 for different types of enclosures

Aspect ratio	Glass balls	Aluminium foam
0.9	3.70588	3.44818
1	3.40632	3.16945
1.2	2.94402	2.73929

Table 4 Values of Nusselt number at R_1=30, α=0.06, M=0.775028(Glass Balls)and M=0.615132(Aluminium foam) for different values of buoyancy ratio, n, in the case of a square enclosure

Buoyancy ratio	Glass balls	Aluminium foam
0	2.19501	2.04237
2	3.40632	3.16945
4	4.17854	3.88797

Different values of aspect ratios are tabulated in Table 3 to get the results of shallow, square and tall porous enclosures. We observe that the heat transport is minimum in case of tall enclosures and maximum in the case of shallow enclosures.

We have tabulated the values of Nusselt number in Table 4 for different values of buoyancy ratio. We observe that the heat transport is more in heat and mass-driven convection than in the case of heat-driven convection.

References

1. Bejan, A.: On the boundary layer regime in a vertical enclosure filled with a porous medium. Lett. Heat Mass Transfer **6**, 93–102(1979)
2. Bejan, A.: Natural convection in a vertical cylindrical well filled with porous medium. Int. J. Heat Mass Transfer **23**, 726–729(1980)
3. Bejan, A.: The boundary layer regime in a porous layer with uniform heat flux from the side. Int. J. Heat Mass Transfer **26**, 1339–1346(1983)
4. Brinkman, H. C.: The viscosity of concentrated suspensions and solutions. J. Chem. Phy. **20**, 571–571(1952)
5. Buongiorno, J.: Convective transport in nanofluids. ASME J. Heat Transfer **128**, 240–250(2006)
6. Corcione, M.: Rayleigh-Bénard convection heat transfer in nanoparticle suspensions. Int. J. Heat Fluid Flow **32**, 65–77(2011)
7. Dastmalchi, M., Sheikhzadeh, G.A., Arani, AAA.: Double-diffusive natural convective in a porous square enclosure filled with nanofluid. Int. J. Therm. Sci. **95**, 88–98(2015)
8. Grosan, T., Revnic, C., Pop, I., Ingham, D.B.: Free convection heat transfer in a square cavity filled with a porous medium saturated by a nanofluid. Int. J. Heat Mass Transfer **87**, 36–41(2015)
9. Hamilton, R.L., Crosser, O.K.: Thermal conductivity of heterogeneous two-component systems. Ind. Eng. Chem. Fundam. **1**, 187–191(1962)
10. Khanafer, K., Vafai, K., Lightstone, M.: Buoyancy-driven heat transfer enhancement in a two-dimensional enclosure utilizing nanofluids. Int. J. Heat Mass Transfer **46**, 3639–3653(2001)
11. Nield, D.A., Kuznetsov, A.V.: Thermal instability in a porous medium layer saturated by a nanofluid. Int. J. Heat Mass Transfer **52**, 5796–5801(2009)
12. Sheikhzadeh, G.A., Dastmalchi, M., Khorasanizadeh, H.: Effects of walls temperature variation on double diffusive natural convection of $Al2O_3$ water nanofluid in an enclosure. Heat Mass Transf. **194**, 1209–1–1209–12(2013)
13. Sheikholeslami, M., Gorji-Bandpy, M., Ganji, D.D., Soleimani, S.: Thermal management for free convection of nanofluid using two phase model. J. Mol. Liq. **194**, 179–187(2014)
14. Siddheshwar, P.G., Abraham, A.: Convection in a ferromagnetic fluid occupying a vertical enclosure. Indian J. Eng. Mater. Sci., **5**, 423–426(1998)
15. Siddheshwar, P.G., Meenakshi, N.: Amplitude equation and heat transport for Rayleigh–Bénard Convection in Newtonian Liquids with Nanoparticles. Int. J. Appl. and Comp. Math. **2**, 1–22(2015)
16. Siddheshwar, P.G., Veena, B.M.: A theoretical study of natural convection of water-based nanoliquids in low-porosity enclosures using single-phase model. J. nanofluids **7**, 1–22(2018)
17. Siddheshwar, P.G., Kanchana, C., Kakimoto, Y., Nakayama, A.: Steady finite-amplitude Rayleigh-Bénard convection in nanoliquids using a two-phase model-theoretical answer to the phenomenon of enhanced heat transfer. ASME J. Heat Transfer **139**, 012402–1–012402–8(2016)
18. Trevisan, O.V., Bejan, A.: Mass and heat transfer by natural convection in a vertical slot filled with porous medium. Int. J. Heat Mass Transfer **29**, 403–415(1986)

19. Trevisan, O.V., Bejan, A.: Mass and heat transfer by high Rayleigh number convection in a porous medium heated from below. Int. J. Heat Mass Transfer **30**, 2341–2356(1987)
20. Vanaki, S.M., Ganesan, P., Mohammed, H.A.: Numerical study of convective heat transfer of nanofluids: A review. Renew. Sustainable Energy Rev. **54**, 1212–1239(2016)
21. Weber, J.W.: The boundary layer regime for convection in a vertical porous layer. Int. J. Heat Mass Transfer **18**, 569–573(1975)
22. Yang, C., Li, W., Sano, Y., Mochizuki, M., Nakayama, A.: On the anomalous convective heat transfer enhancement in nanofluids: a theoretical answer to the nanofluids controversy. ASME J. Heat Transfer **135**, 054504–1–054504–9(2013)

Study of Viscous Fluid Flow Past an Impervious Cylinder in Porous Region with Magnetic Field

D. V. Jayalakshmamma, P. A. Dinesh, N. Nalinakshi, and T. C. Sushma

Abstract The flow of viscous, incompressible and electrically conducting fluid past and impermeable cylinder present in a cylindrical porous region is considered for the steady case in presence of magnetic field applied in vertical direction. The flow is governed by modified Brinkman and Stokes equations in porous and nonporous regions, respectively. The matching boundary conditions are used at the interface with no-slip condition at the solid surface and uniform velocity away from the nonporous region. This boundary layered problem is solved analytically and obtained solutions in terms of modified Bessel's functions.

Keywords Incompressible · Brinkman equation · Stokes equation · No-slip

1 Introduction

The flows of the fluids through/past a porous medium are of principal interest because of its natural occurrence and its importance in industrial, geophysical, and biomedical applications. The study of hydrodynamic flows in presence of magnetic field has attracted many authors due to its vast applications in astrophysical, geophysical, and industrial fields. Many practical problems need a mechanism to control the motion of the fluid past solid bodies with magnetohydrodynamic (MHD) effects.

D. V. Jayalakshmamma (✉)
Department of Mathematics, Vemana Institute of Technology, Bangalore
e-mail: jayalakshmammadv@vemanait.edu.in

P. A. Dinesh
Department of Mathematics, M.S. Ramaiah Institute of Technology, Bangalore, India
e-mail: dineshdpa@msrit.edu

N. Nalinakshi · T. C. Sushma
Department of Mathematics, Atria Institute of Technology, Bangalore, India
e-mail: nalinakshi.n@atria.edu; sushma.tc@atria.edu

B. Rushi Kumar et al. (eds.), *Applied Mathematics and Scientific Computing*,
Trends in Mathematics, https://doi.org/10.1007/978-3-030-01123-9_27

In the literature, Anjali Devi and Raghavachar [1] studied the horizontal flow of a vertically stratified, conducting fluid past a nonconducting sphere in the presence of uniform magnetic field. Kyrlidis et al. [8] presented the study of conducting fluid past axisymmetric bodies in the presence of magnetic field for small inertial and magnetic Reynolds numbers. Chandran et al. [3] have analyzed the effect of magnetic field on the flow of heat transfer past a continuously moving porous plate in a stationary fluid. The flow of conducting fluid around a circular cylinder in the presence of magnetic field applied parallel to the main flow was investigated by Raghava Rao and Sekhar [11]. Jayalakshmamma et al. [5] presented a creeping flow past a composite sphere in presence of magnetic field. The steady flow of two immiscible fluid spheres of different viscosities was analyzed in the presence of unvarying magnetic field by Jayalakshmamma et al. [7].

Pal and Talukdar [10] analyzed the unsteady flow of a laminar two-dimensional oscillatory flow of conducting fluid between two nonconducting parallel plane surfaces in the presence of suction/injection. The effect of the magnetic field on the permeability of a membrane of solid cylindrical particle was considered by Ashish Tiwari et al. [2]. Pankaj Shukla [9] studied an axisymmetric, stokes flow past a swarm of porous cylindrical particles enclosing a solid core. The influence of transverse magnetic field on the flow of conducting fluid was investigated by Jayalakshmamma et al. [6]. Viscous fluid flow in porous media for spherical region with magnetic was investigated by Dinesh et al. [4].

The present study projects on certain practical applications such as metallurgy and metal processing and lubrication and in nuclear reactors, where an additional force such as magnetic field is applied to control the fluid flow. In the view of these applications, in this paper we considered the flow behavior of viscous, incompressible, conducting fluid past a solid cylinder embedded in a cylindrical porous medium in presence of external magnetic field.

2 Mathematical Formulation

The steady flow of viscous, incompressible, and conducting fluid through a porous cylindrical region of radius b comprising a solid cylindrical core of radius a is investigated in the presence of transverse magnetic field. It is assumed that the induced magnetic field is insignificant, as the magnetic Reynolds number is small. Also the flow domain has been divided into two regions as nonporous and porous region. The governing equations which describe the flow of a conducting fluid in nonporous region under the assumption made are modified Stokes equation with the equation of continuity, given, respectively, as:

$$\nabla.\vec{q_1} = 0 \tag{1}$$

$$\nabla p_1 = \mu\nabla^2\vec{q_1} + \mu_h^2\sigma_e\left(\vec{q_1} \times \vec{H}\right) \times \vec{H} \tag{2}$$

where $\vec{q_1} = (u_1, v_1, w_1)$ is the velocity in the nonporous region; μ is the viscosity of the fluid; μ_h^2 is the magnetic permeability; σ_e is the electrical conductivity, which is very small so that the induced magnetic field is negligible; $\vec{H}$ is the uniform magnetic field; and p_1 is the hydrostatic pressure of the nonporous region.

The flow in the porous region $a < r \leq b$ is governed by the modified Brinkman equation along with equation of continuity, given respectively by:

$$\nabla.\vec{q_2} = 0 \tag{3}$$

$$\nabla p_2 = \bar{\mu}\nabla^2\vec{q_2} - \frac{\mu}{k}\vec{q_2} + \mu_h^2\sigma_e\left(\vec{q_2} \times \vec{H}\right) \times \vec{H} \tag{4}$$

where, $\vec{q_2} = (u_2, v_2, w_2)$ is the velocity in the porous region, $\bar{\mu}$ is the Brinkman viscosity, p_2 the hydrostatic pressure of the porous region and k the permeability of the porous region.

In this study, the cylindrical polar coordinates are used. Thus, for an axisymmetric, two-dimensional flow in a cylindrical coordinate system (r, θ, z) with the origin at the center of the cylinder and the axis $\theta = 0$ is chosen along the direction of the uniform velocity u_∞ far from the nonporous region. Also due to axisymmetry, we have $\frac{\partial}{\partial z} = 0$. The flow characteristics of the problem which are described by Eqs. (1)–(4) can be analyzed in terms of nondimensional parameters pertaining to the flow processes. In view of this, the following dimensionless similarity variables are introduced:

$$r^* = \frac{r}{a}, \vec{q_1^*} = \frac{\vec{q_1}}{u_\infty}, \vec{q_2^*} = \frac{\vec{q_2}}{u_\infty}, \vec{H_1^*} = \frac{\vec{H_1}}{H_0}, \vec{p_1^*} = \frac{a\vec{p_1}}{\mu u_\infty}, \vec{p_2^*} = \frac{a\vec{p_2}}{\mu u_\infty} \tag{5}$$

where H_0 is the applied constant magnetic field.

After nondimensionalizing the governing equations (1)–(4) using the nondimensional variables as defined in Eq. (5) for cylindrical polar coordinate system in nonporous region, we get:

$$\frac{\partial}{\partial r}(ru_1) + \frac{\partial v_1}{\partial \theta} = 0 \tag{6}$$

$$-\frac{\partial p_1}{\partial r} = M^2 u_1 - \left(\frac{\partial^2 u_1}{\partial r^2} + \frac{1}{r}\frac{\partial u_1}{\partial r} + \frac{1}{r^2}\frac{\partial^2 u_1}{\partial \theta^2} - \frac{u_1}{r^2} - \frac{2}{r^2}\frac{\partial v_1}{\partial \theta}\right) \tag{7}$$

$$-\frac{1}{r}\frac{\partial p_1}{\partial \theta} = M^2 v_1 - \left(\frac{\partial^2 v_1}{\partial r^2} + \frac{1}{r}\frac{\partial v_1}{\partial r} + \frac{1}{r^2}\frac{\partial^2 v_1}{\partial \theta^2} - \frac{v_1}{r^2} + \frac{2}{r^2}\frac{\partial u_1}{\partial \theta}\right) \tag{8}$$

Here $(u_1, v_1, 0)$ represents the velocity of the fluid in the nonporous region. Similarly, the nondimensionalized governing equation for the porous region takes the form:

$$\frac{\partial}{\partial r}(ru_2) + \frac{\partial v_2}{\partial \theta} = 0 \tag{9}$$

$$-\frac{\partial p_2}{\partial r} = S^2 u_2 - \left(\frac{\partial^2 u_2}{\partial r^2} + \frac{1}{r}\frac{\partial u_2}{\partial r} + \frac{1}{r^2}\frac{\partial^2 u_2}{\partial \theta^2} - \frac{u_2}{r^2} - \frac{2}{r^2}\frac{\partial v_2}{\partial \theta}\right) \tag{10}$$

$$-\frac{1}{r}\frac{\partial p_2}{\partial \theta} = S^2 v_2 - \left(\frac{\partial^2 v_2}{\partial r^2} + \frac{1}{r}\frac{\partial v_2}{\partial r} + \frac{1}{r^2}\frac{\partial^2 v_2}{\partial \theta^2} - \frac{v_2}{r^2} + \frac{2}{r^2}\frac{\partial u_2}{\partial \theta}\right) \tag{11}$$

Here $(u_2, v_2, 0)$ are components of velocity in normal and tangential direction in porous medium, p_2 is the static pressure in porous region and $S^2 = M^2 + \sigma^2$ in which $\sigma = \frac{a}{\sqrt{k}}$ is the porous parameter, $M = \sqrt{\frac{\mu_h^2 \sigma_e H_0^2 a^2}{\mu}}$ is the Hartmann number, and k is the permeability of the fluid.

As the flow is axisymmetric and two dimensional, the stream function $\psi_i(r, \theta)$ (where $i = 1, 2$ correspondingly for nonporous and porous regions) is introduced, which satisfies the equation of continuity in cylindrical polar coordinate system for both nonporous and porous regions, respectively:

$$u_i = \frac{1}{r}\frac{\partial \psi_i}{\partial \theta}; \qquad v_i = -\frac{\partial \psi_i}{\partial r} \tag{12}$$

Here u_i is the normal component of velocity and v_i is the tangential velocity. By eliminating the pressure term from Eqs. (6) and (7) of nonporous region and Eqs. (9) and (10) of porous region by cross differentiation, we get a fourth-order linear partial differential equation in terms of corresponding stream function as:

$$\nabla^4 \psi_1 - M^2 \nabla^2 \psi_1 = 0, \quad b \le r < \infty \tag{13}$$

$$\nabla^4 \psi_2 - S^2 \nabla^2 \psi_2 = 0, \quad a \le r < b \tag{14}$$

where $\nabla^2 = \frac{\partial^2}{\partial r^2} + \frac{1}{r}\frac{\partial}{\partial r} + \frac{1}{r^2}\frac{\partial^2}{\partial \theta^2}$ is Laplacian operator in cylindrical polar coordinate system.

In the present problem, boundary conditions used are as follows: no-slip conditions on the surface of the solid cylindrical core are:

$$u_2(a, \theta) = 0, \quad 0 \le \theta \le 2\pi \tag{15}$$

$$v_2(a, \theta) = 0, \quad 0 \le \theta \le 2\pi \tag{16}$$

The interfacial conditions, continuity of normal and tangential velocity components, and continuity of normal and tangential stress components at the interface of the porous and nonporous region are given by:

$$u_2(b,\theta) = u_1(b,\theta) \quad 0 \le \theta \le 2\pi \tag{17}$$

$$v_2(b,\theta) = v_1(b,\theta) \quad 0 \le \theta \le 2\pi \tag{18}$$

$$\tau_{r\theta(2)}(b,\theta) = \tau_{r\theta(1)}(b,\theta) \quad 0 \le \theta \le 2\pi \tag{19}$$

$$\tau_{rr(2)}(b,\theta) = \tau_{rr(1)}(b,\theta) \quad 0 \le \theta \le 2\pi \tag{20}$$

where $\tau_{r\theta(i)}$ and $\tau_{rr(i)}$ are the dimensionless tangential and normal components of stress tensors, written in cylindrical coordinate as:

$$\tau_{r\theta(i)} = \frac{1}{r}\frac{\partial u_i}{\partial \theta} + \frac{\partial v_i}{\partial r} - \frac{v_i}{r} \tag{21}$$

$$\tau_{rr(i)} = -p_i + 2\frac{\partial u_i}{\partial r} \tag{22}$$

The continuity of the normal stress at the interface of the two regions from the boundary condition (20) shows the continuity of pressure across the interface, since the viscosity of the fluid is equal to the Brinkman viscosity $\bar{\mu} = \mu$. Therefore, Eq. (20) reduces to:

$$p_2(b,\theta) = p_1(b,\theta) \quad 0 \le \theta \le 2\pi \tag{23}$$

Also, the uniform velocity far away from the fluid cylindrical region is given by:

$$\psi_1(r,\theta) \sim r sin\theta \quad as \quad r \to \infty \tag{24}$$

3 Method of Solution

The boundary condition of uniform velocity far away from the porous cylindrical region leads to find the solution for the fourth-order partial differential equations of (13) and (14) by similarity solution method as:

$$\psi_i(r,\theta) = f_i(r) sin\theta \tag{25}$$

Substituting Eq. (25) in Eqs. (13) and (14) in respective regions, we obtain the ordinary differential equation of order four in $f_i(r)$ as:

$$f_i^{iv} + \frac{2}{r}f_i''' - \frac{3}{r^2}f_i'' + \frac{3}{r^3}f_i' - \frac{3}{r^4}f_i - J_i^2\left[f_i'' + \frac{1}{r}f_i' - \frac{1}{r^2}f_i\right] = 0 \tag{26}$$

$$where,\ J_i^2 = \begin{cases} M^2 & i = 1 \\ S^2 & i = 2 \end{cases}$$

The corresponding boundary conditions are:
No-slip condition at the surface of the solid cylinder is given by:

$$f_2(a) = 0 \tag{27}$$

$$f_2'(a) = 0 \tag{28}$$

The continuity of the velocity and stresses at the interface of the porous and nonporous region is given by:

$$f_2(b) = f_1(b) \tag{29}$$

$$f_2'(b) = f_1'(b) \tag{30}$$

$$f_2''(b) = f_1''(b) \tag{31}$$

$$f_2'''(b) - \sigma^2 f_2' = f_1'''(b) \tag{32}$$

Further, the uniform velocity far away from the nonporous region is:

$$f_1(r) \sim r \quad as \quad r \to \infty \tag{33}$$

The fourth-order ordinary differential equation (26) is converted into second-order differential equation with variable coefficient (see Jayalakshmamma et al. [6]) which can be solved by the method of variation of parameter and the obtained complete solution as:

$$f_1(r) = \frac{A_1}{r} + B_1 r + C_1 K_1(Mr) + D_1 I_1(Mr) \quad b \le r < \infty \tag{34}$$

$$f_2(r) = \frac{A_2}{r} + B_2 r + C_2 K_1(Sr) + D_2 I_1(Sr) \quad a < r < b \tag{35}$$

where $A_1, B_1, C_1, D_1, A_2, B_2, C_2$, and D_2 are arbitrary constants. In the fluid region as $r \to \infty$, then $I_1(Mr) \to \infty$. Therefore the solution is valid for $D_1 = 0$, and also due to the boundary condition for uniform velocity far away from the medium, from Eq. (33) we get $B_1 = 1$. Thus Eq. (34) reduces to:

$$f_1(r) = \frac{A_1}{r} + r + C_1 K_1(Mr) \quad b \le r < \infty \tag{36}$$

Hence the stream function in both the regions takes the form

$$\psi_1(r,\theta) = \left(\frac{A_1}{r} + r + C_1 K_1(Mr)\right) sin\theta \quad b \le r < \infty \tag{37}$$

$$\psi_2(r,\theta) = \left(\frac{A_2}{r} + B_2 r + C_2 K_1(Sr) + D_2 I_1(Sr)\right) sin\theta \quad a < r \le b \tag{38}$$

The arbitrary constants present in Eqs. (37) and (38) are evaluated using the boundary conditions; for the want of space, the expressions of constants are not mentioned in this paper. Further, the expression for normal and tangential component of velocities for both porous and nonporous regions can be obtained in terms of stream function from Eq. (12).

4 Results and Discussion

The considered boundary value problem is solved analytically, and expression for stream function is obtained as a function of r with nondimensional parameters.

The effect of magnetic field M for a fixed porous parameter σ on the flow patterns is discussed through the streamlines. For $\sigma = 5$ and for small magnetic field $M = 0.1$, it is noticed that the fluid is flowing past the porous cylinder rather than passing through it, shown in Fig. 1(i). This can be attributed to the lower permeability of the porous medium. For the same σ, when the magnetic field strength is increased, the fluid starts to move inside the porous region. As a result the streamlines are moving closer to the solid surface of a cylinder and the same is illustrated in Fig. 1(ii)–(iv).

The effect of magnetic field on the tangential velocity along the line $\theta = \frac{\pi}{2}$ is analyzed for both the regions and is depicted in Fig. 2. For $\sigma = 25$, a smooth flow is observed at the interface of the two regions for magnetic field of strength $M = 1$. As the magnetic field strength is increased, the tangential velocity increases in the porous medium and accelerates near the boundary of the two regions, reaches its maximum value, and maintains a uniform velocity far away from the porous cylinder. Also, the viscous sublayer decreases near the surface of porous cylindrical region with increase in Hartmann number as given in Fig. 2 (i). For $\sigma = 50$ and increasing Hartmann number, it is observed that the curve is sharpened at the interface, i.e., the viscous sublayer is decreased with an increase in Hartmann number and is shown in Fig. 2 (ii).

5 Conclusions

In this article, the influence of Hartmann number is discussed on the streamline patterns. From the graph, the meandering of streamlines near the surface of the solid cylinder is noticed for the increase in magnetic field strength with fixed porous

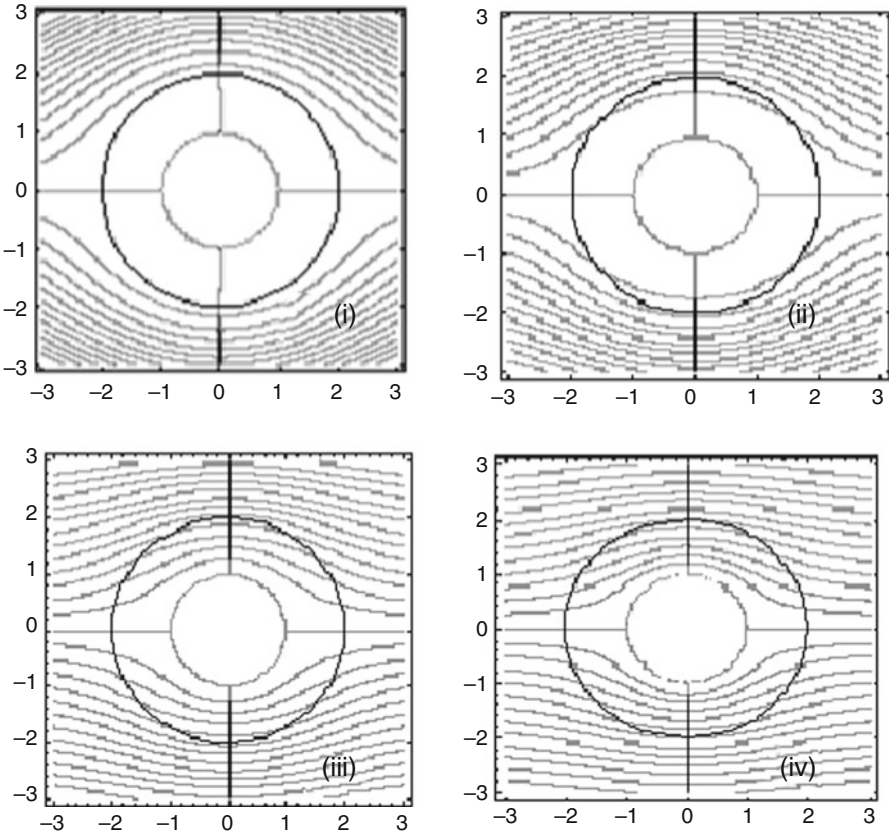

Fig. 1 Streamlines for fixed $\sigma = 5$ and different value of M. (i) $M = 0.1$, (ii) $M = 2$, (iii) $M = 5$, (iv) $M = 10$

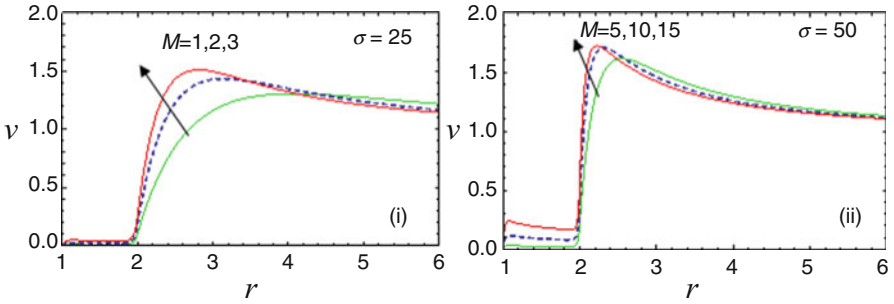

Fig. 2 Variation of tangential velocity for different values of M with fixed σ

parameter. This shows that the fluid flow is effectively controlled by the magnetic field; as a result more amount of fluid flows through the porous region/on the surface of the solid core.

The tangential component of velocity increases with increasing the magnetic field strength for fixed porous parameter, i.e., the tangential component of velocity amplifies and reaches its maximum and maintains the uniform velocity as distance moved away from the surface.

Acknowledgements The authors are grateful to research centers Vemana IT, M.S.R.I.T., and Atria IT, Bangalore, India, for their support and encouragement to carry out our research work.

References

1. Anjali devi, S.P., Raghavachar M. R.:Magneto hydrodynamic stratified flow past a sphere. Int. J. Engng Sci.20(10), 1169–1177 (1982).
2. Ashish, Tiwari, Satya Deo., Anatoly Filipov.: Effectof the Magnetic field on the hydrodynamic permeability of a Membrane, Colloid Journal.74(4), 515–522 (2012).
3. Chandran, P., Sacheti,N.C., Singh,A.K.,: "Hydromagnetic flow and heat transfer past a continuously moving porous boundary". Int. Comm. Heat Mass Trans.23 (6), 889–898 (1996).
4. Dinesh, P.A., Jayalakshmamma D.V., Chandrashekhar D.V.: Exact solution for viscous fluid flow in porous media with magnetic field, Proceedings of the 6th International Conference on Porous Media and Its Applications in Science and Engineering- ICPM6, July 3–8, Waikoloa, Hawaii (2016).
5. Jayalakshmamma, D.V., Dinesh, P.A.,Sankar M,: Analytical study of creeping flow past a composite sphere: solid core with porous shell in presence of magnetic field. Mapana Journal Science.10 (2), 11–24 (2011).
6. Jayalakshmamma, D.V., Dinesh, P.A., Sankar, M., Chandrashekhar, D.V.: "Flow of conducting fluid on solid core surrounded by porous cylindrical region in presence of transverse magnetic field". Mapana Journal Science.13 (3), 13–29 (2014).
7. Jayalakshmamma, D.V., Dinesh, P.A., M. Sankar., Chandrashekhar D.V.: MHD Effect on Relative Motion of Two Immiscible Liquid Spheres", International Journal of Fluid Dynamics and Material Processing. 10(3), 343–357, (2014).
8. Kyrlidis, A., Brown, R. A., Walker, J.S.: Creeping flow of a conducting fluid past axisymmetric bodies in the presence of an aligned magnetic field. Phys. Fluids.A2, 2230–228 (1990).
9. Pankaj Shukla.: Stokes flow through porous cylindrical particle in cell enclosing a solid cylindrical core, Asian Journal of Current Engineering and Math 2, 59–64 (2013).
10. Pal, D., Talukdar, B.: Unsteady hydromagnetic oscillating flow past a porous medium with suction/injection and slip effects. Int. J. Appl. Math. Mech. 7(15), 58–71 (2011).
11. Raghava, Rao, C.V., Sekhar, T.V.S.: "MHD flow past a circular cylinder-a numerical study". Computational Mechanics. 26, 430–436 (2000).

Numerical Solution of Steady Powell-Eyring Fluid over a Stretching Cylinder with Binary Chemical Reaction and Arrhenius Activation Energy

Seethi Reddy Reddisekhar Reddy and P. Bala Anki Reddy

Abstract The present work addresses the two-dimensional boundary layer flow of a Powell-Eyring fluid over a stretching cylinder with binary chemical reaction and Arrhenius Activation energy. Also, considered Cattaneo-Christov heat flux model in the place of conventional Fourier's law of heat conduction. Suitable transforms lead to strongly nonlinear differential equations, which are solved through R-K method along with shooting scheme. The effects of various parameters are shown graphically on velocity, temperature and concentration fields. The numerical values for skin friction($\sqrt{\mathrm{Re}_x} X C_f/2$), local Nusselt($Nu_x \mathrm{Re}_x^{-1/2} X^{-1}$) and Sherwood numbers($Sh_x \mathrm{Re}_x^{-1/2} X^{-1}$) are reported. A relative revision among the earlier published results and the present results for a special case is found to be in an excellent agreement. Rising the values of thermal relaxation time, reduces the temperature at near the cylinder due to domination of mixed convection in the flow.

Keywords Powell-Eyring fluid · Cattaneo-Christov heat flux · MHD · Arrhenius activation energy

Nomenclature

A	Ratio parameter	v	Velocity component in the r direction (ms^{-1})
B	Total magnetic field	u_e	Free stream velocity
B_0	Magnetic field	U_0	Reference velocity
c	Fluid parameter	x, r	Coordinates along and normal to the stretching cylinder (m)
C	Concentration of the fluid $\left(kmol\, m^{-3}\right)$		
C_0	Reference concentration		

S. R. Reddisekhar Reddy · P. Bala Anki Reddy (✉)
Department of Mathematics, S.A.S., Vellore Institute of Technology, Vellore, India
e-mail: reddisekhar.reddy@vit.ac.in; bala.anki@vit.ac.in

B. Rushi Kumar et al. (eds.), *Applied Mathematics and Scientific Computing*,
Trends in Mathematics, https://doi.org/10.1007/978-3-030-01123-9_28

C_w	Stretching cylinder concentration
C_∞	Concentration of the ambient fluid
c_p	Specific heat at constant pressure
D	Mass diffusion coefficient
E_a	Activation energy ($J\ kg^{-1}\ k^{-1}$)
E	Non-dimensional activation energy
F	Dimensionless velocity
J	Current density
k	Thermal conductivity ($w\ m^{-1}\ k^{-1}$)
k_r	Reaction rate
l	Characteristic length
M	Magnetic parameter
n	Unit less exponent fitted rate constant
Nu_x	Local Nusselt number
Pr	Prandtl number
p	Fluid pressure
Re_x	Local Renolds number
Sc	Schmidt number
T	Temperature of the fluid (K)
T_0	Reference temperature
T_w	Cylinder temperature (K)
T_∞	Temperature of the ambient fluid
u	Velocity component in the x direction (ms^{-1})

Greek symbols

υ	Kinematic viscosity
ζ	Similarity variable
β	Fluid parameter
μ	Dynamic viscosity of the fluid
ρ	Density of the fluid ($kg\ m^{-3}$)
$\delta,\ \varepsilon$	Fluid parameters
Φ	Dimensionless concentration
γ	Curvature perameter
Γ	Chemical reaction parameter
Θ	Dimensionless temperature
σ	Electrical conductivity of the fluid
λ_2	Relaxation time for heat flux
Γ	Chemical reaction rate $\left(kmol\ m^{-3}\right)$
Λ	Non-dimensional thermal relaxation time
τ_w	Surface shear stress ($N\ m^{-2}$)

Subscripts

w	Conditions at the wall
∞	Ambient condition

Superscript

$'$	Differentiation with respect to ζ

1 Introduction

The rheology of non-Newtonian fluid models has attained a great importance in technical and growing industrial applications. A few applications of non-Newtonian fluid can be used as shoe manufacturing, manufacturing lubricants for vehicles, metal extrusion and metal spinning, flexible military suits for soldiers, food and medicine industries. Some empirical models of non-Newtonian fluids are Power-law fluids, Williamson fluids, Rivlin-Ericksen fluids, Powell-Eyring fluids, Casson fluids, Viscoelastic fluids, Maxwell fluid, Jeffrey fluid, Walter's liquid B fluids. Among these the Powell-Eyring model [1–3] is the simplest subclass of the rate type. In this model, reduces the Newtonian behavior for both low shear stress and high shear stress. The mathematical model of Powell-Eyring fluid plays an important role in various natural, geophysical and industrial applications. Such applications include the formation and dispersion of fog, enhanced oil recovery,

designing of many chemical processing equipment, damaging of crops due to freezing, environmental pollution, distribution of temperature and moisture over agricultural fields, thermal insulation, groves of fruit trees, packed bed catalytic reactors and underground energy transport. Akbar and Nadeem [4] investigated the importance of peristaltic flow of Eyring-Powell fluid flow with heat and mass transfer analysis in an endoscope. The steady magnetohydrodynamic (MHD) boundary layer flow of Powell-Eyring nanofluid over a stretching cylinder in the presence of thermal radiation effects was discussed by Hayat et al. [5]. Hayat and Nadeem [6] examined the three-dimensional exponential flow of Powell-Eyring fluid flow over an exponentially stretching surface and also, they explained the impact of variable thermal conductivity, non-Fourier's model, using generalized Fick's law, to inscribe the investigation of heat and mass transfer. The objective of the present paper, a numerical analysis is made of the two-dimensional boundary layer flow of a Powell-Eyring nanofluid over a cylinder with Arrhenius Activation energy and Cattaneo-Christov heat flux model. Some recent efforts in the effect of Cattaneo-Christov heat flux model are labelled in ref. no. [7–9]. Some other applications related to magnetohydrodynamic flow was discussed in [10–17].

2 Mathematical Formulation

We examine the two-dimensional (x, r) hydromagnetic Eyring-Powell fluid flow over a stretching cylinder (see Fig. 1). The flow analysis is explored with Cattaneo-Christov heat flux and Arrhenius Activation Energy. In a coordinate system, x and r are the surface of the geometry and vertical to the cylinder respectively. The stretching velocity of the cylinder is $U_w = U_0 (x/l)$. The temperature and concentration distribution are $T = T_w - T_\infty = T_0 (x/l)$ and $C = C_w =$

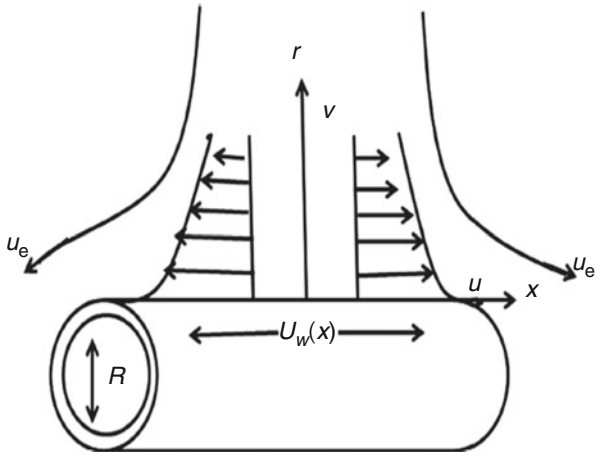

Fig. 1 Physical model of the problem

$C_\infty + C_0\,(x/l)$ respectively. A uniform magnetic field of strength B_0 is implemented in r direction. Here induced magnetic field is neglected due to small magnetic Reynolds number. The system of equations based on [5]. regulating the above considerations are:

$$\frac{\partial\,(rv)}{\partial r} + \frac{\partial\,(ru)}{\partial x} = 0 \tag{1}$$

$$v\frac{\partial u}{\partial r} + u\frac{\partial u}{\partial x} - \left[\begin{array}{l} \frac{\mu}{\rho}\left(\frac{\partial^2 u}{\partial r^2} + \frac{1}{r}\frac{\partial u}{\partial r}\right) + \frac{1}{\rho\beta c}\left(\frac{\partial^2 u}{\partial r^2} + \frac{1}{r}\frac{\partial u}{\partial r}\right) \\ -\frac{1}{6\rho\beta c^3}\left(3\frac{\partial^2 u}{\partial r^2}\left(\frac{\partial u}{\partial r}\right)^2 + \frac{1}{r}\left(\frac{\partial u}{\partial r}\right)^3\right) \end{array}\right] = u_e\frac{du_e}{dx} - \frac{\sigma B_0^2}{\rho}\,(u - u_e) \tag{2}$$

$$v\frac{\partial T}{\partial r} + u\frac{\partial T}{\partial x} + \lambda_2\left[\begin{array}{l} \left(u\frac{\partial u}{\partial x} + v\frac{\partial u}{\partial r}\right)\frac{\partial T}{\partial x} + \left(u\frac{\partial v}{\partial x} + v\frac{\partial v}{\partial r}\right)\frac{\partial T}{\partial r} \\ +2uv\frac{\partial^2 T}{\partial x \partial r} + u^2\frac{\partial^2 T}{\partial x^2} + v^2\frac{\partial^2 T}{\partial r^2} \end{array}\right] = \frac{k}{\rho c_p}\left(\frac{\partial^2 T}{\partial r^2} + \frac{1}{r}\frac{\partial T}{\partial r}\right) \tag{3}$$

$$v\frac{\partial C}{\partial r} + u\frac{\partial C}{\partial x} = D\frac{\partial^2 C}{\partial x^2} - \Gamma^2\,(C - C_\infty)\left(\frac{T}{T_\infty}\right)^n e^{\frac{-E_a}{kT}} \tag{4}$$

The corresponding boundary conditions are:

$$\begin{aligned} &u = U_w = \frac{U_0 x}{l},\ v{=}0,\ T = T_w - T_\infty = T_0\,(x/l)\,,\ C = C_w - C_\infty{=}C_0\,(x/l) \\ &\text{at}\, r = 0 \end{aligned} \tag{5}$$

$$u \to u_e = U_\infty x/l,\ T \to T_\infty,\ C \to C_\infty \text{ as } r \to \infty$$

In Eq. (4), the term $\left(\frac{T}{T_\infty}\right)^n e^{\frac{-E_a}{k^* T}}$ is the modified Arrhenius function in which the Boltzmann constant is $k^* = 8.61 \times 10^{-5} eV/K$ and the range of n is $-1 < n < 1$. We introduce the similarity variables as

$$\begin{aligned} &\zeta = \left(\frac{U_0}{vl}\right)^{\frac{1}{2}}\left(\frac{r^2 - R^2}{2R}\right),\ \xi = (U_w v x)^{\frac{1}{2}} R F(\zeta),\ u = \frac{1}{r}\frac{\partial \xi}{\partial x}, \\ &\Theta\,(\zeta) = \frac{T - T_\infty}{T_w - T_\infty},\quad \Phi\,(\zeta) = \frac{C - C_\infty}{C_w - C_\infty},\quad v = \frac{-1}{r}\frac{\partial \xi}{\partial r} \end{aligned} \tag{6}$$

Equations (2–4) are transformed by means of Eq. (6) and stated below,

$$\begin{aligned} &(1 + 2\gamma\zeta)\,(\varepsilon + 1)\,F''' + FF'' - \left(F'\right)^2 + A^2 + \gamma\,(1 + 2\varepsilon)\,F'' \\ &-\tfrac{4}{3}\varepsilon\delta\gamma\,(1 + 2\gamma\zeta)\left(F''\right)^3 - \varepsilon\delta(1 + 2\gamma\zeta)^2 F'''\left(F''\right)^2 - M^2\left(F' - \mathrm{A}\right) = 0 \end{aligned} \tag{7}$$

$$(1 + 2\gamma\zeta)\,\Theta'' + 2\gamma\Theta' + \mathrm{Pr}\left(F\Theta' - F'\Theta\right) - \Lambda\,\mathrm{Pr}\left(\begin{array}{l} F^2\Theta'' - FF'\Theta' \\ +F'^2\Theta - FF''\Theta \end{array}\right) = 0 \tag{8}$$

$$(1{+}2\gamma\zeta)\,\Phi'' + 2\gamma\Phi' + Sc\left(F\Phi' - F'\Phi\right) - Sc\Gamma\Phi[1{+}\Theta\,(\Theta_w{-}1)]^n e^{\frac{-E}{1+\Theta(\Theta_w - 1)}} = 0 \tag{9}$$

With the boundary conditions are:

$$\begin{aligned} &F'(0) = 1,\ F(0) = 0,\ \Theta(0) = 1,\ \Phi(0) = 1 \\ &F(\infty) = A,\ \Theta(\infty) = 0,\ \Phi(\infty) = 0 \end{aligned} \tag{10}$$

The non-dimensional parameters which are expressed as:

$$\begin{aligned} &\delta = \frac{U_0^3 x^2}{2\nu l^3 c^2},\ \varepsilon = \frac{1}{\mu\beta c},\ \gamma = \left(\frac{l\nu}{U_0 R^2}\right)^{1/2},\ M = \left(\frac{\sigma B_0^2 l}{\rho U_0}\right)^{1/2},\ A = \frac{U_\infty}{U_0} \\ &\Pr = \frac{\mu c_p}{k},\ \ \Lambda = \frac{\lambda_2 U_0}{l},\ Sc = \frac{\nu}{D},\ \Gamma = \frac{k_0^2 l}{U_0},\ E = \frac{E_a}{k^* T_\infty},\ \Theta_w = \frac{T_w}{T_\infty} \end{aligned} \tag{11}$$

Skin friction(C_f), local Nusselt(Nu_x) and Sherwood numbers(Sh_x) are represented as

$$C_f = \frac{2\tau_w}{\rho U_w^2},\ Nu_x = \frac{x q_w}{k(T_w - T_\infty)} \quad \text{and } Sh_x = \frac{x J_w}{D(C_w - C_\infty)}. \tag{12}$$

$$\begin{aligned} &\text{where } \tau_w = \mu\left(\frac{\partial u}{\partial r} + \frac{1}{\beta c}\left(\frac{\partial u}{\partial r}\right) - \frac{1}{6\beta c^3}\left(\frac{\partial u}{\partial r}\right)^3\right)_{r=R},\ \ q_w = -k\left(\frac{\partial T}{\partial r}\right)_{r=R} \\ &\text{and } J_w = -D\left(\frac{\partial C}{\partial r}\right)_{r=R}. \end{aligned} \tag{13}$$

The dimensionless Skin friction, local Nusselt and Sherwood numbers are respectively formed as

$$\begin{aligned} &C_f \frac{\sqrt{\mathrm{Re}_x} X}{2} = (\varepsilon + 1) F''(0) - \frac{1}{3}\varepsilon\delta\left(F''(0)\right)^3,\ Nu_x \mathrm{Re}_x^{-1/2} X^{-1} = -\Theta'(0) \\ &\text{and } Sh_x \mathrm{Re}_x^{-1/2} X^{-1} = -\Phi'(0) \end{aligned} \tag{14}$$

where $\mathrm{Re}_x = \frac{l U_w}{\nu}$ and $X = \sqrt{x/l}$

3 Results and Discussions

In the present study, $\varepsilon = 0.4$, $\delta = 0.5$, $M = 0.2$, $A = 0.3$, $\Theta_w = 1.5$, $n = 0.3$, $E = 1$, $Sc = 1$, $Pr = 0.7$, $\Lambda = 0.5$, $\gamma = 0.2$, $\Gamma = 2.0$ are considered as default values. The effect of ratio of velocities is provided in Fig. 2. It is important to notice that improving the values of A, maximize the velocity profile. Actually, improving the values of ratio velocities means, speed up the flow, which tends to boost up the velocity profile. The characteristics of M on velocity profile is described in Fig. 3. It is recorded that, we increasing the magnetic parameter (M), decreases the Velocity profile. Physically when the Lorentz force increases for large values of M due to resistive force, which tends to the velocity of the fluid reduces. Figure 4 lays out the influence of ϵ on velocity profile. It can be seen that the large values of ϵ the velocity profile increases. This is due to the less viscous which tends to increasing the fluid velocity. Figure 5 elucidates the variation of fluid parameter δ on the velocity profile.

It is found that the velocity of the fluid profile reduces when δ is large. The effect of thermal relaxation time on temperature profile is plotted in Fig. 6. By increasing the thermal relaxation time, reduces the temperature at near the cylinder due to domination of mixed convection in the flow. Rising the values of thermal relaxation parameter takes long time to transfer the heat to its neighbouring particles. Figure 7 elucidates the variation of chemical reaction parameter on concentration profile. It is found that the concentration profile reduces for an increasing the values of chemical reaction parameter. Physically large values of a chemical reaction which generates the fluid species more inefficiently. Variation of non-dimensional activation energy on concentration profile is sketched in Fig. 8. It is noticed that the mass transfer rate increases for large values of E. Variation of temperature ratio parameter on concentration profile is drawn in Fig. 9. It is observed that the mass transfer rate decreases for large values of temperature ratio parameter.

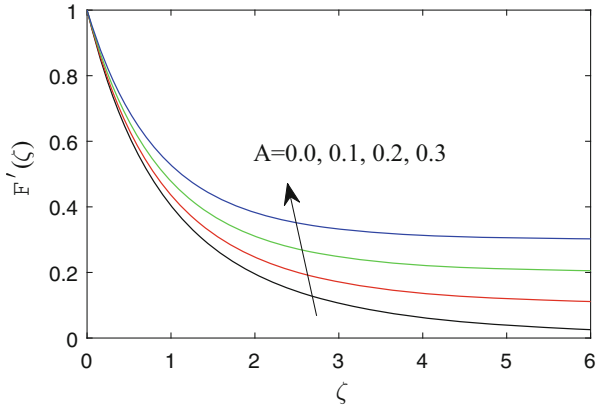

Fig. 2 $F'(\zeta)$ for diverse values of A

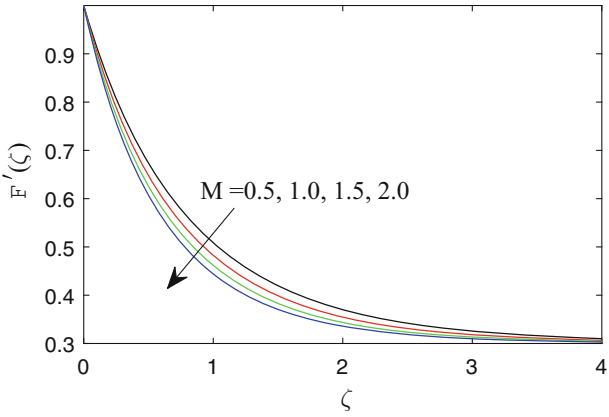

Fig. 3 $F'(\zeta)$ for diverse values of M

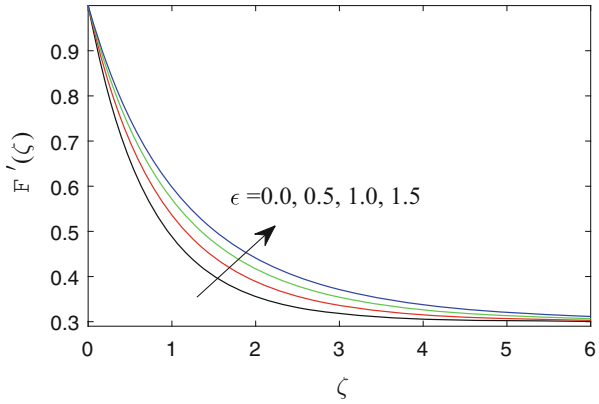

Fig. 4 $F'(\zeta)$ for diverse values of ϵ

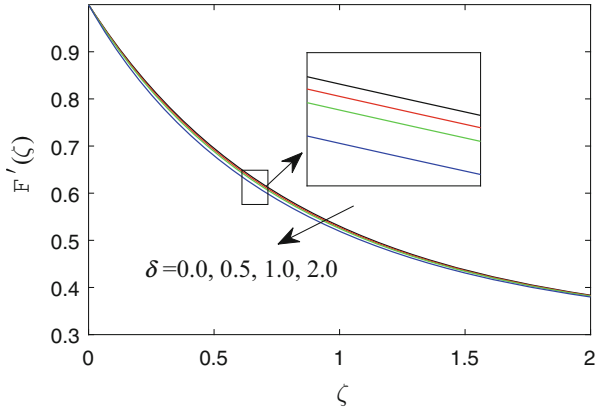

Fig. 5 $F'(\zeta)$ for diverse values of δ

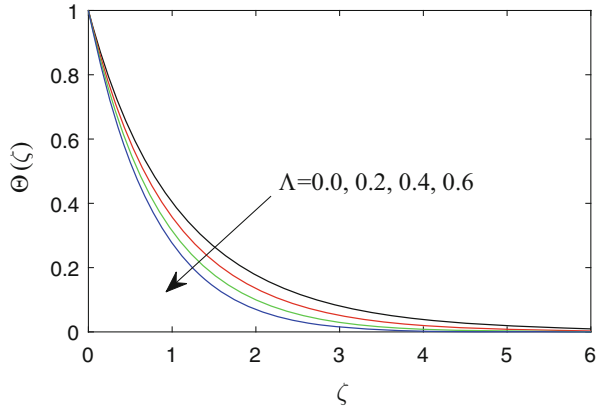

Fig. 6 $\Theta(\zeta)$ for diverse values of Λ

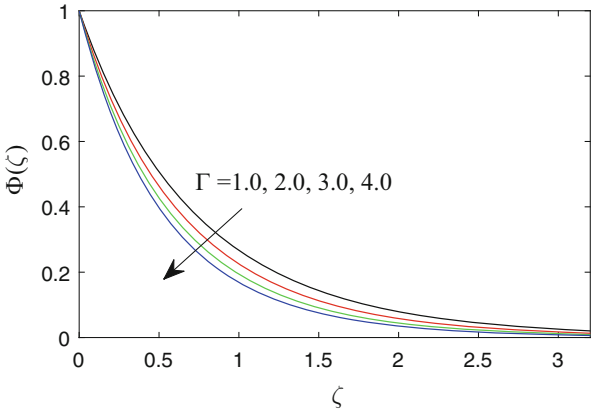

Fig. 7 $\Phi(\zeta)$ for diverse values of Γ

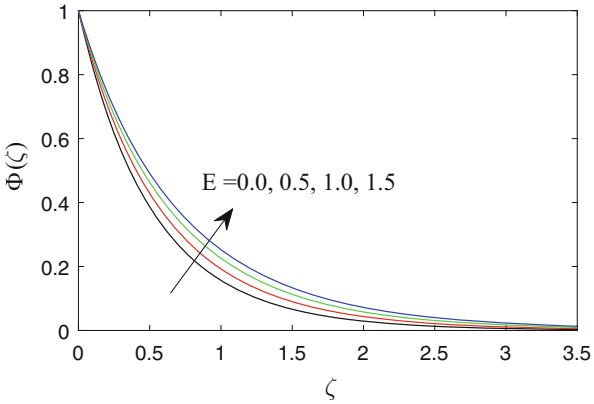

Fig. 8 $\Phi(\zeta)$ for diverse values of E

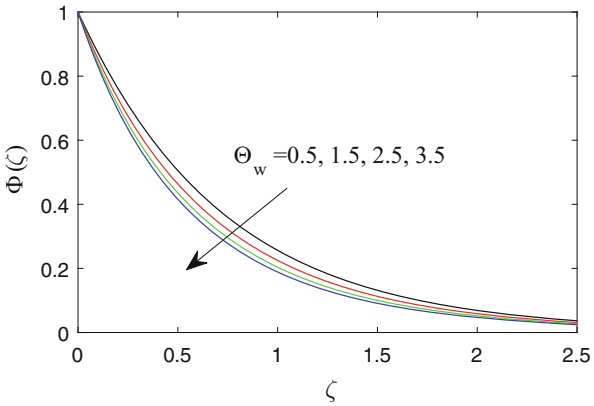

Fig. 9 $\Phi(\zeta)$ for diverse values of Θ_w

Table 1 Numerical values of $\sqrt{\mathrm{Re}_x}XC_f/2$ for different parameters

M	γ	δ	ε	A	$\sqrt{Re_x}XC_f/2$
0.2	0.2	0.5	0.4	0.3	−1.1448
0.4	0.2	0.5	0.4	0.3	−1.2059
0.2	0.6	0.5	0.4	0.3	−1.2988
0.2	0.2	1.0	0.4	0.3	−1.1329
0.2	0.2	0.5	0.6	0.3	−1.2280
0.2	0.2	0.5	0.4	0.5	−0.8904

Table 2 Comparison values of $F''(0)$ and $\sqrt{Re_x}XC_f/2$ for different values of ϵ and δ

δ	ε	$F''(0)$			$\sqrt{Re_x}XC_f/2$		
		Hayath et al. [5]	Javed et al. [1]	Present	Hayath et al. [5]	Javed et al. [1]	Present
0	0	−1	−1	−1	−1	−1	−1
	0.2	−0.91287	−0.9131	−0.912871	−1.09545	−1.0954	−1.0954
	0.4	−0.84516	−0.8452	−0.845154	−1.18322	−1.1832	−1.1832
0.3	0	−1	−1	−1	−1	−1	−1
	0.2	−0.92218	−0.9222	−0.922192	−1.09092	−1.0909	−1.0909
	0.4	−0.85804	−0.8580	−0.858035	−1.17598	−1.1776	−1.1760
0.6	0	−1	−1	−1	−1	−1	−1
	0.2	−0.93221	−0.9322	−0.932209	−1.08625	−1.0862	−1.0862
	0.4	−0.87252	−0.8725	−0.872512	−1.16838	−1.1684	−1.1684

Table 3 Local Nusselt number $-\Theta'(0)$ for diverse parameters

M	γ	δ	ε	Pr	Λ	Θ_w	E	Γ	$-\Theta'(0)$
0.2	0.2	0.5	0.4	0.7	0.5	1.5	1.0	2.0	1.224010
0.4	0.2	0.5	0.4	0.7	0.5	1.5	1.0	2.0	1.213033
0.2	0.6	0.5	0.4	0.7	0.5	1.5	1.0	2.0	1.369423
0.2	0.2	1.0	0.4	0.7	0.5	1.5	1.0	2.0	1.220884
0.2	0.2	0.5	0.6	0.7	0.5	1.5	1.0	2.0	1.236414
0.2	0.2	0.5	0.4	1.0	0.5	1.5	1.0	2.0	1.488515
0.2	0.2	0.5	0.4	0.7	0.6	1.5	1.0	2.0	1.272492
0.2	0.2	0.5	0.4	0.7	0.5	2.0	1.0	2.0	1.224010
0.2	0.2	0.5	0.4	0.7	0.5	1.5	1.5	2.0	1.224010
0.2	0.2	0.5	0.4	0.7	0.5	1.5	1.0	2.5	1.224010

The numerical values of $\sqrt{Re_x}XC_f/2$ for different parameters are presented in Table 1. The magnitude of skin friction increases with an increasing of δ and A. However, it reduces when increasing M, γ and ε. Table 2 shows that the comparison the present values of $F''(0)$ and $\sqrt{Re_x}XC_f/2$ with the existed literature for better accuracy. Tables 3 and 4 provides the impact of numerous physical parameters on $-\Theta'(0)$ and $-\Phi'(0)$ at the cylindrical surface. It is revealed that $-\Theta'(0)$ and $-\Phi'(0)$ increases for fluid parameters when increasing γ and ε. However, it reduces when M and δ increases. The rate of heat transfer coefficient $(-\Theta'(0))$ increases and rate of mass transfer coefficient $(-\Phi'(0))$ decreases with an increasing the thermal relaxation time and Prandtl number.

Table 4 Local Sherwood number $-\Phi'(0)$ for diverse parameters

M	γ	δ	ε	Pr	Λ	Θ_w	E	Γ	$-\Phi'(0)$
0.2	0.2	0.5	0.4	0.7	0.5	1.5	1.0	2.0	2.272187
0.4	0.2	0.5	0.4	0.7	0.5	1.5	1.0	2.0	2.267324
0.2	0.6	0.5	0.4	0.7	0.5	1.5	1.0	2.0	2.440279
0.2	0.2	1.0	0.4	0.7	0.5	1.5	1.0	2.0	2.270477
0.2	0.2	0.5	0.6	0.7	0.5	1.5	1.0	2.0	2.277377
0.2	0.2	0.5	0.4	1.0	0.5	1.5	1.0	2.0	2.263917
0.2	0.2	0.5	0.4	0.7	0.6	1.5	1.0	2.0	2.270577
0.2	0.2	0.5	0.4	0.7	0.5	2.0	1.0	2.0	2.400595
0.2	0.2	0.5	0.4	0.7	0.5	1.5	1.5	2.0	2.108908
0.2	0.2	0.5	0.4	0.7	0.5	1.5	1.0	2.5	2.397559

4 Conclusion

- Velocity decreases with an increase in magnetic parameter and the Eyring-Powell fluid parameter.
- Rising the values of thermal relaxation time, reduces the temperature at near the cylinder due to domination of mixed convection in the flow.
- With the larger values of non-dimensional activation energy and curvature parameters, the concentration distribution decreases.
- The rate of heat transfer coefficient increases and rate of mass transfer coefficient decreases with an increase the thermal relaxation time.
- Skin friction coefficient increases with an increasing in Eyring-Powell fluid parameter δ and ratio parameter.

References

1. Javed, T., Ali, N., Abbas, Z., Sajid, M.: Flow of an Eyring-Powell non-Newtonian fluid over a stretching sheet. Chem. Eng. Commun. **200(3)**, 327–336 (2013)
2. Srinivas Reddy, C., Kishan, N., Madhu M.: Finite element analysis of Eyring-Powell Nano fluid over an exponential stretching sheet. Int. J. Appl. Comput. Math, **4(8)**, 1–13 (2018)
3. Adesanya, S.O., Ogunseye, H.A., Jangili S.: Unsteady squeezing flow of a radiative Eyring-Powell fluid channel flow with chemical reactions. Int. J. Therm. Sci. **125**, 440–447 (2018)
4. Akbar, N.S., Nadeem, S.: Characteristics of heating scheme and mass transfer on the peristaltic flow for an Eyring–Powell fluid in an endoscope. Int. J. Heat Mass Transf. **55**, 375–383 (2012)
5. Hayat, T., Gull, N., Farooq, M., Ahmad, B.: Thermal radiation effect in MHD flow of Powell-Eyring nanofluid induced by a stretching cylinder. J. Aerosp. Eng. **29(1)**, 1–13 (2016)
6. Hayat, T., Nadeem, S.: Aspects of developed heat and mass flux models on 3D flow of Eyring-Powell fluid. Results Phys. **7**, 3910–3917 (2017)
7. Oyelakin, I.S., Mondal, S., Sibanda, P.: Cattaneo-Christov Nanofluid flow and heat transfer with variable properties over a vertical cone in a porous medium. Int. J. Appl. Comput. Math. **3(1)**, 1019–1034 (2017)

8. Dogonchi, A.S., Ganji, D.D.: Impact of Cattaneo–Christov heat flux on MHD nanofluid flow and heat transfer between parallel plates considering thermal radiation effect. J. Taiwan Inst. Chem. Eng. 1–12 (2017)
9. Malik, R., Khan, M., Mushtaq M.: Cattaneo-Christov heat flux model for Sisko fluid flow past a permeable non-linearly stretching cylinder. J. Mol. Liq. **222**, 430–434 (2016)
10. Bala Anki Reddy, P., Bhaskar Reddy, N., Suneetha, S.: Radiation effects on MHD flow past an exponentially accelerated Isothermal vertical plate with uniform mass diffusion in the presence of Heat Source. J. Appl. Fluid Mech. **5(3)**, 119–126 (2012)
11. EL-Kabeir, S. M. M., Ali J. Chamkha, Rashad, A. M.: Heat and mass transfer by MHD stagnation-point flow of a power-law fluid towards a stretching surface with radiation, chemical reaction and Soret and Dufour effects. Int. J. Chem. React. Eng. **8**, 1–18 (2010)
12. Bala Anki Reddy, P.: Magnetohydrodynamic flow of a Casson fluid over an exponentially inclined permeable stretching surface with thermal radiation and chemical reaction. Ain Shams Eng. J. **7**, 593–602 (2016)
13. Rashad, A.M., Modather M., Abdou, M., Chamkha A.J.: MHD free convective heat and mass transfer of a chemically-reacting fluid from radiate stretching surface embedded in a saturated porous medium. Int. J. Chem. React. Eng. **9**, 1–15 (2011)
14. Bala Anki Reddy, P., Suneetha, S.: Effects of homogeneous– heterogeneous chemical reaction and slip velocity on MHD stagnation flow of a micropolar fluid over a permeable stretching/shrinking surface embedded in a porous medium. Front. Heat Mass Transf. **8(24)**, 1–11 (2017)
15. Reddy, S.R.R., Bala Anki Reddy, P., Suneetha S.: Magnetohydrodynamic flow of blood in a permeable inclined stretching surface with viscous dissipation, non-uniform heat source/sink and chemical reaction. Front. Heat Mass Transf. **10(22)**, 1–10 (2018)
16. Chamkha, A.J., Rashad, A. M.: Unsteady heat and mass transfer by MHD mixed convection flow from a rotating vertical cone with chemical reaction and Soret and Dufour effects. Can. J. Chem. Eng. **92(4)**, 758–767 (2014)
17. Mallikarjuna, B., Rashad, A. M., Chamkha, A.J. Hariprasad Raju, S.: Chemical reaction effects on MHD convective heat and mass transfer flow past a rotating vertical cone embedded in a variable porosity regime. Afrik. Mate. **27(3)**, 646–665 (2016)

Effect of Homogeneous-Heterogeneous Reactions in MHD Stagnation Point Nanofluid Flow Toward a Cylinder with Nonuniform Heat Source or Sink

T. Sravan Kumar and B. Rushi Kumar

Abstract The study investigates the effect of homogeneous-heterogeneous reactions in the stagnation point nanofluid flow toward a cylinder. In the presence of uniform magnetic field, thermal radiation, and non uniform heat source or sink. As per the geometry of the flow configuration, the conservation laws are transformed into a nonlinear model. Using the appropriate analogue transformations, the resultant equations are employing RK-4th order approach along with shooting technique to derive closed-form solutions for momentum, angular velocity, temperature, and concentration fields as well as skin friction, local Nusselt number, and Sherwood number. It is observed that heat generation parameter leads to enhance the temperature distribution. The concentration boundary layer thickness decreases for larger homogeneous reaction rate parameter.

Keywords MHD · stagnation point · homogeneous-heterogeneous reactions · nanofluid flow · non-uniform heat source/sink

1 Introduction

The heat and mass transfer is affected by nanofluid over a stretching sheet with thermal radiation. It has tremendous applications in many areas such as stretching of plastic film, industrialization of polymer sheet, crystal growing, electronic chips, filaments and wires, glass blowing, cooling of metallic sheet, artificial fibers, paper production, metallurgical processes, tinning of copper wires, and many others which can be found in Pop and Ingham [1] and Vafai [3]. Nanofluid is a kind of heat and

T. Sravan Kumar
Department of Mathematics, VIT, Vellore, Tamil Nadu, India
e-mail: t.sravankumar2014@vit.ac.in

B. Rushi Kumar (✉)
Department of Mathematics, School of Advanced Sciences, Vellore Institute of Technology, Vellore, Tamil Nadu, India
e-mail: rushikumar@vit.ac.in

B. Rushi Kumar et al. (eds.), *Applied Mathematics and Scientific Computing*, Trends in Mathematics, https://doi.org/10.1007/978-3-030-01123-9_29

mass transfer fluids that contains base fluid and nanoparticles. These nanoparticles are dissolved in the base fluid; it might be water or natural dissolvable.

Nanoparticles used as a part of nanofluids are normally formed metals, oxides, nitriles, and carbides. Base liquid is normally a conductive liquid, for example, water engine oil and $C_2H_6O_2$. Effective thermal conductivity of ethylene glycol is stretched out by up to 40% for a nanofluid including $C_2H_6O_2$ containing around 0.3% vol. copper nanoparticles of mean width <10 nm, analyzed by Choi [4] and Choi et al. [5]. Das et al. [6] examined a two- to fourfold rise in thermal conductivity development for nanofluid containing TiO_2-water or Al_2O_3-water nanoparticles over a small temperature varying from 21° to 51 °C. To study the effects of the concentration and size variation of the nanoparticles, the concentration and size are varied from 0% to 5% and 25 to 100 nm, respectively, over the Reynolds number range of 250–1500 for Au-water nanofluid. Lawrence and Crane [7] investigated the Brownian motion, thermophoresis, and other thermophysical properties of nanofluids. Eastman et al. [8] displayed that an improvement in the thermal conductivity relies on upon the shape, estimate, and thermal attributes of nanoparticles. The existing literature shown that ensures the enlargement of nanoparticles in the base fluid may accomplish an essentially reducing in the heat transfer; for comprehensive review, see (Makinde and Aziz [9], Khan and Pop [10], Nadeem and Haq [11], Nadeem et al. [12], and Sheikholeslami et al. [13]).

The investigation of magnetohydrodynamics with heat and mass transfer within the sight of thermal radiation effects has gained a great consideration due to its diversified applications involved in designs of the fins, steel rolling, manufacturing engineering and various propulsion devices for aircraft, in cooling of reactors in geophysics and astrophysicist. It is associated with examined stellar and solar structures, radio spread by the ionosphere, etc. It is because of the interaction of electromagnetic fields and electrically conducting fluids. Conducting fluid moves through the magnetic field and an electric field, and therefore a current may be started, and in this manner, the current interacts with the magnetic field to make a body force on the fluid. Such interactions occur both in nature and in new man-made devices. In the research center, numerous devices have been made based on the principle of the magnetohydrodynamic interaction directly, such as impetus units and power generators or which include liquid electromagnetic field interactions, for example, electrical discharges, MHD pumps, electron beam dynamics, MHD bearing, traveling wave tubes, etc. Magnetohydrodynamic convective flow issues are very imperative, and some of the works on chemical engineering, planetary and stellar magnetospheres, and aeronautics can be found in (Ellahi [14], Ali [15], Zeeshan et al. [16], Nadeem et al. [17], Noghrehabadi et al. [18], and Mabood et al. [19]).

Most chemically reacting systems involve both heterogeneous and homogenous reactions (biochemical systems, catalysis, and combustion). The simple combustion model helps us to recognize the combustion phenomenon in lots of complicated engineering features such as in rocket engines and aircraft. A model for isothermal heterogeneous-homogeneous reactions in the boundary layer flow of a viscous fluid past a flat plate was presented by Merkin [20].

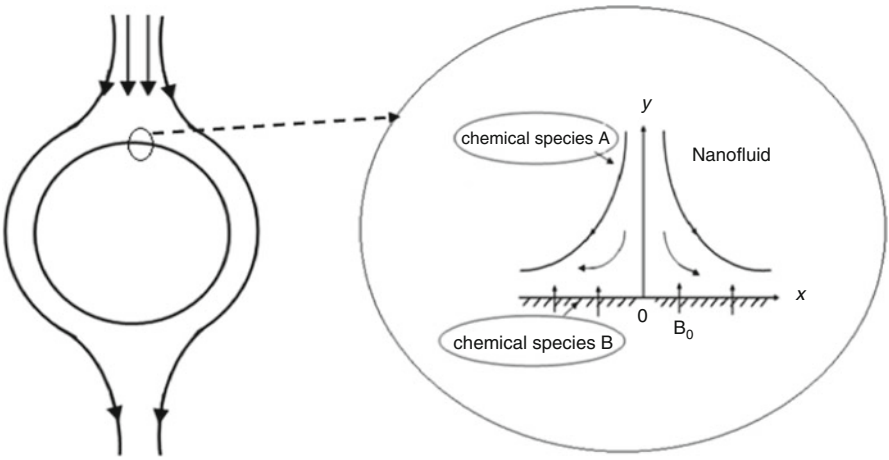

Fig. 1 Schematic nanofluid flow model

In this paper, we have talked about heat and mass transfer examinations; nanofluid model is seen to be decisively applicable to various suitable conditions in wings of polymer taking care of organizations, biomechanics, etc. It is assumed that a simple homogeneous-heterogeneous reaction model as shown in Fig. 1.

2 Mathematical Analysis

Consider a steady, laminar, boundary layer flow of a nanofluid near toward the stagnation point region of a 2D cylinder in the presence of homogeneous-heterogeneous reactions. Uniform magnetic field, thermal radiation, and non uniform heat source or sink are account. The x-coordinate is taken along the sheet, and the y-coordinate is measured normal to the sheet. An external magnetic field of constant strength B_0 is applied normal to the sheet. All the flow properties are assumed to be constant except the smaller variations in density caused by the temperature differences of force vector in the fluid region. The electric field is neglected. We additionally considered a simplest model of homogeneous reaction and heterogeneous reaction involving two chemical species A and B in a boundary layer flow expressed by Chaudhary and Merkin [2] and Merkin [20]:

$$A + 2B \rightarrow 3B, rate = k_1 c_a c_b^2 \tag{1}$$

$$A \rightarrow B, rate = k_s c_a \tag{2}$$

The governing equations describing flow pattern are as follows:

$$\frac{\partial u}{\partial x}+\frac{\partial v}{\partial y}=0 \tag{3}$$

$$u\frac{\partial u}{\partial x}+v\frac{\partial u}{\partial y}=-\frac{1}{\rho}\frac{\partial p}{\partial x}+U_\infty\frac{\partial U_\infty}{\partial x}+\nu\left(\frac{\partial^2 u}{\partial x^2}+\frac{\partial^2 u}{\partial y^2}\right)+\frac{\sigma B_0^2}{\rho}(U_\infty-u) \tag{4}$$

$$u\frac{\partial T}{\partial x}+v\frac{\partial T}{\partial y}=\frac{\kappa}{\rho C_P}\left(\frac{\partial^2 T}{\partial x^2}+\frac{\partial^2 T}{\partial y^2}\right)-\frac{1}{\rho C_P}\frac{\partial q_r}{\partial y}+\frac{q'''}{\rho C_P}$$
$$+\tau\left[D_B\left(\frac{\partial C_b}{\partial x}\frac{\partial T}{\partial x}+\frac{\partial C_b}{\partial y}\frac{\partial T}{\partial y}\right)+\frac{D_T}{T_\infty}\left(\left(\frac{\partial T}{\partial x}\right)^2+\left(\frac{\partial T}{\partial y}\right)^2\right)\right] \tag{5}$$

$$u\frac{\partial C_a}{\partial x}+v\frac{\partial C_a}{\partial y}=D_A\left(\frac{\partial^2 C_a}{\partial x^2}+\frac{\partial^2 C_a}{\partial y^2}\right)-k_1 C_a C_b^2 \tag{6}$$

$$u\frac{\partial C_b}{\partial x}+v\frac{\partial C_b}{\partial y}=D_B\left(\frac{\partial^2 C_b}{\partial x^2}+\frac{\partial^2 C_b}{\partial y^2}\right)+\frac{D_T}{T_\infty}\left(\frac{\partial^2 T}{\partial x^2}+\frac{\partial^2 T}{\partial y^2}\right)+k_1 C_a C_b^2 \tag{7}$$

Associate boundary conditions (4)–(7) are given by:

$$u=U_w=ax,\quad v=0,\quad T=T_w,\quad D_A\frac{\partial C_a}{\partial y}=k_s C_a,\quad D_B\frac{\partial C_b}{\partial y}=-k_s C_a,\quad \text{at}\quad y=0$$
$$u\to U_\infty=bx,\qquad T\to T_\infty,\qquad C_a\to C_\infty,\qquad C_b\to 0,\quad \text{as } y\to\infty \tag{8}$$

The radiative heat flux for an optically thick fluid can be taken from Rosseland approximation, and its formula is derived from the diffusion concept of radiative heat transfer in the following way:

$$q_r=-\frac{4\sigma^*}{3K^*}\frac{\partial T^4}{\partial y} \tag{9}$$

$$q'''=\left[A^*(T_w-T_\infty)f'(\eta)+B^*(T-T_\infty)\right]\left(\frac{\kappa U_w(x)}{x\nu}\right) \tag{10}$$

where A^* is the space dependent and B^* is the temperature-dependent parameter.

Since θ is a dimensionless temperature of the nanofluids defined as $\theta=\frac{(T-T_w)}{(T_w-T_\infty)}$, T^4 appeared in Eq. (9):

$$T^4=(1+(\theta_w-1)\theta)^4\,T_\infty^4, \tag{11}$$

where $\theta=\frac{T_w}{T_\infty}$ and is the wall temperature excess ratio parameter.

The similarity components are also introduced by

$$u = axf'(\eta), v = -\sqrt{a\nu}f(\eta), \xi(\eta) = \frac{C_a}{C_\infty}, \phi(\eta) = \frac{C_b}{C_\infty}, \eta = \sqrt{\frac{a}{\nu}}y,$$
$$\psi = \sqrt{a\nu}xf(\eta) \quad (12)$$

An equation due to mass conservation (1) is fulfilled by presenting a stream function ψ with $u = \frac{\partial \psi}{\partial y}$ and $u = -\frac{\partial \psi}{\partial x}$.

Substituting Eqs. (9)–(12) into Eqs. (4) to (7) transforms into the accompanying nonlinear ODEs.

$$f''' + ff'' - f'^2 + A^2 + M\left(A - f'\right) = 0 \quad (13)$$

$$\left(\left(\frac{1}{Pr} - R\left[1 + (\theta_w - 1)\theta\right]^3\right)\theta'\right)' + f\theta' + Nb\phi'\theta' + Nt\theta'^2$$
$$+\frac{1}{Pr}\left(A^* f' + B^*\theta\right) = 0 \quad (14)$$

$$\frac{1}{Sc_A}\xi'' + f'\xi' - K\xi\phi^2 = 0 \quad (15)$$

$$\frac{1}{\epsilon Sc_A}\left(\phi'' + \frac{Nt}{Nb}\theta''\right) + f\phi' + K\xi\phi^2 = 0 \quad (16)$$

The corresponding boundary conditions become

$$f(0) = 0, f'(0) = 1, \theta(0) = 1, \xi'(0) = K_s\xi(0), \phi'(0) = -\epsilon K_s\xi(0)$$
$$f'(\infty) = A, \theta(\infty) = 0, \xi(\infty) = 1, \phi(\infty) = 0 \quad (17)$$

The dimensionless constants appearing in Eqs. (13) and (16) are defined as follows: $Pr = \frac{\nu}{\alpha}$, $M = \frac{\sigma B_0^2}{a\rho}$, $A = \frac{b}{a}$, $Nb = \frac{\tau D_B C_\infty}{\nu}$, $Nt = \frac{\tau \Delta T D_T}{\nu T_\infty}$, $K = \frac{k_1 C_\infty^2}{a}$, $Sc_A = \frac{\nu}{D_A}$, $K_s = \frac{k_s}{D_A}\frac{1}{\sqrt{\frac{a}{\nu}}}$, $\epsilon = \frac{D_A}{D_B}$, $R = \frac{16\sigma^* T_\infty^3}{3K^*\kappa}$.

It is expected that the diffusion coefficient of chemical species A and B is of a comparable size which leads us to make a further assumption that the diffusion coefficients D_A and D_B are equal, i.e., $\epsilon = 2$ [2]. This assumption leads to the following relation:

$$\xi(\eta) + \theta(\eta) = 1 \quad (18)$$

Equations (15) and (16) under this assumption reduced to

$$\frac{1}{Sc_A}\xi'' + f'\xi' - K\xi\left(1 - \xi\right)^2 = 0 \quad (19)$$

and are subject to the boundary conditions

$\xi'(0) = K_s\xi(0), \xi(\infty) = 1$

3 Results and Discussion

The nonlinear ODEs (13)–(16) with the boundary condition equation (17) have been solved numerically using the shooting technique with fourth-order RK method. The influence of various governing dimensionless parameters is examined, namely, the magnetic parameter (M), Prandtl number (Pr), wall temperature excess ratio parameter (θ_w), radiation parameter (R), Brownian motion parameter (Nb), thermophoresis parameter (Nt), homogeneous reaction rate (K), ratio diffusion constants (ϵ), and Schmidt number (Sc) in transit of flow field $f'(\eta)$, $\theta(\eta)$, $\xi(\eta)$ which are analyzed and discussed through graphs, which are plotted in Figs. 2, 3, 4, 5, 6, 7, 8, 9, 10, and 11. Throughout the computations it is considered that $Pr = 1$, $Nt = 0.05$, $Nb = 1$, $K = 1$, $Sc = 1$, $\epsilon = 1.5$, $A^* = 0.1$, $B^* = 0.1$, $M = 1$, $\theta_w = 1.5$, $R = 0.5$, and $A = 0.1$. The comparative results are reported. The results obtained from this study are very good in agreement. Gives the information of $f''(0)$, $-\theta'(0)$, and $\xi'(0)$ for different values of M, R, θ_w, K, and K_s.

Figure 2 depicts the variation in velocity of nanofluid with respect to magnetic field parameter. It is observed that an increase in M depreciates the velocity profiles of the nanofluid flow. It is because of the physical occurrence that the application of transverse magnetic lines will result in a Lorentz force similar to drag force, which leads to restricting the fluid flow and therefore reducing its velocity. And it is even noticed that the momentum boundary layer thickness decreases with increasing value of M. The effect of the magnetic parameter on the temperature field is shown in Fig. 3; it is noticed that the temperature increases with an increment of the

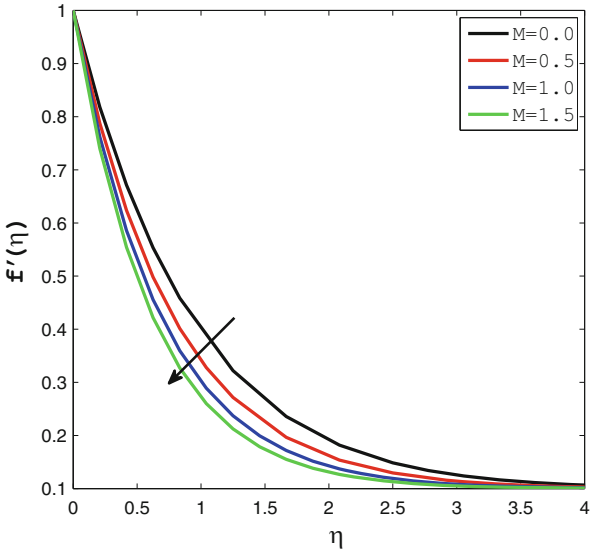

Fig. 2 Influence of M on velocity

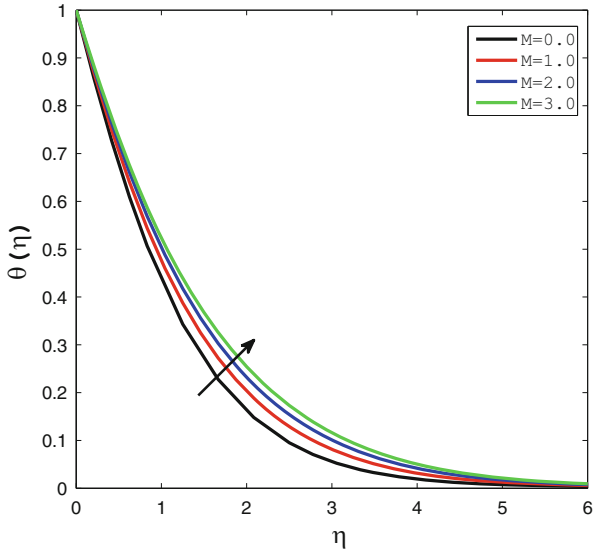

Fig. 3 Influence of M on temperature

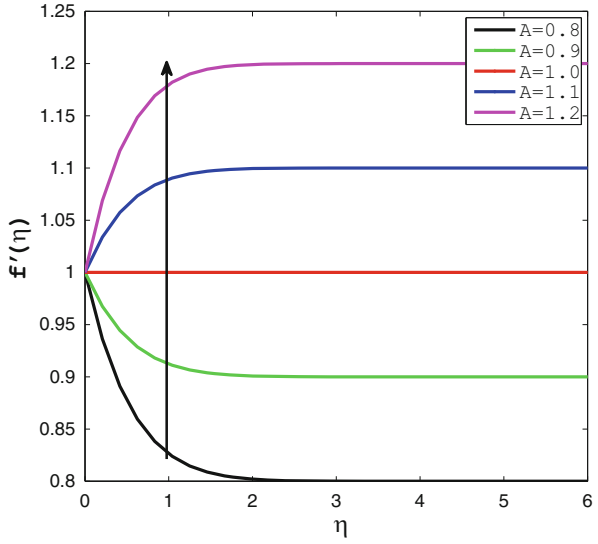

Fig. 4 Influence of A on velocity

magnetic parameter. Owing to the nanofluid has thick thermal boundary layer and also temperature increments in the nanofluid due to its high thermal conductivity. The influence of ratio parameter A on velocity profile is displayed in Fig. 4; it is noticed that velocity profiles increase for $A > 0$ and for $A < 1$, the momentum

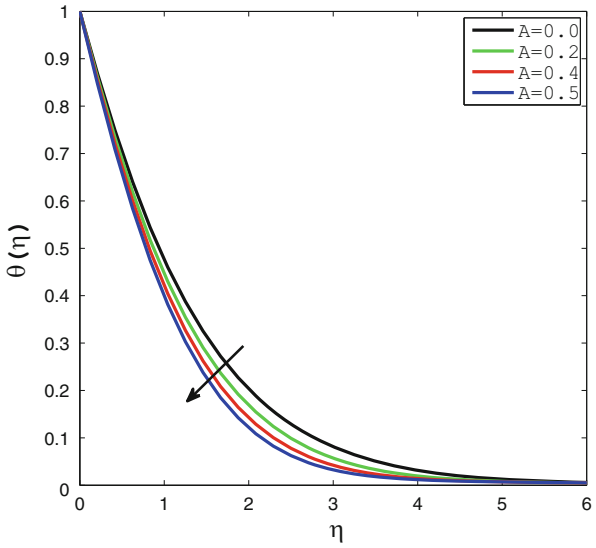

Fig. 5 Influence of A on temperature

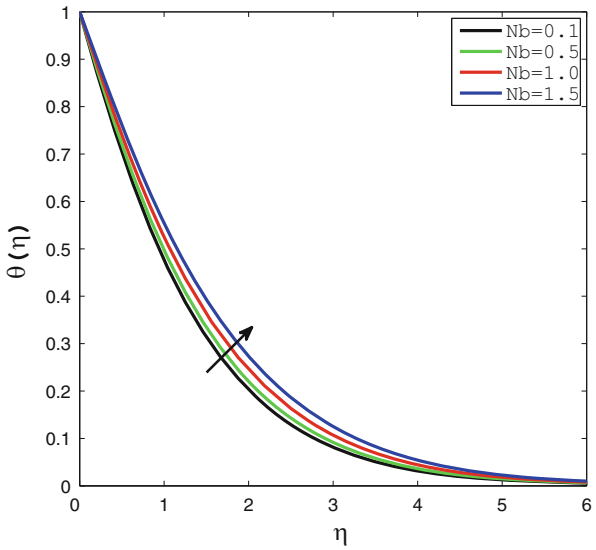

Fig. 6 Influence of Nb on temperature

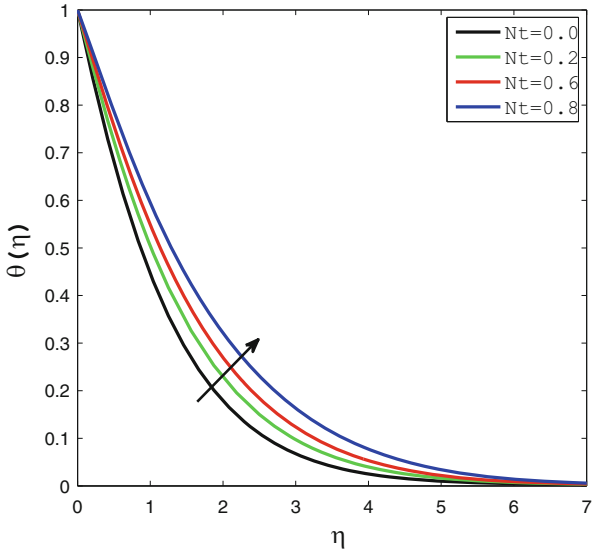

Fig. 7 Influence of Nt on temperature

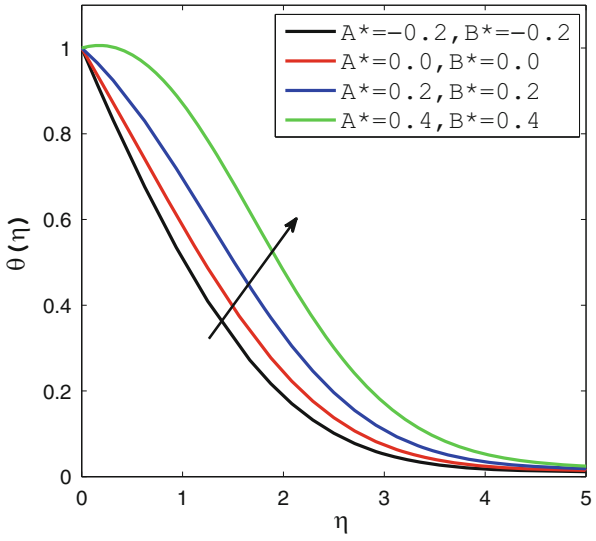

Fig. 8 Influence of A^* and B^* on temperature

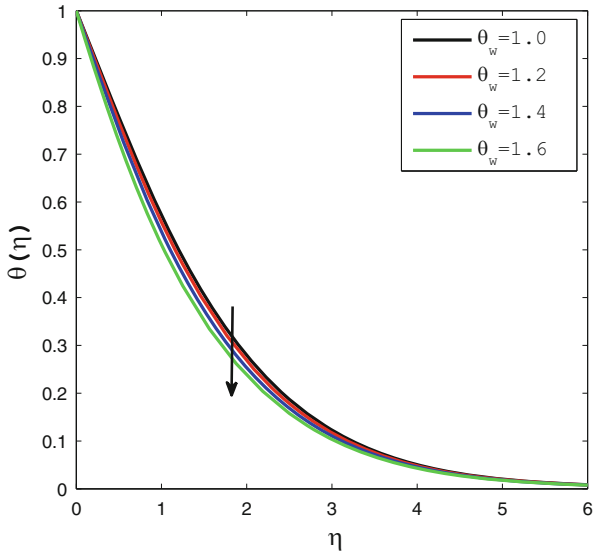

Fig. 9 Influence of θ_w on temperature

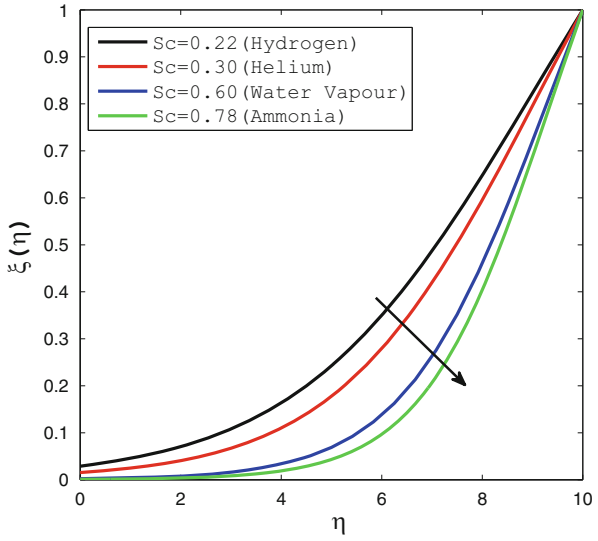

Fig. 10 Influence of *Sc* on concentration

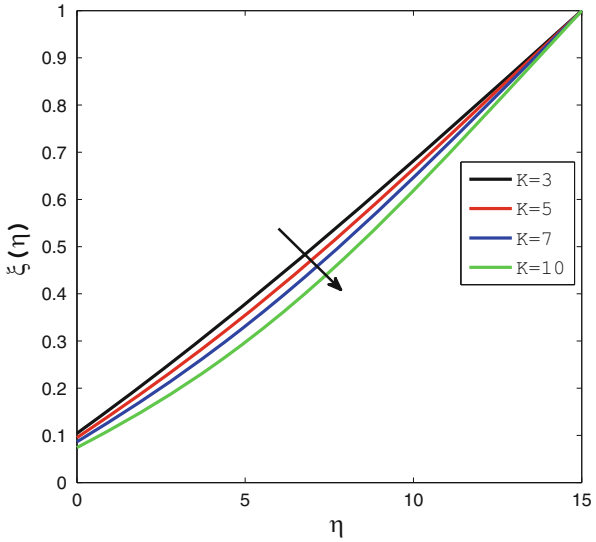

Fig. 11 Influence of Sc on concentration

boundary layer thickness has opposite effects. It is additionally analyzed that there is no pattern of velocity boundary layer for $A = 1$, that is, fluid and sheet move with the same velocity. Figure 5 demonstrates the variation in temperature of nanofluid with respect to ratio parameter. It is observed that an increase in A depreciates the temperature profiles of the nanofluid flow. Consequently, higher estimations of ratio parameter infer higher pressure which gives less resistance to nanofluid motion and thus rate of heat transfer rise.

The behavior of fluid temperature by the influence of nanoparticles, Nb, Nt, Pr, and R, is illustrated in Figs. 6–11. The influences of Nb on the temperature profile are sketched in Fig. 6. It is observed that with rising Brownian motion parameter, the temperature of the fluid increases and, as a consequence, the thermal boundary layer thickness increases with increasing values of Nb. Fig. 7 demonstrate the impacts of thermophoresis parameter on temperature profiles. The temperature of the nanofluid increments with an increment of thermophoresis parameter. We observed that positive thermophoresis parameter shows a cool surface but is negative to a hot surface. For hot surfaces, thermophoresis tends to blow the nanoparticle volume fraction boundary layer far from the surface since a hot surface repels the sub-micrometer-sized particles from it, in this way shaping a generally particle-free layer close to the surface. As an outcome, the nanoparticle circulation is formed just outside, specifically, the impact of escalating the thermophoresis parameter.

In Fig. 10, it is observed that the concentration due to variation in Schmidt number for gases like hydrogen ($Sc = 0.22$), helium ($Sc = 0.30$), water vapor ($Sc = 0.60$), and ammonia ($Sc = 0.78$) is reduced. It is noticed that concentration field is arrived regularly for hydrogen and accrues for ammonia in comparison to

water vapor. Thus, water vapor can be used for maintaining concentration field, and hydrogen can be used for maintaining good concentration field. An increasing Sc leads to decreases in the boundary layer thickness. Figure 11 illustrates that the concentration decreases with increasing values of homogeneous reaction rate parameter.

References

1. Pop, I., Ingham, D.B.: Convective heat transfer. Mathematical and computational modeling of viscous fluids and porous media pergamon. Oxford. (2001)
2. Chaudhary, M. A., and Merkin, J. H.: A simple isothermal model for homogeneous-heterogeneous reactions in boundary-layer flow-I: Equal diffusivities. Fluid Dyn. Res. **16**(6), 311–333 (1995)
3. Vafai, K.: Porous media: Applications in biological systems and biotechnology. CRC Press (2010)
4. Choi, S.U.S.: Enhancing thermal conductivity of fuids with nanoparticles developments and applications of non-Newtonian flows. ASME FED 231/MD. **6**, 699–105 (1995)
5. Choi, S.U.S., Zhang, Z.G., Yu. W., Lockwood. F.E., Grulke. E.A.: Anomalous thermal conductivity enhancement in nanotube suspensions. Appl. Phys. Letts. **79**(14), 2252–2254 (2001)
6. Das, S.K., Putra, N., Thiesen, P., Roetzel, W.: Temperature dependence of thermal conductivity enhancement for nanofluids. J. Heat Trans. **12**, 567–574 (2003)
7. Lawrence, J.C., Flow past a stretching plate. ZAMM. **21**(4), 645–647 (1970)
8. Eastman, J.A., Choi, S.U., Li, S., Yu, W., Thompson, L.J.: Anomalously increased effective thermal conductivities of ethylene glycol-based nanofuids containing copper nanoparticles. Appl. Phys. Letts. **178**, 718–720 (2001)
9. Makinde, O.D., Aziz, A.: Boundary layer flow of a nanofluid past a stretching sheet with a convective boundary condition. Int. J. Therm. Sci. **50**(7), 1326–1332 (2011)
10. Khan, W.A., Pop, I.: Boundary-layer flow of a nanofluid past a stretching sheet. IJHMT. **53**, 2477–2483 (2010)
11. Nadeem, S., Haq, R.U.: Effect of Thermal radiation for magneto-hydrodynamic boundary layer flow of a nanofluid past a stretching sheet with convective boundary conditions. J. Comput. Theor. Nanosci. **11**(1), 32–40 (2014)
12. Nadeem, S., Haq, R.U., Khan, Z.H.: Numerical study of MHD boundary layer flow of a Maxwell fluid past a stretching sheet in the presence of nanoparticles. J. Taiwan Inst. Chem. Eng.. **45**(1), 121–126 (2014)
13. Sheikholeslami, M., Bandpy, M.G., Ellahi, R., Zeeshan, A.: Simulation of MHD CuO-water nanofluid flow and convective heat transfer considering Lorentz forces. J. Magne. Magne. Mater.. **369**, 69–80 (2014)
14. Ellahi, R.: The effects of MHD and temperature dependent viscosity on the flow of non-Newtonian nanofluid in a pipe: analytical solutions. Appl. Mathem. Model. **37**, 1451–1467 (2013)
15. Ali, F.Md., Nazar, R., Arifin, N.Md., Pop, I.: MHD boundary layer flow and heat transfer over a stretching sheet with induced magnetic field. Heat Mass Trans.. **47**(2), 155–162 (2010)
16. Zeeshan, A., Ellahi, R., Siddiqui, A.M., Rahman, H.U.: An investigation of porosity and magneto-hydrodynamic flow of non-Newtonian nanofluid in coaxial cylinders. Int. J. Phys. Sci. **7**(9), 1353–1361 (2012)
17. Nadeem, S., Lee, C.: Boundary layer flow of nanofluid over an exponentially stretching surface. Nanosc. Res. Letts. **7**(1), 94 (2012)

18. Noghrehabadi, A., Pourrajab, R., Ghalambaz, M.: Flow and heat transfer of nanofluids over stretching sheet taking into account partial slip and thermal convective boundary conditions. Heat Mass Trans. **49**(9), 1357–1366 (2013)
19. Mabood, F., Khan, W. A., Ismail, A.I.M.: MHD boundary layer flow and heat transfer of nanofluids over a nonlinear stretching sheet: a numerical study. J. Magne. Magne. Mater. **374**, 569–576 (2015)
20. Merkin, J. H.: A Model for Isothermal Homogeneous-Heterogeneous Reactions in Boundary-Layer Flow. Math. Comput. Model. **24**(8), 125–136 (1996)

Effects of Thermal Radiation on Peristaltic Flow of Nanofluid in a Channel with Joule Heating and Hall Current

R. Latha and B. Rushi Kumar

Abstract The present article has been arranged to study the Hall current and Joule heating effects with thermal radiation on peristaltic flow of nanofluid in a channel with flexible walls. Convective conditions for heat transfer in the formulation are adopted. Viscous dissipation in energy expression is taken into account. Resulting differential systems after invoking small Reynolds number and long wavelength considerations are numerically solved. Runge-Kutta scheme of order four is implemented for the results of axial velocity, temperature, and concentration. Outcomes of new parameters like Brownian motion parameter, thermophoresis parameter, thermal radiation parameter, Prandtl number, and Eckert number on the physical quantities of interest are discussed. It is found that the influence of thermal radiation parameter and the Biot number on the temperature is the same fashion.

Keywords peristaltic flow · Hall current · Nano fluid · heat dissipation · permeability · joule heating.

1 Introduction

Examination as for the flow of non-Newtonian fluid cannot be disregarded in view of its wide applications in combination of fields like industry, physiology, and design engineering. Almost certainly different constitutive relations are recommended for the flow portrayal of such fluids differing in characteristics. Some current specialists are even at this point connected with the flow investigation of such fluids. Regarding peristalsis, the non-Newtonian fluid increased much consideration due to their

R. Latha
Department of Mathematics, VIT, Vellore, Tamil Nadu, India
e-mail: latha.r@vit.ac.in

B. Rushi Kumar (✉)
Department of Mathematics, School of Advanced Sciences, Vellore Institute of Technology, Vellore, Tamil Nadu, India
e-mail: rushikumar@vit.ac.in

B. Rushi Kumar et al. (eds.), *Applied Mathematics and Scientific Computing*, Trends in Mathematics, https://doi.org/10.1007/978-3-030-01123-9_30

different applications in mechanical and physiological procedures. Spontaneous pressing and loosening up development along the walls of tabular structures is named as peristalsis. Stomach-related tract and blood flow in lymphatic transport are a couple of cases that can be seen inside the human body. The wonder is moreover engaged with outlining numerous devices like blood direct machine to blood pump during surgical procedures, dialysis machine, and heart lung machine. A few worms also utilize this wonder for their locomotion. Some important studies which described the peristaltic flows are defined in [1–6]. Kothandapani et al. [7] have analyzed the peristaltic transport of a Jeffery fluid under the effect of magnetic field in an asymmetric channel. They have discussed the problem in wave frame moving with a constant axial velocity under the approximations of long wavelength and low Reynolds number. Peristaltic flow with long wavelength at low Reynolds number has been considered in this study, where a number of waves are small depending on the half width of the channel to the wavelength of the fluid. If the number of waves is small, then the slope of the channel wall is also small, where it is occurring in the human ureter. Another way, the size of the Reynolds number of the fluid flow is small in the human ureter. In each cross section, the pressure gradient and axial velocity are small, when the size of the slope wall is small compared to the longitudinal values. Radius of the channel and size of wavelength both are large compared to half width of the channel, when the long wavelength theory is applicable. Manton [8] points out the fluid mechanics of peristaltic wave with an arbitrary shape in order to get the general properties of peristalsis. Kaimal [9] carried out the peristaltic transport of Newtonian fluid with lubrication theory, and he discussed special phenomena like reflux and trapping. Shapiro et al. [10] found the peristaltic pumping with long wavelengths at low Reynolds number. In the greater part of the MHD flows detailed in the composed work, the Hall current term in Ohm's law was overlooked as it has no significant effect for littler values of the magnetic field. Regardless, when the greater magnetic field is utilized, the influence of Hall current is more significant. Henceforth, the investigation of Hall current effect on MHD flows has extended much significance because of its wide range of utilization, for example, in electric generators and pumps, power transformers, refrigeration cycles, etc. Another imperative part of MHD peristaltic flow is to deal with Hall current. This impact can happen; when the electron-molecule crash repeatable will be low, alternately the magnetic field is strong. Additionally, joule heating happens when the power of an electric current is transformed into heat as it travels through a resistance. It has reasonable applications, in geophysical streams, atomic designing, and biomedical field. A few cases of this impact in daily life are electric stoves, welding irons, electrical radiators, and thermometers. Porous medium is a solid body that contains pores. The definition of the porosity of the porous medium can be given as the ratio of pore volume to the total volume of a given sample of material. Porous medium has very fine holes, the fluid is not flowing through solid, and it is only flowing through the open edge. The phenomenon of porosity is important with regard to tremendous applications such as human lugs, vascular beds, kidney and bone etc. Darcy law is proportionality between the flow velocity and the pressure difference for low speed in an unbounded porous medium. Due to the numerous applications in biomedical engineering,

medicine, and industry, like heat conduction owing the blood flow in tissues, oxygenation process, biomass transfer, heat exchanges in the environment, heat generation, hypothermia, cooling system of industrial equipment, etc., and inspired by the abovementioned studies, in this study, we investigated the influence of wall flexibility and joule heating on the peristaltic transport of a conducting nanofluid in uniform porous channel. The exact solution is obtained for stream function and velocity. Further, R-K Fehlberg integration scheme is applied for solving the energy and concentration equations. Results are obtained and discussed for the flow of uniform geometry at different values of relevant parameters.

2 Mathematical Model and Governing Equations

Consider the peristaltic flow of a conducting nanofluid in a 2D porous uniform or nonuniform channel; it is assumed that the x-axis is along the channel wall and y-axis is perpendicular to it. The flow is formed by a sinusoidal wave propagating along the elastic walls of the channel with a constant speed c. Joule heating, Hall current, and dissipation effects are considered (Fig. 1). The channel wall deformation is defined as:

$$y = \pm\bar{\eta}\left(\bar{x},\ \bar{t}\right) = \pm\left(a\sin\frac{2\pi}{\lambda}\left(\bar{x} - c\bar{t}\right) + d\left(x\right)\right),\ d\left(x\right) = \bar{m}x + d,\quad \bar{m} \ll 1 \tag{1}$$

Consider the following nondimensional variables:

$$x^* = \frac{\bar{x}}{\lambda},\quad y^* = \frac{\bar{y}}{d_1},\quad u^* = \frac{\bar{u}}{c},\quad v^* = \frac{\bar{v}}{c},\quad p^* = \frac{d_1^2}{\lambda\mu c}\bar{p},\quad t^* = \frac{c\bar{t}}{\lambda},$$

$$\mathrm{Re} = \frac{\rho_f c d_1}{\mu},\quad \eta^* = \frac{\bar{\eta}}{d}$$

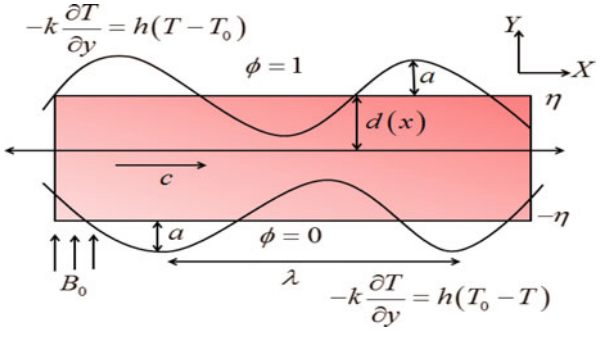

Fig. 1 Geometry of the problem

$$M = \sqrt{\frac{\sigma}{\mu}} B_0 d_1, \quad \delta = \frac{d_1}{\lambda}, \quad R_d = \frac{16\sigma^* T_0^3}{3kk^*}, \quad \theta = \frac{T - T_0}{T_1 - T_0},$$

$$Ec = \frac{c^2}{c_f\,(T_1 - T_0)}, \quad \Pr = \frac{v}{\alpha}$$

$$\sigma = \frac{C - C_0}{C_1 - C_0}, \quad k = \frac{k_1}{d_1^2}, \quad \psi' = \frac{\psi}{cd_1}, \quad u = \frac{\partial \psi}{\partial y}, \quad v = -\delta \frac{\partial \psi}{\partial x},$$

$$Nb = \frac{\tau D_B\,(c_1 - c_0)}{v},$$

$$Nt = \frac{\tau D_T\,(T_1 - T_0)}{T_m v}, \quad Bi = \frac{hd_1}{k}, \quad E_1 = \frac{-\tau d_1^3}{\lambda^3 \mu c}, \quad E_2 = \frac{mcd_1^3}{\lambda^3 \mu},$$

$$E_3 = \frac{dd_1^3}{\lambda^2 \mu}, \quad Sc = \frac{v}{D_B}$$

The governing equations describing flow pattern are as follows:

$$\frac{\partial u}{\partial x} + \frac{\partial v}{\partial y} = 0 \tag{2}$$

$$\mathrm{Re}\left[\delta u \frac{\partial u}{\partial x} + v \frac{\partial u}{\partial y}\right] = -\frac{\partial p}{\partial x} + \left(\delta^2 \frac{\partial^2 u}{\partial x^2} + \frac{\partial^2 u}{\partial y^2}\right) + \frac{M}{(1 + m^2)}(-u + mv) - \frac{u}{k} \tag{3}$$

$$\mathrm{Re}\left[\delta u \frac{\partial v}{\partial x} + v \frac{\partial v}{\partial y}\right] = -\frac{\partial p}{\partial y} + \left(\delta^2 \frac{\partial^2 v}{\partial x^2} + \frac{\partial^2 v}{\partial y^2}\right) + \frac{M}{(1 + m^2)}(v + mu) - \frac{v}{k} \tag{4}$$

$$\mathrm{Re}\left[\delta u \frac{\partial \theta}{\partial x} + v \frac{\partial \theta}{\partial y}\right] = \frac{1}{\Pr}\left(\delta^2 \frac{\partial^2 \theta}{\partial x^2} + \frac{\partial^2 \theta}{\partial y^2}\right) + Nb\left(\delta^2 \frac{\partial \phi}{\partial x}\frac{\partial \theta}{\partial x} + \frac{\partial \phi}{\partial y}\frac{\partial \theta}{\partial y}\right) + Nt\left\{\left(\delta \frac{\partial \theta}{\partial x}\right)^2 + \left(\frac{\partial \theta}{\partial y}\right)^2\right\} + Ec\left[4\left(\delta \frac{\partial u}{\partial x}\right)^2 + \left(\delta \frac{\partial v}{\partial x} + \frac{\partial u}{\partial y}\right)^2\right] + \frac{M^2 Ec}{(1 + m^2)}\left(v^2 + u^2\right) + \frac{Rd}{\Pr}\frac{\partial^2 \theta}{\partial y^2} \tag{5}$$

$$\mathrm{Re}\ Sc\left[\delta u \frac{\partial \phi}{\partial x} + v \frac{\partial \phi}{\partial y}\right] = \left(\delta^2 \frac{\partial^2 \phi}{\partial x^2} + \frac{\partial^2 \phi}{\partial y^2}\right) + \frac{Nt}{Nb}\left(\delta^2 \frac{\partial^2 \theta}{\partial x^2} + \frac{\partial^2 \theta}{\partial y^2}\right) \tag{6}$$

The subject boundary conditions can be put into the forms

$$\begin{aligned} &u = 0, \quad \frac{\partial \theta}{\partial y} = \left\{ \begin{matrix} -Bi\theta \\ -Bi\,(1-\theta) \end{matrix} \right\}, \quad \phi = \left\{ \begin{matrix} 1 \\ 0 \end{matrix} \right\} \quad \text{at } y = \pm\eta \\ &\left[E_1 \frac{\partial^3}{\partial x^3} + E_2 \frac{\partial^3}{\partial x \partial t^2} + E_3 \frac{\partial^3}{\partial t \partial x} \right] \eta = \left(\delta^2 \frac{\partial^2 u}{\partial x^2} + \frac{\partial^2 u}{\partial y^2} \right) \\ &-\mathrm{Re} \left[\delta \frac{\partial u}{\partial t} + \delta u \frac{\partial u}{\partial x} + v \frac{\partial u}{\partial y} \right] + \frac{M^2}{(1+m^2)} (-u + mv) - \frac{u}{k} \end{aligned} \quad \text{at } y = \pm\eta \qquad (7)$$

where $\eta = 1 + \varepsilon \sin 2\pi\,(x - t)$. Now we introduce the stream function in the above nondimensional system as follows:

$$u = \frac{\partial \psi}{\partial y}, \quad v = -\delta \frac{\partial \psi}{\partial x}$$

And adopting long wavelength and low Reynolds number approximations, we obtain

$$\frac{\partial^4 \psi}{\partial y^4} - \left(\frac{M^2}{1+m^2} + \frac{1}{k} \right) \frac{\partial^2 \psi}{\partial y^2} = 0 \qquad (8)$$

$$\frac{(1+Rd)}{\mathrm{Pr}} \left(\frac{\partial^2 \theta}{\partial y^2} \right) + Nb \left(\frac{\partial \phi}{\partial y} \frac{\partial \theta}{\partial y} \right) + Nt \left(\frac{\partial \theta}{\partial y} \right)^2 + Ec \left(\frac{\partial^2 \psi}{\partial y^2} \right)^2 + \frac{M^2 Ec}{(1+m^2)} \left(\frac{\partial \psi}{\partial y} \right)^2 = 0 \qquad (9)$$

$$\frac{\partial^2 \phi}{\partial y^2} + \frac{Nt}{Nb} \frac{\partial^2 \theta}{\partial y^2} = 0 \qquad (10)$$

with the boundary conditions

$$\begin{aligned} &\frac{\partial \psi}{\partial y} = 0 \quad \text{at } y = \pm\eta \\ &\left[E_1 \frac{\partial^3}{\partial x^3} + E_2 \frac{\partial^3}{\partial x \partial t^2} + E_3 \frac{\partial^3}{\partial t \partial x} \right] \eta = \left(\frac{\partial^3 \psi}{\partial y^3} \right) - \left(\frac{M^2}{(1+m^2)} + \frac{1}{k} \right) \frac{\partial \psi}{\partial y} \\ &\frac{\partial \theta}{\partial y} = \left\{ \begin{matrix} -Bi\theta \\ -Bi\,(1-\theta) \end{matrix} \right\}, \quad \phi = \left\{ \begin{matrix} 1 \\ 0 \end{matrix} \right\} \quad \text{at } y = \pm\eta, \end{aligned} \qquad (11)$$

The exact solution of Eq. (8) with boundary conditions (11) has the form

$$\psi = \frac{8\varepsilon\pi^3 \left[(E_1+E_2)\cos 2\pi(x-t) - \frac{E_3}{2\pi} sin 2\pi(x-t) \right]}{\left(\frac{M^2}{1+m^2} + \frac{1}{k} \right)} \left[\frac{\sinh\left(\sqrt{\frac{M^2}{1+m^2} + \frac{1}{k}} \right) y}{\sqrt{\frac{M^2}{1+m^2} + \frac{1}{k}} \cosh\left(\sqrt{\frac{M^2}{1+m^2} + \frac{1}{k}} \right) \eta} - y \right] \qquad (12)$$

3 Numerical Procedure

Equations (9) and (10) with the help of (11) and (12) are solved numerically by employing Runge-Kutta Fehlberg integration scheme with step size as $\eta = 0.001$ and relative error as 0.0001. The set of nonlinear ordinary differential equations of second order in θ and ϕ are first reduced into a system of simultaneous ordinary equations. In order to solve this system using Runge-Kutta Fehlberg integration scheme, one should require the missed initial conditions. However, the values of θ and ϕ are known at$y = h$. These end conditions are used to obtain unknown initial conditions at $y = 0$ using shooting technique. In shooting method, the boundary values calculated have to be matched with the real boundary values. Using trial and error or some scientific approach, one attempts to get as close to the boundary value as possible, the most essential step of this method is to choose the appropriate finite values for far-field boundary condition. We took $y = h$ condition at a large but finite value of y where no considerable variations in temperature and concentration occur.

4 Results and Discussions

The motivation behind this part is to predict the acts of velocity, temperature, and concentration under the effect of rising parameters. Consequently the graphical outcomes are gotten numerically through Runge-Kutta with shooting technique in MATLAB. The appropriate physical clarifications are exhibited in this section. The effects of E_1 , E_2, and E_3 on velocity profile are demonstrated in Figs. 2, 3, and 4. The velocity upgrades with an expansion in E_1 and E_2, while it diminishes whenever$E_3$is expanded. The heart functions as a pump carrying the blood over the veins. The walls of these vessels are expanded in flexibility, and adaptability of these walls upgrades the velocity of the blood flow. Then again, the blood vessels involve the more amount of force to develop and take up the blood expelled from the heart. This prompts diminishing in the velocity of the blood inside the channel wall. The effects of E_1 , E_2, and E_3 on temperature profile are demonstrated in Figs. 5, 6, and 7. The temperature upgrades with an expansion in E_1 and E_2, while it diminishes whenever$E_3$is expanded. The effect of Bi on temperature profile is portrayed in Fig. 8. The decline in temperature profile as Bi enhances. The convective heat transfer reduces the thermal conductivity inside the channel and hence declines the temperature of the fluid. The effects of E_1 , E_2, and E_3 on concentration profile are demonstrated in Figs. 9, 10, and 11. The concentration diminishes with an expansion in E_1 and E_2, while it upgrades whenever E_3 is expanded.

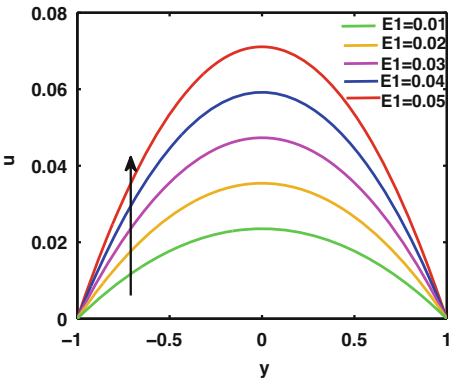

Fig. 2 Velocity for different E_1

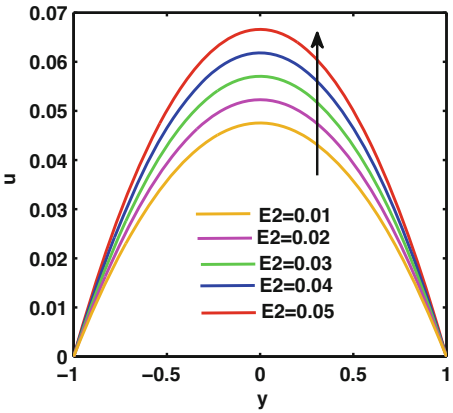

Fig. 3 Velocity for different E_2

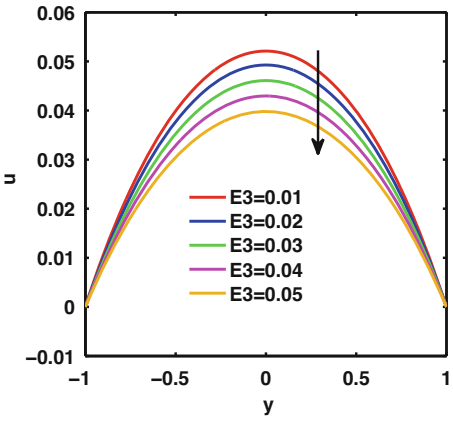

Fig. 4 Velocity for different E_3

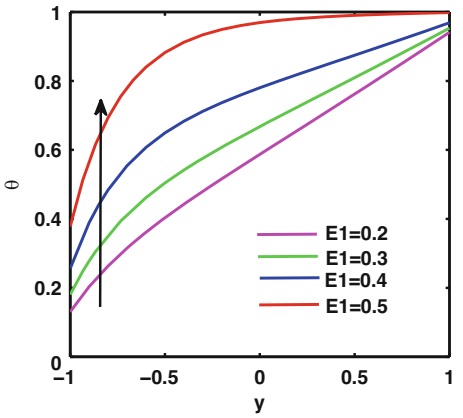

Fig. 5 Temperature for different E_1

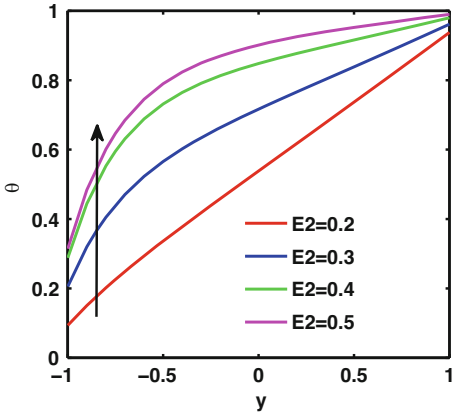

Fig. 6 Temperature for different E_2

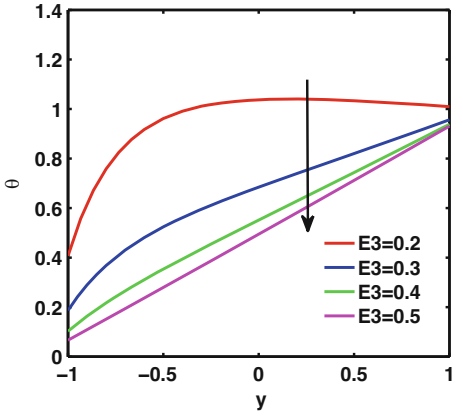

Fig. 7 Temperature for different E_3

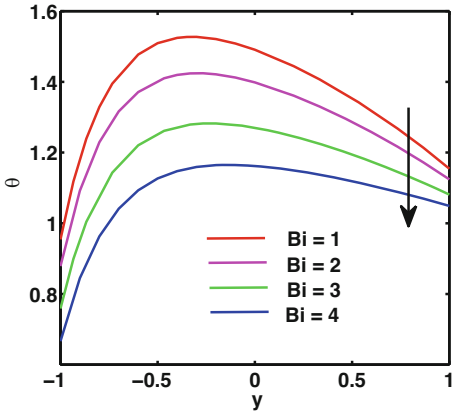

Fig. 8 Temperature for different Bi

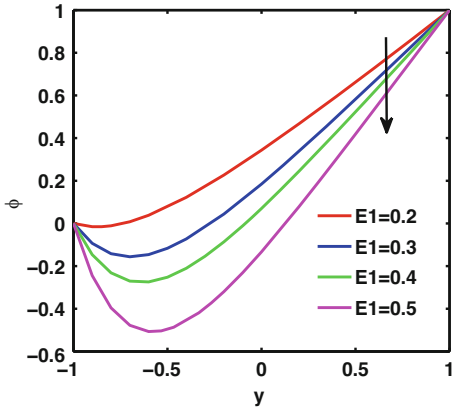

Fig. 9 Concentration for different E_1

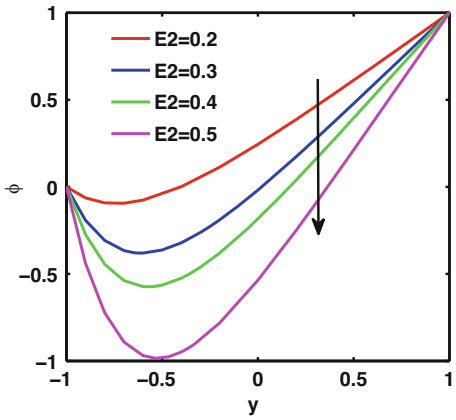

Fig. 10 Concentration for different E_2

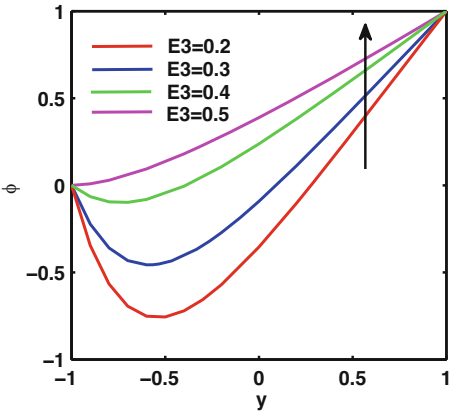

Fig. 11 Concentration for different E_3

5 Conclusions

The major findings of the analysis are as follows:

1. An expanding hall parameter m upgrades the velocity. It causes a diminish in magnetic damping power, and henceforth the velocity upgrades.
2. The effects of E_1 , E_2, and E_3 are the same fashion on velocity and concentration profile; compared to this fashion, the temperature profile is different.
3. Decline in temperature profile as Bi enhances because the convective heat transfer reduces the thermal conductivity inside the channel and hence declines the temperature of the fluid.

References

1. Mekheimer, Kh. S. Abd Elmaboud, Y. : Peristaltic flow of a couple stress fluid in an annulus: application of an endoscope. Phys A. **387**, 2403–15 (2008)
2. Mekheimer, Kh. S. Abd Elmaboud, Y. : The influence of heat transfer and magnetic field on peristaltic transport of a Newtonian fluid in a vertical annulus: an application of an endoscope. Phys. Lett. A. **372**, 1657–65 (2008)
3. Srinivas, S. Kothandapani, M.: Peristaltic transport in an asymmetric channel with heat transfer, a note. Int. Commun. Heat Mass Trans. **35**, 514–22 (2008)
4. Srinivas, S. Gayathri, R.: Peristaltic transport of a Newtonian fluid in a vertical asymmetric channel with heat transfer and porous medium. Appl. Math. Comput. **215**, 185–96 (2009)
5. Srinivas, S. Gayathri, R. Kothandapani, M.: The influence of slip conditions, wall properties and heat transfer on MHD peristaltic transport. Comput. Phys. Commun. **180**, 2115–22 (2009)
6. Srinivas, S. Kothandapani, M.: The influence of heat and mass transfer on MHD peristaltic flow through porous space with compliant walls. Appl. Math. Comput. **213**, 197–208 (2009)
7. Kothandapani, M. Srinivas, S. : Peristaltic transport of a Jeffery fluid under the effect of magnetic field in an asymmetric channel, Int. J. Non-Linear Mech. **43**, 915–924 (2008)

8. Manton, M. J. : Long-wavelength peristaltic pumping at low Reynolds number Journal of Fluid Mech. 68, 467–476 (1975)
9. Kaimal, M. R. : Peristaltic Pumping of a Newtonian Fluid With Particles Suspended in It at Low Reynolds Number Under Long Wavelength Approximations, J. Appl. Mechs. **45**, 32–36 (1978)
10. Shapiro, A. H. Jaffrin, M. Y. Weinberg, S. I. : Peristaltic pumping with long wavelengths at low Reynolds number. J. Fluid Mech. **37**, 799–825 (1969)

Chemically Reactive 3D Nonlinear Magneto Hydrodynamic Rotating Flow of Nanofluids over a Deformable Surface with Joule Heating Through Porous Medium

E. Kumaresan and A. G. Vijaya Kumar

Abstract This article presents a numerical investigation on free convective heat and mass flow characteristics in a 3-dimensional MHD nonlinear boundary layer flow of nanofliuids past a deformed revolving surface through porous medium in the presence of Joule heating and radiation absorption as part of the chemical reaction mechanism. It is assumed that the Ag- water and Cu- water nanofluids which flow in parallel layers in a stream line. The phenomenon presided when modelled the flow transport leads to obtain a coupled nonlinear partial differential equations and further in the process of attaining an approximate solution, the system of equations were transformed in to a set of nonlinear ordinary differential equations using appropriate similarity transformation. The resulting equations were solved numerically with by using the R-K-Felhberg-integration with shooting method. It is found that the temperature increases with increasing radiation absorption parameter, We also seen that the Ag-water nanofluid has high thermal conductivity than Cu-water nanofluid.

Keywords MHD · Nano fluid · Porous medium · Joule heating · Heat source · Radiation absorption · Chemical reaction

1 Introduction

Initially the examination of the 3-D boundary-layer flow is caused by a stretching flat surface in two tangential directions by Wang [1]. Takhar et al. [2] studied 3-D magneto hydrodynamic boundary-layer flow due to the impulsive stretching of the surface in two lateral directions and by suddenly increasing the surface temperature from that of the surrounding fluid. Kumari and Nath [3] presented an

E. Kumaresan · A. G. Vijaya Kumar (✉)
Department of Mathematics, VIT, Vellore, Tamil Nadu, India
e-mail: kumaresan.e2014@vit.ac.in; vijayakumarag@vit.ac.in

B. Rushi Kumar et al. (eds.), *Applied Mathematics and Scientific Computing*,
Trends in Mathematics, https://doi.org/10.1007/978-3-030-01123-9_31

analytical solution by using HAM method for unsteady 3-D magneto hydrodynamic boundary-layer flow and heat transfer due to impulsively stretched plane surface. Choi [4] was pioneer in introducing this colloidal suspension. Boundary layer analysis in the presence of MHD flow of nanofluid has wide range of applications in industrial and engineering problems. Mohaghegh et al. [5] investigated 3-D stagnant-point flow and heat transfer of a dusty fluid toward a stretching sheet. Mondal et al. [6] analyzed the effects of radiation, heat and mass transfer on the unsteady MHD flow of three dimensional casson nanofluids with the help of spectral quasi linearization method. Stanford Shateyi [7] presented numerical analysis of 3-D magneto hydrodynamic nanofluid flow over a stretching sheet with convective boundary conditions through a porous medium. Nayak et al. [8, 9] studied 3-D magneto hydrodynamic nanofluid flow with thermal radiation by using Runga-Kutta method of fourth order along with shooting technique as well as Secant method for better approximation. Jusoh et al. [10] investigated the MHD three dimensional Maxwell nanofluid flow over a permeable stretching/shrinking surface with convective boundary conditions. Chen [11] studied 3-D with power-law stretching in a nanofluid containing gyrotactic microorganisms. Forghani et al. [12] elaborated effect upon Hartmann number on flow and heat transfer of Ag-water nanofluid with variable heat flux. However, most studies revolved around two-dimensional flows. Motivated by this, the primary purpose of this paper is to solve the problem of chemically reactive three-dimensional magneto hydrodynamic rotating flow of nanofluids over a deformable surface with joule heating through porous medium.

2 Mathematical Formulation

We investigate copper and silver nanofluid three-dimensional rotating flow over deformable surface. The surface is deformed with the velocity $u_w = ax$. With invariable angular velocity Ω the fluid is rotated about z-axis (see Fig. 1). The transverse magnetism is also investigated. Surface temperature is adjusted by convection process through the hotted fluid with temperature T_f and T_∞ denotes the ambient temperature.

Relevant equations are:

$$\frac{\partial u}{\partial x} + \frac{\partial v}{\partial y} + \frac{\partial w}{\partial z} = 0 \tag{1}$$

$$u\frac{\partial u}{\partial x} + v\frac{\partial u}{\partial y} + w\frac{\partial u}{\partial z} - 2\Omega v = \frac{1}{\rho_{nf}}\left[\mu_{nf}\frac{\partial^2 u}{\partial z^2} - \sigma_{nf}{B_0}^2 u - \frac{\mu_{nf}}{k}u\right] \tag{2}$$

$$u\frac{\partial v}{\partial x} + v\frac{\partial v}{\partial y} + w\frac{\partial v}{\partial z} + 2\Omega u = \frac{1}{\rho_{nf}}\left[\mu_{nf}\frac{\partial^2 v}{\partial z^2} - \sigma_{nf}{B_0}^2 v - \frac{\mu_{nf}}{k}v\right] \tag{3}$$

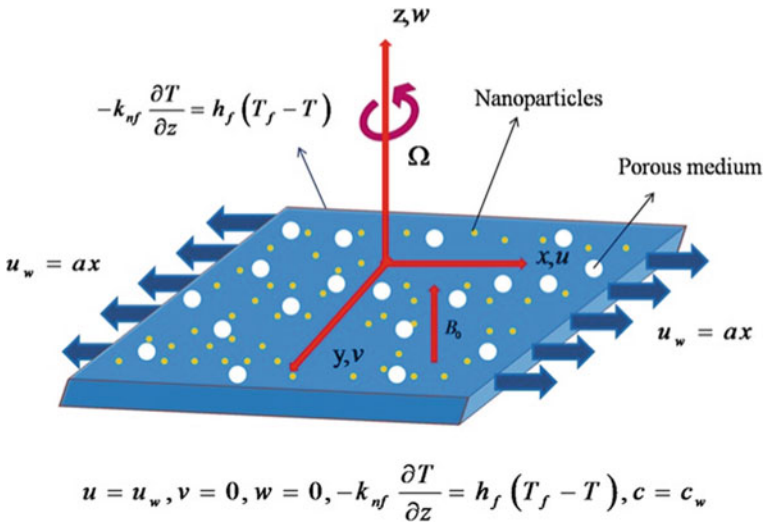

Fig. 1 Physical geometry of the model

$$u\frac{\partial T}{\partial x}+v\frac{\partial T}{\partial y}+w\frac{\partial T}{\partial z}=\alpha_{nf}\frac{\partial^2 T}{\partial z^2}-\frac{1}{(\rho C_p)_{nf}}\frac{\partial q_r}{\partial z}+\frac{\mu_{nf}}{(\rho C_p)_{nf}}\left[\left(\frac{\partial u}{\partial z}\right)^2+\left(\frac{\partial v}{\partial z}\right)^2\right]$$

$$+\frac{\sigma_{nf}B_0{}^2}{(\rho C_p)_{nf}}\left[u^2+v^2\right]+\frac{Q_0}{(\rho C_p)_{nf}}(T-T_\infty)+Q'_1(C-C_\infty) \tag{4}$$

$$u\frac{\partial C}{\partial x}+v\frac{\partial C}{\partial y}+w\frac{\partial C}{\partial z}=D_m\frac{\partial^2 C}{\partial z^2}-k_0(C-C_\infty) \tag{5}$$

The relevant boundary conditions are;

$$u = u_w = ax, v = 0, W = 0, -k_{nf}\frac{\partial T}{\partial z} = h_f\left(T_f - T\right), C = C_W \text{ at } Z = 0.$$

$$u \to 0, v \to 0, T \to T_\infty, C \to C_\infty \text{ as } z \to \infty \tag{6}$$

The properties of nanofluids are given as follows

$$\mu_{nf} = \frac{\mu_f}{(1-\varphi)^{2.5}}, \rho_{nf} = (1-\varphi)_{\rho f} + \varphi\rho_s, (\rho C_P)_{nf} = (1-\varphi)(\rho C_P)_f + \varphi(\rho C_P)_s$$

$$k_{nf} = k_f\left[\frac{k_s+2k_f+2\varphi(k_s-k_f)}{k_s+2k_f+\varphi(k_f-k_s)}\right], \sigma_{nf} = \sigma_f\left[1+\frac{3\left(\sigma_s-\sigma_f\right)\varphi}{\left(\sigma_s+2\sigma_f\right)-\left(\sigma_s-\sigma_f\right)\varphi}\right] \tag{7}$$

The radiative heat flux is denoted by q. Using the Rosseland approximation for radiation, we have:

$$q_r = -\frac{4\sigma^*}{3k^*}\frac{\partial T^4}{\partial z} \tag{8}$$

$$T^4 \cong 4T_\infty^3 T - 3T_\infty^4 \tag{9}$$

Thus, substituting Eq. (9) into Eq. (8) we get

$$\frac{\partial q_r}{\partial z} = -\frac{16\sigma^* T_\infty^3}{3k*}\frac{\partial^2 T}{\partial z^2} \tag{10}$$

Therefore Eq. (4) reduced to

$$u\frac{\partial T}{\partial x} + v\frac{\partial T}{\partial y} + w\frac{\partial T}{\partial z} = \alpha_{nf}\frac{\partial^2 T}{\partial z^2} + \frac{1}{(\rho C_P)_{nf}}\frac{16\sigma^* T_\infty^3}{3k^*}\frac{\partial^2 T}{\partial z^2} + \frac{\mu_{nf}}{(\rho C_p)_{nf}}\left[\left(\frac{\partial u}{\partial z}\right)^2 + \left(\frac{\partial v}{\partial z}\right)^2\right] + \frac{\sigma_{nf}B_0^2}{(\rho C_p)_{nf}}\left[u^2 + v^2\right] + \frac{Q_0}{(\rho C_p)_{nf}}(T - T_\infty) + Q_1'(C - C_\infty) \tag{11}$$

The following similarity transformations are introduced to simply the mathematical analysis of the problem

$$u = axf'(\eta), v = axg(\eta), w = -\sqrt{av_f}f(\eta), \eta = \sqrt{\frac{a}{v_f}}z, \theta(\eta) = \frac{T - T_\infty}{T_f - T_\infty}, \varphi(\eta) = \frac{C - C_\infty}{C_f - C_\infty} \tag{12}$$

Using Eqs. (11) and (12) the governing non-linear partial differential equations (1–5) together with the boundary condition (6) reduce to ordinary differential equations that are locally valid as follows:

Momentum boundary layer equation:

$$f''' - \left[(1-\phi)^{2.5}\frac{\sigma_{nf}}{\sigma_f}Mf' + \frac{(1-\phi)^{2.5}}{A_1}\left[f'^2 - ff'' - 2\lambda g\right] + Kf'\right] = 0 \tag{13}$$

$$g'' - \left[(1-\phi)^{2.5}\frac{\sigma_{nf}}{\sigma_f}Mg + \frac{(1-\phi)^{2.5}}{A_1}\left[f'g - fg' + 2\lambda f'\right] + Kg\right] = 0 \tag{14}$$

Thermal boundary layer equation:

$$\theta'' + \frac{\Pr}{A_2\left(\frac{k_{nf}}{k_f} + R\right)}\left[\frac{A_2 Ec}{(1-\phi)^{2.5}}\left(f''^2 + g'^2\right) + \frac{\sigma_{nf}}{\sigma_f}A_2 MEc\left(f'^2 + g^2\right) + A_2 Q\theta + Q_1\varphi + f\theta'\right] = 0 \tag{15}$$

Concentration boundary layer equation:

$$\varphi'' - k_r Sc\varphi + Scf\varphi' = 0 \tag{16}$$

The corresponding transformed boundary conditions are

$f(\eta) = 0, f'(\eta) = 1, g(\eta) = 0, \frac{k_{nf}}{k_f}\theta'(\eta) = Bi[\theta(\eta) - 1], \varphi(\eta) = 1$ at $\eta = 0$

$$f'(\eta) \to 0, g(\eta) \to 0, \theta(\eta) \to 0, \varphi(\eta) \to 0 \text{as} \eta \to \infty \tag{17}$$

The C_{fx} is the skin friction coefficient along $x$direction, C_{fy} is the skin friction coefficient along $y$direction and Nu_x is the local Nusselt number. They are defined as;

$$C_{fx} = \frac{\tau_{wx}}{\rho_f u_w^2}, C_{fy} = \frac{\tau_{wy}}{\rho_f u_w^2}, Nu_x = \frac{xq_w}{k_f\left(T_f - T_\infty\right)} \tag{18}$$

Where $\tau_{wx} = \tau_{zx}|_{z=0}$and $\tau_{wy} = \tau_{zy}\big|_{z=0}$ are the surface shear stresses and $q_w$is the surface heat flux given by,

$$\tau_{wx} = \mu_{nf}\left.\frac{\partial u}{\partial z}\right|_{z=0}, \tau_{wy} = \mu_{nf}\left.\frac{\partial v}{\partial z}\right|_{z=0}, q_w = -k_{nf}\left.\frac{\partial T}{\partial z}\right|_{z=0} + q_r|_{z=0} \tag{19}$$

Substituting the similarity transformations Eq. (12) into Eqs. (18) and (19), we get

$$\sqrt{Re_x}C_{fx} = (1-\phi)^{-2.5}f''(0), \sqrt{Re_x}C_{fy} = (1-\phi)^{-2.5}g'(0), \frac{Nu_x}{\sqrt{Re_x}} = -\left(\frac{k_{nf}}{k_f} + R\right)\theta'(0)$$

Here $Re_x = \left(u_w x v_f\right)$- local Reynolds number.

3 Results and Discussion

The simplified Eqs. (13)–(16) are nonlinear and coupled. They can be solved numerically using Runge-Kutta fourth order with shooting technique for different values of parameters such as Magnetic field (M), Radiation parameter (R), Chemical reaction parameter (k), porous medium (K), Eckert number (Ec), Heat absorption (Q), Radiation absorption $(Q1)$, Rotation parameter (λ), Prandtl number (Pr), Schmidt number (Sc) and nanoparticle volume fraction (ϕ). The effects of the emerging parameters on the axial velocity $f'(\eta)$, transverse velocity $g(\eta)$, temperature $\theta(\eta)$, concentration $\varphi(\eta)$, skin friction coefficient and the rate of heat transfer profiles are investigated. The physical properties of the pure water and the nanoparticles are given in Table 1. The results of velocity, temperature, concentration, skin

Table 1 Thermophysical properties of water based nanoparticles

Thermo physical properties	Base fluid (water)	Cu (Copper)	Ag(Silver)
$\rho(kg/m^3)$	997.1	8933	10,500
$C_P(J/kg\,K)$	4179	385	235
$k(W/m\,K)$	0.613	401	429
$\sigma\,(\Omega m)^{-1}$	0.05	59.6×106	6.3×107

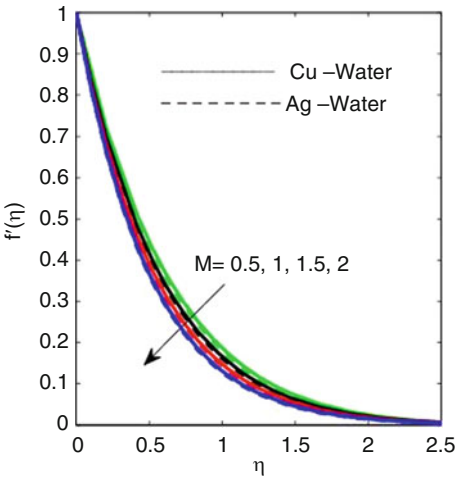

Fig. 2 Influence of M on $f'(\eta)$

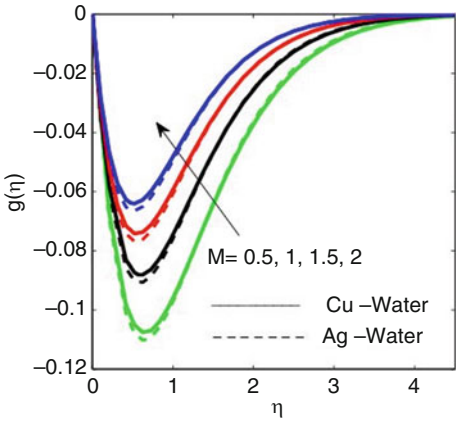

Fig. 3 Influence of M on $g(\eta)$

friction coefficient and the rate of heat transfer profiles have been studied for a different values of physical parameters, during the whole manipulation, we take the values $M = 2$, $\Pr = 6.2$, $R = 2$, $Ec = 0.2$,$K = 0.5$, $Bi = 0.4$, $Sc = 0.78$, $k = 0.5$, $Q = 0.1$, $Q1 = 0.5$, $\lambda = 0.5$, $\phi = 0.05$. In order to highlight the important features of the flow and the heat transfer characteristics, the numerical values are plotted in Figs. 2, 3, 4, 5, 6, 7, 8, 9, 10, and 11. The effect of the transverse magnetic field parameter on $f'(\eta)$, $g(\eta)$ and $\theta(\eta)$ is shown in

Parameter		Skin friction $f''(0)$		Skin friction$g'(0)$		Nusselt number $-\theta'(0)$	
		Cu	Ag	Cu	Ag	Cu	Ag
ϕ	0	−1.892	−1.892	−0.2778	−0.2778	−0.5921	−0.5921
	0.05	−1.97	−1.99	−0.3305	−0.3463	−0.674	−0.7182
	0.08	−2.001	−2.031	−0.3526	−0.3752	−0.7209	−0.8051
	0.1	−2.017	−2.052	−0.3639	−0.3904	−0.7509	−0.8697
M	1.0	−1.706	−1.73	−0.3899	−0.407		
	1.5	−1.841	−1.864	−0.3568	−0.3732		
	2.0	−1.97	−1.99	−0.3305	−0.3463		
	2.5	−2.092	−2.111	−0.3091	−0.3242		
Q	0					−0.2873	−0.294
	0.05					−0.41	−0.4235
	0.07					−0.4865	−0.5062
	0.1					−0.674	−0.7182
$Q1$	0.5					−0.674	−0.7182
	1					−1.259	−0.1331
	1.5					−1.844	−0.1994
	2					−2.429	−2.557
λ	0	−1.941	−1.959	0	0	−0.5932	−0.6212
	0.5	−1.97	−1.99	−0.3305	−0.3463	−0.674	−0.7182
	1	−2.045	−2.071	−0.6335	−0.6618	−0.9787	−1.111
	1.5	−2.146	−2.718	−0.9006	−0.9381	−2.075	−3.146

Figs. 2, 3, and 4 for both Ag-water and Cu -water based nanofluids. From Figs. 2 and 3 it is found that the velocity is decreases in increase the magnetic field parameter because that the reason behind this phenomenon is that application of magnetic field to an electrically conducting nanofluid gives rise to a resistive type force called the Lorentz force. This force has the tendency to slow down the motion of the nanofluid in the boundary layer. However opposite reaction is found for transverse velocity. It is prominent to mention here that magnetic field effect is highly significant on Cu–water nanofluid while compared with Ag-water nanofluid. From Fig. 4 the temperature is increases for increasing magnetic field parameter, further, we also observe that the Cu-water based nanofluid exhibits relatively less thermal conductivity than that of the Ag-water based nanofluid. Figures 5, 6, and 7 present λon $f'(\eta)$, $g(\eta)$ and $\theta(\eta)$. Here the $f'(\eta)$ and $g(\eta)$decreases by increasing λ. The Coriolis force turns to stronger and stronger by escalating λ that leads to increase in $f'(\eta)$ profile. It is notice that the values of $g(\eta)$ are negative which means that the fluid is moving along negative y-axis. Further, for large values of rotation parameter the function $f'(\eta)$ happen to negative near $\eta = 0$, which implies that the fluid flows along x-direction at small region. This is all because of the significant influence of Corioils force along with the stretching influence. It is seen that the temperature significantly increases as strength of Lorentz and Corioils forces are increased.

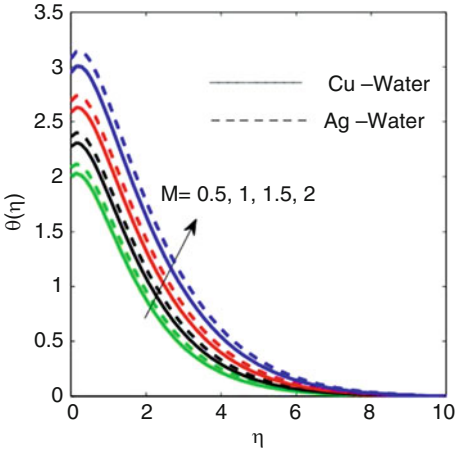

Fig. 4 Influence of M on $\theta\ (\eta)$

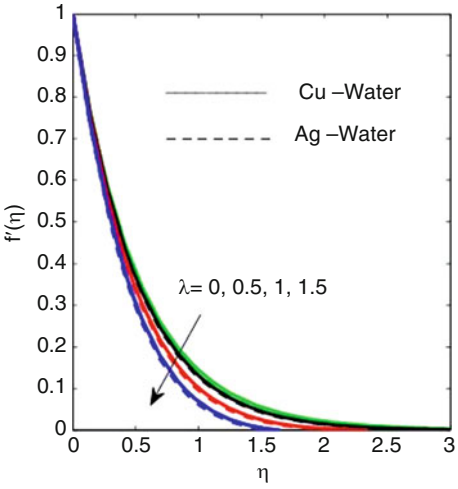

Fig. 5 Influence of λ on $f'\ (\eta)$

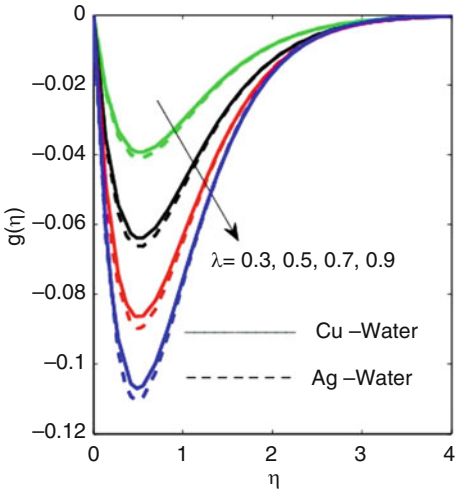

Fig. 6 Influence of λ on $g\ (\eta)$

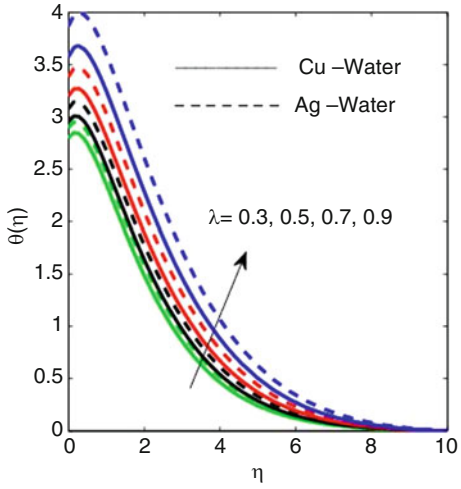

Fig. 7 Influence of λ on $\theta\,(\eta)$

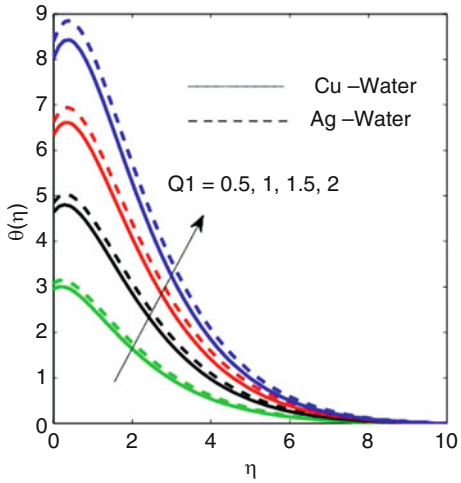

Fig. 8 Influence of $Q1$ on $f'\,(\eta)$

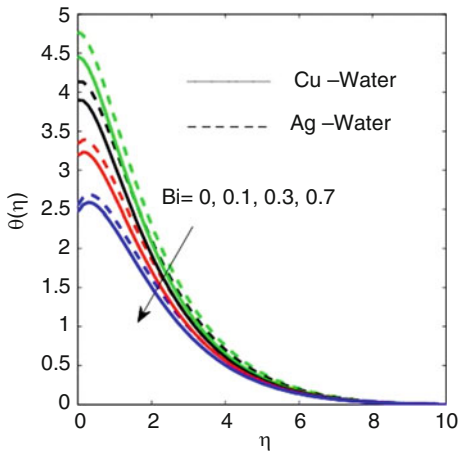

Fig. 9 Influence of Bi on $g\,(\eta)$

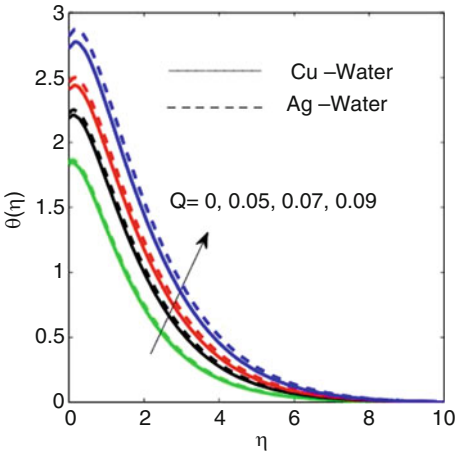

Fig. 10 Influence of Q on θ (η)

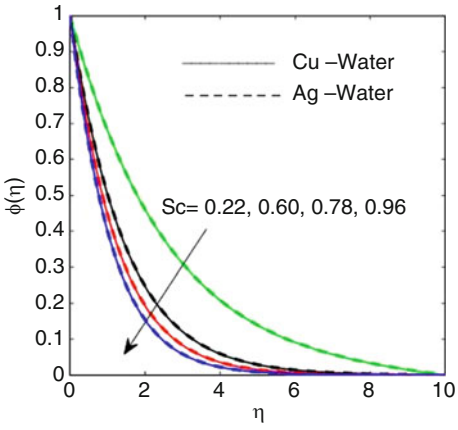

Fig. 11 Influence of Sc on π (η)

The impact of heat generation/absorption and radiation absorption on the dimensionless temperature profiles are shown in Figs. 8 and 10, respectively for both Cu-water and Ag-water based nanofluids. It is evident that the temperature increase with an increase in the heat source parameter. These results qualitatively agree with expectation since the effect of internal heat generation is to increase the rate of heat transport to the fluid there by increasing the temperature, we also observe that an increase the radiation absorption parameter the nanofluid temperature increases for both the fluids. The effect of B_i on temperature profile is show in Fig. 9. On viewing this figure, the temperature of both Cu-water nanofluid and Ag-water nanofluid is increases with the increasing parameter B_i. The concentration profiles are presented for different values Sc in Fig. 11. It is noticed that increase of Schmidt number leads to decrease in concentration of the species.

References

1. Wang, C. Y.: The three-dimensional flow due to a stretching flat surface. Phys. Fluids. **27** (8), 1915–1917 (1984)
2. Takhar, H. S., Chamkha, A. J., Nath, G.: Unsteady three-dimensional MHD-boundary-layer flow due to the impulsive motion of a stretching surface. Acta Mech. **146**, 59–71 (2001)
3. Kumari, M., Nath, G.: Analytical solution of unsteady three-dimensional MHD boundary layer flow and heat transfer due to impulsively stretched plane surface. Commun. Nonlin. Sci. Numeri. Simul. **14** (8), 3339–3350 (2009)
4. Choi, S. U. S.: Enhancing thermal conductivity of fluids with nanoparticles, ASME, USA., FED 231/MD, 99–105, (1995)
5. Mohaghegh, M. R., Asghar, B. R.: Three-dimensional stagnation-point flow and heat transfer of a dusty fluid toward a stretching sheet. J. Heat Trans. **138** (11) 112001 (2016)
6. Sabyasachi, M., Oyelakin, I. S., Sibanda, P.: Unsteady mhd three dimensional casson nanofluid flow over a porous linear stretching sheet with slip condition. FHMT. **8**, (2017)
7. Shateyi, S.: Numerical analysis of three-dimensional MHD nanofluid flow over a stretching sheet with convective boundary conditions through a porous medium. Nanofluid Heat Mass Trans. Eng. Problems, (2017)
8. Nayak, M. K., Akbar, n. S., Tripathi, D., Pandey, V. S.: Three dimensional MHD flow of nanofluid over an exponential porous stretching sheet with convective boundary conditions. J.Thermal Science and Eng. Progress. **3**, 133–140 (2017)
9. Nayak, M. K., Akbar, N. s., Pandey, V. S., Hayat, K., Dharmendra, T.: 3D free convective MHD flow of nanofluid over permeable linear stretching sheet with thermal radiation. Powder Tech. **315**, 205–215 (2017)
10. Rahimah, J., Nazar, R., Pop, I.: Flow and heat transfer of magnetohydrodynamic three-dimensional Maxwell nanofluid over a permeable stretching/shrinking surface with convective boundary conditions. Int. J. Mech. Sci. **124–125**, 166–173 (2017)
11. Chen, H., Chen, J., Yao, G., Chen, K.: Three-dimensional boundary layer flow over a rotating disk with power-law stretching in a nanofluid containing gyrotactic microorganisms. J. Transfer-Asian Res. (2017)
12. Forghani, P. T., Karimipour, A., Afrand, M., Mousavi, S.: Different nano-particles volume fraction and Hartmann number effects on flow and heat transfer of water-silver nanofluid under the variable heat flux, Phys. E: Low-dim. Syst. Nanost. **85**, 271–279 (2017)

MHD Carreau Fluid Flow Past a Melting Surface with Cattaneo-Christov Heat Flux

K. Anantha Kumar, Janke V. Ramana Reddy, V. Sugunamma, and N. Sandeep

Abstract In this article, we presented simultaneous solutions for magnetohydrodynamic Cattaneo-Christov flow of Carreau fluid over a variable thickness melting surface. Firstly, proper transformations are considered to convert the basic flow equations as ODE. The solution of these ODEs is obtained by the consecutive application of shooting and R.K. fourth-order methods. Graphs are plotted with the assistance of MATLAB package to emphasize the impact of various physical parameters on the flow fields. Further, the rate of heat transfer and friction factor are also intended and depicted with the help of a table. Results indicate that fluid velocity has inverse relationship with melting and magnetic field parameters. Also the nonuniform heat source/sink parameters play a key role in heat transfer performance.

1 Introduction

The investigation of non-Newtonian fluid flows due to stretching surface has countless applications in mechanical engineering, biomechanics, aeronautical engineering and some industrial processes like thermal insulation, production of paper, biochemical processes, crystal growth, food processing, pasteurization of milk, hot rolling, glass fibre, plastic sheet extrusion, etc. Carreau fluid is also a non-Newtonian fluid. Hanks and Larsen [5] discussed the non-Newtonian fluid flow through a ring-shaped region. Khan and Azam [8] and Shah et al. [14] have analysed the flow and heat transport phenomenon of Carreau fluid flow over a stretching surface. Further, Kumar et al. [9] analysed the flow and heat transfer attributes of Casson fluid over a stretching surface with cross-diffusion.

K. Anantha Kumar · J. V. Ramana Reddy · V. Sugunamma (✉)
Department of Mathematics, Sri Venkateswara University, Tirupati, India
e-mail: ananthakumar.kempannagari@svuniversity.edu.in; vsuguna@svuniversity.edu.in

N. Sandeep
Department of Mathematics, Central University of Karnataka, Kalaburagi, India

B. Rushi Kumar et al. (eds.), *Applied Mathematics and Scientific Computing*,
Trends in Mathematics, https://doi.org/10.1007/978-3-030-01123-9_32

In 1948, Cattaneo [3] proposed a model to acquire effective heat transfer rate with the inclusion of thermal relaxation time to Fourier's model. Later, Christov [4] proposed the time-derivative model to Cattaneo's model, and it is termed as Cattaneo-Christov heat flux model. This mechanism plays a vital role in various processes like thermization of milk and making of microchips and electronic devices. Hayat et al. [6] utilized this model to examine the heat transport phenomenon. Kumar et al. [10] proposed a model to analyse the heat transfer behaviour of MHD flow over a cone/wedge in the presence of nonuniform heat sink/source.

Babu and Sandeep [2] and Kumar et al. [11] analysed the impact of cross-diffusion on MHD viscoelastic liquid flow over a melting surface. The heat transfer attributes on MHD nanofluid flow over a stretching surface were reported by Sandeep and Animasaun [13]. Recently, Reddy et al. [12] reported the combined influence of heat and mass transport on MHD Casson and Maxwell fluids over a linearly stretched surface. Shateyi [15] analysed the magnetohydrodynamic flow of non-Newtonian fluid past a stretched surface with heat and mass transfer.

The melting heat transport aspect has auspicious importance in mechanical and chemical engineering processes. Hayat et al. [7] presumed a problem to analyse the stagnation point flow of non-Newtonian liquid over a linear surface with melting heat transport. The impact of exponential heat source on non-Newtonian liquid flow via melting surface with variable fluid properties was studied by Adegbie et al. [1].

2 Modelling of the Problem

Here an unsteady, two-dimensional flow of an incompressible Carreau fluid over a linear/nonlinear variable thickness surface is considered. The Cattaneo-Christov heat flux is implemented to scrutinize the heat transport performance. Let us imagine the variable thickness of the sheet is $y = L\,(x + p_1)^{\frac{1-p}{2}}$, where p_1, L are constants and p is the velocity power law index. Here $p = 1$ refers to the flow past a linear surface, and $p > 1$ refers to the flow past a nonlinear stretching surface. The flow is imagined in the region $y \geq 0$. The x and y axes are taken along and normal to the surface, respectively, as depicted in Fig. 1. The varying magnetic field $B(x) = B_0(x + p_1)^{\frac{p-1}{2}}$ is applied normal in the flow direction as displayed in Fig. 1. Here B_0 is the strength of the magnetic field. The impact of variable heat sink/source and melting heat transfer is accounted.

Owing to the afore taken presumptions, the governing equations of the flow are (see Ref. [8])

$$\frac{\partial u}{\partial x} + \frac{\partial v}{\partial y} = 0, \tag{1}$$

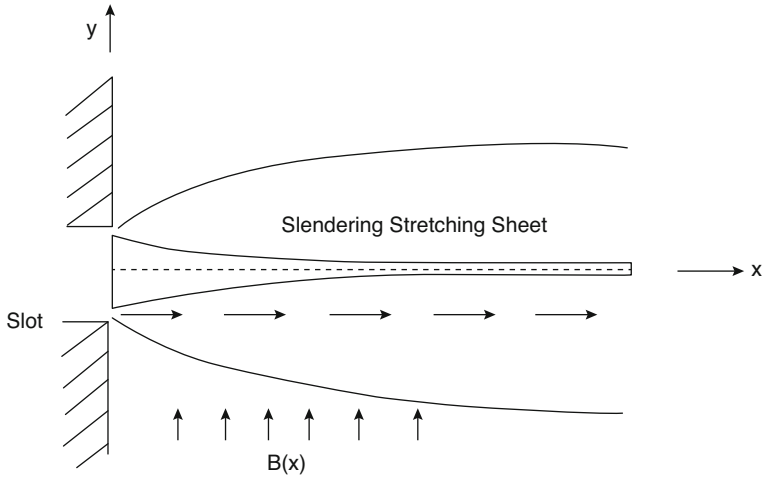

Fig. 1 Flow Geometry

$$\frac{\partial u}{\partial t}+u\frac{\partial u}{\partial x}+v\frac{\partial u}{\partial y}=\nu\frac{\partial^2 u}{\partial y^2}+3\nu\frac{n-1}{2}\Gamma^2\left(\frac{\partial u}{\partial x}\right)^2\frac{\partial^2 u}{\partial y^2}-\frac{\sigma B(x)^2}{\rho}, \tag{2}$$

$$\left.\begin{aligned}\frac{\partial T}{\partial t}+u\frac{\partial T}{\partial x}+v\frac{\partial T}{\partial y}+\delta\left(\frac{\partial^2 T}{\partial t^2}+2u\frac{\partial^2 T}{\partial t\partial x}+2v\frac{\partial^2 T}{\partial t\partial y}+\right.\right.\\ 2uv\frac{\partial^2 T}{\partial x\partial y}+u^2\frac{\partial^2 T}{\partial x^2}+v^2\frac{\partial^2 T}{\partial y^2}+\frac{\partial T}{\partial x}\left(\frac{\partial u}{\partial t}+u\frac{\partial u}{\partial x}+v\frac{\partial u}{\partial y}\right)+\\ \left.\left.\frac{\partial T}{\partial y}\left(\frac{\partial v}{\partial t}+u\frac{\partial v}{\partial x}+v\frac{\partial v}{\partial y}\right)\right)=\frac{k}{\rho C_p}\frac{\partial^2 T}{\partial y^2}+\frac{Q^*}{\rho C_p}\right.\end{aligned}\right\}, \tag{3}$$

Here (u, v) are the velocity components of (x, y) directions, respectively, t is the time, ν is the kinematic viscosity, ρ is fluid density, σ is electrical conductivity of the fluid, n is the non-Newtonian power law index, Γ is the relaxation time, T is the fluid temperature, k is thermal conductivity, C_p is the heat capacitance and δ is relaxation time of the heat flux.

In Eq. (3), the second term in the R.H.S, Q^* is added to discuss the concept of nonuniform heat source or sink, and it is given by (see Ref. [10])

$$Q^*=\frac{ku_s(x,t)}{(x+p_1)\nu}\left(A^*(T_\infty-T_m)f'+B^*(T-T_m)\right), \tag{4}$$

Here $T_m - T_\infty = T_0(x+p_1)^{\frac{(1-p)}{2}}(1-\alpha_1 t)^{-0.5}$; T_m is the melting temperature; T_∞, T_0 are the ambient and reference temperatures of the fluid, respectively; A^*, $B^* > 0$ represents the internal heat source; and A^*, $B^* < 0$ represents the internal heat sink.

The corresponding boundary conditions of the problem are given by (see Ref. [7])

$$\left.\begin{aligned} u = u_s(x,t),\ v = 0,\ k\frac{\partial T}{\partial y} = \frac{[\delta + c_s(T_m - T_0)]}{\rho {c_s}^{-1}} v(x,y),\ T = T_m \quad \text{at} \quad y = \frac{(x+p_1)^{\frac{1-p}{2}}}{L^{-1}}, \\ u \to 0,\ v \to 0,\ T \to T_\infty \qquad as \quad y \to \infty, \end{aligned}\right\} \tag{5}$$

Here $u_s(x,t)$ is the stretching velocity of the sheet, $p_0 > 0$ is a constant, α_1 is the unsteadiness constant, and c_s is the concentration susceptibility.

Consider the following transformations in order to get the non-dimensional expressions of the flow equations (see Ref. [8]):

$$\left.\begin{aligned} u = \frac{\partial \zeta}{\partial y} = \frac{p_0(x+p_1)^p}{(1-\alpha_1 t)} f'(\chi),\ T = T_m + (T_\infty - T_m)\theta(\chi), \\ v = -\frac{\partial \zeta}{\partial y} = -\sqrt{\frac{(p+1)\nu p_0 (x+p_1)^{p-1}}{2(1-\alpha_1 t)}}\left[f(\chi) + \chi\left(\frac{p-1}{p+1}\right) f'(\chi)\right], \end{aligned}\right\} \tag{6}$$

Here $\chi = y\sqrt{\frac{(p+1)p_0}{2\nu}}$ is the similarity variable, $\zeta = \sqrt{\frac{2\nu p_0 (x+p_1)^{p-1}}{(p+1)}} f(\chi)$ is the stream function, f' and θ (functions of χ) signify the dimensional velocity and temperature fields with domain $[\lambda, \infty)$. (u, v) satisfies trivially the equation of continuity.

Using Eqs. (4) and (7) in Eqs. (1)–(3) and (5)–(6), we obtain the nonlinear ODEs in terms of f and θ with the domain $[\lambda, \infty)$. In order to facilitate the computation, we change the domain $[\lambda, \infty)$ into $[0, \infty)$ using the following transformations (see Ref. [2]):

$$F(\eta) = F(\chi - \lambda) = f(\chi),\ \Theta(\eta) = \Theta(\chi - \lambda) = \theta(\chi), \tag{7}$$

Here η is the new similarity variable.

In view of the above transformation, we obtain

$$F''' + FF'' + \frac{3(n-1)We^2}{4(p+1)^{-1}}(F'')^2 F''' = \frac{2\left(p(F')^2 + MF' + A(F' - \chi F'')\right)}{(p+1)}, \tag{8}$$

$$\left.\begin{aligned}\left(\frac{p+1}{2Pr}\right)\Theta''+\frac{1}{2}\left(F\Theta'+(p-1)F\Theta'-A(\Theta+\chi\Theta')\right)-\frac{1}{Pr}\left(A^*F'+\right.\\ B^*\Theta\Big)-\beta\Bigg[\frac{(p+1)^2}{4}F^2\Theta''-\frac{(p^2-1)}{4}FF''\Theta-\frac{(p-3)(p+1)}{2}FF'\Theta'+\\ \frac{(p-1)^2}{4}\left(3\Theta(F')^2+\chi^2F'F''\Theta'+2(p-1)^2\chi(F')^2\Theta'\right)+\alpha_1\left(\frac{A}{2}\left(3\Theta+\right.\right.\\ 5\chi\Theta'+\chi^2\Theta''\Big)-\frac{p+1}{2}\left(5F\Theta'\right)+\frac{p+1}{2}\left(2\chi F\Theta''\right)+\\ \left.\left.\frac{3p-1}{2}\chi F'\Theta'+\frac{p-1}{2}\left(4F'\Theta+\chi F''\Theta-2\chi F\Theta'\right)\right)\Bigg]=0\end{aligned}\right\}, \tag{9}$$

$$\left.\begin{aligned}F'(0)=1, M_l\Theta'(0)=Pr\left(F(0)+\frac{p-1}{p+1}\lambda\right), \Theta(0)=1 \quad at \quad \eta=0,\\ F'(\infty)\to 0, \Theta(\infty)\to 1 \qquad as \quad \eta\to\infty,\end{aligned}\right\} \tag{10}$$

Here ($'$) signifies the derivative w.r.t. η, $We=\left(\frac{\Gamma^2 p_0{}^3(x+p_1)^{3p-1}}{\nu(1-\alpha_1 t)}\right)$ is the Weissenberg number, $M=\frac{\sigma {B_0}^2}{p_0\rho}$is the magnetic field parameter, $A=\frac{\alpha_1(x+p_1)^{1-p}}{p_0}$ is the unsteadiness parameter, $Pr=\frac{\mu C_p}{k}$ is Prandtl number, $\beta=\frac{\delta p_0\sqrt{(x+p_1)^{(1-p)}}}{(1-\alpha_1 t)}$ is the thermal relaxation parameter, $\lambda=L\sqrt{\frac{(p+1)p_0}{2\nu(1-\alpha_1 t)}}$ is the wall thickness parameter, and $M_l=\frac{C_p(T_m-T_\infty)}{(\delta+c_s(T_m-T_0))}$ is the melting parameter.

The physical quantities in view of scientific applications are friction factor (C_f) and heat transfer rate (Nu). These are derived for present problem as

$$C_f=2\sqrt{\frac{p+1}{2}}(Re_x)^{\frac{-1}{2}}\left(1+\frac{(n-1)(P+1)(We)^2(F''(0))F'''(0)}{4}\right)F''(0), \tag{11}$$

$$Nu=-\sqrt{\frac{p+1}{2}}(Re_x)^{\frac{1}{2}}\Theta'(0), \tag{12}$$

where $Re_x=\frac{(x+p_1)u_s}{\nu}$ is the local Reynolds number.

3 Deliberation of Results

The nonlinear ODEs (8) and (9) with the boundary conditions (10) are solved numerically by utilizing the well-known fourth-order Runge-Kutta-based shooting methods. The impact of sundry physical parameters on the fluid temperature and velocity field is shown through plots. Further, we examine the effect of same

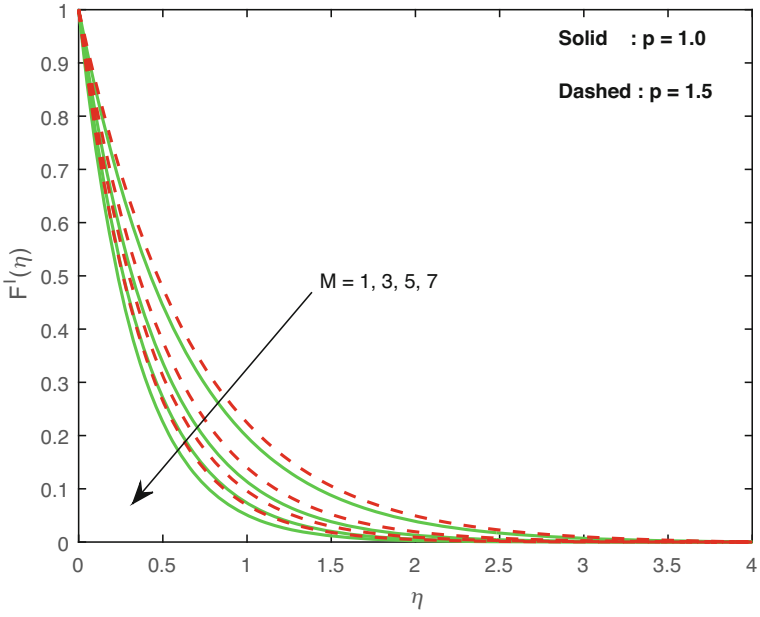

Fig. 2 Impact of M on $F'(\eta)$

parameters on C_f and Nu, and results are displayed in a table. Results are obtained by allotting the values of dimensionless parameters as $We = 0.5$, $p = 1.5$, $M = 5$, $A = 1.2$, $A^* = B^* = 0.3$, $\beta = 0.5$, $\lambda = 0.2$, $Pr = 7$, $\eta = 1$ and $M_l = 0.7$. We have been taken these values as common for the entire analysis of results, unless otherwise stated in figures and tables.

Figure 2 reveals the nature of $F'(\eta)$ for different values of M. It is fascinating to see that the fluid velocity is a decreasing function of M. The attendance of M in an electrically conducting fluid pioneers a force called Lorentz force which acts against the flow direction. This frictional force has a tendency to slow down the flow. Figure 3 displays the impact of $F'(\eta)$ on We. The ratio between relaxation time of the fluid and a particular process time is termed as Weissenberg number. It is discerned that when We increases, the velocity profile and its boundary layer enhance for the flow past a nonlinear surface. But the fluid velocity past a linear surface does not impacted by We.

The influence of thermal relaxation parameter β on velocity and temperature distribution can be seen in Figs. 4 and 5, respectively. We claim that β helps to diminish the velocity and temperature of the fluid. The physical reason for these results is that as we increase the values of β, fluid particles exhibit non-conducting nature owing to which they require more time to bring the heat to their surrounding particles.

The variation in the graphs of $F'(\eta)$ and $\Theta(\eta)$ using different values of M_l is manifested in Figs. 6 and 7 correspondingly. It is fascinating to detect

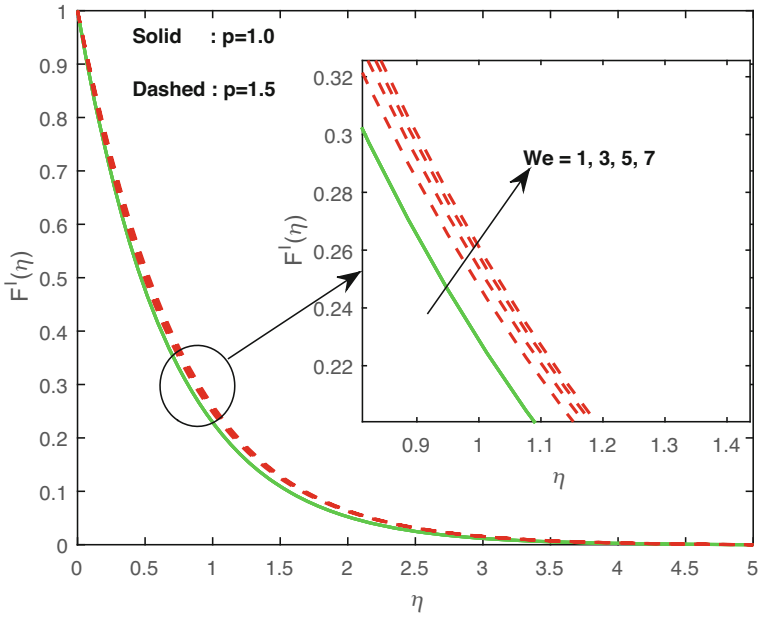

Fig. 3 Impact of We on $F'(\eta)$

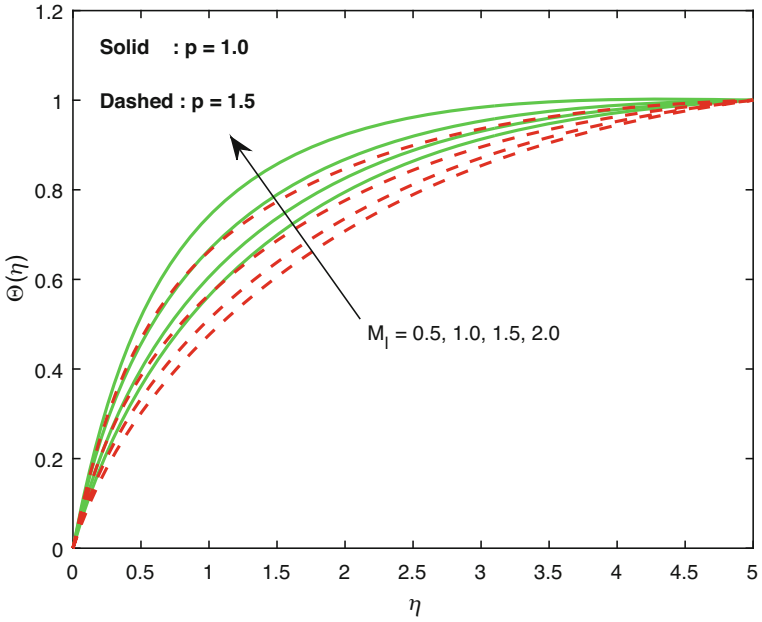

Fig. 4 Impact of β on $F'(\eta)$

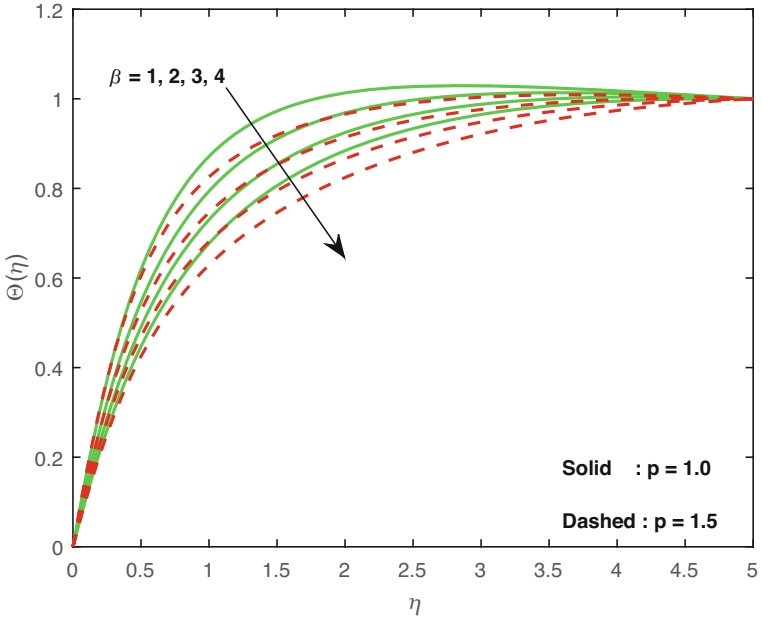

Fig. 5 Impact of β on $\Theta(\eta)$

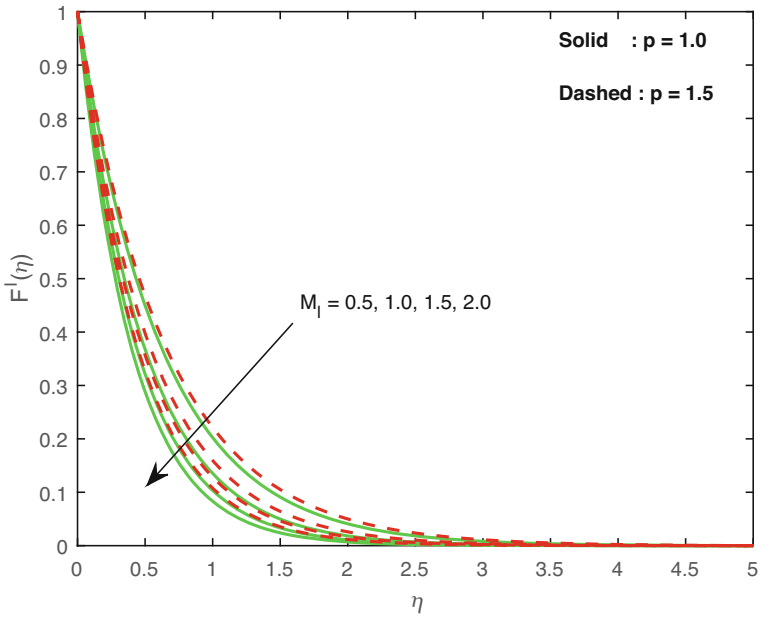

Fig. 6 Impact of M_l on $F'(\eta)$

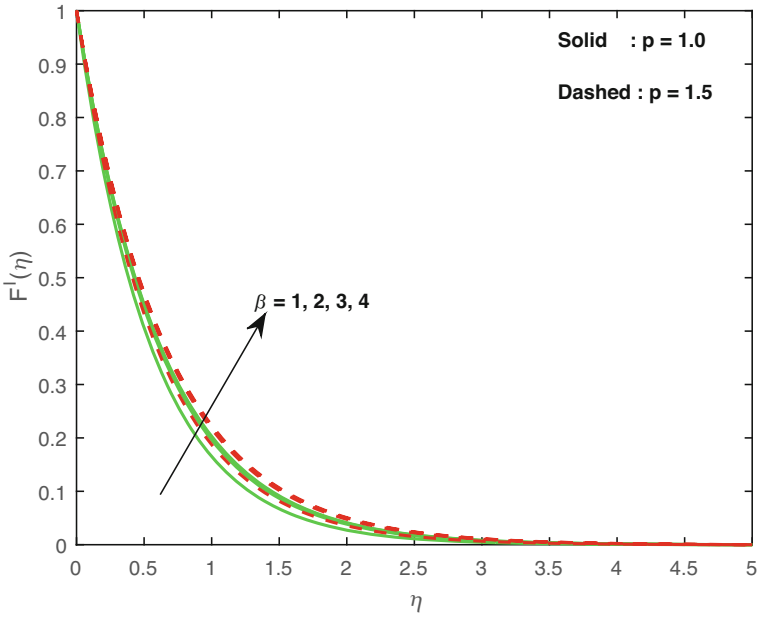

Fig. 7 Impact of M_l on $\Theta(\eta)$

that both the profile velocity and temperature are decreasing functions of M_l. Generally, an increase in M_l causes an enhancement in the potency of the melting, and hence more thermal energy is released from melting sheet to the fluid. It is detected that influence of M_l is more on fluid velocity when compared to temperature.

Figures 8 and 9 are plotted to know the essence of velocity and thermal fields for disparate irregular heat parameter (A^*) values. These figures enable us to conclude that increasing values of A^* enhance the thermal field but a divergent result is perceived for the velocity field. Physically, increasing values of A^* enhances the thermal boundary layer thickness, and hence it serve as an agent to generate heat in the fluid. Owing to this, a magnification in thermal field and a reduction in fluid velocity are observed for raising values of A^*.

From Table 1 it is found that rising values of M, A and Pr enhance the heat transfer rate, but an opposite result is noticed in friction factor. A strength in Weissenberg number causes a reduction in local Nusselt number, but a hike in friction factor is noticed for both cases. Both heat transfer rate and friction factor reduce with rising values of A^*, B^*, M_l and β. Boosting values of λ enhance the friction factor and heat transfer performance for the flow over a nonlinear stretching surface.

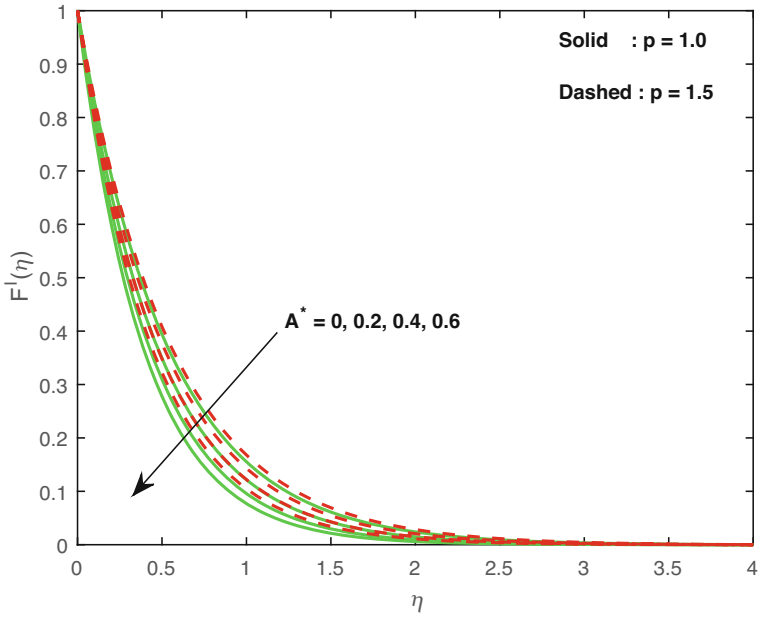

Fig. 8 Impact of A^* on $F'(\eta)$

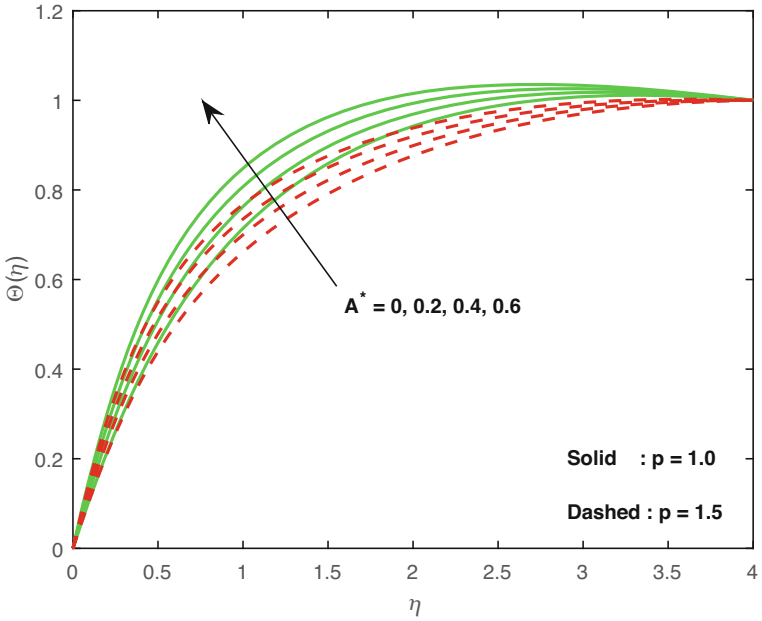

Fig. 9 Impact of A^* on $\Theta(\eta)$

Table 1 Variation of C_f and Nu for sundry physical parameters of the flow past a linera/nonlinear variable thickness surface

λ	β	A^*	M_l	We	C_f $(p = 1.0)$	C_f $(p = 1.5)$	Nu $(p = 1.0)$	Nu $(p = 1.5)$
0.1					−1.4306	−1.4040	−0.5918	−0.9681
0.2					−1.4306	−1.3907	−0.5918	−0.8892
0.3					−1.4306	−1.3773	−0.5918	−0.8123
0.4					−1.4306	−1.3641	−0.5918	−0.7374
	1.0				−3.8501	−3.3694	−2.8557	−2.3722
	2.0				−3.5334	−3.1105	−2.2102	−1.8257
	3.0				−3.4016	−3.0028	−1.9306	−1.5888
	4.0				−3.3261	−2.9410	−1.7670	−1.4500
		0.0			−1.3986	−1.3751	−0.3525	−0.4599
		2.0			−1.4014	−1.3773	−0.4243	−0.5186
		4.0			−1.4041	−1.3795	−0.4962	−0.5773
		6.0			−1.4069	−1.3817	−0.5682	−0.6362
			0.5		−1.2844	−1.2692	−0.9103	−0.9634
			1.0		−1.3487	−1.3291	−1.1880	−1.1983
			1.5		−1.4684	−1.4258	−1.6540	−1.5297
			2.0		−1.6722	−1.5640	−2.2557	−1.8789
				1.0	−1.4341	−1.3409	−1.6715	−0.7553
				3.0	−1.4341	−1.2853	−1.6715	−0.7706
				5.0	−1.4341	−1.2519	−1.6715	−0.7815
				7.0	−1.4341	−1.2288	−1.6715	−0.7899

4 Important Findings

- Fluid velocity suppresses for swelling values of M, A and M_l.
- Temperature field unveils reducing behaviour for higher values of β, Pr and M.
- Temperature gradient raises for higher values of A^*, $B^*$and M_l.
- C_f can be decreased by rising Pr, but a reverse trend is detected for λ and M_l.
- Nusselt number increases with increasing values A and M.

References

1. Adegbie, K.S., Omowaye, A.J., Disu, A.B., Animasaun, I.L.: Heat and mass transfer of upper convected Maxwell fluid flow with variable thermo-physical properties over a horizontal melting surface. Appl. Math. **6**, 1362–1379 (2016)
2. Babu, M.J., Sandeep, N.: MHD non-Newtonian fluid flow over a slendering stretching sheet in the presence of cross-diffusion effects. Alex. Eng. J. **55**, 2193–2201 (2017)
3. Cattaneo, C.: Sulla conduzione del calore. Atti Semin. Mat. Fis. Univ. Modena Reggio Emilia **3**, 83–101 (1948)
4. Christov, C.I.: On frame indifferent formulation of the Maxwell-Cattaneo model of finite speed heat conduction. Mech. Res. Comm. **36**, 481–486 (2009)

5. Hanks, R.W., Larsen, K.M.: The flow of power-law non-Newtonian fluids in concentric Annuli. Ind. Eng. Chem. Fund.**18**, 33–35 (1979)
6. Hayat, T., Farooq, M., Alsaedi, A., Solamy, F.A.: Impact of Cattaneo-Christov heat flux in the flow over a stretching sheet with variable thickness. AIP Adv. **5**, Article Id: 087159 (2015)
7. Hayat, T., Mustafa, M., Shehzad, S.A., Obaidat, S.: Melting heat transfer in the stagnation point flow of an Upper-convected Maxwell (UCM) fluid past a stretching sheet. Int. J. Numer. Meth. Fluids. **68**, (2012) 233–243
8. Khan, M., Azam, M.: Unsteady boundary layer flow of Carreau fluid over a permeable stretching surface. Res. Phys. **6**, 1168–1174 (2016)
9. Kumar, K.A., Reddy, J.V.R., Sandeep, N., Sugunamma, V.: Dual solutions for thermo diffusion and diffusion thermo effects on 3D MHD Casson fluid flow over a stretching surface, Res. J. Pharm. Tech. **9**, 1187–1194 (2016)
10. Kumar, K.A., Reddy, J.V.R., Sugunamma, V., Sandeep, N.: Magnetohydrodynamic Cattaneo-Christov flow past a cone and a wedge with variable heat source/sink. Alex. Eng. J. **57**, 435–443 (2018)
11. Kumar, K.A., Reddy, J.V.R., Sugunamma, V., Sandeep, N.: Impact of cross diffusion on MHD viscoelastic fluid flow past a melting surface with exponential heat source. Multi. Mod. Mat. Str., (2018) https://doi.org/10.1108/MMMS-12--2017-0151
12. Reddy, J.V.R., Kumar, K.A., Sugunamma, V., Sandeep, N.: Effect of cross diffusion on MHD non-Newtonian fluids flow past a stretching sheet with non-uniform heat source/sink: A comparative study. Alex. Eng. J. (2017) https://doi.org/10.1016/j.aej.2017.03.008
13. Sandeep, N., Animasaun, I.L.: Heat transfer in wall jet flow of magnetic-nanofluids with variable magnetic field. Alex. Eng. J. **56**, 263–269 (2017)
14. Shah, R.A., Abbas, T., Idrees, M., Ullah, M.: MHD Carreau fluid slip flow over a porous stretching sheet with viscous dissipation and variable thermal conductivity. Bound. Value Prob. **94**, (2017) https://doi.org/10.1186/s13661-017-0827-4
15. Shateyi, S.: A new numerical approach to MHD flow of a Maxwell fluid past a vertical stretching sheet in the presence of thermophoresis and chemical reaction. Bound. Value Prob. **196**, (2013) https://doi.org/10.1186/1687-2770-2013-196

Effect of Porous Uneven Seabed on a Water-Wave Diffraction Problem

Manas Ranjan Sarangi and Smrutiranjan Mohapatra

Abstract Utilizing the linearized wave theory, the issue of the diffraction of obliquely progressive waves by a little contortion on a porous sea-bed is investigated. By the help of perturbation hypothesis, the related problem is diminished to a boundary value problem (BVP) for the first-order velocity potential function. Then the first-order potential function and, henceforth, the first-order reflection as well as transmission coefficients are evaluated by Fourier transform technique. A particular frame of sinusoidal ripples has been considered for verifying the theoretical results.

1 Introduction

In late decades, there has been a growing interest in the problems of the propagation of waves over a submerged object at the base of a sea because of growing experimental activities in the field of coastal engineering. Different techniques have discussed to analyze the reflected as well as transmitted energy in water waves due to a submerged structure in a sea with rigid base surface.

A diffraction of waves by a little base contortion in a sea with free surface creates exciting problems pulling the attention of different cases for getting their required results (Davies [2], Mohapatra and Bora [6] and Mohapatra [7, 8]). Mei [5] evolved the wave evolution as well as the reflection theory near the case of Bragg resonance for a beach sinusoidal bars. Davies and Heathershaw [3] studied the issue of wave diffraction by a contortion surface in a sea. For the issue of internal waves over a contortion surface, the mild-slope condition was first introduced by Kirby [4], and then Chamberlain and Porter [1] proposed an approximate theoretical hypothesis which originally involves depth averaging, along with the consideration of the

M. R. Sarangi (✉) · S. Mohapatra
VSS University of Technology, Burla, Odisha, India
e-mail: smohapatra_math@vssut.ac.in

B. Rushi Kumar et al. (eds.), *Applied Mathematics and Scientific Computing*,
Trends in Mathematics, https://doi.org/10.1007/978-3-030-01123-9_33

little discrepancy of the rigid bottom surface. Recently, Mohapatra and Sarangi [9] studied a water-wave diffraction problem in a channel which is bounded by an infinite rigid horizontal upper surface, and the bed is having a porous surface with a little bottom contortion.

In the present study, we examine a diffraction problem of obliquely incident progressive waves in a sea where the base is taken as a porous surface having a little contortion. Here, the fluid movement beneath the porous surface of the seabed is not investigated. It is considered that the movement of the fluid particles is such a way that the assuming condition at the porous base surface holds good in this study and only depends on a known parameter D, named as the porosity parameter. Under the typical suspicions of linear wave hypothesis and then by utilizing Fourier transform hypothesis, we evaluated the reflection as well as transmission coefficients approximately in terms of integral involving the frame of the base contortion. We exhibit a particular frame of base contortion, that is, a patch of sinusoidal ripples and the first-order reflection coefficient is portrayed graphically for several estimations of the various parameters.

2 Formulation of the Physical Problem

Assume an incompressible and inviscid fluid flow on a sea with the porous base surface which is having a little contortion. The fluid region is extended horizontally in x-direction, and its depth is taken vertically downward in y-direction. Let the line $x = 0$ indicate the mean position of the free surface and $y = h$ as the base surface. Furthermore, the motion of the fluid is assumed to be irrotational and time harmonic with angular frequency ω. The base surface of the sea is represented as $y = h+\epsilon c(x)$, where the $\epsilon(\ll 1)$ is a measure of the smallness of the contortion and $c(x)$ is a differentiable function. Assuming the linear wave hypothesis, the potential function $\widetilde{\chi}(x, y, z, t)$ in the fluid can be described as

$$\widetilde{\chi}(x, y, z, t) = Re\{e^{i(\nu z-\omega t)}\chi(x, y)\} \text{ on } -\infty < x < \infty,\ 0 < y < h + \epsilon c(x), \tag{1}$$

where ν is the component of the incident field wavenumber along z-direction. The spatial velocity potential function $\chi(x, y)$ follows the modified Helmholtz equation:

$$(\nabla^2_{x,y} - \nu^2)\ \chi = 0 \text{ on } -\infty < x < \infty,\ 0 < y < h + \epsilon c(x), \tag{2}$$

where $\nabla^2_{x,y} = \partial^2/\partial x^2 + \partial^2/\partial y^2$. The linearized conditions near the free surface and at the porous base surface are

$$\chi_y + K\chi = 0 \text{ on } -\infty < x < \infty,\ y = 0, \tag{3}$$

$$\chi_n - D\chi = 0 \text{ on } -\infty < x < \infty,\ y = h + \epsilon c(x), \tag{4}$$

where $K = \omega^2/g$, g denotes the acceleration due to gravity, $\partial/\partial n$ represents the normal derivative to the base surface, and D represents the porous effect parameter on the base surface. In the above fluid region, a train of obliquely incident waves which propagates along the positive horizontal direction is:

$$\chi_0(x, y) = \mathrm{e}^{\mathrm{i}(\sqrt{k^2-\nu^2})x}\ f(k, y), \tag{5}$$

where

$$f(k, y) = \left[\frac{(D/k)\sinh k(h-y) - \cosh k(h-y)}{(D/k)\sinh kh - \cosh kh}\right],\quad -\infty < x < \infty,\ 0 \le y \le h, \tag{6}$$

with $\cosh kh - \left(\frac{D}{k}\right)\sinh kh$ which is non-zero, and the positive number $k \in \mathbb{R}$ needs to satisfy the dispersion condition:

$$\Delta(k) \equiv [(D/k)K + k]\tanh kh - (D + K) = 0. \tag{7}$$

In Eq. (7), there exists a real root $k = u_0(> 0)$ that demonstrates the engendering modes and an infinite number of purely imaginary roots $\mathrm{i}k_n$ $(n \in \mathbb{N})$ that correspond to a set of evanescent modes, where the positive real numbers k_n satisfy the following equation:

$$K + D + [\widetilde{k} + K(D/\widetilde{k})]\tanh \widetilde{k}h = 0. \tag{8}$$

Assuming, for little bottom contortion, ϵ to be small enough, and avoiding the second- and higher-order terms, Eq. (4) can be written as

$$\chi_y - \epsilon\frac{d}{dx}[c(x)\chi_x] - c(x)\nu^2\chi - D[\chi + \epsilon c(x)\chi_y] + O(\epsilon^2) = 0 \quad \text{on } y = h. \tag{9}$$

The far-field condition of $\chi(x, y)$ is

$$\chi \sim \begin{cases} (\mathrm{e}^{-\mathrm{i}kx}R + \mathrm{e}^{+\mathrm{i}kx})\ f(k, y), & x \to -\infty, \\ \mathrm{e}^{+\mathrm{i}kx}T\ f(k, y), & x \to \infty, \end{cases} \tag{10}$$

where R and $T \in \mathbb{C}$, respectively, are the reflection and transmission coefficients and the values of these constants are to be evaluated. Now, the perturbation hypothesis can be utilized to get these constants up to the first order. By utilizing the perturbation hypothesis, the whole fluid domain $-\infty < x < \infty$, $0 \le y \le h + \epsilon c(x)$ is transferred to the uniform finite strip, $-\infty < x < \infty$, $0 \le y \le h$ in the following analysis.

3 Solution of the Problem

Let us consider a train of obliquely transit waves engenders on the porous base contortion of a seabed. When there is no base contortion, the obliquely transit waves will pass on without any disturbance, and, in this case, the only transmission will appear. Now, the above assumption along with the convenient form of the condition (9) proposes that $\chi(x, y)$, R, and T can be formulated in terms of ϵ as:

$$\left.\begin{aligned} &\chi(x, y) = \chi_0(x, y) + \epsilon\ \chi_1(x, y) + O(\epsilon^2),\\ &R = \epsilon\ R_1 + O(\epsilon^2),\\ &T = 1 + \epsilon\ T_1 + O(\epsilon^2), \end{aligned}\right\} \tag{11}$$

where $\chi_0(x, y)$ is given by (5). In the case of a huge reflection, the perturbation series, described in Eq. (11), needs to filter so that it can easily handle for the Bragg resonance case which was studied in Mei [5]. Utilizing Eq. (11) in Eqs. (2), (3), (9), and (10) and then comparing the first-order terms of ϵ in these equations, we obtain a BVP for the function χ_1 which follows:

$$(\nabla^2_{x,y} - \nu^2)\ \chi_1 = 0 \quad \text{on} \quad -\infty < x < \infty,\ 0 \le y \le h + \epsilon c(x), \tag{12}$$

$$\chi_{1y} + K\chi_1 = 0 \quad \text{on} \quad -\infty < x < \infty,\ y = 0, \tag{13}$$

$$\begin{aligned} \chi_{1y} - D\chi_1 &= \frac{\mathrm{i}u_0 \cos\theta \frac{d}{dx}[c(x)\mathrm{e}^{\mathrm{i}u_0 x\cos\theta}] + (D^2 - u_0^2 \sin^2\theta)c(x)\ \mathrm{e}^{\mathrm{i}u_0 x\cos\theta}}{\cosh u_0 h - (D/u_0)\sinh u_0 h}\\ &\equiv U(x, u_0),\quad -\infty < x < \infty,\ y = h, \end{aligned} \tag{14}$$

$$\chi_1 \sim \begin{cases} \mathrm{e}^{-\mathrm{i}kx} R_1\ f(k, y), & x \to -\infty,\\ \mathrm{e}^{+\mathrm{i}kx} T_1\ f(k, y), & x \to \infty. \end{cases} \tag{15}$$

3.1 Fourier Transform Technique

Let us assume that the Fourier transform of the first-order potential χ_1 with respect to the variable x, which is denoted by $\overline{\chi}_1(\xi, y)$, exists and is defined as

$$\overline{\chi}_1(\xi, y) = \int_{-\infty}^{\infty} \mathrm{e}^{-\mathrm{i}\xi x} \chi_1(x, y)\ dx. \tag{16}$$

Taking Fourier transform to Eqs. (12)–(14), we obtain a new BVP for $\overline{\chi}_1(\xi, y)$, that is,

$$\overline{\chi}_{1yy} - \tilde{\xi}^2\ \overline{\chi}_1 = 0,\quad 0 \le y \le h, \tag{17}$$

$$\overline{\chi}_{1y} + K\overline{\chi}_1 = 0, \quad y = 0, \tag{18}$$

$$\overline{\chi}_{1y} - D\overline{\chi}_1 = \overline{U}(\xi, u_0), \quad y = h, \tag{19}$$

where $\overline{\chi}_{1yy}$, $\overline{\chi}_{1y}$, $\overline{\chi}_1$, and $\overline{U}(\xi, u_0)$ are the Fourier transforms of χ_{1yy}, χ_{1y}, χ_1, and $U(x, u_0)$, respectively, and $\tilde{\xi}^2 = \xi^2 + \nu^2$. The solution of the above BVP is

$$\overline{\chi}_1(\xi, y) = \frac{\overline{U}(\xi, u_0)[\cosh \xi(h - y) - (D/\xi) \sinh \xi(h - y)]}{\Delta(\xi)[\cosh \xi h - (D/\xi) \sinh \xi h]}, \tag{20}$$

where

$$\overline{U}(\xi, u_0) = \frac{(D^2 + u_0^2 \cos 2\theta) \sec \theta}{\cosh u_0 h - (D/u_0) \sinh u_0 h} \int_{-\infty}^{\infty} c(x) e^{i(u_0 - \xi)x \cos \theta} dx. \tag{21}$$

$$\Delta(\xi) \equiv [\xi + K(D/\xi)] \tanh \xi h - (D + K). \tag{22}$$

The inverse Fourier transform is defined as

$$\chi_1(x, y) = \frac{1}{2\pi} \int_{-\infty}^{\infty} \mathrm{e}^{\mathrm{i}\xi x} \overline{\chi}_1(\xi, y)\, d\xi. \tag{23}$$

Applying Eq. (23) to Eq. (20), we get the final expression for $\chi_1(x, y)$ as follows:

$$\chi_1(x, y) = \frac{i[\cosh u_0(h - y) - (D/u_0) \sinh u_0(h - y)]}{\Delta'(u_0)[\cosh u_0 h - (D/u_0) \sinh u_0 h]} \times [\overline{U}(-x) e^{-iu_0 x \cos \theta} + \overline{U}(x) e^{iu_0 x \cos \theta}]. \tag{24}$$

3.1.1 Determination of Reflection and Transmission Coefficients

Now to obtain the first-order reflection as well as transmission coefficients, we compare the behaviors of $\chi_1(x, y)$ when $x \to \mp\infty$ from Eq. (24) with the far-field behaviors given in Eq. (15). To get the behavior of $\chi_1(x, y)$ as $x \to \infty$, we turn the contour in the integral having $\mathrm{e}^{\mathrm{i}\xi x}$ in the first quadrant by an angle $\beta (0 < \beta < \pi/2)$ and the contour in the integral having $\mathrm{e}^{-\mathrm{i}\xi x}$ in the fourth quadrant by the same angle β. When x tends to ∞, the integral having $\mathrm{e}^{\mathrm{i}\xi x}$ will just add a term getting from the residue at $\xi = p_0$, whereas there is no result from the integral having $\mathrm{e}^{-\mathrm{i}\xi x}$. Hence, when x tends to ∞, the resultant integral of Eq. (24) is as follows:

$$\chi_1(x, y) = \frac{i[\cosh u_0(h - y) - (D/u_0) \sinh u_0(h - y)]}{\Delta'(u_0)[\cosh u_0 h - (D/u_0) \sinh u_0 h]} \times \overline{U}(x) e^{iu_0 x \cos \theta}. \tag{25}$$

Now comparing the above estimation for $\chi_1(x, y)$ with the corresponding expression in Eq. (15), we obtain

$$T_1 = \frac{i(D^2 - u_0^2) \sec \theta}{\Delta'(u_0)[\cosh u_0 h - (D/u_0) \sinh u_0 h]} \times \int_{-\infty}^{\infty} c(x) dx. \tag{26}$$

In a similar way, taking $x \to -\infty$ in Eq. (24) and then comparing with the corresponding expression in Eq. (15), we get the first-order refection coefficient R_1 as follows:

$$R_1 = \frac{i(D^2 + u_0^2 \cos 2\theta) \sec\theta}{\Delta'(u_0)[\cosh u_0 h - (D/u_0) \sinh u_0 h]} \times \int_{-\infty}^{\infty} c(x) e^{2iu_0 x \cos\theta} dx. \quad (27)$$

Consider a fixed frame of sinusoidal ripples on the base surface of the sea with amplitude a on an otherwise flat base has the form:

$$c(x) = \begin{cases} a \sin lx, & -n\pi/l \le x \le m\pi/l, \\ 0 & \text{otherwise}, \end{cases} \quad (28)$$

where $m, n \in \mathbb{N}$, and l denote the wave number of the patch of sinusoidal ripples. Substituting $c(x)$ from Eq. (28) into Eqs. (26) and (27), we get

$$T_1 = \left\{ \frac{\mathrm{i}a(D^2 - u_0^2) \sec\theta}{\Delta'(u_0)[\cosh u_0 h - (D/u_0) \sinh u_0 h]} \right\} \times \left[\frac{(-1)^n - (-1)^m}{l} \right], \quad (29)$$

$$R_1 = \frac{\mathrm{i}al(D^2 + u_0^2 \cos 2\theta) \sec\theta}{\Delta'(u_0)[\cosh u_0 h - (D/u_0) \sinh u_0 h]} \times \left[\frac{(-1)^n \mathrm{e}^{2\mathrm{i}(u_0 \cos\theta)(-n\pi/l)} - (-1)^m \mathrm{e}^{2\mathrm{i}(u_0 \cos\theta)(-m\pi/l)}}{l^2 - 4u_0^2 \cos^2\theta} \right]. \quad (30)$$

It can be noticed that when $2u_0$ tends to l, the first-order reflection coefficient ends up noticeably unbounded opposite to our presumption that R_1 is a little amount, being the first-order improvement of the minute reflection. Thus, we assume just the cases barring this condition to escape the contradiction emerging out of the Bragg resonant case. Moreover, near the resonance case, R_1 turns a constant multiple of the total number of ripples in the patch of contortion. Also, R_1 raises linearly with the numbers m and n. Though the entire hypothesis collapses when $l = 2u_0$, a huge quantity of reflection of the incident wave energy by this uncommon type of bed surface will produce in the adjacent of the peculiarity at $l = 2u_0$.

3.2 Numerical Results

The various plots in Fig. 1 relate to different incident angles, $\theta = 0, \pi/10, \pi/6$, and $\pi/5$. For each of these plots, $m = 2$, $n = 3$, $Dh = 0.1$, $a/h = 0.1$, and $lh = 1$. It is noticed that when $\theta = 0$ (i.e., for normal incidence case), the extreme estimation of $|R_1|$ is 0.20815, achieved at $u_0 h = 0.50700$ (when $Kh = 0.151$), i.e., whenever the ripple wavenumber lh of the base contortion on the porous seabed turns out to be roughly twice as bigger as the element of the incident wavenumber $u_0 h \cos\theta$ along horizontal direction. The similar observation can be drawn for $\theta > 0$

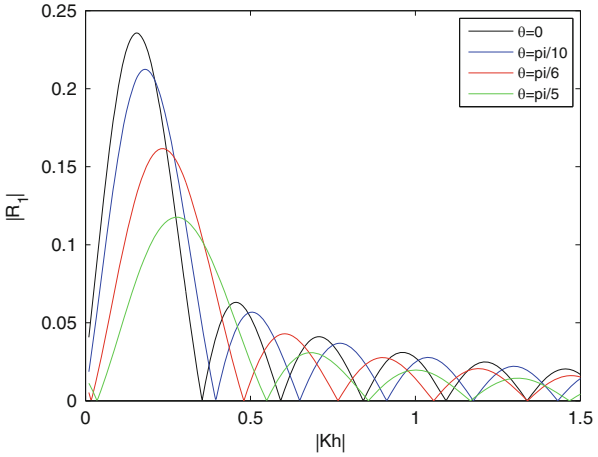

Fig. 1 $|R_1|$ for $Dh = 0.1$, and $\theta = \pi/6$

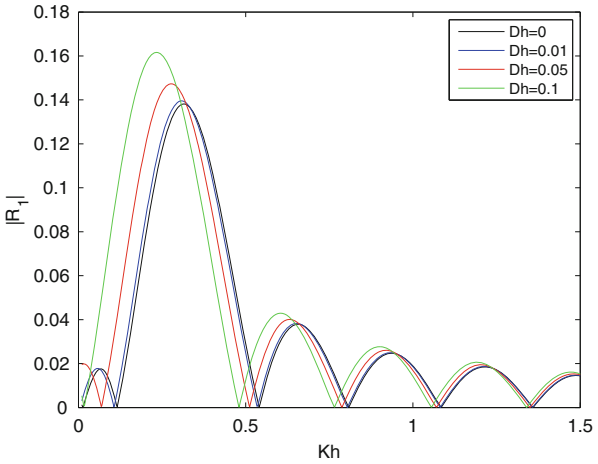

Fig. 2 $|R_1|$ for $m = 2, n = 3$ and $\theta = \pi/6$

(i.e., for oblique incidence case). Another general attribute in Fig. 1 is the oscillating behavior of the absolute value of $|R_1|$ as a function of the wavenumber Kh. As θ increases, the crest estimation of $|R_1|$ reduces. When θ tends to $\pi/4$, the reflection coefficient $|R_1|$ is considerably less as compared to other angles of incident waves. In the normal incidence case, the crest estimation of $|R_1|$ is the highest. In Fig. 2, $|R_1|$ is plotted for various porosity parameters Dh of the seabed, whereas we settled $\theta = \pi/6$, $lh = 1$, $m = 2$, and $n = 3$. This is most apparent in the plots that the crest estimation of $|R_1|$ raises as the porosity parameter of the seabed raises. It demonstrates that $|R_1|$ is pretty sensitive to the changes in the porosity parameter of the seabed. In Fig. 3, various plots relate to a different number of ripples in the fix of

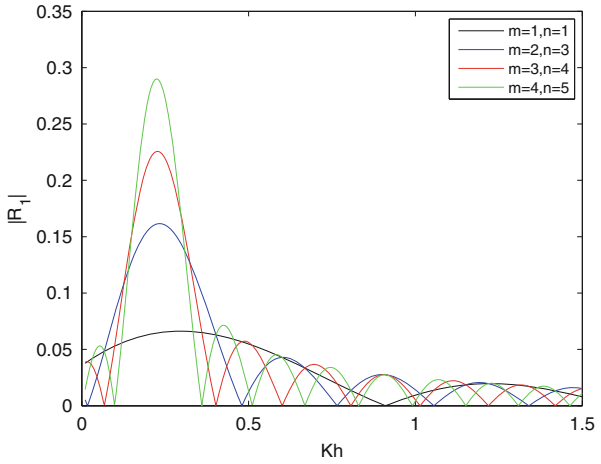

Fig. 3 $|R_1|$ for $Dh = 0.1$, and $\theta = \pi/6$

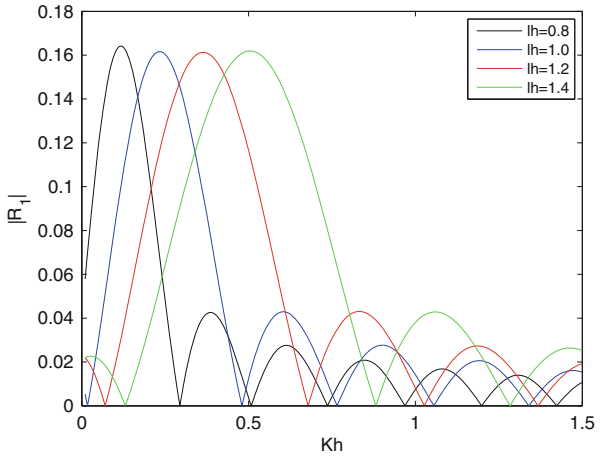

Fig. 4 $|R_1|$ for $m = 2, n = 3$ and $\theta = \pi/6$

contortion on the porous seabed. For each of these plots, we have taken $Dh = 0.1$, $\theta = \pi/6$, and $lh = 1$. It is observed from this figure that when the number of ripples in the fix of the base contortion becomes more, the estimation of $u_0 h \cos\theta$ tends to a number which lies in the neighborhood of $lh/2$ and the crest estimation of $|R_1|$ increases. However, as the number of ripples turns out to be bigger, the reflection coefficient becomes unbounded. Its oscillatory behavior is more perceptible with the number of zeros of $|R_1|$ raised; however the general behavior of $|R_1|$ remains the same as before.

In Fig. 4, various plots relate to particular ripple wavenumbers $lh = 0.8, 1, 1.2$, and 1.4 in the fix contortion on the porous seabed. For all plots in this figure, we

have taken $m = 2, n = 3, Dh = 0.1$, and $\theta = \pi/6$. In this case, also, it has been noticed that the crest estimations of the reflection coefficient are achieved at various estimations of Kh. That means, the estimations of reflection coefficient $|R_1|$ become most extreme, only when $lh \approx 2u_0 h \cos\theta$. That implies when obliquely incident waves propagate over a porous seabed having a little ripple wavenumber in the fix bottom contortion, a considerable amount of reflected energy can be generated.

4 Conclusion

In this paper, the issue of diffraction of obliquely incident progressive waves by a little base contortion on the porous seabed is investigated. In this case, the progressive waves with only one wavenumber exist for any particular frequency. The BVP which is derived from the physical issue is tackled by utilizing perturbation hypothesis in combination with Fourier transform method. For the support of the theoretical results, a special frame of sinusoidal ripples is considered. The first-order approximations to the velocity potential function, reflection, as well as transmission coefficients are evaluated in terms of integrals, and the reflection coefficients are drawn graphically for various parameters. The results obtained here are relied to be subjectively useful for a wide class of water-wave diffraction issues including a bottom contortion on the porous seabed.

References

1. Chamberlain, P.G., Porter, D.: The modified mild-slope equations. J. Fluid Mech., **291**, 393–407 (1995)
2. Davies, A.G.: The reflection of wave energy by undulations of the sea bed. Dyn. Atmos. Oceans, **6**, 207–232 (1982).
3. Davies A.G., Heathershaw A.D.: Resonant reflection of surface water waves by periodic sandbars. J. Fluid Mech., **144**, 419–443 (1984)
4. Kirby, J.T.: A general wave equation for waves over rippled beds. Journal of Fluid Mechanics, **162**, 171–186 (1986)
5. Mei, C.C.: Resonant reflection of surface water waves by periodic sandbars. J. Fluid Mech., **152**, 315–335 (1985)
6. Mohapatra, S., Bora S.N.: Reflection and transmission of water waves in a two-layer fluid flowing through a channel with undulating bed. J. Appl. Math. Mech., **91**, 46–56 (2011)
7. Mohapatra, S.: Scattering of oblique surface waves by the edge of small deformation on a porous ocean bed. J. Mar. Sci. Appl., **14**, 156–162 (2015)
8. Mohapatra, S.: The effect of surface-tension on scattering of water waves by small bottom undulation. ANZIAM J., **58(E)**, E39–E80 (2017)
9. Mohapatra, S., Sarangi, M.R.: A note on the solution of water wave scattering problem involving small deformation on a porous channel-bed. J. Mar. Sci. Appl., **16**, 10–19 (2017)

Nonlinear Wave Propagation Through a Radiating van der Waals Fluid with Variable Density

Madhumita Gangopadhyay

Abstract We examine a quasilinear system of PDEs governing the one-dimensional unsteady flow of a radiating van der Waals fluid in radial, cylindrical and spherical geometry. The local value of the fundamental derivative (Γ) associated with the medium is of order $O(\epsilon)$ and changes sign about the reference state ($\Gamma = 0$); the undisturbed medium is assumed to be spatially variable. An asymptotic method is employed to obtain a transport equation for the system of Navier Stokes equations; the impact of radiation and the van der Waals parameters on the evolution of the initial pulse is studied.

Keywords Hyperbolic system · Mixed nonlinearity · van der Waals fluid · Radiation

1 Introduction

The development of science and technology in the present age has brought forth hypersonic flight, power plants for space exploration, gas-cooled nuclear reactors and fission and fusion reactions in which the temperature attained by the medium is very high and thermal radiation comes into play. An analysis of the resulting flow field therefore calls for a study of both the gas dynamic field and the thermal radiation fields simultaneously.

A linearized and nonlinear analysis of small amplitude disturbances in a perfectly conducting and radiating gas has been considered by Radha and Sharma [8]. Small-amplitude waves in relaxing and radiating gases have been investigated by Clarke and McChesney [2], Vincenti and Kruger [15], Varley and Cumberbatch [14] and Fusco [4]. The ideal gas has been the subject of study in each of these cases. However real gases may not be exactly described by the ideal gas model. The

M. Gangopadhyay (✉)
Department of Mathematics, University of Mumbai, Mumbai, India
e-mail: madumita.gangopadhyay@mathematics.mu.ac.in

B. Rushi Kumar et al. (eds.), *Applied Mathematics and Scientific Computing*,
Trends in Mathematics, https://doi.org/10.1007/978-3-030-01123-9_34

shock-wave phenomena exhibited by real gases may be significantly different from that of an ideal medium [16].

Bethe [1], Zeldovich [17] and Thompson [12] are pioneers in the study of nonlinear waves in real fluids; the formation of negative shock waves in real single-phase fluids was independently identified by Bethe and Zeldovich. Thompson [12] and Thompson and Lambrakis [13] is credited to having identified a class of fluids for which thermodynamic parameter Γ changes sign about a reference line in the pressure-density space. The van der Waals fluid is an example of such a fluid. Some interesting studies related to wave propagation in a van der Waals fluid having mixed nonlinearity can be found in the works of Shukla and Sharma [10] and Fan and Slemrod [3]. In the present paper, we have made an attempt to examine the wave motion in a one-dimensional unsteady flow of a radiating van der Waals gas exhibiting mixed nonlinearity.

The fundamental derivative (Γ) inherent in the medium is of order $O(\epsilon)$ where

$$\Gamma = 1 + \frac{\rho}{c}\left(\frac{\partial c}{\partial \rho}\right)_s,$$

$c = \sqrt{\partial p/\partial \rho}$, being the sound speed, $p = p(\rho, s)$ the pressure, ρ, the fluid density and s, the entropy of the fluid. The behaviour of the wave is significantly different from the cases when $\Gamma > 0$ or $\Gamma < 0$; see, for instance, Kluwick and Cox [5] and Shukla and Sharma [10]. The main purpose of the present study is to investigate the effects of radiation, the van der Waals parameters and the varying medium ahead on the evolving wave.

2 Basic Equations

Estimating the effects of thermal radiation by optically thin approximation of the radiative transfer equation as given by Pai [6] and Penner and Olfe [7], the Euler's equations for the propagation of planar ($m = 0$), cylindrical ($m = 1$) and spherically ($m = 2$) symmetric motion of a radiating gas are given by

$$\frac{\partial \rho}{\partial t} + u\frac{\partial \rho}{\partial x} + \rho\frac{\partial u}{\partial x} + \frac{m\rho u}{x} = 0 \tag{1}$$

$$\frac{\partial u}{\partial t} + u\frac{\partial u}{\partial x} + \frac{1}{\rho}\frac{\partial p}{\partial x} = 0 \tag{2}$$

$$\frac{\partial s}{\partial t} + u\frac{\partial s}{\partial x} + (\gamma - 1)Q = 0, \tag{3}$$

where u is the fluid velocity, ρ the density, p the pressure, γ the constant specific heat ratio, t the time and x the space coordinate. The rate of energy loss by the gas per unit volume through radiation is given by

$$Q = 4\alpha\sigma(T^4 - T_0^4) \tag{4}$$

where T is the temperature, T_0 is the reference temperature of the medium ahead, σ is the Stefan-Boltzmann constant and α is the Planck mean absorption coefficient given by

$$\alpha = K\rho^{\Gamma}T^{\beta}, \tag{5}$$

where K, Γ and β are constants pertaining to the gas. The caloric and thermal equations of state of the van der Waals fluid are given by [16]

$$e = c_v T - a\rho, \quad p = \frac{\rho RT}{1 - b\rho} - a\rho^2, \tag{6}$$

where e is the specific internal energy, T is the absolute temperature, R is the specific gas constant, c_v is the specific heat at constant volume which is a constant assuming the medium to be a polytropic gas and a and b are van der Waals parameters representing, respectively, a measure of attraction between the constituent particles and the effective volume of each particle.

The specific entropy of the van der Waals gas is given by

$$s = R \ln\left(KT^{1/\delta}\frac{1 - b\rho}{\rho}\right) \tag{7}$$

where δ is a dimensionless quantity given by $\delta = R/c_v$, $0 < \delta \leq 2/3$.

The system of Equations (1)–(3) can be written comprehensively as

$$\mathbf{U}_{,t} + A(\mathbf{U})\mathbf{U}_{,x} + \mathbf{F}(\mathbf{U}) = 0, \tag{8}$$

where the variable in the subscript preceded by a comma indicates partial derivative with respect to the variable; $\mathbf{U} = (\rho, u, s)^{tr}$, $\mathbf{F}(\mathbf{U}) = \left(\frac{m\rho u}{x}, 0, (\gamma - 1)Q\right)^{tr}$, and $A(\mathbf{U})$ is a 3×3 matrix given by

$$A(\mathbf{U}) = \begin{bmatrix} u & \rho & 0 \\ p_\rho/\rho & u & p_s/\rho \\ 0 & 0 & u \end{bmatrix}, \tag{9}$$

tr denoting transposition. Assuming the reference state to be spatially variable, we have at time $t = 0$ $u_0 s_{0,x} = 0$, i.e. either $u_0 = 0$ or $s_{0,x} = 0$. If $u_0 = 0$, $p_0 =$ constant, i.e. the medium ahead is stationary and is at a constant pressure. If $s_{0,x} = 0$, then $s_0 =$constant or the medium ahead has a constant entropy. In the subsequent analysis, we assume the undisturbed medium to be at rest with a variable density.

3 Nonlinear High-Frequency Waves

We consider a small-amplitude, high-frequency signal entering the undisturbed medium $U_0 = (\rho_0(x), u_0(x), s_0(x))$. We assume that the perturbations are of size $O(\epsilon)$ and they depend on the fast variable $\xi = \dfrac{\phi(x,t)}{\epsilon^2}$, where ϕ is the phase function identified with the wavefront. Using the method of multiple scales, the solution to Eq. (8) may be expressed as

$$U_i(x,t) = U_i^{(0)}(x) + \epsilon U_i^{(1)}(\xi,x,t) + \epsilon^2 U_i^{(2)}(\xi,x,t) + \epsilon^3 U_i^{(3)}(\xi,x,t) + O(\epsilon^4), \tag{10}$$

where $U_i^{(0)}(x)$ is the known reference state. With this change in variables, Eq. (8) assumes the form

$$\epsilon^2(\mathbf{U}_{,t} + A(\mathbf{U})\mathbf{U}_{,x} + F(\mathbf{U})) + \mathbf{U}_{,\xi}(\phi_{,t} I + A(\mathbf{U})\phi_{,x}) = 0, \tag{11}$$

where I is the 3×3 unit matrix.

The coefficient matrices A and F are expanded in a Taylor's series about $\mathbf{U} = \mathbf{U_0}$ as follows:

$$A_{ij}(U) = A_{ij}^{(0)} + A'_{ijk}(\epsilon U_k^{(1)} + \epsilon^2 U_k^{(2)}) + A''_{ijkl}\epsilon^2 U_k^{(1)} U_l^{(1)} + O(\epsilon^3), \tag{12}$$

$$F_i(U) = F_i^{(0)} + F'_{ij}(\epsilon U_j^{(1)} + \epsilon^2 U_j^{(2)}) + O(\epsilon^2), \tag{13}$$

where $A_{ij}^{(0)} = A_{ij}(U_m^{(0)})$, $A'_{ijk} = \frac{\partial A_{ij}}{\partial U_k}|_{U_m = U_m^{(0)}} and$ $F_i^{(0)} = F_i(U_m^{(0)})$;
the indices i, j, k, etc. take values from 1 to 3. It is assumed that A'_{ijk}, $A''_{ijkl} and F'_{ij}$ are smooth and admit expansions:

$$A'_{ijk} = A'_{0ijk} + \epsilon A'_{1ijk} + O(\epsilon^2) \tag{14}$$

$$A''_{ijkl} = A''_{0ijkl} + \epsilon A''_{1ijkl} + O(\epsilon^2) \tag{15}$$

$$F'_{ij} = F'_{0ij} + \epsilon F'_{1ij} + O(\epsilon^2). \tag{16}$$

Substituting (10) and (12)–(16) in (11) and matching the coefficients of successive powers of ϵ on either sides of the resulting equation, we have the following system of equations:

$$G_{ij} u_{j,\xi}^{(1)} = 0 \tag{17}$$

$$G_{ij} u_{j,\xi}^{(2)} = -u_{j,\xi}^{(1)} A'_{0ijk} u_k^{(1)} \phi_{,x} \tag{18}$$

$$\begin{aligned} G_{ij} u_{j,\xi}^{(3)} = -\phi_{,x} \Big\{ & A'_{0ijk} u_{j,\xi}^{(2)} u_k^{(1)} + A'_{1ijk} u_{j,\xi}^{(1)} u_k^{(1)} + A'_{0ijk} u_{j,\xi}^{(1)} u_k^{(2)} \\ & + A''_{ijkl} u_{j,\xi}^{(1)} u_k^{(1)} u_l^{(1)} \Big\} - u_{i,t}^{(1)} - A_{0ij} u_{j,x}^{(1)} - F'_{0ij} u_j^{(1)} - A'_{0ijk} u_k^{(1)} u_{j,x}^{(0)} \end{aligned} \tag{19}$$

where $G_{ij} = (\delta_{ij}\phi_{,t} + A_{0ij}\phi_x)$, δ_{ij}, being the Kronecker symbol. In order to obtain a nontrivial solution, we assume $\det(G_{ij}) = 0$, i.e. $\phi_t(\phi_t^2 - c_0^2\phi_x^2) = 0$, where $c_0^2 = (1+\delta)\dfrac{(p_0 + a\rho_0^2)}{\rho_0(1-b\rho_0)} - 2a\rho_0$ is the square of the sound speed in the undisturbed van der Waals fluid. Thus the initial signal splits into distinct pulses associated with the different eigen values of (9); $\phi_t = 0$ corresponds to convection of entropy with particle velocity, while $\phi_t = c_0\phi_x$ and $\phi_t = -c_0\phi_x$ are the left and right moving acoustic waves, respectively. We take a simple phase function $\phi(x,t) = x - c_0 t$ and the right running acoustic wave, the left and right eigenvectors of which are, respectively,

$$\mathbf{L} = \left(\frac{c_0}{\rho_0}, 1, \frac{p_{s0}}{\rho_0 c_0}\right), \quad \mathbf{R} = \left(\frac{\rho_0}{c_0}, 1, 0\right)^{tr},$$

tr denoting transposition. Equation (17) implies

$$U^{(1)} = \alpha(\xi, x, t)\mathbf{R}(x,t) \tag{20}$$

where $\alpha(\xi, x, t)$ is a scalar function that can be thought of as the amplitude of the dominant term of the asymptotic solution. Scalar product of Eq. (18) with $\mathbf{L}$ yields

$$L_i A'_{0ijk} R_j R_k \alpha\alpha_{,\xi} = 0, \tag{21}$$

where we assume that $U_j^{(2)}$ is a nontrivial correction to $U_j^{(1)}$. Similarly the scalar product of (19) with $\mathbf{L}$ and subsequent division by $L_i R_i$ yields

$$\alpha_{,t} + V_0\alpha_{,x} + b_j u^{(2)}_{j,\xi}\alpha + c_k u_k^{(2)}\alpha_\xi + \left(\frac{L_i A'_{1ijk} R_j R_k}{L_i R_i} + \frac{L_i A''_{0ijkl} R_j R_k R_l}{L_i R_i}\alpha\right)\alpha\alpha_{,\xi} + \left(\frac{L_i F'_{0ij} R_j + L_i A'_{0ijk} R_k u^0_{j,x} + L_i A_{0ij} R_{j,x}}{L_i R_i}\right)\alpha = 0 \tag{22}$$

$$\text{where} \quad V_0 = \frac{L_i A_{0ij} R_j}{L_i R_i}, \quad b_j = \frac{L_i A'_{0ijk} R_k}{L_i R_i}, \quad c_k = \frac{L_i A'_{0ijk} R_j}{L_i R_i}. \tag{23}$$

Equation (22) describes the evolution of the amplitude function $\alpha(\xi, x, t)$ of the first-order approximation to the signal. Second-order terms are still unknown; in view of Eq. (21), b_j is orthogonal to R_j, and c_k is orthogonal to R_k. Hence each of them lies in the two-dimensional row space of G_{ij} and can be expressed as $b_j = \delta_\lambda G_{\lambda j}$, and $c_k = \beta_\lambda G_{\lambda k}$, $\lambda = 1, 2, \quad j, k = 1, 2, 3$ where δ_λ and β_λ are scalars.

In order to simplify the second-order terms $c_k u_k^{(2)}$ and $b_j u_{j,\xi}^{(2)}$, we consider Eq. (18) above which reduces to

$$G_{ij} u_{j,\xi}^{(2)} = -A'_{0ijk} R_j R_k \alpha \alpha_\xi \tag{24}$$

Integrating with respect to ξ, we have

$$G_{ij} u_j^{(2)} = -\frac{1}{2} A'_{0ijk} R_j R_k \alpha^2 \tag{25}$$

where we assume that $u_j^{(2)} = 0$ when $u_j^{(1)} = 0$. Therefore,

$$c_k u_k^{(2)} = -\frac{1}{2} \beta_\lambda A'_{0\lambda kl} R_k R_l \alpha^2 \tag{26}$$

$$b_j u_{j,\xi}^{(2)} = -\delta_\lambda A'_{0\lambda jl} R_j R_l \alpha \alpha_\xi \tag{27}$$

Using (23), (26) and (27), the evolution equation can be written as

$$\alpha_t + V_0 \alpha_x + (P + Q\alpha)\alpha \alpha_\xi + R\alpha = 0, \tag{28}$$

where

$$P = \frac{L_i A'_{1ijk} R_j R_k}{L_i R_i}, \quad Q = \frac{L_i A''_{0ijkl} R_j R_k R_l}{L_i R_i} - \frac{1}{2}(\beta_\lambda + 2\delta_\lambda) A'_{0\lambda kl} R_k R_l,$$

$$R = \frac{L_i F'_{0ij} R_j + L_i A'_{0ijk} R_k u_{j,x}^{(0)} + L_i A_{0ij} R_{j,x}}{L_i R_i}$$

Since the medium ahead is stationary, $U_0 = (\rho_0(x), 0, s_0(x))$. Expanding the sound speed $c(\rho)$ in a Taylor's series about ρ_0, we have in non-dimensional variables

$$\bar{c}(\bar{\rho}) = 1 + (\bar{\rho} - 1)(\Gamma_0 - 1) + \frac{(\bar{\rho} - 1)^2}{2!}(\Lambda - \Gamma_0 + 2) + O[(\bar{\rho} - 1)^3], \tag{29}$$

where $\bar{c} = \frac{c}{c_0}$, $\bar{\rho} = \frac{\rho}{\rho_0}$, $\Gamma_0 = \frac{\rho_0}{c_0}\Gamma(\rho_0, c_0) = O(\epsilon)$, $\Lambda = \frac{\rho_0^2}{c_0}\frac{\partial \Gamma}{\partial \rho}|_{(\rho_0, s_0)} = O(1)$.

In order to construct the evolution equation (28), we compute the nonzero terms of A'_{ijk} and A''_{ijkl} as follows:

$$A'_{ii2} = 1, \quad A'_{121} = 1, \quad A'_{211} = -\frac{c_0^2}{\rho_0^2} + \frac{2c_0 c_{\rho 0}}{\rho_0}, \quad A'_{213} = \frac{2c_0 c_{s0}}{\rho_0},$$

$$A'_{231} = \frac{2c_0 c_{s0}}{\rho_0} - \frac{p_{s0}}{\rho_0^2}, \; A'_{233} = \frac{p_{ss0}}{\rho_0}, \quad A''_{02111} = \frac{2c_0^2(\Lambda + 6)}{\rho_0^3},$$

where the values have been obtained in the undisturbed reference state; using the above values, Eq. (21) yields

$$\frac{L_i A'_{0ijk} R_j R_k}{L_i R_i} = \frac{c_0}{\rho_0} + c_{\rho 0} = O(\epsilon), \tag{30}$$

which is comparable with the fundamental derivative Γ discussed in the introduction. Using (23), the b_j and c_k are given by

$$b_1 = c_1 = c_{\rho_0}, \quad b_2 = c_2 = 1, \quad b_3 = c_3 = c_{s0}.$$

Hence the values of β_λ and δ_λ are as follows:

$$\beta_1 = \delta_1 = \frac{1}{\rho_0} + \frac{c_0 c_{s0}}{p_{s0}}, \quad \beta_2 = \delta_2 = \frac{\rho_0 c_{s0}}{p_{s0}}.$$

The nontrivial values of F'_{ij} in the medium ahead are computed as:

$$F'_{012} = \frac{m\rho_0}{x}, \quad F'_{031} = \frac{16(\gamma-1)\sigma K^{1-\delta}\delta e^{\delta s_0/R}\rho_0^{\Gamma+\delta-1} T_0^{\beta+3}}{(1-b\rho_0)^{\delta+1}}$$

Using the above values,

$$V_0{=}c_0{=}O(1), \quad P{=}\frac{\Gamma_0}{\epsilon} = O(1), \quad Q = (\Lambda+6)\frac{\rho_0}{c_0} - \frac{3}{c_0} - \frac{3\rho_0 c_{s0}}{p_{s0}}\Gamma_0 = O(1)$$

$$\text{and} \quad R = \frac{mC_0}{2x} + \frac{8(\gamma-1)p_{s,0}\sigma\delta K^{1-\delta}e^{\delta s_0/R}\rho_0^{\Gamma+\delta-1}T_0^{\beta+3}}{c_0(1-b\rho_0)^{\delta+1}} + \frac{3c_{0,x}}{2} - \frac{c_0}{2\rho_0}\rho_{0,x}$$
$$= O(1). \tag{31}$$

Hence P, Q and R are all functions of x for planar, cylindrical or spherical flow. Along a ray $x - c_0 t =$ constant, Eq. (28) reduces to

$$\alpha_t + (P + Q\alpha)\alpha\alpha_\xi + R\alpha = 0. \tag{32}$$

This resembles an inviscid Burgers equation with quadratic and cubic nonlinearities and a source term; P represents Lax's genuine nonlinearity parameter, Q measures the degree of material nonlinearity, and R depicts the impact of the flow geometry, radiation and the van der Waals parameters a and b. Also the effect of the varying medium is inherent in each of P, Q and R. The nonlinearity coefficients P and Q are instrumental in shock formation and the eventual breaking of the wave; the source term however delays the shock formation by bringing about an attenuation in the wave amplitude α due to wave interactions with the varying medium ahead, radiation and the wavefront curvature.

4 Conclusion

In the present work, we have examined a quasilinear system of partial differential equations governing the one-dimensional unsteady planar, cylindrical or spherically symmetric motion of sound waves through a radiating van der Waals gas. The fundamental derivative associated with the medium is of order $O(\epsilon)$ and changes sign about the base state $\Gamma = 0$. A method of multiple scales has been employed which reduces the system of equations to a single equation that determines the evolution of the initial pulse; it contains quadratic and cubic nonlinearities and a source term.

A general property of nonlinear hyperbolic equations is the eventual formation of discontinuities in the propagating signal. Hence the evolving wave gets distorted with time and a shock is formed. But the presence of the source term brings about a decay in the wave amplitude and delays the shock formation. We observe that the quadratic and cubic nonlinearities depend on the initial density and entropy of the medium along with the van der Waals parameters a and b; the source term is influenced by the flow geometry, the van der Waals parameters and radiation. Thus suitable values of the van der Waals parameters and radiation may bring about a considerable decay in the amplitude of the evolving wave and may thereby reduce the possibility of a shock. Shukla et al. [11] have given an in-depth analysis of the solution of a similar evolution equation in the presence of a magnetic field but in the absence of radiation. If $a = b = 0$, the medium reduces to an ideal medium; in the absence of radiation, Eq. (32) matches with the evolution equation of Sharma and Madhumita [9].

Acknowledgements The author wishes to sincerely thank the University Grants Commission, India, for its support through a Major Research Project No. F/788/2012/SR.

References

1. Bethe, H.A.: On the theory of shock waves for an arbitrary equation of state. Tehnical Report No. 545, Office of Scientific Research and Development (1942)
2. Clarke, J.F., McChesney, M.: Dynamicss of Relaxing gases. Butterworth, London (1976)
3. Fan, H., Slemrod, M.: Dynamic flows with liquid/vapor phase transitions. In: Handbook of Mathematical Fluid Dynamics, **1**, pp. 373–420, North Holland, Amsterdam (2002)
4. Fusco, D.: Some comments on wave motions described by nonhomogeneous quasilinear first order hyperbolic systems. Meccanica **17**, 128–137 (1982)
5. Kluwick, A., Cox, E.A.: Nonlinear waves in materials with mixed nonlinearity. Wave Motion **27**, 23–41 (1998)
6. Pai, S.I.: Radiation Gasdynamics. Springer, New York (1966)
7. Penner, S.S., Olfe, D.B.: Radiation and Reentry. Academic Press, New York (1968)
8. Radha, Ch., Sharma, V.D.: High and low frequency small amplitude disturbances in a perfectly conducting and radiating gas. Int.J.Engng Sci. **33**, 2001–2010 (1995)
9. Sharma, V.D., Madhumita G.: Nonlinear wave propagation through a stratified atmosphere. J. Math. Anal. Appl. **311**, 13–22 (2005)

10. Shukla, T.P., Sharma, V.D.: Weakly nonlinear waves in nonlinear fluids. Studies in Applied Mathematics **00**, 1–22 (2016)
11. Shukla, T.P., Madhumita G., Sharma, V.D.: Evolution of planar and cylindrically symmetric magneto-acoustic waves in a van der waals fluid. Int.J.Nonlinear Mechanics **91**, 58–68 (2017)
12. Thompson, P.A.: A fundamental derivative in gas dynamics. Phys. Fluids **14**, 1843–1849 (1971)
13. Thompson, P.A., Lambrakis, K.S.: Negative shock waves. J.Fluid Mech. **60**, 187–207 (1973)
14. Varley, E., Cumberbatch, E., Nonlinear high frequency sound waves. J. Inst. Math. Appl. **2**, 133–143 (1966)
15. Vincenti, W.G., Kruger, C.H.: Introduction to Physical Gasdynamics. Wiley. New York (1965)
16. Zhao, N., Mentrelli, A., Ruggeri, T., Sugiyama, M.: Admissible shock waves and shock induced phase transitions in a van der waals fluid. Phys. Fluids **23**, 086101 (2011)
17. Zeldovich, Y.B.: On the possibility of rarefaction shock waves. Zh. Eksp. Teor. Fiz. **4**, 363–364 (1946)

Effect of Slip and Convective Heating on Unsteady MHD Chemically Reacting Flow Over a Porous Surface with Suction

A. Malarselvi, M. Bhuvaneswari, S. Sivasankaran, B. Ganga, and A. K. Abdul Hakeem

Abstract The influence of slip and convective boundary heating on unsteady forced convective heat transfer of an electrically conducting incompressible fluid over a flat plate in the presence of uniform magnetic field along with chemical reaction is examined. The governing partial differential equations are transformed into ordinary differential equations by applying similarity transformations. Then the reduced equations are solved numerically by shooting technique and Runge-Kutta method and are solved analytically by homotopy analysis method.

Keywords Chemical reaction · Forced convection · MHD · Unsteady flow · Slip effect

1 Introduction

The studies pertaining to the boundary flow along with heat and mass transfer of an electrically conducting fluid play a vital role in many industrial and geophysical problems in current years. It has gained the global attention of many researchers because of its wide applications in industries and engineering. To mention few of them, it is used in cooling of nuclear reactors, rocket engine, production of polymer and metallic sheets and thermal insulation. In the generation of the metallic plates and polymer sheets, perfection of the final product relies upon the rate of cooling. Makinde [1] reported on the natural convection from a moving vertical plate in the

A. Malarselvi · B. Ganga
Department of Mathematics, Providence College for Women, Coonoor, India

M. Bhuvaneswari · S. Sivasankaran (✉)
Department of Mathematics, King Abdulaziz University, Jeddah, Saudi Arabia
e-mail: smsivanandam@kau.edu.sa

A. K. Abdul Hakeem
Department of Mathematics, Sri Ramakrishna Mission Vidhyalaya College of Arts and Science, Coimbatore, India

B. Rushi Kumar et al. (eds.), *Applied Mathematics and Scientific Computing*, Trends in Mathematics, https://doi.org/10.1007/978-3-030-01123-9_35

existence of internal heat generation and convective surface boundary condition. Boundary layer flow and heat transfer of a viscoelastic fluid over a stretching surface was investigated by Eswaramoorthi et al. [2, 3]. Merkin and Pop [4] analysed the forced convective heat transfer over a flat surface of a uniform stream with a convective boundary condition. Bhattacharyya and Layek [5] performed an investigation on the influence of chemical reaction on the boundary flow in the existence of magnetic field over a porous plate.

Nabil et al. [6] discussed the effect of the chemical reaction and radiation on the unsteady MHD free convective flow past a semi-infinite vertical permeable moving plate through a porous medium. Ferdows et al. [7] studied free convective heat transfer and fluid flow in an inclined porous plate. Bhuvaneswari et al. [8] performed Lie group analysis on the convective flow, heat and mass transfer of an incompressible viscous fluid in an inclined surface with first-order homogeneous chemical reaction. Chamkha and Rashad [9] performed the investigation on the Soret and Dufour effects in the unsteady coupled heat and mass transfer by MHD mixed convective flow from a rotating vertical cone with magnetic field in the presence of chemical reaction. Soret and Dufour effects on MHD mixed convection of a stagnation point flow towards a vertical plate in a porous medium with chemical reaction, radiation and heat generation were investigated by Karthikeyan et al. [10]. Soret and Dufour effects on MHD mixed convection stagnation point flow with radiation were investigated by Niranjan et al. [11]. Sivasankaran et al. [12] investigated the effects of chemical reaction and radiation on MHD mixed convection stagnation point flow in a porous medium with slip and convective boundary conditions.

It is observed from the survey of the literature that so far no attempt has been made for analysing the effect of convective surface heating and slip on unsteady MHD boundary layer flow in the presence of chemical reaction over a porous plate. The aim of the present work is to find the numerical and analytical solution of the influence of convective surface heating on hydromagnetic convective boundary layer flow over a porous plate with suction and chemical reaction.

2 Mathematical Formulation

We consider an unsteady two-dimensional hydromagnetic flow of a viscous incompressible electrically conducting fluid and solute distribution with convective surface heating in the presence of chemical reaction over a flat plate. The flow is assumed to be in x direction which is taken along the flat plate and y-axis normal to it. A magnetic field of uniform strength B_0 is applied in the transverse direction of the flow. The surface is maintained at a constant temperature T_w which is higher than free stream temperature T_∞, and the concentration C_w is greater than the concentration in the free stream C_∞. The continuity, momentum, energy and concentration equations describing such type of flow can be written as

$$\frac{\partial u}{\partial x}+\frac{\partial v}{\partial y}=0, \tag{1}$$

$$\frac{\partial u}{\partial t}+u\frac{\partial u}{\partial x}+v\frac{\partial u}{\partial y}=\nu\frac{\partial^2 u}{\partial y^2}+\frac{\sigma B_0^2}{\rho}(u_\infty-u), \tag{2}$$

$$\frac{\partial T}{\partial t}+u\frac{\partial T}{\partial x}+v\frac{\partial T}{\partial y}=\frac{k}{\rho c_p}\frac{\partial^2 T}{\partial y^2} \tag{3}$$

$$\frac{\partial C}{\partial t}+u\frac{\partial C}{\partial x}+v\frac{\partial C}{\partial y}=D\frac{\partial^2 C}{\partial y^2}-K_n(t)(C-C_\infty)^n. \tag{4}$$

where $\nu=\frac{\mu}{\rho}$ is the kinematic viscosity of the fluid, μ is the viscosity, ρ is the fluid density, σ is the electrical conductivity of the fluid, n is the order of chemical reaction, $K_n(t)=k_n(1-\alpha t)$ is the rate of chemical reaction with $\alpha t<1$ and $u_\infty\left(=\frac{ax}{1-\alpha t}\right)$ is the free stream velocity. The boundary conditions subjected to the above-described Eqs. (2)–(4) are as follows:

$$u=U_\infty+l\frac{\partial u}{\partial y},\quad v=v_w=\frac{v_0}{\sqrt{x}},\quad C=C_w,\quad -k\frac{\partial T}{\partial y}=h_f(T_w-T),\quad y=0;$$
$$u\to u_\infty,\quad T\to T_\infty,\quad C\to C_\infty,\quad as\quad y\to\infty. \tag{5}$$

where v_w is the prescribed suction/blowing at the plate and is given by $v_w=v_0/\sqrt{x}$, v_0 is constant with $v_0<0$ which corresponds to suction and $v_0>0$ corresponds to blowing and ψ is the stream function defined in usual notation as $u=\frac{\partial\psi}{\partial y}$ and $v=-\frac{\partial\psi}{\partial x}$. We now introduce the following similarity variable η and dimensionless stream function $f(\eta)$ and temperature $\theta(\eta)$ and concentration $\varphi(\eta)$ as follows:

$$\eta=y\sqrt{\frac{a}{\nu(1-\alpha t)}},\qquad \psi=\sqrt{\frac{a\nu}{(1-\alpha t)}}xf(\eta), \tag{6}$$
$$T=T_\infty+(T_w-T_\infty)\theta(\eta),\qquad C=C_\infty+(C_w-C_\infty)\varphi(\eta).$$

Under the above transformation, the governing momentum, energy and concentration equation can be expressed in a non-dimensional form as

$$f'''(\eta)-f'(\eta)^2+f''(\eta)\left[f(\eta)-\frac{\eta}{2}A\right]-Af'(\eta)+\frac{Ha^2}{Re}\left[1-f'(\eta)\right]=0, \tag{7}$$

$$\left(\frac{1}{Pr}\right)\theta''(\eta)+f\theta'(\eta)-A\left[\frac{3}{2}\theta(\eta)+\frac{\eta}{2}\theta'(\eta)\right]=0, \tag{8}$$

$$\left(\frac{1}{Sc}\right)\phi''(\eta)-\left[\frac{\eta}{2}A-f(\eta)\right]\phi'(\eta)-Cr\phi^n(\eta)=0, \tag{9}$$

$$f(\eta)=s,\ f'(\eta)=1+df''(0),\theta'(\eta)=-Bi(1-\theta(\eta)),\phi(\eta)=1\text{at}\eta=0, \tag{10}$$

$$f'(\eta)\to 0,\ \ \theta(\eta)\to 0,\ \ \phi(\eta)\to 0,\ \ \text{as}\ \ \eta\to\infty. \tag{11}$$

where $Ha = \frac{\sigma B_0^2 x^2}{\rho \nu}$ is the Hartmann number, $Sc = \nu/D$ is the Schmidt number, $Cr = \frac{K_n (C_w - C_\infty)^{n-1}}{u_\infty}$ is the chemical reaction parameter, $A = \frac{\alpha}{a}$ is the unsteadiness parameter, $Pr = \frac{\mu C_p}{k}$ is the Prandtl number, $Re_x = \frac{u_\infty x}{\nu}$ is the local Reynolds number, $s = \frac{-v_0}{\sqrt{\nu U_\infty}}$ is the suction parameter, $d = \frac{\sqrt{U_\infty}}{\sqrt{\nu_x}}$ is the slip parameter and $Bi = -\frac{h_f}{k}\sqrt{\frac{\nu_x}{U_\infty}}$ is the Biot number.

The non-dimensional form of the skin friction or skin friction coefficient at the wall can be calculated as $Cf_x = \frac{\mu \left(\frac{\partial u}{\partial y}\right)_{y=0}}{\rho u_w^2}$ and is given by $Cf_x \left(\sqrt{Re_x}\right) = f''(0)$. The rate of heat transfer at the plate in the form of Nusselt number is given by $Nu_x = \frac{x q_w}{k(T_w - T_\infty)}$ where $q_w = -k \left(\frac{\partial T}{\partial y}\right)_{y=0}$. We get $\frac{Nu_x}{\sqrt{Re_x}} = -\theta'(0)$. The local Sherwood number which is proportional to the rate of solute transfer from the plate and is given by $Sh_x = \frac{x M_w}{D(C_w - C_\infty)}$ where $M_w = D \left(\frac{\partial C}{\partial y}\right)_{y=0}$; using the above result, we finally get $\frac{Sh_x}{\sqrt{Re_x}} = -\phi'(0)$.

The governing partial differential equations are transformed into ordinary differential equations by applying similarity transformations, and then the reduced equations are solved numerically by shooting technique with Runge-Kutta integration scheme.

3 Analytical Solution

The governing boundary layer equations (7)–(9) with the boundary conditions (10) are solved using homotopy analysis method (HAM). The initial approximations of the given problem are

$f_0(\eta) = s + \frac{a}{(1+\lambda)}\left[1 - e^{-\eta}\right]$, $\theta_0(\eta) = \frac{Bi}{(1+Bi)} e^{-\eta}$ and $\phi_0(\eta) = e^{-\eta}$.

These convergent series solution contains the auxiliary parameters h_f, h_θ and h_ϕ. These parameters adjust and control the HAM series solutions. The h_f, h_θ and h_ϕ curves are displayed in Fig. 1. It is concluded from this figure the range values

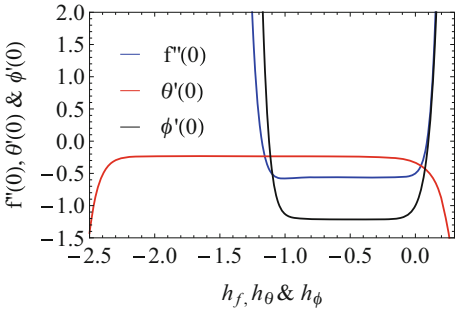

Fig. 1 h-curve for $f''(0)$, $\theta'(0)$ and $\phi'(0)$

of $-0.8 \leq h_f \leq -0.1$, $-2.1 \leq h_\theta \leq -0.5$ and $-0.8 \leq h_\phi \leq -0.2$, respectively. It is observed that our HAM solutions convergence in the whole region of η when $h_f = h_\phi = -0.5$ and $h_\theta = -1$.

4 Results and Discussion

The analysis of fluid flow, heat and mass transfer for various parameters is discussed in order to get the physical insight of the problem in the area of applications. This investigation focuses on the influence of convective heating and slip effect on unsteady incompressible fluid. The velocity profile for various values of slip and suction/injection parameters is displayed in Fig. 2. It is vivid from this figure that velocity is decreased due to the increment in the slip values with Ha = 0.5, A = 1, a = 1, s = 1 and Cr = 0.1. It is elucidated from the graph that the velocity is decreased while the values of s (suction /injection) are increased. The physical phenomenon of the graph is that the existence of the heat generation has the tendency to affect the fluid velocity. The temperature profile for various values of Biot number is displayed in Fig. 3. It is seen that convective heating enhances the temperature boundary layer. It is observed from Fig. 4 that as s (suction /injection) increases, the concentration boundary layer also increases. The effect of chemical reaction parameter over a concentration profile is shown in Fig. 4b. It is depicted from the graph that rising values of chemical reaction parameters diminishes the solutal boundary layer thickness. The influence of unsteady parameter over velocity, temperature and concentration profiles is noted in Fig. 5a–c. It is noticed that the increase of unsteadiness leads to the decrease in the velocity boundary layer for the fixed values of Hartmann number, slip and chemical reaction parameter. The thickness of the temperature boundary layer is increased for the decrement in the unsteady parameter. The concentration boundary layer thickness decreases with increasing unsteady parameter with Ha = 0.2, Bi = 0.1, d = 1 and s = 1.

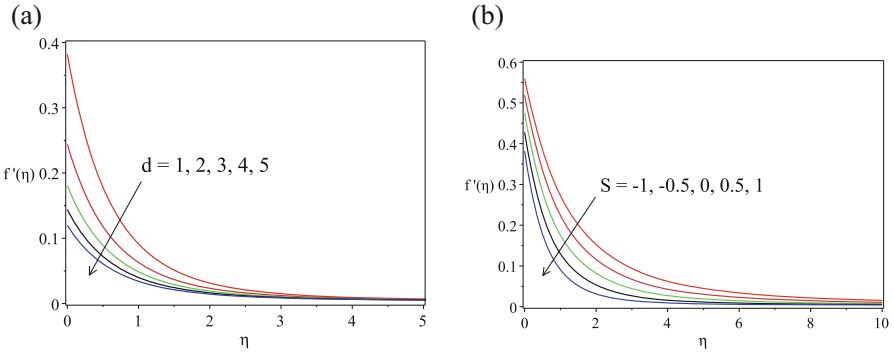

Fig. 2 Velocity profiles for different d and s values with (**a**) Ha = 0.5, A = 1, a = 1, Cr = 0.1, s = 1 and (**b**) Ha = 0.2, Bi = 1, d = 1, a = 1, Cr = 1, A = 1

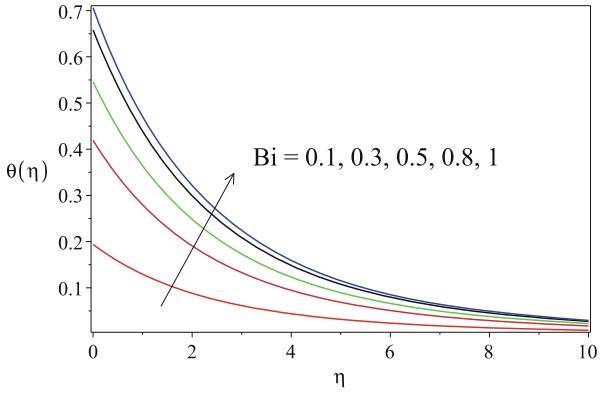

Fig. 3 Temperature profiles for different Biot numbers with Ha = 0.5, A = 1, Cr = 1, a = 1, d = 1, s = 1

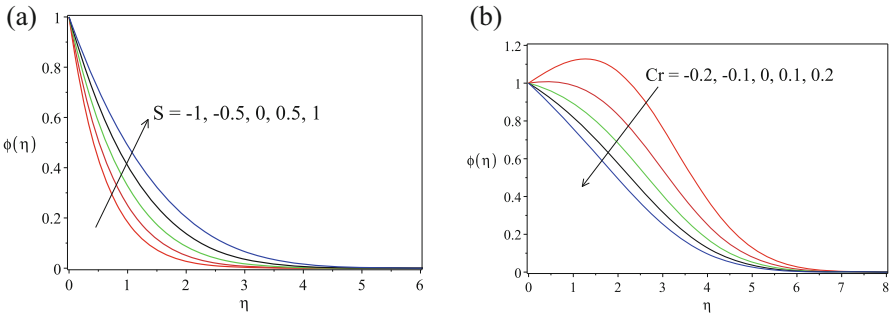

Fig. 4 Concentration profiles for different s and Cr values with (**a**) Ha = 0.2, Bi = 1, d = 1, a = 1, Cr = 1, A = 1 and (**b**) Ha = 0.5, Bi = 1, A = 1, a = 1, d = 1, s = 1

The numerical computation of skin friction, Nusselt number and Sherwood number is obtained and presented in Table 1. It is apparent from the data that the effect of Biot number and suction/injection parameter is to accelerate the local Nusselt number. We infer from the table that the enhancing values of s are to decelerate the local skin-friction coefficient. It is interesting to note that there is a significant decrease in the Sherwood number when raising the values of suction parameter. It is noted that the considerable increase in the rate of solute transfer due the enhancing values of chemical reaction parameter. It is found that increment of slip parameter (d) produces the increment in the coefficient of local skin friction and the rate of solute transfer with Ha = 0.2, A = 1, s = 1 and Bi = 1. The opposite behaviour is found for local Nusselt number with slip parameter. The local skin-friction coefficient is decreased when unsteadiness parameter is increased. It is quite interesting to note that both the rate of heat transfer and the rate of solute transfer are increased because of the increment in the unsteady parameter (A).

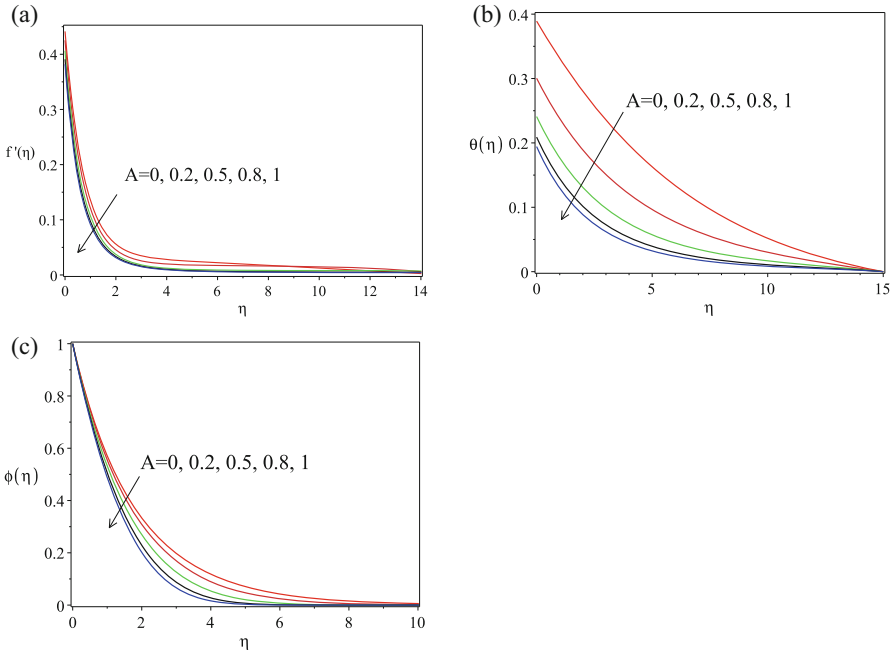

Fig. 5 Velocity, temperature, concentration profiles for different A values with Ha = 0.2, Bi = 0.1, d = 1, a = 1, Cr = 0.1, s = 1

5 Conclusion

In this investigation, we studied the influence of convective heating of an electrically conducting fluid over a flat plate in the existence of uniform magnetic field along with the chemical reaction.

- The velocity profile decreases with the enhancing values of slip parameter, suction/injection parameter and the unsteadiness parameter.
- The Biot number has the great influence on the temperature. It accelerates the dimensionless temperature in the presence (or in the absence) of suction/injection parameter. There is a prominent decrease in the dimensionless temperature due to the incremented values of unsteadiness parameter.
- The raising values of chemical reaction and unsteadiness parameters diminish the thickness of the solutal boundary layer. The enhancing values of suction/injection parameter are to increase concentration boundary layer.
- The effect of Biot number, unsteadiness and suction/injection parameters are to accelerate the local Nusselt number.

Table 1 The calculated values of Cf_x, $-\theta(0)$, $-\phi'(0)$ with $Re = 10$, $Pr = 0.1$, $Sc = 1$ and $a = 1$

Ha	A	Bi	d	s	Cr	Cf_x	$Nu/\sqrt{Re}$	$Sh/\sqrt{Re}$
0.5	1	0.1	1	1	1	−0.609747	0.080605	0.654116
		0.3					0.174233	
		0.5					0.226958	
		0.8					0.273516	
		1					0.293591	
0.5	1	0.1	1	−1	1	−0.437246	0.076748	1.640686
		0.3					0.157158	
		0.5					0.198820	
		0.8					0.233663	
		1					0.248160	
0.5	1	1	1	−1.0	1	−0.440469	0.247960	1.640686
				−0.5		−0.481069	0.258661	1.319565
				0.0		−0.525298	0.269722	1.046737
				0.5		−0.571758	0.281188	0.826351
				1.0		−0.618149	0.293119	0.655800
0.5	1	1	1	1	−0.2	−0.609747	0.293591	−0.160804
					−0.1			−0.034582
					0.0			0.065310
					0.1			0.149839
					0.2			0.224239
0.2	1	1	1	1	1	−0.618149	0.293119	0.655800
			2			−0.377954	0.291575	0.667321
			3			−0.273073	0.290838	0.672868
			4			−0.213974	0.290402	0.676160
			5			−0.175979	0.290114	0.678346
0.2	0.0	1	1	1	1	−0.558514	0.135674	0.584982
	0.2					−0.574788	0.188902	0.597832
	0.5					−0.593714	0.239557	0.618167
	0.8					−0.609046	0.274527	0.640155
	1.0					−0.618149	0.293119	0.655800

- The coefficient of local skin friction is decreased by the incremented values of unsteadiness and suction/injection parameters, and it is boosted with the values of slip parameter.
- The rate of solute transfer is improved by chemical reaction, slip and unsteadiness parameters, and it is decelerated by suction/injection parameter.

References

1. Makinde, O.D.: Similarity solution for natural convection from a moving vertical plate with internal heat generation and a convective boundary condition. Thermal science, **15(1)**, S137–S143 (2011).

2. Eswaramoorthi, S., Bhuvaneswari, M., Sivasankaran,S. Rajan, S.: Effect of radiation on MHD convective flow and heat transfer of a viscoelastic fluid over a stretching surface. Procedia Engineering, **127**, 916–923 (2015).
3. Eswaramoorthi, S., Bhuvaneswari, M., Sivasankaran, S., Rajan, S.: Soret and Dufour effects on viscoelastic boundary layer flow, heat and mass transfer in a stretching surface with convective boundary condition in the presence of radiation and chemical reaction. Scientia Iranica B, **23(6)**, 2575–86 (2016).
4. Merkin J.K, Pop, I.: The forced convective flow of a uniform stream over a flat surface with a convective surface boundary condition. Communication in Nonlinear Science and Numerical Simulation, **16(9)**, 3602–3609 (2011).
5. Bhattacharyya, K., Layek, G.C.: Similarity solution of MHD boundary layer flow with diffusion and chemical reaction over a porous flat plate with suction/blowing. Meccanica , **47(4)**, 1043–1048 (2012).
6. Nabil, T.M., El-dabe, Hassan, M.A., Godh, W.A.: Unsteady magneto hydrodynamic free convection flow past a semi-infinite permeable moving plate through porous medium with chemical reaction and radiation absorption. Journal of Heat Transfer, **135(2)**, 024501 (2012)
7. Ferdows, M., Kaino, K., Sivasankaran, S.: Free convection flow in an inclined porous surface. Journal of porous media, **12(10)**, 997–1003 (2009).
8. Bhuvaneswari, M., Sivasankaran, S., Kim ,Y.J.: Lie group analysis of radiation natural convection flow over an inclined surface in a porous medium with internal heat generation. Journal of porous media, **15(12)**, 1155–1164 (2012).
9. Chamkha, A.J., Rashad, A.M.: Unsteady heat and mass transfer by MHD mixed convection flow from a rotating vertical cone with chemical reaction and soret and dufour effects. Canadian Journal of Chemical Engineering, **92(4)**, 758–767 (2014).
10. Karthikeyan, S., Bhuvaneswari, M., Sivasankaran, S., Rajan, S.: Soret and Dufour effects on MHD mixed convection heat and mass transfer of a stagnation point flow towards a vertical plate in a porous medium with chemical reaction, radiation and heat generation. Journal of Applied Fluid Mechanics, **9(3)**, 1447–1455 (2016).
11. Niranjan, H., Sivasankaran, S., Bhuvaneswari, M.: Chemical reaction, Soret and Dufour effects on MHD mixed convection stagnation point flow with radiation and slip condition. Scientia Iranica B, **24(2)**, 698–706 (2017).
12. Sivasankaran, S., Niranjan, H., Bhuvaneswari, M.: Chemical reaction, radiation and slip effects on MHD mixed convection stagnation-point flow in a porous medium with convective boundary condition. International Journal of Numerical Methods for Heat and Fluid Flow, **27(2)**, 454–470 (2017).

Solution of Wave Equations and Heat Equations Using HPM

Nahid Fatima and Sunita Daniel

Abstract In this paper, the homotopy perturbation method (HPM) has been used to solve some wave equations and a few heat equations. The resultant solution helps to substantiate that HPM is a useful and robust mechanism to solve these equations. An accurate approximation is possible while solving complex and complicated problems using semi-analytical methods, an example of which is the HPM. However, we consider the boundary conditions as one-dimensional when we use this method, and hence these approximations can be considered only for a small range. HPM was developed by J. H. He for solving wave and heat equations. To obtain accurate results for these equations using HPM, standard homotopy technique is merged with the perturbation technique along with some modifications.

1 Introduction

Partial differential equations have wide and varied applications in various fields of science. One has to construct these partial differential equations and also find exact and explicit solutions for them. Because of its importance, solving them and finding the exact solutions of these equations have always been an active area of research. Most of the linear and nonlinear partial differential equations can be split into two components, namely, the integrable component and the non-integrable component. Infinite number of solutions can be found if the equations are integrable. However, if the equations are not integrable, it is difficult for one to find an exact solution, and hence some other techniques have to be used to obtain them.

During the recent years, many methods have been developed for finding the exact solutions of nonlinear equations. Each method has its own merits and demerits, and hence we cannot pinpoint any particular method and say that it is the best method. All the methods which have been developed so far are problem dependent and so

N. Fatima (✉) · S. Daniel
Amity School of Applied Sciences, Amity University Haryana, Gurugram, Haryana, India
e-mail: nfatima@ggn.amity.edu; sdaniel@ggn.amity.edu

B. Rushi Kumar et al. (eds.), *Applied Mathematics and Scientific Computing*,
Trends in Mathematics, https://doi.org/10.1007/978-3-030-01123-9_36

may work for only some type of problems and not for others. Hence we can apply these methods to solve the nonlinear equations which have not yet been solved using them, and we can check if the solutions so obtained by these methods are the same as the exact solutions.

In this paper, we use the homotopy perturbation method to find the accurate solution of the wave and heat equations. Prior to the introduction of this method by J. He, Wazwaz and Gorguis studied the wave equation and nonlinear diffusion equation subject to initial conditions by using Adomian decomposition method [15]. J. He developed the HPM to solve linear and nonlinear, initial, and boundary value problems [8, 10–14, 16]. In this method, we assume the solution to be the sum of an infinite series, and this infinite series converges rapidly to accurate solutions. This method has been used by various authors [2–4, 7, 9, 17] to solve several functional equations. Modified homotopy perturbation method has also been developed and used for solving various partial differential equations [1, 5, 6].

2 Homotopy Perturbation Method

In the current segment, we explain the HPM for a general differential equation with given boundary conditions. We shall then see as to how this method works for various wave and heat equations under different boundary conditions.

Let us assume the function:

$$S(u) - t(r) = 0, \quad r \in \phi \tag{1}$$

with the given condition

$$A\left(u, \frac{\partial u}{\partial \pi}\right) = 0, \quad r \in \lambda \tag{2}$$

where S represents the general operator, $t(r)$ is an analytic function, A is a boundary operator, and λ is the domain boundary. The operator S can be generally split into two operators, K and M, where K is a linear and M a nonlinear operator. Equation (1) now becomes

$$K(u) + M(u) - t(r) = 0. \tag{3}$$

Applying the homotopy method, we now construct a homotopy $v(r, p) : \phi \times [0, 1] \to R$, which satisfies

$$H(v, p) = (1 - p)[K(v) - K(u_0)] + p[S(v) - t(r)] = 0 \tag{4}$$

or

$$H(v, p) = K(v) - K(u_0) + pK(u_0) + pK(u_0) + p[M(v) - t(r)] = 0 \tag{5}$$

where $p \in [0, 1]$ is called homotopy parameter and u_0 is an initial approximation for the solution of (1), which satisfies the boundary condition. Evidently, from Eqs. (4) and (5), we shall have

$$H(v, 0) = K(v) - K(u_0) = 0 \tag{6}$$

$$H(v, 1) = S(v) - t(r) = 0 \tag{7}$$

After performing some manipulations, we get

$$V = v_0 + pv_1 + p^2 v_2 + p^3 v_3 + \ldots \tag{8}$$

Putting $p = 1$ in (8) gives

$$U = \lim_{p \to 1} v = v_0 + v_1 + v_2 + v_3 + \ldots \tag{9}$$

Having discussed the homotopy perturbation method, we shall now solve some examples of wave equations and heat equations and show that the solution derived by this method is precisely the same as the solution found by the analytical procedure.

2.1 Examples of Wave Equations

In this section we consider the various examples of wave equations with different boundary conditions.

2.1.1 Illustration 1

Assume the wave formula

$$u_{rr} - \frac{s^2}{2} u_{ss} = 0 \tag{10}$$

with the initial conditions as

$$U(s, 0) = s^2, \quad u_r = -s^2 \tag{11}$$

By the homotopy method, we get

$$\frac{\partial^2 u}{\partial r^2} = p\left[\frac{\partial^2 u}{\partial r^2} + \frac{s^2}{2} u_{ss} - D_r^2 u\right] \tag{12}$$

Now by HPM we have

$$U = u_0 + pu_1 + p^2u_2 + p^3u_3 + \ldots \tag{13}$$

Using the Eq. (12) in Eq. (11) and correlating the coefficient of different powers of p, the resultant equation will be

$p^0 : \frac{\partial^2 u_0}{\partial r^2} = 0, \frac{\partial u_0}{\partial r} = -s^2, u_0 = s^2 - rs^2$

$p^1 : \frac{\partial^2 u_1}{\partial r^2} = \frac{s^2}{2}(u_0)_{ss}, u_1 = (\frac{r^2}{2!} - \frac{r^3}{3!})s^2$

$p^2 : \frac{\partial^2 u_2}{\partial r^2} = \frac{s^2}{2}(u_1)_{ss}, u_2 = (\frac{r^4}{4!} - \frac{r^5}{5!})s^2$

$p^3 : \frac{\partial^2 u_3}{\partial r^2} = \frac{s^2}{2}(u_2)_{ss}, u_3 = (\frac{r^4}{4!} - \frac{r^5}{5!})s^2$

Continuing this process we get

$U = u_0 + pu_1 + p^2u_2 + p^3u_3 + \ldots$

$U = (s^2 - rs^2) + (\frac{r^2}{2!} - \frac{r^3}{3!})s^2 + (\frac{r^4}{4!} - \frac{r^5}{5!})s^2 + (\frac{r^4}{4!} - \frac{r^5}{5!})s^2 + \ldots$

$U = s^2(1 + \frac{r^2}{2!} + \frac{r^4}{4!} + \ldots) - s^2(\frac{r}{1!} + \frac{r^3}{3!} + \frac{r^5}{5!} + \ldots)$

$U = s^2 \sum_{n=0}^{\infty}(-1)^n \frac{r^n}{n!}$

$U = s^2 e^{-r}$

This is same as the exact solution of the equation given by (10).

2.1.2 Illustration 2

Assume the wave formula

$$u_{rr} - \frac{s^2}{2}u_{ss} = 0 \tag{14}$$

where the conditions are given as

$$U(s, 0) = s^2, \quad u_r = 0 \tag{15}$$

By the homotopy method we get, $U = s^2 \cosh(r)$ which is same as the exact solution.

2.2 *Examples of Heat Equations*

In this section we consider the various examples of heat equations with different boundary conditions.

2.2.1 Illustration 1

Assume the heat formula

$$u_r = i\frac{u}{ss} \tag{16}$$

with the conditions given as

$$U(s,0) = \sinh(s), \qquad u_r = 0 \tag{17}$$

By the homotopy method, we get

$$\frac{\partial^2 u}{\partial r^2} = p\left[\frac{\partial u}{\partial r} + iu_{ss} - D_r u\right] \tag{18}$$

Now by HPM we have

$$U = u_0 + pu_1 + p^2u_2 + p^3u_3 + \ldots \tag{19}$$

Using the formula (19) in formula (18) and analyzing the coefficient of different powers of p, we get

$p^0 : \frac{\partial^2 u_0}{\partial r} = 0, \frac{\partial u_0}{\partial r} = -s^2, u_0 = \sinh(s)$

$p^1 : \frac{\partial^2 u_1}{\partial r} = i(u_0)_{ss}, u_1 = i(r)\sinh(s)$

$p^2 : \frac{\partial^2 u_2}{\partial r} = i(u_1)_{ss}, u_2 = i^2(\frac{r^2}{2!})\sinh(s)$

$p^3 : \frac{\partial^2 u_3}{\partial r} = i(u_2)_{ss}, u_3 = i^3(\frac{r^3}{3!})\sinh(s)$

Continuing this process we get

$U = u_0 + pu_1 + p^2u_2 + p^3u_3 + \ldots$

$U = (1 + ri + i^2\frac{r^2}{2!} + \ldots)\sinh(s)$

$U = s^2(1 + \frac{r^2}{2!} + \frac{r^4}{4!} + \ldots)$

$U = e^{ir}\sinh(s)$

which is same as the accurate solution.

2.2.2 Illustration 2

Assume the heat formula

$$u_r = \lambda u_{ss}, \qquad -\infty < s < \infty, \quad r > o \tag{20}$$

with the initial conditions as

$$U(s,0) = f(s), \quad u_r = 0 \tag{21}$$

By the homotopy method, we get

$$\frac{\partial u}{\partial r} = p\left[\frac{\partial u}{\partial r} + \lambda u_{ss} - D_r u\right] \tag{22}$$

Now by HPM we have

$$U = u_0 + pu_1 + p^2u_2 + p^3u_3 + \ldots \tag{23}$$

Using the Eq. (22) in Eq. (21) and comparing the coefficient of different powers of p, we get

$U = f(s) + \sum_{n=1}^{\infty} \frac{(\lambda r)^n}{n!} f^{2n}(s)$

which is same as the accurate solution.

2.2.3 Illustration 3

Consider the Schrodinger formula

$$u_r + iu_{ss} = 0, \quad -\infty < s < \infty, \quad r > o \tag{24}$$

where the conditions are given as

$$U(s,0) = f(s), \quad u_r = 0 \tag{25}$$

Using the homotopy method, we get

$$\frac{\partial u}{\partial r} = p\left[\frac{\partial u}{\partial r} - iu_{ss} - D_r u\right] \tag{26}$$

Now by HPM we have

$$U = u_0 + pu_1 + p^2u_2 + p^3u_3 + \ldots \tag{27}$$

Using the formula (27) in formula (26) and analyzing the coefficient of different powers of p, we get

$p^0 : \frac{\partial u_0}{\partial r} = 0, \frac{\partial u_0}{\partial r} = 0, u_0 = f(s)$

$p^1 : \frac{\partial u_1}{\partial r} = -i(u_0)_{ss}, u_1 = -i(r)f^{"}(s)$

$p^2 : \frac{\partial u_2}{\partial r} = -i(u_1)_{ss}, u_2 = i^2(\frac{r^2}{2!})f^4(s)$

$p^3 : \frac{\partial^2 u_3}{\partial r} = i(u_2)_{ss}, u_3 = -i^3(\frac{r^3}{3!})f^6(s)$

Continuing this process we get

$U = u_0 + pu_1 + p^2u_2 + p^3u_3 + \ldots$

$U = (1 + ri + i^2\frac{r^2}{2!} + \ldots)\sinh(s)$

$U = f(s) - i(r)f^{"}(s) + i^2(\frac{r^2}{2!})f^4(s) - i^3(\frac{r^3}{3!})f^6(s) + \ldots$

$U = f(s) + \sum_{n=1}^{\infty}\frac{(-ir)^n}{n!}f^{2n}(s)$

which is same as the accurate solution.

3 Conclusion

Successful administration of HPM process was introduced in the above illustrations to achieve explicit solutions for wave and heat equations. Additionally, this method is a productive tool to determine the solution of different types of PDE. The HPM is capable in observing the comparative or analytic explanation of the linear and nonlinear partial differential equation. Since the solution is in the form of infinite series, many complex problems can be made simple using this technique, and hence it takes limited duration to reach a conclusion. This is also a helpful and useful procedure to obtain the solution of differential equations.

References

1. X.Feng, Y.We, Modified homotopy perturbation method for solving the Stoke's equations, Computer and Mathematics with Applications **6(8)**, 2262–2266 (2011).
2. O.Martin, A homotopy perturbation method for solving a neutron transport equation, Applied Mathematics and Computation **217(21)**, 8567–8574 (2011).
3. K.A.Gepreel, The homotopy perturbation method applied to the nonlinear fractional Kolomogrov-Petrovskii-Piskunov equations, Applied Mathematics Letters **24(8)**, 1428–1434 (2011).
4. M. Duman, Asymptotic expansions for the Sturm-Liouville problem by homotopy perturbation method, Applied Mathematics and Computation **216(2)**, 492–496 (2010).
5. M.A.Jafari and A Aminataei, Improvement of the homotopy perturbation method for solving diffusion equations, Physica Scripta **82(1)**, 1–8 (2010).
6. J.Nadjafi, M.Tamamgar, Modified Homotopy perturbation method for solving integral equations, International Journal of Modern Physics B **24 (2)**, 4741–4746 (2010).
7. S. Pamuk, N. Pamuk, He's homotopy perturbation method for continuous population models for single and interacting species, Computers and Mathematics with Applications **59(2)**, 612–621 (2010).

8. J.H He, An elementary introduction to the homotopy perturbation method, Computers and Mathematics with Applications **578(3)**, 410–412 (2009).
9. A. Yildirim, Application of He's homotopy perturbation method for solving the Cauchy reaction-diffusion problem, Computers and Mathematics with Applications **57 (4)**, 612–618 (2009).
10. J.H. He, Non-perturbative methods for strongly nonlinear problems, Dissertation, de-Verlag in Internet GmbH, Berlin (2006).
11. J.H. He, Some asymptotic methods for strongly nonlinear equations, International Journal of Modern Physics B **20 (10)**, 1141–1199 (2006).
12. J.H. He, New interpretation of homotopy perturbation method, International Journal of Modern Physics B **20**, 2561–2568 (2006).
13. J.H. He, Application of homotopy perturbation method to nonlinear wave equations, Chaos, Solitons & Fractals **26**, 695–700 (2005).
14. J.H. He, Homotopy perturbation method for bifurcation of nonlinear problems, International Journal of Nonlinear Sciences and Numerical Simulation **6**, 207–208 (2005).
15. A.M. Wazwaz, A. Gorguis, An analytical study of Fisher's equation by using Adomian decomposition method, Applied Mathematics and Computation **154**, 609–620 (2004).
16. J.H. He, A coupling method of homotopy technique and perturbation technique for nonlinear problems, International Journal of Non-Linear Mechanics **35**, 37–43 (2000).
17. J.H. He, Homotopy perturbation technique, Computer Methods in Applied Mechanics and Engineering **178**, 257–262 (1999).

Nonlinear Radiative Unsteady Flow of a Non-Newtonian Fluid Past a Stretching Surface

P. Krishna Jyothi, G. Sarojamma, K. Sreelakshmi, and K. Vajravelu

Abstract Analysis of nonlinear radiative heat transfer on the MHD Maxwell fluid flow in the boundary layers adjacent to a sheet with continuous stretching is discussed. Numerical solution of the PDEs governing the flow is obtained by the successive application of suitable similarity variables and BVP4c method. The flow variables, surface frictional coefficient, and local gradients of temperature and concentration are discussed through the graphs and tables. Results of the present analysis are compared with the previously published work and are found to be in close agreement.

1 Introduction

We deal with several nonclassical fluids in industries and in our daily routine. For example, polymers, paints, jellies, medicines, physiological fluids, etc. exhibit rheological properties. Maxwell fluid is a special kind of fluid processing the properties of elasticity and viscosity while undergoing deformation. The upper convective Maxwell model is said to be the generalization of Maxwell material with large deformation using the upper convective time derivative. Roy [1] studied the Maxwell fluid flow pattern past an infinite plate when the plate is moving parallel to itself with an arbitrary time-dependent velocity. Assuming the pressure to be uniform and velocity in an exponential form, exact solutions are obtained. Kumari and Nath [2] studied the heat and flow characteristics of a Maxwell fluid of a vertical sheet with exponential stretching. Nonlinear radiative heat flux is significant when the temperature differences in the fluid layers are not small and the energy

P. Krishna Jyothi · G. Sarojamma (✉) · K. Sreelakshmi
Department of Applied Mathematics, Sri Padmavati Mahila Visvavidyalayam, Tirupati, Andhra Pradesh, India
e-mail: jyothikrishna@spmvv.ac.in; sarojamma@spmvv.ac.in; katasreelakshmi@spmvv.ac.in

K. Vajravelu
Department of Applied Mathematics, University of Central Florida, Orlando, FL, USA
e-mail: kuppalapalle.vajravelu@ucf.edu

B. Rushi Kumar et al. (eds.), *Applied Mathematics and Scientific Computing*, Trends in Mathematics, https://doi.org/10.1007/978-3-030-01123-9_37

transport equation contains a new diffusion term owing to energy conservation. Solar power devices, nuclear power generators, and chemical processes involving very high temperatures are some of the areas that contain nonlinear thermal radiative heat transfer. Investigations on nonlinear radiative heat transfer with different aspects in different fluid flow conditions have been studied by Animasaun et al. [3], Mahanthesh et al. [4], Hayat et al. [5], Vijaya et al. [6]. Stratification refers to the formation of layers due to concentration differences, temperature variations, or the presence of fluids with different densities. Double stratification occurs when both heat and mass mechanisms take place simultaneously. Study of mass and energy stratification in fluid flows is very important due to its varied applications. Thermal stratification of reservoirs and oceans; salinity stratification in rivers, estuaries, groundwater reservoirs, and oceans; heterogeneous mixtures in atmosphere; and industrial, food, and manufacturing processes are some of the examples of stratification. Chen and Eichhorn [7] explored the flow characteristics of a free convective fluid flow along a vertical plate with thermally stratification. Singh et al. [8] obtained the flow characteristics of a steady Newtonian fluid flow over a moving vertical plate considering the effect of temperature stratification. Sarojamma et al. [9] investigated dual stratification effect on the oblique stagnation point flow of a nonclassical Casson fluid. In this analysis we investigate the influence of nonlinear thermal radiation, thermal and solutal stratification on the energy, and mass transport in hydromagnetic flow of UCM fluid induced by a surface of continuous linear stretching.

2 Mathematical Formulation

We propose the transfer of mass and heat in a UCM fluid flow due to an unsteady stretching surface. The surface comes forth from a narrow slit at origin (x=0,y=0) and proceeds with a velocity $u_w(x,t) = bx/(1-\alpha t)$, where b and α are positive constants with dimensions of $(time)^{-1}$. The flow is exposed to a variable magnetic field $B(x) = B_0/\sqrt{1-\alpha t}$ applied normally to the surface with B_0 as its initial strength. $T_w(x) = T_0 + m_1 x/(1-\alpha t)$ and $C_w(x) = C_0 + n_1 x/(1-\alpha t)$, respectively, are the temperature and concentration of the sheet, while $T_\infty(x) = T_0 + m_2 x/(1-\alpha t)$ and $C_\infty(x) = C_0 + n_2 x/(1-\alpha t)$ correspond to the ambient fluid where m_1, m_2, n_1, n_2 are dimensional constants and T_0, C_0 are, respectively, the reference temperature and concentration. Governing equations of the problem under study are given here under:

$$\frac{\partial u}{\partial x} + \frac{\partial v}{\partial y} = 0 \tag{1}$$

$$\frac{\partial u}{\partial t} + u\frac{\partial u}{\partial x} + v\frac{\partial u}{\partial y} + \lambda\left(u^2\left(\frac{\partial^2 u}{\partial x^2}\right) + v^2\left(\frac{\partial^2 u}{\partial y^2}\right) + 2uv\left(\frac{\partial^2 u}{\partial x \partial y}\right)\right) = \nu\left(\frac{\partial^2 u}{\partial y^2}\right) - \frac{\sigma B^2}{\rho}\left(u + \lambda v\frac{\partial u}{\partial y}\right) \tag{2}$$

$$\frac{\partial T}{\partial t}+u\frac{\partial T}{\partial x}+v\frac{\partial T}{\partial y}=\frac{k}{\rho C_p}\frac{\partial^2 T}{\partial y^2}+\frac{16\sigma^*}{3k^*\rho C_p}\frac{\partial}{\partial y}(T^3\frac{\partial T}{\partial y})+\frac{Q^*}{\rho c_p}(T-T_\infty) \quad (3)$$

$$\frac{\partial C}{\partial t}+u\frac{\partial C}{\partial x}+v\frac{\partial C}{\partial y}=D\frac{\partial^2 C}{\partial y^2}-K_1(C-C_\infty) \quad (4)$$

where, u and v are fluid velocity components along x and y-axes, respectively; the nomenclature of $\nu, \rho, \sigma, k, c_p, \sigma^*, k^*, \mu, D$ is same as that used in [9]; $\lambda = \lambda_0(1-\alpha t)$ is the relaxation time; λ_0 is a constant; T is fluid temperature; C is fluid concentration; $Q^*(t) = Q_0/(1-\alpha t)$ is heat generation ($Q^* > 0$) or absorption ($Q^* < 0$) coefficient which changes with time; Q_0 being the initial value of heat generation/absorption coefficient; $k_1(t) = k_c/(1-\alpha t)$ is the time-dependent reaction rate; and k_c is a constant.

The pertinent boundary conditions controlling the problem are given by

$$u=u_w, v=0, T=T_w=T_0+\frac{m_1 x}{1-\alpha t}, C=C_w=C_0+\frac{n_1 x}{1-\alpha t} \quad at \quad y=0 \quad (5)$$

$$u\to 0, T\to T_\infty=T_0+\frac{m_2 x}{1-\alpha t}, C\to C_\infty=C_0+\frac{n_2 x}{1-\alpha t} \quad as \quad y\to\infty \quad (6)$$

3 Method of Solution

The stream function $\psi(x, y, t)$ is defined as

$$u=\frac{\partial \psi}{\partial y}=\frac{bx}{1-\alpha t}f'(\eta) \quad (7)$$

$$v=-\frac{\partial \psi}{\partial x}=-\sqrt{\frac{\nu b}{1-\alpha t}}f(\eta) \quad (8)$$

which satisfies Eq. (1). The governing PDEs (3)–(4) can be recast to a set of ODEs on introduction of the given similarity variables

$$\psi(x,y,t)=\sqrt{\frac{\nu b}{1-\alpha t}}xf(\eta), \eta=\sqrt{\frac{b}{\nu(1-\alpha t)}}y, \theta(\eta)=\frac{T-T_\infty}{T_w-T_0}, \phi(\eta)=\frac{C-C_\infty}{C_w-C_0} \quad (9)$$

Substitution of (9) into Eqs. (3) to (4) yields

$$f'''+ff''-(f')^2+\beta(2ff'f''-f^2f''')-S(f'+\frac{\eta}{2}f'')-M(f'-\beta ff'')=0 \quad (10)$$

$$\theta''+Nr[(1+(\theta_r-\theta_s)\theta)^3]\theta''+3Nr[(\theta_r-\theta_s)(1+(\theta_r-\theta_s)\theta)^2](\theta')^2 \quad (11)$$

$$+ Pr(f\theta' - f'\theta - \epsilon_1 f' - S(\epsilon_1 + \theta + \frac{\eta}{2}\theta') + Q\theta) = 0$$

$$\phi'' + Sc(f\phi' - f'\phi - \epsilon_2 f' - S(\epsilon_2 + \phi + \frac{\eta}{2}\phi') - \gamma\phi) = 0 \tag{12}$$

with boundary conditions

$$f(0) = 0, f'(0) = 1, \theta(0) = 1 - \epsilon_1, \phi(0) = 1 - \epsilon_2 \tag{13}$$

$$f'(\infty) \to 0, \theta(\infty) \to 0, \phi(\infty) \to 0 \tag{14}$$

where $\beta = \lambda_0 b$ is the elastic parameter. It may be noted that β is the nondimensional elastic number that involves the relaxation time of the fluid (λ) as well as the kinematical parameter (b). In view of the presence of λ_0, β represents the measure of elasticity of the fluid and is also known as Deborah or Weissenberg number. $S = \alpha/b$ is the unsteadiness parameter, $M = \sigma B_0^2/\rho b$ is the magnetic field parameter, $Pr = (\rho c_p \nu)/k$ is the Prandtl number, $Nr = 16\sigma^* T_\infty^3/3kk^*$ is thermal radiation parameter, $\theta_r = T_w/T_\infty$ and $\theta_s = T_0/T_\infty$ are temperature ratio parameters, $Q = Q_0/\rho c_p b$ is the heat source/sink parameter, $\epsilon_1 = m_2/m_1$ is thermal stratified parameter, $\epsilon_2 = n_2/n_1$ is solutal stratified parameter, $Sc = \nu/D$ is the Schmidt number, and $\gamma = k_c/b$ is the chemical reaction parameter.

The C_f, Nu_x, and Sh_x coefficients of surface drag, heat, and mass transfer, respectively, are defined by

$$C_f = \frac{\tau_w}{\rho u_w^2}, Nu_x = \frac{xq_w}{k(T_w - T_\infty)}, Sh_x = \frac{xm_w}{D(C_w - C_\infty)} \tag{15}$$

where the wall shear stress τ_w, the surface heat flux q_w, and the mass flux m_w are given by

$$\tau_w = ((\mu+k)\frac{\partial u}{\partial y}+kN)_{y=0}, q_w = -K(1+\frac{16\sigma^* T^3}{3Kk^*})(\frac{\partial T}{\partial y})_{y=0}, m_w = -D(\frac{\partial C}{\partial y})_{y=0} \tag{16}$$

Making use of Eq. (16) in Eq. (15), we obtain

$$C_f\sqrt{Re_x} = (1+\beta)f''(0), \frac{Nu_x}{\sqrt{Re_x}}$$

$$= -(1 + Nr[1 + (\theta_r - \theta_s)\theta(0)]^3)\frac{1}{1-\epsilon_1}\theta'(0), \frac{Sh_x}{\sqrt{Re_x}} = -\phi'(0)(\frac{1}{1-\epsilon_2})$$

where $Re_x = u_w x/\nu$ is a local Reynolds number.

The governing Eqs. (10)–(12) are nonlinear equations, and its exact solution is not possible. Hence, we have solved the equations numerically using BVP4c method. The numerical scheme is validated by comparing the present results, i.e., $f''(0)$ with those calculated by Sharidan [10] and Chamkha et al. [11] in Table 1 for

Table 1 Values of $-f''(0)$ for different values of S with $\beta = M = 0$

S	Sharidan et al. [10]	Chamkha et al. [11]	Present results
0.8	−1.261042	−1.261512	−1.261043
1.2	−1.377722	−1.378052	−1.377724

Table 2 Values of $-\theta'(0)$ for values of Pr when $M = S = \beta = \theta_r = \theta_s = Nr = Sc = \gamma = \epsilon_1 = \epsilon_2 = 0$

Pr	Grubka and Bobba [12]	Chen [13]	Present results
0.01	0.0294	0.02942	0.02942
0.72	1.0885	1.08853	1.088623
1.00	1.333	1.3334	1.3334
3.00	2.5097	2.50972	2.50972

a Newtonian fluid in absence of magnetic field (i.e., $\beta = 0, M = 0$). Table 2 gives the comparison of $-\theta'(0)$ with those of [12] and [13]. We observe a good agreement of our results with theirs.

4 Results and Discussion

The intent of this analysis is to explore the effect of nonlinear radiative heat flux and stratifications of thermal and mass on the unsteady flow of a hydromagnetic UCM fluid over a sheet of continuous stretching. Influence of selected flow parameters on the flow variables is examined.

Figure 1 illustrates that the presence of magnetic field suppresses the velocity near the plate, i.e., $0 \leq \eta \leq 5$ and outside this range its influence is negligible. Velocity is seen to decrease with increase in M accompanied by thinning of boundary layers. This reduction is attributed to the Lorentz force generated due to the application of the transverse magnetic field which has a tendency to oppose the flow, and consequently the motion of the fluid slows down leading to the depreciation of velocity. Figure 2 indicates the effect of elastic parameter (β) on velocity. It is clear that velocity decreases with increasing β as expected. Figure 3 shows that increasing unsteadiness parameter enhances the velocity near the boundary and shows an opposite trend away from the boundary. Figure 4 reveals that the temperature ratio parameters θ_r enhances temperature, while θ_s shows an opposite effect as illustrated in Fig. 5. It is seen from Fig. 6 that temperature is depreciated with an increase in ϵ_1. It is clear from Fig. 7 that the mass concentration of the fluid is diluted for an increment in ϵ_2.The plots presented in Fig. 8 elucidate the relation between $C_f Re_x^1/2$ and M for different values of β. All profiles are straight lines with a negative slope showing a reduction with increasing M. It is seen that with increasing β we observe that all the curves of surface drag are parallel indicating a consistent reduction in surface drag. Profiles of Nusselt number drawn in Fig. 9 reveal that it increases with Pr. The profiles originate from higher values of Nusselt number for larger values of ϵ_1. Initially a marginal difference between the curves occurs when $Pr = 0.1$, and the difference increases

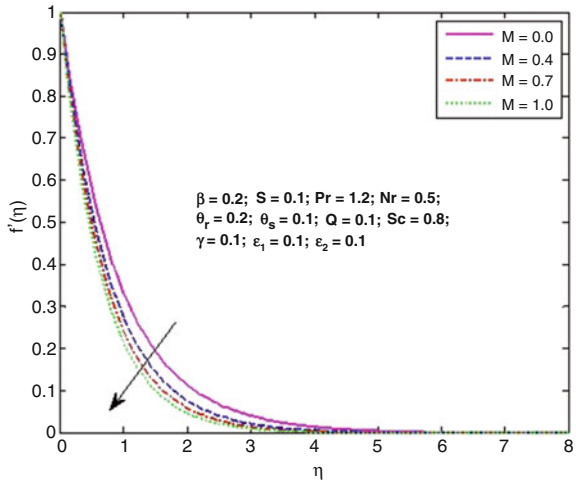

Fig. 1 Variation of M on $f'(\eta)$

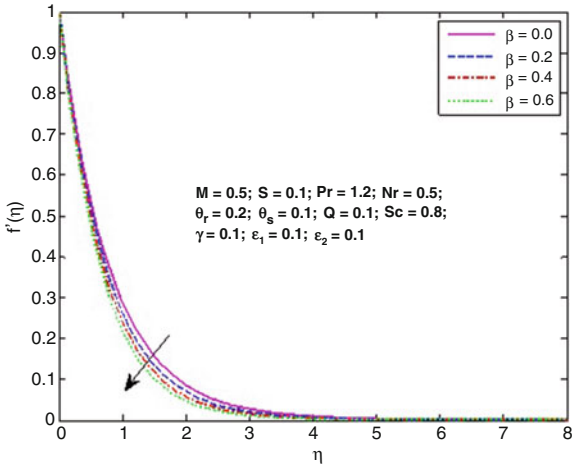

Fig. 2 Variation of β on $f'(\eta)$

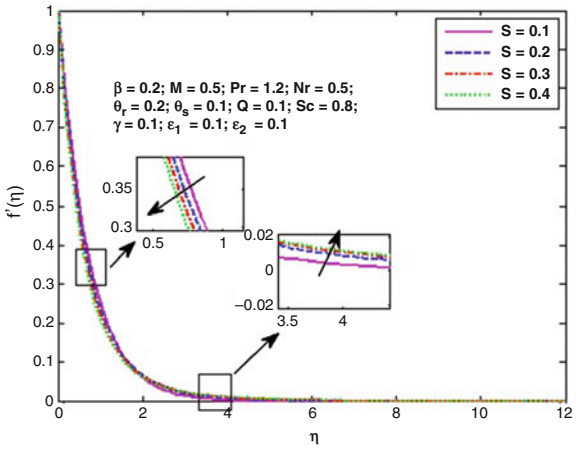

Fig. 3 Variation of S on $f'(\eta)$

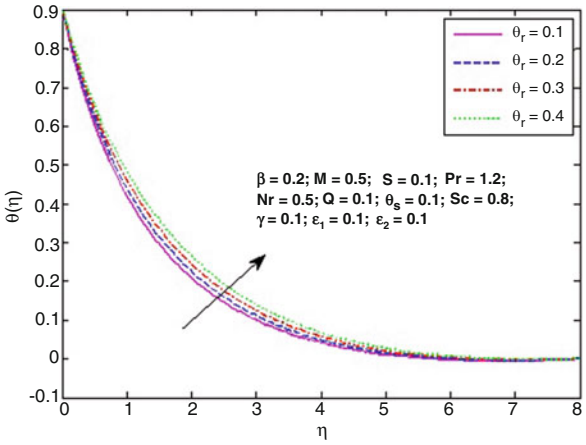

Fig. 4 Variation of θ_r on $\theta(\eta)$

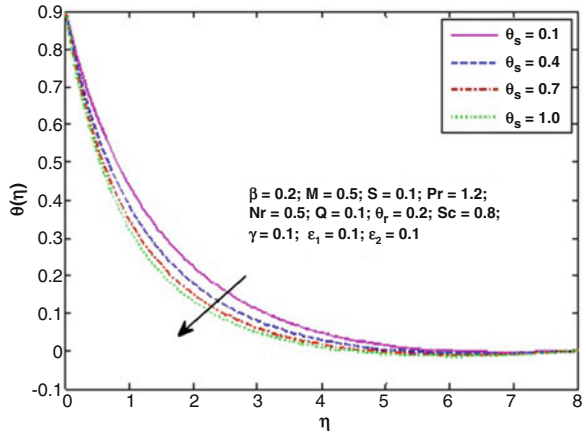

Fig. 5 Variation of θ_s on $\theta(\eta)$

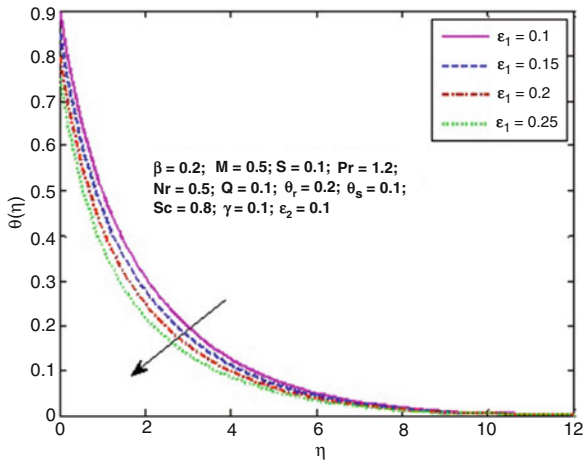

Fig. 6 Variation of ϵ_1 on $\theta(\eta)$

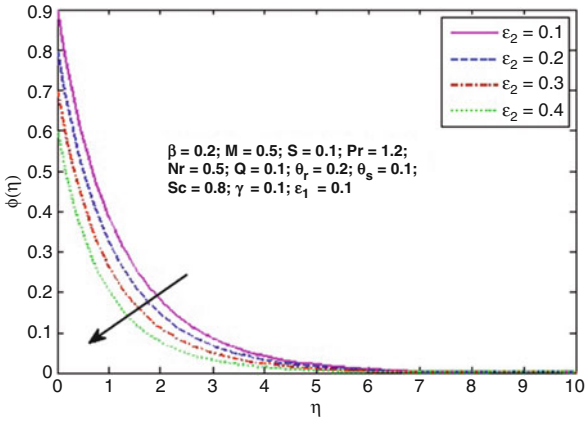

Fig. 7 Variation of ϵ_2 on $\phi(\eta)$

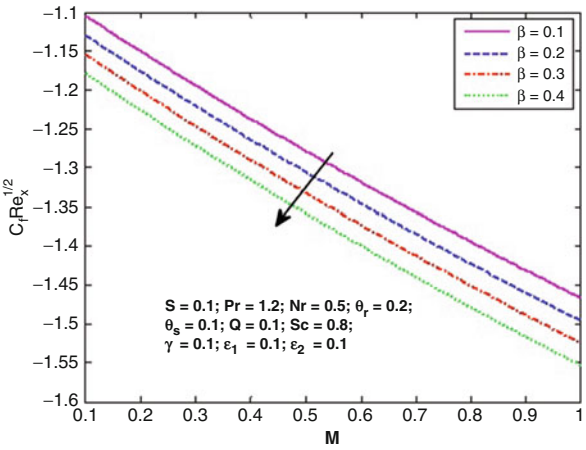

Fig. 8 Variation of skin friction with M for β

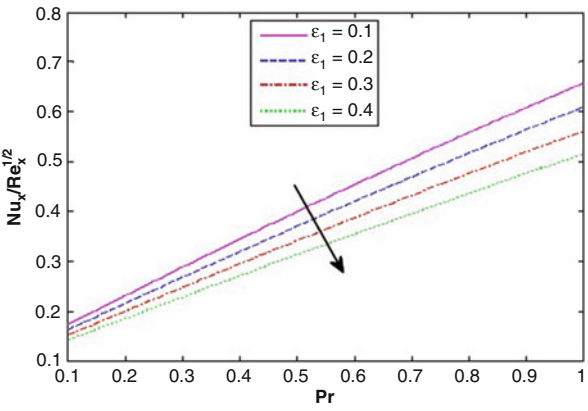

Fig. 9 Variation of Nusselt number with Pr for ϵ_1

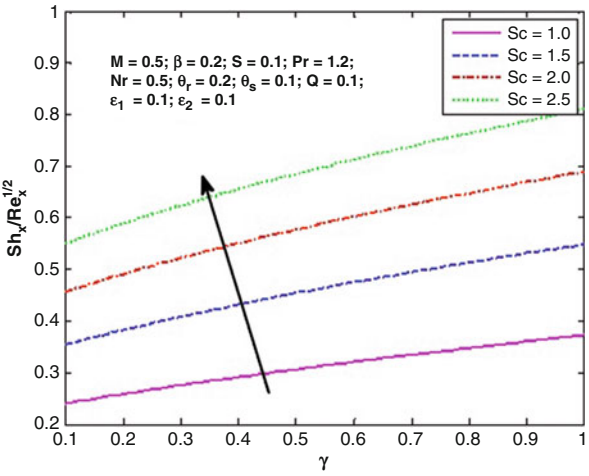

Fig. 10 Variation of Sherwood number with γ for Sc

as Pr tends to 1. Figure 10 shows the relationship between $Sh_x\, Re_x^{-1/2}$ and γ for different values of Sc. We note that Sherwood number enhances with both γ and Sc. However, the enhancement in Sherwood number with Sc is more compared to that of γ.

5 Conclusion

Some of the findings of the study are:

- The elastic parameter is seen to have a reducing influence on velocity.
- The unsteadiness parameter suppressed the velocity near the boundary and accelerated the flow away from the boundary.
- The temperature is seen to be enhanced for increasing values of temperature ratio parameter θ_r.
- The effect of excessive solutal stratification resulted in dilution of species concentration.

References

1. Roy, P. C.: Unsteady flow of a maxwell fluid past a flat plate. Indian J.Pure Appl. Math. 9(2), 157–166 (1978)
2. Kumari, M. and Nath, G.: Steady mixed convection flow of a maxwell fluid over an exponentially stretching verticle surface with magnetic field and viscous dissipation. Meccania. 49, 1263–1274 (2014)

3. Animasaun, I. L., Raju, C. S. K. and Sandeep,N.: Unequal diffusivities case of homogeneous-heterogeneous reactions within viscoelastic fluid flow in the presence of induced magnetic field and nonlinear thermal radiation. Alexandr. Eng. J. (2016)
4. Mahanthesh, B., Gireesha, B. J. and Rama Subba Reddy, G.: Non-linear radiative heat transfer in MHD three dimensional flow of water based nanofluid over a non-linearly stretching sheet with convective boundary condition, Journal of Nigerian Mathematicakl Society. 35, 178–198 (2016)
5. Hayat, T., Imtiaz, M., Alsaedi, A. and Kutbi, M. A. : MHD three dimensional flow of a nano fluid with velocity slip and non-linear thermal radiation. J. Magn. Mater. 396, 31–37 (2015)
6. Vijaya, N., Sreelakshmi, K. and Sarojamma, G.: Non-linear radiation effect on Casson fluid saturated nao-Darcy porous medium, Int. J. Mathematical Archive. 8, 39–52 (2017)
7. Chen, C. and Eichhorn, R.: Natural convectin from a vertical surface to stratified fluid. ASME J. Heat Trans. 98, 446–451 (1976)
8. Singh, G., Sharma, P. R. and Chamkha, A. J.: Effect of thermally stratified ambient fluid on MHD convective flow along a moving non-isothermal verticle plate. Int. J. Physical Sciences. 5, 208–215 (2010)
9. Sarojamma, G., Sreelakshmi, K. and Vajravelu, K.: Effects of dual stratification on non-orthogonal non-Newtonian fluid flow and heat transfer. Int. J. Heat and Technology. 36, 207–214 (2018)
10. Sharidan, S., Mahmood, T. and Pop. I.: Similarity solutions for the unsteady boundary layer flow and heat transfer due to a stretching sheet. Int. J. Appl. Mech. Eng. 11, 647–654 (2006)
11. Chamka, A. J., Aly, A. M. and Mansour, M. A.: Similarity solution for unsteady heat and mass transfer form a stretching surface embedded in a porous medium with suction/injection and chemical reaction effects. Chem. Eng. Commun. 197, 846–858 (2010)
12. Grubka, L. J., Bobba, K. M.: Heat transfer characteristics of a continuous stretching surface with variable temperature. ASME J. Heat Transfer. 107, 248–250 (1985)
13. Chen, C. H.: Laminar mixed convection adjacent to vertical continuously stretching sheets. Heat and Mass Transfer. 33, 471–476 (1998)

Heat Transfer Analysis in a Micropolar Fluid with Non-Linear Thermal Radiation and Second-Order Velocity Slip

R. Vijaya Lakshmi, G. Sarojamma, K. Sreelakshmi, and K. Vajravelu

Abstract This study addresses the thermal energy transport in a slippery sheet-driven flow of a micropolar fluid analysing the effect of radiative heat flux. The solution of PDEs of the governing the flow is derived numerically by the application of self-similarity transformations and Runge-Kutta Fehlberg algorithm along with shooting method. The computational results are discussed graphically for several selected flow parameters. Results of this analysis are compared with the published results and are seen to tally very closely.

Keywords Micropolar liquid · Non-linear radiative heat flux · Second-order velocity slip

1 Introduction

Micropolar fluids are used to model liquids containing arbitrarily oriented rigid spherical particles dispersed in a viscous medium, neglecting the fluids particles deformation. The mechanics of micropolar fluids, emerged from the theory developed by Eringen [1], has been an interesting area of research owing to the wide range of applications in industry. For example, polymeric liquids, real fluids with suspensions, liquid crystals, animal blood and exotic lubricants are modelled by micropolar fluids. Yacob and Ishak [2] obtained dual solutions to the problem of a micropolar fluid due to a sheet of shrinking. Energy transfer in fluids flowing over surfaces of stretching on account of thermal radiation has effective industrial applications in solar power technology, furnace design, solar

R. Vijaya Lakshmi · G. Sarojamma (✉) · K. Sreelakshmi
Department of Applied Mathematics, Sri Padmavati Mahila Visvavidyalayam, Tirupati, Andhra Pradesh, India
e-mail: sarojamma@spmvv.ac.in; katasreelakshmi@spmvv.ac.in

K. Vajravelu
Department of Applied Mathematics, University of Central Florida, Orlando, FL, USA
e-mail: kuppalapalle.vajravelu@ucf.edu

B. Rushi Kumar et al. (eds.), *Applied Mathematics and Scientific Computing*, Trends in Mathematics, https://doi.org/10.1007/978-3-030-01123-9_38

ponds, heat exchangers, satellites and space vehicles. Sarojamma et al. [3] explored dual stratification effect on the oblique stagnation point flow of a non-classical Casson fluid. Recently, researchers are investigating the non-linear thermal radiative heat transfer and consequently the equation governing the temperature becomes strongly non-linear. Mahantesh et al. [4] reported the effects of non-linear thermal radiation coupled with dual diffusion on the 3-D flow of a nanofluid. Wall slip flows with different aspects have been analysed [5, 6]. All these studies pertain to slip flows of first order. However, slip flows with second order occur in many fields of industry. In spite of the need to analyse the slip effect of second order on fluid flows, not much attention has been paid on it. Fang and Aziz [7] analysed the flow of a viscous liquid with second-order slip considering the stretch and shrink effects, respectively. Ibrahim [8] examined the MHD micropolar fluid flow considering the first and second-order slips. Analysis of heat transfer with non-linear thermal radiation and second-order slip flow of a micropolar fluid has not yet been addressed. This investigation addresses the effect of non-linear thermal radiation and velocity slip of order two in a micropolar fluid flow.

2 Mathematical Formulation

We propose a thin elastic sheet which issues from a narrow slit at the origin of a Cartesian co-ordinate system. The sheet at $y = 0$ is taken to be parallel to the x-axis and moves in its own plane with a velocity $u_w = ax$. The surface temperature T_w is assumed as constant. The flow is subjected to a constant transverse magnetic field of strength B_0 which is assumed to be applied in the positive y-direction, normal to the surface. The flow equations after boundary layer approximations are given by

$$\frac{\partial u}{\partial x} + \frac{\partial v}{\partial y} = 0 \tag{1}$$

$$u\frac{\partial u}{\partial x} + v\frac{\partial v}{\partial y} = \frac{(\mu + k)}{\rho}\left(\frac{\partial^2 u}{\partial y^2}\right) + \frac{k}{\rho}\frac{\partial N}{\partial y} - \frac{\sigma B_0^2}{\rho}u + g_1\beta_T\,(T - T_\infty) \tag{2}$$

$$u\frac{\partial N}{\partial x} + v\frac{\partial N}{\partial y} = \frac{\Omega}{\rho j}\frac{\partial^2 N}{\partial y^2} - \frac{k}{\rho j}\left(2N + \frac{\partial u}{\partial y}\right) \tag{3}$$

$$u\frac{\partial T}{\partial x} + v\frac{\partial T}{\partial y} = \frac{K}{\rho c_p}\frac{\partial^2 T}{\partial y^2} + \frac{16\sigma^*}{3k^*\rho c_p}\frac{\partial}{\partial y}\left(T^3\frac{\partial T}{\partial y}\right) \tag{4}$$

The boundary conditions are

$$u = u_w + U_{slip},\, v = 0,\, N = -n\frac{\partial u}{\partial y},\, T = T_w \quad at \quad y = 0 \tag{5}$$

$$u \to 0,\, N \to 0,\, T \to T_\infty, \quad as \quad y \to \infty$$

where, u and v are velocity components along x and y directions, respectively. The nomenclature of u_w, a, μ, k, σ, ρ, j, K, c_p, A, B, K_n, $l = \min\left[\frac{1}{K_n}, 1\right]$, α $(0 \leq \alpha \leq 1)$, λ,ν, Ω, n $(0 \leq n \leq 1)$ can be found in [8] and σ^*, k^* can be found in [3]; g_1 is acceleration due to gravity, β_T is coefficient of thermal expansion, T is the temperature inside the boundary layer, and T_∞ is ambient temperature. Slip velocity at the surface, following Wu [9], is given by

$$U_{slip} = \frac{2}{3}\left(\frac{(3-\alpha l^3)}{\alpha} - \frac{3}{2}\frac{(1-l^2)}{K_n}\right)\lambda\frac{\partial u}{\partial y} - \frac{1}{4}\left(l^4 + \frac{2}{K_n^2}(1-l^2)\right)\lambda^2\frac{\partial^2 u}{\partial y^2}$$

$$U_{slip} = A\frac{\partial u}{\partial y} + B\frac{\partial^2 u}{\partial y^2} \tag{6}$$

N is the microrotation or angular velocity, whose direction of rotation is normal to the $x - y$ plane, Ω is given by $\Omega = (\mu + k/2)j = \mu(1 + \beta/2)j$, where $\beta = k/\mu$ is the material parameter which describes the coupling of the linear and angular motion which arises due to the microrotation of the fluid molecules. Therefore β symbolises the coupling between Newtonian and rotational viscosities. If $\beta \to 0$ we see that $k \to 0$ which corresponds to the case of Newtonian fluid; hence $\beta \to 0$ corresponds to a viscous fluid.

3 Method of Solution

We define

$$u = \frac{\partial \psi}{\partial y} = axf', v = -\frac{\partial \psi}{\partial x} = -\sqrt{a\nu}f \tag{7}$$

where $\psi(x, y)$ is the stream function. We define the following similarity transformations for dimensionless variables

$$\eta = \sqrt{\frac{a}{\nu}}y, \psi = \sqrt{a\nu}xf(\eta), N = ax\sqrt{\frac{a}{\nu}}g(\eta), \theta(\eta) = \frac{T - T_\infty}{T_w - T_\infty} \tag{8}$$

where f, θ, g are dimensionless variables. Using the above similarity transformation and dimensionless variables, the governing equations (1)–(4) are reduced into the ordinary differential equations as follows:

$$(1 + \beta)f''' + ff'' - (f')^2 + \beta g' - Mf' + Gr\theta = 0 \tag{9}$$

$$\left(1 + \frac{\beta}{2}\right)g'' - \beta(2g + f'') + fg' - f'g = 0 \tag{10}$$

$$\theta'' + Nr[(1+(\theta_w-1)\theta)^3]\theta'' + 3Nr[(\theta_w-1)(1+(\theta_w-1)\theta)^2](\theta')^2 + Prf\theta' = 0 \quad (11)$$

With boundary conditions

$$f(0)=0,\ f'(0)=1+h_1 f''(0)+h_2 f'''(0),\ g(0)=-nf''(0),\ \theta(0)=1 \quad at \quad \eta=0 \quad (12)$$

$$f'(\infty)\to 0,\ g(\infty)\to 0,\ \theta(\infty)\to 0 \quad as \quad \eta\to\infty \quad (13)$$

where $M = \frac{\sigma B_0^2}{\rho a}$ is the magnetic parameter, $Gr = g_1\beta_T(T_w - T_\infty)/au_w$ is the thermal Grashof number, $Pr = (\rho c_p \nu)/K$ is the Prandtl number, $Nr = (16\sigma^* T_\infty^3)/(3Kk^*)$ is the thermal radiation parameter, $\theta_w = T_w/T_\infty$ is the temperature ratio parameter and

$h_1 = A\sqrt{a/\nu}$, $h_2 = Ba/\nu$ Nu_x are the first- and second-order velocity slip parameters, respectively.

The skin friction coefficient C_f and local Nusselt number Nu_x are defined by

$$C_f = \frac{\tau_w}{\rho u_w^2},\ Nu_x = \frac{xq_w}{K(T_w - T_\infty)} \quad (14)$$

where the wall shear stress τ_w and the surface heat flux q_w are given by

$$\tau_w = \left((\mu+k)\frac{\partial u}{\partial y} + kN\right)_{y=0},\ q_w = -K\left(1+\frac{16\sigma^* T^3}{3Kk^*}\right)\left(\frac{\partial T}{\partial y}\right)_{y=0} \quad (15)$$

Using Eq. (15) in Eq. (14), we obtain

$$C_f\sqrt{Re_x} = -(1+\beta(1-n))\ f''(0),\ \frac{Nu_x}{\sqrt{Re_x}} = -\left(1+Nr\,[1+(\theta_w-1)\theta(0)]^3\right)\theta'(0)$$

where $Re_x = U_w x/\nu$ is a local Reynolds number.

The set of differential equations (9)–(11) along with the conditions (12) and (13) are solved numerically standard RKF-45 method.

In order to confirm the accuracy of our numerical procedure, we compared our results, viz. $-f''(0)$ for various slip factors h_1 with those of Sahoo and Do [6] and Ibrahim [8] when $\beta = M = h_2 = n = Gr = Pr = Nr = 0$. Values of $-\theta'(0)$ are compared with those of Ishak [10] and Ibrahim [8] for various values of Pr in the absence of β, M, h_1, h_2, n, Gr, Nr and are presented in Table 1. It is seen that there is an excellent agreement with them. Table 2 shows that $-f''(0)$ and $-\theta'(0)$ are compared with Ibrahim [8] in the absence of thermal buoyancy force and thermal radiation for various M, β, h_2. From this we observe that our results are very close to those evaluated by Ibrahim [8].

Table 1 Comparison values of $-f''(0)$ and $-\theta'(0)$ with slip factor h_2 and Pr when $\beta = M = Gr = Nr = \theta_w = h_2 = n = 0$

h_1 ($Pr = 0$)	Sahoo and Do [6] $-f''(0)$	Ibrahim [8] $-f''(0)$	Present results $-f''(0)$	Pr ($h_1 = 0$)	Ishak [10] $-\theta'(0)$	Ibrahim [8] $-\theta'(0)$	Present results $-\theta'(0)$
0.0	1.001154	1.000000	1.000000	0.72	0.4631	0.4636	0.463592
1.0	0.428450	0.430160	0.430160	3.0	1.1652	1.1652	1.165244
2.0	0.282893	0.283980	0.283981	10.0	2.3080	2.3080	2.308009
3.0	0.213314	0.214055	0.214056	100.0	7.7657	7.7657	7.765816

Table 2 Comparison values of $-f''(0)$ and $-\theta'(0)$ with M, β, h_2 when $h_1 = 1, Pr = 1, n = 0.5, Gr = 0, Nr = 0$

M	β	h_2	$-f''(0)$ Ibrahim [8]	$-f''(0)$ Present	$-\theta'(0)$ Ibrahim [8]	$-\theta'(0)$ Present
0.1	0.1	−1	0.3220	0.32197	0.3816	0.38161
0.2			0.3262	0.32620	0.3603	0.36040
0.4			0.3315	0.33147	0.3239	0.32391
0.2	1	−1	0.3173	0.31728	0.4066	0.40659
	2		0.3068	0.30678	0.4431	0.44308
	3		0.2971	0.29709	0.4703	0.47033
0.2	2	−1	0.3068	0.30675	0.4431	0.44315
		−2	0.2588	0.25883	0.4143	0.41438
		−3	0.2262	0.22622	0.3927	0.39281

4 Results and Discussion

Influence of the various physical parameters that emerged in this study on the flow variables has been presented through graphs and discussed.

Figure 1 shows the variation of the material parameter (β) on the velocity, and its influence is seen to increase the velocity. From Fig. 2 for any value of β , microrotation is observed to diminish near the boundary till $\eta = 0.75$, and afterwards it increases and eventually satisfies the free stream condition. Further microrotation is seen to enhance with β.

Figure 3 indicates that presence of magnetic field suppresses the velocity due to the Lorentz force developed as a result of the applied magnetic field which has a tendency to resist the fluid flow. Also, increase in the strength of magnetic field causes further reduction in the velocity due to stronger Lorentz forces. Magnetic field is seen to have a decreasing influence on the microrotation.

Figure 4 displays the variation of both velocity and microrotation in the boundary layer for different values of Gr. It is seen that velocity increases with increase in the buoyancy parameter Gr as thermal buoyancy assists the fluid flow in the boundary layer. The microrotation is observed to diminish near the boundary till $\eta = 1.4$, and later it increases up to $\eta = 7$ and eventually attains the free stream velocity. It can be noticed that temperature has an exactly opposite trend to that of the two velocities for the same variation of Gr.

Influence of first-order slip parameter on both velocity and microrotation components is to reduce in their magnitude as illustrated in Fig. 5. Second-order slip variations on velocities are plotted in Fig. 6. The impact of second-order slip parameter on velocities is qualitatively similar to that of first-order slip parameter.

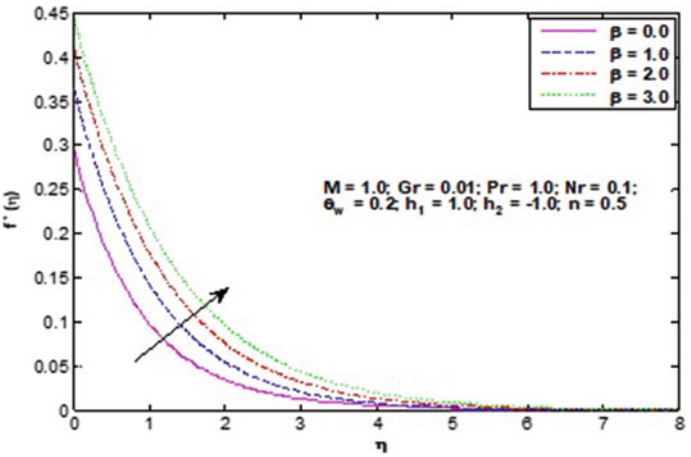

Fig. 1 Effect of β on f'

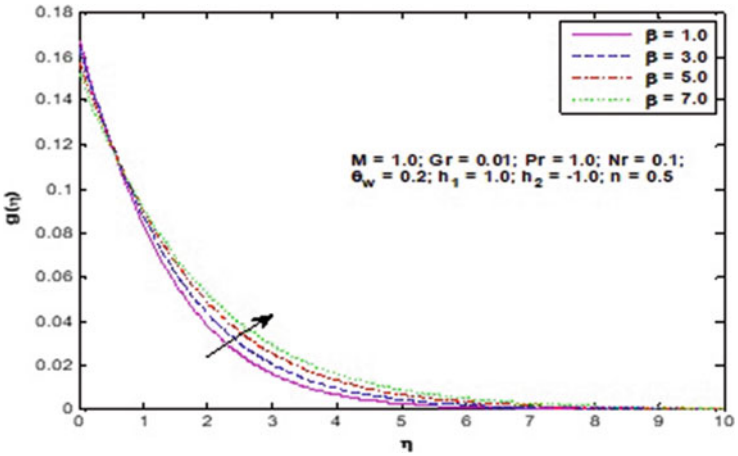

Fig. 2 Effect of β on g

Figure 7 indicates the variation of thermal radiation parameter on temperature. When $\theta_w > 1$, i.e., when heat flow takes place from boundary to the fluid, the temperature is increased as Nr increases. For the same set of values of Nr, a reversal trend is seen in temperature when $\theta_w < 1$ since heat flow is towards the boundary.

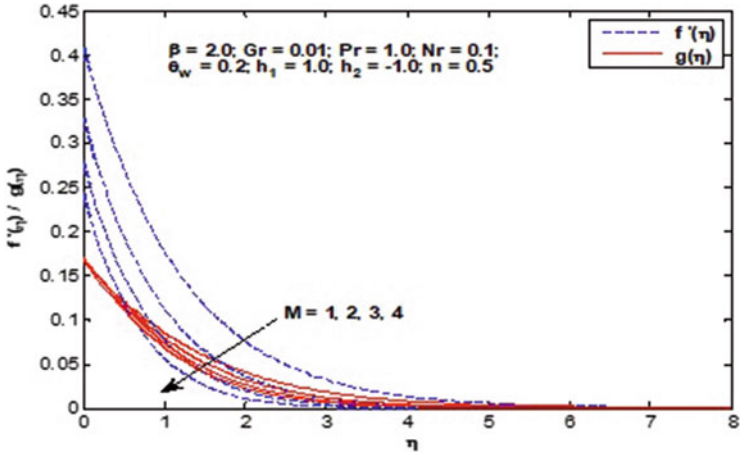

Fig. 3 Effect of M on f', g

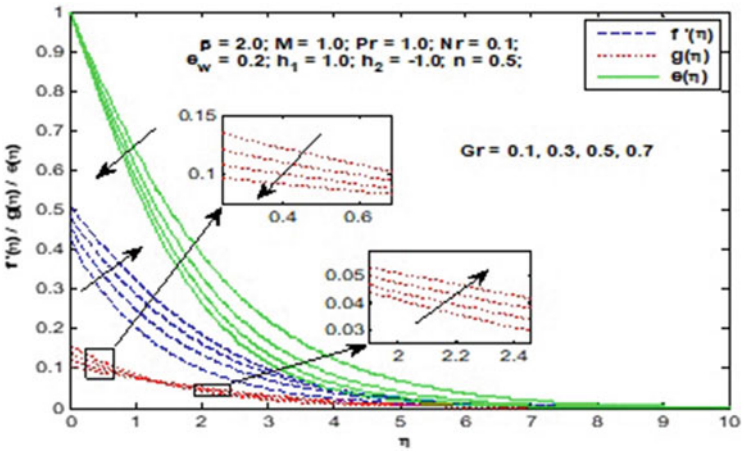

Fig. 4 Effect of Gr on f', g, θ

The effect of (n) on microrotation g is shown in Fig. 8. The microrotation g is found to increase rapidly near the boundary with increasing values of n due to larger velocity gradients and away from the boundary velocity shows an opposite trend.

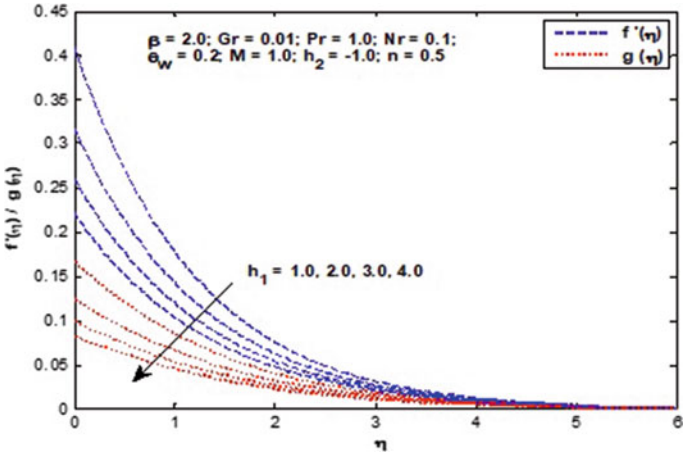

Fig. 5 Effect of h_1 on f', g

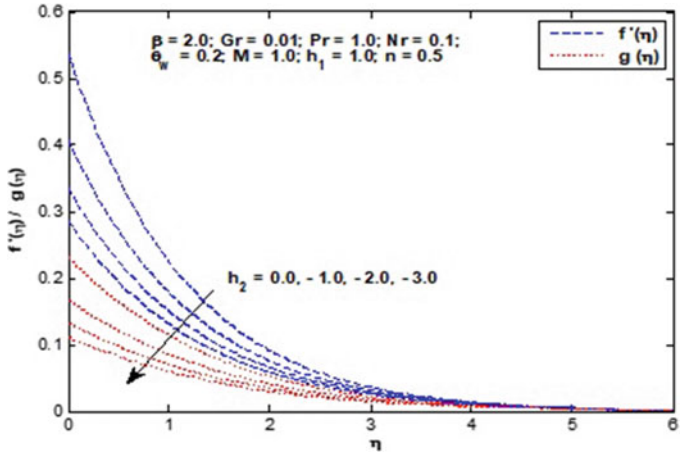

Fig. 6 Effect of h_2 on f', g

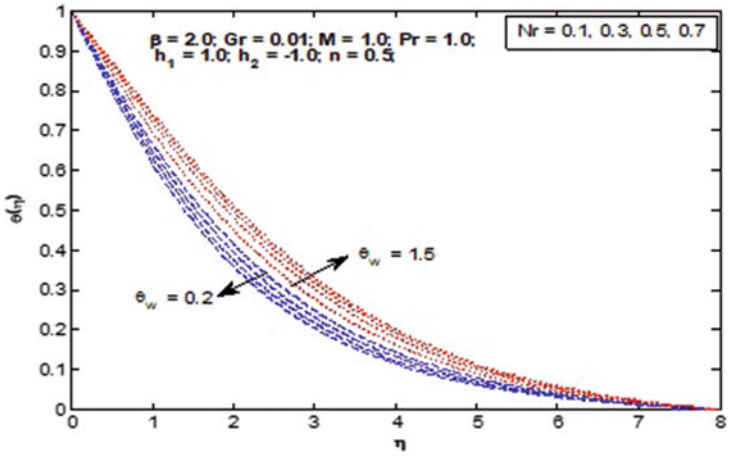

Fig. 7 Effect of Nr on θ

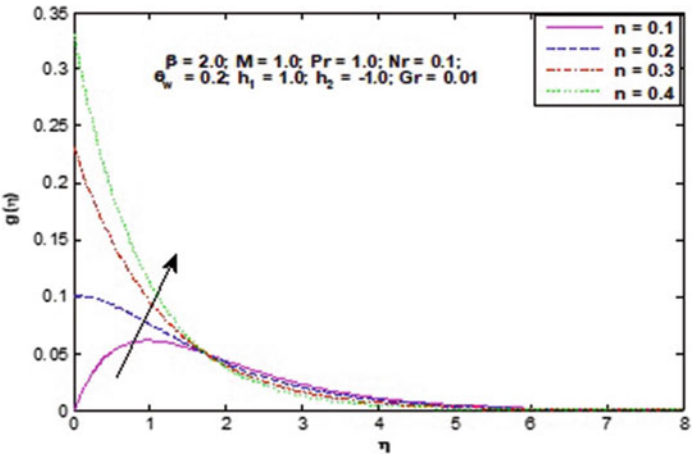

Fig. 8 Effect of n on g

5 Conclusion

Some of the highlights of the analysis are:

- Microrotation across the flow shows a decreasing trend near the boundary, while it increases in the region for an increment in (Gr).
- Microrotation is seen to have an increasing trend for with increase in n.
- Thinner momentum boundary layers are formed for higher values of the slip parameters.

References

1. Eringen, A.C.: Theory of micropolarfluids. J. Math. Mech. **16**, 1–8 (1966)
2. Yacob, N.A. and Ishak, A.: Micropolar fluid flow over a shrinking sheet. Meccanica **47**, 293–299 (2012)
3. Sarojamma, G. Sreelakshmi, K. and Vajravelu, K.: Effects of dual stratification on non-orthogonal non-Newtonian fluid flow and heat transfer. J. Heat and Tech. **36**, 207–214 (2018)
4. Mahanthesh, B. Gireesha, B.J. and Rama Subba Reddy, G.: Nonlinear radiative heat transfer in MHD three-dimensional flow of water based nanofluid over a non-linearly stretching sheet with convective boundary condition. J. Nigerian Mathematical Society **35**, 178–198 (2016)
5. Wang, C.Y.: Flow due to a stretching boundary with partial slip an exact solution of the Navier Stokes equation. Chem. Eng. Sci. **57**, 3745–3747 (2002)
6. Sahoo, B. and Do, Y.: Effects of slip on sheet-driven flow and heat transfer of a third grade fluid past a stretching sheet. Int. Comm. Heat and Mass Trans. **37**, 1064–1071 (2010)
7. Fang, T. and Aziz, A.: Viscous flow with second order slip velocity over a stretching sheet. Z Natuforsch **65**, 1087–1092 (2010)

8. Ibrahim, W.: MHD boundary layer flow and heat transfer of micropolar fluid past a stretching sheet with second order slip. J. Braz. Soc. Mech. Sci. Eng. **39**, 791–799 (2017)
9. Wu, L.: A slip model for rarefied gas flows at arbitrary Knudsen number. Appl. Phys. Lett. **93**, 253103-1-3 (2008)
10. Ishak, A.: Thermal boundary layer flow over a stretching sheet in micropolar fluid with radiation effect. Meccanica **45**, 367–373 (2010)

Analytical Study on Heat Transfer Behavior of an Orthotropic Pin Fin with Contact Resistance

M. A. Vadivelu, C. Ramesh Kumar, and M. M. Rashidi

Abstract In this paper, analytical solutions for dimensionless fin temperature distribution and dimensionless fin heat transfer rate are derived and offered for a two-dimensional orthotropic, pin fin structure with contact resistance at the fin base in a convective environment. Fin performance was evaluated based on the different forms of ratio of conductive resistance to convective resistance parameters Bi_r, Bi_z, Bi_c, thermal conductivity ratio K^*, and dimensionless length of fin contact space at the base δ^*. The detailed discussions on dimensionless parameters lead to the deterministic design and optimization of polymer composite fin structures under all types of convective situations in many real-time applications.

1 Introduction

The present-day heat sink domain requires high performance materials with high economic factors. Thermal sink management plays a vibrant part in the qualitative and quantitative performance parameters of all the heat transfer units. The production of thermal systems using conventional materials depends on mechanical and economic constraints such as higher weight, manufacturability, corrosion, and continuous maintenance [4, 6, 7].

The new system designs pertain to shape, surface area enlargements, fin structure variations, alignment of tubes and fins, and advancements using regenerators. These kinds of modification and adjustments can be performed on the thermal systems only by embracing polymer materials owing to its low density, low thermal expansion coefficient value, and ease in the manufacturing of the complicated shapes of the desired systems.

M. A. Vadivelu (✉) · C. Ramesh Kumar
Automotive Research Center, Vellore Institute of Technology, Vellore, India
e-mail: vadivelu.ma2014@vit.ac.in; crameshkumar@vit.ac.in

M. M. Rashidi
Department of Civil Engineering, University of Birmingham, Birmingham, UK
e-mail: m.m.rashidi@bham.ac.uk

B. Rushi Kumar et al. (eds.), *Applied Mathematics and Scientific Computing*,
Trends in Mathematics, https://doi.org/10.1007/978-3-030-01123-9_39

Although polymer materials are insulators, the perfect reinforcement of fillers can make these materials produce heat sinks with less effort. Recent developments in polymer composite materials provide a path to achieving high thermal conductivity with the help of carbon fillers, fibers, and graphite fillers. Contemporary research into the use of single-wall carbon nanotubes, multi-wall carbon nanotubes, and graphene in a polymer matrix may lead to supplementary enhancements in such composites [4, 6]. Conventional polymeric materials have low thermal conductivity value of 0.1–0.6 W/m-K, but the addition of carbon fiber and filler enhances the thermal conductivity of resulting polymer composites [1, 4, 7]. The addition of continuous carbon fiber improves the value of thermal conductivity to 300 W/m-K in the fiber axial direction [4]. However, these types of composites exhibit very low thermal conductivity values in another direction perpendicular to the fiber axis. For these kinds of problem, one-dimensional heat equation-based solutions are not valid [2, 3, 5].

In this research, temperature distribution and the heat transfer rate of the pin fin of a orthotropic nature were derived and presented. The effect of the orthotropic nature on pin fin performance was discussed with the help of parametric analysis. The two-dimensional orthotropic cylindrical coordinate-based energy equations for the pin fin with a contact resistance problem was solved and the solutions are presented. The effects of the thermal conductivity parameter, the contact resistance parameter, and the Biot number on the overall performance of the pin fin system are analyzed (Fig. 1).

2 Mathematical Formulations

By considering a convective environment at the fin's base, sides, and tip, the steady-state energy equation with no internal heat generation for a orthotropic fin in a cylindrical coordinate system can be written as:

$$\frac{1}{r}\frac{\partial}{\partial r}\left(rk_r\frac{\partial T}{\partial r}\right)+k_z\frac{\partial^2 T}{\partial z^2}=0. \tag{1}$$

The contact resistance at fin base was assumed, with uniform contact conductance. The convective film coefficients at the fin's base, sides, and tip are assumed to be

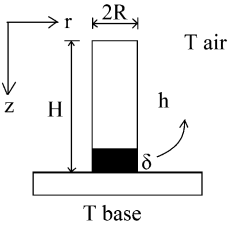

Fig. 1 Representation of present pin fin problem with contact resistance

uniform and different in nature. By taking δ as a thickness of the contact space at the fin base, the boundary conditions are introduced as:

$$r = 0, 0 \le r \le R, \frac{\partial T}{\partial r} = 0 \tag{2}$$

$$z = 0, 0 \le z \le H, k_z \frac{\partial T}{\partial z} = h(T - T_\infty) \tag{3}$$

$$r = R, 0 \le r \le R, -k_r \frac{\partial T}{\partial r} = h(T - T_\infty) \tag{4}$$

$$z = H - \delta, 0 \le z \le H, k_z \frac{\partial T}{\partial z} = h_c(T_b - T) \tag{5}$$

$$z = H, 0 \le z \le H, T = T_b. \tag{6}$$

By presenting the following nondimensional parameters

$$\theta = \frac{(T - T_\infty)}{(T_b - T_\infty)}, \gamma = \frac{r}{R}, \varphi = \frac{z}{H} \tag{7}$$

$$K^* = \frac{k_r}{k_z}, \omega = \frac{R}{H}, \delta^* = 1 - \frac{\delta}{H}, \tag{8}$$

and different Biot numbers as representatives of different convective environments

$$Bi_r = \frac{hR}{k_r}, Bi_z = \frac{hH}{k_z} Bi_c = \frac{(h_c \delta)}{k_z} Bi_{gm} = \frac{hR}{(k_r k_z)^{\frac{1}{2}}}. \tag{9}$$

The two-dimensional energy equation for the present problem can be formulated as

$$K^* \frac{\partial^2 \theta}{\partial \gamma^2} + \frac{K^*}{\gamma} \frac{\partial \theta}{\partial \gamma} + \omega^2 \frac{\partial^2 \theta}{\partial \varphi^2} = 0 \tag{10}$$

and subjected to the boundary conditions

$$\gamma = 0, 0 \le \gamma \le 1, \frac{\partial \theta}{\partial \gamma} = 0 \tag{11}$$

$$\varphi = 0, 0 \le \varphi \le 1, \frac{\partial \theta}{\partial \varphi} = Bi_z \theta \tag{12}$$

$$\gamma = 1, 0 \le \gamma \le 1, \frac{\partial \theta}{\partial \gamma} = -Bi_r \theta \tag{13}$$

$$\varphi = \delta^*, 0 \le \varphi \le 1, \frac{\partial \theta}{\partial \varphi} = Bi_c(1-\theta) \tag{14}$$

$$\varphi = 1, 0 \le \varphi \le 1, \theta = 1. \tag{15}$$

3 Solution Procedure

The solution of the two-dimensional, orthotropic pin fin system with contact resistance at the fin base can be solved with the help of the separation of variables method. The dimensionless temperature distribution θ of the present fin system can be expressed in terms of two variables, which are the function of two major coordinates. Let

$$\theta = \frac{P(\gamma)}{S(\varphi)}. \tag{16}$$

The solution for the proposed fin system based on the above formulations can be expressed in terms of a Bessel function as:

$$\theta = \left[CJ_0\left(\frac{\beta\gamma}{(K^*)^{\frac{1}{2}}}\right) + DY_0\left(\frac{\beta\gamma}{(K^*)^{\frac{1}{2}}}\right)\right]\left[Asinh\left(\frac{\beta\varphi}{\omega}\right) + Bcosh\left(\frac{\beta\varphi}{\omega}\right)\right]. \tag{17}$$

By substituting the required boundary conditions in Eq. (17), we obtain:

$$\theta = \frac{T - T_\infty}{T_b - T_\infty}$$
$$= 2\sum_{n=1}^{\infty} \frac{\alpha_n Bi_c J_1(\alpha_n) J_0(\alpha_n \gamma)\left[\frac{Bi_z}{\gamma} sinh(\tau\varphi) + cosh(\tau\varphi)\right]}{J_0^2(\alpha_n)[Bi_r^2 + \alpha_n^2][(Bi_z + Bi_c)cosh(\tau\delta^*) + (\tau + \frac{Bi_c Bi_z}{\tau})sinh(\tau\delta^*)]} \tag{18}$$

where

$$\alpha_n = \frac{\beta_n}{(K^*)^{\frac{1}{2}}}, \tau = \frac{\beta_n}{\omega}. \tag{19}$$

The dimensionless form of heat conduction by the pin fin from the fin base is expressed as:

$$Q = \sum_{n=1}^{\infty} \frac{[Bi_r^2 Bi_c]\left[\frac{Bi_z}{\gamma} sinh(\tau\varphi) + cosh(\tau\varphi)\right]}{\alpha_n[Bi_r^2 + \alpha_n^2][\tau(Bi_z + Bi_c)cosh(\tau\delta^*) + (\tau + \frac{Bi_c Bi_z}{\tau})sinh(\tau\delta^*)]}. \tag{20}$$

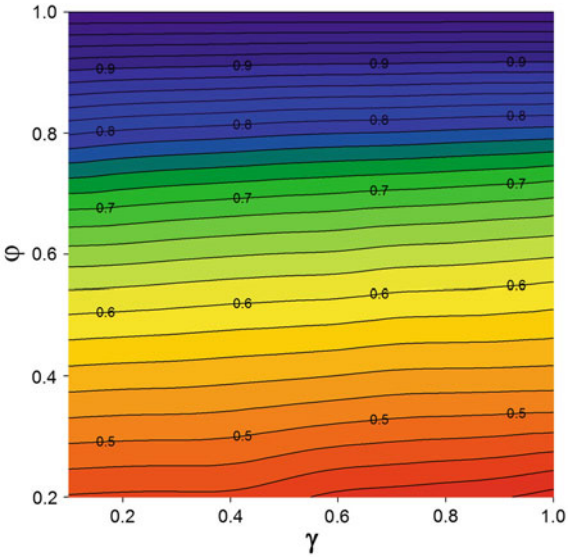

Fig. 2 Dimensionless temperature distribution plots for an orthotropic pin fin with an aspect ratio (H/R) of 10 and zero contact resistance for radial and axial Biot numbers 0.1 and 0.1

The eigenvalues are calculated by the following equation based on a Bessel function and the convective boundary condition as:

$$J_1(\alpha_n) = \frac{Bi_r}{\alpha_n} J_0(\alpha_n). \tag{21}$$

4 Results and Discussion

The closed-form semi-analytical solution for the present orthotropic pin fin problem was formulated. Solutions were performed on MATLAB using the algebraic mathematical expressions developed in the previous section. Eigenvalues were calculated based on Eq. (21) to execute the calculation of fin performance parameters. For the complete research, the fin aspect ratio (H/R) was maintained at 10.

The temperature distribution in the two-dimensional orthotropic pin fin was shown in Figs. 2 and 3. The temperature distributions of the two-dimensional orthotropic pin fin in the absence of contact resistance are also depicted in Figs. 2 and 3 for various radial and axial Biot numbers. The effect of contact resistance was neglected to intensify the effect of radial thermal conductivity and the Biot number on the pin fin performance. The first image in Fig. 2 displays the isotropic fin system-based temperature contours due to Biz = Bir.

Although Fig. 2 related to the isotropic system, it shows an observable temperature gradient in the radial direction compared with others. This comparison shows the dominant behavior of radial direction heat transfer at higher values of Biz, which obviously reduces the overall heat transfer rate of the fin system for a fixed thermal conductivity ratio.

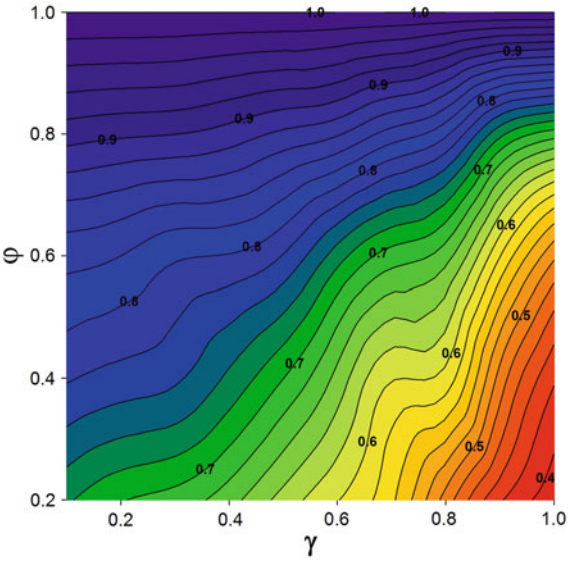

Fig. 3 Dimensionless temperature distribution plots for an orthotropic pin fin with an aspect ratio (H/R) of 10 and zero contact resistance for radial and axial Biot numbers 2.0 and 0.1

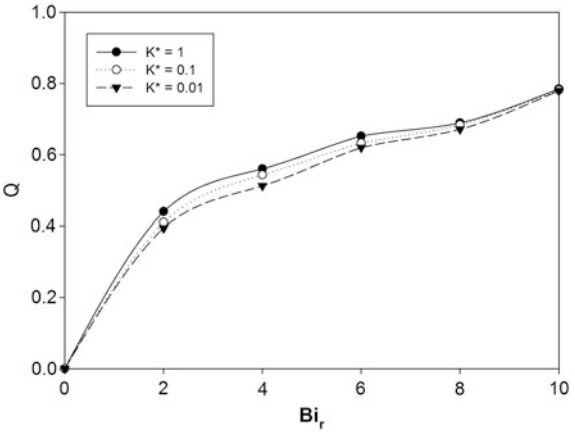

Fig. 4 Dimensionless heat transfer rate (Q) plots for an orthotropic pin fin with an aspect ratio (H/R) of 10 and zero contact resistance for various radial Biot numbers and thermal conductivity ratios, K*

Figure 3 encompasses the effect of a larger radial Biot number, which corresponds to high thermal resistance in that direction and consequently a high temperature gradient in that particular direction. Further improvement in the axial directional Biot number to ten times that of the above case does not improve the temperature distribution of the fin system.

The dimensionless heat transfer rate of the pin fin system with orthotropic nature is plotted in Figs. 4 and 5 for different values of radial and axial Biot numbers in the absence of contact resistance. The plots were constructed for the fin aspect ratio (H/R) of 10. Figure 4 represents the effect of the radial Biot number, Bir, on the heat transfer rate for various thermal conductivity ratios, K*. The dimensionless heat transfer rate of the pin fin system significantly increases with the continuous

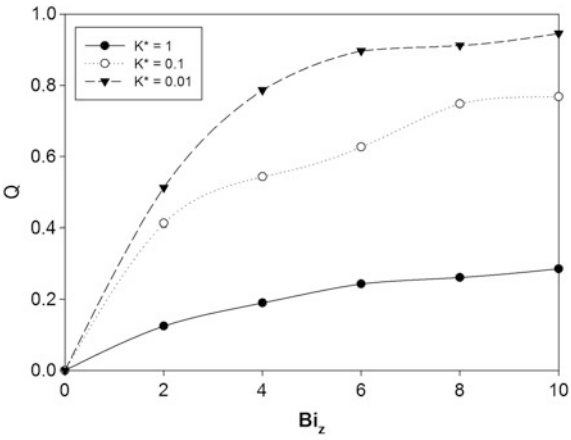

Fig. 5 Dimensionless heat transfer rate (Q) plots for an orthotropic pin fin with an aspect ratio (H/R) of 10 and zero contact resistance for various axial Biot numbers and thermal conductivity ratios, K*

hike in radial Biot number as shown in Fig. 4. However, the heat transfer rate is considerably independent of the thermal conductivity ratio for larger Biot numbers. The dimensionless heat transfer rate of the pin fin system increases when the thermal conductivity ratio increases for a particular interval of the radial Biot number. The effect of the thermal conductivity ratio on the heat transfer rate for a respective radial Biot number shrinks when the value of K* approaches 1, an isotropic natural limit, as shown in Fig. 4.

Plot 4 also demonstrates that the effect of the thermal conductivity ratio on the heat transfer rate for a particular radial heat convective environment is insignificant in nature. The polymer composites with low radial thermal conductivity properties can be adopted for the application of heat transfer with a high axial convective environment. Similarly, Fig. 5 represents the effect of the axial Biot number on the heat transfer rate for different values of the thermal conductivity ratio. The dimensionless heat transfer rate Q decreases with increases in K* values over all ranges of axial Biot number, as shown in Fig. 5. Figure 6 represents the effect of the contact Biot number or contact resistance on the dimensionless heat transfer rate for different values of the radial Biot number and the thermal conductivity ratio. As discussed in Fig. 4, here also, the thermal conductivity ratio does not have a significant effect on the heat transfer rate.

In contrast, the contact Biot number has a significant effect on the dimensionless heat transfer rate. As predicted, the low contact Biot number 0.01 shows a higher heat transfer rate compared with other cases owing to lower contact resistance δ/L or high conduction through the contact area.

5 Conclusion

The heat transfer performance characteristics of the fin system formulated by polymeric materials can be investigated using the methods presented in this research article. The effect of the thermal conductivity ratio, the radial Biot number, and the

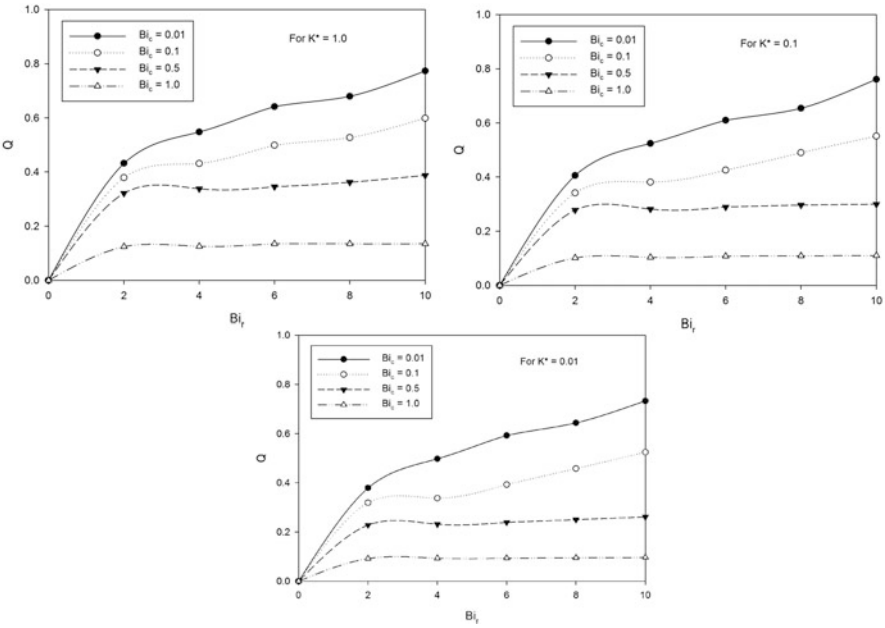

Fig. 6 Dimensionless heat transfer rate (Q) plots for an orthotropic pin fin with an aspect ratio (H/R) of 10 for various radial Biot numbers, contact Biot numbers, and thermal conductivity ratios, K*

contact Biot number on the dimensionless heat transfer rate was investigated and presented. The adverse effect of contact resistance on the heat transfer performance of the fin system was extensively covered. It is expected that the investigation performed, solutions provided, and results declared in this research can be adopted to design the extended surfaces based on polymer composites.

Nomenclature

Symbol

Bi Biot number
H Fin height in meters
h Convective heat transfer coefficient in W/m^2K
K Thermal conductivity ratio
k Thermal conductivity in W/mK
Q Dimensionless heat transfer rate
R Fin outer radius in meters
r Radial co-ordinate

T Temperature in °C
z Axial co-ordinate

Greek Symbol

δ Contact thickness
γ Dimensionless radial co-ordinate
φ Dimensionless axial co-ordinate
ω Reciprocal of aspect ratio
θ Dimensionless temperature

Subscripts

b base
c contact
gm geometric mean
∞ Ambient

Superscripts

* Dimensionless

References

1. Bahadur, R., Bar-Cohen, A.: Thermal design and optimization of natural convection polymer pin fin heat sinks. IEEE Trans. Compon. Packag. Technol., **28(2)**, 238–246(2005).
2. Bahadur, R., Bar-Cohen, A.: Orthotropic thermal conductivity effect on cylindrical pin fin heat transfer. Intl. J. Heat Mass Transfer **50**, 1155–1162(2007).
3. Kundu, B., Lee, K. S.: Thermal design of an orthotropic flat fin in fin-and-tube heat exchangers operating in dry and wet environments. Intl. J. Heat Mass Transfer **54**, 5207–5215 (2011).
4. Vadivelu M. A., Ramesh Kumar C., Joshi, G. M.: Polymer composites for thermal management: a review. Composite Interfaces, **23(9)**, 847–872 (2016).
5. Zubir, S. M, Arif, A.F.M.: Thermal analysis and optimization of orthotropic pin fins: A closed-form analytical solution. J. Heat Transfer, **132 (1–8)**, March 2010.
6. Zweben, C.: Advanced composites and other advanced materials for electronic packaging thermal management. Materials – International Symposium on Advanced Packaging Materials. Braselton, GA, 11–14 March 2001.
7. Zweben, C.: Emerging high-volume commercial applications for thermally conductive carbon fibers. Proceedings of the 6th International Business Conference on the Global Outlook for Carbon Fiber. San Diego, CA, 5–7 November 2003.

Numerical Investigation of Developing Laminar Convection in Vertical Double-Passage Annuli

Girish N, M. Sankar, and Younghae Do

Abstract This work numerically explored the developing laminar natural convection in the vertical double-passage cylindrical annuli. The double-passage annuli are designed from three upright coaxial cylindrical tubes with the intermediate cylinder treated as a thin and conductive baffle. In the present study, two thermal conditions are imposed, namely, interior or exterior cylindrical wall is constantly heated, whereas the opposite wall is thoroughly insulated. Using the boundary layer approximation, the nonlinear and coupled governing partial differential equations are numerically solved by employing an implicit finite difference technique. The flow and thermal distributions, heat transfer rates are portrayed for various axial locations, Grashof number and baffle position. The results reveal that the velocity and temperature profiles significantly altered with Grashof number and axial locations. Further, the baffle location plays a major role in controlling the heat transfer in the annular passages.

1 Introduction

The development of free, forced, and mixed convection is explored numerically by many researchers under various thermal boundary conditions, with or without viscous dissipation in different geometries, namely, in vertical channels designed by parallel plates, vertical pipes, vertical annulus formed by concentric cylinders,

Girish N
Department of Mathematics, JSS Academy of Technical Education, Bangalore, India
e-mail: girishn@jssateb.ac.in

M. Sankar (✉)
Department of Mathematics, School of Engineering, Presidency University, Bangalore, India
e-mail: msankar@presidencyuniversity.in

Y. Do
Department of Mathematics, KNU-Center for Nonlinear Dynamics, Kyungpook National University, Daegu, Republic of Korea
e-mail: yhdo@knu.ac.in

B. Rushi Kumar et al. (eds.), *Applied Mathematics and Scientific Computing*,
Trends in Mathematics, https://doi.org/10.1007/978-3-030-01123-9_40

and double-passage channels formed by inserting baffle in vertical channel. Aung et al. [1] made a combined numerical and experimental study on developing laminar convection by considering constant wall temperature and constant wall heat fluxes in a vertical passage and also revealed that numerical solutions approached to exact solutions for fully developed flow. Aung and Worku [2] investigated developing flow and flow reversal using finite difference method in a vertical channel by considering asymmetric thermal temperatures and found that buoyancy effect considerably increases the hydrodynamic entry length whereas decreases thermal development distance. Utilizing finite difference scheme, Davis and Perona [3] investigated developing natural convection in a vertical tube maintained either CWT or CHF thermal conditions and found that both heating conditions have significant effects on heat transfer rate. The development of laminar mixed convection has been numerically examined by El-Shaarawi and Sarhan [4] in vertical concentric annuli for isothermal and adiabatic thermal conditions. El-Din [5] investigated developing laminar convective flow numerically in a vertical double-passage channel to reveal the consequence of thin perfectly conductive baffle. After a thorough literature survey, it has been found that the influence of baffle insert on developing natural convection in vertical annulus has not been attempted in the literature. The aim of present work is to study the impact of baffle position on developing buoyancy-driven convection in the vertical double-passage annuli.

2 Mathematical Formulation

The physical configuration and coordinate system for the present study, as shown in Fig. 1, are the vertical double-passage annuli, designed from three upright coaxial cylinders with the intermediate cylinder (or baffle) assumed to be thin and highly conductive. The annulus is of finite length, open at both ends with the radii of inner, middle, and outer cylinders, and are r_i, r_m, and r_o, respectively. In the present analysis, two boundary conditions are considered for temperature, viz., case (I) refers to the thermal condition where the interior cylinder is kept at isothermal and outer cylinder is maintained at adiabatic, and case (O) refers to isothermal outer cylinder and insulated inner cylinder. The temperature difference between the annular walls generates an ascending buoyancy-driven convective flow in the passages between three cylindrical boundaries. The fluid, with a flat velocity profile, is assumed to pass through the annulus whose value is same as that of the average vertical velocity inside the annuli gaps and with a constant temperature having the magnitude of ambient temperature. The physical properties of the fluid taken to be constant, however, obey the Boussinesq approximation. Also the axisymmetric flow is assumed to be steady; internal heat generation and viscous dissipation effects are neglected. Further, the Prandtl boundary layer assumptions are imposed, and, in the energy equation, the axial diffusion term is ignored compared to the radial diffusion term. Under the above assumptions, the dimensionless equations governing the

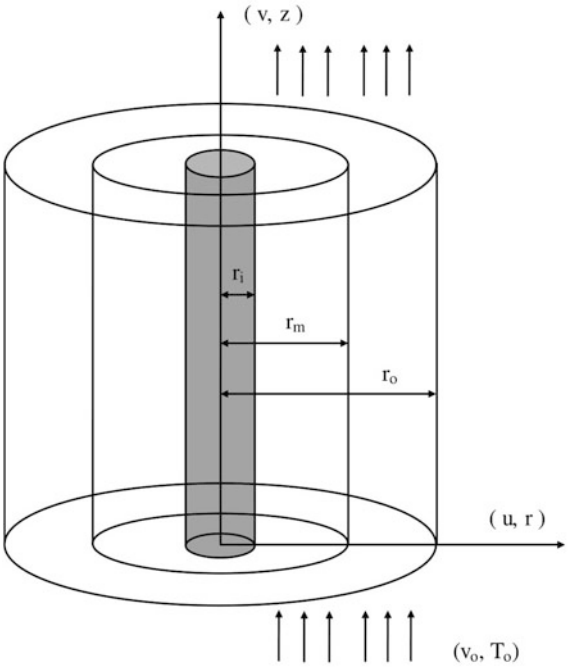

Fig. 1 Physical configuration and coordinate system

conservation of mass, momentum, and energy are as follows (El-Shaarawi and Sarhan [6]):

$$\frac{\partial U}{\partial R} + \frac{U}{R} + \frac{\partial V}{\partial Z} = 0 \tag{1}$$

$$U\frac{\partial V}{\partial R} + V\frac{\partial V}{\partial Z} = -\frac{\partial P}{\partial Z} + \frac{\partial^2 V}{\partial R^2} + \frac{1}{R}\frac{\partial V}{\partial R} + \frac{\theta}{16(1-\lambda)^4} \tag{2}$$

$$U\frac{\partial \theta}{\partial R} + V\frac{\partial \theta}{\partial Z} = \frac{1}{\mathrm{Pr}}\left[\frac{\partial^2 \theta}{\partial R^2} + \frac{1}{R}\frac{\partial \theta}{\partial R}\right] \tag{3}$$

The continuity equation is recast into the below mentioned integral form for both passages.

$$Q = (N^2 - \lambda^2)V_0 = 2\int_{\lambda}^{N} RV\,dR \;\;\&\;\; Q = (1 - N^2)V_0 = 2\int_{N}^{1} RV\,dR \tag{4}$$

The above dimensionless equations are made using the following relations:

$$U = \frac{ur_0}{\nu},\; V = \frac{vr_0^2}{l\nu Gr},\; \theta = \frac{T - T_0}{T_w - T_0},\; R = \frac{r}{r_0},\; Z = \frac{z}{lGr},\; \lambda = \frac{r_i}{r_o},\; Pr = \frac{\nu}{\alpha},$$

$$Q = \frac{q}{\pi l \nu Gr},\ V_0 = \frac{v_0 r_0^2}{l \nu Gr},\ P = \frac{p * r_0^4}{\rho_0 l^2 \nu^2 Gr^2},\ Gr = \frac{g\beta D^4 (T_w - T_0)}{l\nu^2}, N = \frac{r_m}{r_o}.$$

Here Pr and Gr are the Prandtl and Grashof numbers and λ is the radius ratio. The corresponding dimensionless boundary conditions are

$$U_1 = U_2 = 0,\ V_1 = V_2 = 0,\ \theta_1 = \theta_2 = 0,\ P = \frac{-V_0^2}{2} \text{ at } Z = 0, \text{ and } \lambda < R < 1.$$

$$U_1 = U_2 = 0,\ V_1 = V_2 = 0, \begin{cases} \theta_1 = 1 & \text{for case (I)} \\ \frac{\partial \theta_1}{\partial R} = 0 & \text{for case (O)} \end{cases} \text{ at } R = \lambda \text{ and } Z \geq 0,$$

$$U_1 = U_2 = 0,\ V_1 = V_2 = 0,\ \theta_1 = \theta_2 \text{ for case(I) and case (O) at } R = N \text{ and } Z \geq 0$$

$$U_1 = U_2 = 0,\ V_1 = V_2 = 0, \begin{cases} \frac{\partial \theta_2}{\partial R} = 0 & \text{for case (I)} \\ \theta_2 = 1 & \text{for case (O)} \end{cases} \text{ at } R = 1 \text{ and } Z \geq 0,$$

$$P_1 = 0, P_2 = 0 \quad \text{at} \quad Z = \frac{1}{Gr} = L$$

From the temperature distribution, the local Nusselt number, a major parameter of practical interest in the analysis of convective heat transfer at any cross section, may be calculated. Thus, the global Nusselt number across the cylindrical boundary is given by

$$\overline{Nu} = \frac{\int_0^L Nu dZ}{\int_0^L dZ} = \frac{1}{L}\int_0^L Nu dZ, \text{ where } Nu = -\frac{\partial \theta}{\partial R} \text{ is the local Nusselt number.}$$

3 Numerical Solution

Since the model equations governing the physical problem are nonlinear and coupled, a general analytical solution is not possible. Hence, a group of coupled differential equations subjected to the chosen boundary conditions are numerically solved by an implicit finite difference technique used previously by many authors for both parallel plates and annular geometries with great success. Since we consider a boundary layer type flow in our investigation, the solution of governing equations is marched in the downstream direction. Initially, we take two guess values of Q such that the product of pressure at the annulus exit is negative. Then the method of bisection is used to obtain the exact value of Q for which the pressure becomes zero at the exit of the annulus. Further, it is found that for the same value of Q, the overall mass balance at the upper and lower portions of the annulus are same.

4 Results and Discussion

In this section, we presented the numerical simulations to illustrate the effect of baffle position and Grashof number on the flow and thermal distributions and on heat transfer rates. Figure 2 illustrates the influence of Grashof number on radial velocity profiles for both the thermal cases (I) and (O). The development of radial velocity at different heights of the channel length is plotted in Fig. 2 for two different values of Gr, namely, 5×10^2 and 5×10^3, by fixing the radius ratio at $\lambda = 0.5$, and the baffle is positioned in the middle of the annulus. The magnitude of radial velocity increases with an increase in the value of Gr in passage-1 for case (I) but decreases with channel height, and maximum velocity is observed in passage-1 for $Z = 0.16$, near the annulus entrance. At higher values of Grashof number, $Gr = 5 \times 10^3$, the phenomenon of flow reversal is witnessed in passage-2 for both case (I) and case (O).

The development of axial velocity is presented in Fig. 3 by fixing $\lambda = 0.5$ and $N = 0.75$ at different locations of the channel to analyze the effect of Grashof number. It can be noticed that the axial velocity strength decreases with an increase in the Grashof number but it remains invariant with channel length for lower value of $Gr = 5 \times 10^2$ for both the thermal cases, but for $Gr = 5 \times 10^3$ slight variation in velocity profile is visible in passage-1 for case (I), whereas it appears in passage-2 for case (O). Also, the maximum velocity appears in the first passage for both the

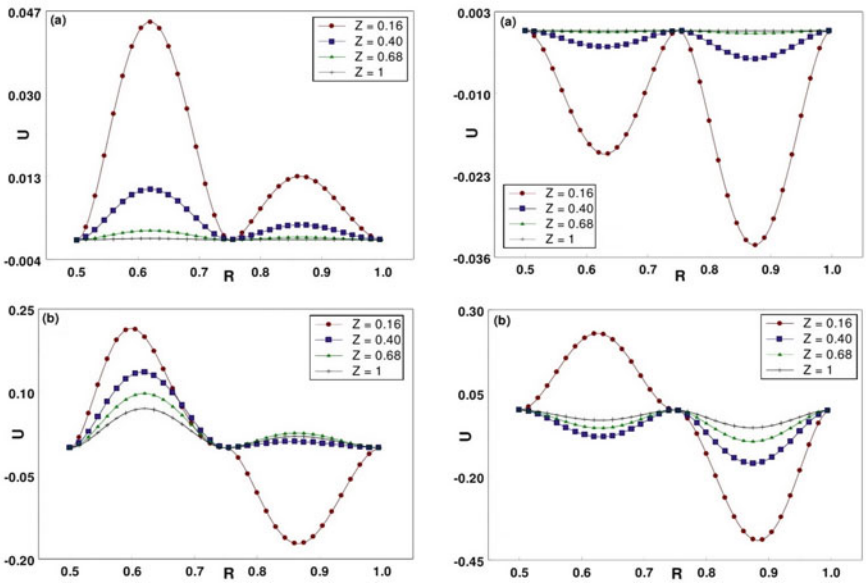

Fig. 2 Development of radial velocity profiles at $\lambda = 0.5$ and $N = 0.75$ for different Gr. (**a**) $Gr = 5 \times 10^2$ and (**b**) $Gr = 5 \times 10^3$ for case (I) (left) and case (O) (right)

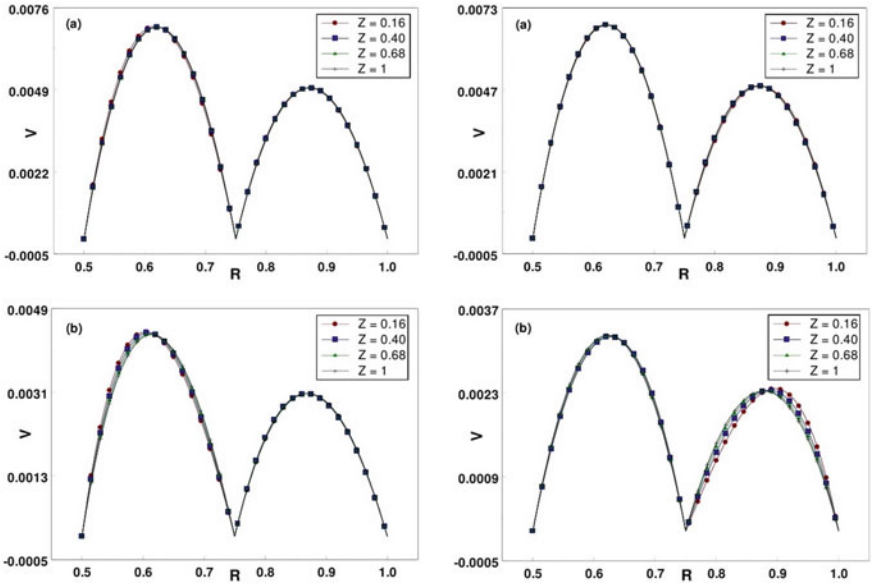

Fig. 3 Development of axial velocity profiles at $\lambda = 0.5$ and $N = 0.75$ for different Gr. (**a**) $Gr = 5 \times 10^2$ and (**b**) $Gr = 5 \times 10^3$ for case (I) (left) and case (O) (right)

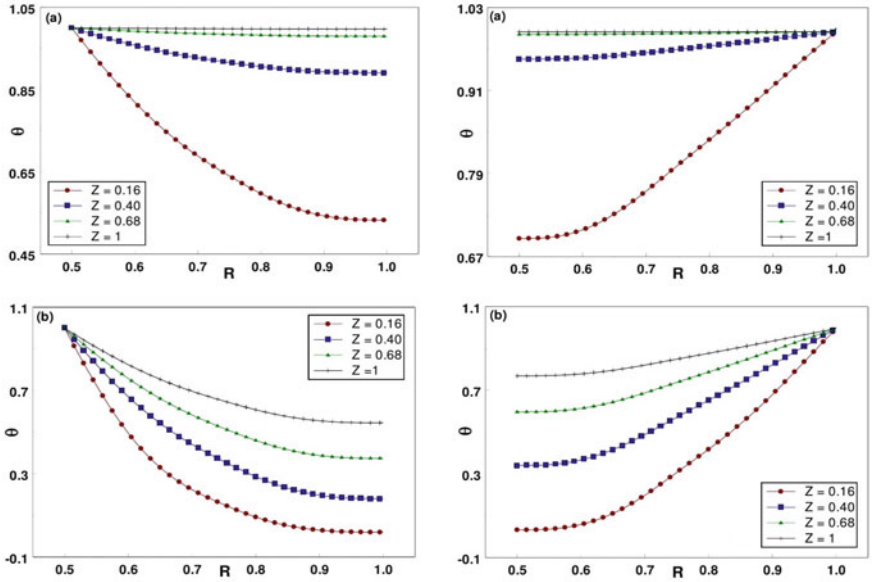

Fig. 4 Development of temperature profiles at $\lambda = 0.5$ and $N = 0.75$ for different Gr. (**a**) $Gr = 5 \times 10^2$ and (**b**) $Gr = 5 \times 10^3$ for case (I) (left) and case (O) (right)

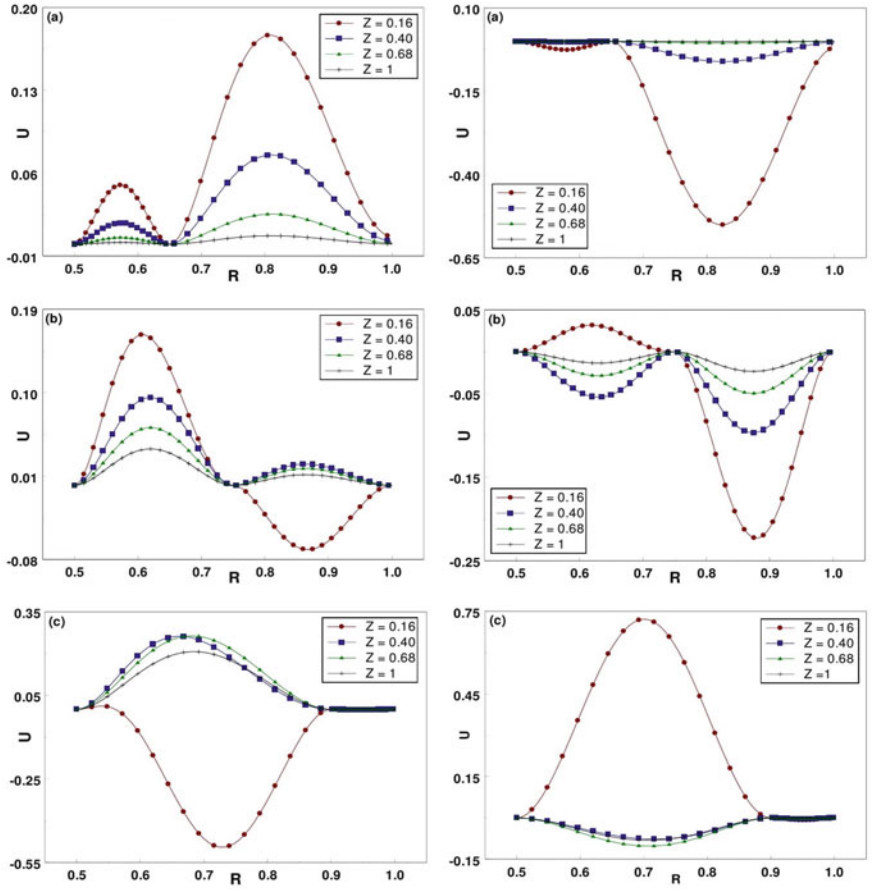

Fig. 5 Development of radial velocity profiles at $\lambda = 0.5$ and $Gr = 3 \times 10^2$ for different N. (**a**) $N = 0.65$, (**b**) $N = 0.75$ and (**c**) $N = 0.90$, for case (I) (left) and case (O) (right)

thermal cases. Figure 4 depicts variation in thermal distributions for different values of Gr. The magnitude of temperature declines with an intensification of Grashof number toward the outer wall but increases with channel height in case (I), whereas in case (O) temperature profiles increase toward outer wall due to opposite thermal conditions.

The influence of baffle position on radial velocity distributions is portrayed in Fig. 5 for four distinct values of Z by fixing $\lambda = 0.5$ and $Gr = 3 \times 10^3$. For a wider passage, a significant variation in velocity profile is observed, whereas a minor variation in velocity profile is observed in narrow passage. However, velocity variation is insignificant in the narrow passage formed by positioning the baffle near to outer wall. Also, the velocity profiles for case (O) are mirror images of case (I) due to opposite thermal conditions. The effect of baffle position and Grashof

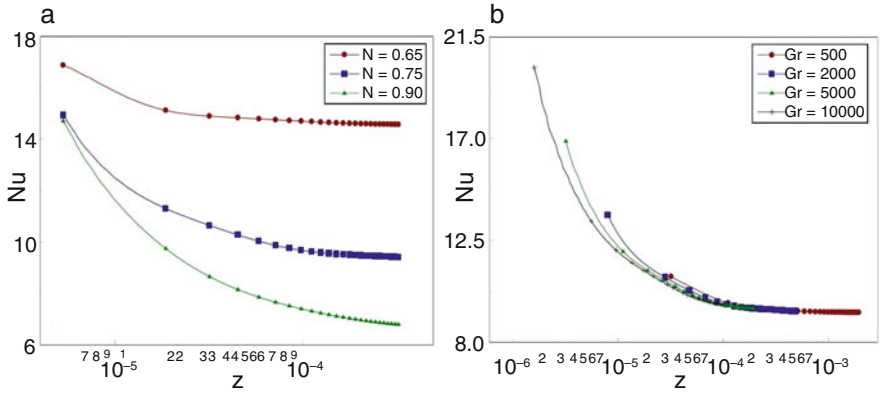

Fig. 6 Development of local Nusselt number distributions at (**a**) $\lambda = 0.5$ and $Gr = 3 \times 10^2$ for different N (left) and (**b**) $\lambda = 0.5$ and $N = 0.75$ for different values of Gr (right) for case (I)

number on heat transfer rate is shown in Fig. 6 for case (I). The local Nusselt number enhancement could be achieved either by increasing the values of Gr or moving baffle closer to isothermal wall.

5 Conclusions

The developing natural convection in the vertical double-passage annuli is numerically investigated in this analysis. Based on the influences of Grashof number and baffle position on the development of velocity and temperature profiles, and also on heat transfer rate, the following conclusions are drawn:

The radial velocity increases with increase in the values of Gr but decreases with channel height in passage-1 for case (I). Flow reversal phenomenon in radial velocity profiles are observed in passage-2 for case (O) for both the values of Gr and at all locations of the channel. Axial velocity decreases with an increase in the values of Gr, but velocity profile remains invariant with channel length. Temperature decreases with an increase in Gr toward the adiabatic wall. In wider passages, the variation in radial velocity is significant.

Acknowledgements The authors MS and GN are, respectively, grateful to the management of Presidency University, Bengaluru and J S S Academy of Technical Education, Bengaluru, and to VTU, Belgaum, India, for their support and encouragement. M. Sankar gratefully acknowledges the financial support provided by the Vision Group of Science and Technology, Government of Karnataka under Grant Number KSTePS/VGST-KFIST (L1)/2017. Also, Y. Do was supported by the National Research Foundation of Korea (NRF) grant funded by the Korea Government (MSIP) (No. NRF-2016R1A2B4011009).

References

1. Aung, W., Fletcher, L. S., Sernas, V.: Developing laminar free convection between vertical flat plates with asymmetric heating. Int. J. Heat Mass Transfer **15 (11)**, 2293–2308 (1972)
2. Aung, W., Worku, G.: Developing flow and flow reversal in a vertical channel with asymmetric wall temperatures. J. Heat Transfer **108 (2)**, 299–304 (1986)
3. Davis, L. P., Perona, J. J.: Development of free convection flow of a gas in a heated vertical open tube. Int. J. Heat Mass Transfer **14 (7)**, 889–903 (1971)
4. El-Shaarawi, M. A. I., Sarhan, A.: Free convection effects on the developing laminar flow in vertical concentric annuli. J. Heat Transfer **102 (4)**, 617–622 (1980)
5. El-Din, M. M. S.: Developing laminar convection in a vertical double-passage channel. Heat Mass Transfer. **38 (1-2)**, 93–96 (2001)
6. El-Shaarawi, M. A. I., Sarhan, A.: Developing laminar free convection in a heated vertical open-ended concentric annulus. Ind. Eng. Chem. Fundam. **20 (4)**, 388–394 (1981)

Heat and Mass Transfer on MHD Rotating Flow of Second Grade Fluid Past an Infinite Vertical Plate Embedded in Uniform Porous Medium with Hall Effects

M. Veera Krishna, M. Gangadhar Reddy, and A. J. Chamkha

Abstract We discussed Hall effects on unsteady hydromagnetic natural convective rotating flow of second grade fluid past an impulsively moving vertical plate entrenched in a fluid inundated porous medium, while temperature of the plate has a temporarily ramped profile. Analytical solutions of the governing equations are obtained by Laplace transform technique. The precise solution is also obtained in case of unit Schmidt number. The analytical phrases for skin friction due to primary and secondary flows and Nusselt number are derived for both ramped temperature and isothermal plates. Expression for Sherwood number is also obtained. The velocity, temperature, and concentration are displayed graphically, whereas those of skin friction, Nusselt number, and Sherwood number are presented in tabular form with reference to momentous flow parameters.

Nomenclature

u, w	Fluid velocity in x and z direction	K_1	Permeability of the porous medium
g	Acceleration due to gravity	q_r	Radiative flux vector
k^*	Rossland mean absorption coefficient	k	Thermal conductivity of the fluid

M. Veera Krishna (✉) · M. Gangadhar Reddy
Department of Mathematics, Rayalaseema University, Kurnool, Andhra Pradesh, India

A. J. Chamkha
RAK Research and Innovation Center, American University of Ras Al Khaimah, Ras Al Khaimah, United Arab Emirates

Prince Sultan Endowment for Energy and Environment, Prince Mohammad Bin Fahd University, Al-Khobar, Kingdom of Saudi Arabia
e-mail: achamkha@pmu.edu.sa

B. Rushi Kumar et al. (eds.), *Applied Mathematics and Scientific Computing*, Trends in Mathematics, https://doi.org/10.1007/978-3-030-01123-9_41

C_p	Specific heat at constant pressure	D	Chemical molecular diffusivity
q	The velocity vector,	H	The magnetic field intensity vector,
E	The electric field,	J	The current density vector,
U_0	Uniform velocity of the plate	M^2	Hartmann number,
m	Hall parameter	R	Rotation parameter,
K	Permeability parameter,	Gr	Thermal Grashof number,
Gc	Mass Grashof number,	Pr	Prandtl number
N	Thermal radiation parameter and	Sc	The Schmidt number
$H(t-1)$	Unit step function	B_0	Strength of magnetic field
K	Permeability parameter	$erfc(x)$	Complementary error function

Greek Symbols

τ_e	The electron collision time	ω_e	The cyclotron frequency
β	Volumetric coefficient of thermal expansion	Ω	Uniform angular velocity
β^*	Volumetric coefficient of expansion for species concentration	σ^*	Stefan-Boltzmann constant.
μ_e	The magnetic permeability	ν	Coefficient of kinematic viscosity
ρ	Fluid density	σ	Electrical conductivity
θ	Fluid temperature	ϕ	Species concentration
θ_∞	Free stream temperature	λ	Visco elastic parameter

1 Introduction

Natural convective stream persuaded by thermal and solutal buoyancy forces performing above bodies through dissimilar geometries in a fluid-soaked porous medium is prevalent in a large number of usual development together which has assorted as well as ample collection of industrial applications. Taking into account the priority of aforesaid fluid flow issues, vast moreover in detail research works have been borne out by several researchers [1, 2] performed. Many researchers [3–7] studied in-depth survey of usual convection boundary layer flow above several geometrical bodies with heat and mass transfer in spongy(porous) and non-spongy media. Recently, Veera Krishna and Swarnalathamma [8] deliberated the peristaltic MHD stream of Williamson fluid. Swarnalathamma and Veera Krishna [9] discussed the ideological and computational attention of peristaltic hemodynamic flow of couple stress fluids. MHD-free convective rotating flow deliberated by Veera Krishna and Gangadhar Reddy [10]. Veera Krishna and Subba Reddy [11] studied unsteady MHD convective flow of second grade fluid. Veera Krishna et al. [12] performed

heat and mass transfer on unsteady MHD oscillatory flow of blood all the way through spongy arteriole. In this paper, we have discussed the things of Hall effects on unsteady hydromagnetic usual convective rotating flow of second grade fluid past an impetuously moving vertical plate entrenched in a fluid inundated porous medium. El-Kabeir et al.[14] studied the problem on heat transfer in an unsteady, three-dimensional, laminar, boundary layer flow of a viscous, incompressible, and electrically conducting fluid over inclined permeable surface embedded in porous medium in the existence of a stable magnetic field and heat generation/absorption effects by making use of Lie group method. The coupled heat and mass transfer in fleeting flow by a mixed convection boundary layer past an impervious vertical stretching sheet embedded in a fluid-soaked porous medium in the existence of a chemical reaction effect by Rashad [15]. The effects of chemical reaction on mixed convection flow along a sphere in non-Darcian porous media studied by Rashad [16]. The Soret and Dufour effects on unsteady coupled heat and mass transfer by mixed convection flow over a vertical cone rotating in an current fluid with a time-dependent angular velocity in the presence of a magnetic field and chemical reaction studied by Ali and Rashad [17]. El-Kabeir et al. [18] deliberated the thermal diffusion as well as diffusion-thermo effects on heat and mass transfer by fleeting free convection flow of above an impetuously initiated isothermal vertical plate embedded in a inundated porous medium. In this paper, we discussed Hall effects on unsteady hydromagnetic natural convective rotating flow of second grade fluid past an impulsively moving vertical porous plate.

2 Formulation and Solution of the Problem

We considered unstable hydromagnetic natural convective flow of an electrically conducting, viscous, incompressible , and optically substantial revolving fluid over an infinite upright plate entrenched in a consistent porous medium in a very revolving structure taking Hall current into account. The physical configuration of the problem is as shown in Fig. 1. The temperature of plate is raised or lowered, whereas $0 < t \leq t_0$, and it is maintained at consistent temperature when $t > t_0$ (t_0 being characteristic time). Moreover, at time $t > t_0$, species concentration at the surface of the plate is lifted to invariable species concentration and is maintained thenceforth. Since plate is of infinite extent in x and z directions, all physical quantities except pressure depend on y and t only. The equations for governing flow through porous medium in a rotating frame taking Hall current into account, under Boussinesq approximation, are specified by

$$\frac{\partial u}{\partial t} + 2\Omega w = \nu \frac{\partial^2 u}{\partial y^2} + \frac{\alpha_1}{\rho} \frac{\partial^3 u}{\partial y^2 \partial t} - \frac{\sigma B_0^2}{\rho(1+m^2)}(u + mw) - \frac{\nu}{K_1} u + g\beta(\theta - \theta_\infty) + g\beta^*(\phi - \phi_\infty) \tag{1}$$

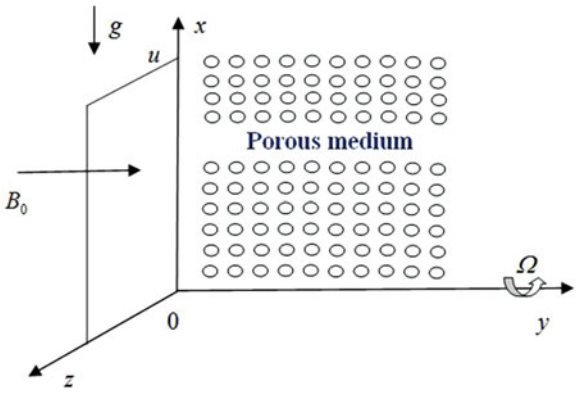

Fig. 1 The physical configuration of the problem

$$\frac{\partial w}{\partial t} - 2\Omega u = \nu \frac{\partial^2 w}{\partial y^2} + \frac{\alpha_1}{\rho}\frac{\partial^3 w}{\partial y^2 \partial t} + \frac{\sigma B_0^2}{\rho(1+m^2)}(mu - w) - \frac{\nu}{K_1} w \tag{2}$$

$$\rho C_p \frac{\partial \theta}{\partial t} = k\frac{\partial^2 \theta}{\partial y^2} - \frac{\partial q_r}{\partial y} \tag{3}$$

$$\frac{\partial \phi}{\partial t} = D\frac{\partial^2 \phi}{\partial y^2} \tag{4}$$

Initial and boundary conditions are

$$u = w = 0, \theta = \theta_\infty, \phi = \phi_\infty \text{ for } y \geq 0 \text{ and } t \leq 0, \tag{5}$$

$$u = U_0, w = 0 \text{ at } y = 0 \text{ for } t > 0, \phi = \phi_w \text{ at } y = 0 \text{ for } t > 0, \tag{6}$$

$$\theta = \theta_w \text{ at } y = 0 \text{ for } t > t_0, \theta = \theta_\infty + (\theta_w - \theta_\infty)\frac{t}{t_0} \text{ at } y = 0 \text{ for } 0 < t \leq t_0, \tag{7}$$

$$w \to 0; \theta \to \theta_\infty; \phi \to \phi_\infty \text{ as } y \to \infty \text{ for } t > 0. \tag{8}$$

For an optically substantial fluid, discharge, and self-importance, we adopted Rosseland approximation for radiative flux vector q_r [13],

$$q_r = -\frac{4\sigma^*}{3k^*}\frac{\partial \theta^4}{\partial y}, \tag{9}$$

Assume little temperature disparity among θ and θ_∞, θ^4 is extended in Taylor series concerning θ_∞ to linearize Eq. (9), after leaving second and greater order terms in $\theta - \theta_\infty$,

$$\theta^4 \cong 4\theta_\infty^3\theta - 3\theta_\infty^4 \tag{10}$$

Equation (3) with the help of Eq. (9) as well as (10) reduces to

$$\frac{\partial\theta}{\partial t} = \frac{k}{\rho C_p}\frac{\partial^2\theta}{\partial y^2} + \frac{1}{\rho C_p}\frac{16\sigma^*\theta_\infty^3}{3k^*}\frac{\partial^2\theta}{\partial y^2} \tag{11}$$

Introducing the dimensionless variables,

$$y^* = \frac{y}{U_0 t_0}, u^* = \frac{u}{U_0}, w^* = \frac{w}{U_0 t_0}, t^* = \frac{t}{t_0}, \theta^* = \frac{\theta - \theta_\infty}{\theta_w - \theta_\infty}, \phi^* = \frac{(\phi - \phi_\infty)}{(\phi_w - \phi_\infty)},$$

$$M^2 = \frac{\sigma B_0^2 \nu}{\rho U_0^2}, R^2 = \frac{\nu\Omega}{U_0^2}, m = w_e t_e, K = \frac{K_1 U_0^2}{\nu^2}, \alpha = \frac{U_0^2\alpha_1}{\rho\nu^2},$$

$$Gr = \frac{g\beta\nu(\theta_w - \theta_\infty)}{U_0^3}, Gc = \frac{g\beta^*\nu(\phi_w - \phi_\infty)}{U_0^3}, Pr = \frac{\nu\rho C_p}{k}, N = \frac{16\sigma^*\theta_\infty^3}{3kk^*}, Sc = \frac{\nu}{D}$$

Using dimensionless variables, Eqs. (1), (2), (4), and (11) are

$$\frac{\partial u}{\partial t} + 2R^2 w = \frac{\partial^2 u}{\partial y^2} + \alpha\frac{\partial^3 u}{\partial y^2 \partial t} - \frac{M^2}{(1+m^2)}(u + mw) - \frac{u}{K} + Gr\theta + Gc\phi \tag{12}$$

$$\frac{\partial w}{\partial t} - 2R^2 u = \frac{\partial^2 u}{\partial y^2} + \alpha\frac{\partial^3 u}{\partial y^2 \partial t} + \frac{M^2}{(1+m^2)}(mu - w) - \frac{w}{K}, \tag{13}$$

$$\frac{\partial\theta}{\partial t} = \frac{(1+N)}{P_c}\frac{\partial^2\theta}{\partial y^2}, \tag{14}$$

$$\frac{\partial\phi}{\partial t} = \frac{1}{Sc}\frac{\partial^2\phi}{\partial y^2}, \tag{15}$$

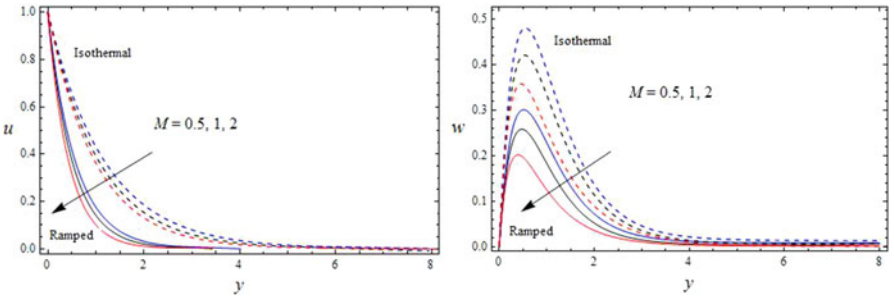

Fig. 2 The velocity profile for u and w against M with $R = 1$, $K = 0.5$, $m = 1$, $\alpha = 1$, $Pr = 0.71$, $N = 1$, $Sc = 0.22$, $Gr = 3$, $Gc = 5$, $t = 0.2$

Characteristic time t_0 is according to the dimensionless method discussed as $t_0 = \nu/U_0^2$. Combining Eqs. (12) and (13),

$$\frac{\partial F}{\partial t} = \frac{\partial^2 F}{\partial y^2} + \alpha \frac{\partial^3 F}{\partial y^2 \partial t} - \lambda F + Gr\theta + Gc\phi \tag{16}$$

Where $F = u + iw$ as well as $\lambda = M^2/(1-im) + (1/K) - 2iR^2$. The dimensionless initial and boundary conditions are

$$F = 0, \theta = 0, \phi = 0 \text{ for } y \geq 0 \text{ and } t \leq 0 \tag{17}$$

$$F = 1 \text{ at } y = 0 \text{ for } t > 0, \phi = 1 \text{ at } y = 0 \text{ for } t > 0, \tag{18}$$

$$\theta = t \text{ at } y = 0 \text{ for } 0 < t \leq 1, \theta = 1 \text{ at } y = 0 \text{ for } t > 1, \tag{19}$$

$$F \to 0; \theta \to 0; \phi \to 0 \text{ as } y \to \infty \text{ for } t > 0. \tag{20}$$

Taking Laplace transforms to Eqs. (14)–(16) and using initial and boundary conditions, we obtain velocity, temperature, and concentration.

3 Results and Discussion

We noticed that Fig. 2 portrays the impact of magnetic field on the primary velocity u along with secondary velocity w for both plates. It is evident starting Figs. 2 and 3 that, for the plates, u as well as w decreases on growing M in an area close to the plate and the same nature the area left from the plate. It is evident from Fig. 3 that

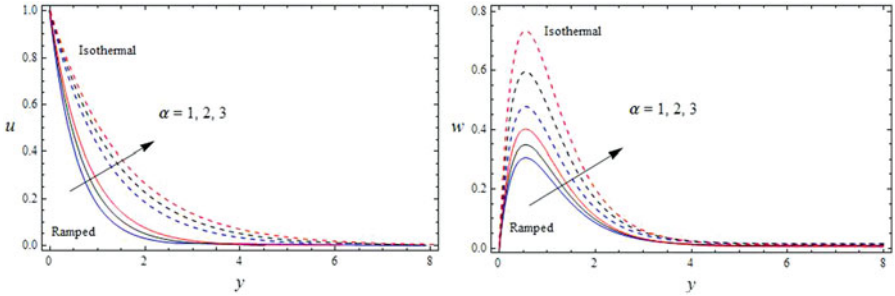

Fig. 3 The velocity profile for u and w against α with $M = 0.5$, $R = 1$, $K = 0.5$, $m = 1$, $Pr = 0.71$, $N = 1$, $Sc = 0.22$, $Gr = 3$, $Gc = 5$, $t = 0.2$

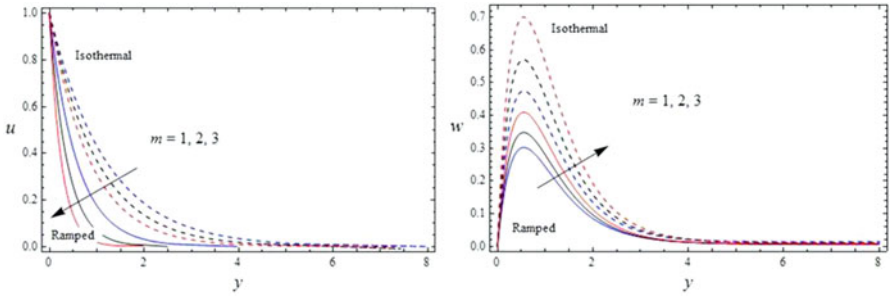

Fig. 4 The velocity profile for u and w against m with $M = 0.5$, $R = 1$, $K = 0.5$, $\alpha = 1$, $Pr = 0.71$, $N = 1$, $Sc = 0.22$, $Gr = 3$, $Gc = 5$, $t = 0.2$

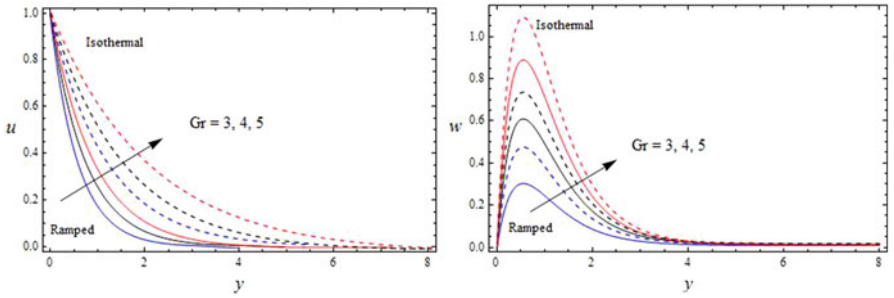

Fig. 5 The velocity profile for u against Gr with $M = 0.5$, $R = 1$, $K = 0.5$, $m = 1$, $\alpha = 1$, $Pr = 0.71$, $N = 1$, $Sc = 0.22$, $Gc = 5$, $t = 0.2$

both u and w enhance with increasing second grade fluid parameter for both plates. It is professed from Fig. 4 that, in both cases, u decreases on rising m, whereas w increases on enhancing m all over the boundary layer region. For both cases, Hall current tends to speed up secondary fluid velocity throughout the boundary layer region which is dependable that Hall current brings secondary flow in the entire fluid region. Figure 5 depicts the possessions of thermal buoyancy forces on the primary

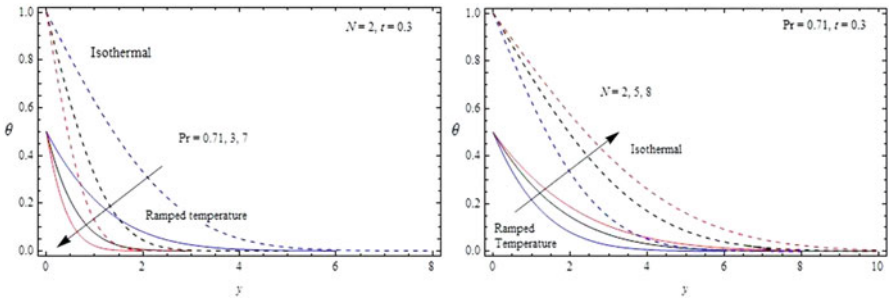

Fig. 6 The temperature profile against N and Pr with $t = 0.5$

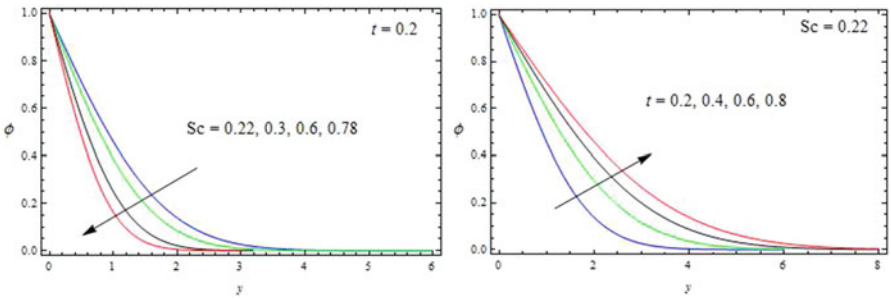

Fig. 7 The concentration profile against Sc and t

and secondary fluid velocities. We noticed that, in both cases, u and w increase on increasing Gr. We also noticed from Fig. 6 that the temperature enhances with increasing N for both plates. Therefore thermal radiation is inclined to increase fluid temperature all over the boundary layer region in both cases. Hence thermal radiation offers diffuse energy, since an enhance in N implies a reduce in k^* for fixed values of θ_∞ and k. It is evident that fluid temperature reduces with growing Pr. Figure 7 divulges that ϕ diminishes with increasing Sc whereas increases with rising t. We noticed that, from the Table 1, the skin friction τ_x enhances and τ_z decreases with growing M for the ramped temperature; the reversal behavior is observed for isothermal plate. For both plates τ_x reduces and τ_z increases with rising m, Gr, Gc, N, and t, whereas τ_x enhances and τ_z decreases with increasing Pr or Sc. Therefore, for plates, Hall current, thermal and concentration buoyancy forces, thermal and mass diffusions, and thermal radiation have propensity to decrease τ_x, while these physical quantities have turnover effect on τ_z. For both the plates, τ_x and τ_z increases with increasing R or α. Rotation tends to enhance both τ_x and τ_z for both plates. Both τ_x and τ_z increase for the ramped temperature and decrease for isothermal plate on increasing K. From Table 2, the Nusselt number Nu reduces with increasing N and is augmented on increasing time for both

cases, whereas it is diminished initially and then increases with the growth of Pr. Likewise from Table 3, Sherwood number enhances with increasing Schmidt number at the plate and reduces with increasing on time.

Table 1 Skin friction

											Ramped temperature		Isothermal plate	
M	K	R	α	m	Pr	Gr	Gc	N	Sc	t	$-\tau_x$	τ_z	$-\tau_x$	τ_z
0.5	0.5	1	1	1	0.71	3	5	2	0.22	0.2	2.85669	1.98552	2.15589	2.41522
1											3.14528	1.54278	1.85662	2.66089
1.5											3.41014	1.35524	1.70014	2.87490
	1										3.25445	2.32566	1.70544	1.85447
	1.5										3.64785	2.66502	1.24458	1.41178
		2									3.25547	2.14478	2.48012	2.85546
		3									3.65289	2.58790	2.87485	3.22145
			2								3.11145	2.29044	2.47996	2.88878
			3								3.52256	2.62546	2.80995	3.14520
				2							2.45226	2.22214	1.89958	2.66985
				3							2.22147	2.55489	1.52415	2.99968
					3						3.32202	1.82568	2.33256	2.22101
					7						3.66589	1.70145	2.61889	2.01255
						4					2.56996	2.33652	2.05685	2.66587
						5					2.01452	2.50785	1.88959	2.80145
							6				2.45228	2.15025	1.88019	2.85565
							7				2.14458	2.36960	1.52289	3.21014
								3			2.71245	1.99552	2.01455	2.45228
								4			2.60447	2.00145	1.89965	2.47885
									0.3		2.99258	1.80025	2.35562	2.22014
									0.6		3.14522	1.65278	2.52887	2.01478
										0.5	2.71145	2.13325	2.01025	2.89782
										0.8	2.51004	2.41890	1.89046	3.20478

Table 2 Nusselt number

N	Pr	t	Nu ramped temperature	Nu isothermal plate
2	0.71	0.5	0.274469	0.194079
5			0.194079	0.137235
8			0.158465	0.112052
	3		0.164682	0.150333
	7		0.439151	0.245493
		0.3	0.564190	0.398942
		0.8	0.861814	0.609394

Table 3 Sherwood number

Sc	t	Sh
0.22	0.2	−0.591727
0.3		−0.690988
0.6		−0.977205
0.78		−1.114190
	0.4	−0.418414
	0.6	−0.341634
	0.8	−0.295864

4 Conclusions

For both plates, Hall current and rotation tends to accelerate w and decelerate u throughout the boundary layer region. u and w are accelerated with increasing time throughout the boundary layer region. Thermal radiation and thermal diffusion tends to enhance fluid temperature throughout the boundary layer region. Mass diffusion tends to enhance concentration throughout the boundary layer region. Rotation and second grade fluid parameter tend to enhance τ_x and τ_z. Nu reduces with increasing N and is augmented on increasing time.

References

1. Nakayama, A., Hossain, M.A.: An integral treatment for combined heat and mass transfer by natural convection in a porous medium. Int J Heat Mass Transfer. **38**, 761–5 (1995)
2. Chamkha, A.J., Takhar, H.S.: Soundalgekar ,V.M.: Radiation effects on free convection flow past a semi-infinite vertical plate with mass transfer. Chem Eng J. **84** , 335–42 (2001)
3. Ganesan, P., Palani, G.: Natural convection effects on impulsively started inclined plate with heat and mass transfer. Heat Mass Transfer. **39** , 277–83 (2003)
4. Eckert, E.R., Drake, R.M.: Analysis of Heat and Mass Transfer. Mc-Graw Hill NY (1972)
5. Gebhart, B.,Jaluria, Y., Mahajan, R.L., Sammakia,B.: Buoyancy Induced Flow and Tran. (1998).
6. Nield, D.A., Bejan, A.: Convection in Porous Media. 3rd Ed. Springer NY (2006)
7. Pop, A., Ingham, D.B. : Convective Heat Transfer: Mathematical and Computational Modelling of Viscous Fluids and Porous Media. Oxford Pergamon (2001)
8. Veera Krishna, M., Swarnalathamma, B.V.: Convective heat and mass transfer on MHD peristaltic flow of Williamson fluid with the effect of inclined magnetic field. AIP Conf Proc. (2016) https://doi.org/10.1063/1.4946512
9. Swarnalathamma, B.V., Veera Krishna, M.: Peristaltic hemodynamic flow of couple stress fluid through a porous medium under the influence of magnetic field with slip effect. AIP Conf Proc. (2016) https://doi.org/10.1063/1.4946654
10. Veera Krishna, M., Gangadhar Reddy, M. : MHD free convective rotating flow of visco-elastic fluid past an infinite vertical oscillating porous plate with chemical reaction. IOP Conf Ser Mater Sci Eng.**149**:012217. (2016) https://doi.org/10.1088/1757-899X/149/1/012217
11. Veera Krishna, M., Subba Reddy, G.: Unsteady MHD convective flow of Second grade fluid through a porous medium in a Rotating parallel plate channel with temperature dependent source. IOP Conf Ser Mater Sci Eng. **149**:012216. (2016) https://doi.org/10.1088/1757-899X/149/1/012216

12. Veera Krishna, M., Swarnalathamma, B.V., Prakash, J. : Heat and mass transfer on unsteady MHD Oscillatory flow of blood through porous arteriole, Applications of Fluid Dynamics. Lecture Notes in Mechanical Engineering, **XXII**, 207–224 (2018) https://doi.org/10.1007/978-981-10-5329-0_14.
13. Sparrow, E.M., Cess, R,D.: Radiation heat transfer. Brooks/Cole Belmont Calif. (1966).
14. EL-Kabeir, S.M.M., EL-Hakiem, M.A., Rashad,A.M. : Lie Group Analysis Of Unsteady MHD Three Dimensional By Natural Convection From An Inclined Stretching Surface Saturated Porous Medium . J. Comp. App. Math. **213**, 582–603 (2008)
15. Rashad, A.M.: Heat And Mass Transfer In Transient Flow By Mixed Convection Boundary Layer Over A Stretching Sheet Embedded In A Porous Medium With Chemically Reactive Species. Journal of Porous Media. **13** , 75–85 (2010)
16. Rashad, A.M. : Effect Of Chemical Reaction On Heat And Mass Transfer By Mixed Convection Flow About A Solid Sphere In A Saturated Porous Media, International Journal of Numerical Methods for Heat and Fluid Flow . Int. J. Num. Methods for Heat and Fluid Flow . **21**(4) , 418–433 (2011)
17. Chamkha, Ali.J., Rashad, A.M. : Unsteady Heat and Mass Transfer by MHD Mixed Convection Flow from a Rotating Vertical Cone with Chemical Reaction and Soret and Dufour Effects . Canadian Journal of Chem. Eng. **92**(4), 758–767 (2014)
18. EL-Kabeir, S.M.M., Modather, M., Rashad, A.M. : Heat And Mass Transfer By Unsteady Natural Convection Over A Moving Vertical Plate Embedded In A Saturated Porous Medium With Chemical Reaction, Soret And Dufour Effects. J. App. Fluid Mech. **8**(3), 453–463 (2015)

High-Power LED Luminous Flux Estimation Using a Mathematical Model Incorporating the Effects of Heatsink and Fins

A. Rammohan, C. Ramesh Kumar, and M. M. Rashidi

Abstract High-power light emitting diode (HPLED) is an emerging technology in automotive, aerospace, domestic, and industrial lighting applications. Application of HPLED in the above mentioned areas are challenging, as effective cooling is required for maximal luminous output and longer life. This chapter deals with estimation of the total luminous flux of HPLED using a mathematical model for a given heat sink configuration, and electric and thermal conditions. The parameters that are considered in this model are voltage, current, the power of HPLED, the number of the LEDs in the module, thermal parameters such as the junction temperature of LED, heat sink and fin temperature, ambient temperature, and thermal resistances. The proposed model will be helpful for designing and predicting the luminous output of LED and also arriving at optimal heat sink and fin configurations for a given design.

1 Introduction

A light-emitting diode (LED) is an opto-semiconductor device that produces light when power is supplied using forward bias. In other words, LED is a semiconductor device that transforms electrical energy into light energy. The intensity of light emitted by the LED is governed by the current flowing through the LED [5]. Hence, the illumination of the LED can be controlled in a straightforward manner by changing the current supplied. Even though the LED has greater efficacy than

A. Rammohan (✉)
TIFAC-CORE, Vellore Institute of Technology, Vellore, India
e-mail: rammohan.a@vit.ac.in

C. Ramesh Kumar
Automotive Research Center, Vellore Institute of Technology, Vellore, India
e-mail: crameshkumar@vit.ac.in

M. M. Rashidi
Department of Civil Engineering, University of Birmingham, Birmingham, UK
e-mail: m.m.rashidi@bham.ac.uk

B. Rushi Kumar et al. (eds.), *Applied Mathematics and Scientific Computing*,
Trends in Mathematics, https://doi.org/10.1007/978-3-030-01123-9_42

conventional halogen and CFL lamps, LEDs still generate heat. Dissipating the heat generated is difficult as these are very compact systems. As heat transfer is directly proportional to area and compact size, the junction temperature increases owing to the accumulation of heat. This extreme temperature has unwanted effects such as chromaticity shift and catastrophic failure. Considering these effects, thermal management is an important aspect of high-power lighting design [1]. For the given set of operating conditions, the internal thermal resistances of the LEDs have a direct impact on the junction temperature. The higher the internal thermal resistance, the more rapidly the junction temperature rises. Thermal management of LED involves the design of a heat sink, its thickness, and the number of fins based on the operating conditions [6]. The operating conditions include a number of LEDs in the array and also the operating location, such as in the headlights of an automobile, streetlights or in industrial flood lighting etc. This chapter deals with the estimation of total luminous flux by considering the photo-electrothermal model along with the effects of temperature and thermal resistance. The developed model is simulated in MATLAB. By using this model for a given luminescence, it is possible to estimate the number of fins and the length of the fins.

2 Thermal Model of High-Power LED

The study of LED thermal behavior is a necessity for every new HPLED product designed before introduction onto the market. The thermal behavior directly relates to the life of HPLED [3]. With increased power, the introduction of polymer-based materials, complex shapes, and increased chip density, the estimation of the heat dissipation of an HPLED package is becoming challenging to model.

2.1 Junction Temperature of High-Power LED

In a typical high-power LED system, the LED is soldered onto a printed circuit board (PCB) through solder points and further to the metal core or FR4 (fire retardant 4), which is usually attached to the heat sink. Also, to maximize heat transfer between the heat sink and the PCB, a good thermal interface material (TIM) is required to fill air voids in the surface roughness of the surfaces. This TIM is a thermal grease that has better thermal conductivity. TIMs are generally in the form of grease, pads, and epoxy. Thermal grease (gel) also helps in bonding the surfaces, making it possible to rework the surfaces aids to stress relief [2, 4]. Various temperatures between junction and ambient are given in Eq. (1) and the details are shown in Fig. 1:

$$T_{junc-ambient} = T_{junc-sp} + T_{sp-pcb} + T_{pcb-TIMa} + T_{heatsink-ambient} \tag{1}$$

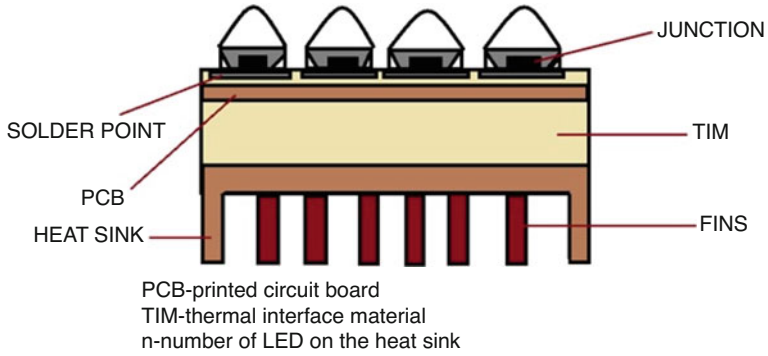

Fig. 1 LED assembly with heatsink and fins

where,

$T_{junc-ambient}$ is a temperature between LED junction and ambient
$T_{junc-sp}$ is a temperature between LED junction and solder point
T_{sp-pcb} is a temperature between the solder point and the PCB
$T_{pcb-TIMa}$ is a temperature between the PCB and the thermal interface material (TIMa)
$T_{heatsink-ambient}$ is a temperature between heatsink and ambient

The generated heat at the junction of an HPLED has to be conducted outward to the ambient temperature through the heat sink and cooling fins. Considering the HPLED construction shown in Fig. 1, the solder point, PCB, and TIM performance solely depend on the design of the manufacturer. In general, standard LED manufacturers provide the material properties of the solder point, PCB, and TIM in the data sheet and application notes. In the proposed model, the junction, heatsink, and fin resistances are considered relatively high compared with all other resistances [2] in the LED. The luminous flux solely depends on (V_f), current (I_f) and the junction temperature [5]. Practically, the heat sink should be designed in such a way as to dissipate the heat at a maximum junction temperature of around 120 °C and above.

2.2 Modeling the Total Luminous Flux of High-Power LED

Consider χ_v as the total luminous flux value [5] of a high-power LED consisting of N number of LED in the array.

$$\chi_v = N \times \xi \times P_d \tag{2}$$

$$\xi = E_o[1 + k_e(T_j - T_o)] \tag{3}$$

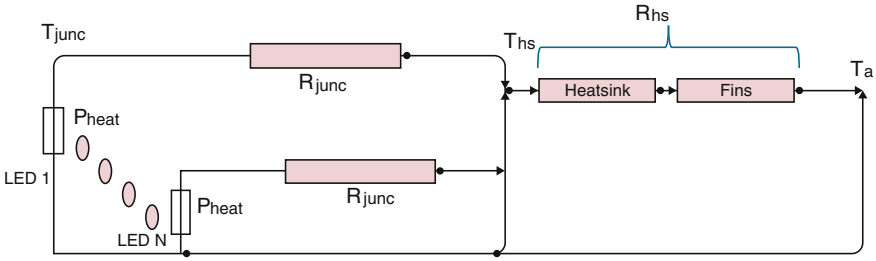

Fig. 2 Dynamic model of LED including thermal resistance of heatsink and fins

ξ is the luminous efficacy (lumen/watt) and P_d is the total power of one LED in watts. E_o is the rated efficacy at the rated temperature T_o (typically 25 °C in most LED data sheets) [5] and k_e is the relative rate of reduction of efficacy with the rise in temperature. Suppose that ξ reduces by 35% over a temperature increase of 100 °C, then the $k_e = -0.035$. In general, the LED power is defined as $P_d = V_f I_f$, where V_f is a forward voltage and I_f is a forward current of the LED. Once a portion of the power has been utilized to convert into light energy, then the remaining energy is dissipated as heat. Thus, the heat generated in one LED is given as $P_h = k_h \times P_d = k_h \times V_f \times I_f$ where k_h is a constant value, should be less than 1, and represents the part of the LED power that is converted into heat. For example, if 80% of the LED power is dissipated as heat, then $k_h = 0.80$. A simplified dynamic thermal equivalent circuit of the LED system is shown in Fig. 2, assuming that the N numbers of the LED in the array are fixed on the single heatsink and fins with a total thermal resistance of R_{h_s} and the LED consist of junction thermal resistance, which is given asR_{junc}. Practically, the TIM may be used among the LEDs and the heatsink to guarantee the perfect thermal contact. The thermal resistance of such compound is comparatively small when compared with junction resistance of LEDs and is not considered in the proposed model. Based on these considerations, the steady-state heatsink temperature T_{hs} can be stated as:

$$T_{hs} = T_{amb} + R_{hs}(N \times P_{heat}) \tag{4}$$

where T_{amb} is the ambient temperature and R_{hs} is the heatsink resistance of the LED.

$$T_{junc} = T_{hs} + (R_{junc} \times P_{heat}) \tag{5}$$

The junction thermal resistance is given by:

$$R_{junc} = R_{jcoo}(1 + k_{junc} \times P_d) \tag{6}$$

where $Rjcoo$ is the rated junction-to-case thermal resistance at 25 °C and k_{junc} is a positive coefficient

$$T_{junc} = T_{amb} + R_{hs}(N \times P_h) + R_{junc} \times k_h \times P_d \tag{7}$$

$$T_{junc} = T_{amb} + (R_{junc} + NR_{hs})k_h P_d \tag{8}$$

where T_{junc} is the junction temperature and R_{hs} is a total heatsink and fin thermal resistance, which was modeled separately. Further, substituting Eqs. (7) and (8) to obtain the total luminous flux [5] given in Eq. (10):

$$\chi_v = E_o\{1 + k_e[T_{amb} + (R_{junc} + NR_{hs})k_h P_d - T_o]\} \tag{9}$$

$$\chi_v = NE_o\{[1 + k_e(T_{amb} - T_o)]P_d + [k_e k_h(R_{jcoo} + NR_{hs})]P_d^2\} \tag{10}$$

2.3 Modelling the Overall Efficiency and the Total Thermal Resistance of the Heatsink with Fins

The thermal resistance of the heatsink played an important role in thermal management. The heat flow between the integrated chip (IC) die and the ambient air is designed based on a series of resistances [6]. The following resistances need to considered from the LED junction to the heat sink, and from the heat sink to the fins, and then to the ambient temperature. The sum of these resistances is the total thermal resistance from the junction temperature to the ambient temperature. Thermal resistance is generally defined as the temperature rise per unit of power, which is similar to common electrical resistance, and is represented in units of degrees Celsius per watt (°C/W).The temperature rise in the LED junction over ambient can be calculated with the help of total thermal resistances. The nomenclature for the heat transfer from a heatsink and fin array is shown in Fig. 3.

Let us consider A_f as the total area of fins and A_t as the total exposed area, including the fins. Then, the exposed parent area on the LED side is given by $A_{ex} = A_t - A_f$. The total heat transferred from the exposed LED-mounted parent area is given in Eq. (11). The total heat transfer is then given in Eq. (13).

$$Q_{total} = Q_{ex} + Q_{fin} = [A_{ex} \times h \times \theta_b] + A_f \times h \times \theta_b \times \eta \tag{11}$$

$$\theta_b = T_b - T_{amb} \tag{12}$$

$$Q_{total} = A_e \times h \times \theta_b \left[1 - \frac{A_f}{A_t} \times (1 - \eta)\right] \tag{13}$$

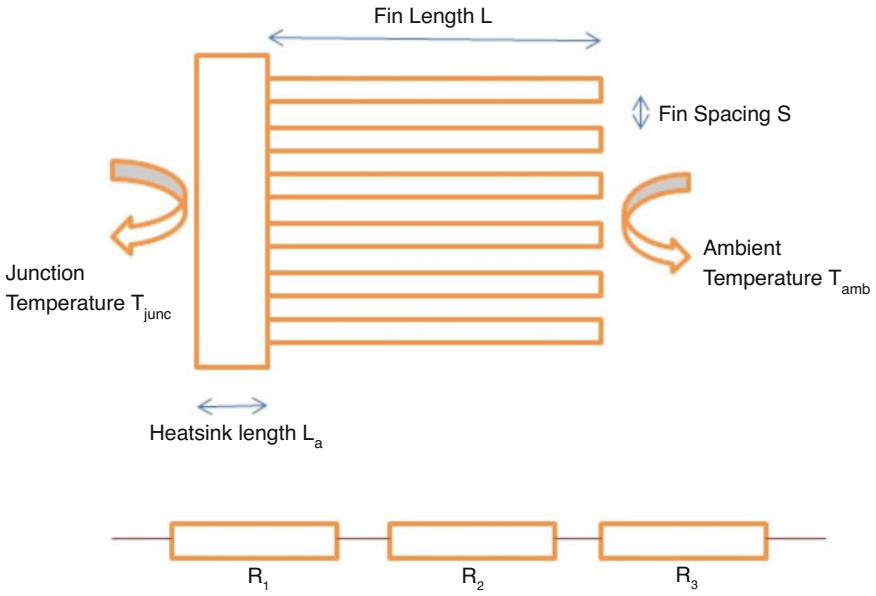

Fig. 3 Heat sink and fins with thermal resistances

In the derived Eq. (13), the η is the efficiency of every individual fin array and θ_b is the temperature excess on the LED side (based structure) with respect to ambient temperature. Also, h, h_a and h_b are heat transfer coefficients by convection in the heatsink and fins respectively. The maximum possible heat transfer rate is given in Eq. (14). Based on this, the overall efficiency is denoted as $\eta_{surface}$ in Eq. (15) [6].

$$Q_{maximum} = A_t \times h \times \theta_b \tag{14}$$

$$\eta_{surface} = \frac{Q_{total}}{Q_{maximum}} = \left[1 - \frac{A_f}{A_t} \times (1 - \eta)\right] \tag{15}$$

The fin efficiency is calculated using Eq. (16)

$$\eta = \frac{tanh(\omega)}{\omega} \tag{16}$$

where the nondimensional fin parameter $\omega = mL$ and the fin parameter m is given as $m = \sqrt{\frac{h}{k \times t}}$. The total exposed area of the heatsink and fin is calculated [6] as given in Eq. (17) and the area of the fins is given in Eq. (18).

$$A_t = [2 \times L \times W \times nf] + [S \times W \times (nf - 1)] \tag{17}$$

$$A_f = 2 \times L \times W \times nf \tag{18}$$

where A_t is a totally exposed area, A_f is the area of the fins, nf is the number of fins, W is the fin array width, S is the space between the fins, and L is length of the fin. Also, the total heat sink resistance is given in Eq. (19) based on Fig. 3.

$$R_{hs} = R1 + R2 + R3 = \frac{1}{h_a \times A} + \frac{L_a}{k \times A} + \frac{1}{h_b \times A_t \times \eta_{surface}} \tag{19}$$

where, $R1$ = inside film resistance, $R2$ = conduction resistance of the heatsink, $R3$ = thermal resistance of the fins, and L_a is length of the heatsink. The total heat transfer is given based on the thermal resistance [6] in Eq. (20).

$$Q_{ht} = \frac{T_{junc} - T_{amb}}{R_{h_s}} \tag{20}$$

where T_{junc} is the temperature directly available on the parent surface (heatsink), which is exposed from the LED junction, and T_{amb} is the ambient temperature, which is same as that mentioned in Eq. 12. The following assumptions are made to model the above equations:

- The analysis is performed for one-dimensional, steady-state heat conduction and the material properties are assumed to be constant
- The fin tip is assumed to be insulated at the end
- As per the datasheets of the LED, the junction temperature is a minimum of about 25 °C, 85 °C as peak and 105 °C is extremely high.

3 Simulation Results and Analysis

The above equations are modeled in SIMULINK, which is available in the MATLAB tool as a model-based design. The following data are considered for simulation based on the CREE LED datasheet and the total luminous output executed.

$Ke = -0.0045$, $Kjc = 0.13$, $Eo = 78.5$ lumen/Watt, $N = 8$, $Rjcoo = 8$, $Vf = 34.54$ V, $If = 0.25$ A, $h = 16.5$ W/m^2 °C, $t = 0.0006$ m, $k = 187$ W/m °C, $L = 0.035$ m, $La = 0.017$ m
$nf = 8$, $S = 0.004$ m, $W = 0.098$ m, $T1 = 65$°C, $T2 = 22$°C
$ha = 270$ W/m^2 °C, $h2 = 45$ W/m^2 °C

The total luminous output is 546.2 lumens based on Eq. (10). The heatsink resistance is calculated as 1.79 by the tool. This heatsink resistance is directly substituted for the total luminous flux to obtain the optimal output, which is the novelty in our proposed model. The fin efficiency is calculated as 0.944.

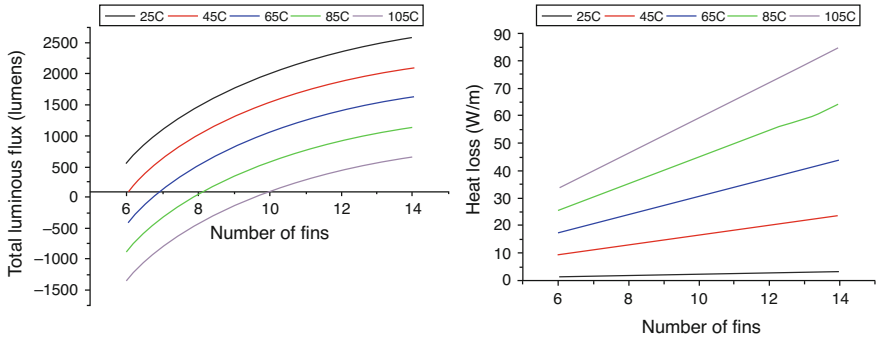

Fig. 4 Number of fins with heat loss and total luminous output

Figure 4 is simulated output, which clearly shows that:

- The number of fins on the x-axis and the heat loss or transfer and total luminous flux on the y-axis
- The number of fins increased from 6 to 14 and the junction temperature at the base of the heatsink given by the LED is 25, 45, 65, 85, and 105 °C
- When the junction temperature increases the heat loss is increased along with an increase in the number of fins
- The optimal thermal management for the required luminous flux can also be calculated from the proposed design. For example, under 85 °C, it is not optimal to fix fewer than eight fins. This means that the best luminous output is obtained if the designer uses more than eight fins. The negative results shown in Fig. 4 are not optimal for choosing the number of fins under a particular temperature.

From Fig. 5 the simulated output, which clearly shows that:

- The fin length is on the x-axis and thermal resistance, heat loss, total luminous flux on the y-axis
- The fin length is increased from 0.035 m to 0.08 m with 0.05 m on each step and the given junction temperature at the base of the heatsink is 85 °C
- When the fin length is increased, the thermal resistance is decreased and the heat transfer and total luminous flux are also increased.
- The optimal thermal management for the required luminous flux, which can also be calculated from the proposed design by varying the fin length, is proven. For example, under 85 °C, although the fin length is 0.055 m, the total luminous flux is 208.5 lumens, thermal resistance is 1.667 and heat loss is 37.79 W.

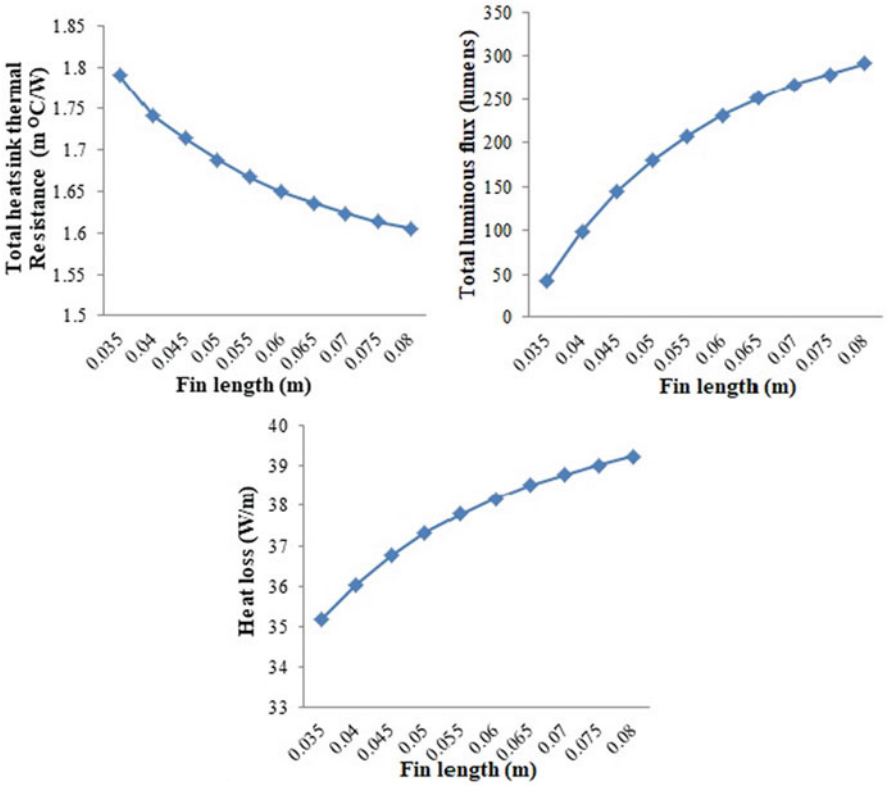

Fig. 5 Variation of fin length with thermal resistance, total luminous flux, and heat loss

4 Conclusion

In this paper, a mathematical model is proposed for the thermal management of a high-power LED by considering electrical and thermal aspects. In this model, heatsink resistance is modeled separately and included in the total luminous flux equation. The model helps to easily estimate the total luminous flux and required thermal management. The simulated results show that with an increase in the number of fins or an increase in the fin length, the total luminous flux improves, whereas the thermal resistance decreases. This mathematical model can also help to predict the life of an LED while relating the operating hours using this total luminous flux model.

References

1. Vipradas, A., Takawale, A., Tripathi, S., Swakul, V.: A parametric study of a typical high power LED package to enhance overall thermal performance. 13th IEEE ITHERM Conference (2012) https://doi.org/978-1-4244-9532-0
2. Wang, C.-P., Kang, S.-W., Lin, K. M., Chen, T.-T., Fu, H.-K., and Chou, P.-T.: Analysis of thermal resistance characteristics of power LED module, IEEE Trans. Electron Devices, **61(1)**, 105–110(2014)
3. Fu H.-K., Wang C.-P., Chiang, H.-C., Chen, T.-T., Chen, C. L., Chou, P. T.: Evaluation of temperature distribution of LED module, Microelectron Reliab., **53**, 554–559(2013)
4. Huang, H., Cai, M., Tian, K., Chen, Y., Jia, H., Yang, D.: Thermal resistance analysis of high power LED module under power cycling test. 15th International Conference on Electronic Packaging Technology (2014). https://doi.org/978-1-4799-4707-2
5. Hui S. Y., Qi Y. X.: General photo-electro-thermal theory for light emitting diode (LED) systems, IEEE TRANS. Power Electron., **24(8)**, 1967–1977(2009)
6. Venkateshan S. P.: Heat transfer, 2nd edn. Ane Books Pvt. Ltd. (2011)

Soret and Dufour Effects on Hydromagnetic Marangoni Convection Boundary Layer Nanofluid Flow Past a Flat Plate

D. R. V. S. R. K. Sastry, Peri K. Kameswaran, Precious Sibanda, and Palani Sudhagar

Abstract The present study explores the effects of thermal radiation, chemical reaction, viscous dissipation, Soret and Dufour on Marangoni convection over a steady and laminar boundary layer flow. A nanofluid, consisting of copper, silver, and alumina metallic nanoparticles suspended in water, is considered. Similarity transformations are used to solve the governing equations of motion. The transformed ordinary differential equations are then solved numerically using MATLAB 'bvp4c' residual method. The upshots of various physical properties influenced by Eckert, Nusselt, Sherwood, Soret, and Dufour numbers are delineated.

1 Introduction

The low sedimentation and high stability uniquely brought nanofluids into the focus of research. Choi [1] identified that nanofluids possess high thermal conductivity compared to base fluids however small volume fraction might be. Free convection boundary layer flow over a horizontal plate is studied by Aziz et al. [2]. Natural convection boundary layer flow of Cheng-Minkowycz is examined by Nield and Kuznetsov [3]. Convection about vertical plate over porous medium is explained by Cheng and Minkowycz [4]. They considered heat transfer applications over a dike. Vajravelu and Hadjinicolaou [5] elucidated how internal heat generation along with viscous dissipation effects heat transfer rate. Over a few decades, the study of magnetic field has a great impact over sciences, engineering, and allied sciences

D. R. V. S. R. K. Sastry (✉)
Department of Mathematics, SASTRA Deemed University, Thanjavur, Tamil Nadu, India
e-mail: sastry@maths.sastra.edu

P. K. Kameswaran · P. Sudhagar
VIT, Vellore, Tamil Nadu, India

P. Sibanda
School of Mathematics, Statistics and Computer Science, University of KwaZulu-Natal (UKZN), Scottsville, Pietermaritzburg, South Africa

B. Rushi Kumar et al. (eds.), *Applied Mathematics and Scientific Computing*,
Trends in Mathematics, https://doi.org/10.1007/978-3-030-01123-9_43

applications, especially in the metallurgy, cooling of strips or filaments in thinning of copper wires. Joshi and Gebhart [6] explored the combined effect of conduction and viscous dissipation on MHD free convection flow along a vertical flat plate. The temperature or concentration gradients produce energy flux. The energy flux caused by temperature gradient is named as thermo-diffusion effect or Soret effect. Further, the energy flux generated by concentration gradient is known as diffusion thermo or Dufour effect. Adrian [7] considered a numerical study over the heat and mass transfer in presence of Soret and Dufour effects for the natural convection flow over a vertical surface embedded in a saturated porous medium along with magnetic effect. Weaver and Viskanta [8] identified that the coupled interaction is significant when the gradients of temperature and concentration are large. The combined effect of Soret and Dufour over a non-Newtonian mixed convection flow was discussed by Mahdy [9]. The combined effects of thermophoresis and chemical reaction over a mixed convection flow were explained by Kairi and Murthy [10].

On the other hand, the dissipative layers which may develop along the liquid-gas or liquid-liquid interfaces are named as Marangoni boundary layers. The convection induced by the variations of surface tension along the interface is termed as Marangoni convection. This may be either thermal Marangoni effect or solute Marangoni effect. Thermal Marangoni effect is due to variation of surface tension due to temperature gradient, and solute Marangoni effect is because of variation in the surface tension due to concentration differences explored by Magyari and Chamkha [11]. Marangoni convection in nanofluids has a considerable interest of research as it has tremendous industry applications. Considerable work on Marangoni convection was executed by Christopher and Wang [12], Golia and Viviani [13] and Zhang and Zheng [14]. Further Mahdy and Ahmed [15] recently had a reconnaissance of Soret and Dufour effects over heat and mass transfer in a Marangoni boundary layer magnetohydrodynamic flow.

In the present paper, we have examined the combined Soret and Dufour effects on heat and mass transfer in Marangoni convection nanofluid flow over a flat surface. The fluid is influenced by viscous forces and thermal radiation.

2 Flow Analysis

A steady laminar thermosolutal Marangoni boundary layer flow is considered along flat plate. The fluid is opined to be viscous, Newtonian, and electrically conducting in presence of transverse magnetic field of uniform strength. A water-based nanofluid contains three different types of nanoparticles: copper (Cu), silver (Ag), and alumina (Al_2O_3). Moreover no electric field exists, and Hall effect is negligible. Further assume magnetic Reynolds number is small so that Maxwell's equations become disconnected from the Navier-Stokes equations. The interface temperature and concentration are presumed to be quadratic functions of the distance x along the interface. These suppositions assure the existence of similarity solution. Assume that the temperature of the plate is $T(x)$ and that of the ambient

fluid is T_∞. A uniform magnetic field B_0 is applied in the horizontal direction normal to the plane. Consider a Cartesian coordinate system (x, y), where x and y are the coordinates measured along the interface and normal to it. The above flow assumptions set the boundary layer equations of a viscous and incompressible fluid expound mass, linear momentum, energy, and concentration in the following dimensional form,

$$\frac{\partial u}{\partial x} + \frac{\partial v}{\partial y} = 0 \tag{1}$$

$$u\frac{\partial u}{\partial x} + v\frac{\partial u}{\partial y} = \frac{\mu_{nf}}{\rho_{nf}}\frac{\partial^2 u}{\partial y^2} - \frac{\delta}{\rho_{nf}}B_0^2 u \tag{2}$$

$$u\frac{\partial T}{\partial x} + v\frac{\partial T}{\partial y} = \alpha_{nf}\frac{\partial^2 T}{\partial y^2} - \frac{1}{(\rho c_p)_{nf}}\frac{\partial q_r}{\partial y} - \frac{\mu_{nf}}{(\rho c_p)_{nf}}\left(\frac{\partial u}{\partial y}\right)^2 + D_T\frac{\partial^2 h}{\partial y^2} \tag{3}$$

$$u\frac{\partial h}{\partial x} + v\frac{\partial h}{\partial y} = D\frac{\partial^2 h}{\partial y^2} + D_h\frac{\partial^2 T}{\partial y^2} - k_0(h - h_\infty) \tag{4}$$

along with the boundary conditions

$$v = 0, T = T_\infty + ax^2, h = h_\infty + bx^2, \mu_{nf}\frac{\partial u}{\partial y} = \gamma\frac{\partial T}{\partial x} + \gamma^*\frac{\partial h}{\partial x} \quad at \quad y = 0$$

$$and \quad u \to 0, T \to T_\infty, h \to h_\infty \quad as \quad y \to \infty \tag{5}$$

where u and v indicate velocity components along x and y directions, respectively. ρ, T, and h denote fluid density, temperature, and concentration, respectively. Moreover T_∞ and h_∞ quantify temperature and concentration of the fluid far from the surface. c_p means specific heat at constant pressure. D denotes the species diffusivity. D_h and D_T betoken the coefficients that measure mass fluxes through temperature and concentration gradients, respectively. k_0 and δ stand for chemical reaction parameter and electric conductivity of the fluid. The coefficients a and b are dimensional constants. According to Boussinesq approximation, the interface governing equation with interface surface tension σ_0 may be written as

$$\sigma = \sigma_0[1 - \gamma(T - T_\infty) - \gamma^*(h - h_\infty)] \quad where\ \gamma = -\frac{\partial\sigma}{\partial T}, \gamma^* = -\frac{\partial\sigma}{\partial h} \tag{6}$$

With respect to the species volume fraction, the effective quantities representing viscosity, density, thermal diffusivity, heat capacitance, and thermal conductivity of the nanofluid are defined, respectively, as

$$\mu_{nf} = \frac{\mu_f}{(1-\phi)^{2.5}}, \quad \rho_{nf} = (1-\phi)\rho_f + \phi\rho_s, \quad \alpha_{nf} = \frac{k_{nf}}{(\rho c_p)_{nf}}, \tag{7}$$

$$(\rho c_p)_{nf} = (1-\phi)(\rho c_p)_f + \phi(\rho c_p)_s, \quad k_{nf} = k_f \left(\frac{k_s + 2k_f - 2\phi(k_f - k_s)}{k_s + 2k_f + \phi(k_f - k_s)} \right) \tag{8}$$

The subscripts nf, f, and s stand for nanofluid, base fluid, and solid species, respectively. In fluid mechanics majority of the existing solutions are similarity solutions which reduce the number of independent variables. Henceforth one can transform the governing equations of motion to a system of ordinary differential equations. For this, we introduce the following similarity transformations:

$$\psi = Axf(\eta), \quad \eta = By, \quad \theta(\eta) = \frac{T - T_\infty}{ax^2}, \quad \chi(\eta) = \frac{h - h_\infty}{bx^2} \tag{9}$$

where

$$A = \left(\frac{a\mu_f \frac{d\sigma}{dT}|_h}{\rho_f^2} \right)^{\frac{1}{3}}, B = \left(\frac{a\rho_f \frac{d\sigma}{dT}|_h}{\mu_f^2} \right)^{\frac{1}{3}} \tag{10}$$

Employing Rosseland approximation to the temperature, (3) reduces to

$$u\frac{\partial T}{\partial x} + v\frac{\partial T}{\partial y} = \alpha_{nf}(1 + N_r)\frac{\partial^2 T}{\partial y^2} - \frac{\mu_{nf}}{(\rho c_p)_{nf}} \left(\frac{\partial u}{\partial y} \right)^2 + D_T \frac{\partial^2 h}{\partial y^2} \tag{11}$$

Exerting the similarity transformations given in (9) along with (10), Eqs. (2), (4) and (11) mutate to

$$f''' = (1-\phi)^{2.5}[(1-\phi) + \phi\frac{\rho_s}{\rho_f}](f'^2 - ff'') + M^2(1-\phi)^{2.5}f' \tag{12}$$

$$\theta''(\beta_1 + Nr) = \frac{Pr\ Ec\ f''^2}{(1-\phi)^{2.5}} + \beta_2 \left[Pr(2f'\theta - f\theta') - D_f\chi'' \right] \tag{13}$$

$$\chi'' = S_c(2\chi f' - f\chi' + K^*\chi) - S_r\theta'' \tag{14}$$

where $\beta_1 = \frac{k_s + 2k_f - 2\phi(k_f - k_s)}{k_s + 2k_f + \phi(k_f - k_s)}$ and $\beta_2 = (1-\phi) + \phi\frac{\rho(cp)_s}{\rho(cp)_f}$. The similarity transformation further alters the boundary conditions as follows

$$f(0) = 0, \theta(0) = 1, \chi(0) = 1, \frac{1}{(1-\phi)^{2.5}} f''(0) = -2(1 + Ma)$$
$$f'(\infty) = 0, \theta(\infty) = 0, \chi(\infty) = 0 \tag{15}$$

The quantities with no dimensions which are appearing in above equations the Hartmann number $M = \frac{\delta^{1/2} B_0 \mu^{1/6}}{\rho^{1/3} \frac{d\sigma}{dT}|_h^{1/3} a^{1/3}}$, Prandtl number $Pr = \frac{\nu_f (\rho c_p)_f}{k_f}$, Schmidt number $Sc = \frac{\nu_f}{D}$, Soret number $Sr = \frac{D_h (T - T_\infty)}{D(h - h_\infty)}$, scaled chemical reaction parameter $K^* = \frac{k_0 \mu_f^{1/3} \rho_f^{1/3}}{\frac{d\sigma}{dT}|_h^{2/3} a^{2/3}}$, Dufour number $D_f = \frac{(h - h_\infty) D_T}{\alpha_{nf} (T - T_\infty)}$, ratio of solutal and thermal Marangoni numbers $Ma = \frac{\Delta h \frac{d\sigma}{dh}|_T}{\Delta T \frac{d\sigma}{dT}|_h}$, viscous parameter $Ec = \left[\frac{1}{cp_f}\right] \left\{ \frac{a\left(\frac{d\sigma}{dt}\right)|_h^4}{\rho_f^2 \mu_f^2} \right\}^{\frac{1}{5}}$, and radiation parameter $Nr = \frac{16\sigma^* T_\infty^3}{3k^* k_{nf}}$ where σ^* and k^* are Stefan-Boltzmann constant and mean absorption coefficient, respectively. The quantities of practical interest in this study are Nusselt number Nu_x and Sherwood number Sh_x which quantify the rate of heat and mass transfers, respectively. These may be formulated in non-dimension form by the use of transformation as follows

$$\frac{Nu_x}{\frac{k_n f}{k_f} Bx} = -\theta'(0), \quad \frac{Sh_x}{Bx} = -\chi'(0) \tag{16}$$

where Bx, $\frac{k_n f}{k_f}$ remain non-dimension quantities.

3 Results and Discussions

A numerical solution is found for Eqs. (12)–(14) along with boundary conditions (15) using MatLab, fourth-order boundary value problem-solver. This is a residual control-based adaptive mesh solver. Instead of uniform mesh, this provides a uniform grid of data points x over the interval $\frac{1}{2x}$ and solve accordingly. The relative tolerance is taken up to 10^{-10}. The maximum value for similarity variable is $\eta_{\max} = 15$ which represents the conditions far away from the fluid. The value of $\eta_{\max}$ is found to each iteration loop by the assignment statement $\eta_{\max} = \eta_{\max} + \Delta\eta$ on taking step size $\Delta\eta = 0.05$. Profiles are drawn for standard values of parameters $M = Nr = Sc = Ec = 1$, $Sr = D_f = \phi = Ma = K^* = 0.2$.

Kinetic energy will be converted to internal energy by work done against viscous stream representing viscous dissipation. The heat developed during this process enhances the velocity of the fluid particles. So more viscous dissipation triggers more velocity. This results a descent in temperature profiles which can be observed from Fig. 1. Temperature profiles are shown in Fig. 2 against Dufour number. It is noted that enhancing Dufour number causes a decrease in thermal boundary layer. The effect of Soret number on species concentration is observed in Fig. 3. It is noticed that concentration gears up by increasing Soret number; in particular, silver particles possess more mass diffusion than that of the others. Schmidt number, ratio of mass and thermal diffusivity, provides the relation between hydrodynamic and mass boundary layers. Increasing this value will suppress concentration boundary layer. The same is witnessed in Fig. 4.

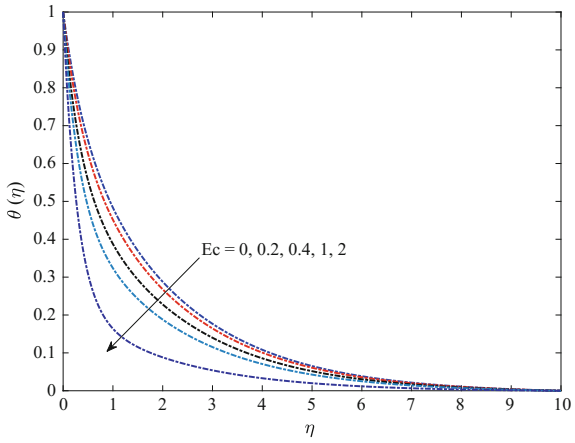

Fig. 1 Effect of Eckert number on temperature distribution

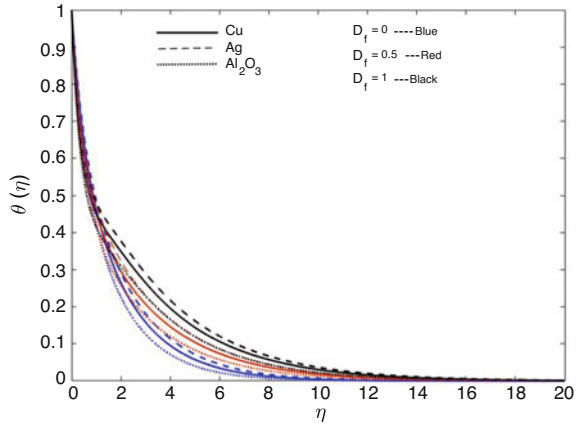

Fig. 2 Effect of Dufour number on temperature distribution

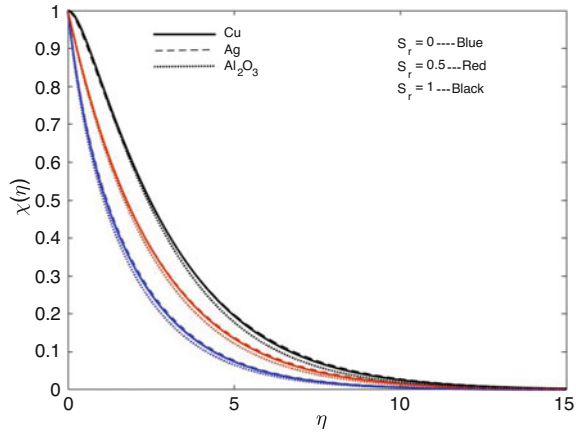

Fig. 3 Effect of Soret number on concentration distribution

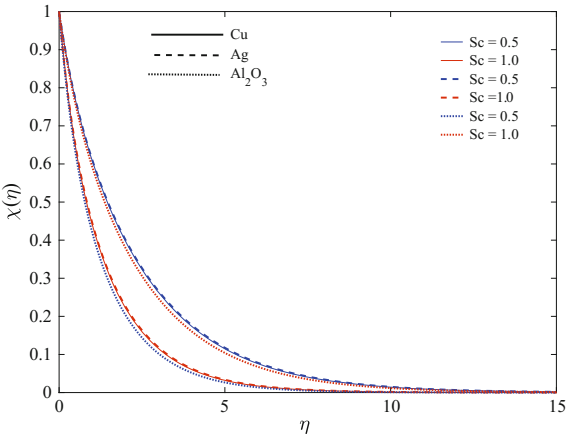

Fig. 4 Effect of Schmidt number on concentration distribution

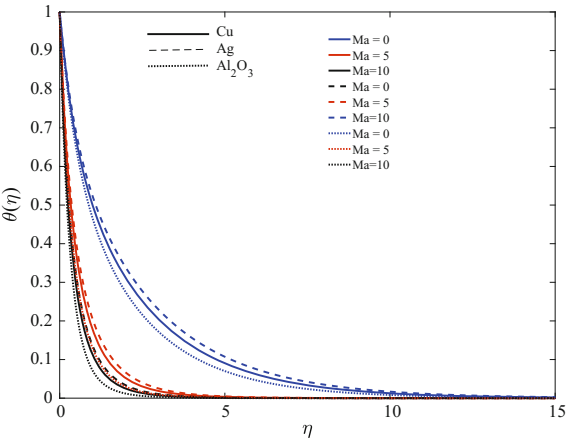

Fig. 5 Effect of Marangoni number on temperature

It is clear from Figs. 5 and 6 that thermosolutal surface tension ratio plays an impressive role in the temperature and concentration profiles. A decrease in this ratio encounters an increase in both fluid temperature and concentration. This finding is obtained due to the increase in the values of Ma demand and the increase in the marangoni convection which produces more induced flows within the boundary layer. As a consequence, the resulting flows will propagate within the boundary layers causing the maximum velocity obtained at the wall which reduces the temperature boundary layer. We observe from Fig. 7 the impact of Soret number on Nusselt numbers. As Soret number is a consequence of the temperature gradient, it is clearly observed that an increase in Soret number enhances the heat transfer. Further it is noted that heat transfer is more in alumina as it is more conductive.

Figures 8 and 9 address the Dufour effect on heat and mass transfer, respectively. Heat transfer rate increases, and mass transfer rate decreases with the increase

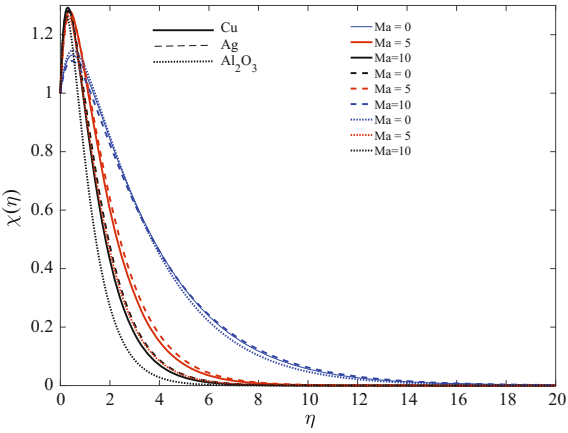

Fig. 6 Effect of Marangoni number on concentration

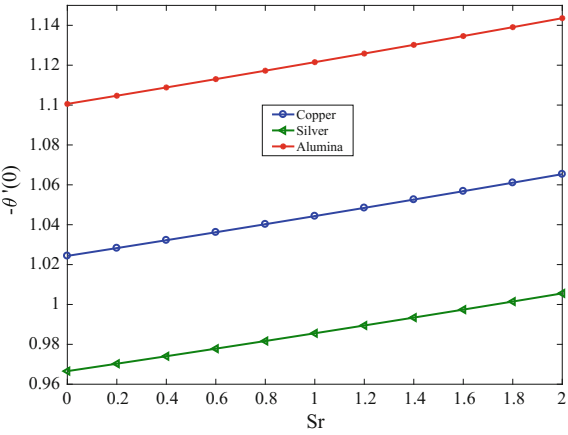

Fig. 7 Effect of Soret number on heat transfer

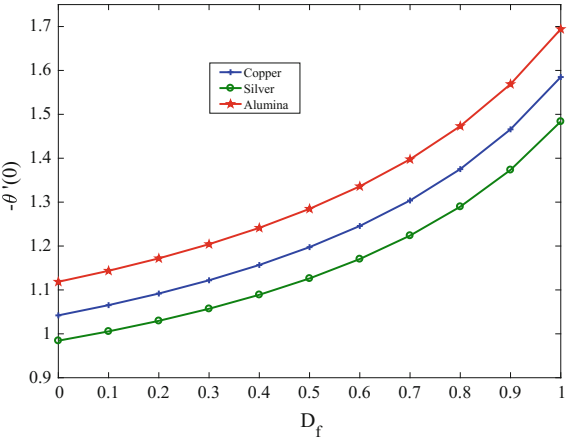

Fig. 8 Effect of Dufour number on heat transfer

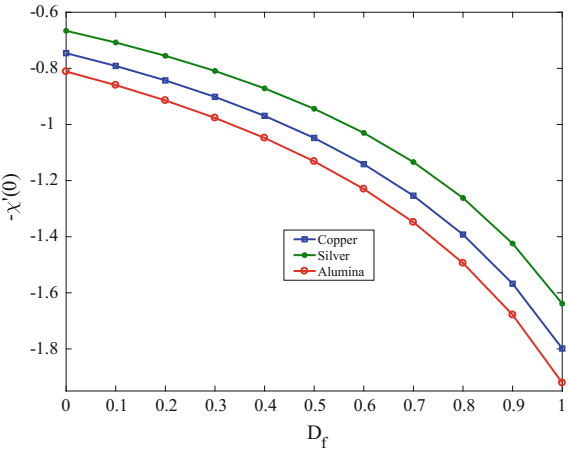

Fig. 9 Effect of Dufour number on mass transfer

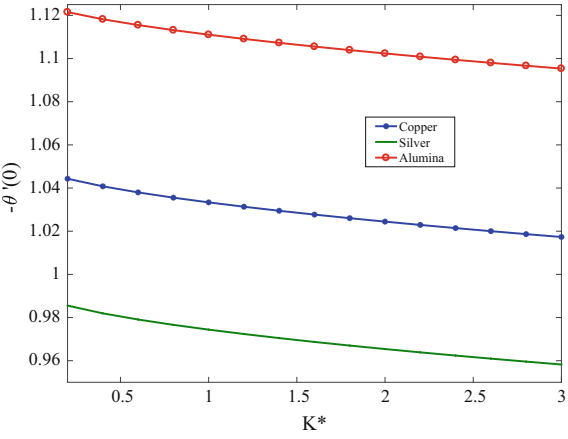

Fig. 10 Effect of chemical reaction parameter on heat transfer

of Dufour number. The alumina and silver species have higher and lower heat transfer rates, respectively. A complete reversal is observed in case of Sherwood number.

Figures 10 and 11 unveil the effect of chemical reaction parameter on heat and mass transfer. Heat transfer rate is monotonically decreasing with an increase in the chemical reaction. Chemical reaction increases the mass transfer rate in all the species and is significant at large values of this parameter. This is particularly high for silver nanoparticles, as silver species diffuse quickly. Figure 12 uncovers the resistivity of magnetic field on copper nanofluid movement. Magnetic field instigates a resistance for the movement of the fluid, known as Lorentz force, which is more predominant within the boundary layer.

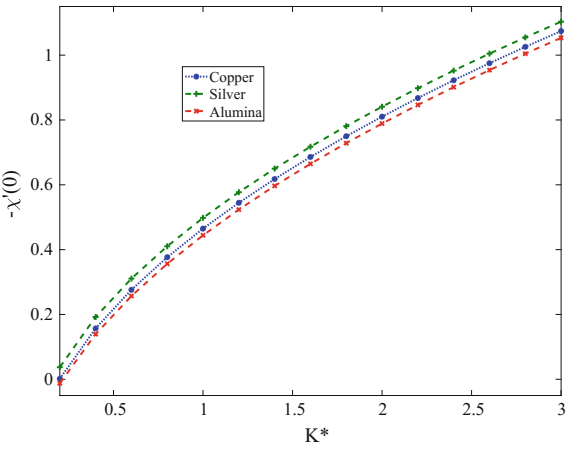

Fig. 11 Effect of chemical reaction parameter on mass transfer

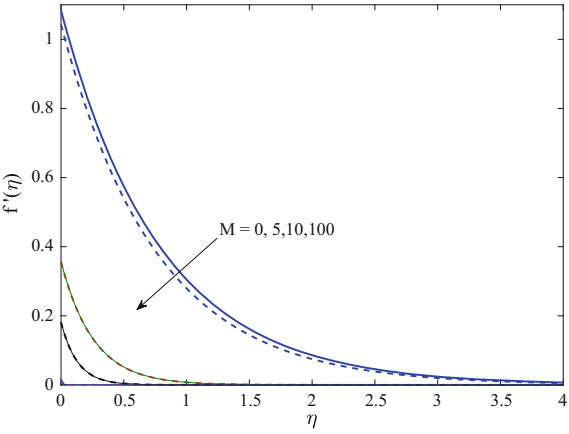

Fig. 12 Effect of magnetic parameter on velocity

4 Conclusions

A viscous nanofluid Marangoni convection chemically reacted flow over a flat plate subjected to the radiation under Soret and Dufour effects is analyzed. The following conclusions are made:

1. A descent in thermal boundary layer is observed when Dufour number increases
2. Increase of Soret number enhances species concentration
3. The mass diffusion in silver particles is high
4. Increase of marangoni convection parameter retrains both temperature and species concentration
5. A descent in temperature profiles is observed with respect to increase of viscosity

Acknowledgements The first author is thankful to the Department of Science and Technology, Government of India for providing financial support under FIST programme $SR\backslash FST\backslash MSI - 107\backslash 2015$

References

1. Choi, S.U.S.: Enhancing thermal conductivity of fluids with nanoparticles. ASME Fluids Eng. Division. **231**, 99–105 (1995)
2. Aziz, A., Khan, W.A., Pop, I.: Free convection boundary layer flow past a horizontal flat plate embedded in porous medium filled by nanofluid containing gyrotactic microorganisms. International Journal of Thermal Sciences. **56**, 48–57 (2012)
3. Nield, D.A., Kuznetsov, A.V.: The Cheng-Minkowycz problem for natural convective boundary layer flow in a porous medium saturated by a nanofluid. Int. J. Heat Mass Transf. **52**, 5792–5795 (2009)
4. Cheng, P., Minkowycz, W.J.: Free convection about a vertical flat plate embedded in a porous medium with application to heat transfer from a dike. J. Geophys. Res. **28**, 2040–2044 (1977)
5. Vajravelu, K., Hadjinicolaou, A.: A Heat transfer in a viscous fluid over a stretching sheet with viscous dissipation and internal heat generation. Int. Commun. Heat Mass Transfer. **20**, 417–430 (1993)
6. Joshi, Y., Gebhart, B.: Effect of pressure stress work and viscous dissipation in some natural convection flows. Int. J. Heat Mass Transfer. **29**, 377–388 (1981)
7. Adrian, P.: Influence of a magnetic field on heat and mass transfer by natural convection from vertical surfaces in porous media considering Soret and Dufour effects. Int. J. Heat Mass Transfer. **47**, 1467–1472 (2004)
8. Weaver, J.A., Viskanta, R.: Natural convection due to horizontal temperature and concentration gradients (2): species inter diffusion, Soret and Dufour effects. Int. J. Heat Mass Transfer. **34**, 3121–3133 (1991)
9. Mahdy, A.: Soret and Dufour effect on double diffusion mixed convection from a vertical surface in a porous medium saturated with a non-Newtonian fluid. J. Non Newtonian Fluid Mech. **165**, 568–575 (2010)
10. Kairi, R.R., Murthy, P.V.S.N.: The effect of melting and thermo-diffusion on natural convection heat mass transfer in a non-Newtonian fluid saturated non-Darcy porous medium. Open Transp. Phenom. J. **1**, 7–14 (2009)
11. Magyari, E., Chamkha, A.J.: Exact analytical results for the thermosolutal MHD marangoni boundary layers. Int. J. Therm. Sci. **47**, 848–857 (2008)
12. Christopher, D.M., Wang, B.: Prandtl number effects for Marangoni convection over a flat surface. Int. J. Therm. Sci. **40**, 564–570 (2001)
13. Golia, C., Viviani, A.: Marangoni buoyant boundary layers. Aerotec. Missili. Spaz. **64**, 29–35 (1985)
14. Yan Zhang, Liancun Zheng: Analysis of MHD thermosolutal marangoni convection with the heat generation and a first-order chemical reaction. Chem. Eng. Sci. **69**, 449–455 (2012)
15. Mahdy, A., Ahmed, S.E.: Thermosolutal marangoni boundary layer magnetohydrodynamic flow with the Soret and Dufour effects past a vertical flat plate. Engineering Science and Technology, an International Journal. **18**, 24–31 (2015)

Part VII
Graph Theory

An Algorithm for the Inverse Distance-2 Dominating Set of a Graph

K. Ameenal Bibi, A. Lakshmi, and R. Jothilakshmi

Abstract Let $G = (V, E)$ be a simple, finite, connected, and undirected graph. Let $D \subseteq V(G)$ be the non-empty subset of $V(G)$ such that D is the minimum distance-2 dominating set in the graph $G = (V, E)$. If $V - D$ contains a distance-2 dominating set $D^{'}$ of G, then $D^{'}$ is called an inverse distance-2 dominating set with respect to D. The inverse distance-2 domination number ${\gamma_{\leq 2}}^{-1}(G)$ of G is the minimum cardinality of the minimal inverse distance-2 dominating set of G. In this paper, we presented an algorithm for finding an inverse distance-2 dominating set of a graph.

1 Introduction

All graphs considered here are simple, finite, connected, and undirected. In this paper, the terms and notations used may be found in [7, 8]. A non-empty set $D \subseteq V(G)$ is said to be a dominating set of G if every vertex in $V - D$ is adjacent to at least one vertex in D [2]. A dominating set D is called a minimal dominating set if no proper subset of D is a dominating set. The domination number $\gamma(G)$ is the minimum cardinality taken over all the minimal dominating sets of G [12, 16].

Kulli V.R. and Sigarkanti S.C. introduced the concept of inverse domination in graph in 1991 [10].

Let D be a minimum dominating set in a graph $G = (V, E)$. If $V - D$ contains a dominating set $D^{'}$ of G, then $D^{'}$ is called an inverse dominating set with respect to D [3]. The inverse domination number $\gamma^{-1}(G)$ of G is the cardinality of a smallest inverse dominating set of G [13, 14].

K. A. Bibi · A. Lakshmi
PG and Research Department of Mathematics, D.K.M College for Women (Autonomous), Vellore, India

R. Jothilakshmi (✉)
PG and Research Department of Mathematics, Mazharul Uloom College, Ambur, India

B. Rushi Kumar et al. (eds.), *Applied Mathematics and Scientific Computing*, Trends in Mathematics, https://doi.org/10.1007/978-3-030-01123-9_44

Fig. 1 Figure (a)

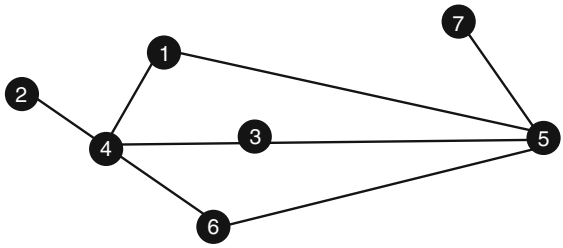

A non-empty set D in a graph $G = (V, E)$ is a distance-2 dominating set if every vertex in $V - D$ is within the distance two of at least one vertex in D [6]. The distance-2 domination number $\gamma_{\leq 2}(G)$ of G equals the minimum cardinality of a minimal distance-2 dominating set in G [5, 11].

A distance-2 dominating set D is called a minimal distance-2 dominating set if no proper subset of D is a distance-2 dominating set (Fig. 1).

Definition 1 Let D be the minimum distance-2 dominating set in a graph $G = (V, E)$. If $V - D$ contains a distance-2 dominating set D' of G, then D' is called an inverse distance-2 dominating set with respect to D. The inverse distance-2 domination number ${\gamma_{\leq 2}}^{-1}(G)$ of G is the cardinality of the smallest inverse distance-2 dominating set of G [4, 15].

Example 1 Here minimum distance-2 dominating set is $\{1\}$,$\gamma_{\leq 2}(G) = 1$, and inverse distance-2 dominating set is $\{3\}$, ${\gamma_{\leq 2}}^{-1}(G) = 1$.

We use the following algorithm which is presented in [1], and it is utilized in this algorithm.

2 Proposed Algorithm for Minimum Distance-2 Dominating Set

This algorithm gives the minimum distance-2 dominating set of a graph.

The algorithm works with the following steps.

Step 1: All the vertices in V are initialized with white color.

Step 2: We select a vertex in V which has the maximum degree (in case we have any vertices that are equal to the maximum degree, arbitrarily select any one), changes from white color to red color and sends a notification to all its neighbors within the distance two. On receiving this notification, the white color neighbor vertices within the distance two turn into green color.

Step 3: Now we select any one white color vertex in V.

Case 1: If the white color vertex has maximum degree (in case we have any vertices that are equal to the maximum degree, we select any one) and not adjacent to any green color vertex in the remaining vertices of V.

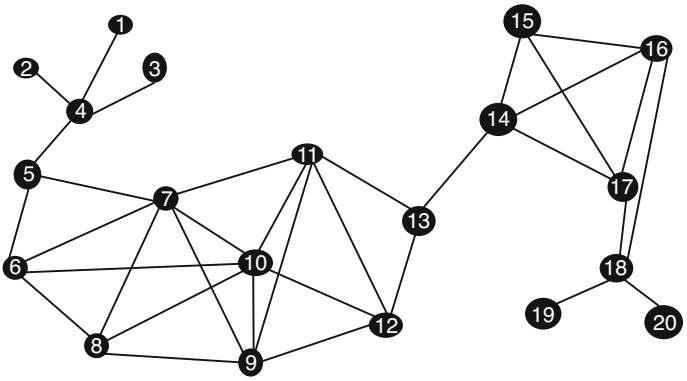

Fig. 2 Figure (b)

Case 2: If the green color vertex which is exactly at the distance two and has more than one pendent vertex, then change the green color vertex into red color vertex.

Step 4: Repeat the above process (Steps 2–3) until there is no more white color vertex in the graph.

Step 5: Now, all the red color vertices in the graph form a minimum distance-2 dominating set.

Example 2 Consider the following graph with 20 vertices in V. Now, by applying the vertex sorting procedure in [9], i.e., arranging the vertices in the decreasing order of their degrees, we can deduce $V = \{7, 10, 9, 11, 4, 6, 8, 12, 14, 16, 17, 18, 5, 13, 15, 1, 2, 3, 19, 20\}$.

Step 1: All 20 vertices are initialized with white color as shown in Fig. 2.

Step 2: We select a vertex 7 in V (here the maximum degree is 6) which has maximum degree (in case we have two vertices 7 and 10 that are equal to maximum degree 6, we select vertex 7); change its color to red and send a notification to all its neighbors within the distance two. On receiving this notification, the white color neighbor vertices within the distance two are turn into green color (vertices 4,5,6,8,9,10,11,12, and 13) as shown in Fig. 3.

Step 3: Now we select any one white color vertex in V.

Case 1: If we select the white color vertex 17 which has maximum degree 4 (here vertices14, 16, and 18 have the same degree, so we select any one) and not adjacent to any green color vertex in the remaining vertices of V.

Step 4: Repeat the above process; the vertex 17 changes its color to red and sends a notification to all its neighbors within the distance two. On receiving this notification, the white color neighbor vertices within the distance two are turned into green color (vertices 14,15,16,18,19, and 20) as shown in Fig. 3.

Case 2: If the green color vertex 4 which is exactly at the distance two and has more than one pendent vertex (pendent vertices 1, 2, 3), then change the green color vertex into red color vertex as shown in Fig. 3.

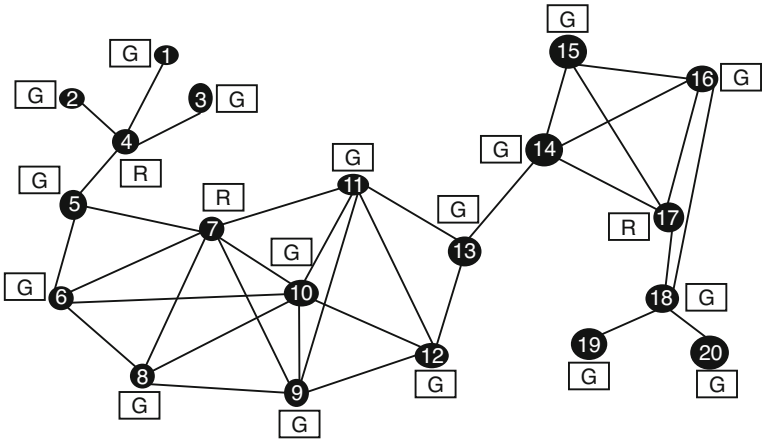

Fig. 3 Figure (c)

Step 4: Now there are no more white color vertex in the graph.

Step 5: Now, all the red color vertices in the graph form a minimum distance-2 dominating set, i.e., the minimum distance-2 dominating set is $D = \{4, 7, 17\}$.

3 Proposed Algorithm for Inverse Distance-2 Dominating Set

Step 1: First we find the minimum distance-2 dominating set in a graph using the above algorithm. And also mark those vertices in red color and the remaining vertices in green color.

Step 2: Now we consider only green color vertices to finding an inverse distance-2 dominating set in G. Select a green color vertex which has the maximum degree in G (red color vertices are not included). Change its color into blue color, and send a notification to all its neighbors within the distance two. On receiving this notification, the green color neighbor vertices within the distance two are turned into yellow color (if any red color vertices are in the distance, don't change the color).

Step 3: Now we select any one green color vertex in V.

Case 1: If any green color vertex has the maximum degree (in case we have any vertices having equal maximum degree, we select any one) and not adjacent to any yellow color vertex in the remaining green color vertices of V.

Case 2: If any yellow color vertex which is exactly at the distance two to at least a blue color vertex and has more than one pendent vertex, then change the yellow color vertex into blue color vertex.

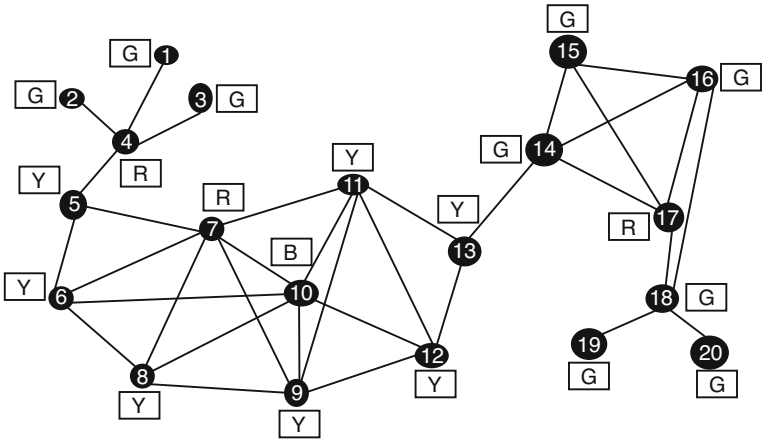

Fig. 4 Figure (d)

Case 3: If any yellow color vertex which is one and only vertex adjacent to a red color vertex exactly at the distance two and the red color vertex has one or more than one pendent vertices, then change the yellow color vertex into blue color vertex.

Step 4: Repeat the above process (Steps 2–3) until there is no more green color vertex in the graph.

Step 5: Now, all the blue color vertices in the graph form an inverse distance-2 dominating set D' of the graph.

Example 3 Consider the following graph with 20 vertices in V.

Step 1: First, we find the minimum distance-2 dominating set D in a graph G using the above algorithm. Also mark those vertices in red color and the remaining vertices in green color as shown in Fig. 3.

Step 2: Now, we consider only green color vertices to find an inverse distance-2 dominating set in G. We select a vertex 10 in V which has the maximum degree 6, change its color to blue, and send a notification to all its neighbors within the distance two. (Red color vertices are not included.) Change its color into blue color, and send a notification to all its neighbors within the distance two. On receiving this notification, the green color neighbor vertices within the distance two are turned into yellow color (if any red color vertices are in the distance, don't change the color) (vertices 5, 6, 8, 9,11, 12, and 13) as shown in Fig. 4.

Step 3: Now we select any one green color vertex in V.

Case 1: If we select the green color vertex 16 which has the maximum degree 4 (here vertices 16 and 18 have the same degree, so we select any one) and not adjacent to any yellow color vertex in the remaining green color vertices of V as shown in Fig. 5.

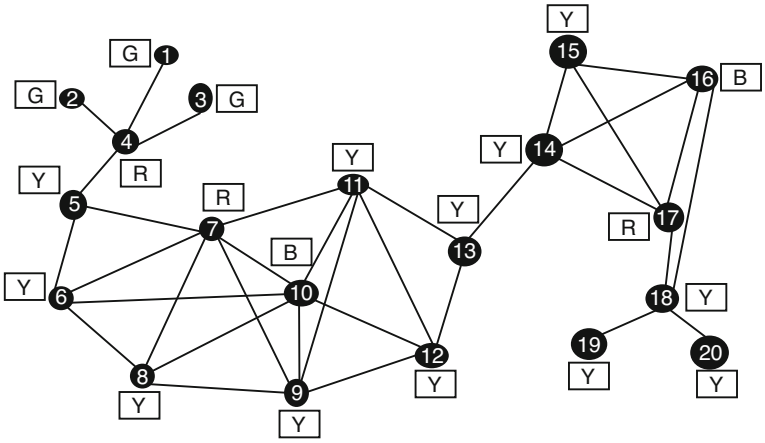

Fig. 5 Figure (e)

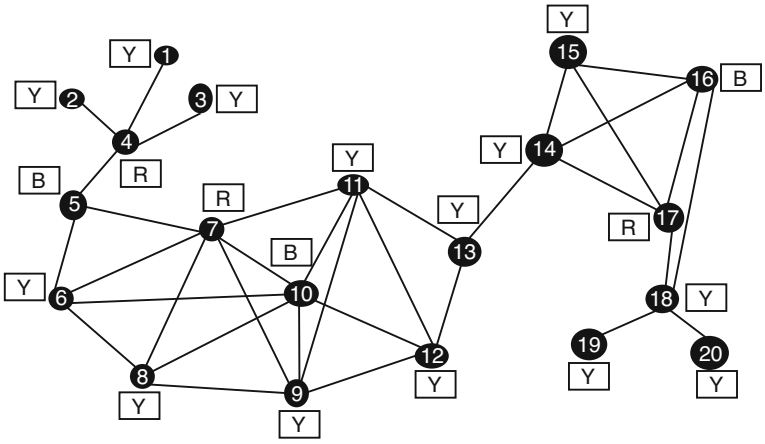

Fig. 6 Figure (f)

Case 3: If we select the yellow color vertex 5 which has one and only adjacent to a red color vertex 4 exactly at the distance two and the red color vertex has more than one pendent vertices, then change the yellow color vertex into blue color vertex as shown in Fig. 6.

Step 4: Repeat the above process (Steps 2–3) until there is no more green color vertex in the graph.

Step 5: Now, all the blue color vertices in the graph form an inverse distance-2 dominating set $D^{'} = \{5, 10, 16\}$ of the graph.

References

1. K. Ameenal Bibi, A. Lakshmi and R. Jothilakshmi, (2017), *An Algorithm for Minimal and Minimum distance - 2 dominating sets of Graph*, Global Journal of pure and applied Mathematics, ISSN -0978-1768 vol.13, No.2, pp. 1117–1126.
2. E.J. Cockayne, S.T. Hedetniemi, (1977) *"Towards a Theory of Domination in Graphs"*, Networks, 7, pp. 247–261.
3. T.H. Cormen, C.E. Leiserson, R.L. Riest and C. Stein, *"Introduction to Algorithms",* 2^{nd} Edition, MIT Press, 2001.
4. B. Das and V. Bharghavan , *"Routing in Ad Hoc Networks Using Minimum Connected Dominating set"*, in Proceedings of International Conference on Communications' 97, Montreal, Canada. June 1997.
5. J.R Griggs and J.P. Hutchinson, *"On the r-domination number of a graph"*, Discrete Mathematics, 101, 1992, pp. 65–72.
6. S. Guha and S. Khuller, "Approximation Algorithm for connected dominating sets", Algorithmica, vol. 20, no.4, pp. 374–387. Apr. 1998.
7. F. Harary, *"Graph Theory"*, Addison – wesley, Massachusetts, 1969.
8. T.W. Haynes, S.T. Hedetniemi, P.J. Slater, *"Fundamentals of Domination in Graphs"*, Marcel Dekker Publishers, New York, 1998.
9. Mallikarjun Avula, Seong-Moo and Seungjin Park, *"Constructing Minimum Connected Dominating Set in Mobile Ad Hoc Networks"*, published in International journal on applications of graph theory in wireless ad hoc networks and sensor networks, Vol 4, No.2/3, Sep 2012, pp. 15–27.
10. Mano Yadav, Vinay Rishiwal, G. Arora and S. Makka, "Modified Minimum Connected Dominating set formation for Wireless Adhoc Networks", in Journal of Computing, Vol 1, Issue 1, Dec 2009, pp. 200–203.
11. K. Sakai, M.T. Sun and W.S. Ku and Hiromi Okada, *"Maintaining CDS in Mobile Ad hoc Networks"*, wireless Algorithms Systems and Applications, Lecture Note in Computer Science, 2008, Vol 5258, pp. 141–153.
12. P.J. Slater,*"R-Domination in Graphs*," Journal of Association for Computer Machinery, 23(3), July 1976, pp. 446–450.
13. N. Sridharan, V.S.A. Subramanian and M.D. Elias, *"Bounds on the Distance Two- Domination Number of a Graph, Graphs and Combinatorics"*, Journal of Association for Computer Machinery,18(3), 2002, pp. 997–675.
14. S.K. Vaidya, N.J. Kothari, *"Distance k-domination of some path related graphs"*, International Journal of Mathematics and Soft Computing, Vol. 4, 2014, pp. 1–5.
15. D.B. West, *Introduction to Graph Theory,* 2^{nd} Ed., Prentice Hall, Upper Saddle River, NJ, 2001, pp.116–118.
16. J. Wu and H.L. Li, *"On Calculating Connected Dominating Set for Efficient Routing in Ad Hoc Wireless Networks"*, in Proceedings of the 3^{rd} ACM International Workshop on Discrete Algorithms and Methods for Mobile Computing and Communications, 1999, pp 7–14.

γ-Chromatic Partition in Planar Graph Characterization

M. Yamuna and A. Elakkiya

Abstract A uniquely colorable graph G whose chromatic partition contains at least one γ-set is termed as a γ-uniquely colorable graph. We characterize the planarity of these graphs using the domination number of G.

1 Introduction

Dominating sets are used for characterizing graph properties. In [4] Zhou studied the dominating—χ—color number, $d_\chi(G)$. Three parameters involving independent domination are introduced by Arumugam et al. in [2]. In [9], Yamuna et al. have obtained a characterization of planar graphs when the graph G and $\bar{G}$ are γ stable. In [10, 11], Yamuna et al. introduced γ-uniquely colorable graphs and also provided the constructive characterization of γ-uniquely colorable trees and characterized planarity of complement of γ-uniquely colorable graphs. In [12, 13], Yamuna et al. introduced non-domination subdivision stable graphs (NDSSs) and characterized planarity of complement of NDSS graphs . In [8], Pinciu proved that for outer planar graphs where all bounded faces are three cycles, the problem of determining $\gamma_c(G)$ is equivalent to an art gallery problem. In [3], Battle et al. declared that every planar graph with nine points has a complement which is non planar. In [1], Akiyama et al. have characterized all graphs when G and $\bar{G}$ are outer planar. In [7], Enciso et al. have classified planar graph based on the complement of G.

M. Yamuna (✉) · A. Elakkiya
Department of Mathematics, Vellore Institute of Technology, Vellore, India
e-mail: myamuna@vit.ac.in

B. Rushi Kumar et al. (eds.), *Applied Mathematics and Scientific Computing*,
Trends in Mathematics, https://doi.org/10.1007/978-3-030-01123-9_45

2 Terminology

We consider simple undirected connected graphs G = (V, E), $|V|$ = n, $|E|$ = m. K_5 and $K_{3,3}$ are termed as Kuratowski's graph. For graph properties we refer to Harary [5]. A chromatic partition of a graph G is the partition of V (G) into disjoint-independent sets with smallest cardinality. If the minimum cardinality is unique, then G is said to be uniquely colorable. A set of vertices D in a graph G = (V, E) is a dominating set if every vertex of V-D is adjacent to some vertex of D. If D has the smallest possible cardinality of any dominating set of G, then D is called a minimum dominating set—abbreviated MDS. The cardinality of any MDS for G is called the domination number of G, and it is denoted by γ (G). A γ set denotes a dominating set for G with minimum cardinality. For domination properties, we refer to Haynes et al. [6].

3 Result and Discussion

3.1 γ—Uniquely Colorable Graphs

A uniquely colorable graph G whose chromatic partition contains at least one γ-set is termed as a γ-uniquely colorable graph (Fig. 1).
Since the chromatic partition contains at least one γ-set whenever P = $\{V_1, V_2, \ldots, V_k\}$ is a γ-chromatic partition, V_1 shall always denote a γ—set. So $|V_i| \geq |V_1|$ for every i = 2, 3, . . . , k

3.2 Characterization of Planarity of γ-Uniquely Colorable Graphs

The graph in Fig. 2a is planar and γ-uniquely colorable graph, while the graph in Fig. 2b is γ-uniquely colorable but not planar. So not all γ-uniquely colorable graphs are planar.

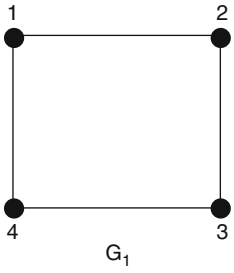

Fig. 1 γ-uniquely colorable graphs with γ-chromatic partition {1, 3}, {2, 4}

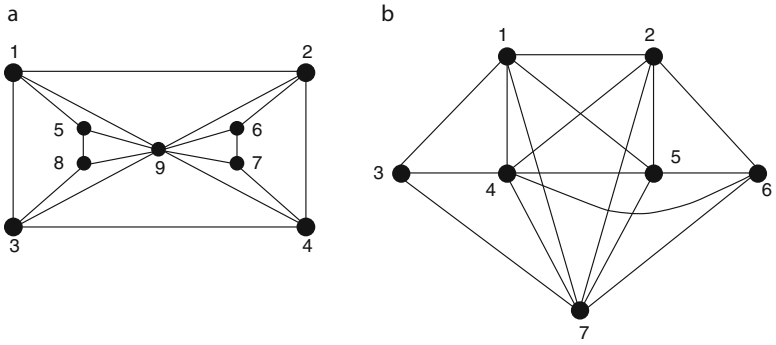

Fig. 2 Planar and nonplanar γ-uniquely colorable graph

Planar graphs are often characterized by the following famous theorems that use Kuratowski's graphs.

R_1. G is planar if and only if G does not contain K_5 or $K_{3,3}$ as a subgraph or any graph homeomorphic to K_5 or $K_{3,3}$ as a subgraph.

R_2. A graph is planar if and only if it does not have a subgraph contractible to K_5 or $K_{3,3}$.

We use these theorems for characterizing the planarity of γ—uniquely colorable graphs in this section.

Theorem 1 *A γ-uniquely colorable graph is planar if*

1. *γ (G) = 2 such that*
   - *$|P| = 2$*
   - *$|P| = 3$, $|V_i| = 2 \; \forall \; i = 1, 2, 3$ and*
2. *$3 \leq \gamma$ (G) ≤ 5 , $|P| = 2$, $|V_1| = |V_2|$*

Proof

1. γ (G) = 2, $|P| = 2$, $|V_1| = |V_2| = 2$
   Since $|V(G)| = 4$, G is always planar.
   γ (G) = 2 , $|P| = 2$, $|V_1| = 2$, $|V_2| = 3$
   Since $|V(G)| = 5$, $K_{3,3}$ is not possible.
   $\langle V_i \rangle$ is independent for i = 1, 2, implies $\langle V(G) \rangle$ is not K_5, implies G is always planar.
   γ (G) = 2, $|P| = 2$, $|V_1| = 2$, $|V_2|$ = k, $k \geq 5$.
   Let $V_1(G) = \{a_1, a_2\}$, $V_2(G) = \{b_1, b_2, \ldots, b_k\}$, $k \geq 4$. $\langle V_i(G) \rangle$ is independent, implies G is a bipartite graph with partition V_1, V_2. $\langle V_i \rangle$ is not K_5 or $K_{3,3}$. The graph G can have maximum 2k edges, since deg (b_i) = 2 for i = 1 to k . It is not possible to have five vertices of degree 4 or six vertices of degree 3 directly or by using edge contraction (since deg (b_i) = 2, the degree of the merged vertices does not change). In this case, it is never possible to have up to five vertices of degree 4 and six vertices of degree 3 with or without edge contraction.

By this discussion, we can conclude that when γ (G) = 2 , $|P| = 2$, G is always planar.

Let γ (G) = 5 , $V_1 = \{a_1, a_2, a_3, a_4, a_5\}$, $V_2 = \{b_1, b_2, b_3, b_4, b_5\}$. If $K_{3,3}$is a subgraph of G say $\langle a_1, a_2, a_3, b_1, b_2, b_3\rangle$ is $K_{3,3}$. Since G is a connected bipartite graph with partition V_1, V_2, a_4, a_5 are adjacent to at least one b_i. Similarly b_4 and b_5 are adjacent to at least one a_i. Remaining is the adjacency between a_4, a_5, b_4, and b_5 and the remaining vertices. Since G is connected, graph degree of any vertex is at least one. Let us consider the following possibilities when degree of at least one a_i or b_i = 1 , i = 4, 5 which is shown in Fig. 3.

In all the cases, $|\gamma(G)| < 5$, a contradiction to our assumption that γ (G) = 5.

All remaining possible γ-uniquely colorable graphs have at least one edge in addition to the edges in the above cases, which implies γ (G) < 5 in all possible cases implies $K_{3,3}$ is not a subgraph of G.

A. Since $K_{3,3}$ is not a subgraph of G, $K_{3,3}$ can be generated only upon edge contractions. If we choose five vertices in any V_i say in V_1 and one vertex in V_2, then for every two vertices in V_1, we require a distinct vertex in V_2 which is not possible, since we require additional ten vertices. Similarly if we choose four vertices from V_1 and two vertices from V_2, we need additional six vertices which is not possible. If three vertices from V_1 and three vertices from V_2 are chosen, then we need additional three vertices in each V_i, i = 1, 2 which is again not possible. Hence determining $K_{3,3}$ by edge contractions from G is not possible.

K_5 cannot be a subgraph of G, since G is a bipartite graph. If G is non planar, then K_5 can be generated by edge contractions only. Since $\langle V_i\rangle$, i = 1, 2 is independent, any edge between vertices in V_i can be created by edge contractions only. To create K_5 by edge contractions if we pick five vertices from any V_i say we pick a_i , i = 1 to 5, then to create edge between vertices in V_1 every pair of vertices in V_1 should be adjacent to a distinct vertex in V_2. Since $|V_1| = 5$, we require at least ten vertices in V_2 which is not possible.

Similarly, to create K_5 if we choose four vertices in V_1, then we require at least six vertices in V_2 which is not possible. So to create K_5, we can choose a maximum of three vertices in any V_i, i = 1, 2. To create K_5, let us choose a_1, a_2, a_3, b_1, b_2. To create K_5, we need edges between $\{a_1, a_2\}$, $\{a_1, a_3\}$, $\{a_2, a_3\}$, $\{b_1, b_2\}$,implies, we need three distinct b_i and at least one a_i adjacent to these pairs say a_1, a_2 adjacent to b_3, a_1, a_3 adjacent to b_4, a_2, a_3 adjacent to b_5, b_1, b_2 adjacent to a_4. a_5 is the only remaining vertex. Let $\langle a_1, a_2, a_3, b_1, b_2\rangle$ be $K_{2,3}$. The partial structure of graph G is as seen in Fig. 4.

$\{a_2, a_5, b_2, b_4\}$ is a γ set of cardinality 4, a contradiction since γ (G) = 4, implies K_5 cannot be generated from G by edge contraction. We have assumed $\langle a_1, a_2, a_3, b_1, b_2\rangle$ is $K_{2,3}$. Suppose $\langle a_1, a_2, a_3, b_1, b_2\rangle$ is not $K_{2,3}$, then the missing edges should be generated by edge contractions only. The only remaining vertex that can be used for edge contraction is a_5. $\langle V_i\rangle$ is independent. Hence a_5 cannot be used to create an edge between a_i, b_j, implies K_5 cannot be generated from G by edge contraction in this case.

Fig. 3 Partial graph structure

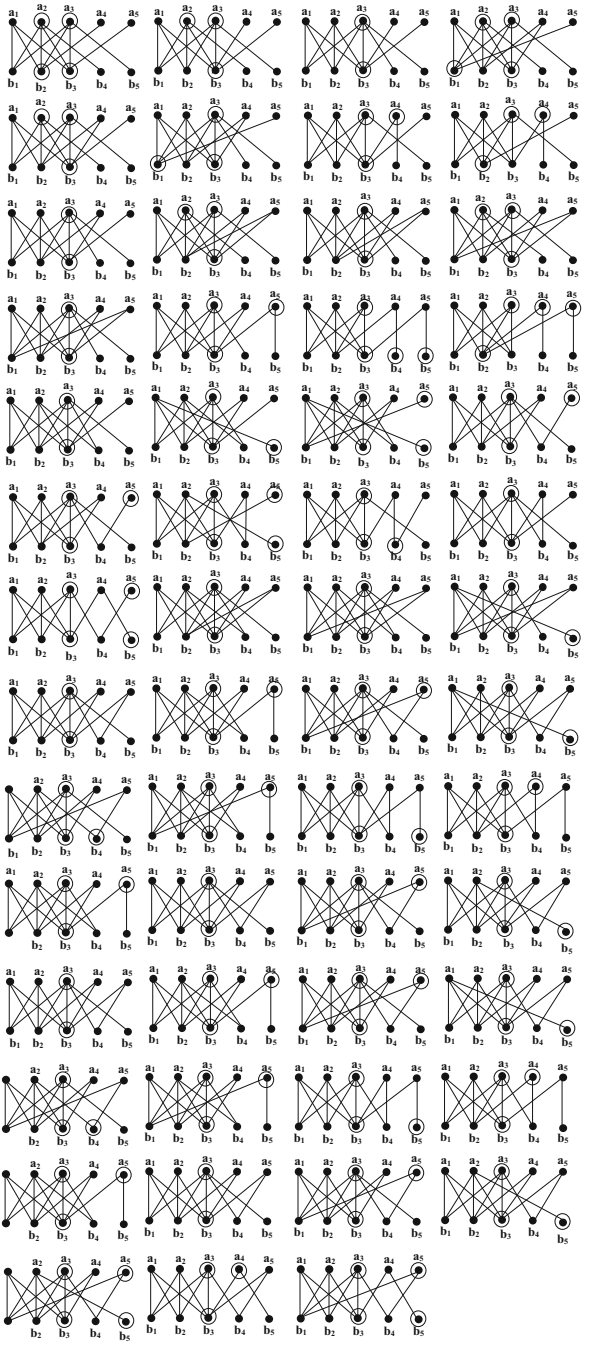

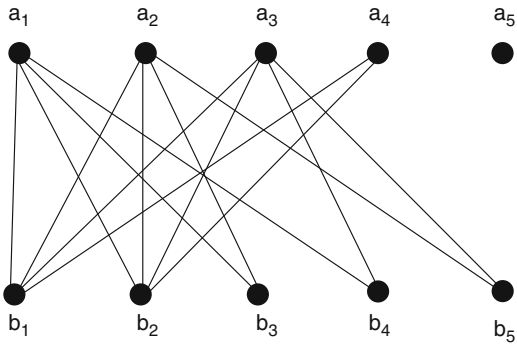

Fig. 4 Partial graph structure

From the above discussion, we conclude that K_5 cannot be a subgraph of G nor can be generated by edge contractions. In every other cases, when this is not true, $\langle a_1, a_2, a_3, b_1, b_2 \rangle$, is not K_5 (since the remaining edges cannot be create by edge contraction).

2. $|P| = 2$, such that $|V_1| = |V_2|$, γ (G) = 4
   Let $\gamma(G) = 4$, $V_1 = \{a_1, a_2, a_3, a_4\}$, $V_2 = \{b_1, b_2, b_3, b_4\}$. If $K_{3,3}$is a subgraph of G say $\langle a_1, a_2, a_3, b_1, b_2, b_3 \rangle$ is $K_{3,3}$. Since G is a connected bipartite graph with partition V_1, V_2, a_4 is adjacent to at least one b_i, and b_4 is adjacent to at least one a_i, i = 1, 2, 3, 4. Since G is a connected graph, degree of any vertex is at least one. Let us consider the following possibilities when degree of a_4 or b_4 is 1.

   a. a_4 is adjacent to b_4 and b_4 adjacent to some a_i, i = 1, 2, 3.
   In this case a_i, b_j, b_4 is a γ—set for G where i, j = 1 or 2 or 3.

   b. a_4 is adjacent some b_i and b_4 adjacent to some a_j, i , j = 1, 2, 3.
   In this case a_i, b_j is a γ—set for G.
   In both cases, $\gamma(G) \leq 4$, a contradiction to our assumption that$\gamma(G) = 4$.

   c. a_4 is adjacent to b_4, and a_4 is adjacent to some b_i, i = 1, 2, 3. This is analogues to a.

   All remaining possible γ-uniquely colorable graphs have at least one edge in addition to the edges in a, b, and c which implies $K_{3,3}$ is not a subgraph of G. By (A), we know that determining $K_{3,3}$ by edge contraction from G is not possible. K_5 cannot be a subgraph of G, since G is a bipartite graph. If G is non planar, then K_5 can be generated by edge contraction only. Since $\langle V_i \rangle$, i = 1, 2 is independent any edge between vertices in V_i can be created by edge contractions only. To create K_5 by edge contraction, if we pick four vertices from any V_i say we pick a_i, i = 1 to 4 then to create edges between these vertices in V_1 every pair of vertices in V_1 should be adjacent to a distinct in V_2. Since $|V_1| = 4$, we require at least six vertices in V_2 which is not possible. Similarly, if we choose three vertices in V_1, then we require at least three additional vertices (apart from the two used for creating K_5) which is not possible and implies that K_5 cannot be generated from G by edge contraction. From the above discussion, we conclude that K_5 cannot be a subgraph of G nor G can be generated by edge contraction.

3. $|P| = 2$, such that $|V_1| = |V_2|$, γ (G) = 3
   Let $\gamma(G) = 3$, $V_1 = \{a_1, a_2, a_3\}$, $V_2 = \{b_1, b_2, b_3\}$. $K_{3,3}$ is not a subgraph of G, since $\gamma(G) = 3$. Since $|V(G)| = 6$, $K_{3,3}$ cannot be determined by edge contraction. K_5 cannot be a subgraph of G, since G is a bipartite graph. If G is nonplanar, then K_5 should be generated by edge contractions only. Since $\langle V_i \rangle$, i = 1, 2 is independent edges between vertices in V_i can be generated edge contractions. To create K_5 by edge contractions if we randomly pick any five vertices say a_1, a_2, a_3, b_1, b_2, then we require at least four additional vertices to create edge between the independent pairs which is not possible. Hence K_5 cannot be generated by edge contractions.
4. $|P| = 3$ such that $|V_1| = |V_2| = |V_3| = 2$, γ (G) = 2
   Since $|P| = 3$, $|V_1| = 2$, and $\langle V_i \rangle$, i = 1, 2, 3, when we randomly pick five vertices, there is no edge between at least two pairs of vertices, implies K_5 cannot be a subgraph of G. Since $|V(G)| = 6$, when we partition V(G) into two sets say V (G) = $X_1 \cup X_2$, then $\exists$ one V_i, i = 1, 2, 3 such that $X_j \cap V_i \neq \phi$, j = 1, 2, implies there exist at least one vertex say u $\in X_1$, v $\in X_2$, such that u not adjacent to $K_{3,3}$ cannot be a subgraph of G. Since $|V(G)| = 6$, determining $K_{3,3}$, by edge contractions from G is not possible. If G is non planar, then K_5 can be generated by edge contractions. Since $\langle V_i \rangle$, i = 1, 2 is independent, any edge between vertices in V_i can be created by edge contractions only. To create K_5 by edge contractions if we pick two vertices from V_1, V_2 and one from V_3, then to create edge between vertices in V_1 ,V_2, we need two distinct vertices which is not possible since $|V(G)| = 6$. Hence determining K_5 by edge contractions from G is not possible.
   In all the cases, K_5 or $K_{3,3}$ is not a subgraph of G, and K_5 or $K_{3,3}$ cannot be determined by edge contractions. So we conclude that G is planar when it satisfies the condition of the theorem. □

4 Conclusion

γ sets are not in wide use to characterize graph planarity. In this paper, we define a new kind of partition containing a γ set and hence use it for characterizing a group of graphs as planar graphs.

References

1. Akiyama, J., Harary, F.: A Graph and its Complement with Specified Properties. I: Connectivity, Internat. J. Math Science. **2**, 223–228 (1979).
2. Arumugam, A. Ismail Sahul Hamid, I., Muthukamatchi, A.: Independent domination and graph colorings. Proceeding. of ICDM. 195–203 (2006).
3. Battle, B.J., Harary, F., Yukihiro: Every planar graph with nine points has a non planar complement. Communicated by Roger Lyndon. **68**, 569–571 (1962).

4. Bing Zhou: On the maximum number of dominating classes in graph coloring. Open Journal of Discrete Mathematics. **6**, 70–73 (2016).
5. Harary, F. 2011. *Graph Theory*. Addison Wesely, Narosa Publishing House.
6. Haynes,T. W., Hedetniemi, S. T. and Slater, P. J. 1998. *Fundamentals of Domination in Graphs*, Marcel Dekker, New York.
7. Rosa, I., Enciso Ronald, Dutton, D.: Global Domination in Planar Graphs. http://www.cs.ucf.edu/ renciso/Global Domination in Planar Grap.pdf.
8. Val Pinciu: Dominating Sets for Outerplanar Graphs. http://citeseerx.ist.psu.edu/viewdoc/download?doi=10.1.1.412.8672&rep=rep1&type=pdf.
9. Yamuna, M., Karthika,K.: Planar Graph Characterization - Using γ - Stable Graphs, WSEAS Transactions on Mathematics.**13**, 493–504 (2014).
10. Yamuna, M., Elakkiya, A.: γ - Uniquely colorable graphs, IOP Conf. Series: Materials Science and Engineering. **263** (2017).
11. Yamuna, M., Elakkiya, A.: Planar graph characterization of γ - Uniquely colorable graphs, IOP Conf. Series: Materials Science and Engineering. **263** (2017).
12. Yamuna, M., Elakkiya, A.: Non domination subdivision stable graphs, IOP Conf. Series: Materials Science and Engineering. **263** (2017).
13. Yamuna, M., Elakkiya, A.: Planar graph characterization of NDSS graphs, IOP Conf. Series: Materials Science and Engineering. **263** (2017).

Coding Through a Two Star and Super Mean Labeling

G. Uma Maheswari, G. Margaret Joan Jebarani, and V. Balaji

Abstract In this paper, a technique of coding a message is presented using the super mean labeling on a two star graph $K_{1,\,m} \cup K_{1,\,n},\ m \leq n$. A method of fixing the super mean labeling on any two star graph is provided after stating a few observations for a super mean labeling on a two star graph in order to use the combination of the two for coding.

2010 Mathematics Subject Classification 05C78

1 Introduction

A countless directions are available to the mind which moves in the pursuit of knowledge. Any concept selected for the search comforts one's mind when one is able to find a result of utility however insignificant it may be. A few techniques for coding a message secretly using super mean labeling on a two star graph $K_{1,\,m} \cup K_{1,\,n},\ m \leq n$ are presented through GMJ code.

GMJ code stands for: (1) Graph message jumble code. A coding technique to communicate a message through graphs jumbling letters is named as GMJ code. (2) It also refers to the name of one of the researchers of this paper (Gabriel Margaret Joan) who has conceived this method of coding. Also, a rule for the super mean labeling on any two stars is provided which will facilitate the assignment of numbers.

G. Uma Maheswari · V. Balaji (✉)
Department of Mathematics, Sacred Heart College, Tirupattur, India
e-mail: balajiv@shct.edu

G. Margaret Joan Jebarani
Department of Mathematics, Auxilium College, Vellore, India

B. Rushi Kumar et al. (eds.), *Applied Mathematics and Scientific Computing*,
Trends in Mathematics, https://doi.org/10.1007/978-3-030-01123-9_46

1.1 Literature Review

Much work is done by researchers on super mean labeling [2, 3, 6, 7]. Jeyanthi et al. have discussed super mean labeling on several infinite families of graphs [1]. The concept of coding labeled trees was introduced by Caminiti et al. [5]. Using graph theory and cryptography, a paper was presented by Read [4]. Motivated by this work, we have introduced a few techniques of coding by using super mean labeling on a two-star graph.

2 Prerequisites

Definition 1 (Super Mean Labeling) Let G be a (p, q) graph and $f : V(G) \rightarrow \{1,2,3,\cdots,p+q\}$ be an injection. For each edge $e=uv$,, let $f^*(e)=\frac{f(u)+f(v)}{2}$ if $f(u)+f(v)$ is even and $f^*(e)=\frac{f(u)+f(v)+1}{2}$ if $f(u)+f(v)$ is odd. Then f is called super mean labeling if $f(V) \cup \{f^*(e) : e \in E(G)\} = \{1,2,3,\cdots,p+q\}$. A graph that admits super mean labeling is called a super mean graph.

2.1 A Rule for Labeling

1. Some observations on super mean labeling of $K_{1,m} \cup K_{1,n}, m \leq n$ are listed. Here p and q represent the number of vertices and edges, $p = 2+m+n, q = m+n, p+q = 2+2m+2n$. The numbers from 1 to $2+2m+2n$ must be assigned to the top vertices and the pendant vertices, and in the process, the edge values get allotted. Repetition is not permitted. Here $f(u)$, $f(v)$, $f(u_i)$, and $f(v_j)$ are the numbers assigned to the top vertices and the pendant vertices, and $f^*(uu_i)$ and $f^*(vv_j)$ are the numbers assigned to the edges of the first and the second star, respectively. The rule for getting the edge values is $f^*(uu_i) = \frac{f(u)+f(u_i)}{2}$or $f^*(uu_i) = \frac{f(u)+f(u_i)+1}{2}$ where the edge connects u and u_i. Note that the edge value can be the actual or adjusted mean. The average of the largest and the previous number is $\frac{(2+2m+2n)+(2+2m+2n-1)}{2} = 2+2m+2n$. As repetition is not allowed, this combination is not considered. Hence neither the edge value nor the pendant vertices can exceed $2+2m+2n$. So it becomes possible to label a two-star $K_{1,m} \cup K_{1,n}$ through super mean labeling for all values of m and n without omitting any number between 1 and $(p+q)$ with $m \leq n$.
2. If ($f(u)$ and $f(u_i)$) or ($f(v)$ and $f(v_i)$) are both odd or both even, then the edge value is the actual mean. If they are not alike, then the edge value assumes the adjusted mean.
3. When f(u) is odd and if $f(u_i) = 2s$, $f(u_{i+1}) = 2s+1$,, they lead to same edge value and hence to be avoided, that is, $\frac{1+6}{2}$ and $\frac{1+7}{2}$ have the same edge value

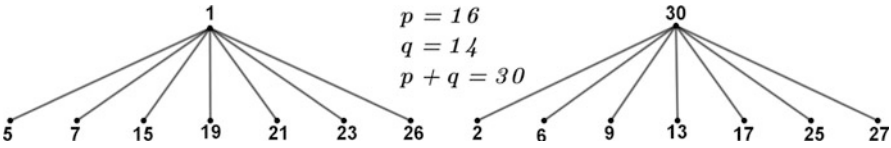

Fig. 1 $K_{1,7} \cup K_{1,7}$

4 when $f(u) = 1$. When $f(u_i) = 2s + 1$ and $f(u_{i+1}) = 2s + 2$, they give different edge values and hence can be assigned. That is, $\frac{1+7}{2} = 4$ and $\frac{1+8}{2} = 5$ give different edge values.

Also when f(u) is even, the situation is reversed. These are to be noted while labeling the numbers to the pendant vertices.

Step 1: Take 1 and $p + q$ as $f(u)$ and $f(v)$, respectively. $f(u_i) \neq 2$, for the edge value becomes 2, but $f(v_i) = 2$ is permitted.

Step 2: If $f(u_1) = 3$, then $f(v_1) = 4$ and if $f(u_1) = 5$, then $f(v_1) = 2$. That is, assign a value to u_1 and assign the next possible least integer to v_1 of the second star, the u_2 and v_2 are labeled proceeding in the same manner. Once or twice we may have to continue with assigning to $u_i's$ successively in order to avoid any repetition. This procedure makes labeling a two star graph easy using super mean labeling. A two star graph with super mean labeling is given above (Fig. 1).

2.2 GMJ Coding Method

By assigning numbers to the 26 alphabets of English in a different manner, choosing a suitable labeled graph with a given clue mathematical or non-mathematical, finding the number in the graph for each letter of each word of the given message, and presenting the letter codes in a unique way in some form such as a horizontal string and the codes by a picture shuffling the order of the letters in order to increase the secrecy of the coded message is named as GMJ coding method.

2.3 Procedure for Encoding

Step 1: A suitable two star graph has to be taken. A clue, mathematical or non-mathematical is stated to find the two star graph which is to be used.

Step 2: By using the super mean labeling on this two star, numbers from 1 to $(p+q)$ are assigned to the top vertices and the pendant vertices and thereby the edge values get fixed. The rule given in 2.1 (step 2) goes a long way in fixing the super mean labeling on the two star.

Step 3: The 26 alphabets of English are divided in some way (using GMJ coding), and the numbers attached to the alphabets are noted down.

Step 4: The Greek letters α and $\beta$are used to refer to the first and second star, respectively. T, E_i and P_i denote the top vertex, the ith pendant vertex, and the ith edge value in order. For example, $\alpha(P_i)$ denotes the number assigned to the ith pendant vertex of the first star.

Step 5: The message to be coded is written (wordwise).

Step 6: By using the notations stated in step 4, the coding is written along a horizontal string with (1,1) denoting the space between the words.

Step 7: Present the coding in a shape desired, shuffling the order of the letters.

Step 8: For decoding the message, the instructions given for coding and a knowledge of super mean labeling on any two-star graph $K_{1,\,m} \cup K_{1,\,n}$, $m \leq n$ are required.

Illustration 1

1. Message: Valleyside Bamboo Bridge.

2. Clue: A special prime twinkling perfect one. (Special prime -2, it is the only even number which is prime, twinkling-referring to a Star. So, a two star is understood. First perfect number is 6. Therefore the required graph is ($K_{1,\,6} \cup K_{1,\,6}$.)

3. Labeling: The super mean labeling done for $K_{1,\,6} \cup K_{1,\,6}$ is shown below
$K_{1,\,6} \cup K_{1,\,6}$, $p = 14$, $q = 12$, $p + q = 26$
$f(u) = 1$, $f(u_1) = 5$, $f(u_2)v7$, $f(u_3) = 15$, $f(u_4) = 19$, $f(u_5) = 21$, $f(u_6) = 23$,
$f(v) = 26$, $f(v_1) = 2$, $f(v_2) = 6$, $f(v_3) = 9$, $f(v_4) = 13$, $f(v_5) = 17$, $f(v_6) = 24$.

1	26	2	25	3	24	4	23	5	22	6	21	7	20	8	19	9	18	10	17	11	16	12	15	13	14
A	B	C	D	E	F	G	H	I	J	K	L	M	N	O	P	Q	R	S	T	U	V	W	X	Y	Z

4. Numbering of alphabets: OFEB The numbers 1–13 and 14–26 are allotted to the odd- and even-positioned alphabets moving forward and backward from A to C to E and Z to X to V and so on; this method is named as OFEB (odds forward, evens backward).

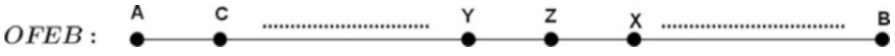

We express the numbering of alphabets in terms of a function for encoding.
For decoding we reverse the process. Coding is done word by word using OFEB to get the number for any letter and search for it in the two star graph labeled.

$$\begin{array}{lll} g(2k+1) = k+1 & \text{for} & k = 0, 1, \cdots, 12 \\ g(2k) = (27-k) & \text{for} & k = 1, 2, \cdots, 13 \end{array}$$

5. Coding: (wordwise) Valleyside - $\beta(E_2)\alpha(T)\alpha(P_5)\alpha(P_5)\alpha(E_1)\beta(P_4)\alpha(E_4)\alpha(P_1)\beta(E_6)\alpha(E_1)$
bamboo - $\beta(T)\alpha(T)\alpha(P_2)\beta(T)\alpha(E_3)\alpha(E_3)$
bridge - $\beta(T)\beta(E_3)\alpha(P_1)\beta(E_6)\alpha(E_2)\alpha(E_1)$

6. Horizontal string: $\beta(E_2)\alpha(T)\alpha(P_5)\alpha(P_5)\alpha(E_1)\beta(P_4)\alpha(E_4)\alpha(P_1)\beta(E_6)\alpha(E_1)(1,1)\beta(T)\alpha(T)\alpha(P_2)$

$\beta(T)\alpha(E_3)\alpha(E_3)(1,1)\beta(T)\beta(E_3)\alpha(P_1)\beta(E_6)\alpha(E_2)\alpha(E_1)$ (1)

Illustration 2
For the same shape, graph, and sentence, a different coding pattern is used just for comparison.

1	6	7	2	8	9	10	11	3	12	13	14	15	16	17	4	18	19	20	21	22	23	24	25	5	26
A	B	C	D	E	F	G	H	I	J	K	L	M	N	O	P	Q	R	S	T	U	V	W	X	Y	Z

1. Numbering of alphabets: PSNF The alphabets in the position 1^2, 2^2, 3^2, 4^2 and 5^2 are given the numbers 1, 2, 3, 4, 5.
Then the letter B gets the number 6, C gets the number 7, and E gets the number 8 and so on. This method is named as PSNF (perfect square numbered first).

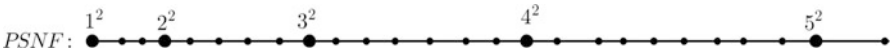

The function for encoding is given below

$$\begin{array}{ll} g(n^2) = n \text{ for } n = 1, 2, 3, 4, 5. & g(n^2+k) = 5+k, \text{ for } n = 1, k = 1, 2 \\ g(n^2+k) = 7+k, \text{ for } n = 2, k = 1, 2 \ldots, 4. & g(n^2+k) = 11+k, \text{ for } n = 3, k = 1, 2, \ldots, 6 \\ g(n^2+k) = 17+k, \text{ for } n = 4, k = 1, 2, \ldots, 8. & g(n^2+k) = 25+k, \text{ for } n = 5, k = 1 \end{array}$$

Coding is done word by word using PSNF to get the number for any letter and search for it in the two star graph labeled.

2. Horizontal string: $\alpha(P_6)\alpha(T)\beta(E_1)\beta(E_1)\alpha(E_3)\alpha(P_1)\beta(E_4)\alpha(E_1)\beta(P_1)\alpha(E_3)(1,1)\beta(P_2)\alpha(T)\alpha(P_3)$

$\beta(P_2)\beta(P_5)\beta(P_5)(1,1)\beta(P_2)\alpha(P_4)\alpha(E_1)\beta(P_1)\alpha(E_4)\alpha(E_3)$ (2)

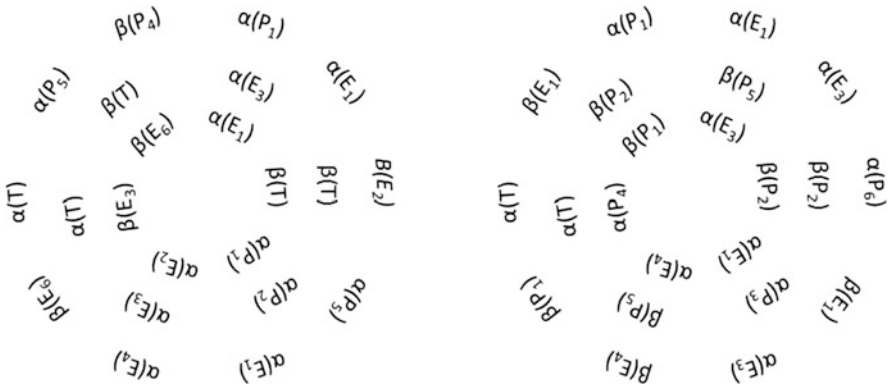

Fig. 2 Coded message (OFEB) Coded message (PSNF)

For the same sentence the codings are different with respect to the two methods OFEB and PSNF are seen from (1) and (2) and so the Illustrations 1 and 2 are given (Fig. 2).

Illustration 3

1. Message: The documents are in your purple briefcase intact.

2. Clue: Thrice the special prime and thrice its power. (Thrice the special prime $3 \times 2 = 6$ and thrice its power $2^3 = 8$)

3. Labeling: The super mean labeling done for $K_{1,6} \cup K_{1,8}$ is shown below

$K_{1,6} \cup K_{1,8}$, $p = 16, q = 14, p + q = 30$

$f(u) = 1$, $f(u_1) = 3$, $f(u_2) = 9$, $f(u_3) = 12$, $f(u_4) = 21$, $f(u_5) = 26$, $f(u_6) = 29$, $f(v) = 30$, $f(v_1) = 4$, $f(v_2) = 6$, $f(v_3) = 8$, $f(v_4) = 10$, $f(v_5) = 13$, $f(v_6) = 16$. $f(v_7) = 24$, $f(v_8) = 25$.

Numbering of alphabets and writing the coding are done as in Illustration 1 using OFEB.

4. Coding: (wordwise) After coding horizontal string is written (Fig. 3).

5. Horizontal string: $\beta(E_1)\beta(E_6)\alpha(P_1)(1,1)\beta(P_8)\beta(P_2)\alpha(E_1)\alpha(E_4)\alpha(E_3)$
$\alpha(P_1)\beta(E_4)\beta(E_1)\beta(P_4)(1,1)$
$\alpha(T)\beta(E_3)\alpha(P_1)(1,1)\alpha(E_2)\beta(E_4)(1,1)\beta(P_5)\beta(P_2)\alpha(E_4)\beta(E_3)(1,1)\beta(E_2)$
$\alpha(E_4)\beta(E_3)\beta(E_2)\alpha(P_4)\alpha(P_1)(1,1)\alpha(P_5)\beta(E_3)\alpha(E_2)\alpha(P_1)\beta(P_7)\alpha(E_1)\alpha(T)$
$\beta(P_4)\alpha(P_1)(1,1)\alpha(E_2)\beta(E_4)\beta(E_1)\alpha(T)\alpha(E_1)\beta(E_1)$

Illustration 4

1. Message: City 5 tallest building floor 34 room number 6.

2. Clue: Completeness and abundance marching together. (The number 7 stands for completeness and the number 8 for abundance)

$$\beta(E_4)\alpha(E_2)$$
$$\alpha(T)\alpha(P_1)\beta(E_3)$$
$$\beta(E_1)\alpha(P_1)\beta(E_6)$$
$$\beta(P_8)\alpha(E_1)\alpha(E_3)\beta(E_4)\beta(P_4)\beta(P_2)\alpha(E_4)\alpha(P_1)\beta(E_1)$$
$$\alpha(p_5)\alpha(E_2)\beta(P_7)\alpha(T)\alpha(P_1)\beta(E_3)\alpha(P_1)\alpha(E_1)\beta(P_4)$$
$$\beta(E_2)\beta(E_3)\alpha(P_4)\alpha(E_4)\beta(E_2)\alpha(P_1)$$
$$\alpha(E_2)\beta(E_1)\alpha(E_1)\beta(E_4)\alpha(T)\beta(E_1)$$
$$\beta(P_5)\alpha(E_4)\beta(P_2)\beta(E_3)$$

Fig. 3 Coded message (OFEB)

3. Labeling: The super mean labeling done for $K_{1,7} \cup K_{1,8}$ is shown below

$$K_{1,7} \cup K_{1,8},\ p = 17, q = 15,\ p + q = 32$$

$f(u) = 1$, $f(u_1) = 3$, $f(u_2) = 9$, $f(u_3) = 12$, $f(u_4) = 14$, $f(u_5) = 24$, $f(u_6) = 29$, $f(u_7) = 31$, $f(v) = 32$, $f(v_1) = 4$, $f(v_2) = 6$, $f(v_3) = 10$, $f(v_4) = 11$, $f(v_5) = 17$, $f(v_6) = 20$, $f(v_7) = 23$, $f(v_8) = 27$.

14	13	15	12	16	11	17	10	18	9	19	8	20	7	21	6	22	5	23	4	24	3	25	2	26	1
A	B	C	D	E	F	G	H	I	J	K	L	M	N	O	P	Q	R	S	T	U	V	W	X	Y	Z

4. Numbering of alphabets: EBOF The numbers 1–13 are allotted to the even-positioned alphabets moving backward from Z to X to V and so on. And the numbers 14–26 are allotted to the odd-positioned alphabets moving forward starting from A to C to E and so on. This method is named as EBOF (evens backward, odds forward).

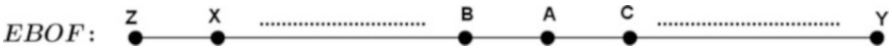

We express the numbering of alphabets in terms of a function for encoding. For even-positioned alphabets, the function g is given by,

$$g(k+1) = \left(\frac{27-k}{2}\right) \quad for \quad k = 1, 3, 5, \ldots, 25$$

For odd-positioned alphabets, the function g is given by,

$$g(k) = \left(\frac{27+k}{2}\right) \quad for\ k = 1, 3, 5, \ldots, 25.$$

For decoding we reverse the process.
By using EBOF and the super mean labeling on $K_{1,7} \cup K_{1,8}$, the message is encoded.

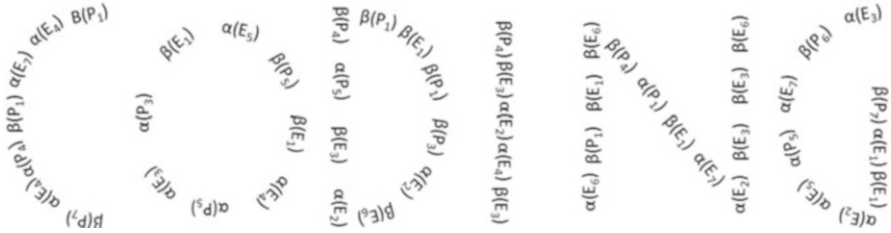

Fig. 4 Coded message (EBOF)

5. Coding: (wordwise) After coding Horizontal string is written (Fig. 4).

6. Horizontal string: $\alpha(E_6)\beta(E_1)\beta(P_1)\beta(E_6)(1,1)\beta(P_4)\beta(E_1)\alpha(P_1)\alpha(E_7)(1,1)$ $\beta(P_1)\alpha(P_4)\alpha(E_4)\alpha(E_4)\alpha(E_7)\beta(P_7)\beta(P_1)(1,1)\alpha(E_5)\alpha(P_5)\beta(E_1)\alpha(E_4)\alpha(P_3)$ $\beta(E_1)\alpha(E_3)\beta(P_5)(1,1)\beta(P_4)\alpha(E_4)\beta(E_3)\beta(E_3)\alpha(E_2)(1,1)\beta(P_1)\beta(P_3)\beta(E_1)$ $\alpha(E_2)\beta(P_1)\beta(E_6)(1,1)\beta(P_4)\beta(E_3)\alpha(P_5)\alpha(E_2)(1,1)\alpha(E_2)\beta(E_3)\beta(E_3)\beta(P_6)$ $(1,1)\alpha(E_3)\alpha(P_5)\beta(P_6)\alpha(E_5)\alpha(E_7)\alpha(E_2)(1,1)\beta(P_7)\beta(E_1)\alpha(E_1)$.

Illustration 5

1. Message: Stop be silent for zero six days.

2. Clue: One more than perfect single two less than perfect double. (Here perfect single refers to the first perfect number 6, one more than 6 is 7, perfect double is $6 \times 2 = 12$,2 less than this is 10, so the graph is $K_{1,\,7} \cup K_{1,\,10}$)

3. Labeling: The super mean labeling done for $K_{1,\,7} \cup K_{1,\,10}$ is shown below

$$K_{1,\,7} \cup K_{1,\,10},\ p = 19,\ q = 17,\ p + q = 36$$

$f(u) = 1$, $f(u_1) = 3$, $f(u_2) = 9$, $f(u_3) = 12$, $f(u_4) = 14$, $f(u_5) = 30$, $f(u_6) = 33$, $f(u_7) = 35$, $f(v) = 36$, $f(v_1) = 4$, $f(v_2) = 6$, $f(v_3) = 10$, $f(v_4) = 11$, $f(v_5) = 13$, $f(v_6) = 15$, $f(v_7) = 19$, $f(v_8) = 22$, $f(v_9) = 27$, $f(v_{10}) = 31$.

Numbering of alphabets and writing the coding are done as in Illustration 4 using EBOF.

4. Coding: (wordwise) After coding Horizontal string is written.

5. Horizontal string: $\beta(E_3)\beta(P_1)\beta(E_2)\beta(P_2)(1,1)\beta(P_5)\alpha(E_5)(1,1)\beta(E_3)\alpha(E_7)$ $\alpha(E_4)\alpha(E_5)\alpha(E_3)\beta(P_1)(1,1)\beta(P_4)\beta(E_2)\alpha(E_2)(1,1)\alpha(T)\alpha(E_5)\alpha(E_2)\beta(E_2)$

$$(1,1)\beta(E_3)\alpha(E_7)\alpha(E_1)(1,1)\alpha(P_3)\alpha(P_4)\beta(E_6)\beta(E_3). \tag{3}$$

Illustration 6

For the same shape, graph, and sentence, different coding pattern is used just for comparison. By using PSNF and the super mean labeling on $K_{1,\,7} \cup K_{1,\,10}$, the message is encoded.

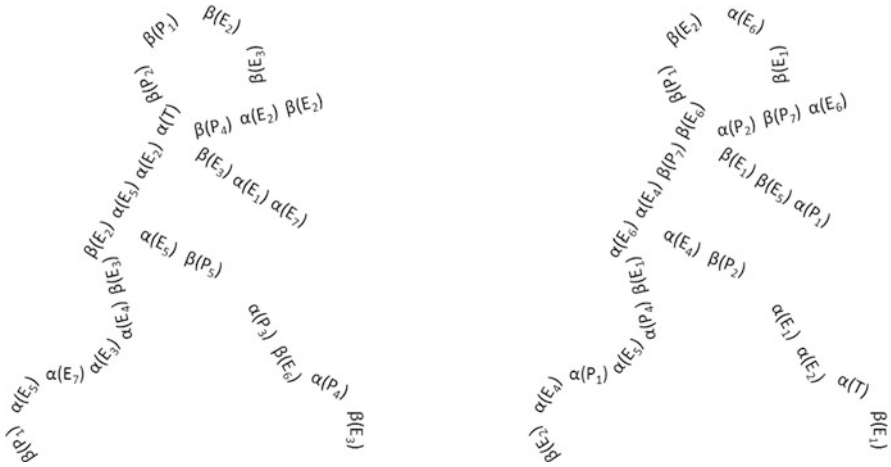

Fig. 5 Coded message (EBOF) Coded message (PSNF)

1. Horizontal string: $\beta(E_1)\beta(E_2)\alpha(E_6)\beta(P_1)(1,1)\beta(P_2)\alpha(E_4)(1,1)\beta(E_1)$
$\alpha(P_1)\alpha(P_4)\alpha(E_4)\alpha(E_5)\beta(E_2)(1,1)\alpha(P_2)\alpha(E_6)\beta(P_7)(1,1)\beta(E_6)\alpha(E_4)\beta(P_7)$

$\alpha(E_6)(1,1)\beta(E_1)\alpha(P_1)\beta(E_5)(1,1)\alpha(E_1)\alpha(T)\alpha(E_2)\beta(E_1)$

(4)

For the same sentence, the codings are different with respect to the two methods EBOF and PSNF are seen from (3) and (4) and so the Illustrations 5 and 6 are given (Fig. 5).

3 Conclusion and Future Work

In this paper we have used the super mean labeling on any suitable two-star graph for communicating some messages through different types of numbering of alphabets OFEB, EBOF, and PSNF for coding. The coded messages are given in pictures in order to make the understanding of the messages a bit difficult. Some more different techniques using super mean labeling on a three star graph for encoding messages are intended to be done.

References

1. P. Jeyanthi, D. Ramya and P. Thangavelu, On super mean graphs, AKCE Int.J.Graphs.combin., 6(1), (2009),103–112.
2. R.Ponraj and D.Ramya, on super mean graphs of order 5, Bulletin of pure and Applied sciences, (section E Maths and Statistics)., 25E (2006),143–148.

3. D. Ramya and P. Jeyanthi, Super mean labeling of some classes of graphs, International J.Math.combin.,1(2012), 83–91.
4. R.C Read, Graph Theory and the Amateur Cryptogapher Computer Math Applic., 34(11), 1997, 121–127.
5. Saverio Caminiti, Irene Finocchi and Rosella peterschi, On coding labeled trees, Theoretical computer science., 382(2007)97–108.
6. R.Vasuki and A.Nagarajan, Some results on super mean graphs, International Journal of Mathematical Combinatorics., 3 (2009), 82–96.
7. R.Vasuki and A. Nagarajan, On the construction of new classes of super mean graphs, Journal of Discrete Mathematical Sciences and Cryptography.,13 (3),(2010), 277–290.

Computing Status Connectivity Indices and Its Coindices of Composite Graphs

K. Pattabiraman and A. Santhakumar

Abstract This article is devoted to present the first status connectivity indices and its coindices of some composite graphs such as join, Cartesian product, corona product, and composition of two given connected graphs.

Mathematics Subject Classification 05C12, 05C76

1 Introduction

A mathematical measure which correlates to the chemical structures of simple finite graph is called topological index. In view of study in $QSAR/QSPR$, it plays a remarkable role. In theoretical chemistry, topological indices are widely used for modeling physicochemical, pharmacologic, toxicologic, nanoscience, biological, and other properties of chemical compounds. In fact the first topological index, namely, Wiener index, is proposed by Wiener [9]. For more details, see [3, 5–7].

Let v be a vertex in G. The sum of its distance from every other vertex in G is called the status [4] of v in G, and it is denoted by $\sigma_G(v)$, that is, $\sigma_G(v) = \sum_{u \in V(G)} d_G(u, v)$. Here $d_G(u, v)$ denotes the distance between u and v in G. The status of a vertex is also called as transmission of a vertex [4].

The Wiener index $W(G)$ of a connected graph G is defined as the sum of the distances between all pairs of vertices of G. This is equivalent to $W(G) = \frac{1}{2} \sum_{u,v \in V(G)} d_G(u, v) = \frac{1}{2} \sum_{u \in V(G)} \sigma_G(v)$.

K. Pattabiraman (✉)
Department of Mathematics, Annamalai University, Annamalainagar, India

A. Santhakumar
Department of Mathematics, CK College of Engineering and Technology, Cuddalore, India

B. Rushi Kumar et al. (eds.), *Applied Mathematics and Scientific Computing*,
Trends in Mathematics, https://doi.org/10.1007/978-3-030-01123-9_47

The first and second Zagreb indices of G are denoted by $M_1(G)$ and $M_2(G)$ which are defined as $M_1(G) = \sum u \in V(G)(d_G(u))^2 = \sum_{uv \in E(G)} (d_G(u) + d_G(v))$ and $M_2(G) = \sum_{uv \in E(G)} d_G(u)d_G(v)$, respectively. They are widely used in QSPR and QSAR studies as well; see [2]. Likewise, Ashrafi et al. [1] introduced the first and second Zagreb coindices of G denoted by $\overline{M}_1(G)$ and $\overline{M}_2(G)$ which are defined as $\overline{M}_1(G) = \sum_{uv \notin E(G)})(d_G(u)+d_G(v))$ and $\overline{M}_2(G) = \sum_{uv \notin E(G)} d_G(u)d_G(v)$, respectively.

Certainly the role of Zagreb indices is as motivating idea for first status connectivity index and its coindex which are furnished by Ramane and Yalnaik in [8]. Consequently of this, the first status connectivity index and its coindex of G denoted by $S_1(G)$ and $\overline{S}_1(G)$ are defined as $S_1(G) = \sum_{uv \in E(G)} \left(\sigma_G(u) + \sigma_G(v)\right)$ and $\overline{S}_1(G) = \sum_{uv \notin E(G)} \left(\sigma_G(u) + \sigma_G(v)\right)$, respectively. The first status connectivity index is equivalent to $S_1(G) = \sum_{u \in V(G)} d_G(u)\sigma_G(u)$. Here $d_G(u)$ is the degree of a vertex $u \in V(G)$.

Ramane and Yalnaik [8] gave the various upper and lower bounds for the status connectivity indices of a graph G. In addition, they have discussed the linear regression analysis of the distance-based indices with the boiling points of benzenoid hydrocarbons, and the linear model based on the status index is better than the models corresponding to the other distance-based indices. Hence, we obtain the exact formulae for first status connectivity indices and its coindices of composite graphs such as join, Cartesian product, corona product, and composition of two given connected graphs.

2 Composite Graphs

In this section, we obtain the first status connectivity indices and its coindices of join, Cartesian product, corona product, and composition of two given connected graphs.

Lemma 1 *If G is a graph with n vertices, then $\overline{S}_1(G) = 2(n-1)W(G) - S_1(G)$.*

Proof By the formula of $\overline{S}_1(G)$, we have $\overline{S}_1(G) = \sum_{uv \notin E(G)} (\sigma_G(u) + \sigma_G(v)) = \sum_{\{u,v\} \subseteq V(G)} (\sigma_G(u) + \sigma_G(v)) - \sum_{uv \in E(G)} (\sigma_G(u) + \sigma_G(v)) = 2(n-1)W(G) - S_1(G)$.

A path and cycle on n vertices are denoted by P_n and C_n, respectively. It is known that [8] $S_1(P_n) = \frac{1}{3}n(n-1)(2n-1)$ and $S_1(C_n) = \frac{n^3}{2}$ when n is even, and $\frac{n(n^2-1)}{2}$ otherwise. Similarly, one can easily observe that $W(P_n) = \frac{n(n^2-1)}{6}$ and $W(C_n) = \frac{n^3}{8}$ when n is even, and $\frac{n(n^2-1)}{8}$ otherwise.

2.1 Cartesian Product

The Cartesian product of G and H is denoted by $G \square H$, and it has the vertex set $V(G \square H) = V(G) \times V(H)$ and $(r_1, s_1)(r_2, s_2) \in E(G \square H)$ if $r_1 = r_2$ and $s_1 s_2 \in E(H)$ or $r_1 r_2 \in E(G)$ and $s_1 = s_2$.

Theorem 1 *If G and H are connected graphs with n_1, n_2 vertices and m_1, m_2 edges, respectively, then* $S_1(G \square H) = n_2^2 S_1(G) + n_1^2 S_1(H) + 4n_1 m_1 W(H) + 4n_2 m_2 W(G)$.

Proof From the structure of $G \square H$, the distance between (u_i, v_r) and (u_k, v_s) in $G \square H$ is $d_G(u_i, u_k) + d_H(v_r, v_s)$. Moreover, $d_{G \square H}((u_i, v_r)) = d_G(u_i) + d_H(v_r)$. By the definition of $\sigma(u)$ for $G \square H$ and $(u_i, v_r) \in V(G \square H)$, we have $\sigma_{G \square H}((u_i, v_r)) = \sum_{u_k \in V(G)} \sum_{v_s \in V(H)} \Big(d_G(u_i, u_k) + d_G(v_r, v_s) \Big) = n_2 \sigma_G(u_i) + n_1 \sigma_H(v_r)$. Hence

$$\begin{aligned}
S_1(G \square H) &= \sum_{(u_i, v_r) \in V(G \square H)} d_{G \square H}((u_i, v_r)) \sigma_{G \square H}((u_i, v_r)) \\
&= \sum_{u_i \in V(G)} \sum_{v_r \in V(H)} \Big(d_G(u_i) + d_H(v_r) \Big) \Big(n_2 \sigma_G(u_i) + n_1 \sigma_H(v_r) \Big) \\
&= \sum_{u_k \in V(G)} \sum_{v_r \in V(H)} \Big(n_2 d_G(u_i) \sigma_G(u_i) + n_1 d_G(u_i) \sigma_H(v_r) \\
&\quad + n_2 d_H(v_r) \sigma_G(u_i) + n_1 d_H(v_r) \sigma_H(v_r) \Big) \\
&= n_2^2 S_1(G) + n_1^2 S_1(H) + 4n_1 m_1 W(H) + 4n_2 m_2 W(G).
\end{aligned}$$

Let $G_1, G_2, \ldots, G_n$ be graphs with vertex set $V(G_i)$ and edge set $E(G_i)$, $1 \le i \le n$. The Cartesian product of $G_1, G_2, \ldots, G_n$ is denoted by $\prod_{i=1}^{n} G_i$. Obviously, $\left| V(\prod_{i=1}^{n} G_i) \right| = \prod_{i=1}^{n} |V(G_i)|$. By induction on n, it is easily verified that $\left| E(\prod_{i=1}^{n} G_i) \right| = \prod_{i=1}^{n} |V(G_i)| \sum_{i=1}^{n} \frac{|E(G_i)|}{|V(G_i)|}$. The proof of the following theorem follows from mathematical induction on number of graphs.

Theorem 2 *If $G_1, G_2, \ldots, G_n$ are connected graphs, then* $S_1(\prod_{i=1}^{n} G_i) = \sum_{i=1}^{n} S_1(G_i) \prod_{j=1, j \neq i}^{n} \big| V(G_j) \big|^2 + 4 \sum_{i,j=1 \, i \neq j}^{n} W(G_i) \big| V(G_j) \big| \big| E(G_j) \big| \prod_{k=1, i \neq k \neq j}^{n} |V(G_k)|^2$.

Corollary 1 *If G is a graph, then* $S_1(\square G^n) = S_1(\overset{n}{\underset{i=1}{\square}} G) = n\,|V(G)|^{2n-3}\left\{|V(G)|\ S_1(G) + 4(n-1)\,|E(G)|\,W(G)\right\}$.

Example 1 Suppose Q_n denotes the hypercube of dimension n. Then $S_1(Q_n) = S_1(\square K_2^n) = 2^{2n-1}n^2$.

Using Theorems 1 and 2 and $S_1(P_n)$,$S_1(C_n)$,$W(P_n)$ and $W(C_n)$, we obtain the exact value of S_1 for various graphs.

Example 2 The graphs $L_n = P_n\square K_2$, $R = P_n\square C_m$, $S = C_m\square C_n$, and $T = P_m\square P_n$ are known as ladder, C_4 nanotubes, C_4 nanotorus, and grid, respectively. The exact first status connectivity index and coindex of these graphs are given below.

(i) $S_1(L_n) = 2n\left[2n^2 + n - 2\right]$.

(ii) $$S_1(R) = \begin{cases} \frac{nm^2}{6}\left[8n^2 - 10n + 6mn - 3m + 2\right], & m \text{ is even} \\ \frac{nm}{6}\left[8n^2 - 16n + 6m^2n - 3m^2 + 5\right], & m \text{ is odd.} \end{cases}$$

(iii) $$S_1(S) = \begin{cases} nm(n+m)(nm-1), & m \text{ and } n \text{ are odd} \\ n^2m(m^2+nm-1), & m \text{ is odd and } n \text{ is even} \\ nm^2(n^2+nm-1), & m \text{ is even and } n \text{ is odd} \\ n^2m^2(n+m), & m \text{ and } n \text{ are even.} \end{cases}$$

(iv) $S_1(T) = \frac{nm}{3}\left[4nm(m+n) - 2(n^2+m^2) - 6mn - m - n + 4\right]$.

Theorem 3 *If G and H are graphs with n_1, n_2 vertices and m_1, m_2 edges, respectively, then* $\overline{S}_1(G\square H) = 2n_2\left[n_2(n_1n_2-1) - 2m_2\right]W(G) + 2n_1\left[n_1(n_1n_2 - 1) - 2m_1\right]W(H) - n_2^2S_1(G) - n_1^2S_1(H)$.

Proof By Theorem 1, Lemma 1 and this fact that [10], $W(G\square H) = n_2^2W(G) + n_1^2W(H)$, the proof is straightforward.

Using Theorem 3, we obtain the following.

Example 3 *(i)* $\overline{S}_1(L_n) = \frac{4m}{3}[2m^3 - m^2 - 5m + 3]$.

(ii) $$\overline{S}_1(R) = \begin{cases} \frac{nm^2}{12}\left[4n^3m + 3n^2m^2 - 43mn - 32n^2 + 60n + 18n - 8\right], \\ \qquad m \text{ is even} \\ \frac{nm}{12}\left[4m^2n^3 - 43nm^2 - 7n^2m + 3n^2m^2 - 48n^2 + 18m^2 + 4m \right. \\ \qquad \left. + 99n - 30\right], \ m \text{ is odd.} \end{cases}$$

$$(iii)\ \overline{S}_1(S) = \begin{cases} \frac{nm}{4}(nm-1)(nm^2+mn^2-5n-5m), & m \text{ and } n \text{ are odd} \\ \frac{nm}{4}(n^2m^3-6n^2m+m^2n^3-5nm^2+5n), & m \text{ is odd and } n \text{ is even} \\ \frac{nm}{4}(n^2m^3+n^3m^2-6nm^2-5mn^2+5m), & m \text{ is even and } n \text{ is odd} \\ \frac{n^2m^2}{4}(n+m)(nm-5), & m \text{ and } n \text{ are even.} \end{cases}$$

$$(iv)\ \overline{S}_1(T) = \frac{nm}{3}\Big[n^2m^2(m+n)-6nm(n+m)+2(n^2+m^2)+2(n+m)+6mn-4\Big].$$

2.2 Join

The *join* $G + H$ of G and H is denoted by $G + H$, and it is defined as the union $G \cup H$ together with all the edges joining $V(G)$ and $V(H)$. From the structure of $G + H$, the distance between two vertices u and v of $G + H$ is

$$d_{G+H}(u,v) = \begin{cases} 1, & \text{if } uv \in E(G) \text{ or } uv \in E(H) \text{ or } (u \in V(G) \text{ and } v \in V(H)) \\ 2, & \text{otherwise.} \end{cases}$$

Moreover, the degree of a vertex v in $V(G + H)$ is $d_G(v) + |V(H)|$ whenever $v \in V(G)$ and $d_H(v) + |V(G)|$ when $v \in V(H)$.

Theorem 4 *If G and H are graphs with n_1, n_2 vertices and m_1, m_2 edges, respectively, then $S_1(G+H) = (2m_1+n_1n_2)(2n_1+n_2-2)+(2m_2+n_1n_2)(2n_2+n_1-2) - M_1(G) - M_1(H) - 2n_1n_2(m_1+m_2)$.*

Proof Let $u \in V(G)$. Then from the structure of $G + H$, we obtain:

$$\begin{aligned} \sigma_{G+H}(u) &= \sum_{v\in V(G)\ u\neq v, uv\notin E(G)} (2) + \sum_{v\in V(G),\ u\neq v, uv\in E(G)} (1) + \sum_{v\in V(H)} (1) \\ &= 2n_1 + n_2 - 2 - d_G(u). \end{aligned}$$

Similarly, if $v \in V(H)$, then $\sigma_{G+H}(v) = 2n_2 + n_1 - 2 - d_G(v)$. Hence by the definition of S_1, we have

$$\begin{aligned} S_1(G+H) &= \sum_{u\in V(G)} \Big(d_G(u)+n_2\Big)\Big(2n_1+n_2-2-d_G(u)\Big) \\ &\quad + \sum_{u\in V(H)} \Big(d_H(u)+n_1\Big)\Big(2n_2+n_1-2-d_H(u)\Big) \\ &= \sum_{u\in V(G)} \Big((2n_1+n_2-2)d_G(u)-(d_G(u))^2+n_2(2n_1+n_2-2)-n_2d_G(u)\Big) \\ &\quad + \sum_{u\in V(H)} \Big((2n_2+n_1-2)d_H(u)-(d_H(u))^2+n_1(2n_2+n_1-2)-n_1d_H(u)\Big) \end{aligned}$$

$$= (2m_1 + n_1n_2)(2n_1 + n_2 - 2) - M_1(G) - 2n_1n_2m_1$$
$$+ (2m_2 + n_1n_2)(2n_2 + n_1 - 2) - M_1(H) - 2n_1n_2m_2.$$

According to [10], we know that $W(G + H) = |V(G)|(|V(G)| - 1) + |V(H)|(|V(H)| - 1) + |V(G)||V(H)| - |E(G)| - |E(H)|$ by this formula, Theorem 4 and Lemma 1, we obtain the following theorem.

Theorem 5 *If G and H are graphs with n_1, n_2 vertices and m_1, m_2 edges, respectively, then $\overline{S}_1(G+H) = n_1n_2(n_1+n_2+6)+6(m_1+m_2-n_1m_1-m_2n_2)-4(m_1n_2+m_2n_1)+2n_1n_2(m_1+m_2)+2(n_1+n_2)+2(n_1^3+n_2^3)-4(n_1^2+n_2^2)+M_1(G)+M_1(H)$.*

By using Theorems 4 and 5, we get the following.

Corollary 2 *If G is a graph with n vertices and m edges, then (i) $S_1(G + K_q) = 2m(2n + nq + q - 2) + nq(3n + 3q - 4) + q(q - 1)(n + q - nq - 1) - M_1(G)$.*

(ii) $\overline{S}_1(G + K_q) = 2(n^3 + q^3) - 4(n^2 + q^2) + 2(n + q) + nq(n + 2m + q + 6) - 2m(3n + 2q - 3) + q(q - 1)(2n + 4q + nq + 2) + M_1(G)$.

Corollary 3 *Let $K_{p,q} = \overline{K}_p + \overline{K}_q$. Then (i) $S_1(K_{p,q}) = pq(3p + 3q - 4)$.*
(ii) $\overline{S}_1(K_{p,q}) = 2(p^3 + q^3) - 4(p^2 + q^2) + 2(p + q) + pq(p + q + 6)$.

One can observe that $M_1(C_n) = 4n,\ n \geq 3,\ M_1(P_1) = 0,\ M_1(P_n) = 4n - 6,\ n > 1$. Using Corollary 2, $M_1(C_n)$ and $M_1(P_n)$, we compute the formulae for status connectivity indices and it coindices of *fan graph* $P_n + K_1$ and *wheel graph* $C_n + K_1$.

Example 4

(i) $S_1(P_n + K_1) = 9n^2 - 11n + 8$ and $\overline{S}_1(P_n + K_1) = 2n^3 - 7n^2 + 19n - 6$.

(ii) $S_1(C_n + K_1) = 9n^2 - 7n$ and $\overline{S}_1(C_n + K_1) = 2n^3 - 7n^2 + 15n$.

2.3 Composition

The *composition* of G and H is denoted by $G[H]$, and it has the vertex set $V(G) \times V(H)$. Two vertices (u_i, v_r) and (u_k, v_s) are adjacent in $G[H]$ if and only if $u_iu_k \in E(G)$ or $[u_i = u_k \text{ and } v_rv_s \in E(H)]$.

Theorem 6 *Let G and H be two connected graphs with n_1, n_2 vertices and m_1, m_2 edges, respectively. Then $S_1(G[H]) = n_2^3S_1(G) + 4n_2m_1W(G) - n_1M_1(H) + 4n_2^2m_1(n_2 - 1) + 4n_1m_2(n_2 - 1) - 4m_1m_2n_2$.*

Proof For the composition of two graphs, $d_{G[H]}((u, v)) = n_2d_G(u) + d_H(v)$. Moreover, the distance between two vertices (u_i, v_r) and (u_k, v_s) of $G[H]$ is

$$d_{G[H]}((u_i, v_r), (u_k, v_s)) = \begin{cases} d_G(u_i, u_k) & u_i \neq u_k \\ 2 & u_i = u_k,\ v_rv_s \notin E(H) \\ 1 & u_i = u_k,\ v_rv_s \in E(H). \end{cases} \quad \text{Let } (u_i, v_r) \in$$

$V(G[H])$. Then

$$\begin{aligned}\sigma_{G[H]}((u_i, v_r)) &= \sum_{(u_k,v_s)\in V(G[H]),\ u_i\neq u_k} d_G(u_i, u_k) \\ &\quad + \sum_{(u_i,v_s)\in V(G[H])} d_{G[H]}((u_i, v_r), (u_i, v_s)) \\ &= n_2\sigma_G(u_i) + d_H(v_r) + 2(n_2 - 1 - d_H(v_r)) \\ &= n_2\sigma_G(u_i) + 2(n_2 - 1) - d_H(v_r). \qquad (1)\end{aligned}$$

By the definition of S_1, we have

$$\begin{aligned}S_1(G[H]) &= \sum_{(u_i,v_r)\in V(G\square H)} d_{G[H]}((u_i, v_r))\sigma_{G[H]}((u_i, v_r)) \\ &= \sum_{u_i\in V(G)}\sum_{v_r\in V(H)} \Big(n_2 d_G(u_i)+d_H(v_r)\Big)\Big(n_2\sigma_G(u_i)+2(n_2-1)-d_H(v_r)\Big), \text{ by (1)} \\ &= \sum_{u_i\in V(G)}\sum_{v_r\in V(H)} \Big[n_2^2 d_G(u_i)\sigma_G(u_i) + 2(n_2 - 1)n_2 d_G(u_i) - n_2 d_G(u_i)d_H(v_r) \\ &\quad + n_2 d_H(v_r)\sigma_G(u_i) + 2(n_2 - 1)d_H(v_r) - (d_H(v_r))^2\Big] \\ &= n_2^3 S_1(G) + 4n_2 m_1 W(G) - n_1 M_1(H) + 4n_2^2 m_1(n_2 - 1) \\ &\quad + 4n_1 m_2(n_2 - 1) - 4m_1 m_2 n_2.\end{aligned}$$

Recall from [10] that $W(G[H]) = |V(H)|^2\,(W(G)+|V(G)|)-|V(G)|\,(|V(H)| + |E(H)|)$. According to $W(G[H])$ and $S_1(G[H])$, we get the following.

Theorem 7 *If G and H are graphs with n_1, n_2 vertices and m_1, m_2 edges, respectively, then* $\overline{S}_1(G[H]) = 2n_2\Big[n_2(n_1n_2 - 1) - 2m_1\Big]W(G) - n_2^3 S_1(G) - n_1 M_1(H) + 2n_1(n_1n_2)(n_2^2 - n_2 - m_2) - 4(n_2 - 1)(n_2^2 m_1 + n_1 m_2) - 4m_1 m_2 n_2$.

Using Theorems 6 and 7, we get the following.

Corollary 4 *If G be a connected graph with n vertices and m edges, then*

(i) $S_1(G[K_q]) = q^3 S_1(G) + 4qmW(G) + q(q - 1)(2mq + nq - n)$.

(ii) $\overline{S}_1(G[K_q]) = 2q[q(nq - 1) - 2m]W(G) - q^3 S_1(G) + q(q - 1)[nq^2 - 6mq - 3nq + 3n - q]$.

Using Corollary 4, we obtain the status connectivity indices and its coindices of open fence graph $P_n[K_2]$ and closed fence graph $C_n[P_2]$.

Example 5

(i) $S_1(P_n[K_2]) = \frac{4}{3}(n - 1)(n^3 + 4n^2 - 3n + 9)$.

(ii) $S_1(C_n[K_2]) = \begin{cases} n(n^3 + 4n^2 + 10), & n \text{ is even} \\ n(n^3 + 4n^2 - n + 6), & n \text{ is odd.} \end{cases}$

(iii) $\overline{S}_1(P_n[K_2]) = \frac{4}{3}n(n-1)(n^2+3n+2) + 2(11n+10)$.

(iv) $\overline{S}_1(C_n[K_2]) = \begin{cases} n^3(n-5) + 2(11n-2), & n \text{ is even} \\ n(n^2-1)(n-5) + 2(11n-2), & n \text{ is odd.} \end{cases}$

2.4 Corona Product

The *corona product* of G and H is denoted by $G \circ H$ and obtained by taking one copy of G and $|V(G)|$ copies of H and by joining each vertex of the ith copy of H to the ith vertex of G, where $1 \leq i \leq |V(G)|$.

Theorem 8 *Let G and H be two connected graphs with n_1, n_2 vertices and m_1, m_2 edges, respectively. Then* $S_1(G \circ H) = (n_2+1)S_1(G) + 4(n_2+1)(m_2+n_2)W(G) - n_1M_1(H) + n_1(2m_2+n_2)(2n_1n_2+n_1-2) + n_1(n_2(2m_1+n_1n_2) - 2m_2)$.

Proof If H_i is the ith copy of H, $i = 1, 2, \ldots, n_1$. Let $v \in V(H_i)$ and the ith vertex of G be u_i. Then by the structure of $G \circ H$, we obtain, $\sigma_{G\circ H}(v) = (n_2 + 1)\sigma_G(u_i) + 2n_1n_2 + n_1 - d_H(v) - 2$ and $\sigma_{G\circ H}(u_i) = (n_2+1)\sigma_G(u_i) + n_1n_2$. According to the definition of first status connectivity index, we get

$$S_1(G \circ H) = \sum_{i=1}^{n_1} \sum_{v \in V(H_i)} \Big(d_H(v)+1\Big)\Big((n_2+1)\sigma_G(u_i) + 2n_1n_2 + n_1 - d_H(v) - 2\Big)$$
$$+ \sum_{u_i \in V(G)} \Big(d_G(u_i)+n_2\Big)\Big((n_2+1)\sigma_G(u_i) + n_1n_2\Big) = A_1 + A_2, \text{ where}$$

$$A_1 = \sum_{i=1}^{n_1} \sum_{v \in V(H_i)} \Big(d_H(v)+1\Big)\Big((n_2+1)\sigma_G(u_i) + (2n_1n_2+n_1-2) - d_H(v)\Big)$$
$$= \sum_{i=1}^{n_1} \sum_{v \in V(H_i)} \Big((n_2+1)d_H(v)\sigma_G(u_i) + (2n_1n_2+n_1-2)d_H(v) - (d_H(v))^2$$
$$+(n_2+1)\sigma_G(u_i) + (2n_1n_2+n_1-2) - d_H(v)\Big)$$
$$= 2(2m_2+n_2)(n_2+1)W(G) - n_1M_1(H) + (2m_2+n_2)n_1(2n_1n_2+n_1-2)$$
$$-2n_1m_2.$$

$$A_2 = \sum_{u_i \in V(G)} \Big(d_G(u_i) + n_2\Big)\Big((n_2+1)\sigma_G(u_i) + n_1 n_2\Big)$$

$$= \sum_{u_i \in V(G)} \Big((n_2+1)d_G(u_i)\sigma_G(u_i) + n_1 n_2 d_G(u_i) + n_2(n_2+1)\sigma_G(u_i) + n_1 n_2^2\Big)$$

$$= (n_2+1)S_1(G) + 2n_2(n_2+1)W(G) + 2n_1 n_2 m_1 + n_1^2 n_2^2.$$

Adding A_1 and A_2, we obtain the desired result.

Using the formula [10], $W(G \circ H) = |V(G)|\,|V(H)|\,(|V(G)|\,|V(H)| + |V(G)| - 1) + (|V(H)|+1)^2 W(G) - |V(G)|\,|E(H)|$, $S_1(G \circ H)$ and Lemma 1, we get the following.

Theorem 9 *If G and H are graphs with n_1, n_2 vertices and m_1, m_2 edges, respectively, then* $\overline{S}_1(G \circ H) = 2(n_2+1)\big[(n_2+1)(n_1 n_2 + n_1 - 1) - 2(m_2 + n_2)\big]W(G) + n_1 M_1(H) - (n_2+1)S_1(G) + n_1 n_2\big[2(n_1 n_2 + n_1 - 1) - (2m_1 + n_1 n_2)\big] - 2n_1 m_2\big[n_1 n_2 + n_1 - 2\big] - n_1(2m_2 + n_2)(2n_1 n_2 + n_1 - 2)$.

Conclusion Ultimately, the degree and distance-based topological indices are widely used in mathematical chemistry which are helpful to study the properties of molecules. In this article, we have discussed two indices of various graph operations. Furthermore, as we found in this as tide, one can estimate the value of same indices for more classes of graphs.

References

1. Ashrafi A.R, Doslić T, Hamzeh A (2010) The Zagreb coindices of graph operations. Discrete Appl. Math. 158:1571–1578.
2. Devillers J, Balaban A.T Eds.(1999) Topological indices and related descriptors in QSAR and QSPR. Gordon and Breach, Amsterdam, The Netherlands.
3. Dobrynin A.A, Entringer R, Gutman I (2001) Wiener index of trees: Theory and applications. Acta Appl. Math. 66:211–249.
4. Harary F (1959) Status and contrastatus. Sociometry 22:23–43.
5. Pattabiraman K, Paulraja P(2012) On some topological indices of the tensor product of graphs. Discrete Appl. Math. 160: 267–279.
6. Pattabiraman K, Paulraja P(2012) Wiener and vertex PI indices of the strong product of graphs. Discuss. Math. Graph Theory 32:749–769.
7. Pattabiraman K, Paulraja P(2011) Wiener index of the tensor product of a path and a cycle. Discuss. Math. Graph Theory 31 :737–751.
8. Ramane H. S, Yalnaik A.S (2016) Status connectivity indices of graphs and its applications to the boiling point of benzenoid hydrocarbons. J. Appl. Math. Comput. https://doi.org/10.1007/s12190-016-1052-5
9. Wiener H (1947) Structural determination of the paraffin boiling points. J. Amer. Chem. Soc. 69: 17–20.
10. Yeh Y.N, Gutman I (1994) On the sum of all distances in composite graphs. Discrete Math. 135:359–365.

Laplacian Energy of Operations on Intuitionistic Fuzzy Graphs

E. Kartheek and S. Sharief Basha

Abstract The concept of Laplacian energy of an intuitionistic fuzzy graph is extended to Laplacian energy in operations on intuitionistic fuzzy graph. In this paper, we have obtained the value of Laplacian energy in different operations such as union and join between two intuitionistic fuzzy graphs. Also we study the relation between the Laplacian energy in the operations on two intuitionistic fuzzy graphs.

1 Introduction

Fuzzy set has emerged as a potential area of interdisciplinary research, and fuzzy graph theory is of recent interest. The concept of a fuzzy graph relation was defined by Zadeh [3], and it has found applications in the analysis of cluster patterns. Rosenfeld [1] considered the fuzzy relations on fuzzy sets and developed the structure of fuzzy graphs.

In this paper we are concerned with simple graphs. Let G be a graph with n vertices and m edges, and we say this G is a (n, m) graph.

Let d_i be the degree of ith vertex of G,i=1,2,. . . ,n. The spectrum of the graph G, consisting of the numbers $\lambda_1, \lambda_2, \ldots, \lambda_n$, is the spectrum of its adjacency matrix [2]. The Laplacian spectrum of the graph G ,consisting of the numbers $\mu_1, \mu_2, \ldots, \mu_n$, is the spectrum of its Laplacian matrix.

In this paper we introduce the concept of Laplacian energy of operations on intuitionistic fuzzy graphs. Section 2 consists of different operations such as union and join of two intuitionistic fuzzy graphs definition, and in this section ,we present the Laplacian energy of union and join of two intuitionistic fuzzy graphs . We give the conclusion in the last section.

E. Kartheek · S. Sharief Basha (✉)
Applied Algebra Division, School of Advanced Sciences, VIT University, Vellore, Tamilnadu, India

B. Rushi Kumar et al. (eds.), *Applied Mathematics and Scientific Computing*,
Trends in Mathematics, https://doi.org/10.1007/978-3-030-01123-9_48

2 Laplacian Energy of Some Operations on Intuitionistic Fuzzy Graphs

2.1 Laplacian Energy of Union of an Intuitionistic Fuzzy Graph

Definition 1 Union of Intuitionistic Fuzzy Graph Let $G_1 = (V_1, E_1)$and $G_2 = (V_2, E_2)$ be two intuitionistic fuzzy graphs with $V_1 \bigcap V_2 = \phi$ and $G = G_1 \bigcap G_2 = \left(V_1 \bigcap V_2, E_1 \bigcap E_2\right)$.

Then the union of intuitionistic fuzzy graphs $G_1$and G_2 is an intuitionistic fuzzy graph defined by

$$\left(\mu_1 \bigcup \mu_1'\right)(v) = \begin{cases} \mu_1(v) \ \ if \ v \in V_1 - V_2 \\ \mu_1'(v) \ \ if \ v \in V_2 - V_1 \end{cases} \left(\gamma_1 \bigcup \gamma_1'\right)(v) = \begin{cases} \gamma_1(v) \ \ if \ v \in V_1 - V_2 \\ \gamma_1'(v) \ \ if \ v \in V_2 - V_1 \end{cases}$$

$$\left(\mu_1 \bigcup \mu_1'\right)(v_i v_j) = \begin{cases} \mu_{2ij} \ if \ e_{ij} \in E_1 - E_2 \\ \mu_{2ij}' \ if \ e_{ij} \in E_2 - E_1 \end{cases} \left(\gamma_1 \bigcup \gamma_1'\right)(v_i v) = \begin{cases} \gamma_{2ij} \ if \ e_{ij} \in E_1 - E_2 \\ \gamma_{2ij}' \ if \ e_{ij} \in E_2 - E_1 \end{cases}$$

Where (μ_1, γ_1) and $\left(\mu_1', \gamma_1'\right)$ refer to the vertex membership and nonmembership of $G_1$and G_2,respectively;$(\mu_2, \gamma_2)$and $\left(\mu_2', \gamma_2'\right)$ refer to the edge membership and nonmembership of G_1 and G_2,respectively (Fig. 1).

Adjacency matrices of G_1 and G_2 are given below

$$A(G_1) = \begin{bmatrix} 0 & (0.1, 0.6) & (0.2, 0.8) \\ (0.1, 0.6) & 0 & (0.5, 0.2) \\ (0.2, 0.8) & (0.5, 0.2) & 0 \end{bmatrix} A(G_2) = \begin{bmatrix} 0 & (0.1, 0.7) \\ (0.1, 0.7) & 0 \end{bmatrix}$$

The membership and nonmembership values of G_1

$$A\left(\mu_{ij}(G_1)\right) = \begin{bmatrix} 0 & 0.1 & 0.2 \\ 0.1 & 0 & 0.5 \\ 0.2 & 0.5 & 0 \end{bmatrix} A\left(\gamma_{ij}(G_1)\right) = \begin{bmatrix} 0 & 0.6 & 0.8 \\ 0.6 & 0 & 0.5 \\ 0.8 & 0.2 & 0 \end{bmatrix}$$

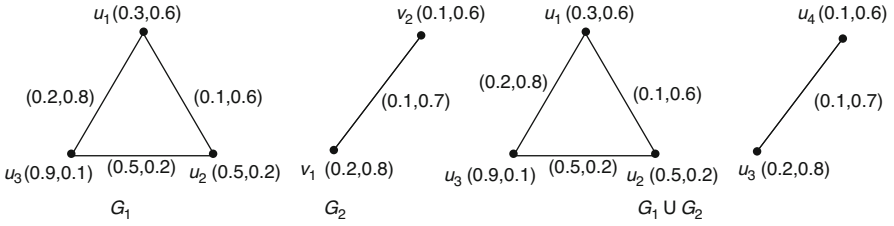

Fig. 1 G_1, G_2 *and* $G_1 U G_2$

and $A\left[\mu_{ij}\left(G_2\right)\right] = \begin{bmatrix} 0 & 0.1 \\ 0.1 & 0 \end{bmatrix}$, $A\left[\gamma_{ij}\left(G_2\right)\right] = \begin{bmatrix} 0 & 0.7 \\ 0.7 & 0 \end{bmatrix}$

$$L\left[\mu_{ij}\left(G_1\right)\right] = \begin{bmatrix} 0.3 & -0.1 & -0.2 \\ -0.1 & 0.6 & -0.5 \\ -0.2 & -0.5 & 0.7 \end{bmatrix}, L\left[\gamma_{ij}\left(G_1\right)\right] = \begin{bmatrix} 1.4 & -0.6 & -0.8 \\ -0.6 & 0.8 & -0.5 \\ -0.8 & -0.2 & 1.0 \end{bmatrix}$$

$$spec \quad \left[L\left(\mu_{ij}\left(G_1\right)\right)\right] = \{0\,,\ 0.4394\,,\ 1.1606\ \}$$

$$spec \quad \left[L\left(\gamma_{ij}\left(G_1\right)\right)\right] = \{\ 0\,,\ 1.0708\,,\ 2.1292\ \}$$

$$LE\left[\mu_{ij}\left(G_1\right)\right] = \left|0 - \frac{2\,(1.6)}{3}\right| + \left|0.4394 - \frac{2\,(1.6)}{3}\right| + \left|1.1606 - \frac{2\,(1.6)}{3}\right|$$

$$= 1.0666 + 0.6272 + 0.0939 = 1.7877$$

$$LE\left[\gamma_{ij}\left(G_1\right)\right] = \left|0 - \frac{2\,(3.2)}{3}\right| + \left|0.4394 - \frac{2\,(3.2)}{3}\right| + \left|2.1292 - \frac{2\,(3.2)}{3}\right|$$

$$= 2.1333 + 1.0625 + 0.0041 = 3.1999$$

Similarly the membership and nonmembership values of G_2

$$A\left(\mu_{ij}(G_2)\right) = \begin{bmatrix} 0 & 0.1 \\ 0.1 & 0 \end{bmatrix} \text{ and } A\left(\gamma_{ij}(G_2)\right) = \begin{bmatrix} 0 & 0.7 \\ 0.7 & 0 \end{bmatrix}$$

$$L\left(\mu_{ij}(G_2)\right) = \begin{bmatrix} 0.1 & -0.1 \\ -0.1 & 0,1 \end{bmatrix} \text{ and } L\left(\gamma_{ij}(G_2)\right) = \begin{bmatrix} 0.7 & -0.7 \\ -0.7 & 0,7 \end{bmatrix}$$

$$Spec\left[L\left(\mu_{ij}\left(G_2\right)\right)\right] = \{0, 0.2\}$$

$$Spec\left[L\left(\gamma_{ij}\left(G_2\right)\right)\right] = \{0, 1.4\}$$

$$LE\left[\mu_{ij}\left(G_2\right)\right] = \left|0 - \frac{2\,(0.1)}{2}\right| + \left|0.2 - \frac{2\,(0.1)}{2}\right| = 0.1 + 0.1 = 0.2$$

$LE\left[\gamma_{ij}\left(G_2\right)\right] = \left|0 - \frac{2(0.7)}{2}\right| + \left|1.4 - \frac{2(0.7)}{2}\right| = 0.7{+}0.7 = 1.4$Adjacency matrix of $G_1 \bigcup G_2$ is given below

$$A\left[G_1 \bigcup G_2\right] = \begin{bmatrix} 0 & (0.1, 0.6) & (0.2, 0.8) & 0 & 0 \\ (0.1, 0.6) & 0 & (0.5, 0.2) & 0 & 0 \\ (0.2, 0.8) & (0.5, 0.2) & 0 & 0 & 0 \\ 0 & 0 & 0 & 0 & (0.1, 0.7) \\ 0 & 0 & 0 & (0.1, 0.7) & 0 \end{bmatrix}$$

The membership matrix of $G_1 \bigcup G_2$is

$$\mu_{ij}\left[G_1 \bigcup G_2\right] = \begin{bmatrix} 0 & 0.1 & 0.2 & 0 & 0 \\ 0.1 & 0 & 0.5 & 0 & 0 \\ 0.2 & 0.5 & 0 & 0 & 0 \\ 0 & 0 & 0 & 0 & 0.1 \\ 0 & 0 & 0 & 0.1 & 0 \end{bmatrix}$$

$$L\left[\mu_{ij}\left[G_1 \bigcup G_2\right]\right] = \begin{bmatrix} 0.3 & -0.1 & -0.2 & 0 & 0 \\ -0.1 & 0.6 & -0.5 & 0 & 0 \\ -0.2 & -0.5 & 0.7 & 0 & 0 \\ 0 & 0 & 0 & 0.1 & -0.1 \\ 0 & 0 & 0 & -0.1 & 0.1 \end{bmatrix}$$

$$Spec\left[\left(\mu_{ij}\left(G_1 \cup G_2\right)\right)\right] = \{0, 0, 0.2,\ 0.4394,\ 1.1606\}$$

$$\begin{aligned} LE\left[\mu_{ij}\left(G_1 \cup G_2\right)\right] &= \left|0 - \tfrac{2(1.8)}{5}\right| + \left|0 - \tfrac{2(1.8)}{5}\right| + \left|0.2 - \tfrac{2(1.8)}{5}\right| \\ &\quad + \left|0.4394 - \tfrac{2(1.8)}{5}\right| + \left|1.1606 - \tfrac{2(1.8)}{5}\right| \\ &= 0.72 + 0.72 + 0.52 + 0.2806 + 0.4406 = 2.6812 \end{aligned}$$

$$A\ [\gamma_{ij}\left[G_1 \bigcup G_2\right]] = \begin{bmatrix} 0 & 0.6 & 0.8 & 0 & 0 \\ 0.6 & 0 & 0.2 & 0 & 0 \\ 0.8 & 0.2 & 0 & 0 & 0 \\ 0 & 0 & 0 & 0 & 0.7 \\ 0 & 0 & 0 & 0.7 & 0 \end{bmatrix} L\left[\mu_{ij}\left[G_1 \bigcup G_2\right]\right]$$

$$= \begin{bmatrix} 1.4 & -0.6 & -0.8 & 0 & 0 \\ -0.6 & 0.8 & -0.2 & 0 & 0 \\ -0.8 & -0.2 & 1.0 & 0 & 0 \\ 0 & 0 & 0 & 0.7 & -0.7 \\ 0 & 0 & 0 & -0.7 & 0.7 \end{bmatrix}$$

$$Spec\left[\left(\mu_{ij}\left(G_1 \bigcup G_2\right)\right)\right] = \{0, 0, 1.0708\,, 1.4, 2.1292\}$$

$$\begin{aligned} LE\left[\mu_{ij}\left(G_1 \cup G_2\right)\right] &= \left|0 - \frac{2\,(4.6)}{5}\right| + \left|0 - \frac{2\,(4.6)}{5}\right| + \left|1.0708 - \frac{2\,(4.6)}{5}\right| \\ &\quad + \left|1.4 - \frac{2\,(4.6)}{5}\right| + \left|2.1292 - \frac{2\,(4.6)}{5}\right| \\ &= 1.86 + 1.84 + 0.7592 + 0.44 + 0.2892 = 5.1784 \end{aligned}$$

We observed here that

$$LE\left[\mu_{ij}\left(G_1\right)\right] + LE\left[\mu_{ij}\left(G_2\right)\right] \leq LE\left[\mu_{ij}\left(G_1 \bigcup G_2\right)\right] \text{and also}$$

$$LE\left[\gamma_{ij}\left(G_1\right)\right] + LE\left[\gamma_{ij}\left(G_2\right)\right] \leq LE\left[\gamma_{ij}\left(G_1 \bigcup G_2\right)\right]$$

3 Laplacian Energy of Join of Two Intuitionistic Fuzzy Graph

Definition 2 The join of two intuitionistic fuzzy graphs G_1 and G_2 is an intuitionistic fuzzy graph$G_1 + G_2 - \left(V_1 \bigcup V_2, E_1 \bigcup E_2\right)$ defined by

$$\left(\mu_1 + \mu_1'\right)(v) = \left(\mu_1 \bigcup \mu_1'\right)(v) \;\; if\; v \in V_1 \bigcup V_2$$

$$\left(\gamma_1 + \gamma_1'\right)(v) = \left(\gamma_1 \bigcup \gamma_1'\right)(v) \;\; if\; v \in V_1 \bigcup V_2$$

$$\begin{aligned}\left(\mu_2 + \mu_2'\right)\left(v_i v_j\right) &= \left(\mu_2 \bigcup \mu_2'\right)\left(v_i v_j\right) \;\; if\; v_i v_j \in E_1 \bigcup E_2 \\ &= \min\left(\mu_1\left(v_i\right), \mu_1'\left(v_j\right)\right) \;\; if\; v_i v_j \in E'\end{aligned} \text{ and}$$

$$\begin{aligned}\left(\gamma_2 + \gamma_2'\right)\left(v_i v_j\right) &= \left(\gamma_2 \bigcup \gamma_2'\right)\left(v_i v_j\right) \;\; if\; v_i v_j \in E_1 \bigcup E_2 \\ &= \max\left(\gamma_1\left(v_i\right), \mu_1'\left(v_j\right)\right) \;\; if\; v_i v_j \in E'\end{aligned}$$

In the previous section we already find (Fig. 2)

$$LE\left(G_1\right) = (1.77877, 3.1999)$$

$$LE\left(G_2\right) = (0.2, 1.4)$$

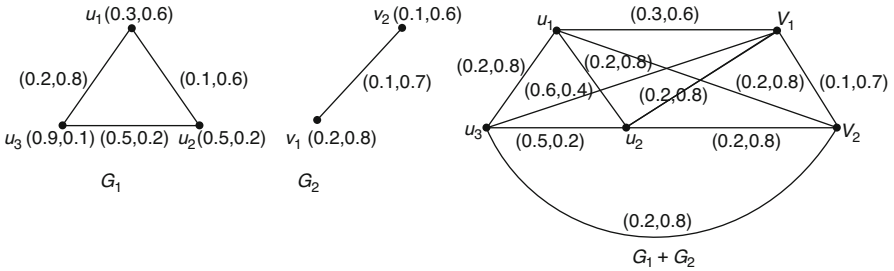

Fig. 2 G_1, G_2 *and*$G_1 + G_2$

Now we will verify the Laplacian energy of join of two intuitionistic fuzzy graphs $G = G_1 + G_2$

$$A(G_1 + G_2) = \begin{bmatrix} 0 & (0.1, 0.6) & (0.2, 0.8) & (0.3, 0.6) & (0.2, 0.8) \\ (0.1, 0.6) & 0 & (0.5, 0.0) & (0.2, 0.8) & (0.2, 0.8) \\ (0.2, 0.8) & (0.5, 0.0) & 0 & (0.6, 0.4) & (0.2, 0.8) \\ (0.3, 0.6) & (0.2, 0.8) & (0.6, 0.4) & 0 & (0.1, 0.7) \\ (0.2, 0.8) & (0.2, 0.8) & (0.2, 0.8) & (0.1, 0.7) & 0 \end{bmatrix}$$

$$A\left[\mu_{ij}((G_1 + G_2))\right] = \begin{bmatrix} 0 & 0.1 & 0.2 & 0.3 & 0.2 \\ 0.1 & 0 & 0.5 & 0.2 & 0.2 \\ 0.2 & 0.5 & 0 & 0.6 & 0.2 \\ 0.3 & 0.2 & 0.6 & 0 & 0.1 \\ 0.2 & 0.2 & 0.2 & 0.1 & 0 \end{bmatrix} L\left[\mu_{ij}((G_1 + G_2))\right]$$

$$= \begin{bmatrix} 0.8 & -0.1 & -0.2 & -0.3 & -0.2 \\ -0.1 & 1.0 & -0.5 & -0.2 & -0.2 \\ --0.2 & -0.5 & 1.5 & -0.6 & -0.2 \\ -0.3 & -0.2 & -0.6 & 1.2 & -0.1 \\ -0.2 & -0.2 & -0.2 & -0.1 & 0.7 \end{bmatrix}$$

$$Spec\left[L\left(\mu_{ij}(G_1 + G_2)\right)\right] = \{0.0204,\ 2.0557,\ 1.3463,\ 0.9135,\ 0.8641\}$$

$$LE\left[\mu_{ij}(G_1 + G_2)\right] = \left|0.0204 - \tfrac{2(2.6)}{5}\right| + \left|2.0557 - \tfrac{2(2.6)}{5}\right| + |1.3463 - \tfrac{2(2.6)}{5}| + \left|0.9135 - \tfrac{2(2.6)}{5}\right| + \left|0.8641 - \tfrac{2(2.6)}{5}\right|$$

$$= 1.0196 + 1.0157 + 0.3063 + 0.1265 + 0.1759 = 2.2922$$

$$A\left[\gamma_{ij}((G_1 + G_2))\right] = \begin{bmatrix} 0 & 0.6 & 0.8 & 0.6 & 0.8 \\ 0.6 & 0 & 0 & 0.8 & 0.8 \\ 0.8 & 0 & 0 & 0.4 & 0.8 \\ 0.6 & 0.8 & 0.4 & 0 & 0.7 \\ 0.8 & 0.8 & 0.8 & 0.7 & 0 \end{bmatrix} L\left[\gamma_{ij}((G_1 + G_2))\right]$$

$$= \begin{bmatrix} 2.8 & -0.6 & -0.8 & -0.6 & -0.8 \\ -0.6 & 2.2 & 0 & -0.8 & -0.8 \\ -0.8 & 0 & 2.0 & -0.4 & -0.8 \\ -0.6 & -0.8 & -0.4 & 2.5 & -0.7 \\ -0.8 & -0.8 & -0.8 & -0.7 & 3.1 \end{bmatrix}$$

$$Spec\left[L\left(\gamma_{ij}(G_1 + G_2)\right)\right] = \{3.8883, 3.5029, 3.2064, 2.6023, 0.\}$$

$$LE\left[\gamma_{ij}\left(G_1+G_2\right)\right] = \left|3.8883-\tfrac{2(6.3)}{5}\right| + \left|3.5029-\tfrac{2(6.3)}{5}\right| + \left|3.2064-\tfrac{2(..36)}{5}\right| + \left|2.60223-\tfrac{2(6.3)}{5}\right| + \left|0-\tfrac{2(6.3)}{5}\right| = 1.3683+0.9829+0.6864+0.5177+2.52 = 6.0753$$

Here also we observed that

$LE\left[\mu_{ij}\left(G_1\right)\right] + LE\left[\mu_{ij}\left(G_2\right)\right] \leq LE\left[\mu_{ij}\left(G_1+G_2\right)\right]$ and also

$$LE\left[\gamma_{ij}\left(G_1\right)\right] + LE\left[\gamma_{ij}\left(G_2\right)\right] \leq LE\left[\gamma_{ij}\left(G_1+G_2\right)\right]$$

4 Conclusion

The Laplacian matrix and energy for an intuitionistic fuzzy graph are defined. Some results on Laplacian spectra of intuitionistic fuzzy graphs may reveal more analogous results of these kinds and will be discussed in the forthcoming papers.

References

1. Rosenfeld.A, Fuzzy Graphs, in Zadeh.L.A, Fu. K.cS, Tanaka.K and Shimura.M (eds.), Fuzzy Sets and their Applications to Cognitive and Decision Process, Academic Press, New York, 75–95, (1975).
2. Sharief Basha.S and E. Kartheek, Laplacian Energy of an Intuitionistic Fuzzy Graph, Indian Journal of Science and Technology, 8(33) 1–7, (2015).
3. Zadeh.L.A., Fuzzy sets , Information and Control,, (8)338–353, (1965).

Wiener Index of Hypertree

L. Nirmala Rani, K. Jennifer Rajkumari, and S. Roy

Abstract Binary trees are enormously used in data structure as they can be easily stored, manipulated, and retrieved. The most straightforward and extensive applications of binary trees are in the study of computer searching and sorting methods, binary identification problems, and variable binary codes. Many complex networks are easily classified and analyzed by the usage of binary tree representations. A binary tree is defined as a tree in which there is exactly one vertex of degree two and each of the remaining vertices is of degree one or three. Every binary tree is a rooted tree with odd number of vertices. A special type of binary tree known as hypertree is an interconnection topology which combines the easy expansibility of tree structures with the compactness of the hypercube. In this paper we find the Wiener index of hypertree.

1 Interconnection Networks and Graphs

Food webs, protein interactions, airline travel routes, computer chip wiring, and telephone call graphs are all networks that are models of phenomena surrounding us. Social activity-based visual networks like Facebook and Orkut, exhibiting the association of a person with friends and others, mobile communication networks without which the human race become paralyzed and desperate, satellite communication (audio and visual) networks that are essential for the blissful existence of human race on this earth, and space communication networks to explore the wonderful creations of celestial bodies and calculate the effect of

L. Nirmala Rani
Anandarayan Kottai, Dindigul, Tamil Nadu, India

K. Jennifer Rajkumari
IEEE, Electrical Engineering, Stanford University, CA, USA

S. Roy (✉)
Department of Mathematics, Vellore Institute of Technology, Vellore, India
e-mail: roy.santiago@vit.ac.in

B. Rushi Kumar et al. (eds.), *Applied Mathematics and Scientific Computing*,
Trends in Mathematics, https://doi.org/10.1007/978-3-030-01123-9_49

their orbital forces on this earth and human race are a few of the innumerable number of natural networks in the creation of this universe and also man-made networks that are invented or constructed for the sustenance of human race in this universe. Having methods and tools to better understand these networks and their dynamics is beneficial for knowledge advancement and better design of future systems.

We categorize and explore these networks as graph-related indicators. Presentation of any concept through a diagram will facilitate a better understanding of the concept. Problems related to Mathematics, Science, Engineering, and even real-life situations can be diagrammatically represented by points on a plane and joining a few pairs of points with lines. Such a mathematical abstraction is the foundation of graph theory. Graph serves as a mathematical model to analyze successfully many concrete real-life problems.

2 Topological Indices

A topological index is a structural invariant real number related to a graph. Several topological indices have been defined, and many of them have found applications as means to model chemical, pharmaceutical, and other properties of molecules. Usage of topological indices in chemistry began in 1947 when chemist Harold Wiener developed the most widely known topological descriptor, the Wiener index, and used it to determine physical properties of types of alkanes known as paraffins. There are many topological indices such as Hyper-Wiener index, Eata index, PI index, Alpha index, Gamma index, Harary index, Hyper-Harary index, Kirchhoff index, Pasareti index, Detour index, Hyper-Detour index, Hosoya index, Shimbel index, etc. [1–5, 10].

3 Shortest Path Problems

In this competitive and time-conscious era, the shortest path concept between two vertices or nodes in networks or between the sources and destinations is very much needed. The shortest path problem is to find a shortest path in a graph such that the sum of the weights of its constituent edges is minimized. The shortest path problem can be defined for undirected, directed, or mixed. There are different types of shortest path graph problems. (1) The single-source shortest path problem is to find shortest paths from a source vertex v to all other vertices in the graph. (2) The single-destination shortest path problem is to find shortest paths from all vertices in the directed graph to a single destination vertex v. (3) The all-pairs shortest path problem is to find shortest paths between every pair of vertices (u, v) in the graph.

Shortest path problem has been extensively used in all interconnection networks and especially in routing between the sending station and receiving station.

4 Wiener Index

It is a topological invariant based on the all-pairs shortest path problem in networks, named after its inventor Wiener [5]. It is defined as half the sum of shortest paths between any two vertices of an undirected graph. It is calculated in many ways.

(1) Multiply the number of vertices on each side of an edge and add all such contributions. Let T be a tree with n vertices and e as one of its edges. Let $n_1(e)$ and $n_2(e) = n - n_1(e)$ be the numbers of vertices of the two parts of $T - e$. Then the wiener index formula is given by: $W = \sum_e^{p-1} n_1(e)n_2(e)$.
(2) The Wiener edge decomposition formula which is valid only for acyclic graphs has been generalized by Lukovits and Gutman in 1994 to be applicable to cycle containing systems . The general edge-decomposition formula is given by $E = \sum_e \sum_{i \le j} [p_{ij}(e)/p_{ij}]$ where p_{ij} is the total number of paths between vertices i and j that are of length $l(i, j)$. The number of such paths that contain the edge e is denoted by $p_{ij}(e)$.
(3) The Wiener index W of a graph G is equal to half the sum of the off-diagonal elements of the distance matrix D : $W = \frac{1}{2} \sum_{i=1}^{p} \sum_{j=1}^{p} [D]_{ij}$ where $[D]_{ij}$ represents the length of a shortest path between vertices i and j in G.
(4) Consequently, Wiener index based on all pairs shortest path problem is defined as half the sum of all shortest paths between unordered pairs of vertices of a graph. Wiener index has been calculated for many graphs [6–13].

Before proceeding to find the Wiener index of hypertree, we recall some of the basic concepts and definitions of tree, complete tree, and hypertree.

5 Complete Binary Tree

A tree is a connected graph without any cycles. The most common type of tree is the binary tree. A rooted binary tree represents a data structure with a hierarchical relationship among its various elements. In many ways we can systematically list all nodes of a tree. There are three important listing or ordering, namely, preorder, inorder, and postorder as we trace the tree counterclockwise starting from the root. For preorder, we list a node the first time we pass it. For inorder, we list a leaf the first time we pass it but list an interior node the second time we pass it. For postorder, we list a node the last time we pass it [19]. A binary tree T_r, for any nonnegative integer r, in which each internal node has exactly two

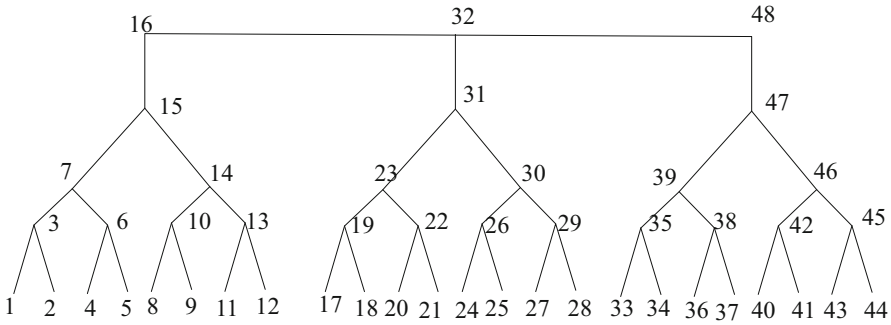

Fig. 1 3-Rooted complete binary tree T_4^3 with postorder

descendants, described as left and right children of the parent node, and all the leaves at the same level is known as complete binary tree of height $r - 1$. Each level i, $1 \leq i \leq r$, contains 2^{i-1} vertices. T_r has exactly $2^r - 1$ vertices. The 1-rooted complete binary tree T_r^1 is obtained from a complete binary tree T_r by attaching to its root a pendant edge. The new vertex , called as the root of T_r, is considered to be at level 0. The n-rooted complete binary T_r^n is obtained by taking n vertex disjoint 1-rooted complete binary trees T_r^1 on 2^r vertices each, with roots say $r_1, r_2, r_3, ..., r_n$ and adding the edges (r_i, r_{i+1}), $1 \leq i \leq n - 1$. The number of vertices and the edges of T_r^n are $n(2^r)$ and $n(2^r - 1)$ [17]. See Fig. 1 for a 3-rooted complete binary tree are used in embedding of hypercubes, grids [14], cycles and wheels [15], and recursive circulants [16] and in many multiprocessor networks [18].

6 Hypertree

The basic skeleton of a hypertree is a complete binary tree T_r. A hypertree is a hypergraph H if there is a tree T such that the hyperedges of H induce subtrees in T. A hypertree is also called as a subtree hypergraph or arboreal hypergraph [19–21]. The nodes of the hypertree are labelled as follows: the root node is kept at level 1 with a label 1. The left and right children of this root node are labelled by appending a 0 and 1. Successively the labels of left and right children of any parent node are formed by appending a 0 and 1 to their parent node, respectively. See Fig. 2a. The decimal labels of the hypertree in Fig. 2a are depicted in Fig. 2b. The children of the parent node y are labelled as $2y$ and $2y + 1$. Additional links in a hypertree are horizontal, and two nodes in the same level r of the tree are joined if their label difference is 2^{r-2}. A hypertree with r level is denoted as $HT(r)$. It has $2^r - 1$ vertices and $2(2^{r-1} - 1)$ edges. A hypertree is an interconnection topology for multicomputer

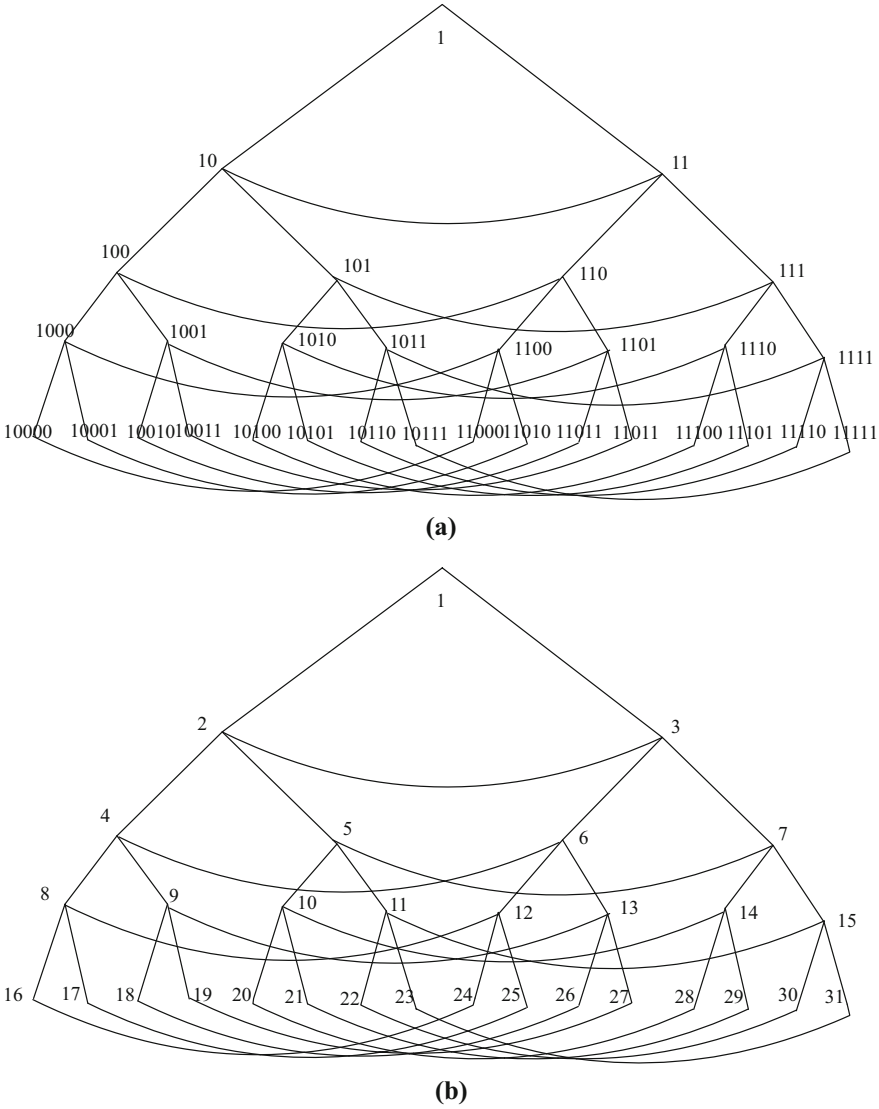

Fig. 2 (**a**) $HT(5)$ with binary labels. (**b**) $HT(5)$ with decimal labels

systems which combines the best features of the binary tree and the hypercube. This topology is particularly facinative for implementation of multiprocessor networks of the future, where a complete computer with a significant amount of memory can fit on a single VLSI chip. Hypertrees are used in fault tolerance and transmission delay in interconnection networks [22, 23].

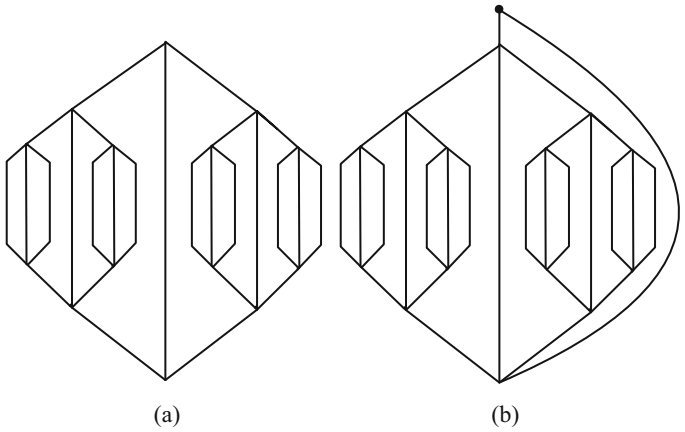

Fig. 3 (**a**) Extended theta mesh $EMT(5)$. (**b**) Extended rooted theta mesh $ITM(5)$

6.1 Extended Theta Mesh

Let T_r be a complete binary tree, $r \geq 1$. A graph which is obtained from two copies of complete binary tree T_r, say T_r^1 ,T_r^2 by joining each vertex of T_r^1 with the corresponding vertex of T_r^2 by an edge, is called an extended theta mesh and is denoted by $ETM(r)$. See Fig. 3a. It has $2^{r+1} - 2$ vertices. A graph obtained from $ETM(r)$ by identifying a pendant vertex is known as identified extended theta mesh with $2^r - 1$ vertices and denoted as $ITM(r)$. See Fig. 3b. It has been proved that $ITM(r)$ is isomorphic to $HT(r)$ [23].

Definition 1 Let G be a connected undirected graph with vertex set $V(G)$ and edge set $E(G)$. The Wiener index $D(G)$ of G is defined as half the sum of all shortest distances $d(v_i, v_j)$ between the unordered pairs v_i, v_j of vertices of G., i.e., $D(G) = \frac{1}{2} \sum_{v_i, v_j \in V(G)} d(v_i, v_j)$ [6–12].

In this paper, without using distance matrix, we use a Lemma based on edge-cut techniques to compute the Wiener index of a hypertree.

6.2 Edge-Cut Partition Lemma

Lemma 1 ([24]) *Let G be a graph on n vertices. Let $\{S_1, S_2, \ldots, S_m\}$ be a partition of $E(G)$ such that each S_i is an edge cut of G and the removal of edges of S_i leaves G into two components G_i and G_i'. Also each S_i satisfies the following conditions*

(i) For any two vertices $u, v \in G_i$, a shortest path between u and v has no edges in S_i.

(ii) For any two vertices $u, v \in G'i$, a shortest path between u and v has no edges in S_i .

(iii) For any two vertices $u \in G_i$ and $v \in G'_i$, a shortest path between u and v has exactly one edge in S_i .

Then the congestion on S_i is given by $c(S_i) = |V(G_i)|(n - |V(G_i)|)$, and Wiener index of G is given by $W(G) = \sum_{i=1}^{m} |V(G_i)|(n - |V(G_i)|)$.

Theorem 1 *Let G be a hypertree $HT(n)$, $n \geq 2$. Then the Wiener index of G is given by $W(G) = (4n - 12)2^{2n} + (6n + 10)2^n + 2$.*

Proof Let $S_{2^{n-1}}^{2^2-2}$ denote the set of 2^{n-1} edge cuts each cutting G into two components with one component having exactly $2^2 - 2$, i.e., two vertices. Let $S_{2^{n-2}}^{2^3-2}$ denote the set of 2^{n-2} edge cuts each cutting G into two components with one component having exactly $2^3 - 2$, i.e., six vertices. Let $S_{2^{n-3}}^{2^4-2}$ denote the set of 2^{n-3} edge cuts each cutting G into two components with one component having exactly $2^4 - 2$, i.e., 14 vertices. In general let $S_{2^{n-i}}^{2^{i+1}-2}$; $i = 1, 2, 3, \ldots, n-1$ denote the set of 2^{n-i} edge cuts each cutting G into two components with one component having exactly $2^{i+1} - 2$ vertices. Now consider the pair (k, j) where $k = 1$, $j = 2^n - 1$.

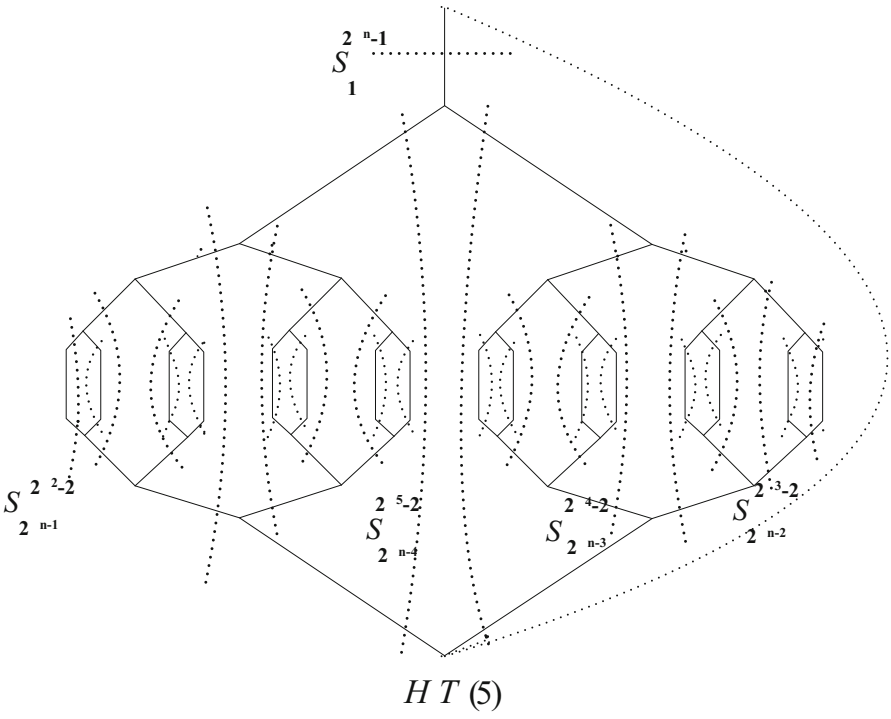

Fig. 4 Edge cut of hypertree $HT(5)$

For $i = 1, 2, 3, \ldots, n-1$ let $S = S_{2^{n-i}}^{2^{i+1}-2} \bigcup (k, j)$. Edge cut of hypertree $HT(5)$ as shown in Fig. 4. Now S satisfies all the conditions of the Edge-Cut Lemma. Let $c(S)$ be the congestion on S. Hence by the Edge-Cut Lemma, the Wiener index is given by

$$\begin{aligned} W(G) = C(S) &= c(S_{2^{n-i}}^{2^{i+1}-2}) + c(k, j) \\ &= \sum_{i=1}^{n-1} 2^{n-i}(2^{i+1} - 2)((2^{n+1} - 1) - (2^{i+1} - 2)) + 2^{n+1} - 2 \\ &= (4n - 12)2^{2n} + (6n + 10)2^n + 2. \end{aligned}$$

7 Conclusion

In this paper we have found the Wiener index of hypertree $HT(r)$. Finding Wiener index of Ringtree is challenging and the problem remains open.

References

1. Saad, Y., Schultz, M. H.: Topological properties of hypercubes. IEEE Trans. Comput. **37(7)**, 867–872 (1988).
2. Ivanciuc, O., Ivanciuc, T., Balaban, A. T.: Design of topological indices. Part 10. Parameters based on electronegativity and covalent radius for the computation of molecular graph descriptors for heteroatom-containing molecules. J. Chem. Inf. Comput. Sci. **38**, 395–401 (1998)
3. Luiu, B., Nikoli, S., Trinajsti, N.: Distance-Related Molecular Descriptors. Internet Electronic Journal of Molecular Design. **7**, 195–206 (2008).
4. Balaban, A. T.: Topological indices based on topological distances in molecular graphs. Pure Appl. Chem. **55**, 199–206 (1983).
5. Wiener, M.: Structural determination of paraffin boiling points. J. Am. Chem. Soc. **69**, 17–20 (1947).
6. Gutman, I., Yeh, Y. N., Lee, S. L., Luo,Y. L.: Some recent results in the theory of the Wiener number. Indian J. Chem. **32A**, 651–661 (1993).
7. A.Graovac, T. Pisanski, On the Wiener index of a graph. J. Math. Chem. **8**, 53–62 (1991).
8. Gutman, I., Furtula, B., Petrovi, M.: Terminal Wiener index. J. Math. Chem. **46**, 522–531 (2009).
9. Dobrynin, A. A., Entringer, R., Gutman, I.: Wiener index of trees: theory and applications. Acta Appl. Math. **66**, 211–249 (2011).
10. Randi, M.: On generalization of Wiener index for cyclic structures. Acta Chim. Slov. **49**, 483–496 (2002).
11. Khadikar, P. V., Deshpande, N. V., Kale, P. P., Dobrynin, A. A., Gutman, I., DĆmĆtor, G.: The Szeged index and an analogy with the Wiener index. J. Chem. Inf. Comput. Sci. **35**, 547–550 (1995).
12. Mohar, B., Pisanski, T.: How to compute the Weiner index of a Graph. J. Math. Chem. **2**, 267–277 (1988).

13. Zhang, X. D., Xiang, Q.-Y., Xu, L.-Q., Pan, R.-Y. The Wiener index of trees with given degree sequences. Math. Comput. Chem. **60**, 623–644 (2008).
14. Opatrn, J., Sotteau, D.: Embeddings of complete binary trees into grids and extended grids with total vertex-congestion 1. Discrete Appl. Math. **98**, 237–254 (2000).
15. Rajasingh, I., Quadras, J., Manuel, P., William, A.: Embedding of cycles and wheels into arbitrary trees. Networks. **44(3)**,173–178 (2004).
16. Lim, H-S., Park, J-H., Chwa, K-Y.: Embedding trees in recursive circulants, Discrete applied Mathematics, **69(1–2)**,83–89 (1996).
17. Rajasingh, I., Manuel, P., Rajan, B., Arockiaraj, M.: Wirelength of hypercubes into certain trees. Discrete Applied Mathematics. **1601(18)**, 2778–2786 (2012).
18. Goodman, J.R., Sequin, C.H.: A multiprocessor interconnection topology. IEEE Transactions on Computers. **30(12)**, 923–933 (1981).
19. Papa, D. A., Markov, I. L.: Hypergraph Partitioning and Clustering: In Approximation Algorithms and Metaheuristics. CRC Press, (2007).
20. Heuvel, J. V. D., Johnson, M.: Transversals of subtree hypergraphs and the source location problem in digraphs. Networks, **51(2)**, 113–119 (2008).
21. Akram, M., Dudek, W. A.: Intuitionistic fuzzy hypergraphs with applications. Information Sciences. **218**, 182–193 (2013).
22. Brandstadt, A., Chepoi, V. D., Dragan, F. F.: The algorithmic use of hypertree structure and maximum neighbourhood orderings, Discrete Applied Mathematics. **82**, 43–77 (1998).
23. Sundara Rajan, R., Jeyagopal, R., Rajasingh, I., Rajalaxmi, T. M., Parthiban, N.: Combinatorial properties of Root-fault hypertree. Procedia Computer Science. **57**, 1096–1103 (2015).
24. Manuel, P., Rajasingh, I., Rajan, B., Sundara Rajan, R.: A New Approach to Compute Wiener Index. Journal of Computational and Theoretical Nanoscience. **10**, 1–7 (2013).

Location-2-Domination for Product of Graphs

G. Rajasekar, A. Venkatesan, and J. Ravi Sankar

Abstract Locating-2-Dominating Set is denoted as $R_2^D(G)$, and in this chapter the Location-2-domination number for direct and Cartesian product of graphs, namely $P_n \square P_m$, $P_n \square S_m$, $P_n \square W_m$, $C_n \square C_m$, $P_n \times P_m$, $P_n \times S_m$, $C_n \times P_m$, $C_n \times C_m$, are being found.

Keywords Cartesian product of graphs · Direct product of graphs · Domination number · Location-2-domination number

Mathematics Subject Classification 05C76, 05C69

1 Introduction

Throughout this chapter, we follow the terminology and notation of Harary [8]. Cockayne and Hedetniemi [4] introduced and defined the concept of the dominating set as a subset S of vertices from V, which is called a dominating set for G if every vertex of G is either a member of S or adjacent to a member of S. A dominating set of G is called a minimum dominating set if G has no dominating set of smaller

G. Rajasekar (✉)
Department of Mathematics, Jawahar Science College, Neyveli, India

A. Venkatesan
Department of Mathematics, St. Joseph's College of Arts and Science College (Autonomous), Cuddalore, India

J. Ravi Sankar
Department of Mathematics, School of Advanced Sciences, Vellore Institute of Technology, Vellore, India

B. Rushi Kumar et al. (eds.), *Applied Mathematics and Scientific Computing*, Trends in Mathematics, https://doi.org/10.1007/978-3-030-01123-9_50

cardinality. The cardinality of the minimum dominating set of G is called the dominating number for G and is denoted by $\gamma(G)$ [3].

Harary and Haynes [2] introduced and defined the concept of double domination in graphs as a dominating set S of G, which is called a double dominating set if every vertex in $V - S$ is adjacent to at least two vertices in S. Given a dominating set S for graph G, for each u in $V - S$, let $S(u)$ denote the set of vertices in S that are adjacent to u. The locating-dominating set was introduced by Slater [7], which is defined as a dominating set S. If for any two vertices u and w in $V - S$, $S(u)$ is not equal to $S(w)$ and the minimum cardinality of the location domination number is denoted by $RD(G)$ [4, 8]. The Cartesian product $G \square H$ of graphs G and H is the graph with the vertex set $V(G) \times V(H)$, and the edge set is $(u, a)(v, b) \in E(G \square H)$ if and only if $a = b$ and $uv \in E(G)$ or $u = v$ and $ab \in E(H)$[1]. The direct product $G \times H$ of graphs G and H is the graph with the vertex set $V(G) \times V(H)$ and the edge set is $(u, a)(v, b) \in E(G \times H)$ if and only if $uv \in E(G)$ and $ab \in E(H)$ [9].

2 Preliminaries

2.1 Location-2-Domination

Definition 1 ([5]) A set $S \subseteq V$ is a Location-2-Dominating set of G if S is a 2-Dominating set of G and if for any two vertices $u, v \in V - S$ such that $N(u) \cap S \neq N(v) \cap S$. The minimum cardinality of Location-2-Dominating is denoted by $R_D^2(G) = |S|$

2.2 Location-2-Domination for Simple Graphs

Theorem 1 ([5]) *Location-2-Domination number of a Path P_n is*
$R_D^2(P_n) = \frac{n-1}{2} + 1$; *n is odd,*
$R_D^2(P_n) = \frac{n}{2} + 1$; *n is even*

Theorem 2 ([5]) *For any cycle C_n,*
$R_D^2(G) = \frac{n}{2}$; *n is even,*
$R_D^2(G) = \frac{n-1}{2} + 1$; *n is odd for $n \neq 4$*

Theorem 3 ([6]) *In Location-2-Domination for any graph, the vertex $\{v\}$ is a pendant vertex, then $v \in R_2^D(G)$ only.*

3 Location-2-Domination for Cartesian Product of Graphs

Theorem 4 *For the graph $G(= P_n \square S_m)$, $R_2^D(G) = R_2^D(P_n) + \frac{m(n-1)}{2}$, n is odd and $R_2^D(G) = \frac{n}{2}(m + 1)$, n is even.*

Proof Clearly, $|V(G)| = n(m+1)$. Let S denote the Location-2-Dominating set. Here the path plays a major role in dominating the graph G. Now, the vertex set can be partitioned into two ways, one is vertex set of P_n vertices and another is a vertex set of S_m vertices, i.e., $v = \{v_1, v_2, v_3, \ldots, v_n\}$ and $u = \{(u_{1_1}, u_{1_2}, u_{1_3}, \ldots, u_{1_m}), (u_{2_1}, u_{2_2}, \ldots, u_{2_m}), \ldots, (u_{n_1}, u_{n_2}, \ldots, u_{n_m})\}$. Clearly, each v_i is adjacent to v_{i+1} and u_{i_j} where $i = 1, 2, 3, \ldots, n$, $j = 1, 2, \ldots, m$. Also, there is no edge from v_i to $u_{(i+1)_j}$, then the collection of the Location-2-Dominating set contains both v and u. This is not the case for a single vertex set.

Case (i) Suppose n is odd and m can be either even or odd, i.e., the path of length is odd; thus, by the Theorem 1, collect the vertices $\{1, 3, 5, \ldots, n\}$ from the set v and $\{(u_{1_2}, u_{1_4}, \ldots, u_{1_{m-1}}), (u_{2_2}, u_{2_4}, \ldots, u_{2_{m-1}}), \ldots, (u_{n_2}, u_{n_4}, \ldots, u_{n_{m-1}})\}$ from the u set only. Therefore, $|S| = \frac{n+1}{2} + \frac{m(n-1)}{2}$.

Case (ii) Suppose n is even, m is either odd or even, then clearly the path of length is even; thus, by the Theorem 1, collect the vertices from v-set, which are $\{1, 3, \ldots, n-1\}$ *or* $\{2, 4, \ldots, n\}$, but from the u-set they have $N(v-(1, 3, \ldots, n-1))$ or $N(v-(2, 4, \ldots, n))$ vertices m times. Therefore, $|S| = \frac{n}{2} + m\left(\frac{n}{2}\right) = \frac{n}{2}(m+1)$.

Theorem 5 *For the graph* $G(= P_n \square W_m)$, $m \geq 5$ *we have,*

$$R_2^D(G) = \begin{cases} \binom{\frac{n+2}{2}}{} R_2^D(W_m) + \binom{\frac{n-2}{2}}{}, & n \text{ is even, } m \text{ is either even or odd} \\ \binom{\frac{n+1}{2}}{} R_2^D(W_m) + \binom{\frac{n-1}{2}}{}, & n \text{ is odd, } m \text{ is either even or odd} \end{cases}$$

Proof Let the S-set denote the Location-2-Dominating set of G and the vertices of G are $\{(w_1, v_1), \ldots, (w_m, v_1), \ldots, (w_1, v_n), \ldots, (w_m.v_n)\}$. Clearly, $|G| = nm$ and vertices (w_i, v_j), (w_i, v_{j+1}) for $i = 1, 2, \ldots, m$, $j = 1, 2, \ldots, n$, (w_i, v_j), (w_{i+1}, v_j) for $i = 1, 2, \ldots, m$, $j = 1, 2, \ldots, n$, (w_n, v_j), $(w_i.v_j)$ for $i = 1, 2, \ldots, m-1$, $j = 1, 2, \ldots, n$ and (w_n, v_j), (w_n, v_{j+1}) for $j = 1, 2, \ldots, n$ are adjacent, but the adjacency order (w_i, v_j) to (w_{i+1}, v_j) for $i = 1, 2, \ldots, m, j = 1, 2, \ldots, n$ forms a n different cycle of length $m-1$. From G, now define $C_1, C_2, \ldots, C_n$ are the collection of the vertex $\{(w_1, v_1), \ldots, (w_m, v_1)\}, \{(w_1, v_2), \ldots, (w_m, v_2)\}, \ldots, \{(w_1, v_n)(w_m, v_n)\}$ respectively, that is, each C_i $i = 1, 2, \ldots, n$ gives a wheel graph. Now let us collect the S-set as follows:

Case (i) Suppose that n, m is even, that is, the path of the length is even. Now collect the vertex possibly from C_1 and C_n are (w_i, v_1) and (w_i, v_n) for $i = 1, 3, \ldots, m-1$ respectively. This gives $\frac{m}{2}$ vertices from C_1 and C_n separately. Also from $C_3, C_5, \ldots, C_{n-3}, C_{n-1}$, collect the vertices $\{(w_i, v_3), (w_i, v_5), \ldots, (w_i, v_{n-1})\}$ $i = 2, 4, \ldots, m$ this also gives $\frac{m}{2}$ vertices from $C_3, C_5, \ldots, C_{n-1}$ respectively; therefore, $C_1, C_3, \ldots, C_{n-3}, C_{n-1}, C_n$ are given $\frac{m}{2}$ vertices separately, i.e., $\frac{n+2}{2}$ times $\frac{m}{2}$ vertices, and collect the vertices from

$C_2, C_4, \ldots, C_{n-4}, C_{n-2}$ is $\left(w_n, v_j\right)$, $j = 2, 4, \ldots, n-2$ i.e.$\frac{n-2}{2}$ times, which gives a single vertex, that is, $|S| = \left(\frac{n+2}{2}\right)\left(\frac{m}{2}\right) + \left(\frac{n-2}{2}\right)$.

Case (ii) Suppose that n is even and m is odd. Now collect the vertex from C_1 and C_n, (w_i, v_1) and (w_i, v_n) for $i = 1, 3, \ldots, m$ respectively. This gives $\frac{m-1}{2}$ vertices from C_1 and C_n separately. Also from $C_3, C_5, \ldots, C_{n-3}, C_{n-1}$ collect the vertices $\{(w_i, v_3), (w_i, v_5), \ldots, (w_i, v_{n-1})\}$ $i = 2, 4, \ldots, m-1$. This also gives $\frac{m-1}{2}$ vertices from $C_3, C_5, \ldots, C_{n-1}$ respectively; therefore, $C_1, C_3, \ldots, C_{n-3}, C_{n-1}, C_n$ gives $\frac{m-1}{2}$ vertices separately, that is, $\frac{n+2}{2}$ times$\frac{m-1}{2}$ vertices, and the collection of vertices from $C_2, C_4, \ldots, C_{n-4}, C_{n-2}$ is $\left(w_n, v_j\right)$, $j = 2, 4, \ldots, n-2$, that is, $\frac{n-2}{2}$ times, which gives a single vertex.

Therefore, $|S| = \left(\frac{n+2}{2}\right)\left(\frac{m-1}{2}\right) + \left(\frac{n-2}{2}\right)$.

Case (iii) Suppose that n is odd and m is even. Now collect the vertex possibly from C_1 and C_n, (w_i, v_1) and (w_i, v_n) for $i = 1, 3, \ldots, m-1$ respectively. This gives $\frac{m}{2}$ vertices from C_1 and C_n separately. Also from $C_3, C_5, \ldots, C_{n-2}$ collect the vertices $\left\{w_i, v_j\right\}$ $i = 2, 4, \ldots, m$, $j = 3, 5, \ldots, n-2$ respectively. This also gives $\frac{m}{2}$ vertices from $C_3, C_5, \ldots, C_{n-2}$ separately; therefore, $C_1, C_3, \ldots, C_{n-2}, C_n$ are given $\frac{m}{2}$ vertices separately, i.e., $\frac{n+1}{2}$ times $\frac{m}{2}$ vertices, and collect the vertices from $C_2, C_4, \ldots, C_{n-1}$ is $\left(w_n, v_j\right)$, $j = 2, 4, \ldots, n-1$ only, i.e., $\frac{n-1}{2}$ times, which gives a single vertex. Therefore, $|S| = \left(\frac{n+1}{2}\right)\left(\frac{m}{2}\right) + \left(\frac{n-1}{2}\right)$.

Case (iv) Suppose that n is odd and m is odd. Now collect the vertex from C_1 and C_n, (w_i, v_1) and (w_i, v_n) for $i = 1, 3, \ldots, m$ respectively. This gives $\frac{m-1}{2}$ vertices from C_1 and C_n separately. Also from $C_3, C_5, \ldots, C_{n-2}$ collect the vertices $\{(w_i, v_3), (w_i, v_5), \ldots, (w_i, v_{n-2})\}$ $i = 2, 4, \ldots, m-1$. This also gives $\frac{m-1}{2}$ vertices from $C_3, C_5, \ldots, C_{n-2}$ respectively; therefore, $C_1, C_3, \ldots, C_{n-2}, C_n$ gives $\frac{m-1}{2}$ vertices separately, that is, $\frac{n+1}{2}$ times $\frac{m-1}{2}$ vertices, and collect the vertices from $C_2, C_4, \ldots, C_{n-3}, C_{n-1}$ is $\left(w_n, v_j\right)$, $j = 2, 4, \ldots, n-1$, i.e., $\frac{n-1}{2}$ times, which gives a single vertex.

Therefore, $|S| = \left(\frac{n+1}{2}\right)\left(\frac{m-1}{2}\right) + \left(\frac{n-1}{2}\right)$.

Theorem 6 *For the Graph* $G(= P_n \square P_m)$. *Then*

$$R_2^D(G) = \begin{cases} \frac{nm}{2}, & n \text{ is even}, \ m \text{ is either even or odd} \\ \frac{nm-1}{2}, & n \text{ is odd}, m \text{ is odd} \end{cases}, m \neq 2, n \neq 2$$

Proof Let G be a $P_n \square P_m$, the vertex set of G is namely $\left\{(v_i u_j)\right\} i = 1, 2, \ldots, n$ $j = 1, 2, \ldots, m$. Clearly, $|G| = nm$, let S-set denoted the Location-2-Domination of G, that is, $R_2^D(G) = |S|$.

Case (i) Suppose that n is even and m is even. Clearly, $|G| = nm$ gives the even number of vertices. From G form a maximum length of the closed path

P. Clearly, P containing the vertices namely $P = \{v_1u_1, v_1u_2, \ldots, v_1u_m, v_2u_m, v_2u_{m-1}, \ldots, v_2u_2, \ldots, v_3u_2, v_3u_3, \ldots, v_3u_m, \ldots, v_1u_1\}$. Clearly, $|P| = nm$ and thus P is a cycle of even length; thus, according to the Theorem 2, $R_2^D(G) = |S| = \frac{nm}{2}$.

Case (ii) Suppose that n is even and m is odd, then clearly, $|G| = nm$. This gives an even number of vertices according to Case (i). Again we obtain a cycle of even length and thus $R_2^D(G) = |S| = \frac{nm}{2}$.

Case (iii) Suppose that n is odd and m is odd, $|G| = nm$ gives an odd number of vertices. Now define $|S| = |S_1|+|S_2|$, where $|S_1|$ denote the Location-2-Domination for $P_{n-1}\Box P_m$ and $|S_2|$ denote the Location-2-Domination for $P_1\Box P_m$. Given that n is odd, $n-1$ gives an even number of vertices; thus, $P_{n-1}\Box P_m$ gives a duplication of Case (ii), that is, $|S_1| = \frac{(n-1)m}{2}$. $P_1\Box P_m$ gives a path of an odd length. Also, every vertex of $P_1\Box P_m$ is adjacent to $P_{n-1}\Box P_m$. For our convenience, remove the vertices $\{v_nu_1\}$ and $\{v_nu_m\}$ only from $P_1\Box P_m$, $P_1\Box P_m$ remains with a path of an odd length, according to Theorem 1; hence, $|S_2| = \frac{(m-2)-1}{2} + 1 = \frac{m-1}{2}$.

Therefore, $R_2^D(G) = |S| = |S_1| + |S_2| = \frac{(n-1)m}{2} + \frac{m-1}{2} = \frac{nm-1}{2}$.

Theorem 7 *For any Graph* $G(= C_n\Box C_m)$, *then*

$$R_2^D(G) = \begin{cases} \frac{nm}{2}, & n \text{ is even, } m \text{ is either even or odd} \\ \frac{nm-1}{2}, & n \text{ is odd}, m \text{ is odd} \end{cases}$$

Proof Let G be a $C_n\Box C_m$ graph. Clearly, $|G| = nm$, let S -set denoted the Location-2-Domination of G, that is, $R_2^D(G) = |S|$. The vertex set of G is namely $\{v_iu_j\}$. $1 \le i \le n$, $1 \le j \le m$.

Case (i) Suppose that n is even and m is even with $n = m$ *or* $n \ne m$. Clearly, $|G| = nm$ gives the even number of the vertex set. Now collect the vertex set, namely $\{v_iu_j\}$ $i = 1, 3, 5, \ldots, n-1$ $j = 1, 3, 5, \ldots, m-1$. and v_iu_j, $i = 2, 4, 6, \ldots, n$, $j = 2, 4, 6, \ldots, m$., that is, $|S| = \left(\frac{n}{2}\right)\left(\frac{m}{2}\right) + \left(\frac{n}{2}\right)\left(\frac{m}{2}\right) = \frac{nm}{2}$. herefore $R_2^D(G) = |S| = \frac{nm}{2}$.

Case (ii) Suppose that n is odd and m is even with $m = n$ or $n \ne m$, once again, the Case (i) result can be used.

Case (iii) Suppose that n is odd and m is odd with $m = n$ or $n \ne m$. Clearly, G has an odd number of vertices. Now the vertices of S are v_iu_j $i = 1, 3, 5, \ldots, n$, $j = 2, 4, 6, \ldots, m-1$ and v_iu_j , $j = 1, 3, 5, \ldots, m$, $i = 2, 4, 6, \ldots, n-1$, that is, $\frac{m+1}{2}$ vertices are collected $\frac{n-1}{2}$ times and $\frac{m+1}{2}$ vertices are collected $\frac{n+1}{2}$ times. Therefore, $|S| = \left(\frac{n-1}{2}\right)\left(\frac{m+1}{2}\right) + \left(\frac{n+1}{2}\right)\left(\frac{m-1}{2}\right) = \frac{nm-1}{2}$ and hence, $R_2^D(G) = |S| = \frac{nm-1}{2}$.

4 Location-2-Domination for Direct Product of Graphs

Theorem 8 *For Graphs P_n and P_m, $m \neq 3$,*

$$R_2^D(P_n \times P_m) = \begin{cases} \frac{nm}{2} + 2, & n,\ m\ is\ even \\ \frac{nm}{2} + 2, & either\ n\ is\ odd,\ m\ is\ even\ (or)\ n\ is\ even\ m\ is\ odd \\ \frac{n(m+1)}{2}, & n, m\ is\ odd\ but\ n < m \\ \frac{m(n+1)}{2}, & n, m\ is\ odd\ but\ n > m \end{cases}$$

Proof Let us label the vertices of $G = (P_n \times P_m)$ as $\{v_{ij}\}$ for $1 \leq i \leq n$ and $1 \leq j \leq m$, clearly $|G| = nm$. And let $S-$set denote the Location-2-Dominating set, from G, $d_G(v_{11}) = d_G(v_{1m}) = d_G(v_{n1}) = d_G(v_{nm}) = 1$. So, by Theorem 3 $v_{11}, v_{1m}, v_{n1}, v_{nm}$ all belong to the S-set only in all of the following cases. Also, $d_G(v_{1j}) = d_G(v_{nj}) = d_G(v_{i1}) = d_G(v_{im}) = 2$ for $i = 2, 3, \ldots, n-1$ and $j = 2, 3, \ldots, m-1$, also $d_G(v_{ij}) = 4$ for $2 \leq i \leq n-1, 2 \leq j \leq m-1$.

Case (i) Suppose that n, m is even, now collect the $S-$set, namely $\{v_{ij}\}$ for $1 \leq i \leq n$ and $j = 1, 3, \ldots, m-1$ or $i = 1, 3, \ldots, n-1$ and $1 \leq j \leq m$. This collection clearly contains either v_{11} and v_{1m} or v_{n1} and v_{nm} only. This gives $\frac{n}{2}$ times m vertices; also, the only remaining vertices are two pendant vertices, that is, $|S| = \frac{nm}{2} + 2$. Therefore, $R_2^D(G) = \frac{nm}{2} + 2$.

Case (ii)(a) Suppose that n is odd and m is even, now collect the $S-$ set namely $\{v_{ij}\}$ for $1 \leq i \leq n$ and $j = 1, 3, \ldots, m-1$; also, the two remaining vertices are pendant vertices v_{1m} and v_{nm}, that is, $|S| = \frac{nm}{2} + 2$. Therefore, $R_2^D(G) = \frac{nm}{2} + 2$.

(b): Suppose that n is even and m is odd. Now collect the $S-$ set, namely $\{v_{ij}\}$ for $i = 1, 3, \ldots, n-1$ and $1 \leq j \leq m$. In this case, two pendant vertices v_{n1} and v_{nm} are the only remaining vertices; hence, $|S| = \frac{nm}{2} + 2$. Therefore, $R_2^D(G) = \frac{nm}{2} + 2$.

Case (iii) Suppose that n, m is odd. If $n < m$, now collect the dominating set possibly by $\{v_{ij}\}$ for $i = 1, 2, 3, \ldots, n$ and $j = 1, 3, \ldots, m$. Then, the collection of vertices gives $\frac{(m+1)}{2}$ times n vertices, that is, $|S| = \frac{n(m+1)}{2}$. Therefore, $R_2^D(G) = \frac{n(m+1)}{2}$. If $n > m$, now collect the dominating set, possibly by $\{v_{ij}\}$ for $i = 1, 3, \ldots, n$ and $j = 1, 2, 3, \ldots, m$; hence, the collection of vertices gives $\frac{(n+1)}{2}$ times m vertices, that is, $|S| = \frac{m(n+1)}{2}$. Therefore $R_2^D(G) = \frac{m(n+1)}{2}$.

Theorem 9 *For graphs $P_3 \times P_m$, we have $R_2^D(P_3 \times P_m) = 2m$, and m is either even or odd.*

Proof Let the vertices $G = P_3 \times P_m$ be $\{v_{ij}\}$ for $i = 1, 2, 3$, $1 \leq j \leq m$. From G, $d_G(v_{11}) = d_G(v_{1m}) = d_G(v_{31}) = d_G(v_{3m}) = 1$. And $d_G(v_{12}) = d_G(v_{13}) = , \ldots, = d_G(v_{1(m-1)}) = d_G(v_{32}) = d_G(v_{33}) =, \ldots, = d_G(v_{3(m-1)}) = 4$. Now collect the $S-$set, possibly by $\{v_{ij}\}$ for $i = 1, 3$ and $1 \leq j \leq m$. Clearly, it gives $2m$ vertices, $|S| = 2m$. Therefore, $R_2^D(G) = 2m$. Suppose that any one vertex omitting

from $\{v_{ij}\}$ for $i = 1, 3$ and $1 \leq j \leq m$, or adding any one vertex from $\{v_{2j}\}$ for $1 \leq j \leq m$, it clearly contradicts the definition of the Location-2-Dominating set or increases the cardinality of the $S-$set.

Theorem 10 *For P_n and C_m, $m \neq 2, 4$,*

$$R_2^D(P_n \times C_m) = \begin{cases} \frac{nm}{2}, & n, m \text{ is even} \\ \frac{nm}{2}, & n \text{ is odd}, m \text{ is even (or) } m \text{ is even}, n \text{ is odd} \\ \frac{n(m+1)}{2}, & n, m \text{ is odd but } n < m \\ \frac{m(n+1)}{2}, & n, m \text{ is odd but } n > m \end{cases}$$

Proof Clearly, $| P_n \times C_m | = nm$, now label the vertices of $P_n \times C_m$ as $\{v_{ij}\}$ for $1 \leq i \leq n, 1 \leq j \leq m$. Also, the $2m$ vertices have the degree 2 and the remaining $m(n-2)$ vertices have the degree 4. Let $S-$ set denote the Location-2-Dominating set.

Case (i) Suppose that n, m is even. Now collect the $S-$set possibly by $\{v_{ij}\}$ for $i = 1, 2, 3, \ldots, n$; $j = 1, 3, 5, \ldots, m-1$ or $i = 1, 3, \ldots, n-1$; $j = 1, 2, 3, \ldots, m$ or $i = 1, 2, 3, \ldots, n$; $j = 2, 4, \ldots, m$ or $i = 2, 4, \ldots, n$; $1, 2, 3, \ldots, m$. Then, such a collection gives $n\left(\frac{m}{2}\right)$ or $m\left(\frac{n}{2}\right)$ vertices, that is, $|S| = \frac{nm}{2}$.

Case (ii) Suppose that n is odd and m is even. In this sense, collect the vertices by $\{v_{ij}\}$ for $i = 1, 2, 3, \ldots, n$ and $j = 1, 3, 5, \ldots, m-1$. Clearly, $\frac{m}{2}$ times n vertices are contained in S. Therefore, $|S| = \frac{nm}{2}$. Suppose that $S = \{v_{ij}\}$, $i = 1, 3, \ldots, n-1$ and $j = 1, 2, 3, \ldots, m$. Clearly, $\frac{(n+1)}{2}$ times m vertices contained in S, which contradicts the minimum cardinality.

Case (iii) Suppose that n, m is odd, proof is followed by Theorem 8.

Theorem 11 *For $G = P_n \times C_2$, $n \neq 3$, $R_2^D(G) = \begin{cases} n+2, & n \text{ is even}, \\ n+1, & n \text{ is odd} \end{cases}$*

Proof Clearly, by the observation $P_n \times C_2$ is isomorphic to $P_n \times P_2$. Therefore, the proof is followed by Theorem 10.

Theorem 12 *For $G = P_n \times C_4$, $n \neq 3$, $R_2^D(G) = \begin{cases} 3n+1, & n \text{ is odd} \\ 3n, & n \text{ is even} \end{cases}$*

Proof Label the vertices of G as $\{v_{ij}\}$, $i = 1, 2, \ldots, n$ and $j = 1, 2, 3, 4$. Clearly, $d_G(v_{ij}) = 4$, $i = 1, 2, \ldots, n$ and $j = 1, 4$, $d_G(v_{ij}) = 2$, $i = 1, 2, \ldots, n$, $j = 2, 3$.

Case (i) Suppose that n is odd, Clearly, $2(n+1)$ times $d_G(v_{ij}) = 4$, and $2(n-1)$ times $d_G(v_{ij}) = 2$. Now collect the $S-$set possibly by $\frac{n+1}{2}$ times $d_G(v_{ij}) = 4$ and $\frac{n-1}{2}$ times $d_G(v_{ij}) = 2$, that is, $|S| = 4\left(\frac{n+1}{2}\right) + 2\left(\frac{n-1}{2}\right) = 3n+1$.

Case (ii) Suppose that n is even. Clearly, $2n$ times $d_G(v_{ij}) = 4$ and $2n$ times $d_G(v_{ij}) = 2$. Now collect the $S-$set, possibly by $\frac{n}{2}$ times $d_G(v_{ij}) = 4$ and $\frac{n}{2}$ times $d_G(v_{ij}) = 2$, that is, $|S| = 4\left(\frac{n}{2}\right) + 2\left(\frac{n}{2}\right) = 3n$.

Theorem 13 *For Graphs* P_n $(n \neq 3)$ *and* S_m, $R_2^D(P_n \times S_m) = nm$, $n, m = 1, 2, 3, \ldots$

Proof Clearly, $|G| = n(m+1)$. Label the vertices of the graph with $\{v_{ij}\}$, $i = 1, 2, \ldots, n$ and $j = 1, 2, \ldots, m+1$. Also, $d_G(v_{ij}) = 1$ for $i = 1, n$ and $j = 2, 3, 4, \ldots, m+1$ and $d_G(v_{i1}) = m$ for $i = 2, 3, \ldots, n-1$ and $d_G(v_{ij}) = 2$, for $i = 2, 3, \ldots, n-1$, $j = 2, 3, \ldots, m+1$. Clearly, according to the theorem $\{v_{ij}\}$ for $i = 1, n$ and $j = 2, 3, 4, \ldots, m+1$, all are members of S. Observing G, $\{v_{ij}\}$ for $i = 2, 3, \ldots, n-1$ and $j = 2, 3, \ldots, m+1$, all are neighbors of $\{v_{(i-1)1}\}$ and $\{v_{(i+1)j}\}$. Clearly, $\{v_{i1}\} \not\in S$ for $i = 1, 2, 3, \ldots, n$ and $\{v_{ij}\} \in S$ only for $i = 2, 3, \ldots, n-1$, $j = 2, 3, \ldots, m+1$. Therefore, $|S| = 2m + (n-2)m = nm$. Suppose that any one vertex from $\{v_{i1}\} \in S$ for $i = 1, 2, 3, \ldots, n$ and $\{v_{ij}\} \not\in S$ for $i = 2, 3, \ldots, n-1$, $j = 2, 3, \ldots, m+1$. Clearly, it contradicts the definition of Location-2-Domination or increases the cardinality.

Theorem 14 *For* $n, m \geq 5$, $R_2^D(C_n \times C_m) = \begin{cases} \frac{nm}{2}, & n, m \text{ is even} \\ \frac{(n-1)m}{2}, & n \text{ is odd } m \text{ is even} \\ \frac{n(m-1)}{2}, & n \text{ is even } m \text{ is odd} \\ \frac{(n-1)m}{2}, & n, m \text{ is odd } n < m \\ \frac{n(m-1)}{2}, & n, m \text{ is odd } n > m \end{cases}$

Proof Let us label the vertex set of $C_n \times C_m$ as $\{v_{ij}\}$, $1 \leq i \leq n$, $1 \leq j \leq m$ and in this graph each vertex has degree four.

Case (i) Suppose that if n, m is even, then the collection of $S-$set can be of the form $\{v_{ij}\}$ for $i = 1, 2, 3, \ldots, n-1$ and $j = 1, 3, 5, \ldots, m-1$ or $i = 1, 3, \ldots, n-1$ and $j = 1, 2, 3, \ldots, m-1$ or $i = 1, 2, 3, \ldots, n$ and $j = 2, 4, \ldots, m$ or $i = 2, 4, \ldots, n$ and $j = 1, 2, 3, \ldots, m$. Clearly, $|S| = \frac{nm}{2}$. Suppose that if the $S-$set is none of the above forms, then it contradicts the minimum cardinality.

Case (ii) Suppose that n is odd m is even, by observation of the graph G, $S = \{v_{ij}\}$ $i = 1, 3, \ldots, n-2$ and $j = 1, 2, \ldots, m$. This gives $\left(\frac{n-1}{2}\right)$ times $\frac{m}{2}$ vertices i.e., $|S| = \frac{(n-1)m}{2}$

Case (iii) Suppose that n is even and m is odd, only the pattern of vertex set selection is different from Case (ii).

Case (iv) Suppose that n, m is odd. If $n < m$, collect the set S as $\{v_{ij}\}$, $i = 1, 2, 3, \ldots, n$ and $j = 1, 3, \ldots, m$. This gives $\left(\frac{m-1}{2}\right)$ times n vertices, i.e., $|S| = \frac{n(m-1)}{2}$. Suppose that $S = \{v_{ij}\}$, $i = 1, 3, \ldots, n$ and $j = 1, 2, \ldots, m$. Clearly, this gives $|S| = \frac{n(m+1)}{2} + 1$ vertices and is not the minimum cardinality. If $n > m$, then take the set $S = \{v_{ij}\}$, $i = 1, 3, \ldots, n$ and $j = 1, 2, 3, \ldots, m$. This gives $\left(\frac{n-1}{2}\right)$ times m vertices, that is, $|S| = \frac{m(n-1)}{2}$.

Remark 1 $R_2^D(C_2 \times C_m) = n\ ,\ m \neq 2.$

Remark 2 $R_2^D(C_3 \times C_m) = \begin{cases} \frac{3m}{2},\ m\ is\ even,\ m \neq 2 \\ \frac{3(m-1)}{2}, \qquad\qquad m\ is\ odd \end{cases}$

Remark 3 $R_2^D(C_4 \times C_m) = \frac{m}{2}\ ,\ m \neq 2, 4.$

5 Conclusion

In this chapter, the Locating-2-Dominating set and the Location-2-Domination number for direct and Cartesian products of graphs, namely $P_n \square P_m$, $P_n \square S_m$, $P_n \square W_m$, $C_n \square C_m$, $P_n \times P_m$, $P_n \times S_m$, $C_n \times P_m$ and $C_n \times C_m$ were found.

References

1. Faudree, R.J., Schelp, R.H.: The domination number for the product of graphs. Congr. Numer., **79**, 29–33 (1990).
2. Harary, F., Haynes, T.W.: Double domination in graphs. Ars Combin., **55**, 201–213 (2000).
3. Haray, F.: *Graph theory*, Addison Wesley, Reading MA, 1969.
4. Haynes, T.W., Hedetniemi, S.T., Salter. P.J.: *Fundamentals of domination in graphs*, Marcel Decker, Inc., New York, 1997
5. Rajasekar, G., Venkatesan, A.: Location-2-Domination for simple graphs. Global Journal of Pure and Applied Mathematics, **13**, No:9, 5049–5057 (2017).
6. Rajasekar, G., Venkatesan, A.: Location-2-Domination for special kinds of simple graphs. International Journal of Pure and Applied Mathematics, **117**, No:5 , 13–20 (2017).
7. Slater, P.J.: Dominating and reference sets in a graph. J. Math. Phys. Sci., 22 (1988), 445–455.
8. Slater, P.J.: Domination and location in acyclic graphs. Wiley online library, 55–64 (1987) https://onlinelibrary.wiley.com/.
9. Sitthiwirattham, T.: Domination on Kronecker product of P_n. Applied Mathematical Sciences, **6**, No. 87, 4345–4352 (2012).

Local Distance Pattern Distinguishing Sets in Graphs

R. Anantha Kumar

Abstract Let $G = (V, E)$ be a connected graph and $W \subseteq V$ be a nonempty set. For each $u \in V$, the set $f_W(u) = \{d(u, v) : v \in W\}$ is called the *distance pattern* of u with respect to the set W. If $f_W(x) \neq f_W(y)$ for all $xy \in E(G)$, then W is called a *local distance pattern distinguishing set* (or a $LDPD$-set in short) of G. The minimum cardinality of a $LDPD$-set in G, if it exists, is the $LDPD$-number of G and is denoted by $\varrho'(G)$. If G admits a $LDPD$-set, then G is called a $LDPD$-graph. In this paper we discuss the $LDPD$-number $\varrho'(G)$ of some family of graphs and the relation between $\varrho'(G)$ and other graph theoretic parameters. We characterized several family of graphs which admits $LDPD$-sets.

Keywords LDPD-set · LDPD-number · Local metric set

1 Introduction

By a graph $G = (V, E)$, we mean a finite, undirected, and connected graph with neither loops nor multiple edges. The order and size of G are denoted by n and m, respectively. For graph theoretic terminology, we refer to Chartrand and Lesniak [7].

The distance $d(u, v)$ between two vertices u and v in G is the length of a shortest u-v path in G. The open neighborhood $N(v)$ of the vertex v consists of the set of all vertices adjacent to v, that is, $N(v) = \{w \in V : vw \in E\}$. The eccentricity of u is $e(u) = \max\{d(u, v) : v \in V\}$. For a vertex $v \in V(G)$, the ith neighborhood of v is $N_i(v) = \{u \in V(G) : d(u, v) = i\}$. By an ordered set of vertices, we mean a set $W = \{w_1, w_2, \cdots, w_k\}$ on which the ordering $(w_1, w_2, \cdots, w_k)$ has been imposed. For an ordered subset $W = \{w_1, w_2, \cdots, w_k\}$ of $V(G)$, we refer to the k-vector (ordered k-tuple) $r(v|W) = (d(v, w_1), d(v, w_2), \cdots, d(v, w_k))$ as the (metric)

R. Anantha Kumar (✉)
MEPCO Schlenk Engineering College (Autonomous), Sivakasi, India
e-mail: ananthakumar@mepcoeng.ac.in

B. Rushi Kumar et al. (eds.), *Applied Mathematics and Scientific Computing*,
Trends in Mathematics, https://doi.org/10.1007/978-3-030-01123-9_51

representation of v with respect to W. The set W is called a *resolving set* for G if $r(u|W) = r(v|W)$ implies $u = v$ for all $u, v \in V(G)$. Hence if W is a resolving set of cardinality k for a graph G of order n, then the set $\{r(v|W) : v \in V(G)\}$ consists of n distinct k-vectors. A resolving set of minimum cardinality is called a *basis* for G, and the *metric dimension* of G is defined to be the cardinality of a basis of G and is denoted by $dim(G)$. The idea of resolving set has appeared in the literature previously. In [5] and later in [6], Slater introduced the concept of a resolving set for a connected graph G under the term locating set. He referred to a minimum resolving set as a reference set for G. He called the cardinality of a minimum resolving set (reference set) as the location number of G. Independently, Harary and Melter [2] discovered these concepts as well but used the term metric dimension.

In [1] Ananthakumar and Germina studied the concept of DPD-sets instead of considering the k-vector of distances, which simply takes the set of all distances from vertex v to the vertices in W.

Definition 1 Let $G = (V, E)$ be a connected graph. Let M be a nonempty subset of V, and let $u \in V(G)$. The distance pattern of u with respect to the set M is $f_M(u) = \{d(u, v) : v \in M\}$. If f_M is an injective function on V, then the set M is called a *distance pattern distinguishing set* (or DPD-set in short) of G. The minimum cardinality of a DPD-set in G, if it exists, is the DPD-number of G, and it is denoted by $\varrho(G)$.

Later, Okamato et al. [3] introduced the concept of local metric dimension of a graph.

Definition 2 Let $G = (V, E)$ be a connected graph. For an ordered set $W = \{w_1, w_2, \ldots, w_k\} \subseteq V$ of k distinct vertices in a nontrivial connected graphs G, the metric code of a vector v of G with respect to W is the k-vector, $code(v) = (d(v, w_1), d(v, w_2), \ldots, d(v, w_k))$. The set W is a *local metric set* of G if $code(u) \neq code(v)$ for every pair u, v of adjacent vertices of G. The minimum positive integer k for which G has a local metric set of cardinality k is the *local metric dimension* $lmd(G)$ of G.

In this paper, instead of considering the k-vector of distances, we simply take the set of all distances from vertex v to the vertices in W and investigate under what condition this assignment of the set of distances to the vertices has the property that adjacent vertices receive distinct sets.

We need the following definitions and theorems:

Definition 3 ([4]) Let $G = (V, E)$ be a connected graph of order $n \geq 2$. Two vertices u and v of G are *distance similar* if $d(u, x) = d(v, x)$ for all $x \in V - \{u, v\}$.

Definition 4 ([9]) Given an arbitrary graph G, the *trestled graph* of index k, denoted by $T_k(G)$, is the graph obtained from G by adding k-copies of K_2 for each edge uv of G and joining u and v to the respective end vertices of each K_2.

Definition 5 ([8]) The *core* of the graph G is obtained by successively deleting end vertices until none remain.

Theorem 1 ([1]) *If G is a graph having three pairwise distance similar vertices x, y, and z, then G is not a* DPD-graph. *Further if G is a DPD-graph having exactly two* distance similar *vertices x, y, then exactly one of x, y lies in every DPD-set M of G.*

Theorem 2 ([1]) *The cycle C_n is a DPD-graph if and only if $n \geq 7$. Further $\varrho(C_n) = 3$ for all $n \geq 7$.*

2 Main Results

In this section we are finding the $LDPD$-number of several family of graphs and discuss the relation between $\varrho'(G)$, $\varrho(G)$, and $lmd(G)$.

Definition 6 Let $G = (V, E)$ be a connected graph and let $W \subseteq V$ be a nonempty set. For each $u \in V(G)$, the set $f_W(u) = \{d(u, v) : v \in W\}$ is called the *distance pattern* of u with respect to the set W. If $f_W(x) \neq f_W(y)$ for all $xy \in E(G)$, then the set W is called a *local distance pattern distinguishing set* (or a $LDPD$-set in short) of G. If G admits a *LDPD-set*, then G is called a $LDPD$-graph. The minimum cardinality of a $LDPD$-set in G, if it exists, is the $LDPD$-number of G and is denoted by $\varrho'(G)$.

Observation 3

(1) It is obvious that if G admits a DPD-set M, then M is a $LDPD$-set of G; hence $\varrho'(G) \leq \varrho(G)$. But there are graphs having $LDPD$-set but not a DPD-set. For example, the star $K_{1,n}$, $n \geq 3$ does not have a DPD-set by Theorem 1, but any vertex of $K_{1,n}$ is a $LDPD$-set.

(2) If G is a $LDPD$-graph, then every $LDPD$-set is a local metric set, and hence $lmd(G) \leq \varrho'(G)$.

(3) Let G be any nontrivial graph. Then $V(G)$ is a $LDPD$-set of G if and only if there exist no edge $uv \in E(G)$ such that $e(u) = e(v)$. For example, consider $G_1 = P_{2n+1}$ and $G_2 = P_{2n+1} \circ K_1$(Corona of P_{2n+1} and K_1). Then the sets $V(G_1)$ and $V(G_2)$ are $LDPD$-sets of G_1 and G_2, respectively.

(4) Let u, v be any two adjacent distance similar vertices in a graph G. Then exactly one vertex of u, v belongs to every $LDPD$-set and local metric set of G if it exists.

Example 1 For the graph G given in Fig. 1, $W = \{v_1, v_2, v_3\}$ is a $LDPD$-set of G. Here $\{v_1, v_4\}$, $\{v_2, v_5\}$, and $\{v_3, v_6\}$ are the set of all adjacent distance similar vertices of G, and by (4) of Observation 3, $\varrho'(G) = 3$.

Theorem 4 *Let G be any nontrivial connected graph. Then $\varrho'(G) = 1$ if and only if G is a bipartite graph.*

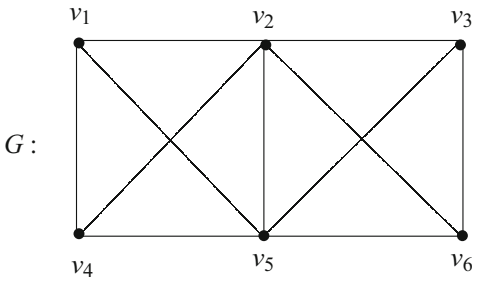

Fig. 1 LDPD-graph with LDPD-number is 3

Proof Let G be any bipartite graph and let $v \in V(G)$. Then $N_i(v)$ is an independent set for each $i,\ i = 1, 2, \ldots, e(v)$ (eccentricity of v), and hence $\{v\}$ is a $LDPD$-set of G and $\varrho'(G) = 1$.

Conversely assume that $W = \{v\} \subseteq V(G)$ be a $LDPD$-set of G. Then $N_i(v)$ is an independent set for each $i, i = 1, 2, \ldots, e(v)$. Let $V_1 = \{v\} \cup \left(\bigcup_{i=1}^{\left\lfloor \frac{e(v)}{2} \right\rfloor} N_{2i}(v) \right)$ and $V_2 = \left(\bigcup_{i=0}^{\left\lfloor \frac{e(v)}{2} \right\rfloor} N_{2i+1}(v) \right)$. Now V_1 and V_2 are independent sets. Thus $V_1 \cup V_2$ is a bipartition of $V(G)$ which implies G is a bipartite graph.

Corollary 1 *For the n-dimensional hypercube* $Q_n, n \geq 3,\ \varrho'(Q_n) = 1$.

Theorem 5 *Let G be any complete k-partite graph with $k \geq 3$. Then G is a $LDPD$-graph if and only if $k = 3$ and G is not isomorphic to K_3. Further if G is a $LDPD$-graph, then $\varrho'(G) = \min\{|V_i| : |V_i| \geq 2\} + 1$.*

Proof Let $V_1 \cup V_2 \cup \cdots \cup V_k$ be the k-partition of $V(G)$, and let W' be any $LDPD$-set of G. Let $u \in V_i \cap W'$ and $v \in V_j \cap W'$, $i \neq j$. Since the vertices in same partite sets are distance similar, $|V_i \cap W| \leq 1$ for all $i = 1, 2, \ldots k$. Also if $|V_i \cap W'| = |V_j \cap W'| = 0$, then $f_{W'}(u) = f_{W'}(v) = \{1\}$ where $u \in V_i$ and $v \in V_j$, which is a contradiction. Hence we have $k = 3,\ |V_1 \cap W'| \geq 2,\ |V_2 \cap W'| = 1$ and $|V_3 \cap W'| = 0$. Also if G isomorphic to K_3, then it is easy to check that G has no $LDPD$-set. Conversely assume G is a complete tripartite graph and $G \neq K_3$. Let $V(G) = V_1 \cup V_2 \cup V_3$ be the tripartition of $V(G)$ with $|V_1| \geq 2$. Let $W = V_1 \cup \{y\}$, where $y \in V_2$.

Then $f_W(x) = \begin{cases} \{0, 1, 2\} & if\ \ x \in V_1 \\ \{1, 2\} & if\ \ x \in V_2 - \{y\} \\ \{1\} & if\ \ x \in V_3 \\ \{0, 1\} & if\ \ x = y. \end{cases}$ Hence W is a $LDPD$-set of G. Further, $\varrho'(G) = \min\{|V_i| : |V_i| \geq 2\} + 1$.

Theorem 6 *Let G be any unicyclic graph. Then G is a $LDPD$-graph if and only if G is not isomorphic to C_3 or C_5. Further if G is a $LDPD$-graph, then*

$$\varrho'(G) = \begin{cases} 1 & if \quad Gisbipartite \\ 3 & if \quad G \cong C_{2k+1} \\ 2 & otherwise. \end{cases}$$

Proof Let G be a unicyclic graph and G is not isomorphic to C_3 or C_5. Let C be the unique cycle in G whose length is denoted by $l(C)$. If $l(C)$ is even, then G is a bipartite graph. Hence by Theorem 4 $\varrho'(G) = 1$.

Suppose G is the cycle C_{2k+1}, $k \geq 3$. Then by Theorem 2, (1) of Observation 3, and Theorem 4, we have G is a $LDPD$-graph and $2 \leq \varrho'(G) \leq 3$. Now we prove that there is no $LDPD$-set of cardinality two in G. Let $W_1 = \{v_i, v_j\}$ be any subset of $V(G)$. Let P_1 and P_2 be the distinct paths joining v_i and v_j. Then exactly one of $l(P_1)$ or $l(P_2)$ is odd, say $l(P_1)$ is odd and $centre(P_1) = \{x, y\}$ for some $xy \in E(G)$. Then $f_{W_1}(x) = f_{W_1}(y) = \{rad(P_1), rad(P_1) + 1\}$. Hence W_1 is not a $LDPD$-set. Therefore $\varrho'(G) = 3$.

Now we assume that G properly contains C_{2k+1} for some $k \geq 1$. Label the vertices of C_{2k+1} by $v_1, v_2, \ldots, v_{2k+1}$ such that there exist $x \in V(G) - V(C_{2k+1})$ which is adjacent to v_2. Then $W_2 = \{v_1, x\}$ is a $LDPD$-set, for $f_{W_2}(v_i) = \{i - 1\}$ if $2 \leq i \leq k + 1$, $f_{W_2}(v_i) = \{2(k + 1) - i, 2(k + 2) - i\}$ if $k + 3 \leq i \leq 2k + 1$, $f_{W_2}(v_{k+2}) = \{k, k + 1\}$ and if $uv \in E(G) - E(C_{2k+1})$, then $f_{W_2}(u) = f_{W_2}(v) + 1$ or $f_{W_2}(v) = f_{W_2}(u) + 1$. Hence adjacent vertices receives distinct sets. Therefore $\varrho'(G) = 2$.

Conversely if G is isomorphic to C_3 or C_5, then it is easy to check that G has no $LDPD$-set.

Proposition 1 *Let G be the sequential join graph $K_2 + K_2 + \cdots + K_2$ k-times. Then G is a $LDPD$ graph if and only if k is odd. Further if G is a $LDPD$-graph, then $\varrho'(G) = k$.*

Proof Let $V(G) = \bigcup_{i=1}^{k} V_i(K_2)$, where $V_i(K_2) = \{u_i, v_i\}$ for $i = 1, 2, \ldots, k$. Let W be any $LDPD$-set of G if it exists. Then $|V_i(K_2) \cap W| = 1$ for all $i = 1, 2, \ldots, k$ by (4) of Observation 3. We assume that $W = \{u_1, u_2, \ldots, u_k\}$. Then $f_W(u_i) = \{0, 1, 2, \ldots, e(u_i)\}$ and $f_W(v_i) = \{1, 2, \ldots, e(u_i)\}$ for all $i = 1, 2, \ldots, k$. So it is enough to check the injectivity of f for the adjacent vertices $x, y \in W$ and $x, y \in V - W$ with $e(x) = e(y)$. Without loss of generality, assume $x, y \in V - W$ and $e(x) = e(y)$. Then $f_W(x) = f_W(y)$ and $x, y \in centre(G)$ hence $diam(G)$ is odd, which implies k is even. Conversely suppose k is odd. Then $f_W(u_i) = f_W(u_{k+1-i}) = \{0, 1, 2, \ldots, k - i\}$ for all $i = 1, 2, \ldots, \lfloor \frac{k}{2} \rfloor$, $f_W(u_{\lfloor \frac{k}{2} \rfloor + 1}) = \{0, 1, 2, \ldots, \lfloor \frac{k}{2} \rfloor\}$, $f_W(v_i) = f_W(v_{k+1-i}) = \{1, 2, \ldots, k - i\}$ for all $i = 1, 2, \ldots, \lfloor \frac{k}{2} \rfloor$ and $f_W(v_{\lfloor \frac{k}{2} \rfloor + 1}) = \{1, 2, \ldots, \lfloor \frac{k}{2} \rfloor\}$. Therefore W is a $LDPD$-set of G and $\varrho'(G) = k$.

The following theorem shows that identifying any number of trees at any set of vertices to a $LDPD$-graph results a $LDPD$-graph.

Theorem 7 *Let H be any $LDPD$-graph with $\varrho'(H) = k$. Let G be a graph with $core(G) = H$. Then $\varrho'(G) \leq k$.*

Proof Given that $core(G) = H$, G can be decomposed into the subgraphs $H, T_1, T_2, \ldots, T_t$ where T_i^s are the trees with exactly one vertex of T_i that is identified to say $u_i \in V(H)$ for all $i = 1, 2, \ldots, t$. Let W be any $LDPD$-set of H of cardinality k. We prove that W is a LDPD-set of G. Since W is a $LDPD$-set of H and $d_G(x, y) = d_H(x, y)$ for all $x, y \in V(H)$, we have $f_W(u) \neq f_W(v)$ for all $uv \in E(H)$. Let $uv \in E(G) - E(H)$. Without loss of generality, assume that $uv \in E(T_i)$ for some i, $1 \leq i \leq t$ and $d(v, u_i) = d(u, u_i) + 1$. Then $f_W(u) = f_W(v) + 1$ hence W is a $LDPD$-set of G and $\varrho'(G) \leq k$.

Remark 1 The bound $\varrho'(G) \leq k$ in Theorem 7 can be sharp and strict also. For example,

(1) Let H_1 be the sequential join graph $K_2 + K_2 + K_2$. Let G_1 be the graph obtained from H_1 by identifying the center of $K_{1,2}$ at exactly one vertex of H_1. Then $\varrho'(H_1) = 3$ by Proposition 1, and it can be verified that $\varrho'(G_1) = 3$.
(2) Let $H_2 = C_{2k+1}$, $k \geq 3$. Let G_2 be any unicyclic graph that contains H_2 as a proper subgraph. Then $\varrho'(H_2) = 3$ and $\varrho'(G_2) = 2$ by Theorem 6.

Theorem 8 *Let G be any $LDPD$-graph. Then the trestled graph $T_k(G)$ of G is also a $LDPD$-graph. Further $\varrho'(T_k(G)) \leq \varrho'(G)$.*

Proof Let $V(G) = \{v_1, v_2, \ldots, v_n\}$, and let $e_i^1 = v_i^1 v_t^1, e_i^2 = v_i^2 v_t^2, \ldots, e_i^k = v_i^k v_t^k$ be the edges of $T_k(G)$ corresponding to the edge $e_i = v_i v_t \in E(G)$ for all $i = 1, 2, \ldots, m$. Let W be any $LDPD$-set of G. Since $d(v_i^j, x) = d(v_i, x) + 1$ and $d(v_t^j, x) = d(v_t, x) + 1$ for all $j = 1, 2, \ldots, m$, $x \in W$ and $v_i, v_t \in V(G)$, we have $f_W(v_i^j) = f_W(v_i) + 1$. and $f_W(v_t^j) = f_W(v_t) + 1$. Also $f_W(v_i) \neq f_W(v_j)$ for all $v_i v_j \in E(G)$ as W is a $LDPD$-set of G, it follows that $f_W(v_i^j) \neq f_w(v_t^j)$ for all $j \in \{1, 2, \ldots, k\}$ and $e_i = v_i v_t \in E(G)$ hence W is a $LDPD$-set of $T_k(G)$. Therefore $\varrho'(T_k(G)) \leq \varrho'(G)$.

Remark 2 The converse of the above theorem need not be true. That is if $T_k(G)$ is a $LDPD$-graph, then G need not be a $LDPD$-graph. For example, consider $G = C_5$ and $T_1(G)$. Then G is not a $LDPD$-graph by Theorem 6, but one can check that $T_1(C_5)$ has a $LDPD$-set.

Although not all the graphs have $LDPD$-set, here we present a technique to embed any graph as $LDPD$-graph.

Theorem 9 *Let G be any graph of order at least four. Then G can be embedded into a $LDPD$-graph.*

Proof Let $V(G) = \{v_1, v_2, \ldots, v_n\}$. Let G' be the graph obtained from G by identifying exactly one leaf of path P_{in+1} at v_i for all $i = 1, 2, \ldots, n$, respectively.

Let $W = \{v'_1, v'_2, \ldots, v'_n\} \subseteq V(G')$, where v'_i is a pendent vertex of G' and $v'_i \in V(P_{in+1})$ for all $i = 1, 2, \ldots, n$. Now we prove that W is a $LDPD$-set of G'. Since $in \in f_W(v_i)$, for all $i = 1, 2, \ldots, n$ and $in \notin f_W(v_j)$ for $i \neq j$, we have $f_W(v_i) \neq f_W(v_j)$ for all $v_i v_j \in E(G)$. Let $uv \in E(G') - E(G)$. Without loss of generality, assume that uv is an edge of the path P_{in+1} for some i, $1 \leq i \leq n$ and $d(v, v_i) = d(u, v_i) + 1$. Then $f_W(v) = \{\{f_W(u) - \{d(u, v_i)\}\} + 1\} \cup \{d(v, v_i)\}$ hence $f_W(u) \neq f_W(v)$. Therefore W is a $LDPD$-set of G'.

3 Some Realization Results

Already we observed that $\varrho'(G) \geq lmd(G)$ and $\varrho(G) \geq \varrho'(G)$, in this section we show that the strict in equality can be made as large as possible.

Theorem 10 *Given any positive integer k, there exists a graph G such that* $\varrho'(G) = lmd(G) = k$.

Proof When $k = 1$, let $G = K_2$. Then $\varrho'(G) = lmd(G) = 1$.

When $k \geq 2$, let $G = K_1 + kK_2$, where $V(K_1) = \{x\}$ and $V_i(K_2) = \{u_i, v_i\}$ for $i = 1, 2, \ldots, k$. Since u_i and v_i are adjacent distance similar vertices in G, exactly one of u_i or v_i say u_i belongs to every $LDPD$-set and local metric set of G for all $i = 1, 2, \ldots, k$. Let $W = \{u_1, u_2, \ldots, u_k\}$. Then $f_W(u_i) = \{0, 2\}$, $f_W(v_i) = \{1, 2\}$ for all $i = 1, 2, \ldots, k$, $f_W(x) = \{1\}$ and $\{u_1, u_2, \ldots, u_k\}$, $\{v_1, v_2, \ldots, v_k\}$ are independent sets; hence W is a $LDPD$-set. Therefore $\varrho'(G) = k$ by (4) of Observation 3.

The codes of x, u_i, v_i are the k-tuples, $code(x) = (1, 1, \ldots, 1)$,

$code(u_i) = (2, 2, \ldots, 0, 2, 2, \ldots, 2)$ (0 occurs only in the ith coordinate) and $code(v_i) = (2, 2, \ldots, 1, 2, 2, \ldots, 2)$ (1 occurs only in the ith coordinate), respectively. Hence $lmd(G) = k$ by (4) of Observation 3.

Theorem 11 *Given any positive integer k, there exists a graph G such that* $\varrho'(G) - lmd(G) = k$.

Proof Let H_i be the graph obtained from $3K_3 : (a_i, b_i, c_i) \cup (v_i, u_i, w_i) \cup (d_i, e_i, f_i)$ and $P_3 : (x_i, y_i, z_i)$ by identifying the vertex a_i and x_i at v_i and identifying the vertex d_i at w_i. Now let G be the graph obtained from the path $P_{2k-1} : (w'_1, w'_2, \ldots, w'_{2k-1})$ and $\{H_i : i = 1, 3, 5, \ldots, 2k-1\}$ by identifying a vertex w_i of H_i to a vertex w'_i of P_{2k-1} for all $i = 1, 3, 5, \ldots, 2k-1$, respectively.

Now in G, $\{b_i, c_i\}$ and $\{e_i, f_i\}$ are set of adjacent distance similar vertices; hence exactly one of b_i or c_i and one of e_i or f_i belong to every $LDPD$-set and local metric set of G for each $i = 1, 3, 5, \ldots, 2k-1$. Without loss of generality, we assume that every $LDPD$-set and local metric set of G contain b_i and e_i for all $i = 1, 3, 5, \ldots, 2k-1$. Let W_1 be any $LDPD$-set G. If $|V(H_i) \cap W_1| = 2$ for some i, $i \in \{1, 3, 5, \ldots, 2k-1\}$, then $W_1 \cap V(H_i) = \{b_i, e_i\}$ and $f_{W_1}(v_i) = f_{W_1}(u_i)$, a contradiction. Hence $|V(H_i) \cap W_1| \geq 3$ for all $i = 1, 3, 5, \ldots, (2k-1)$.

Let $W = \{b_i, e_i, z_i : i = 1, 3, 5, \ldots, 2k-1\}$. Let $xy \in E(G)$. If $xy \in \{v_ic_i,\ v_iy_i, v_iw_i,\ u_if_i,\ u_iw_i\}$, then $\max f_W(x) \neq \max f_W(y)$. If $x = v_i$ and $y = u_i$, then $3 = d(u_i, z_i) \in f_{W_1}(y)$ but $3 \notin f_{W_1}(x)$ hence $f_W(x) \neq f_W(y)$. Let $xy = w_i'w_{i+1}'$. Without loss of generality, assume that i is odd. Then $2 \in f_W(w_i')$ but $2 \notin f_W(w_{i+1}')$. Also W is an independent set; hence W is a $LDPD$-set of G. Therefore $\varrho'(G) = 3k$.

Let $W_2 = \{b_i, e_i : i = 1, 3, 5, \ldots, (2k-1)\}$ be an ordered subset of $V(G)$. Now we prove that W_2 is a local metric set of G. In G, $d(c_i, e_i) = d(v_i, e_i) + 1$, $d(f_i, b_i) = d(u_i, b_i) + 1$, $d(y_i, b_i) = d(v_i, b_i) + 1$ and $d(z_i, b_i) = d(y_i, b_i) + 1$, we have $code(v_i) \neq code(c_i)$ and $code(u_i) \neq code(f_i)$, $code(y_i) \neq code(v_i)$ and $code(z_i) \neq code(y_i)$. Now $d(w_i', b_i) = d(u_i, b_i) = d(v_i, b_i) + 1$ and $d(w_i', e_i) = d(u_i, e_i) + 1$; hence $code(w_i')$, $code(u_i)$, and $code(v_i)$ are mutually distinct. When $w_i'w_{i+1}' \in E(G)$ and i is odd, $d(w_{i+1}', b_i) = d(w_i', b_i) + 1$; hence $code(w_i') \neq code(w_{i+1}')$. Also W_2 is an independent set; therefore, W_2 is a local metric set and $lmd(G) = 2k$ by (4) of Observation 3. Thus $\varrho'(G) - lmd(G) = 3k - 2k = k$.

Theorem 12 *Given any positive integer $k \geq 3$, there exists a graph G such that $\varrho'(G) = \varrho(G) = k$.*

Proof When $k = 3$ consider $G = C_7$. Then by Theorems 2 and 6, $\varrho'(G) = \varrho(G) = 3$.

Assume $k \geq 4$. Let G be the graph obtained from the path $P_{\binom{k}{2}+1} : (v_1, v_2, \ldots, v_{\binom{k}{2}+1})$ and $H_i = C_3 : (x_i, u_i, w_i)$, $i = 1, 2, 4 \ldots, \binom{i}{2}+1, \ldots, \binom{k}{2}+1$ by identifying a vertex x_i of H_i at v_i for all $i = 1, 2, 4, \ldots, \binom{i}{2}+1, \ldots, \binom{k}{2}+1$, respectively. Since u_i and w_i are adjacent distance similar vertices by (4) of Observation 3, exactly one of u_i or w_i say u_i, $i = 1, 2, 4, \ldots, \binom{i}{2}+1, \ldots, \binom{k}{2}+1$ belongs to every DPD and $LDPD$ sets of G. Let $W = \{u_1, u_2, u_4, \ldots, u_{\binom{k}{2}+1}\}$. Now we prove that W is a DPD-set of G.

Let $x = v_i$, $y = v_j$ or $x = w_i$, $y = w_j$ or $x = u_i$, $y = u_j$ or $x = v_i$, $y = w_j$ with $i < j$. If $d(x, cen(G)) \neq d(y, cen(G))$, then $\max f_W(x) \neq \max f_W(y)$. If $d(x, cen(G)) = d(y, cen(G))$, then $\{d(y, u_1), d(y, u_2)\} \subseteq f_W(y)$ but $\{d(y, u_1), d(y, u_2)\} \not\subset f_W(x)$, hence $f_W(x) \neq f_W(y)$. Now consider the case $x = v_i$, $y = w_i$, and then $\max f_W(x) < \max f_W(y)$. Therefore W is a DPD-set and hence $\varrho(G) = k$. Let
$W_1 = \{u_1, u_2, u_4, \ldots, u_{\binom{k}{2}+1}\}$. Since W_1 is a DPD-set, W_1 is a $LDPD$-set also and hence $\varrho'(G) = k$.

4 Conclusion

In this paper the study of local distance pattern distinguishing sets and local distance pattern distinguishing number of a graph are initiated, and it is studied for some family of graphs. Also relation between LDPD-number and other graph theoretic parameters are studied.

Acknowledgements The author is thankful to Professor S. Arumugam for suggesting this problem. Also the author is very much grateful to the constant support of MEPCO Schlenk Engineering College (Autonomous), Sivakasi.

References

1. Ananthakumar, R., Germina, K.A. Distance Pattern Distinguishing Sets in Graphs. Adv. Stud. Contemp. Math(kyungshang). **21**, 107–114 (2011)
2. Harary, F., Melter, R. A. On the metric dimension of a graph. Ars Combin. **2**, 191–195 (1976)
3. Okamoto, F., Phinezy, B., Zhang, P. On Local Metric Dimension of a Graph. JCMCC. **72**, 243–259 (2010)
4. Saenpholphat, V., Zhang, P. Connected Resolvability of Graphs. Czech. Math. **53**(128), 827–840 (2003)
5. Slater, P. J. Leaves of trees. Congr. Numer. **14**, 549–559 (1975)
6. Slater, P. J. Domination and location in acyclic graphs. Networks. **17**, 55–64 (1987)
7. Chartrand, G., Lesniak, L.: Graphs and Digraphs. Chapman and Hall, CRC, (2005)
8. Chartrand, G., Zhang, P.: Chromatic Graph Theory. Chapman and Hall, CRC, (2009)
9. Haynes, T.W., Hedetniemi, S.T., Slater, P.J.: Fundamentals of Domination in Graphs. Marcel Dekker, Inc., New York, (1998)

Construction of Minimum Power 3-Connected Subgraph with k Backbone Nodes in Wireless Sensor Networks

D. Pushparaj Shetty and M. Prasanna Lakshmi

Abstract Minimizing the total power in a wireless sensor network (WSN) has great significance, since the nodes are powered by a small battery of limited capacity. By using an appropriate topology, the energy utilization of the network can be minimized which results in an increased lifetime of a WSN. In reality, WSN is modeled as an undirected graph in which each vertex represents a sensor node and an edge represents the link between the two sensor nodes. We define a distance function that maps a pair of vertices to a positive real number, i.e., Euclidean distance between the two vertices. On this initial topology, we construct a reduced topology satisfying special connectivity constraints like bi-connectivity, k-connectivity, bounded diameter, degree restricted, etc. We assign power to each node as the maximum distance of all its adjacent edges, and total power of the network is the sum of the powers of all the vertices. Fault tolerance addresses the issue of a node or link failure in a WSN. Fault-tolerant network aims at k-connectivity in the network so that there exist at least k vertex disjoint paths between any two sensor nodes of the network. Minimum power 2-connected subgraph (MP2CS) problem is to contrive a 2-connected network with minimum total power. It is proved that MP2CS problem is NP-hard. Minimum power k backbone node 2-connected subgraph (MPkB2CS) problem is a special case of MP2CS problem, which seeks a power assignment satisfying 2-connectivity with k backbone nodes. In this paper, the problem of finding a 3-connected network for a given set of nodes, which minimizes the total power with k backbone nodes, is addressed which is termed as MPkB3CS problem. We propose an algorithm for MPkB3CS problem and establish that the proposed algorithm has an approximation ratio of $4k + 1$, for $k \geq 3$.

Keywords Wireless sensor networks · Graph algorithms · Topology control problem · Range assignment · Approximation algorithm

D. Pushparaj Shetty · M. Prasanna Lakshmi (✉)
National Institute of Technology Karnataka, Mangaluru, India
e-mail: prajshetty@nitk.edu.in; ma14f03@nitk.edu.in

B. Rushi Kumar et al. (eds.), *Applied Mathematics and Scientific Computing*,
Trends in Mathematics, https://doi.org/10.1007/978-3-030-01123-9_52

Mathematics Subject Classification 05C85

1 Introduction

A wireless sensor network (WSN) is a set of specialized sensor nodes with a communication infrastructure, in which each sensor node processes the data and gathers the sensory information and communication between sensor nodes is facilitated in the network. A WSN has applications in several domains [1] like environment monitoring, remote medical systems, surveillance, biological detection, etc. To facilitate the communication between the sensor nodes of a WSN, we assign transmission power to every node of the network. So, any sensor node can communicate with all the nodes in its transmission range directly. Since the nodes require power to communicate with other nodes, it is a requisite task to connect the nodes in such a way that the total power utilized by the resultant network is minimized.

A replica of WSN is an undirected graph $G = (V, d)$, in which each vertex $v \in V$ represents a sensor node and the edge joining two vertices represents the communication link between the nodes. In this context, we deploy the sensor nodes in a Euclidean plane and define distance function $d : V \times V \to \mathbb{R}^+$, which maps a pair of vertices to a positive real number, i.e., the Euclidean distance between the two vertices. Every node is represented by its coordinates. Let $x = (x_1, x_2)$ and $y = (y_1, y_2)$ be the two vertices, and the Euclidean distance between these two vertices is computed by using distance formula given by $d(x, y) = \sqrt{(x_1 - x_2)^2 + (y_1 - y_2)^2}$. On this initial topology, power assignment leads to a reduced topology, which satisfies certain connectivity constraints.

For a given set of deployed vertices in a two-dimensional plane, power of a vertex v in graph G is defined as follows:

$$P(v) = \max\{d(vu) \mid uv \in E(G)\} \tag{1}$$

and the total power of the graph is $\sum_{i=1}^{n} P(v_i)$.

In minimum power assignment problem for given deployed set of nodes of a WSN, our objective is an assignment of transmission range to each sensor node of the network, so that the resultant-induced graph satisfies the required constraints [5] and also minimizes the total power consumption of the network. A topology control problem is to coordinate all the sensor nodes by assigning particular transmission range to each sensor node, in order to build the network that satisfies certain properties [13]. Properties include connectivity, bi-connectivity, broadcast, etc. In [12], Ramanathan and Regina Hain studied the topology control problem by adjusting the transmission power in a multi-hop WSN.

2 Related Work

Node (or link) failure in a network affects the communication in the entire network. To avoid this, it is necessary to construct a fault-tolerant network. This ensures that there exist two or more alternate paths between nodes, so that node failure in the network does not affect the entire network communication. Fault-tolerant network can be achieved by obtaining a network with two or high connectivity in which every two nodes are connected by two or more distinct paths [15].

2.1 Minimum Power Topology with Connectivity Constraints

Strong minimum energy topology (SMET) problem aims at transmission range assignment to each sensor node, which results in a strongly connected network. Cheng et al. [4] have studied SMET problem and proved that this problem is NP-hard. Authors also proposed two heuristics, i.e., power assignment based on MST (minimum spanning tree) and incremental power heuristic. MP2CS problem seeks a power assignment in which the reduced topology satisfies the following constraints: (1) reduced topology is 2-connected and (2) the total power consumption of the network is minimized. Nutov [9] gave an approximation algorithm for MPkCS problem for any fixed k. The approximation ratios are as follows: 3 for $k = 2$, 4 for $k = 3$, $k + 3$ for $k \in \{4, 5\}$, and $3(k - 1)$ for any constant k. Panda and Shetty [11] proved that MP2CS problem is NP-complete and proposed an MST-augmentation-based heuristic, i.e., MST-aug-leaf for the same problem. Authors also studied minimum power k backbone 2-connected subgraph (MPkB2CS) problem, and approximation ratios are as follows: 2 for $k = 3$: and $\frac{3(k+1)}{2}$ for $k \geq 3$.

2.2 Fault Tolerance

Vempala and Vetta [14] proposed an algorithm of approximation ratio 4/3, for finding a minimum 2-edge-connected and 2-vertex-connected subgraph for a given undirected graph. Xiuying and Zhao [7] proposed approximation algorithms for computing minimum 2-connected r-hop dominating set. Azharuddin et al. [2] proposed algorithms for distributed clustering and routing which run in polynomial time and are energy efficient and fault tolerant. Zheng et al. [16] proposed an approximation algorithm for computing r-hop 2-connected dominating set of WSNs and presented simulation results. Lyold et al. [8] studied a problem which seeks a minimum total power 2-node-connected network and developed an approximation algorithm of performance guarantee $2(2 - 2/n)(2 + 1/n)$ that approaches eight asymptotically. Calinescu and Wan [3] proved that the problem of minimum power bi-connectivity is NP-hard. The authors presented an MST-augmentation-based algorithm of approximation four for the minimum power bi-connectivity problem.

In this paper, we undertake MPkB3CS problem and present an algorithm to compute minimum power k backbone node 3-connected subgraph. We also prove that it is of $4k + 1$-approximation ratio. The rest of the paper is arranged in the following way: Section 3 explains the problem statement. Section 4 presents the proposed algorithm for MPkB3CS problem, and Sect. 5 concludes the paper.

3 Problem Formulation

Hierarchical topology plays a very significant role in the establishment of WSNs because it would be effective to arrange the sensors systematically to form clusters that result in a hierarchical structure. Hierarchical topology improves the scalability and efficiency of a WSN [10]. So, we consider MPkB3CS problem for a given complete graph and establish the 3-connectivity, which consists of k *backbone nodes*, minimizing the total power consumption. In this configuration, we have k *backbone nodes* and $n - k$ *client nodes*. The communication between any two client nodes is achieved through the backbone nodes. The k backbone nodes are connected to form a 3-connected subgraph, and then each client node is joined to three backbone nodes to attain 3-connectivity in the network. Minimum power k backbone node 3-connected subgraph (MPkB3CS) problem is formulated as follows:
Problem: Minimum Power k Backbone node 3 Connected Subgraph (MPkB3CS).
Input: A complete graph K_n, a positive integer k.
Output: 3-connected minimum power spanning subgraph with k backbone nodes.

4 MPkB3CS Problem for k=3

For any three backbone nodes (or vertices) x, y, and z, we connect these vertices by a cycle graph xyz. Now, we join remaining $n-3$ client nodes to all the three backbone node x, y, and z to obtain a 3-connected network. It is obvious that 3-connectivity of the network is achieved. For the given n nodes, we have $\binom{n}{3}$ combinations of three vertices, and to connect each of the $n - 3$ client node with three backbone nodes takes a total of $O(n)$ running time. Hence, we arrive at the following theorem:

Theorem 1 *MPkB3CS problem for k=3 can be optimally solved in* $O(n^4)$ *time.*

4.1 MPkB3CS Problem for Any Positive Integer k

In this section, we propose an algorithm for MPkB3CS problem with k backbone nodes to build a 3-connected network for the given set of deployed nodes that minimizes the total power of the induced network. Nutov [9] proved that MPkCS problem admits a 4-approximation algorithm for $k = 3$. This algorithm is based on an algorithm of approximation ratio $k+1$ for Min-Power k-Inconnected subgraph [9]

problem. The main idea of this algorithm [9] for MPkCS problem is to pick cheapest $k-1$ edges for each vertex and augmenting minimum cost edge set so that the resultant graph become k-connected. Authors proved that MPkCS algorithm is of polynomial time and has an approximation ratio 4 for $k = 3$. In the proposed algorithm, initially, we construct 3-connected minimum power subgraph that is formed by k backbone nodes using an approximation algorithm explained in [6]. Next, we establish 3-connectivity by joining each client node with first, second, and third nearest vertices from the set of backbone nodes, i.e., $\{v_1, v_2, v_3, \ldots, v_k\}$. This procedure is demonstrated in Algorithm 1.

Theorem 2 ([9]) *The MP3CS problem has a 4-approximation ratio of running time $O(n^4)$.*

Algorithm 1: MPkB3CS

Input: A complete graph K_n, positive integer k.
Output: A 3-connected subgraph H with k backbone nodes, minimizing the total power.

```
1  begin
2      Min = ∞.
3      for each V_k ⊆ V such that (|V_k| = k) do
4          determine the 3-connected minimum power subgraph of backbone nodes
           v1, v2, v3, ..., vk, say H' using the 4-approximation algorithm by Nutov.
5          for each client node u ∈ V do
6              Let u1, u2 and u3 be the first, second and third nearest backbone vertices
               respectively to u.
7              H' = H' ∪ {uu1, uu2, uu3}
8          end
9          if P(H') ≤ Min then
10             Min = P(H')
11             H = H'
12         end
13     end
14     Return H
15 end
```

Figure 1 consists of an undirected weighted graph with 14 vertices which is presented to illustrate the resultant subgraph obtained by the MPkB3CS Algorithm for $k = 3$. Following theorem validates the 3-connectivity of the resultant structure obtained by the MPkB3CS algorithm.

Theorem 3 ([15]) *If G is k-connected and G' is obtained by adding a new vertex which has at least k neighbors in G, then G' is k-connected.*

Theorem 4 *The resultant subgraph obtained by the MPkB3CS algorithm is 3-connected.*

Proof In the algorithm, initially, we consider 3-connected subgraph, i.e., H induced by the k backbone nodes $v_1, v_2, v_3, \ldots, v_k$. Further, we join each client node v_i for

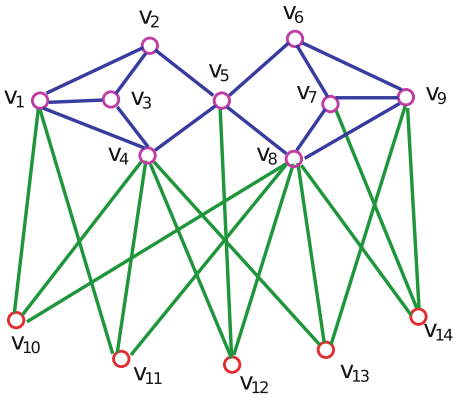

Fig. 1 Resultant network by MPkB3CS algorithm

$i = k+1, k+2, \ldots, n$, with its first, second, and third nearest nodes from the set of backbone nodes to establish 3-connectivity of the resultant network. From Theorem 3, since H is 3-connected and each client node has three backbone nodes as its neighbors in H, the graph obtained after adding any client node always becomes 3-connected (See Fig. 1).

Theorem 5 *MPkB3CS has an approximation ratio of* $4k+1$.

Proof Let H be the resultant 3-connected subgraph obtained by MPkB3CS algorithm and H' be the optimal solution of MPkB3CS problem. Let $v_1, v_2, v_3 \ldots, v_k$ be the backbone nodes and $v_{k+1}, v_{k+2}, v_{k+3} \ldots, v_n$, be the client nodes from the given set of n nodes. Without any loss of generality, we suppose that the sets H and H' consist same set of backbone nodes. Let H_1' be the optimally connected minimum power subgraph of k backbone nodes. Since we join each client node with its three nearest backbone nodes, we have:

$$P_H(v_i) \leq P_{H'}(v_i), \quad \text{for } i = k+1, k+2, \ldots, n. \tag{2}$$

Now considering the backbone nodes, let $m' = \max\{d(xy) \mid xy \in H'\}$ and $m = \max\{d(xy) \mid xy \in H\}$. Now, we have the following two cases possible:

Case i If $m' < m$

Since the maximum value of all the edges in the resultant subgraph H is m, the two endpoints of the edge with $d(xy) = m$ will be assigned power m. We are sure that at least one of those two endpoints x, y will be a backbone node ($\because$ there is no edge between any two client nodes). Therefore, $P_H(v_i) \leq m$, for $i = 1, 2, \ldots, k$, and using Theorem 2 we have:

$$km \leq \sum_{i=1}^{k} P_H(v_i) \leq 4P(H_1') \ . \tag{3}$$

Now, we consider

$$P_H(v_i) \leq m, \text{ for } i = 1, 2, 3, \ldots, k$$

$$\Rightarrow \sum_{i=1}^{k} P_H(v_i) \leq km$$

$$\Rightarrow \sum_{i=1}^{k} P_H(v_i) + \sum_{i=k+1}^{n} P_H(v_i) \leq km + \sum_{i=k+1}^{n} P_H(v_i)$$

$$\Rightarrow P(H) \leq km + \sum_{i=k+1}^{n} P_H(v_i)$$

$$\Rightarrow P(H) \leq km + \sum_{i=k+1}^{n} P_{H'}(v_i) \qquad (\because Eq.(2))$$

$$\Rightarrow P(H) \leq k4P(H'_1) + P(H') \qquad (\because \text{Theorem } 2)$$

$$\Rightarrow P(H) \leq k4P(H') + P(H')$$

$$\Rightarrow P(H) \leq (4k+1)P(H').$$

Case ii If $m' \geq m$

Since m' is the maximum, the two endpoints of the edge with $d(xy) = m'$ will be assigned power m'. Therefore, $P(H') \geq 2m'$ and we have:

$$m' \leq P(H')/2. \tag{4}$$

Similar to Case (i), in this case also, we have:

$$P_H(v_i) \leq m, \text{ for } i = 1, 2, 3, \ldots, k$$

$$\Rightarrow \sum_{i=1}^{k} P_H(v_i) \leq km$$

$$\Rightarrow \sum_{i=1}^{k} P_H(v_i) \leq km'$$

$$\Rightarrow \sum_{i=1}^{k} P_H(v_i) + \sum_{i=k+1}^{n} P_H(v_i) \leq km' + \sum_{i=k+1}^{n} P_H(v_i)$$

$$\Rightarrow P(H) \leq k\frac{P(H')}{2} + \sum_{i=k+1}^{n} P_H(v_i) \qquad (\because Eq.(4))$$

$$\Rightarrow P(H) \leq k\frac{P(H')}{2} + P(H')$$

$$\Rightarrow P(H) \leq \frac{k+2}{2}P(H')$$

Theorem 6 *MPkB3CS admits a running time of* $O(n^{k+4})$.

Proof In this algorithm, step 4 takes $O(n^4)$ running time which computes a 3-connected minimum power subgraph using the algorithm given by Nutov [9]. The loop in step 5 takes $O(n^2)$ time since it finds the first, second, and third nearest vertices to each client node. And the comparison in step 9 takes constant running time. This procedure is repeated for each subset of k backbone nodes, which takes $O(n^k)$ time. Hence the MPkB3CS algorithm is $O(n^{k+4})$ running time.

5 Conclusion

In this research, we have considered minimum power k backbone node 3-connected subgraph (MPkB3CS) problem for $k = 3$ and extended the study to any positive integer k. We proposed an algorithm which is of approximation ratio $4k + 1$.

Acknowledgements The authors would like to acknowledge the National Institute of Technology Karnataka, Surathkal, for the support in this research work.

References

1. Akyildiz, I.F., Su, W., Sankarasubramaniam, Y., Cayirci, E.: Wireless sensor networks: a survey. Computer Networks 38(4), 393–422 (2002), https://doi.org/10.1016/S1389-1286(01)00302-4
2. Azharuddin, M., Kuila, P., Jana, P.K.: Energy efficient fault tolerant clustering and routing algorithms for wireless sensor networks. Computers & Electrical Engineering 41, 177–190 (2015), https://doi.org/10.1016/j.compeleceng.2014.07.019
3. Călinescu, G., Wan, P.: Range assignment for high connectivity in wireless ad hoc networks. In: Ad-Hoc, Mobile, and Wireless Networks, Second International Conference, ADHOC-NOW 2003 Montreal, Canada, October 8-10, 2003, Proceedings. pp. 235–246 (2003), http://doi.org/10.1007/978-3-540-39611-6-21
4. Cheng, X., Narahari, B., Simha, R., Cheng, M.X., Liu, D.: Strong minimum energy topology in wireless sensor networks: Np-completeness and heuristics. IEEE Trans. Mob. Comput. 2(3), 248–256 (2003), http://doi.org/10.1109/TMC.2003.1233530
5. Fuchs, B.: On the hardness of range assignment problems. Networks 52(4), 183–195 (2008), https://doi.org/10.1002/net.20227
6. Lando, Y., Nutov, Z.: On minimum power connectivity problems. J. Discrete Algorithms 8(2), 164–173 (2010), https://doi.org/10.1016/j.jda.2009.03.002
7. Li, X., Zhang, Z.: Two algorithms for minimum 2-connected r-hop dominating set. Inf. Process. Lett. 110(22), 986–991 (2010), https://doi.org/10.1016/j.ipl.2010.08.008
8. Lloyd, E.L., Liu, R., Marathe, M.V., Ramanathan, R., Ravi, S.S.: Algorithmic aspects of topology control problems for ad hoc networks. MONET 10(1-2), 19–34 (2005), https://doi.org/10.1023/B:MONE.0000048543.95178.f5
9. Nutov, Z.: Approximating minimum-power k-connectivity. In: Ad-hoc, Mobile and Wireless Networks, 7th International Conference, ADHOC-NOW 2008, Sophia-Antipolis, France, September 10-12, 2008, Proceedings. pp. 86–93 (2008), http://doi.org/10.1007/978-3-540-85209-4-7
10. Panda, B.S., Shetty, D.P.: Strong minimum energy hierarchical topology in wireless sensor networks. J. Comb. Optim. 32(1), 174–187 (2016), https://doi.org/10.1007/s10878-015-9869-7
11. Panda, B.S., Shetty, D.P.: Minimum range assignment problem for two connectivity in wireless sensor networks. In: Distributed Computing and Internet Technology - 10th International Conference, ICDCIT 2014, Bhubaneswar, India, February 6-9, 2014. Proceedings. pp. 122–133 (2014), http://doi.org/10.1007/978-3-319-04483-5-14
12. Ramanathan, R., Hain, R.: Topology control of multihop wireless networks using transmit power adjustment. In: Proceedings IEEE INFOCOM 2000, The Conference on Computer Communications, Nineteenth Annual Joint Conference of the IEEE Computer and Communications Societies, Reaching the Promised Land of Communications, Tel Aviv, Israel, March 26-30, 2000. pp. 404–413 (2000), https://doi.org/10.1109/INFCOM.2000.832213

13. Santi, P.: Topology control in wireless ad hoc and sensor networks. Wiley (2005)
14. Vempala, S., Vetta, A.: Factor 4/3 Approximations for Minimum 2-Connected Subgraphs, pp. 262–273. Springer Berlin Heidelberg, Berlin, Heidelberg (2000), https://doi.org/10.1007/3-540-44436-X-26
15. West, D.B., et al.: Introduction to graph theory, vol. 2. Prentice hall Upper Saddle River (2001)
16. Zheng, C., Yin, L., Zhang, Y.: Constructing r-hop 2-connected dominating sets for fault-tolerant backbone in wireless sensor networks. In: 2012 8th International Conference on Wireless Communications, Networking and Mobile Computing. pp. 1–4 (Sept 2012)

Fuzzy Inference System Through Triangular and Hendecagonal Fuzzy Number

A. Felix, A. D. Dhivya, and T. Antony Alphonnse Ligori

Abstract A fuzzy inference system works on the basis of fuzzy if-then rules to mimic human intelligence for quantifying the vagueness/uncertainty, which arises in many real-world problems. In this paper, fuzzy inference system is designed using triangular and hendecagonal fuzzy number that represent the value for the linguistic environment. The factors of T2DM mellitus play a critical role in affecting each and every individual health without their knowledge. In this paper, the factor of "Blood Glucose", medical term known as hyperglycemia, is analyzed through this fuzzy inference system (FIS).

Keywords Triangular Fuzzy Number · Hendecagonal Fuzzy number · Linguistic Variables · Inference system

Mathematics Subject Classification 03B52, 15B15, 94D05

1 Introduction

In the beginning, the inference systems were based on crisp logic, but it is not well opted to manage the progressiveness phenomena under uncertain environment. Therefore, the concept of fuzzy inference system (FIS) on the basis of fuzzy set theory was introduced by Zadeh [16]. Since FIS becomes quite popular and interesting as well, it has been successfully applied in many applications like

A. Felix (✉)
Department of Mathematics, SAS, VIT, Chennai, India
e-mail: felix.a@vit.ac.in

A. D. Dhivya
Department of Mathematics, Loyola College, Chennai, India

T. Antony Alphonnse Ligori
Department of Mathematics, Gaeddu College of Business Studies, Gedu, Bhutan

B. Rushi Kumar et al. (eds.), *Applied Mathematics and Scientific Computing*,
Trends in Mathematics, https://doi.org/10.1007/978-3-030-01123-9_53

automatic control, classification of the data, decision analysis, expert systems, times series predictions, pattern recognition, and computer vision [16]. The success of the FIS is just the human of way of thinking and reasoning as well, and it has multidisciplinary nature [11]. FIS has a variety of other names, such as fuzzy rule-based system, fuzzy expert system [7], fuzzy model [4, 13, 14], fuzzy associative memory [8], fuzzy logic controller [10], and fuzzy inference system [1, 3, 9, 12, 15].

FIS can be designed either from the expert knowledge or data based [6]. The basic structure of a FIS consists of three conceptual components: a rule base (a selection of fuzzy rules), a database (defines the membership functions), and a reasoning mechanism (performs the inference procedure upon the rules and given facts to derive a reasonable output). Moreover, fuzzy logic to a real application requires three steps, fuzzification, inference process, and defuzzification. This system shows the quality of factors and nonlinear mapping between symptoms, factors, and complications. FIS can be helpful to achieve classification tasks, medical diagnosis, decision support tools, and process control. FIS has twofold identity to handle linguistic concepts and nonlinear mapping from its input set into output set. This mapping is accomplished by a fuzzy number of IF-THEN rules, each of which describes the essence of the mapping. IF-THEN rules built from expert knowledge which is called fuzzy expert systems or fuzzy controllers. Recently, soft computing researchers showed their interested on diagnosing many diseases in the medical field to assist the medical practitioner. Therefore, this paper harvests a new model called improved fuzzy inference system using triangular and hendecagonal fuzzy number dealing with fuzzy positive and negative ideal solution to predict the mellitus earlier stage and avoid the end-stage complication.

2 Theoretical Background

In this section, some basic definitions are reviewed.

Definition 1 A fuzzy set [16] $\widetilde{A}$ in X is characterized by a membership function $\mu_{\widetilde{A}}(x)$ which associates each point in X, to a real number in the interval [0, 1]. The value of $\mu_{\widetilde{A}}(x)$ represents "grade of membership" of $x \in \mu_{\widetilde{A}(x)}$.

Definition 2 The α-cut of the fuzzy set $\widetilde{A}$ of X is defined as $\widetilde{A}_\alpha = \{x \in X / \mu_{\widetilde{A}}(x) \geq \alpha\}$, where $\alpha \in [0, 1]$.

Definition 3 A fuzzy set $\widetilde{A}$ defined on the set of real numbers $\mathbb{R}$ is said to be a fuzzy number if its membership function $\widetilde{A} : \mathbb{R} \rightarrow [0, 1]$ has the following characteristics.

(i) $\widetilde{A}$ is convex
(ii) $\widetilde{A}$ is normal
(iii) $\widetilde{A}$ is piecewise continuous.

Definition 4 A triangular fuzzy number $\widetilde{A}$ denoted by (a_1, a_2, a_3), and the membership function is defined as

$$\mu_{\tilde{A}}(x) = \begin{cases} \frac{x-a_1}{a_2-a_1}, \text{ for } a_1 \le x \le a_2 \\ \frac{a_3-x}{a_3-a_2}, \text{ for } a_2 \le x \le a_3 \\ 0, \quad \text{elsewhere.} \end{cases}$$

Theorem 1 *Let* $\tilde{A} = (a_1, a_2, a_3)$ *and* $\tilde{B} = (b_1, b_2, b_3)$ *be two triangle fuzzy numbers. The addition, subtraction, and multiplication operations of* $\tilde{A}$ *and* $\tilde{B}$*, denoted by* $\tilde{A} \oplus \tilde{B}$*,* $\tilde{A} \ominus \tilde{B}$*, and* $\tilde{A} \otimes \tilde{B}$*, respectively, yield another triangular fuzzy number.*

(i) $\tilde{A} \oplus \tilde{B} = (a_1 + b_1, a_2 + b_2, a_3 + b_3)$
(ii) $\tilde{A} \ominus \tilde{B} = (a_1 - b_3, a_2 - b_2, a_3 - b_3)$
(iii) $\tilde{A} \otimes \tilde{B} = (a_1 b_1, a_2 b_2, a_3 b_3)$

Definition 5 A hendecagonal fuzzy number $\widetilde{H}_D$ denoted as (a_1, a_2, a_3, a_4, a_5, a_6, a_7, a_8, a_9, a_{10}, and a_{11}) and the membership function is defined as

$$\mu_{\widetilde{H}_D}(x) = \begin{cases} \frac{1}{5}\frac{(x-a_1)}{(a_2-a_1)}, & a_1 \le x \le a_2 \\ \frac{1}{5} + \frac{1}{5}\frac{(x-a_2)}{(a_3-a_2)}, & a_2 \le x \le a_3 \\ \frac{2}{5} + \frac{1}{5}\frac{(x-a_3)}{(a_4-a_3)}, & a_3 \le x \le a_4 \\ \frac{3}{5} + \frac{1}{5}\frac{(x-a_4)}{(a_5-a_4)}, & a_4 \le x \le a_5 \\ \frac{4}{5} + \frac{1}{5}\frac{(x-a_5)}{(a_6-a_5)}, & a_5 \le x \le a_6 \\ 1 - \frac{1}{5}\frac{(x-a_6)}{(a_7-a_6)}, & a_6 \le x \le a_7 \\ \frac{4}{5} - \frac{1}{5}\frac{(x-a_7)}{(a_8-a_7)}, & a_7 \le x \le a_8 \\ \frac{3}{5} - \frac{1}{5}\frac{(x-a_8)}{(a_9-a_8)}, & a_8 \le x \le a_9 \\ \frac{2}{5} - \frac{1}{5}\frac{(x-a_9)}{(a_{10}-a_9)}, & a_9 \le x \le a_{10} \\ \frac{1}{5}\frac{(a_{11}-x)}{(a_{11}-a_{10})}, & a_{10} \le x \le a_{11} \\ 0, & \text{otherwise.} \end{cases}$$

2.1 Arithmetic Operation on α-Cut

Definition 6 A hendecagonal fuzzy number (Fig. 1) [5] $\widetilde{H}_D$ can also be defined as $\widetilde{H}_D = A_1(p), B_1(q), C_1(r), D_1(s), E_1(t), A_2(p), B_2(q), C_2(r), D_2(s), E_2(t)$, $p \in [0, 0.2]$, $q \in [0.2, 0.4]$, $r \in [0.4, 0.6]$ $s \in [0.6, 0.8]$, and $t \in [0.8, 1]$, where [3mm] $A_1(p) = \frac{1}{5}\frac{(x-a_1)}{(a_2-a_1)}$, $B_1(q) = \frac{1}{5} + \frac{1}{5}\frac{(x-a_2)}{(a_3-a_2)}$, $C_1(r) = \frac{2}{5} + \frac{1}{5}\frac{(x-a_3)}{(a_4-a_3)}$, $D_1(s) = \frac{3}{5} + \frac{1}{5}\frac{(x-a_4)}{(a_5-a_4)}$, $E_1(t) = \frac{4}{5} + \frac{1}{5}\frac{(x-a_5)}{(a_6-a_5)}$, $E_2(t) = 1 - \frac{1}{5}\frac{(x-a_6)}{(a_7-a_6)}$, $D_2(s) = \frac{4}{5} - \frac{1}{5}\frac{(x-a_7)}{(a_8-a_7)}$, $C_2(r) = \frac{3}{5} - \frac{1}{5}\frac{(x-a_8)}{(a_9-a_8)}$, $B_2(q) = \frac{2}{5} - \frac{1}{5}\frac{(x-a_9)}{(a_{10}-a_9)}$, $A_2(p) = \frac{1}{5}\frac{(a_{11}-x)}{(a_{11}-a_{10})}$ Here,

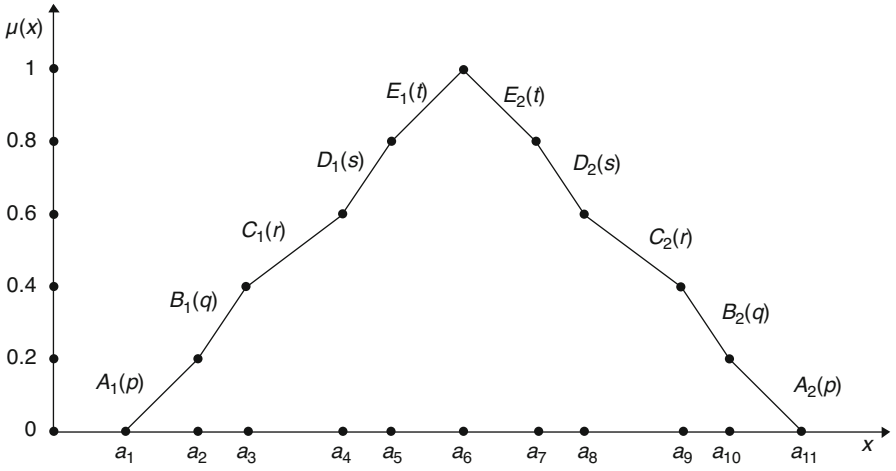

Fig. 1 The hendecagonal fuzzy number

- $A_1(p)$, $B_1(q)$, $C_1(r)$, $D_1(s)$, $E_1(t)$, is bounded and continuous increasing function over [0, 0.2),[0.2, 0.4), [0.4, 0.6), [0.6, 0.8), and [0.8, 1], respectively.
- $A_2(p)$, $B_2(q)$, $C_2(r)$, $D_2(s)$, $E_2(t)$, is bounded and continuous decreasing function over [0, 0.2), [0.2, 0.4), [0.4, 0.6), [0.6, 0.8), and [0.8, 1], respectively.

Definition 7 The α-cut of the fuzzy set of the universe of discourse X is defined as $\widetilde{H_{D\alpha}} = \{x \in X / \mu_{\widetilde{A}}(x) \geq \alpha\}$, where $\alpha \in [0, 1]$.

$$\widetilde{H_{D\alpha}} = \begin{cases} [A_1(\alpha), A_2(\alpha)], & \text{for } \alpha \in [0, 0.2) \\ [B_1(\alpha), B_2(\alpha)], & \text{for } \alpha \in [0.2, 0.4) \\ [C_1(\alpha), C_2(\alpha)], & \text{for } \alpha \in [0.4, 0.6) \\ [D_1(\alpha), D_2(\alpha)], & \text{for } \alpha \in [0.6, 0.8) \\ [E_1(\alpha), E_2(\alpha)], & \text{for } \alpha \in [0.8, 1] \end{cases}$$

Definition 8 If $A_1(x) = \alpha$ and $A_2(x) = \alpha$, then α-cut operations interval $\widetilde{H_{D\alpha}}$ is obtained as

1. $[A_1(\alpha), A_2(\alpha)] = [5\alpha(a_2 - a_1) + a_1, -5\alpha(a_{11} - a_{10}) + a_{11})]$
   Similarly, we can obtain α-cut operations interval $\widetilde{D}_\alpha$ for $[Q_1(\alpha), Q_2(\alpha)]$, $[R_1(\alpha), R_2(\alpha)]$, and $[S_1(\alpha), S_2(\alpha)]$ as follows:
2. $[B_1(\alpha), B_2(\alpha)] = [5\alpha(a_3 - a_2) + 2a_2 - a_3, -5\alpha(a_{10} - a_9) + 2a_{10} - a_9]$
3. $[C_1(\alpha), C_2(\alpha)] = [5\alpha(a_4 - a_3) + 3a_3 - 2a_4, -5\alpha(a_9 - a_8) + 3a_9 - 2a_8]$
4. $[D_1(\alpha), D_2(\alpha)] = [5\alpha(a_5 - a_4) + 4a_4 - 3a_5, -5\alpha(a_8 - a_7) + 4a_8 - 3a_7]$
5. $[D_1(\alpha), D_2(\alpha)] = [5\alpha(a_6 - a_5) + 5a_5 - 3a_6, -5\alpha(a_7 - a_6) + 5a_7 - 3a_6]$

Hence, α-cut of hendecagonal fuzzy number

$$\widetilde{H_{D\alpha}} = \begin{cases} [5\alpha(a_2 - a_1) + a_1, -5\alpha(a_{11} - a_{10}) + a_{11})], & \text{for } \alpha \in [0, 0.2) \\ [5\alpha(a_3 - a_2) + 2a_2 - a_3, -5\alpha(a_{10} - a_9) + 2a_{10} - a_9], & \text{for } \alpha \in [0.2, 0.4) \\ [5\alpha(a_4 - a_3) + 3a_3 - 2a_4, -5\alpha(a_9 - a_8) + 3a_9 - 2a_8], & \text{for } \alpha \in [0.4, 0.6) \\ [5\alpha(a_5 - a_4) + 4a_4 - 3a_5, -5\alpha(a_8 - a_7) + 4a_8 - 3a_7], & \text{for } \alpha \in [0.6, 0.8) \\ [5\alpha(a_6 - a_5) + 5a_5 - 3a_6, -5\alpha(a_7 - a_6) + 5a_7 - 3a_6], & \text{for } \alpha \in [0.8, 1] \end{cases}$$

Theorem 2 *If* $\widetilde{A}=(a_1, a_2, a_3, a_4, \ldots, a_9, a_{10}, a_{11})$ *and* $\widetilde{B}=(b_1, b_2, b_3, b_4, \ldots, b_9, b_{10}, b_{11})$ *are the hendecagonal fuzzy numbers, then* $\widetilde{C}=\widetilde{A}\oplus\widetilde{B}$ *is also a hendecagonal fuzzy number* $\widetilde{A} \oplus \widetilde{B}=(a_1 + b_1, a_2 + b_2, a_3 + b_3, a_4 + b_4, \ldots, a_9 + b_9, a_{10} + b_{10}, a_{11} + b_{11})$.

Theorem 3 *If* $\widetilde{A}=(a_1, a_2, a_3, a_4, \ldots, a_9, a_{10}, a_{11})$ *and* $\widetilde{B}=(b_1, b_2, b_3, b_4, \ldots, b_9, b_{10}, b_{11})$ *are the hendecagonal fuzzy numbers, then* $\widetilde{P}=\widetilde{A}\otimes\widetilde{B}$ *is also a hendecagonal fuzzy number* $\widetilde{A} \otimes \widetilde{B}=(a_1b_1, a_2b_2, a_3b_3, a_4b_4, \ldots, a_9b_9, a_{10}b_{10}, a_{11}b_{11})$.

Theorem 4 *If* $\widetilde{A}=(a_1, a_2, a_3, a_4, \ldots, a_9, a_{10}, a_{11})$ *and* $\widetilde{B}=(b_1, b_2, b_3, b_4, \ldots, b_9, b_{10}, b_{11})$ *are the hendecagonal Fuzzy Numbers, then* $\widetilde{D}=\widetilde{A} \oslash \widetilde{B}$ *is also a hendecagonal fuzzy number:*

$\widetilde{A} \oslash \widetilde{B}=\left(\frac{a_1}{b_{11}}, \frac{a_2}{b_{10}}, \frac{a_3}{b_9}, \frac{a_4}{b_8}, \ldots, \frac{a_8}{b_4}, \frac{a_9}{b_3}, \frac{a_{10}}{b_2}, \frac{a_{11}}{b_1}\right)$

Definition 9 A linguistic variable/term is a "variable whose values is not crisp number but word or sentence in a natural language" [15].

2.2 AND Operation in Linguistic Variables

The intersection of two fuzzy sets $\widetilde{A}$ and $\widetilde{B}$ with the linguistic variables are again fuzzy set $\widetilde{C}$ with linguistic variable, which is defined as the minimum between linguistic variables of $\widetilde{A}$ and $\widetilde{B}$. This is called the minimum criterion of linguistic variables. The fuzzy if-then rules are framed in Tables 1 and 2.

The linguistic values are represented by triangular and hendecagonal fuzzy numbers in Tables 3 and 4.

Table 1 Linguistic fuzzy IF-THEN rules

S/C	NI	VLI	LI	M	HI	VHI	VVHI
NI	Too mild	Too mild	Too mild	Too mild	Too mild	Too mild	Too mild
VLI	Too mild	Mild	Mild	Mild	Mild	Mild	Mild
LI	Too mild	Mild	Moderate	Moderate	Moderate	Moderate	Moderate
M	Too mild	Mild	Moderate	M severe	M severe	M severe	M severe
HI	Too mild	Mild	Moderate	M severe	Severe	Severe	Severe
VHI	Too mild	Mild	Moderate	M severe	Severe	Very Severe	Very Severe
VVHI	Too mild	Mild	Moderate	M severe	Severe	V severe	SC

Table 2 Transforming linguistic variables to medical terms using fuzzy IF-THEN rule

Linguistic variables	Health condition
No influence	Too mild
Very low influence	Mild
Low influence	Moderate
Medium	Moderate severe
High influence	Severe
Very high influence	Very severe
Very very high influence	Serious condition

Table 3 Triangular fuzzy linguistic scale

Linguistic term	Representation of LT	Triangular FN
Too mild	TM	(0.1,0.3.0.5)
Mild	M	(0.3,0.5,0.7)
Moderate	MR	(0.5,0.7,0.9)
Severe	S	(0.7,0.9,1)
Very severe	VS	(0.9,1,1)

Table 4 Hendecagonal fuzzy linguistic scale

Linguistic term	Notation	Hendecagonal FN
Too mild	TM	(0,0,0,0,0,0,0.03,0.06,0.09,0.12,0.15)
Mild	M	(0,0.03,0.06,0.09,0.12,0.15,0.18,0.21,0.24,0.27,0.30)
Moderate	MR	(0.15,0.18,0.21,0.24,0.27,0.30,0.33,0.36,0.39,0.42,0.45)
Moderate severe	MRS	(0.30,0.33,0.36,0.39,0.42,0.45,0.48,0.51,0.54,0.57,0.60)
Severe	S	(0.48,0.51,0.54,0.57,0.60,0.63,0.66,0.69,0.72,0.75,0.78)
Very severe	VS	(0.63,0.66,0.69,0.72,0.75,0.78,0.81,0.84,0.87,0.90,0.93)
Serious condition	SC	(0.78,0.81,0.84,0.87,0.90,0.93,0.96,0.99,1,1,1)

2.3 Blood Glucose

Glucose is the major source of energy for all cells. Without enough glucose, our body cannot perform its normal functions. The three most frequently prescribed blood sugar tests to determine the glucose level in the blood are FBS, PPBS, and RBS. The abovementioned tests are to monitor, confirm, or rule out T2DM. The state of increased blood sugar level ($\geq$140 mg/dl) is known as hyperglycemia and the decreased blood sugar level is hypoglycemia ($\leq$70 mg/dl) [2].

2.4 Hyperglycemia

Hyperglycemia is a condition where our blood glucose level is too high if we do not eat healthy foods or do not exercise. Illness, stress, and hormones can also be a reason to raise our blood glucose. The symptoms of hyperglycemia are increased thirst, excessive hunger, frequent urination, dry mouth, fatigue or feeling

tired, blurry vision, weight loss, and slow-healing sores leading to neuropathy, retinopathy, nephropathy, and cardiovascular problems.

3 Algorithm for Fuzzy Inference System

This fuzzy system is constructed using triangular and hendecagonal fuzzy number.

Fuzzification

Step-1 Construct two uncertain linguistic relation matrices over symptoms S and complications C, respectively, from the linguistic set UL= {NI, VLI, LI, M, HI,VHI, VVHI} with the help of expert opinion, where $(T2DM)_S$—symptoms and $(T2DM)_C$—complications.

Inference Process Database

Step-2 Construct the matrix $(T2DM)_1 = (T2DM)_S \times (T2DM)_C$ using fuzzy IF-THEN rules, which is defined in the form of linguistic fuzzy logic (LFL).

Step-3 A fuzzy linguistic scale is utilized to convert the linguistic variables into triangular, hendecagonal fuzzy number.

Step-4 Find the fuzzy positive ideal solution (FPIS) and fuzzy negative ideal solution (FNIS) for the triangular, hendecagonal fuzzy matrix, and it can be defined as

$P^+ = (x_1^+, x_2^+, \ldots, x_n^+)$, where $x_j^+ = \max_i\{x_{ij_3}\}$, $x_j^+ = \max_i\{x_{ij_{11}}\}$, $i = 1, 2, \ldots, m$; $j = 1, 2, \ldots, n$.
$P^- = (x_1^-, x_2^-, \ldots, x_n^-)$, where $x_j^+ = \min_i\{x_{ij_1}\}$ for both fuzzy numbers, $i = 1, 2, \ldots, m$; $j = 1, 2, \ldots, n$.

Step-5 The distance of each patient from P^+ and P^- can be given by

$$d_i^+ = \sum_{i=1}^{n} d(x_{ij}, x_j^+), \quad i = 1, 2, \ldots, m$$

$$d_i^- = \sum_{i=1}^{n} d(x_{ij}, x_j^-), \quad i = 1, 2, \ldots, m$$

where

$$d(\widetilde{A}, \widetilde{B}) = \sqrt{\frac{1}{3}\left[\sum_{i=1}^{3}(a_i - b_i)^2\right]}$$

$$d(\widetilde{A}, \widetilde{B}) = \sqrt{\frac{1}{11}\left[\sum_{i=1}^{11}(a_i - b_i)^2\right]}$$

Defuzzification

Step-6 The patient's P_i, $(i = 1, 2, \ldots, m)$ health condition is determined by the closeness coefficient

$$PP_i = \frac{d_i^+}{d_i^+ + d_i^-}, \quad PP_i \in [0, 1]$$

4 Adaptation of the Problem to the Proposed Fuzzy Inference System

This section investigates the validity of proposed FIS to analyze the effect of hyperglycemia in T2DM.

At step-1, the expert's (Subaju Patient) voice was recorded by the unsupervised method that what influenced her to come hospital. From her statements, hyperglycemia symptoms are taken as factors. The matrix table for Patient-Symptoms $(T2DM)_S$, Symptoms-Complications $(T2DM)_C$ were constructed with the help of medical practitioner. For instance, IF the P_1 have high level of increased thirsty and very low level of cardiovascular problem, THEN health condition of P_1 is determined at step-2 using (Tables 5, 6, 7).

Next, the linguistic fuzzy IF-THEN rule from Table 1 is used to predict the patient's actual health condition through linguistic variables from Table 2 as medical term. Using IF-THEN rules in the previous step, the patient's actual health condition is Mild. Here, the linguistic variables are converted into triangular and hendecagonal fuzzy numbers. Then, (FPIS) and (FNIS) are determined. Next, using the closeness coefficient formula, the patient health condition is determined. This closeness coefficient for the triangular and hendecagonal matrices are tabulated in Tables 8 and 9.

Table 5 Expert data of $(T2DM)_S$ of hyperglycemia using linguistic variables

$(T2DM)_S$	Increased thirst	Hunger	Frequent urination	Dry mouth	Feeling tired	Blurry vision
P_1	H	L	VH	H	L	H

Table 6 Expert data of $(T2DM)_C$ of hyperglycemia using linguistic variables

$(T2DM)_C$	Cardiovascular	Neuropathy	Nephropathy	Retinopathy
Increased thirst	VL	L	H	NI
Hunger	L	VL	H	L
Frequent urination	NI	L	VH	VL
Dry mouth	H	L	VL	VL
Feeling tired	L	VL	NI	NI
Blurry vision	L	VH	H	VH

Table 7 Expert data of $(T2DM)_1$ of hyperglycemia using linguistic variables

$(T2DM)_1$	Cardiovascular	Neuropathy	Nephropathy	Retinopathy
Increased thirst	Mild	Moderate	Severe	Too mild
Hunger	Moderate	Mild	Moderate	Moderate
Frequent urination	Too mild	Moderate	Very severe	Mild
Dry mouth	Severe	Moderate	Mild	Mild
Feeling tired	Moderate	Mild	Too mild	Too mild
Blurry vision	Moderate	Severe	Severe	Very severe

Table 8 Triangular fuzzy distance measurement and closeness coefficient

PHC	$d_1^{TR^+}$	$d_1^{TR^-}$	PP_i^{TR}	Rank
Cardiovascular	2.4516	3.3321	0.5761	2
Neuropathy	2.2588	2.3924	0.5143	3
Nephropathy	2.0088	3.7331	0.6501	1
Retinopathy	2.8884	2.8697	0.4983	4

Table 9 Hendecagonal Fuzzy distance measurement and closeness coefficient

PHC	$d_1^{HD^+}$	$d_1^{HD^-}$	PP_i^{HD}	Rank
Cardiovascular	2.74818	1.82538	0.3991	2
Neuropathy	2.91928	1.93586	0.3987	3
Nephropathy	3.06838	2.59566	0.4582	1
Retinopathy	4.06378	1.58942	0.2811	4

This closeness coefficient for all alternatives indicates that the patient is presently affected with high grade of nephropathy. From the result, it is observed that the ranking for both is same but the values of hendecagonal are more optimized than the values of triangular. Hence, when the expert opinions are taken under uncertain environment, there is no clear information and no accurate solution for the problem. Therefore, if we increase the uncertain linguistic term, then the uncertainty of the problem would give more information about it and give clear idea to solve the problem.

5 Conclusion

This present study determined that the Subaju Patient was more affected by nephropathy $\succ$ cardiovascular $\succ$ neuropathy $\succ$ retinopathy. Hence, this FIS pave a way to the doctor to precede the treatment step by step according to the result so that it will help the patient to avoid the end stage complication. Therefore, the improved fuzzy inference system with linguistic fuzzy logic, FPIS and FNIS using triangular and hendecagonal fuzzy number is more suitable to fetch out the patient's actual health condition.

References

1. Ajay Kumar Shrivastava., Akash Rajak., Niraj Singhal.: Modeling Pulmonary Tuberculosis using Adaptive Neuro Fuzzy Inference System, International Journal of Innovative Research in Computer Science & Technology, **4(1)**, 24–27 (2016)
2. Ajmalahamed, A., Nandhini, K.M., Krishna Anand.: Designing A Rule Based Fuzzy Expert Controller For Early Detection And Diagnosis of Diabetes, *ARPN Journal of Engineering and Applied Sciences*, **9(5)**, 819–827 (2014)
3. Ambilwade, R.P., Manza., Ravinder Kaur, R. : Prediction of Diabetes Mellitus and its Complications using Fuzzy Inference System, International Journal of Emerging Technology and Advanced Engineering, Certified Journal, **6(7)**, 80–86 (2016)
4. Faran Baig., Saleem, M., Yasir Noor., Imran Khan, M.: Design Model Of Fuzzy Logic Medical Diagnosis Control System, International Journal On Computer Science And Engineering (IJCSE), **3(5)**, 2093–2108 (2011)
5. Devadoss, AV., Dhivya, A.D., Felix, A.: A Hendecagonal Fuzzy Number and Its Vertex Method, International Journal of Mathematics And its Applications, **4(1-B)**, 87–98 (2016)
6. Guillaume, S.: Designing Fuzzy Inference Systems from Data: An Interpretability-Oriented Review, IEEE Transactions on Fuzzy Systems, **9(3)**, 426–443 (2001)
7. Kandel, A. Fuzzy Expert Systems. CRC Press, Inc., Boca Raton, FL (1991).
8. Kosko, B.: Neural Networks and Fuzzy Systems: A dynamical systems approach. Prentice Hall, Upper Saddle River, NJ (1991)
9. Leonardo Yunda., David Pacheco Jorge Millan.: A Web-based Fuzzy Inference System Based Tool for Cardiovascular Disease Risk Assessment, NOVA, **13(24)**, 7–16 (2015)
10. Mamdani, E.H., Assilian, S.: An Experiment in Linguistic Synthesis with a Fuzzy Logic Controller. International Journal of Man-Machine Studies, **7(1)**, 1-13 (1975)
11. Nauck, M.A., Wollschläger, D., Werner, J.: Effects of subcutaneous glucagon-like peptide 1 (GLP-1 [7-36 amide]) in patients with NIDDM. Diabetologia, **39(12)**, 1546–1553 (1996)
12. Shristi Tiwari., Deepti Choudhary., Shubi Sharda.: Prediction Of Lung Cancer Using Fuzzy Inference System, International Journal of Current Innovation Research, **2(6)**, 392–395 (2016)
13. Sugeno, M., Kang, G.T.: Structure Identification of Fuzzy Model, Fuzzy Sets and Systems, **28**, 15–33 (1988)
14. Takagi, T., Sugeno.: Fuzzy Identification of Systems and Its Applications to Modeling and Control. IEEE Transactions on Systems, Man, and Cybernetics, **15**, 116–132 (1985)
15. Zadeh, L.A.: Soft Computing and Fuzzy Logic, IEEE software, **11(6)**, 48–56 (1994)
16. Zadeh, L.A.: Fuzzy sets, Information and Control, **8**, 338–353 (1965)

Computation of Narayana Prime Cordial Labeling of Book Graphs

B. J. Balamurugan, K. Thirusangu, B. J. Murali, and J. Venkateswara Rao

Abstract In this article, we compute the Narayana prime cordial labeling of book graphs using prime and Narayana numbers.

Keywords and phrases: Narayana numbers · Prime numbers · NPC graphs

1 Introduction

A labeling of a graph G is a process of allocating numbers or labels to the nodes of G or lines of G or both through mathematical functions [1]. The basic notion of graph labeling is found in [7]. The vital application of labeled graphs can be found in science, engineering and technology and we refer [4] for the same. For graph labeling literature, we refer to [2]. We refer to the textbook by Harary [3] for notations, concepts, and terminology in graph theory.

The Narayana numbers [5], a recent development in number theory, occur in various combinatorial problems. The applications of Narayana numbers play an important role in various topics of mathematics, especially in cryptography. The Narayana numbers have been used in multiple input and output communication systems, in RNA secondary structure configuration, and in partition of graphs

B. J. Balamurugan (✉)
School of Advanced Sciences, VIT University, Chennai Campus, Chennai, Tamil Nadu, India
e-mail: balamurugan.bj@vit.ac.in

K. Thirusangu
Department of Mathematics, SIVET College, Gowrivakkam, Chennai, Tamil Nadu, India
e-mail: kthirusangu@gmail.com

B. J. Murali
Research and Development Centre, Bharathiar University, Coimbatore, Tamil Nadu, India
e-mail: muralibjpgm@gmail.com

J. Venkateswara Rao
Department of Computing and Mathematics, Mekelle University, Mekelle, Tigrai, Ethiopia
e-mail: venkatjonnalagadda@yahoo.co.in

B. Rushi Kumar et al. (eds.), *Applied Mathematics and Scientific Computing*,
Trends in Mathematics, https://doi.org/10.1007/978-3-030-01123-9_54

in terms of trees. Since the Narayana numbers and labeled graphs have many interesting practical applications, we are concerned in computing the Narayana prime cordial labeling of graphs. We introduced this labeling pattern in [6] and proved that the graphs, viz., (i) paths, (ii) cycles, and (iii) helm graphs, are Narayana prime cordial graphs. In this article, we compute the Narayana prime cordial labeling of book graphs.

2 Narayana Numbers [5]

For definition and properties of Narayana numbers we refer [5].

Definition 1 ([5]) Let $\mathbb{N}_0$ be the set of nonnegative integers and let $k, n \in \mathbb{N}_0$. The Narayana numbers can be defined as

$$N(n,k) = \frac{1}{n}\binom{n}{k}\binom{n}{k+1}; 0 \leq k < n \text{ where } \binom{n}{k} = \frac{n!}{(n-k)!k!}$$

The Narayana numbers discovered by Narayana are highly associated with the Catalan numbers [8]. That is, $C_n = \frac{1}{n+1}\binom{2n}{n}$ and $\sum_{k=0}^{n-1} N(n,k) = C_n$ where C_n is a Catalan number.

For example, the Narayana numbers $N(n,k)$ where $0 \leq k < n \leq 8$ are given in the following triangular array. Here the sum of each row is a Catalan number [8].

$n\|k$	0	1	2	3	4	5	6	7
1	1	1						
2	1	1						
3	1	3	1					
4	1	6	6	1				
5	1	10	20	10	1			
6	1	15	50	50	15	1		
7	1	21	105	175	105	21	1	
8	1	28	196	490	490	196	28	1

3 Narayana Prime Cordial Labeling of Book Graphs

This section introduces the Narayana prime cordial labeling [6] of a graph $G = (V, E)$ and shows that the book graphs are Narayana prime cordial graphs.

Definition 2 Let $G(V, E)$ be a simple graph. A 1-1 function $\ell : V \to \mathbb{N}_0$ is called a Narayana prime cordial labeling of the Graph G if there exists an edge function $\ell^* : E \to \{0, 1\}$ satisfying the two conditions, viz.,

(i) For every $uv \in E, u, v \in V$

$$\begin{aligned}
\ell^*(uv) = 1 \ &\text{if } p|N(\ell(u), \ell(v)), \text{ where } \ell(u) > \ell(v) \text{ and } \ell(u) = p^m \\
&\text{for some } m \in \mathbb{N}_0; 1 \le \ell(v) \le \ell(u) - 2 \text{ where } p \text{ is a prime number} \\
= 1 \ &\text{if } p|N(\ell(v), \ell(u)), \text{ where } \ell(v) > \ell(u) \text{ and } \ell(v) = p^m \\
&\text{for some } m \in \mathbb{N}_0; 1 \le \ell(u) \le \ell(v) - 2 \text{ where } p \text{ is a prime number.} \\
= 0 \ &\text{if } p \not| N(\ell(u), \ell(v)), \text{ where } \ell(u) > \ell(v) \text{ and } \ell(u) = p^m - 1 \\
&\text{for some } m \in \mathbb{N}_0; 0 \le \ell(v) \le \ell(u) - 1 \text{ where } p \text{ is a prime number} \\
= 0 \ &\text{if } p \not| N(\ell(v), \ell(u)), \text{ where } \ell(v) > \ell(u) \text{ and } \ell(v) = p^m - 1 \\
&\text{for some } m \in \mathbb{N}_0; 0 \le \ell(u) \le \ell(v) - 1 \text{ where } p \text{ is a prime number.}
\end{aligned}$$

(ii) $|e_{\ell^*}(0) - e_{\ell^*}(1)| \le 1$ where $e_{\ell^*}(0)$ and $e_{\ell^*}(1)$ denote the total number of edges having the number 0 and the total number of edges having the number 1, respectively.

Definition 3 Let $G = (V, E)$ be a simple graph. If G assumes a Narayana prime cordial labeling, then it is known as a Narayana prime cordial graph.

Remark 1 We call the Narayana prime cordial labeling of a graph as NPC labeling of a graph for simplicity in this paper.

Definition 4 One edge union of cycles of same length is called a book graph. The common edge is called the base edge of the book graph.

Let m copies of cycles of length $n \ge 3$ is denoted as B_n^m.

If $n = 3, 4, 5$, and 6, then book graphs have triangular, rectangular or quadrilateral, pentagonal, and hexagonal pages, respectively. The book graph B_n^m has $m(n-2)+2$ vertices and $m(n-1)+1$ edges.

Theorem 1 *A book graph with triangular pages admits a NPC labeling.*

Proof Let B_3^m be a book graph with triangular pages.

Let $V = \{u_0, v_0\} \cup \{v_i | 1 \le i \le m\}$ be the vertex and $E = E_1 \cup E_2 \cup E_3$ where $E_1 = \{u_0 v_0\}$, $E_2 = \{u_0 v_i | 1 \le i \le m\}$, and $E_3 = \{v_0 v_i | 1 \le i \le m\}$ be the edge set of B_3^m. Then B_3^m has $m+2$ vertices and $2m+1$ edges.

Define a 1-1 function $\ell : V \to \mathbb{N}_0$ such that

$\ell(u_0) = 1$

$\ell(v_0) = 2$

$\ell(v_i) = 2^{i+1}; 1 \le i \le m$ and $i \equiv 1 \pmod 2$

$\ell(v_i) = 2^{i+1} - 1; 1 \le i \le m$ and $i \equiv 0 \pmod 2$

and an edge function $\ell^* : E \to \{0, 1\}$ defined as in the Definition 2.

In this labeling pattern

Case (i) When $m \equiv 0 \pmod 2$, $m+1$ edges of the set E receive the label 0, and m edges receive the label 1.

That is $e_{\ell^*}(0) = m + 1$ and $e_{\ell^*}(1) = m$ and therefore $|e_{\ell^*}(0) - e_{\ell^*}(1)| \le 1$.

Case (ii) When $m \equiv 1 \pmod 2$, $\frac{2(m-1)}{2} + 1 = m$ edges of E receive the label 0 and $\frac{2(m-1)}{2} + 2 = m + 1$ edges receive the label 1. That is, $e_{\ell^*}(0) = m$ and $e_{\ell^*}(1) = m + 1$ and therefore $|e_{\ell^*}(1) - e_{\ell^*}(0)| \leq 1$.

Hence in both cases, B_3^m admits a NPC labeling.

The NPC labeling of B_3^4 and B_3^5 are given in Figs. 1 and 2, respectively.

Example 1

Fig. 1 NPC labeling of B_3^4

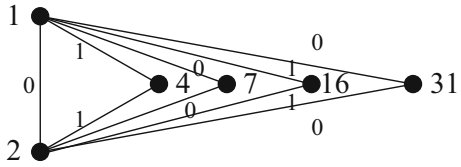

Fig. 2 NPC labeling of B_3^5

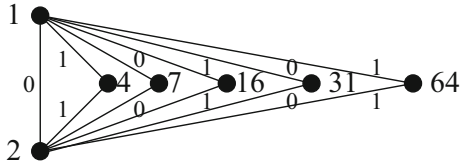

Theorem 2 *A book graph with rectangular pages (or quadrilateral pages) is a NPC graph.*

Proof Let B_4^m be a book graph with rectangular pages.

Let $V = \{u_0, v_0\} \cup \{v_{1,i} | 1 \leq i \leq m\} \cup \{v_{2,i} | 1 \leq i \leq m\}$ be the vertex set of B_4^m.

Let $E = \{u_0 v_0\} \cup E_1 \cup E_2 \cup E_3$ be the edge set of B_4^m where $E_1 = \{u_0 v_{1,i} | 1 \leq i \leq m\}$, $E_2 = \{v_{1,i} v_{2,i} | 1 \leq i \leq m\}$, $E_3 = \{v_0 v_{2,i} | 1 \leq i \leq m\}$.

Now B_4^m has $2m + 2$ vertices and $3m + 1$ edges.

Case (i) When $m \equiv 0 \pmod 2$, define a 1-1 function $\ell : V \to \mathbb{N}_0$ such that

$\ell(u_0) = 1$

$\ell(v_0) = 2$

$\ell(v_{i,1}) = p_1^{i+1}, i = 1, 2$

$\ell(v_{i,2}) = p_2^{i+1} - 1, i = 1, 2$

$\ell(v_{i,3}) = p_3^{i+1}, i = 1, 2$

$\ell(v_{i,4}) = p_4^{i+1} - 1, i = 1, 2$

$\ldots$

$\ell(v_{i,m}) = p_m^{i+1} - 1 \; i = 1, 2$

where $p_1, p_2, \ldots, p_m$ are distinct prime numbers and an edge function $\ell^* : E \to \{0, 1\}$ as in the Definition 2.

In this type of labeling pattern, E has $\frac{3m}{2}+1$ edges with label 0 and $\frac{3m}{2}$ edges with label 1. That is, $e_{\ell^*}(0) = \frac{3m}{2}+1$ and $e_{\ell^*}(1) = \frac{3m}{2}$ and therefore $|e_{\ell^*}(0) - e_{\ell^*}(1)| \leq 1$.

Case (ii) When $m \equiv 1 \pmod 2$, define a 1-1 function $\ell : V \to \mathbb{N}_0$ such that

$\ell(u_0) = 1$
$\ell(v_0) = 2$
$\ell(v_{i,1}) = p_1^{i+1}, i = 1, 2$
$\ell(v_{i,2}) = p_2^{i+1} - 1, i = 1, 2$
$\ell(v_{i,3}) = p_3^{i+1}, i = 1, 2$
$\ell(v_{i,4}) = p_4^{i+1} - 1, i = 1, 2$
$\ldots$
$\ell(v_{i,m-1}) = p_{m-1}^{i+1} - 1, i = 1, 2$
$\ell(v_{1,m}) = p_m^2 - 1$
$\ell(v_{2,m}) = p_m^2$

and an edge function $\ell^* : E \to \{0, 1\}$ as in the Definition 2.

This vertex function and edge function enable the graph such that $\frac{3m+1}{2}$ edges receive the label 0 and $\frac{3m+1}{2}$ edges with receive the label 1. That is, $e_{\ell^*}(0) = \frac{3m+1}{2} + 1$ and $e_{\ell^*}(1) = \frac{3m+1}{2}$, and therefore $|e_{\ell^*}(0) - e_{\ell^*}(1)| \leq 1$ is satisfied in both cases.

Therefore B_4^m is a NPC graph. The NPC labeling of B_4^m is given in the Fig. 3.

Example 2

Fig. 3 NPC labeling of B_4^m

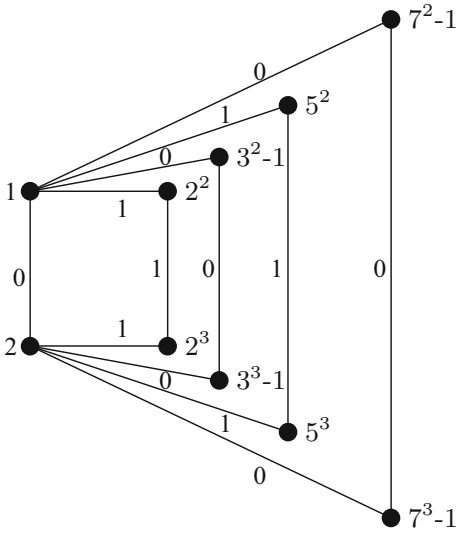

Theorem 3 *The book graph B_n^m is a NPC graph.*

Proof Let B_n^m be a book graph with m copies of n cycles, $n \geq 3$. Then B_n^m has $m(n-2)+2$ vertices and $m(n-1)+1$ edges.

Let $V = \{u_0, v_0\} \cup V_1 \cup V_2 \cup V_3 \cup \cdots \cup V_m$ be vertex set of B_n^m where

$V_1 = \{v_{1,i} | 1 \leq i \leq n-2\}$,
$V_2 = \{v_{2,i} | 1 \leq i \leq n-2\}$,
$V_3 = \{v_{3,i} | 1 \leq i \leq n-2\}$,
$\ldots$,
$V_m = \{v_{m,i} | 1 \leq i \leq n-2\}$.
Let $E = \{u_0v_0\} \cup E_1 \cup E_2 \cup E_3 \cup \cdots \cup E_m$ be edge set of the B_n^m where
$E_1 = \{u_0v_{1,1}\} \cup \{v_{1,i}v_{1,i+1} | 1 \leq i \leq n-3\} \cup \{v_{1,n-2}v_0\}$,
$E_2 = \{u_0v_{2,1}\} \cup \{v_{2,i}v_{2,i+1} | 1 \leq i \leq n-3\} \cup \{v_{2,n-2}v_0\}$,
$E_3 = \{u_0v_{3,1}\} \cup \{v_{3,i}v_{3,i+1} | 1 \leq i \leq n-3\} \cup \{v_{3,n-2}v_0\}$,
$\ldots$,
$E_m = \{u_0v_{m,1}\} \cup \{v_{m,i}v_{m,i+1} | 1 \leq i \leq n-3\} \cup \{v_{m,n-2}v_0\}$.

Case (i) Let $m \equiv 0 \pmod 2$ and $n \equiv 0 \pmod 2$. Define a 1-1 function $\ell : V \to \mathbb{N}_0$ such that

$\ell(u_0) = 1, \ell(v_0) = 2$
$\ell(v_{1,i}) = p_1^{i+1}; 1 \leq i \leq n-2$
$\ell(v_{2,i}) = p_2^{i+1} - 1; 1 \leq i \leq n-2$
$\ell(v_{3,i}) = p_3^{i+1}; 1 \leq i \leq n-2$
$\ldots$
$\ell(v_{m,i}) = p_m^{i+1} - 1; 1 \leq i \leq n-2$

where p_1, p_2, and p_m are distinct primes such that $p_1 \leq p_2 < p_3 < \cdots < p_m$ and an edge function $\ell^* : E \to \{0, 1\}$ as in the Definition 2. In this labeling pattern, $\frac{m(n-1)}{2} + 1$ edges have the label 0, and $\frac{m(n-1)}{2}$ edges have the label 1. That is, $e_{\ell^*}(0) = \frac{m(n-1)}{2} + 1$, and $e_{\ell^*}(1) = \frac{m(n-1)}{2}$; therefore, $|e_{\ell^*}(0) - e_{\ell^*}(1)| \leq 1$.

Case (ii) Let $m \equiv 0 \pmod 2$ and $n \equiv 1 \pmod 2$, and define the vertex function and edge function as in Case (i). These functions will enable the graph such that $\frac{m(n-1)}{2} + 1$ edges receive the label 0 and $\frac{m(n-1)}{2}$ edges receive the label 1. That is $e_{\ell^*}(0) = \frac{m(n-1)}{2} + 1$ and $e_{\ell^*}(1) = \frac{m(n-1)}{2}$ and therefore $|e_{\ell^*}(0) - e_{\ell^*}(1)| \leq 1$.

Case (iii) When $m \equiv 1 \pmod 2$ and $n \equiv 0 \pmod 2$, define a 1-1 function $\ell : V \to \mathbb{N}_0$ such that

$\ell(u_0) = 1, \ell(v_0) = 2$
$\ell(v_{1,i}) = p_1^{i+1}; 1 \leq i \leq n-2$
$\ell(v_{2,i}) = p_2^{i+1} - 1; 1 \leq i \leq n-2$
$\ell(v_{3,i}) = p_3^{i+1}; 1 \leq i \leq n-2$
$\ldots$
$\ell(v_{m-1,i}) = p_{m-1}^{i+1} - 1; 1 \leq i \leq n-2$

$$\ell(v_{m,i}) = \begin{cases} p_m^{i+1}; & 1 \leq i \leq \frac{n-2}{2} + 1 = \frac{n}{2} \\ p_m^{i+1} - 1; & \frac{n}{2} < i \leq n-2 \end{cases}$$

where $p_1, p_2, p_3, \ldots, p_m$ are distinct primes, such that $p_1 < p_2 < p_3 < \cdots < p_m$ and an edge function $\ell^* : E \to \{0, 1\}$ as in the Definition 2. In this type of labeling

pattern, E has $\frac{m(n-1)+1}{2}$ edges with label 0 and $\frac{m(n-1)+1}{2}$ edges with label 1. That is, $e_{\ell^*}(0) = \frac{m(n-1)+1}{2}$ and $e_{\ell^*}(1) = \frac{m(n-1)+1}{2}$ and therefore $|e_{\ell^*}(0) - e_{\ell^*}(1)| \leq 1$.

Case (iv) When $m \equiv 1 \pmod 2$ and $n \equiv 1 \pmod 2$, define a 1-1 function $\ell : V \to \mathbb{N}_0$ such that

$\ell(u_0) = 1, \ell(v_0) = 2$

$\ell(v_{1,i}) = p_1^{i+1}; 1 \leq i \leq n-2$

$\ell(v_{2,i}) = p_2^{i+1} - 1; 1 \leq i \leq n-2$

$\ell(v_{3,i}) = p_3^{i+1}; 1 \leq i \leq n-2$

$\ldots$

$\ell(v_{m-1,i}) = p_{m-1}^{i+1} - 1; 1 \leq i \leq n-2$

$$\ell(v_{m,i}) = \begin{cases} p_m^{i+1}; & 1 \leq i \leq \frac{n-2}{2} \\ p_m^{i+1} - 1; & \frac{n-1}{2} < i \leq n-2 \end{cases}$$

where $p_1, p_2, p_3, \ldots, p_m$ are prime numbers, such that $p_1 < p_2 < p_3 < \cdots < p_m$ and an edge function $\ell^* : E \to \{0, 1\}$ as in the Definition 2. In this type of labeling pattern, E has $\frac{m(n-1)+1}{2}+1$ edges with label 0 and $\frac{m(n-1)+1}{2}$ edges with label 1. That is, $e_{\ell^*}(0) = \frac{m(n-1)+1}{2}+1$ and $e_{\ell^*}(1) = \frac{m(n-1)+1}{2}$ and therefore $|e_{\ell^*}(0)-e_{\ell^*}(1)| \leq 1$.

From Cases (i), (ii), (iii), and (iv), we conclude that B_n^m is a NPC graph.

4 Conclusion

In this manuscript, we proved that the graphs, viz., (i) B_3^m, (ii) B_4^m, and (iii) B_n^m (generalized Book graph), admit a NPC labeling with suitable examples.

References

1. Acharya, B.D., Hegde, S.M.: Arithmetic Graphs. J. Graph Theory. **14**(3), 275–299 (1990)
2. Gallian, J.A.: A Dynamic Survey of Graph Labeling. Electronic Journal of Combinatorics. **17** (DS6) (2016)
3. Harary, F.: Graph Theory. Addison-Wesley, Reading Mass (1972)
4. Lakshmi Prasana, N., Saravanthi, K., Nagalla Sudhakar: Applications of Graph Labeling in Major Areas of Computer Science. International Journal of Research in Computer and Communication Technology. **3**(8) (2014)
5. Miklos Bona, Bruce E. Sagan: On divisibility of Narayana numbers by primes. Journal of Integer Sequences. **8** (2005)
6. Murali, B.J., Thirusangu, K., Balamurugan, B.J.: Narayana prime cordial labeling of graphs. International Journal of Pure and Applied Mathematics. **117**(13), 1–8 (2017)
7. Rosa, A.: On Certain Valuations of the Vertices of a Graph, In Theory of Graphs (Internat. Sympos. Rome. 1966), 349–359 (1967) Gordan and Breach. Newyork. Dunod. Paris
8. Thomas Koshy, Catalan Numbers with Applications, Oxford University Press (2009)

Quotient-3 Cordial Labeling for Path Related Graphs: Part-II

P. Sumathi and A. Mahalakshmi

Abstract A simple graph $G(V, E)$ has order p and size q. Let $f : V(G) \to \mathbb{Z}_4 - \{0\}$ be a function. For each $E(G)$ define $f^* : E(G) \to \mathbb{Z}_3$ by $f^*(uv) = \left\lceil \frac{f(u)}{f(v)} \right\rceil \pmod 3$ where $f(u) \geq f(v)$. The function f is said to be quotient-3 cordial labeling if the difference between the number of vertices (edges) labeled with $i(k)$ and the number of vertices (edges) labeled with $j(l)$ by atmost 1. $1 \leq i, j \leq 3$, $i \neq j$, and $0 \leq k, l \leq 2$, $k \neq l$. Here it is proved that some path-related graphs like $(P_n; P_2)$, $S(P_n; P_2)$, $[P_n; S_m]$ $m \neq 1$, $S[P_n; S_2]$, $Twig(Tg_n)$, and $S(Tg_n)$ are quotient-3 cordial.

Keywords Star · path · twig · subdivision graph · quotient-3 cordial.

Mathematics Subject Classification 05C78

1 Introduction

All the graphs considered here are finite, simple, undirected, and nontrivial. Graph theory has a good development in the graph labeling and has a broad range of applications. Refer to Gallian [3] for more information. Cahit [1] has introduced the concept of cordial labeling. Based on this labeling, more papers published in cordial labeling such as mean cordial labeling, $H1$- and $H2$-cordial labeling of some graphs [2], 3 product cordial labeling, etc. With the reference of these labelings, we have introduced quotient-3 cordial labeling. A graph G is said to be quotient-3 cordial if it receives quotient-3 cordial labeling. Number of vertices labeled with i is denoted

P. Sumathi (✉)
Department of Mathematics, C. Kandaswami Naidu College for Men, Anna Nagar, Chennai, India

A. Mahalakshmi (✉)
Department of Mathematics, Saveetha Engineering College, Thandalam, Chennai, India
e-mail: mahalakshmia@saveetha.ac.in

B. Rushi Kumar et al. (eds.), *Applied Mathematics and Scientific Computing*,
Trends in Mathematics, https://doi.org/10.1007/978-3-030-01123-9_55

by $v_f(i)$, and the number of edges labeled with k is denoted by $e_f(k)$, $1 \leq i \leq 3$, $0 \leq k \leq 2$.

2 Preliminaries

Definition 1 ([6]) A graph $(P_n; P_2)$ is obtained from a path P_n by attaching an end vertex of P_2 with every vertex of P_n through an edge.

Definition 2 ([6]) A graph $[P_n; S_m]$ is obtained by joining the root of a star S_m at every vertex of a path P_n.

Definition 3 ([4]) A Twig graph Tg_n, $n \geq 1$ is obtained by attaching two vertices to every internal vertex of a path through an edge.

Definition 4 ([5]) A new graph is obtained from G by subdividing all the edges of G with a new vertex called subdivision of G, and it is denoted by $S(G)$.

3 Main Result

Definition 5 ([7]) A simple graph $G(V, E)$ has order p and size q. Let $f : V(G) \to \mathbb{Z}_4 - \{0\}$ be a function. For each $E(G)$ define $f^* : E(G) \to \mathbb{Z}_3$ by $f^*(uv) = \left\lceil \frac{f(u)}{f(v)} \right\rceil \pmod 3$ where $f(u) \geq f(v)$. The function f is said to be quotient-3 cordial labeling if the difference between the number of vertices (edges) labeled with $i(k)$ and the number of vertices (edges) labeled with $j(l)$ by atmost 1. $1 \leq i, j \leq 3, i \neq j$, and $0 \leq k, l \leq 2, k \neq l$.

Theorem 1 *A graph $(P_n; P_2)$ is quotient-3 cordial.*

Proof Let $G = (P_n; P_2)$
Let $V(G) = \{u_i, v_i, w_i : 1 \leq i \leq n\}$
$E(G) = \{[(u_i u_{i+1}) : 1 \leq i \leq n-1] \cup [(u_i v_i), (v_i w_i) : 1 \leq i \leq n]\}$
Here $|V(G)| = 3n$, $|E(G)| = 3n - 1$.
Define $f : V(G) \to \mathbb{Z}_4 - \{0\}$
$f(u_i) = 1, 1 \leq i \leq n$
$f(v_i) = 3, 1 \leq i \leq n$
$f(w_i) = 2, 1 \leq i \leq n$
For all n, $v_f(1) = v_f(3) = v_f(2) = n$.
$e_f(1) = n - 1, e_f(0) = e_f(2) = n$
Clearly the graph $(P_n; P_2)$ is quotient-3 cordial.

Theorem 2 *The subdivision of $(P_n; P_2)$ is quotient-3 cordial.* (Table 1)

Proof Let $G = S(P_n; P_2)$
Let $V(G) = \{[u_i : 1 \leq i \leq 2n-1] \cup [x_i, y_i, v_i, w_i : 1 \leq i \leq n]\}$
$E(G) = \{[(u_i u_{i+1}) : 1 \leq i \leq 2n-2] \cup [(u_{2i+1} v_{i+1}) : 0 \leq i \leq n-1] \cup [(v_i w_i), (w_i x_i), (x_i y_i) : 1 \leq i \leq n]\}$

Table 1 $(P_n; P_2)$

Nature of n	$v_f(1)$	$v_f(2)$	$v_f(3)$	$e_f(0)$	$e_f(1)$	$e_f(2)$
$n \equiv 0 \pmod 2$	$2n$	$2n$	$2n-1$	$2n-1$	$2n$	$2n-1$
$n \equiv 1 \pmod 2$	$2n-1$	$2n$	$2n$	$2n-1$	$2n$	$2n-1$

Here $|V(G)| = 6n-1$, $|E(G)| = 6n-2$.
Define $f : V(G) \to \mathbb{Z}_4 - \{0\}$
For all n, $f(u_1) = 1$, $f(v_1) = 3$, $f(w_1) = 3$, $f(x_1) = 2$, $f(y_1) = 2$
Labeling of u_i and $2 \le i \le 2n-1$ is given below.
$f(u_i) = 3$, if $i \equiv 0 \pmod 2$
$f(u_i) = 1$, if $i \equiv 1 \pmod 2$
Labeling of v_i, w_i, x_i, y_i and $2 \le i \le n$ is given below.
For $2 \le i \le n$
$f(v_i) = 2$
$f(w_i) = 2$
$f(x_i) = f(y_i) = 1$, if $i \equiv 0 \pmod 2$
$f(x_i) = f(y_i) = 3$, if $i \equiv 1 \pmod 2$

Theorem 3 [8] *The graph* $[P_n; S_m]$, $m \neq 1$ *is quotient-3 cordial* (Table 2).

Proof Let $G = [P_n; S_m]$
Let $V(G) = \{[u_i, v_{ij} : 1 \le i \le n, 1 \le j \le m]\}$
$E(G) = \{[(u_i u_{i+1}) : 1 \le i \le n-1] \cup [(u_i v_{ij}) : 1 \le i \le n, 1 \le j \le m]\}$
Let $|V(G)| = n(1+m)$, $|E(G)| = n(1+m) - 1$
Define $f : V(G) \to \mathbb{Z}_4 - \{0\}$
For all i, $f(u_i) = 1$
Labeling of v_{ij}, $1 \le i \le n$, and $1 \le j \le m$ is given below.

Case (i) When $n \equiv 0 \pmod 3$
Out of mn vertices, $\left(\frac{mn+n}{3}\right)$ vertices are labeled by 3, $\left(\frac{mn+n}{3}\right)$ vertices are labeled by 2, and the remaining vertices are labeled by 1.

Case (ii) When $n \equiv 1 \pmod 3$

Subcase (i) When $m \equiv 0 \pmod 3$
Out of mn vertices, $\left(\frac{mn+n-1}{3}\right)$ vertices are labeled by 3, $\left(\frac{mn+n-1}{3}\right)$ vertices are labeled by 2, and assign label 1 for the remaining vertices.

Subcase (ii) When $m \equiv 1 \pmod 3$
Out of mn vertices, $\left(\frac{mn+n-2}{3}\right) + 1$ vertices are labeled by 3, $\left(\frac{mn+n-2}{3}\right)$ vertices are labeled by 2, and the remaining vertices are labeled by 1.

Subcase (iii) When $m \equiv 2 \pmod 3$
Out of mn vertices, $\left(\frac{mn+n}{3}\right)$ vertices are labeled by 3, $\left(\frac{mn+n}{3}\right)$ vertices are labeled by 2, and the remaining vertices are labeled by 1.

Table 2 $[P_n; S_m]$

	Nature of m					
	$m \equiv 0 \pmod 3$			$m \equiv 1 \pmod 3$		
Nature of n	$v_f(1)$	$v_f(2)$	$v_f(3)$	$v_f(1)$	$v_f(2)$	$v_f(3)$
$n \equiv 0 \pmod 3$	$\left(\frac{mn+n}{3}\right)$	$\left(\frac{mn+n}{3}\right)$	$\left(\frac{mn+n}{3}\right)$	$\left(\frac{mn+n}{3}\right)$	$\left(\frac{mn+n}{3}\right)$	$\left(\frac{mn+n}{3}\right)$
$n \equiv 1 \pmod 3$	$\left(\frac{mn+n-1}{3}\right)+1$	$\left(\frac{mn+n-1}{3}\right)$	$\left(\frac{mn+n-1}{3}\right)$	$\left(\frac{mn+n-2}{3}\right)+1$	$\left(\frac{mn+n-2}{3}\right)$	$\left(\frac{mn+n-2}{3}\right)+1$
$n \equiv 2 \pmod 3$	$\left(\frac{mn+n-2}{3}\right)+1$	$\left(\frac{mn+n-2}{3}\right)$	$\left(\frac{mn+n-2}{3}\right)+1$	$\left(\frac{mn+n-1}{3}\right)+1$	$\left(\frac{mn+n-1}{3}\right)$	$\left(\frac{mn+n-1}{3}\right)$

	Nature of m					
	$m \equiv 0 \pmod 3$			$m \equiv 1 \pmod 3$		
Nature of n	$e_f(0)$	$e_f(1)$	$e_f(2)$	$e_f(0)$	$e_f(1)$	$e_f(2)$
$n \equiv 0 \pmod 3$	$\left(\frac{mn+n}{3}\right)$	$\left(\frac{mn+n}{3}\right)-1$	$\left(\frac{mn+n}{3}\right)$	$\left(\frac{mn+n}{3}\right)$	$\left(\frac{mn+n}{3}\right)-1$	$\left(\frac{mn+n}{3}\right)$
$n \equiv 1 \pmod 3$	$\left(\frac{mn+n-1}{3}\right)$	$\left(\frac{mn+n-1}{3}\right)$	$\left(\frac{mn+n-1}{3}\right)$	$\left(\frac{mn+n-2}{3}\right)+1$	$\left(\frac{mn+n-2}{3}\right)$	$\left(\frac{mn+n-2}{3}\right)$
$n \equiv 2 \pmod 3$	$\left(\frac{mn+n-2}{3}\right)+1$	$\left(\frac{mn+n-2}{3}\right)$	$\left(\frac{mn+n-2}{3}\right)$	$\left(\frac{mn+n-1}{3}\right)$	$\left(\frac{mn+n-1}{3}\right)$	$\left(\frac{mn+n-1}{3}\right)$

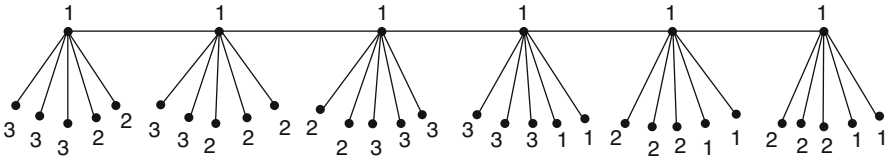

Fig. 1 A quotient-3 cordial of $[P_6; S_5]$

Case (iii) When $n \equiv 2 \pmod 3$

Subcase (i) When $m \equiv 0 \pmod 3$
Out of mn vertices, $\left(\frac{mn+n-2}{3}\right)+1$ vertices are labeled by 3, $\left(\frac{mn+n-2}{3}\right)$ vertices are labeled by 2, and assign label 1 for the remaining vertices.

Subcase (ii) When $m \equiv 1 \pmod 3$
Out of mn vertices, $\left(\frac{mn+n-1}{3}\right)$ vertices are labeled by 3, $\left(\frac{mn+n-1}{3}\right)$ vertices are labeled by 2, and the remaining vertices are labeled by 1.

Subcase (iii) When $m \equiv 2 \pmod 3$
Out of mn vertices, $\left(\frac{mn+n}{3}\right)$ vertices are labeled by 3, $\left(\frac{mn+n}{3}\right)$ vertices are labeled by 2, and assign label 1 for the remaining vertices.
When $m \equiv 2 \pmod 3$ and for all n
$v_f(1) = v_f(2) = v_f(3) = \frac{mn+n}{3}$
$e_f(0) = e_f(2) = \frac{mn+n}{3}$, $e_f(1) = \frac{mn+n}{3} - 1$

Illustration 1 *A quotient-3 cordial of* $[P_6; S_5]$ (Fig. 1)
See Fig. 1.

Theorem 4 *The graph* $S[P_n; S_2]$ *is quotient-3 cordial.*

Proof Let $G = S[P_n; S_2]$
Let $V(G) = \{[u_i : 1 \le i \le 2n-1] \cup [v_{ij}, w_{ij} : 1 \le i \le n, 1 \le j \le 2]\}$
$E(G) = \{[(u_i u_{i+1}) : 1 \le i \le 2n-2] \cup [(u_{2i-1} v_{ij}) : 1 \le i \le n, 1 \le j \le 2] \cup [(v_{ij} w_{ij}) : 1 \le i \le n, 1 \le j \le 2]\}$
Here $|V(G)| = 6n-1$, $|E(G)| = 6n-2$.
Define $f : V(G) \to \mathbb{Z}_4 - \{0\}$
$f(u_i) = 1, 1 \le i \le 2n-1$
$f(v_{ij}) = 3, 1 \le i \le n-1, 1 \le j \le 2$
$f(v_{ij}) = 3$, when $i = n$, $j = 1$
$f(v_{ij}) = 1$, when $i = n$, $j = 2$
$f(w_{ij}) = 2, 1 \le i \le n, 1 \le j \le 2$
For all n, $v_f(1) = v_f(2) = 2n$, $v_f(3) = 2n-1$
$e_f(0) = 2n-1 = e_f(1)$, $e_f(2) = 2n$

Theorem 5 *Twig graph* Tg_n *is quotient-3 cordial.*

Proof Let $G = Tg_n$
Let $V(G) = \{[u_i : 1 \le i \le n+2] \cup [v_i, w_i : 1 \le i \le n]\}$

$E(G) = \{[(u_i u_{i+1}) : 1 \le i \le n+1] \cup [(u_{i+1} v_i), (u_{i+1} w_i) : 1 \le i \le n]\}$
Here $|V(G)| = 3n+2$, $|E(G)| = 3n+1$.
Define $f : V(G) \to \mathbb{Z}_4 - \{0\}$
$f(u_i) = 3, 1 \le i \le n+1$
$f(u_i) = 2, i = n+2$
$f(v_i) = 1, 1 \le i \le n$
$f(w_i) = 2, 1 \le i \le n$
For all n, $v_f(1) = n$, $v_f(2) = v_f(3) = n+1$
$e_f(0) = n = e_f(1)$, $e_f(2) = n+1$

Theorem 6 *The graph $S(Tg_n)$ are quotient-3 cordial.*

Proof Let $G = S(Tg_n)$
Let $V(G) = \{[u_i : 1 \le i \le 2n+3] \cup [v_i, w_i, x_i, y_i : 1 \le i \le n]\}$
$E(G) = \{[(u_i u_{i+1}) : 1 \le i \le 2n+2] \cup [(v_i w_i), (w_i u_{2i+1}), (u_{2i+1} x_i), (x_i y_i) : 1 \le i \le n]\}$
Here $|V(G)| = 6n+3$, $|E(G)| = 6n+2$.
Define $f : V(G) \to \mathbb{Z}_4 - \{0\}$
$f(u_i) = 2, 1 \le i \le 2n+1$
$f(u_i) = 1, i = 2n+2$
$f(u_i) = 3, i = 2n+3$
$f(v_i) = 1, 1 \le i \le n$
$f(w_i) = 3, 1 \le i \le n$
$f(x_i) = 3, 1 \le i \le n$
$f(y_i) = 1, 1 \le i \le n$
For all n, $v_f(1) = 2n+1 = v_f(2) = v_f(3)$
$e_f(0) = 2n+1 = e_f(2)$, $e_f(1) = 2n$

Illustration 2 *A quotient-3 cordial of $S(Tg_5)$* (Fig. 2)
See Fig. 2.

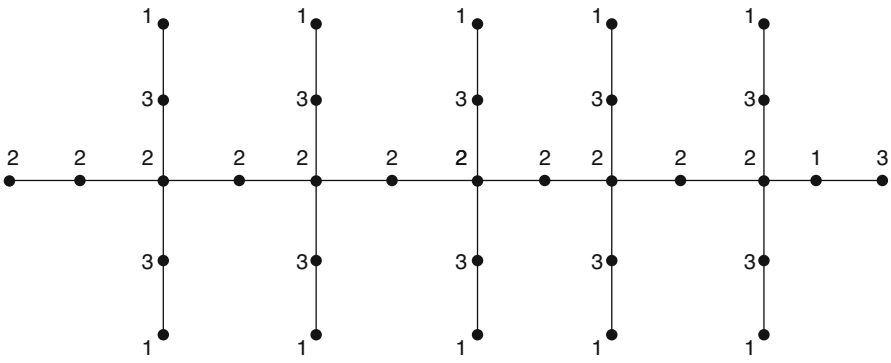

Fig. 2 A quotient-3 cordial of S(Tg_5)

4 Conclusion

Here some path-related graphs have been discussed for quotient-3 cordial. Some more special graphs have to be discussed in future work.

Acknowledgement Register our sincere thanks to the referees offered valuable feedback and suggestions.

References

1. Cahit, I.: Cordial Graphs: A weaker version of Graceful and Harmonious graphs. Ars combin. **23**, 201–207 (1987)
2. Freeda, S, Chellathurai, R.S.: H-1 and H2-cordial labeling of some graphs. Open J. Discrete Math. **2**, 149–155 (2012)
3. Joseph A. Gallian: A Dynamic survey of Graph Labeling. Nineteenth edition, December 23 (2016)
4. Nellai Murugan, A. and Heerajohn, S.: Special Class of Mean Square Cordial Graphs. International Journal of Applied Research. **1**(11), 128–131 (2015)
5. Sankar, K. and Sethuraman, G.: Graceful and Cordial labeling of Subdivision of Graphs. Electronic Notes in Discrete Mathematics. **53**, 123–131 (2016)
6. Selvam Avadayappan and Vasuki, R.: New Families of Mean Graphs. International J. Math. Combin., **2**, 68–80 (2010)
7. Sumathi, P., Mahalakshmi, A., Rathi, A.: Quotient-3 Cordial Labeling for Star Related Graphs. Global Journal of Pure and Applied Mathematics **13**(7), 3909–3918 (2017)
8. Sumathi, P., Mahalakshmi, A., Rathi, A.: Quotient-3 Cordial Labeling for path related graphs part-I. International Journal of Pure and Applied Mathematics **115**(9), 249–258 (2017)

Relation Between k-DRD and Dominating Set

S. S. Kamath, A. Senthil Thilak, and Rashmi M

Abstract In this paper, a new parameter on domination is defined by imposing a restriction on the degrees of vertices in the dominating set. For a positive integer k, a dominating set D of a graph G is said to be a *k-part degree restricted dominating set* (k-DRD-set), if for all $u \in D$ there exists a set $C_u \subseteq N(u) \cap (V - D)$ such that $|C_u| \leq \lceil \frac{d(u)}{k} \rceil$ and $\bigcup_{u \in D} C_u = V - D$. The minimum cardinality of a k-part degree restricted dominating set of G is called the *k-part degree restricted domination number* of G and is denoted by $\gamma_{\frac{d}{k}}(G)$. Here, we determine the k-part degree restricted domination number of some well-known graphs, relation between dominating and k-DRD set, and an algorithm which verifies whether a given dominating set is a k-DRD set or not.

Keywords *Dominating set; Independent dominating set; k-part degree restricted dominating set.*

2010 Mathematics Subject Classification 05C69

1 Introduction

A graph G is a triple consisting of a vertex set V, an edge set E, and a relation that associates two vertices with each edge, namely, its end points. Throughout this paper by a graph, we mean, a finite, undirected graph with no loops or multiple edges having vertex set V and edge set E, unless otherwise specified. We denote the order of graph G by n. The notation and terminologies not defined in this paper are as in [1, 2, 5].

S. S. Kamath (✉) · A. Senthil Thilak · R. M
Department of Mathematical and Computational Sciences, National Institute of Technology Karnataka, Surathkal, Srinivasnagar, Mangalore, India
e-mail: shyam@nitk.edu.in; thilak@nitk.ac.in; ma14f01@nitk.edu.in

B. Rushi Kumar et al. (eds.), *Applied Mathematics and Scientific Computing*, Trends in Mathematics, https://doi.org/10.1007/978-3-030-01123-9_56

A subset $D \subseteq V$ is called a *dominating set* of G, if every vertex not in D is adjacent to at least one vertex in D. The *domination number* of G is the minimum cardinality taken over all dominating sets of G and is denoted by $\gamma(G)$ [3].

Most of the applications and research in the world today hinges on information system; therefore, there is an enormous traffic of data through different communication systems. In a communication network, when a link or a node is carrying so much data, its quality of service often gets compromised, and also there is a possibility of the loss of data. In order to handle such a situation, one needs to remodel the network, so that the neighborhood of the vertex has some prevalent influence. This has prompted us to introduce the new concept, namely, "*k-part degree restricted domination*," in which each vertex v can dominate at most $\lceil \frac{d(v)}{k} \rceil$ other vertices in a given graph instead of all the vertices of the neighborhood of v. In other words, every $u \in D$ dominates at most $\lceil \frac{d(u)}{k} \rceil$ vertices in $V - D$, and we define it as follows.

Definition 1 For a positive integer k, a dominating set D of a graph G is said to be a k-part degree restricted dominating set if for all $u \in D$, there exists a set $C_u \subseteq N(u) \cap (V - D)$ such that $|C_u| \leq \lceil \frac{d(u)}{k} \rceil$ and $\bigcup_{u \in D} C_u = V - D$.

The *k-part degree restricted domination number* of G is the minimum cardinality taken over all the k-part degree restricted dominating set of G and is denoted by $\gamma_{\frac{d}{k}}(G)$. A k-DRD set of cardinality $\gamma_{\frac{d}{k}}$ in G is called a $\gamma_{\frac{d}{k}}$-set of G.

The concept of k-part degree restricted domination is studied for $k = 2$ in [4].

1.1 k-Part Degree Restricted Domination Number of Some Well-Known Graphs

1. $\gamma_{\frac{d}{k}}(P_n) = \lceil \frac{n}{2} \rceil$, for all $k \geq 2$.
2. $\gamma_{\frac{d}{k}}(C_n) = \lceil \frac{n}{2} \rceil$, for all $k \geq 2$.
3. $\gamma_{\frac{d}{k}}(W_n) = \begin{cases} \lceil \frac{n-(m+1)}{2} \rceil + 1 & \text{if } n \equiv 1(mod\ k) \text{ and } k < n-1 \\ \lceil \frac{n-(m+2)}{2} \rceil + 1 & \text{if } n \not\equiv 1(mod\ k) \text{ and } k < n-1 \\ \lceil \frac{n-2}{2} \rceil + 1 & \text{if } k \geq n-1 \end{cases}$

   where $m = \lfloor \frac{n-1}{k} \rfloor$ and $k \geq 3$.
4. $\gamma_{\frac{d}{2}}(W_n) = \begin{cases} 1 + \lceil \frac{n-1}{6} \rceil & \text{if } n \text{ is odd.} \\ 1 + \lceil \frac{n-2}{6} \rceil & \text{if } n \text{ is even.} \end{cases}$
5. Let G be a prism graph. Then $\gamma_{\frac{d}{2}}(G) = \begin{cases} \frac{n}{3} & \text{if } n \equiv 0(mod\ 3) \\ \frac{n+2}{3} & \text{if } n \equiv 1(mod\ 3) \\ \frac{n+1}{3} & \text{if } n \equiv 2(mod\ 3) \end{cases}$

   and $\gamma_{\frac{d}{k}}(G) = \frac{n}{2}$ for all $k \geq 3$.

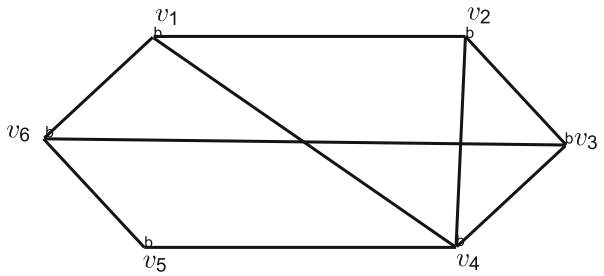

Fig. 1 Here, $\{v_2, v_5\}$ is a dominating set but not a 2-DRD set. Since $d(v_2) = 3$, order of C_{v_2} cannot exceed 2. Similarly, since $d(v_5) = 2$, order of C_{v_5} cannot exceed 1, $|C_{v_5} \cup C_{v_2}| \leq 3 < |V - D| = 4$. Hence, $\{v_2, v_5\}$ cannot be a 2-DRD set of G though it is a dominating set of G. Also note that $D = \{v_4, v_5, v_6\}$ is a $\gamma_{\frac{d}{3}}$-set, but $V - D = \{v_1, v_2, v_3\}$ is not a dominating set

As an immediate consequence of the definition of k-DRD set, we can observe the following:

1. Every graph G has a trivial k-DRD set, namely, $V(G)$.
2. Every k-DRD set is a dominating set, but not conversely; see Fig. 1.
3. The case $k = 1$ is the classical domination number, $\gamma(G) = \gamma_{\frac{d}{1}}(G)$.
4. $\gamma_{\frac{d}{k}}(G) \leq \gamma_{\frac{d}{k+1}}(G)$ for all $k \geq 1$.
5. For every k-DRD set D of a graph G, we can partition the set $V - D$ with the collection of sets $\{C_u : u \in D\}$.
6. Suppose G is a graph without isolated vertices and D is a $\gamma_{\frac{d}{k}}$-set of G, then $V - D$ need not be a k-DRD set or a dominating set, see Fig. 1.

2 Relation Between Dominating Set and k-DRD Set

We know that every dominating set is not a k-DRD set; it is, however, true only for some graphs $\gamma_{\frac{d}{k}}(G) = \gamma(G)$. But looking at the dominating set, it is difficult to determine whether it is a k-DRD set or not; clearly for any dominating set D, if $|V - D| > \sum_{u \in D} \lceil \frac{d(u)}{k} \rceil$, then D is not a k-DRD set. If $|T_u| > \sum_{u \in N(u) \cap D} \lceil \frac{d(u)}{k} \rceil$ for at least one $u \in V - D$, where $T_u = \{v \in V - D | N(v) \cap D \subseteq N(u) \cap D\} \cup \{u\}$, then also D is not a k-DRD set. For any connected graph G, $1 \leq \gamma(G) \leq \frac{n}{2}$. We can characterize the graphs for which $\gamma(G) = \gamma_{\frac{d}{k}}(G) = 1$ and $\gamma(G) = \gamma_{\frac{d}{k}}(G) = \frac{n}{2}$, which are as follows:

Proposition 1 *For $k > 1$, $\gamma(G) = \gamma_{\frac{d}{k}}(G) = 1$ if and only if $G = K_1$ or $G = K_2$.*

Proposition 2 *For a graph G with even order n, no isolated vertices and for any $k > 1$, $\gamma(G) = \gamma_{\frac{d}{k}}(G) = \frac{n}{2}$ if and only if the components of G are cycle C_4 or the corona $H \circ K$ for any connected graph H.*

Proposition 3 *For any graph G, if $\gamma(G) < \lceil \frac{n}{m+1} \rceil$, where $m = \lceil \frac{\Delta(G)}{k} \rceil$, then $\gamma(G) < \gamma_{\frac{d}{k}}(G)$.*

Proof Let D be a $\gamma_{\frac{d}{k}}$-set of G. Since order of C_u cannot exceed $\lceil \frac{\Delta(G)}{k} \rceil$, for any $u \in D$, we have $\left\lceil \frac{n}{\lceil \frac{\Delta(G)}{k} \rceil + 1} \right\rceil \leq \gamma_{\frac{d}{k}}(G)$. Hence, result holds.

Proposition 4 *For $k > 1$ and an independent γ-set D of a tree T, if $d(u) > 1$ for all $u \in D$, then D is not a k-DRD set.*

Proof Suppose D is a k-DRD set, then there exists a partition $\{C_u : u \in D\}$ of $V - D$ such that $|C_u| \leq \lceil \frac{d(u)}{k} \rceil$. Since D is independent and $d(u) > 1$, C_u is a proper subset of $N(u)$ for every $u \in D$. Let $w_1 \in N(u) - C_u$ for some $u \in D$. Since $\bigcup_{u \in D} C_u = V - D$, $w_1 \in C_v$ for some $u \neq v$. Since C_v is a proper subset of $N(v)$, $N(v) - C_v \neq \phi$. Choose a vertex w_2 from $N(v) - C_v$. Furthermore, $w_2 \notin C_u$. If $w_2 \in C_u$, then u, w_1, v, w_2 will form a cycle, a contradiction. Continuing the above process, we get a vertex which is not in any C_u, $u \in D$, contradiction to the fact that D is a k-DRD set.

2.1 Construction of C_u for Every u in a Dominating Set D

We have some results which tells when a given dominating set is a k-DRD set, but our aim is to determine whether a given dominating set D is k-DRD set or not. For this first we have to find C_u for all $u \in D$. In this section we are giving some procedure to find C_u for every $u \in D$. Let $D = \{v_1, v_2, \ldots v_k\}$ and choose a vertex v_1 from D. If $|N(v_1) \cap (V - D)| \leq \lceil \frac{d(v_1)}{k} \rceil$, then $C_{v_1} = N(v_1) \cap (V - D)$. Otherwise choose $\lceil \frac{d(v_1)}{k} \rceil$ number of vertices from the set $N(v_1) \cap (V - D)$ and name that set as C_{v_1}. For $k \geq i \geq 2$, if $|N(v_i) \cap (V - (D \cup (\bigcup_{j=1}^{i-1} C_{v_j})))| \leq \lceil \frac{d(v_i)}{k} \rceil$, then $C_{v_i} = N(v_i) \cap (V - (D \cup (\bigcup_{j=1}^{i-1} C_{v_j})))$. Otherwise choose $\lceil \frac{d(v_i)}{k} \rceil$ number of vertices from the set $N(v_i) \cap (V - (D \cup (\bigcup_{j=1}^{i-1} C_{v_j})))$ and name it as C_{v_i}. Let A be the collection of vertices v in D such that $|C_v| < \lceil \frac{d(v)}{k} \rceil$. If $\bigcup_{v_i \in D} C_{v_i} = V - D$, then D is a k-DRD set. If $(V - D) - \bigcup_{v_i \in D} C_{v_i} \neq \phi$, then we have the following results. In this section, we use $S = V - (\bigcup_{v_i \in D} C_{v_i} \cup D)$ and $A = \{v : |C_v| < \lceil \frac{d(v)}{k} \rceil\}$ as constructed above.

Theorem 1 *A dominating set D of a graph G is a k-DRD set if and only if for every vertex $u \in S$ there exists a path $P_u = u, v_1, v_2, \ldots v_{2l+1}$ satisfying the following.*

1. *For each i, $0 \leq i \leq l$, $v_{2i+1} \in D$.*
2. *For each i, $0 < i \leq l$, $v_{2i} \in C_{v_{2i-1}}$.*
3. *$|C_{v_{2l+1}}| < \lceil \frac{d(v_{2l+1})}{k} \rceil$.*
4. *If the paths $P_{u_1} P_{u_2} .., P_{u_m}$ end at the same vertex say v, then $\lceil \frac{d(v)}{k} \rceil - |C_v| \geq m$.*
5. *For every $u, w \in S$, $V(P_u) \cap V(P_w) \cap (V - D) = \phi$.*

Proof Let D be a k-DRD set. Then for each $u \in D$, there exists $C'_u \subseteq N(u) \cap (V - D)$ such that $|C'_u| \leq \lceil \frac{d(u)}{k} \rceil$ and $\bigcup_{u \in D} C'_u = V - D$. Now for each $u \in S$, we construct a path P_u, which satisfies above conditions. Consider a vertex u from S. Since D is k-DRD set, $u \in C'_{v_1}$ for some $v_1 \in D$. By the construction of C_u for $u \in D$, $|C_{v_1}| = \lceil \frac{d(v_1)}{k} \rceil$, therefore $C_{v_1} - C'_{v_1} \neq \phi$. Consider a vertex v_2 from $C_{v_1} - C'_{v_1}$. Since D is a k-DRD set $v_2 \in C'_{v_3}$ for some $v_3 \in D$. If $|C_{v_3}| < \lceil \frac{d(v_3)}{k} \rceil$, then $P'_u = u, v_1, v_2, v_3$. If $|C_{v_3}| = \lceil \frac{d(v_3)}{k} \rceil$, then $C_{v_3} - C'_{v_3} \cup \{v_2\} \neq \phi$; choose a vertex v_4 from $C_{v_3} - C'_{v_3} \cup \{v_2\}$. Then $v_4 \in C'_{v_5}$ for some v_5. If $|C_{v_5}| < \lceil \frac{d(v_5)}{k} \rceil$, then $P'_u = u, v_1, v_2, v_3, v_4, v_5$. Suppose $|C_{v_5}| = \lceil \frac{d(v_5)}{k} \rceil$. Then we can choose $v_6 \in C_{v_5} - C'_{v_5} \cup \{v_2, v_4\}$ and continue the process. Since D, C_v, $v \in D$ are finite and vertex of C_v can be chosen at most once in the process, the above process has to terminate. So after some finite steps, we get a vertex v_k such that k is odd, $v_{k-1} \in C'_k$,and $|C_{v_k}| < \lceil \frac{d(v_k)}{k} \rceil$. Now for a chosen vertex u in S, we have a path $u, v_1, v_2 \ldots, v_k$ such that $v_{2i+1} \in D$, for $0 \leq i \leq \frac{k-1}{2}$, $v_{2i} \in C_{v_{2i-1}}$, $0 < i \leq \frac{k-1}{2}$, and $|C_{v_k}| < \lceil \frac{d(v_k)}{k} \rceil$.

Let $P'_u = u, u_1, u_2, u_3, \ldots, u_l$ and $P'_v = v_1, v_2, v_3, \ldots v_k$ be two paths. Suppose $u_{2j} = v_{2i}$. Then by the construction $u_{2j} \in C_{u_{2j-1}}$ and $v_{2i} \in C_{v_{2i-1}}$, hence $v_{2i-1} = u_{2i-1}$. Now $v_{2i-2}, u_{2i-2} \in C'_{v_{2i-1}}$ and there exists two vertices in $C'_{v_{2i-1}}$ not in $C_{v_{2i-1}}$. If v_{2i-1} is not an end vertex of path, then $C_{v_{2i-1}}$ has two more vertices which is not in $C'_{v_{2i-1}}$; hence, we can continue the process as above, and we can find one new path P_u such that $V(P_u) \cap V(P_v) \cap (V - D) = \phi$.

Assume that $v_k = u_l$, $\lceil \frac{d(v_k)}{k} \rceil - |C_{v_k}| = 1$ and there is no other such paths for u, v. Then we have following construction:

Let $B_1 = N(u, v) \cap D$, $B'_1 = \bigcup_{u \in B_1} C_u$. For $i > 1$ $B_i = N(B'_{i-1}) \cap D$ and $B'_i = \bigcup_{u \in B_i} C_u$. Since V is finite, there exist $m, n \in N$ such that $B_j = B_{j+1} = B_{j+2}$ for all $j \geq m$ and $B'_l = B'_{l+1} = B'_{l+2}$ for all $l \geq n$. Now $|B'_n| > \sum_{u \in N(B'_n) \cap D} \lceil \frac{d(u)}{k} \rceil$, contradiction to the fact that D is a k-DRD set.

Conversely, we construct C'_u for all $u \in D$ which dominates all the vertices of S. First consider a vertex u of S; then there exists a path $u, v_1, v_2, ..v_k$ satisfying the above conditions. Define $C'_{v_{2i+1}} = C_{v_{v_{2i+1}}} \cup \{v_{2i}\} - \{v_{2i+2}\}$, *forall* i, $\frac{k-3}{2} \geq i \geq 1$, $C'_{v_1} = C_{v_1} \cup \{u\} - \{v_2\}$, $C'_{v_k} = C_{v_k} \cup \{v_{k-1}\}$. Since $|C_{v_k}| < \lceil \frac{d(v_k)}{k} \rceil$, $|C'_{v_k}| \leq \lceil \frac{d(v_k)}{k} \rceil$. Also observe that $|C'_{v_{2i+1}}| = |C_{v_{2i+1}}| \leq \lceil \frac{d(v_{2i+1})}{k} \rceil$ for all i, $\frac{k-3}{2} \geq i \geq 0$ and $u \in C'_{v_1}$ is dominated by D. Since such path exists for all the vertices in S, $\bigcup_{v \in D} C'_v = V - D$. Hence, D is a k-DRD set.

Corollary 1 *For any dominating set D of a tree T, if $\langle S \rangle$ is connected and $|S| \geq |A|$, then D is not a k-DRD set.*

Corollary 2 *For any connected dominating set D of a tree T, D is a k-DRD set if and only if $S = \phi$.*

From Theorem 1, we observe that for a given dominating set, if we are able to find such paths, then D is a k-DRD set. In Sect. 2.2, we develop an algorithm to find such paths for a given graph with respect to a given dominating set D.

Throughout the Sect. 2.2, we consider the graph labeled by natural numbers. Initially we find C_u for each $u \in D$ as defined above. If $\bigcup_{v \in D} C_v = V - D$, then D is a k-DRD set. Suppose $(V - D) - \bigcup_{v \in D} C_v = S \neq \phi$, then we have to check whether vertices of S can be included in some C_u, $u \in D$. We define set A as the collection of all the vertices in D with $|C_u| < \lceil \frac{d(u)}{k} \rceil$. By depth-first search we find the existence of path, from vertices in S to vertices in A, which satisfies the conditions in Theorem 1. If such path exists for all the vertices in S, then D is a k-DRD set; otherwise, D is not a k-DRD set.

Theorem 2 *A γ-set D of a connected graph G is a k-DRD set if and only if, for every subset A of $V - D$, $\sum_{u \in N(A) \cap D} \left\lceil \frac{d(u)}{k} \right\rceil \geq |A|$.*

Proof Let $A \subseteq V - D$. Then $A \subseteq \bigcup_{u \in N(A) \cap D} C_u$, which implies $|A| \leq |\bigcup_{u \in N(A) \cap D} C_u| \leq \sum_{u \in N(A) \cap D} \left\lceil \frac{d(u)}{k} \right\rceil$. Conversely assume that, for any subset A of $V - D$, $\sum_{u \in N(A) \cap D} \left\lceil \frac{d(u)}{k} \right\rceil \geq |A|$. For every $u \in D$, we construct C_u as defined above. Suppose D is not a k-DRD set. Then we can find a vertex $w \in V - D$ such that $w \notin C_u$ for any $u \in D$ and no P_w path satisfying the conditions in Theorem 1. Since D is a dominating set, w is adjacent to at least one vertex in D. Note that $|C_v| = \lceil \frac{d(v)}{k} \rceil$ for all $v \in N(w) \cap D = B_1$ (otherwise uv is a path satisfying the conditions in Theorem 1). Let $\bigcup_{v \in B_1} C_v = B_2$. Then $|C_u| = \lceil \frac{d(u)}{k} \rceil$ for all $u \in N(B_2) \cap D$; otherwise w, v, x, u forms a path satisfying the condition in Theorem 1, where $x \in C_u$. Continuing in this manner, we get the set of vertices $\{w_1, w_2, \ldots, w_l\}$ such that $|C_{w_i}| = \lceil \frac{d(w_i)}{k} \rceil$ for all i, $1 \leq i \leq l$ and $N(\bigcup_{k=1}^{l} C_{w_k}) \cap D \subseteq \{w_1, w_2, \ldots, w_l\}$. Consider $A = \bigcup_{k=1}^{l} C_{w_k} \cup \{w\}$.

Then $N(A) \cap D \subseteq \{w_1, w_2, \ldots, w_l\}$ and $\sum_{u \in N(A) \cap D} |C_u| \leq \sum_{i=1}^{m} |C_{w_i}| = \sum_{i=1}^{m} \left\lceil \frac{d(w_i)}{k} \right\rceil = |A| - 1 < |A|$, a contradiction. Hence D is a k-DRD set.

Corollary 3 *Let G be a connected graph and D be a γ-set of order less than or equal to 2. Then D is a k-DRD set of G if and only if $|Pn(u, D) \cap (V - D)| \leq \left\lceil \frac{d(u)}{k} \right\rceil$ for all $u \in D$ and $|V - D| \leq \sum_{u \in D} \left\lceil \frac{d(u)}{k} \right\rceil$, where $Pn(u, D)$ is the private neighborhood of u.*

Corollary 4 *For a given graph G having D as a γ-set, we can find a super graph of G having same vertex set V and D as $\gamma_{\frac{d}{k}}$ -set if and only if*

$$\gamma(G) \geq \begin{cases} \lceil \frac{n-\gamma(G)}{m} \rceil & \text{if } n \equiv 1 (mod\ k) \\ \lceil \frac{n-\gamma(G)}{m+1} \rceil & \text{if } n \not\equiv 1 (mod\ k) \end{cases}, \text{ where } m = \lfloor \tfrac{n-1}{k} \rfloor.$$

2.2 An Algorithm to Verify Whether a Given Dominating Set is k-DRD Set or Not

The main idea of Algorithm 1 is as follows: First for every vertex i in V, we find degree $d(i)$; for every vertex i in D we find neighborhood N_i in $V - D$ and vertex of maximum degree Δ. We add a vertex of minimum degree from N_i to C_i; repeat this step by adding vertex of next minimum degree to C_i until either order of C_i is $\lceil \frac{d(i)}{k} \rceil$ or N_i becomes empty; update $V - D$ by removing the elements of C_i along with i. Repeat this procedure for each vertex in D, which gives a set C_i for each $i \in D$. If $\bigcup_{i \in D} C_i = V - D$, then D is a k-DRD set. Otherwise from Theorem 1 for each vertex in S, we have to check the existence of path. Here we use depth-first search with stack function P to find such paths. Also note that Top= 0 means $P = \phi$ and P(Top)= i means P$\cup\{i\}$. We can observe that, either a vertex of degree one or its neighborhood vertex should be in k-DRD set; therefore, for any $i \in D$ while adding vertices to C_i, we give first preference to a vertex of minimum degree in N_i.

Theorem 3 *Algorithm 1 runs in $O(n^3)$ time.*

Proof For a given graph G and its dominating set D, calculating the degree of each vertex in V takes $O(n^2)$ time. Similarly to determine the neighborhood of each vertex in $V - D$ takes $O(n^2)$ time. Since cardinality of neighborhood of any vertex is at most n-1, constructing C_v for each vertex $v \in D$ takes $O(n^3)$ time. We find path using DFS which takes $O(n^2)$ time if it exists. In total to find such paths for each vertex in S, it takes $O(n^3)$ running time. Hence, complexity of the algorithm is $O(n^3)$.

Algorithm 1: Test for dominating set to be a k-DRD set

Input: A simple graph $G = (V, E)$, adjacency matrix $[a_{ij}]_{n\times n}$, positive integer k, γ-set D, maximum degree Δ.
Output: D is a k-DRD set or not.

begin
  $D' = V - D$, **for** $i \in V$ **do**
    $d(i) = 0$ **for** *each* $j \in V$ **do**
      $d(i) = d(i) + a_{ij}$
    end
  end
  for $i \in D$ **do**
    $N_i = \phi$ **for** *each* $j \in D'$ **do**
      if $a_{ij} = 1$ **then**
        $N_i = N_i \cup \{j\}$
      end
    end
    $C_i = \phi$ **while** $|C_i| < \lceil \frac{d(i)}{k} \rceil$ && $N_i \neq \phi$ **do**
      $d'_\Delta = \Delta$
      for *each* $j \in N_i$ **do**
        if $d(j) \leq d'_\Delta$ **then**
          $d'_\Delta = d(j), d_\Delta = j$
        end
      end
      $C_i = C_i \cup \{d_\Delta\}, N_i = N_i - \{d_\Delta\}$
    end
    $D' = D' - C_i$
  end
  if $\bigcup_{i\in D} C_i = D'$ **then**
    stop, D is k-DRD set
  end
  else
    $S = D' - \bigcup_{i\in D} C_i$, $A = \{j \in D : |C_j| < \lceil \frac{d(j)}{k} \rceil\}$ **if** $A = \phi$ **then**
      stop, D-is not a k-DRD set
    end
    else
      for *all* $i \in S$ **do**
        $P = call\ Path(i)$, $P = v_o, v_1, v_2, \ldots v_k$, $\frac{k-3}{2} = m$ **for** $l = 1, 2, .., m$ **do**
          $C_{v_{2l+1}} = (C_{v_{2l+1}} \cup \{v_{2l}\})$-$\{v_{2l+2}\}$
        end
        $C_{v_1} = (C_{v_1} \cup \{v_o\}) - \{v_2\}$ $C_{v_k} = C_{v_k} \cup \{v_{k-1}\}$
      end
      stop, D-is a k-DRD set
    end
  end
end

Algorithm 2: Push(i)

```
1 begin
2 |  Top=Top+1
3 |  P(Top)=i
4 end
```

Algorithm 3: Pop

```
1 begin
2 |  P(Top)=Null
3 |  Top=Top-1
4 end
```

Algorithm 4: Path(i)

```
1  begin
2  |  for all g ∈ V do
3  |  |  Visited[g]=0
4  |  end
5  |  Top = 0, Visited[i]=1, Push(i)
6  |  while P ≠ φ do
7  |  |  j=P(Top)
8  |  |  if j ∈ D then
9  |  |  |  N_j= {v ∈ C_j : Visited[v] = 0}
10 |  |  end
11 |  |  else
12 |  |  |  N_j= {v ∈ D : a_jv = 1, Visited[v] = 0}
13 |  |  end
14 |  |  if N_j ≠ φ then
15 |  |  |  choose a vertex l from N_j, Push(l),Visited[l] = 1
16 |  |  |  if l ∈ A then
17 |  |  |  |  return P
18 |  |  |  end
19 |  |  end
20 |  |  else
21 |  |  |  pop()
22 |  |  end
23 |  end
24 |  if P = φ then
25 |  |  stop,D is not a k-DRD set
26 |  end
27 end
```

3 Conclusion

This paper elaborates the relation between dominating set and k-DRD set. We have also presented an algorithm to verify whether a given dominating set is k-DRD set or not. As a future work, we will study the relation between k-DRD set and other domination invariants.

References

1. Bondy, J.A., Murty, U.S.R.: Graph theory, Springer (2008)
2. Cormen, T.H., Leiserson, C.E., Rivest, R. L., Stein, C.: Introduction to Algorithms. MIT Press (2009)
3. Haynes, T.W., Hedetniemi, S., Slater, P.: Fundamentals of domination in graphs, CRC press (1998)
4. S.S.Kamath, A. Senthil Thilak, M.Rashmi.: 2-part degree restricted domination in graphs. In: IWCAAM'16, pp. 211–221. SHANLAX (2016)
5. West, D.B.: Introduction to Graph Theory, Vol. 2. Prentice Hall (2001)

The b-Chromatic Number of Some Standard Graphs

A. Jeeva, R. Selvakumar, and M. Nalliah

Abstract b-Coloring of G is a coloring which is proper such that in each color class there exists a vertex which is called as representative vertex that has at least one neighbor in each of the remaining color classes. The highest positive integer k such that the k-colors can be used to color the vertices of G along with b-coloring is the b-chromatic number of G, denoted by $b(G)$. For a given graph G with n vertices, G^* is constructed (Jeeva et al., Indian J Math 59(2):255–261, 2017). In the research paper, we find out the b-chromatic number of Mycielskian, splitting, shadow, middle, and total graph of G^*.

1 Introduction

Throughout the manuscript, we mentioned every graph is simple, finite, connected, and undirected graph. A pair of a graph $G = (V, E)$ consists of the vertex set V and the edge set E; the order and size of G are n and m, respectively. Consider, a coloring is a proper vertex k-coloring having a nonempty partition say $P = \{v_1, v_2, \ldots, v_k\}$.The color classes are obtained from P such that each V_i should be independent in G. The chromatic number of G, denoted by $\chi(G)$ is the smallest integer k, where k-colors will be used to color the vertices of G. A proper k-coloring is a b-coloring; it has the property that there exist a vertex in every color class which is called as representative vertex that has at least one neighbor in each of the remaining color classes. The representative vertex is also called as b-vertex. The parameter b-chromatic number $b(G)$, introduced by Irving and Manlove [2], is the largest integer k for which G having a b-coloring using k-colors, also they derived

A. Jeeva · R. Selvakumar (✉)
Department of Mathematics, Vellore Institute of Technology, Vellore, India
e-mail: jeeva.a2012@vit.ac.in; rselvakumar@vit.ac.in

M. Nalliah
Department of Mathematics, School of Advanced Sciences, Vellore Institute of Technology, Vellore, Tamil Nadu, India
e-mail: nalliah.moviri@vit.ac.in

B. Rushi Kumar et al. (eds.), *Applied Mathematics and Scientific Computing*,
Trends in Mathematics, https://doi.org/10.1007/978-3-030-01123-9_57

the upper bound of $b(G)$, $b(G) \leq \Delta(G) + 1$. Specifically they noted that a graph G has a b-chromatic coloring using m-colors and G must have at least m vertices of degree $m - 1$. The largest integer m such that G may have m vertices of degree at least $m - 1$ is the m-degree of a graph G, denoted $m(G)$. It follows that for every graph G we have to see that $b(G) \leq m(G)$. A graph having a vertex that has degree at least $m(G)$ is called as dense vertex [3]. Kouider and El Sahili proved [4] the b-chromatic number of d-regular graph with girth five and without cycles of length six is $d + 1$. Also, they stated that every d-regular graph G satisfies $m(G) = d + 1$. The b-chromatic number of some upper and lower bounds for the Cartesian product of two graphs given by Kouider and Maheo [5]. Kouider and Zaker investigated [6] some upper bounds of the b-chromatic number of many classes of graphs with different graph parameters. Several authors have studied the b-chromatic number of Mycielskian, splitting, shadow, middle, and total graph in [7–12].

Definition 1 ([7]) The Mycielski graph $\mu(G)$ is forming from G by taking the vertices of G with $v_1, \cdots, v_n$ as an isomorphic subgraph, along with $n + 1$ new vertices say $u, u_1, \cdots, u_n$. Here we are taking the vertex u_i corresponding to each v_i of G and central vertex u. Then adding an edge between each u_i to u and each u_i to the neighbors of v_i in G.

Definition 2 ([8]) The splitting graph $Splt(G)$ is constructed from G in such a way that, for each $v \in G$, takes an additional vertex v_0 and add v_0 to all the vertices of G which is adjacent to v.

Definition 3 ([9]) Let G' and G'' be the two copies of G. Then the shadow graph $D_2(G)$ is formed from G by adding an edge between each u' in G' to the neighbors of the corresponding u'' in G''.

Definition 4 ([11]) The middle graph of G, is constructed from G in the following way. The vertex set of $M(G)$ is the combination of vertex set and edge set which is called as union, and a and b are two vertices of $M(G)$ which is adjacent in $M(G)$; it will be satisfied at least one condition given the below statements.

1. Both are edges in $E(G)$ say a and b, which is adjacent in G.
2. Both are incident in G say a and b, where a is in $V(G)$ and b is in $E(G)$.

Definition 5 ([11]) The total graph of G is formed from G in the following way. The vertex set of $T(G)$ is the union of vertex set and edge set of G, and a and b are two vertices of $T(G)$ which is adjacent in $T(G)$; it should be satisfied one condition. The conditions are given below.

1. Both are vertices in $V(G)$ say a and b, which is adjacent in G.
2. Both are edges in $E(G)$ say a and b, which is adjacent in G.
3. Both are incident in G say a and b, where a is in $V(G)$ and b is in $E(G)$.

The authors defined a new family of graphs say G^*, and they proved the following lemma in [1].

Definition 6 [1] Let us consider G is any graph. The graph G have n vertices with vertex set $\{v_1, v_2, \cdots, v_n\}$. Then the graph G^* is obtained by adding a set U_i of new vertices of size $|U_i| = n - 1 - d_i$, here d_i denoted as degree of v_i of G , make all the vertices of U_i adjacent to v_i , and add edges arbitrarily between the vertices in U_i. Many graphs G^* can be obtained from one arbitrary graph G with every vertex v_i and have degree $n - 1$, and all other vertices have degree at most $n - 1 - d_i$. The collection of all graphs G^* is denoted by $\mathscr{F}(G)$.

Lemma 1 ([1]) *Let G^* be any graph of $\mathscr{F}(G)$. Then the b-chromatic number of G^* is n.*

2 Main Results

Here, we have to investigate the b-chromatic number of abovementioned standard graphs with replacing G by G^*.

Theorem 1 *Let $G^* \in \mathscr{F}(G)$.Then $b(\mu(G^*)) = n + 1$.*

Proof Let $V(\mu(G^*)) = \{w, v_i \cup U_i^{'} \cup V(G^*)$,where $U_i = u_i^j, 1 \leq i \leq n, 1 \leq j \leq n - 1 - d_i\}$, where $V(G^*)$ is indicated the vertex set of G^* . Clearly the graph $\mu(G^*)$ has $n + 1$ vertices, that $n + 1$ vertices of degree at least n, and hence $m(\mu(G^*)) = n + 1$.Therefore $b(\mu(G^*)) \leq (m(\mu(G^*)) = n + 1$. Now, we define a color map f as follows.

$$f(x) = c(v_i), where\ x = v_i\ or\ v_i^{'} \in V(\mu(G^*))$$

$$f(y) = c(u_i^j), where\ y = u_i^j\ or\ u_i^{j'} \in V(\mu(G^*))$$

$$f(w) = n + 1$$

where f is a color map obtained from Lemma 1 [1] in which we have to use in the same manner. Therefore, we get a proper b-coloring of $\mu(G^*)$ with $n+1$ colors and $b(\mu(G^*)) \geq n + 1$. Thus $b(\mu(G^*)) = n + 1$.

Theorem 2 *Let $G^* \in \mathscr{F}(G)$. Then $b(splt(G^*)) = n$*

Proof Let $V(splt(G^*)) = \left\{\{v_i \cup U_i^{'}\} \cup V(G^*)\right\}$. Clearly we see that the graph $splt(G^*)$ having n vertices of degree at least $n - 1$ and hence $m(splt(G^*)) = n$. Therefore $b(splt(G^*)) \leq m(splt(G^*)) = n$. Now we define a color map g by

$$g(u) = f(u)\ for all\ u \in V(splt(G^*))$$

where f is the color map obtained from the above Theorem 1. Therefore we get a proper b-coloring with n-colors and hence $b(splt(G^*)) \geq n$. Thus $b(splt(G^*)) = n$.

In similar way we have to investigate the shadow graph which also admits the same color map, and hence we obtain the following theorem.

Theorem 3 *Let $G^* \in \mathscr{F}(G)$. Then $b(D_2(G^*)) = n$.*

Now we consider the graph G_e^* formed from G by adding an edge e between u_i^j to u_i^{j+1}, $1 \le i \le n$, $j = 1$ in U_i.

Theorem 4 *Let $G \cong C_n$ be a cycle on n vertices. Then $b(M(G_e^*)) = n + 2$.*

Proof Let $M(V(G_e^*)) = \{v_i, u_i^j \cup y_i, w_i^j, x_i, 1 \le i \le n,\ 1 \le j \le n - 1 - d_i\}$. Clearly the graph $M(G_e^*)$ has $n + 2$ vertices of degree at least $n + 1$ and hence $b(M(G_e^*)) \le m(M(G_e^*)) = n + 2$. Now, we define a color map f as follows.

$$
\begin{aligned}
f(y_i) &= i, 1 \le i \le n \\
f(w_i^1) &= n + 1 \\
f(w_i^2) &= n + 2 \\
f(v_i) &= i + 2, 1 \le i \le n - 2 \\
f(v_{n-2+i}) &= i, i = 1, 2 \\
f(w_i^j) &= \{i + j(mod\ n), 1 \le i \le n, 3 \le j \le n - 1 - d_i\} \\
f(u_i^j) &= \begin{cases} i + 1 & 1 \le i \le n - 1,\ 1 \le j \le n - 1 - d_i \\ 1 & i = n \end{cases} \\
f(x_i) &= n - 2 + i(mod\ n)
\end{aligned}
$$

Therefore we get a proper b-coloring of $M(G_e^*)$ with $n + 2$ colors and $b(M(G_e^*)) \ge n + 2$. Thus $b(M(G_e^*)) = n + 2$. This procedure is explained through the following example (Refer Fig. 1) with $n = 6$.

Theorem 5 *Let $G \cong C_n + \frac{n}{2}K_2$. Then $b(M(G_e^*)) = n + 2$.*

Proof Let $M\left(V(G_e^*)\right) = \left\{\{v_i, u_i^j \cup w_i^j, x_i, 1 \le i \le n,\ 1 \le j \le n - 1 - d_i\} \cup \left\{y_i, 1 \le i \le n + \frac{n}{2}\right\}\right\}$. Clearly the graph $M(G_e^*)$ has $n + 2$ vertices of degree at least $n + 1$ and hence $b(M(G_e^*)) \le m(M(G_e^*)) = n + 2$. Now, we define a color map g as follows.

$$
\begin{aligned}
f(y_i) &= \begin{cases} i & 1 \le i \le n. \\ n + 1, & n + 1 \le i \le n + \frac{n}{2} \end{cases} \\
f(w_i^1) &= n + 2 \\
f(v_i) &= i + 2\ 1 \le i \le n - 2 \\
f(v_{n-2+i}) &= i\ i = 1, 2 \\
f(w_i^j) &= \{i + j + 1(mod\ n)\ 1 \le i \le n, 2 \le j \le n - 1 - d\}
\end{aligned}
$$

Fig. 1 Middle graph of C_{6e}^*

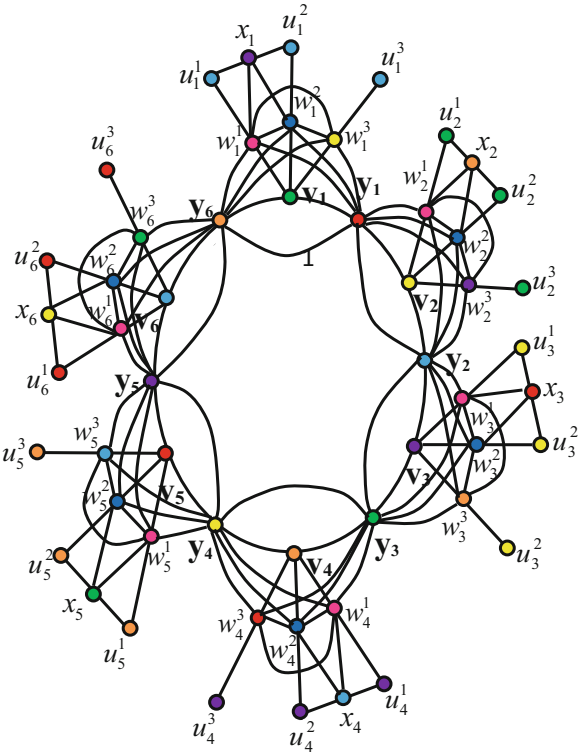

$$f(u_i^j) = \begin{cases} i+1 & 1 \le i \le n-1,\ 1 \le j \le n-1-d_i \\ 1 & i = n \end{cases}$$

$$f(x_i) = n - 2 + i\,(mod\ n)$$

Therefore we get a proper b-coloring of $M(G_e^*)$ with $n+2$ colors and $b(M(G_e^*)) \ge n+2$. Thus $b(M(G_e^*)) = n+2$. This procedure is explained through the following example (Refer Fig. 2) with $n = 6$.

Theorem 6 *Let C_n be a cycle on n vertices. Then $b(T(G_e^*) = 2n-2$*

Proof Let $T\left(V(G_e^*)\right) = \left\{\left\{v_i, u_i^j \cup y_i, w_i^j, x_i\right\}, 1 \le i \le n, 1 \le j \le n-1-d_i\right\}$. Clearly the graph $T(G_e^*)$ has at least $2n-2$ vertices of degree at least $2n-3$ and hence $b(T(G_e^*)) \le m(T(G_e^*)) = 2n-2$. Now, we define a color map $f : V(G_e^*) \longrightarrow [2n-2]$ where $[2n-2] = \{1, 2, \ldots, 2n-2\}$ as follows.

$$f(v_i) = i, 1 \le i \le n$$

$$f(y_i) = n + i, 1 \le i \le n-2$$

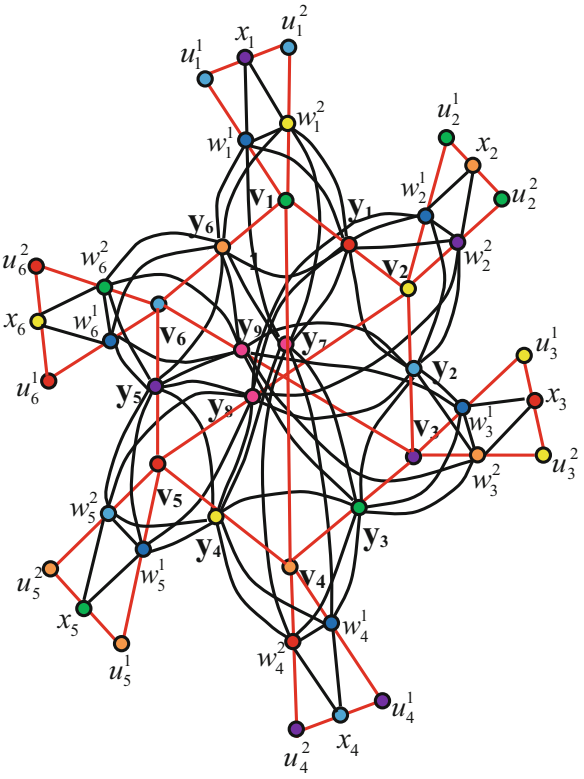

Fig. 2 Middle graph of $(C_6 + 3K_2)$

$$f(y_n) = f(y_{n-2})$$
$$f(y_{n-1}) = f(y_{n+1})$$

Consider

$$N(y_i) = \begin{cases} w_i^j, w_{i+1}^j, v_i, v_{i+1}, y_{i+1}, y_n, i = 1 \\ w_i^j, w_{i+1}^j, v_i, v_{i+1}, y_{i-1}, y_{i+1}, 2 \le i \le n-1 \\ w_i^j, w_1^j, v_1, v_n, y_{i-1}, y_{i+1}, i = n \end{cases}$$

Set

$N(y_i) - v_i, v_{i+1}, y_{i+1}, y_n = S_i$, where $S_i = \{w_i^j, w_{i+1}^j\}, i = 1$

$N(y_i) - v_i, v_{i+1}, y_{i-1}, y_{i+1} = S_i$, where $S_i = \{w_i^j, w_{i+1}^j\}, 2 \le i \le n-1$

$N(y_i) - v_1, v_n, y_1, y_{i-1} = S_i$, where $S_i = \{w_i^j, w_1^j\}, i = n$

Let C_i be the set of $2n$-2 colors.

$$f(S_i) = \begin{cases} C_i - \{f(y_i), f(v_i), f(v_{i+1}), f(y_{i+1}), f(y_n)\}, i = 1 \\ C_i - \{f(y_i), f(v_i), f(v_{i+1}), f(y_{i-1}), f(y_{i+1})\} - \{colored\ w_i^j\}, \\ \qquad 2 \leq i \leq n-1 \end{cases}$$

Consider

$$N(v_i) = \begin{cases} w_i^j, y_i, y_n, v_{i+1}, v_n, i = 1 \\ w_i^j, y_i, y_{i-1}, v_{i+1}, v_{i-1}, 2 \leq i \leq n-1 \\ w_i^j, y_{i-1}, y_i, v_{i-1}, v_1, i = n \end{cases}$$

If each neighbor of v_i receives different colors, then

$$f(u_i^j) = \begin{cases} C_i - \{f(N(v_i)), f(v_i)\}, 1 \leq i \leq n, 1 \leq j \leq n-4 \\ f(y_i), j = n-3 \end{cases}$$

If exactly two neighbors of v_i receive same color, then
$f(u_i^j) = C_i - \{f(N(v_i)), f(v_i)\}, 1 \leq i \leq n, 1 \leq j \leq n-3$
$f(x_i) = i, 1 \leq i \leq n.$

Therefore we get a proper b-coloring of $T(G_e^*)$ with $2n-2$ colors and $b(T(G_e^*)) \geq 2n-2$. Thus $b(T(G_e^*)) = 2n-2$.

3 Conclusion

We feel difficult to find out the b-chromatic number of abovementioned standard graphs for G^* with respect to other families of base graph G, which is still open.

References

1. Jeeva, A., Selvakumar, R., Nalliah, M.: Families of greater achromatic graphs. Indian Journal of Mathematics **59**(2) (2017) 255–261
2. Irving, R.W., Manlove, D.F.: The b-chromatic number of a graph. Discrete Applied Mathematics **91**(1–3) (1999) 127–141
3. Havet, F., Sales, C.L., Sampaio, L.: b-coloring of tight graphs. Discrete Applied Mathematics **160**(18) (2012) 2709–2715
4. Amine El Sahili, A., Kouider, M.: About b-colouring of regular graphs. Utilitas Mathematica **80** (11 2009)
5. Kouider, M., Mahéo, M.: Some bounds for the b-chromatic number of a graph. Discrete Mathematics **256**(1–2) (2002) 267–277
6. Kouider, M., Zaker, M.: Bounds for the b-chromatic number of some families of graphs. Discrete Mathematics **306**(7) (2006) 617–623

7. Lisna, P., Sunitha, M.: The b-chromatic number of mycielskian of some graphs. International Journal of Convergence Computing **2**(1) (2016) 23–40
8. Sampathkumar, E., Walikar, H.: On splitting graph of a graph, j. Karnatak Univ. Sci **25**(13) (1980) 13–16
9. Thilagavathy, K., Santha, A.: The achromatic and b-chromatic number of shadow graph of some graphs. Asian Journal of Research in Social Sciences and Humanities **7**(3) (2017) 838–843
10. Vaidya, S.K., Shukla, M.S.: b-chromatic number of splitting graph of wheel. Mathematical Combinatorics **2** (2015) 69–76
11. Vivin, J.V., Venkatachalam, M.: A note on b-coloring of fan graphs. Journal of Discrete Mathematical Sciences and Cryptography **17**(5–6) (2014) 443–448
12. Vivin, J.V., Vekatachalam, M.: On b-chromatic number of sun let graph and wheel graph families. Journal of the Egyptian Mathematical Society **23**(2) (2015) 215–218

Encode-then-Encrypt: A Novel Framework for Reliable and Secure Communication

Rajrupa Singh, C. Pavan Kumar, and R. Selvakumar

Abstract Achieving a reliable and secure communication is the major challenge in the context of data communication and storage. In this paper, *Encode-then-Encrypt* framework is defined using linear error correcting codes and elliptic curves to address these challenges as a single solution rather than addressing them separately. The working of the proposed framework is explained in detail by taking Reed-Solomon codes (with a set of encoding and decoding algorithms) and elliptic curves of characteristic 2 (with a set of encryption and decryption algorithms). We have outlined the advantages of using such elliptic curves and error correcting codes over any other cryptosystem defined in the existing literature. The proposed framework can be implemented as a part of any real-time communication system to ensure reliability and security.

Keywords Encode · Encrypt · Reed-Solomon Codes · Elliptic Curve Cryptography

Mathematics Subject Classification (2010) 14G50

R. Singh
School of Advanced Sciences (SAS), Vellore Institute of Technology, Vellore, India
e-mail: rajrupa.singh@vit.ac.in

R. Selvakumar (✉)
Department of Mathematics, Vellore Institute of Technology, Vellore, India
e-mail: rselvakumar@vit.ac.in

C. Pavan Kumar
School of Computer Science and Engineering (SCOPE), Vellore Institute of Technology, Vellore, India
e-mail: pavankumarc.2013@vit.ac.in

B. Rushi Kumar et al. (eds.), *Applied Mathematics and Scientific Computing*,
Trends in Mathematics, https://doi.org/10.1007/978-3-030-01123-9_58

1 Introduction

Reliability and security aspects have become an integral part of information transmission. Both aspects have received significant interest from researchers in the recent past. Reliability is largely achieved by the use of coding theory techniques and security by the cryptographic techniques. Proper combination of techniques of coding theory and cryptography will make it possible to achieve the goals of reliable and secure communication even at the higher layers of communication stack other than physical layer. Also, these two challenges are addressed separately in the literature rather than addressing both reliability and security issues jointly or as a single entity.

In a cryptographic protocol, it is the expectation of a recipient that a message has not been modified during the transmission in anyway whereas in case of coding theory protocols, the original message can be reconstructed from received message correcting errors. Reconstruction of original message from the received ones is achieved by adding redundancy to the message. Added redundancy is also termed as parity. There are many applications where both information security and error correction capabilities are required (e.g., in networks, secure packet delivery, secure document management, secure biometrics storage etc., to name a few). In such cases, a sequential execution of encoding and encryption operations has to be performed.

In the late 1980s, McEliece used Goppa codes to construct a public key cryptosystem which was called McEliece system [1]. Such notion can be broadly called as cryptocoding [2]. Similarly, Kak [3] proposed a novel cryptocoding scheme based on arithmetic D-sequences, which are decimal expansions of the fractions. Further, Rao [4] proposed the private key variant of McEliece public key cryptosystem.

Thereafter, cryptography and channel coding techniques were combined together which were separate disciplines originally. The National Science Foundation (NSF) in 1997 established a special working group which emphasized the importance of joint encryption and error correction technique but did not give a specific embodiment [5].

In this paper, we propose a secure communication framework based on linear error correcting codes and elliptic curves. The reason behind choosing these two techniques is that they both involve the elements of a finite field and the elliptic curves can be easily generated for encryption without changing the field. It will increase efficiency, especially in practical realizations.

The paper is organized as follows. In Sect. 2 the preliminaries required for proposing the *Encode-then-Encrypt* framework is discussed. In Sect. 3 the outline of proposed *Encode-then-Encrypt* scheme based on linear error correcting codes and elliptic curves is proposed. In Sect. 4, realization of proposed encode-then-encipher scheme is demonstrated using Reed-Solomon codes and elliptic curve of characteristic greater than 3. In particular the generating of Elliptic curve over the same field as that of Reed-Solomon codes along with the decoder to output the original message. Section 5 deals with the conclusion.

2 Preliminaries

Preliminaries required to define the proposed cryptosystem are discussed in this section.

2.1 Linear Error Correcting Codes

A message m of length k is encoded into a codeword of length n. This encoding $Enco$ can be defined as a one-to-one map or a function as [6], $Enco : \Sigma^k \rightarrow \Sigma^n$ which can also be written equivalently as $M \rightarrow \Sigma^n$, where Σ is symbol from a finite alphabet. M is message space consisting of all messages m that have to be encoded.

Similarly, decoding function $Deco$ is an onto map defined as follows in the absence of channel noise. $Deco : \Sigma^n \rightarrow \Sigma^k$. Challenge of a good decoding function is to successfully recover original message from the received codeword.

2.2 Galois Field

A basic result from number theory is that if p is prime, then the set of integers modulo p is a field denoted by $\mathbb{Z}_p$. However, that is true if and only if p is prime. It has been proved that for any prime p and any natural number r there exists a unique finite field of order p^r, known as Galois field [7]. These fields can be constructed with the help of $\mathbb{Z}_p[x]$, the set of polynomials with coefficients in $\mathbb{Z}_p$. Also, it can be shown that any finite field of size p^r is isomorphic to a Galois field.

2.3 Elliptic Curve Cryptography over F_{2^n}

A cubic equation $P(x)$ of the form

$$y^2 + xy = x^3 + ax^2 + b \tag{1}$$

with coefficients a and b from the Galois field $\mathbb{F}_{2^n}$ and $b \neq 0$ forms an elliptic curve [7, 8].

A set of points x and y from $\mathbb{F}_{2^n}$ is said to be on the curve $P(x)$ if it satisfies the Eq. (1). Also, the "point at infinity" denoted by O is also assumed to be over the elliptic curve.

The set of points that satisfies the elliptic curve E over F_{2^n} given in Eq. (1) are

$$E_{\mathbb{F}_{2^n}}(a, b) = \{(x, y) | (x, y) \in \mathbb{F}_{2^n}^2\} \cup \{O\}$$

3 Outline of the System

In this section we define set of five sequential algorithms of the proposed framework to carry out the'encode-then-encrypt' scheme. General outline of the proposed framework is given in Fig. 1 and Table 1 gives the notations used in this paper.

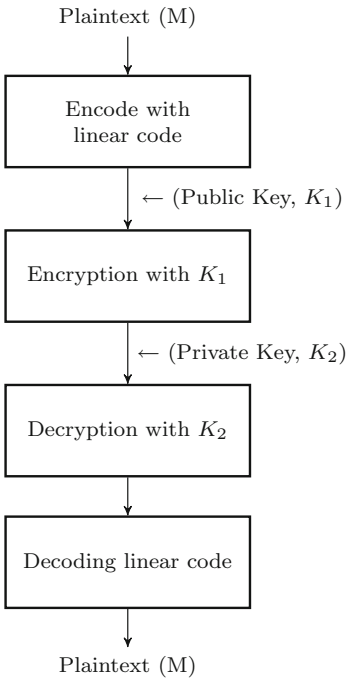

Fig. 1 Encode-then-encrypt cryptosystem

Table 1 Notations

Symbols	Meanings
S	Sender
R	Receiver
k	Length of message m
C	Codeword
$E_{\mathbb{F}_{2^n}}$	Elliptic curve
PK_S	Set of public keys of sender S
PK_R	Set of public keys of receiver R
PR_S	Private key for the sender S
PR_R	Private key for the receiver R
SPB_S	Shared public key from sender S to receiver R
SPB_R	Shared public key from receiver R to sender S
BP	Base point of elliptic curve

3.1 System Initialization and Key Generation

Before we get into the working of the individual algorithms step-by-step, we will make the following assumptions and declarations of the parameters that we require in order to define our cryptosystem:

1. Message m is assumed to be of finite length k and the length of codeword C is n.
2. A base point BP is chosen from the points of the Elliptic Curve $E_{\mathbb{F}_{2^n}}$ such that it is a generator point and also it's order is equal to the order of the underlying field. This point is kept as public.
3. Both the sender and receiver will randomly choose their respective private keys PR_S and PR_R.

System initialization and key generation will be performed in two phases. In initialization phase, sender S will compute its shared public key SPK_S from its secret key PR_S and base point (BP) of elliptic curve E. Similarly, receiver R will compute shared public key SPK_R from its secret key PR_R and base point BP of elliptic curve E.

In the key generation phase, sender will generate set of public keys $PK_S = \{pk_1, pk_2\}$ from its private key PR_S and the shared public key SPK_R of receiver R. Similarly, the receiver R will generate public keys $PK_R = \{pk_1, pk_2\}$ from its private key PR_R and from shared public key SPK_S of sender S.

In Table 2 detailed computation of both initialization phase and key generation phase are provided. Public keys PK_S and PK_R computed, respectively, at both sender S and R are the same. This is analogous to Diffie-Hellman key exchange algorithm [9].

Table 2 Initialization and key generation phase

Sender S	Receiver R
Public base point BP: (b_1, b_2) of elliptic curve $E_{\mathbb{F}_{2^n}}$	
Initialization phase	*Initialization phase*
PR_S: Secret Key	PR_R: Secret Key
$SPK_S = PR_S \times BP$	$SPK_R = PR_R \times BP$
$= PR_S \times (b_1, b_2)$	$= PR_R \times (b_1, b_2)$
$= PR_S b_1, PR_S b_2$	$= PR_R b_1, PR_R b_2$
SPK_S and SPK_R will be shared by sender and receiver	
Key generation phase	*Key generation phase*
$PK_S = PR_S \times SPK_R$	$PK_R = PR_R \times SPK_S$
$= PR_S \times (PR_R b_1, PR_R b_2)$	$= PR_R \times (PR_S b_1, PR_S b_2)$
$= (PR_S PR_R b_1, PR_S PR_R b_2)$	$= PR_R PR_S b_1, PR_R PR_S b_2$
$=(pk_1, pk_2)$	$=(pk_1, pk_2)$
Public keys PK_S and PK_R computed at sender and receiver are same	

3.2 Encode

Encode algorithm $Enco()$ will map the messages $m \in M$ of length k to the space of messages (also called as codeword) of same symbol of length n. The algorithm $Enco(m, k)$ will take message m of length k as input and produce output codeword C of length n by adding r ($r = n - k$) number of redundant or parity bits. It should be noted that while mapping (or while encoding) no information is lost. The pseudocode of $Enco()$ is given in Algorithm 1.

3.3 Encrypt

Algorithm $Encr()$ will take the codeword C and the public key PK_S generated by $KeyGen()$ as input and produce output ciphertext or the encrypted text E. The pseudocode for $Encr()$ is given in Algorithm 2.

Algorithm 1 $Enco()$

Input: message m of length k
Output: codeword C of length n
1: $Enco(m_0, \ldots, m_k) \rightarrow (m_0, \ldots, m_{k+r})$
2: Return codeword C

Algorithm 2 $Encr()$

Input: codeword C of length n
Output: encrypted text E of length n
1: $Encr(m_0, \ldots, m_{k+r}) \rightarrow (e_0, \ldots, e_{k+r})$
2: Return ciphertext E

3.4 Decrypt

Algorithm $Decr()$ will take the ciphertext E as input and produces codeword c of length n as output. The pseudocode for $Decr()$ is given in Algorithm 3.

3.5 Decode

Algorithm $Deco()$ will take the codeword C as input and decodes it to message m of length k. The pseudocode for $Deco()$ is given in Algorithm 4.

Algorithm 3 $Decr()$

Input: ciphertext E of length n
Output: codeword C of length n
1: $Decr(e_0, \ldots, m_k) \rightarrow (m_0, \ldots m_{k+r})$
2: Return codeword C

Algorithm 4 $Deco()$

Input: codeword C of length n
Output: message m of length k
1: $Deco(m_0, \ldots m_{k+r}) \rightarrow (m_0, \ldots, m_k)$
2: Return message m

4 An Example of the Proposed Cryptosystem

In this section, we demonstrate the proposed *Encode-then-Encrypt* scheme with an example of (7, 5) Reed-Solomon (RS) code and a nonsingular elliptic curve of characteristic 2 over a finite field $E_{\mathbb{F}_{2^3}}(g^3, 1)$.

As in any other error-correcting codes, RS codes are represented by parameters n and k where n is the length of codeword and k is the length of message m. r is the number of bytes required for error correction (also termed as forward error correction (FEC) bytes) and $d = n - k$. The maximum codeword length n is given by $n = 2^{s-1}$ where s is the symbol size in bytes. Unlike other error correcting codes, RS codes encode the message word to codeword as a group and not bit by bit. The group of message word to be encoded are also called as digits.

Here we are using RS-codeword with following specifications: RS(7, 5), $s = 3$, $t = 2$, i.e., $five$ symbols are data and two symbols are used for error correction. As there are 2-FEC symbols, RS(7, 5) can only identify and correct one error symbol for each codeword.

4.1 Initialization and Key Generation

In the cubic equation (1), we substitute the coefficients $a = g^3$ and $b = 1$ from the field to obtain elliptic curve equation. The resulting elliptic curve equation will be

$$y^2 + xy = x^3 + g^3x^2 + 1 \tag{2}$$

The points that satisfies the elliptic curve Eq. (2) are as follows:

$E_{\mathbb{F}_{2^3}}(g^3, 1) = \{(0, 1),\ (g, g^2),\ (g, g^4),\ (g^2, 1),\ (g^2, g^6),\ (g^3, g^2),\ (g^3, g^5),\ (g^4, g^4),\ (g^5, 1),\ (g^5, g^4),\ (g^6, g),\ (g^6, g^5) \cup (O)\}$

The order of the group is $O(E_{2^3}(g^3, 1)) = 13$ which is a prime order and according to Lagrange's theorem all the non-zero elements of the group will be the generator elements. For a base point BP we can select any non-zero element say $(g^2, 1)$ and compute the public keys as in Table 3.

4.2 Encode

For encoding a message using RS encoder, three polynomials are used; this will constitute the $Enco()$ (Algorithm 1) defined in the previous section. Polynomials are used to generate the codewords, namely, Galois field polynomial, generator polynomial and encoding polynomial.

Table 3 Initialization and key generation phase

Sender S	Receiver R
Public base point BP: $(g^2, 1)$ of elliptic curve $E_{2^3}(g^3, 1)$	
Initialization phase PR_S: $3 < O(E_{2^3}(g^3, 1))$ $SPK_S = 3 \times (g^2, 1)$ $= g^3 \times (g^2, 1)$ $= (g^5, g^3)$	*Initialization phase* PR_R: $4 < O(E_{2^3}(g^3, 1))$ $SPK_R = 4 \times (g^2, 1)$ $= g^2 \times (g^2, 1)$ $= (g^4, g^2)$
SPK_S and SPK_R will be shared by sender and receiver	
Key generation phase $PK_S = g^3 \times (g^4, g^2)$ $= (g^7, g^5)$ $= (g^0, g^5)$ $=(1, g^5)$	*Key generation phase* $PK_R = g^2 \times (g^5, g^3)$ $= (g^7, g^5)$ $= (g^0, g^5)$ $=(1, g^5)$
Public keys PK_S and PK_R computed at sender and receiver are same	

Table 4 Elements of $GF(2^3)$ from $p(x) = x^3 + x + 1$

0	a^0	a^1	a^2	a^3	a^4	a^5	a^6
0	$x^0 = x^7$	x^1	x^2	x^3	x^4	x^5	x^6
000	001	010	100	011	110	111	101
0	1	2	4	3	6	7	5

4.2.1 Galois Field (GF) Polynomial

This polynomial is used to generate the finite field(Galois field). The irreducible polynomial that cannot be reduced further acts equivalent to a prime number and hence generates the elements of the field.

In this example, we are taking $s = 3$, i.e., each message point is represented by 3-bit symbol. So, the appropriate Galois field will be $GF(2^3)$. The irreducible polynomial over $GF(2^3)$ can be taken as $P(x) = x^3 + x + 1$ or $x^3 + x^2 + 1$ to generate field of eight elements of each 3-bit symbol as given in Table 4. In this example, we consider $x^3 + x + 1$ to generate the Galois field.

The decimal equivalent for the irreducible polynomial $x^3 + x + 1$ will be $P(x) = 1x^3 + 0x^2 + 1x + 1 = 1011_2 = 11_{10}$.

4.2.2 Generator Polynomial

The generator polynomial is used to generate the encoding polynomial. It is of the form $G(x) = (x - a^1)(x - a^2)(x - a^3) \ldots (x - a^{2t})$ where $a^1, a^2, a^3, \ldots, a^{2t}$ are the values of a in the Galois Field and $2t$ determines how many FEC symbols are generated.

4.2.3 Encoding Polynomial

The role of an encoding polynomial is to generate the RS codewords by using the factors from the generator polynomial. Here in this example, we have RS(7,5) with $s = 3$, $t = 2$, that means 2 FEC symbols are used to identify and correct codewords with 1-error symbol. The factors $(x - a^1)$ and $(x - a^2)$ are taken out of the generator polynomial irrespective of position of its occurrence in the codeword.

$$G(x) = (x - a^1)(x - a^2) \tag{3}$$

From the properties of a finite field, adding and subtracting of elements are same in the field $GF(2^n)$ field, hence $(x - a^1) = (x + a^1)$ and $(x - a^2) = (x + a^2)$. Hence the encoding polynomial in Eq. (3) can be rewritten as

$$G(x) = (x + a^1)(x + a^2) \tag{4}$$

In $GF(2^3)$ field we have $a^1 = 2$ and $a^2 = 4$ from the Table 4. By substituting the values in Eq. (4), we get $G(x) = (x+2)(x+4) = x^2+6x+3$. (As $x^3+x+1 = 11_{10}$(in decimal)). Hence, $8 \equiv 3(\text{mod}11)$.

Thus the obtained encoding polynomial that is used to generate RS(7,5) codeword is

$$G(x) = x^2 + 6x + 3 \tag{5}$$

Also, $G(x)$ can be represented as 163. Here we use the RS(7,5) code with $s = 3$ and $t = 2$, all together 7-symbols contained with 5-data symbols and 2-FEC symbols in it. In order to append the 2-FEC symbols with the 5-data symbols, it is required to multiply the bit string by x^2 so that the message is shifted to the left by two places.

A message 12345 to be encoded is represented by its equivalent message polynomial as $(1x^4 + 2x^3 + 3x^2 + 4x + 5)$. To shift it by two symbols to append the error correction symbol, message polynomial has to be multiplied by x^2, such that $M(x) = x^6 + 2x^5 + 3x^4 + 4x^3 + 5x^2 + 0x + 0$. By dividing $M(x)$ with $G(x)$, FEC symbols are obtained, where $G(x)$ represents the encoding polynomial $x^2 + 6x + 3$. We get remainder as 63. Adding the remainder 63 to $M(x)$, the codeword $C(x)$ will be obtained. $C(x) = 1x^6 + 2x^5 + 3x^4 + 4x^3 + 5x^2 + 6x + 3$ or $C(x) = 00101001110010111 0011$. This is systematic form of encoding as the error correction part is embedded in the codeword with message symbols appearing first followed by FEC symbols.

4.3 Encrypt

Encoded word or codeword will be encrypted using elliptic curve, this will constitute the $Encr()$ (Algorithm 2) defined in the previous section. Since we are

working on the field $GF(2^3)$, the generating polynomial is g^3+g+1. The elements of the field $GF(2^3)$ will be $GF(2^3) = \{0, 1, g^1, g^2, g^3, g^4, g^5, g^6\}$

Since the codeword is 00101001110010111001 1 we are mapping each 3-bit symbol from the codeword to a point on the elliptic curve which will be declared before encrypting the message.

We can choose any method to map the codeword symbols on the points of the elliptic curve. Here, we are taking the XOR value of coordinate of points of the curve, i.e., for a point (g^6, g^5) on the curve, the XOR value will be $g = 010$. The 3-bit symbol of the codeword that is equivalent to this XOR-ed value of point on elliptic curve will be mapped. Also, there may be possibility that more than two points on the curve can have the same XOR value, in that case we can select any one of them randomly. For example, the point (g, g^2) corresponds to the codeword symbol 110, also $(g^5, 1) = g^5 + 1 = 110$. In such cases we can select either (g, g^2) or $(g^5, 1)$. But both sender and receiver should mutually agree upon such selection of mapping table.

Here is the mapping table for the codeword that is mutually agreed by both the sender and the receiver: $(001) \rightarrow (0, 1), (010) \rightarrow (g^6, g^5), (011) \rightarrow (g^3, g^2), (100) \rightarrow (g, g^4), (101) \rightarrow (g^2, 1), (110) \rightarrow (g^5, 1), (011) \rightarrow (g^3, g^5)$.

Mapping process from Codewords to corresponding points on the curve and subsequent encrypted points (C_1, C_2) are given in Table 5. Points C_1 and C_2 are computed as $C_1 = m_2k_1+m_1$ and $C_2 = m_2+m_2k_1k_2+m_1k_2$. Outline of encryption process is given in Fig. 2 and calculation of points C_1 and C_2, i.e., encrypted points is given in Table 5.

Table 5 Encryption mapping table

001	010	011	100	101	110	011
(0,1)	(g^6, g^5)	(g^3, g^2)	(g, g^4)	$(g^2, 1)$	$(g^5, 1)$	(g^3, g^5)
$C_1 = m_2k_1 + m_1$ and $C_2 = m_2 + m_2k_1k_2 + m_1k_2$						
$(1, g^4)$	(g, g)	(g^5, g^5)	(g^2, g^5)	(g^6, g^5)	(g^4, g^6)	(g^2, g^4)

Fig. 2 Encryption process

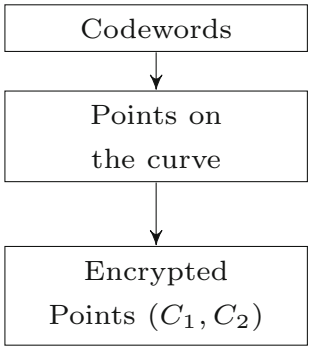

Fig. 3 Encryption process

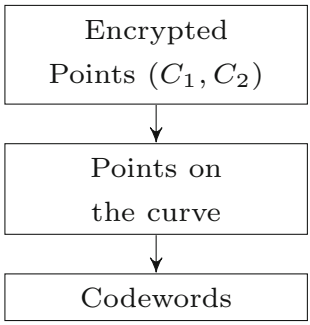

Table 6 Decryption mapping table

$(1, g^4)$	(g, g)	(g^5, g^5)	(g^2, g^5)	(g^6, g^5)	(g^4, g^6)	(g^2, g^4)
$m_1 = C_2 + k_2 C_1$ and $m_2 = C_1 + m_2 k_1$						
(0,1)	(g^6, g^5)	(g^3, g^2)	(g, g^4)	$(g^2, 1)$	$(g^5, 1)$	(g^3, g^5)
001	010	011	100	101	110	011

4.4 Decryption

Decryption process will decrypt the encrypted points on the curve C_1 and C_2 to the points on the elliptic curve. Decryption process and corresponding points calculation from encrypted points are given in Fig. 3 and Table 6 respectively.

4.5 Decode

Once the codeword is obtained, we perform the decoding operation on it to get back the original message. We introduce a small error in the codeword so that we can prove the error detection and correction part in our cryptosystem. The decoding process works as follows, for a detailed account on decoding process readers are referred to [10]

1. creating a polynomial syndrome to quantify the error for syndrome calculation
2. defining an error detection polynomial using Euclidean algorithm
3. locating the coefficient of the error symbol using Chien Search Algorithm
4. correction of the error symbol using Forney Algorithm

In the earlier section, we considered the received codeword as $R(x) = 1x^6 + 2x^5+3x^4+4x^3+5x^2+6x+3$. Now we introduce an error into the received codeword during the transmission over the channel $E(x) = 3x^3$ i.e. $4x^3$ changes to $7x^3$. So the received codeword with error becomes $R(x) = 1x^6+2x^5+3x^4+7x^3+5x^2+6x+3$. If we divide $R(x)$ by the encoding polynomial, i.e., $G(x) = x^2 + 6x + 3$, the remainder is $3x+3$. This shows the indication of presence of an error in the received codeword.

4.5.1 Syndrome Calculation

The syndrome calculation is done by the receiver part. The values of the finite field a is substituted into the received codeword to find the roots of R(x). The roots of the codeword are used to create a syndrome polynomial. Since we have 3-bit symbol message, so we will get three roots for the codeword, $a^0 = 1$, $a^1 = 2$, and $a^2 = 4$, and hence three syndromes S_0, S_1, and S_2, respectively.

S_0 is calculated by substituting a^0 in each term of $R(x)$ and XOR-ing every element. All final values are taken modulo 11_{10}.
$x^6 = a^0 = 001$, $2x^5 = 2(a^0)^5 = 2$, $3x^4 = 3(a^0)^5 = 3$, $7x^3 = 7(a^0)^3 = 7$, $5x^2 = 5(a^0)^2 = 5$, $6x = 6(a^0) = 6$, 3. Taking XOR of all the elements, $S_0 = 7$
S_1 is calculated by substituting a^1 in each term of $R(x)$ and XOR-ing every element. All final values are taken modulo 11_10.
$x^6 = a^1 = 2$, $2x^5 = 2(a^1)^5 = 1$, $3x^4 = 3(a^1)^5 = 6$, $7x^3 = 7(a^1)^3 = 0$, $5x^2 = 5(a^1)^2 = 6$, $6x = 6(a^1) = 5$, 3. Taking XOR of all the elements, $S_1 = 5$
S_2 is calculated by substituting a^2 in each term of $R(x)$ and XOR-ing every element. All final values are taken modulo 11_{10}.
$x^6 = a^2 = 1$, $2x^5 = 2(a^2)^5 = 4$, $3x^4 = 3(a^2)^5 = 5$, $7x^3 = 7(a^2)^3 = 0$, $5x^2 = 5(a^2)^2 = 3$, $6x = 6(a^2) = 3$, 3. Taking XOR of all the elements, $S_2 = 4$.
Thus, the syndrome polynomial for $R(x)$ is defined by the syndromes S_0, S_2 and S_3 as $S(x) = 4x^2 + 5x + 7$.

4.5.2 Error Detection Polynomial Using Euclidean Algorithm

Here we are using Euclidean algorithm to find a common divisor for the syndrome polynomial $S(x)$ and the finite field polynomial x^3. The quotient of the division is denoted as $\Delta(x)$ that locates the exponent of $R(x)$ at which error is located and the remainder of the division is denoted as $\Omega(x)$ that determines the magnitude of the error.

On using Euclidean algorithm for the polynomials $(x^3, 4x^2 + 5x + 7)$, we get $\Delta(x) = 7x + 4$ and $\Omega(x) = x + 1$.

4.5.3 Chien Search Algorithm for Locating the Coefficient

Here we substitute the inverse of $a^n x^n$ i.e. $a^{-n}x^{-n}$ into the error locator polynomial $\Delta(x) = 7x + 4$ for each value of a. The exponent location that returns a values of 0 is the location of the error. As $S(x)$ contains the error information of the codeword, $R(x)$ and $\Delta(x)$ are derived using $S(x)$. Thus, the coefficient that is responsible for the error gets canceled out and returns 0, and other coefficient returns a non-zero value follows:

$\Delta(x^{-6})$=$7(a^{-6} + 4)$=$7a^1 + 4 = 5 + 4 = 1$
$\Delta(x^{-5})$=$7(a^{-5} + 4)$=$7a^2 + 4 = 1 + 4 = 5$
$\Delta(x^{-4})$=$7(a^{-4} + 4)$=$7a^3 + 4 = 2 + 4 = 6$

$\Delta(x^{-3})$=7$(a^{-3}+4)$=7$a^4+4=4+4=0$
$\Delta(x^{-2})$=7$(a^{-2}+4)$=7$a^5+4=3+4=7$
$\Delta(x^{-1})$=7$(a^{-1}+4)$=7$a^6+4=6+4=2$
$\Delta(x^{-0})$=7$(a^{-0}+4)$=7$a^0+4=7+4=3$

Thus, we get 0 for the coefficient of x^3, and it can be concluded that the error in $R(x)$ is located to the position x^3.

4.5.4 Error Correction of the Magnitude Using Forney Algorithm

Till now we have located the error position, i.e., it is located to the coefficient of x^3; here we will define the magnitude of the error by how much it differs the actual value in $R(x)$ using the $\Omega(x)$ defined above.

Forney Algorithm is of the form

$$e_j = x_j \frac{\Omega(X^{-1})}{\Delta(X^{-1})}$$

where j is the position of the error in the $R(x)$ codeword. $\Delta(X) = 7X + 4$ even powers of x are deleted and dividing by x gives 7.

$e_j = a^3 \frac{(a^{-3}+1)}{7} = a^3 \frac{(a^4+1)}{7} = 3\frac{6+1}{7} = \frac{3.7}{7} = 3.$

Magnitude of the error is 3. Therefore the corrected error is 7(111) XOR 3(011) = 4(100). So the corrected codeword $R(x) = x^6 + 2x^5 + 3x^4 + 4x^3 + 5x^2 + 6x + 3$.

Thus, the proposed framework provides reliability by means of correcting errors that appears during communication and also provides security so that only authorized users (with keys) can get access to encrypted data.

5 Conclusion

A single *Encode-then-Encrypt* framework is proposed in this paper. Initially general framework is provided that can use any linear error correcting codes and elliptic curves. Later, the proposed framework is explained in detail by selecting RS codes and cryptographically strong elliptic curves of order 2. We have demonstrated that both reliability and security issues arising in the context of communication and storage are addressed by our proposed framework.

References

1. McEliece, R.: A public-key cryptosystem based on algebraic coding tehory. DSN Progress Report (1978) 42–44
2. Gligoroski, D., Knapskog, S.J., Andova, S.: Cryptcoding-encryption and error-correction coding in a single step. In: Security and Management. (2006) 145–151

3. Kak, S.C.: Joint encryption and error-correction coding. In: Security and Privacy, 1983 IEEE Symposium on, IEEE (1983) 55–55
4. Rao, T.: Joint encryption and error correction schemes. In: ACM SIGARCH Computer Architecture News. Volume 12., ACM (1984) 240–241
5. National Science Foundation: Report of the working group on cryptology and coding theory, https://www.nsf.gov/pubs/1998/nsf9814/nsf9814.htm (1997)
6. Sudan, M.: Coding theory: tutorial amp; survey. In: Proceedings 2001 IEEE International Conference on Cluster Computing. (Oct 2001) 36–53
7. Koblitz, N.: A course in number theory and cryptography. Volume 114. Springer Science & Business Media (1994)
8. Stallings, W.: Cryptography and network security: principles and practices. Pearson Education India (2006)
9. Bos, J.W., Halderman, J.A., Heninger, N., Moore, J., Naehrig, M., Wustrow, E.: Elliptic curve cryptography in practice. In: International Conference on Financial Cryptography and Data Security, Springer (2014) 157–175
10. Moon, T.K.: Error correction coding: mathematical methods and algorithms. (2005)

New Bounds of Induced Acyclic Graphoidal Decomposition Number of a Graph

Mayamma Joseph and I. Sahul Hamid

Abstract An induced acyclic graphoidal decomposition (*IAGD*) of a graph G is a collection ψ of nontrivial induced paths in G such that every edge of G lies in exactly one path of ψ and no two paths in ψ have a common internal vertex. The minimum cardinality of an *IAGD* of G is called the induced acyclic graphoidal decomposition number denoted by $\eta_{ia}(G)$. In this paper we present bounds for $\eta_{ia}(G)$ in terms of cut vertices and simplicial vertices of G.

1 Introduction

The graphs considered here are connected, simple, nontrivial, finite, and undirected. The order and size of a graph $G = (V, E)$ are denoted by n and m, respectively. For terms not defined here, we refer to [11].

A *decomposition* of a graph G is a collection ψ of its subgraphs such that every edge of G lies in exactly one member of ψ. A *path* P in a graph G is a sequence $(v_1, v_2, \ldots, v_k)$ of distinct vertices such that the vertices v_i and v_{i+1} are adjacent for each $i = 1, 2, \ldots, (k-1)$. Here we refer to P as a $v_1 - v_k$ path. The vertices v_1 and v_k are called the end vertices, and all the remaining vertices are called *internal vertices* of P. A *cycle* is a sequence $(v_1, v_2, \ldots, v_k, v_1)$ of distinct vertices such that the vertices v_i and v_{i+1} are adjacent for each $i = 1, 2, \ldots, (k-1)$ and v_k is adjacent to v_1. A cycle is also called a *closed path*.

Decomposition of graphs into paths/cycles is a problem that has caught the attention of several researchers because of its theoretical and practical significance. The pioneering works in *path decomposition* can be seen in [5, 6] and [10].

M. Joseph (✉)
Department of Mathematics, CHRIST (Deemed to be University), Bangalore, India
e-mail: mayamma.joseph@christuniversity.in

I. Sahul Hamid
Department of Mathematics, The Madura College, Madurai, India
e-mail: sahulhamid@maduracollege.edu.in

B. Rushi Kumar et al. (eds.), *Applied Mathematics and Scientific Computing*,
Trends in Mathematics, https://doi.org/10.1007/978-3-030-01123-9_59

Graphoidal decomposition introduced by Acharya and Sampathkumar [1] is a type of path decomposition defined as follows.

Definition 1.1 ([1]) A graphoidal decomposition (GD) of a graph G is a collection ψ of nontrivial paths and cycles of G such that:

(i) Every vertex of G is an internal vertex of at most one member of ψ
(ii) Every edge of G is in exactly one member of ψ.

Several parameters related to *GD* were later found out. Some of them can be seen in [2, 3, 7] and [8].

An *induced path* in a graph G is a path $P = (v_1, v_2, \ldots, v_k)$ such that there exists no edge of G that connects two nonadjacent vertices of P. In other words, an induced path is a *chordless path*, where by the term *chord of a path* P, we mean an edge between two nonadjacent vertices of P. The study of induced paths in a graph assume an importance because of its relevance in the field of information networks. Although there are some studies on induced path decompositions of a graph, several aspects of induced path decompositions are yet to be explored and investigated. In this paper an attempt is made to extend the study of *induced acyclic graphoidal decomposition* introduced by Arumugam [2].

2 Induced Acyclic Graphoidal Decomposition Number

Acharya and Sampathkumar[1] defined the graphoidal decomposition number of a graph as follows:

Definition 2.1 Given a graph G, the minimum cardinality of a GD is called the graphoidal decomposition number of G and is denoted by $\eta(G)$.

As a variation of *GD* of a graph G, Arumugam [2] defined the concept of induced acyclic graphoidal decomposition and the related parameter of induced acyclic graphoidal decomposition number as follows.

Definition 2.2 ([2]) An induced acyclic graphoidal decomposition (IAGD) of a graph G is a graphoidal decomposition ψ in which every member of ψ is an induced path. The minimum cardinality of an IAGD of G is called the induced acyclic graphoidal decomposition number of G and is denoted by $\eta_{ia}(G)$ or η_{ia}.

For the graph G given in Fig. 1, of the three induced acyclic graphoidal decompositions ψ_1, ψ_2, and ψ_3 of different cardinalities, two are presented in Fig. 2, each induced path in these collections being depicted by different types of edges.

$$\psi_1 = \{(b, a, d), (b, c, d), (e, f, g), (b, e), (d, g)\}$$
$$\psi_2 = \{(e, b, a, d, g), (b, c, d), (e, f, g)\}$$
$$\psi_3 = \{(b, a, d, g, f), (d, c, b, e, f)\}$$

Fig. 1 Graph G

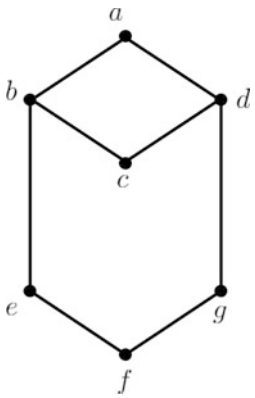

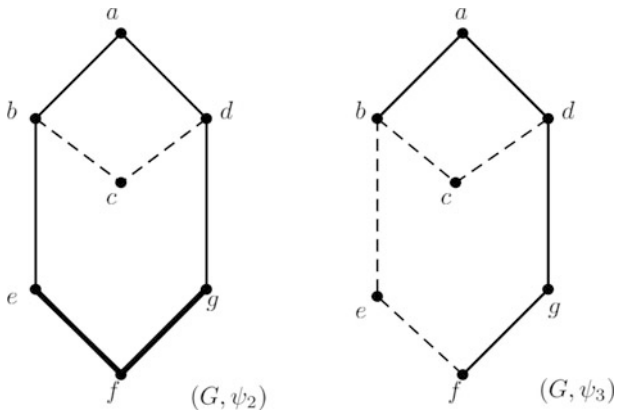

Fig. 2 Induced acyclic graphoidal decompositions of graph G

In fact ψ_3 is a minimum *IAGD* of G because for graphs other than paths, any *IAGD* must be of cardinality at least two. Thus $\eta_{ia}(G) = 2$.

Singh and Das [7] have determined the value of induced acyclic graphoidal decomposition number for complete graphs, complete bipartite graphs, wheels, unicyclic graphs, and bicyclic graphs. Hamid and Joseph [9] have studied this parameter $\eta_{ia}(G)$ further and obtained certain bounds of $\eta_{ia}(G)$, characterized graphs attaining some of these bounds, and investigated graphs admitting an *IAGD* satisfying some specified properties.

Given an *IAGD*, ψ of G, a vertex v, is said to be *interior* to ψ if v is an internal vertex of an element of ψ and is called *exterior* to ψ otherwise. The following theorem proved by Arumugam and Suseela [4] which is similar to the corresponding result on graphoidal decomposition gives an expression for $\eta_{ia}(G)$ in terms of the size of G and the interior vertices.

Theorem 2.3 ([9]) *For every induced acyclic graphoidal decomposition ψ of a graph G, let t_ψ denote the number of vertices interior to ψ, and let $t_{ia}(G) =$*

max t_ψ, *where the maximum is taken over all the induced acyclic graphoidal decompositions* ψ *of* G. *Then* $\eta_{ia}(G) = m - t_{ia}(G)$.

Remark 2.4 From Theorem 2.3, it follows that $\eta_{ia}(G) \geq m - n$ and the equality is obtained only if there exists an IAGD ψ such that all the vertices of G are interior to ψ. Hence the existence of an edge-disjoint collection S of internally disjoint induced paths of G such that every vertex of G is an internal vertex of an element in S ensures $\eta_{ia}(G) = m - n$. This is because S together with the edges of G not belonging to members of S yield an IAGD ψ of G with $t_{ia}(G) = n$.

3 Bounds for η_{ia}

From the definition of *IAGD*, it follows that for any graph G, $m - n \leq \eta_{ia}(G) \leq m$. Hamid and Joseph [9] have proved that if d is the diameter and $\Delta(G)$ is the highest degree among all the vertices of G, then $\Delta(G) - 1 \leq \eta_{ia}(G) \leq m - d + 1$. They have also characterized graphs with $\eta_{ia}(G) = m - d + 1$ and $\eta_{ia}(G) = \Delta(G) - 1$ in the particular case when $\Delta(G) = 3$. As observed earlier, for the determination of the value of $\eta_{ia}(G)$, we need to know the maximum number of vertices that can be made interior to some induced path in G. Hence it is important to examine the nature of the vertices and classify them accordingly so that improved bounds for η_{ia} could be obtained. First we will examine the relationship $\eta_{ia}(G)$ has with the cut vertices of G. By *cut vertex* of a connected graph G, we mean a vertex of a graph whose removal disconnects G. A graph having at least one cut vertex is called a *separable graph*. The following theorem gives an upper bound for $\eta_{ia}(G)$ for separable graphs in terms of the number of its cut vertices.

Theorem 3.1 *If* $c \geq 1$ *denote the number of cut vertices of* G, *then* $\eta_{ia}(G) \leq m - c$.

Proof Consider a graph G with at least one cut vertex. Let x be a cut vertex of G. Then there exist vertices u and v such that (u, x, v) is an induced path. Therefore it is possible to obtain an *IAGD* ψ such that x is interior to ψ. This is true for all the cut vertices of G. Hence if c is the number of cut vertices of G, then $t_{ia} \geq c$. Therefore by Theorem 2.3, $\eta_{ia}(G) = m - t_{ia} \leq m - c$.

Remark 3.2 The above bound is sharp. For example, consider the paw G as given in Fig. 3. We have $m = 4$ and the cut vertex x is the only vertex that can be made interior to any *IAGD* of G. Hence $t_{ia}(G) = 1 = c$ so that $\eta_{ia}(G) = 3$.

Given a graph G, a vertex v is said to be *simplicial* if its neighborhood forms a complete graph. For a complete graph, all its vertices are simplicial.

Next theorem gives a bound for $\eta_{ia}(G)$ in terms of the number of *simplicial vertices* of G.

Theorem 3.3 *Let* s *denote the number of simplicial vertices in a graph* G. *Then* $\eta_{ia} \geq m - n + s$.

Proof Suppose u is a simplicial vertex of a graph G. Then the vertices adjacent to u are mutually adjacent. Therefore there exists no induced path of the form (v_i, u, v_j) for any $v_i, v_j \in V(G)$. That is, there exists no induced path of length more than one in G that contain the vertex u. Hence u is not an interior vertex of any *IAGD* of G. This being true for all simplicial vertices, we have $t_{ia} \leq n - s$ so that $\eta_{ia} = m - t_{ia} \geq m - n + s$.

The graphs G and H given in Fig. 4 are such that $\eta_{ia}(G) = 2$ and $\eta_{ia}(H) = 3$. In the first case, $\eta_{ia}(G) = m - n + s$, and for the other graph, $\eta_{ia}(H) > m - n + s$.

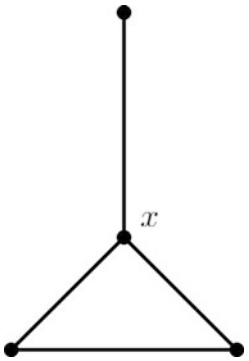

Fig. 3 Graph G with $\eta_{ia}(G) = 3$

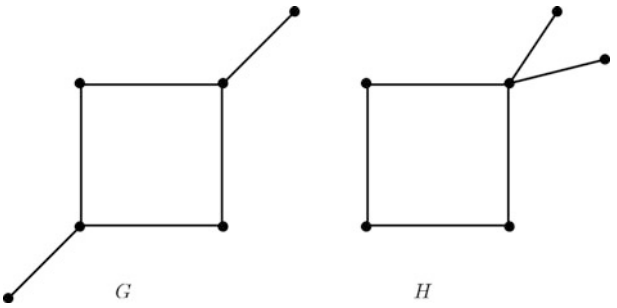

Fig. 4 Graphs G and H

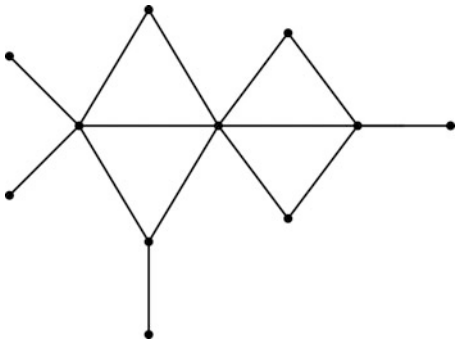

Fig. 5 Graph G with $\eta_{ia}(G) = m - n + s = m - c$

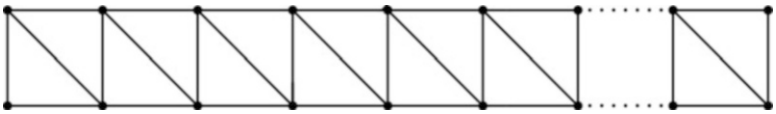

Fig. 6 Triangulated ladder

Remark 3.4 From the preceding theorems, it follows that if G is a graph such that every vertex of G is a simplicial vertex or a cut vertex, then $\eta_{ia}(G) = m - n + s = m - c$ where c is the number of cut vertices and s is the number of simplicial vertices of G. The graph given in Fig. 5 is an example for such a graph.

Now we will present some families of graphs such that $\eta_{ia}(G) = m - n + s$. One such graph is the triangulated ladder presented in Fig. 6.

Theorem 3.5 *If L is the triangulated ladder graph, then $\eta_{ia}(L) = m - n + s$.*

It was observed that relation $\eta_{ia}(G) = m - n + s$ is true in general for chordal graphs having at least one pair of simplicial vertices say, u and v such that neighborhood of $N[u] \neq N[v]$ which leads to the following conjecture.

Conjecture 3.6 If G is a chordal graph having at least two simplicial vertices u and v such that $N[u] \neq N[v]$, then $\eta_{ia}(G) = m - n + s$.

The following is a general problem that is to be addressed further.

Problem 3.7 Characterize chordal graphs having s simplicial vertices where $s \geq 2$ such that $\eta_{ia}(G) = m - n + s$.

An *ear* of a graph G is a maximal path whose internal vertices have degree two in G. Therefore every ear of G is an induced path. An *ear decomposition* of G is a decomposition $P_0, P_1, P_2, \ldots, P_k$ such that P_0 is a cycle and P_i for $i \geq 1$ is an ear of $P_0 \cup P_1 \cup P_2 \ldots \cup P_i$. Whitney [12] has obtained a characterization of two-connected graphs in terms of ear decomposition.

Theorem 3.8 ([12]) *A graph is two-connected if and only if it has an ear decomposition. Furthermore, every cycle in a two-connected graph is an initial cycle of some ear decomposition.*

It has been proved in [9] that $\Delta(G) - 1 \leq \eta_{ia}(G)$. They have also characterized graphs with $\eta_{ia}(G) = \Delta(G) - 1$ in the particular case when $\Delta(G) = 3$. The general case appears to be very challenging. However, Whitney's theorem is useful in finding a necessary and sufficient condition for a graph G that satisfies the equation $\eta_{ia}(G) = \Delta(G) - 1$. Partial solutions to this problem have been obtained. For example, if G is a separable graph with a cut vertex w of degree Δ such that each of its component is a triangle-free two-connected graph containing the vertex w, then $\eta_{ia}(G) = \Delta - 1$. The general question for two-connected graphs is still unsolved.

Problem 3.9 Characterize the two-connected graphs G such that $\eta_{ia}(G) = \Delta - 1$.

References

1. Acharya, B. D., Sampathkumar, E.: Graphoidal covers and graphoidal covering number of a graph. Indian J.pure appl.Math. **18(10)**, 882–890 (1987)
2. Arumugam, S.: Path covers in graphs. Lecture Notes of the National Workshop on Decompositions of Graphs and Product Graphs held at Annamalai University, Tamil Nadu, during January 3–7, (2006)
3. Arumugam, S., Hamid, I. S.: Simple graphoidal covers in graphs. J. Combin. Math. Combin. Comput. **64**, 79–95 (2008)
4. Arumugam, S and Suseela, J. S.: Acyclic graphoidal covers and path partitions in a graph, *Discrete Mathematics*, **190**, 67–77 (1998)
5. Harary, F.: Covering and packing in graphs I. Ann. N. Y. Acad. Sci. **175**, 198–205 (1970)
6. Peroche, B.: The path number of some multipartite graphs. Annals of Discrete Math. **9**, 195–197 (1980)
7. Singh, K. R., Das, P. K.: Induced acyclic graphoidal covers in a graph. World Academy of Science, Engineering and Technology. **68**, 38–44 (2010)
8. Hamid, I. S., Joseph, M.: Further results on induced graphoidal decomposition. Discrete Mathematics, Algorithms and Applications.**5(1)** (2013) https://doi.org/10.1142/S1793830913500067
9. Hamid, I. S., Joseph, M: Decomposing graphs into internally-disjoint induced paths. SCIENTIA. Series A: Mathematical Sciences. **27** 47–57(2016)
10. Stanton, R. G., Cowan, D. D., James, L.O.: Some results on path numbers. Proc. Louisiana Conf. on Combinatorics.Graph Theory and Computing, 112–135 (1970)
11. West, D. B.: Introduction to Graph Theory, Second Edition. Prentice Hall of India, New Delhi (2005)
12. Whitney,H.: Congruent graphs and the connectivity of graphs, *Amer. J. Math* **54**, 150–168 (1932)

Dominating Laplacian Energy in Products of Intuitionistic Fuzzy Graphs

R. Vijayaragavan, A. Kalimulla, and S. Sharief Basha

Abstract The Laplacian energy of an intuitionistic fuzzy graph concept is extended to dominating Laplacian energy in various products of intuitionistic fuzzy graph. In this paper, we have obtained the value of dominating Laplacian energy in two products such as Cartesian product and tensor product. Also we study the relation between the dominating Laplacian energy in the products in two intuitionistic fuzzy graphs.

1 Introduction

It is fairly well known that graphs are simply models of relations. A graph is a convenient way of representing information involving relationship between objects. The objects are represented by vertices and relations by edges. When there is vagueness in the description of the objects or in its relationships or in both, it is natural that we need to design a "fuzzy graph model." Fuzzy graph is a symmetric binary fuzzy relation on a fuzzy subset. The concept of fuzzy sets and fuzzy relations was introduced by L.A. Zadeh in 1965 [11] and further studied in [1]. It was Rosenfeld [7] who considered fuzzy relations on fuzzy sets and developed the theory of fuzzy graphs in 1975.

R. Vijayaragavan
Department of Mathematics, Thiruvalluvar University, Serkadu, Vellore, TN, India

A. Kalimulla
Thiruvalluvar University, Serkadu, Vellore, TN, India
e-mail: akalimulla@email.address

S. Sharief Basha (✉)
Applied Algebra Division, School of Advanced Sciences, VIT University, Vellore, Tamilnadu, India
e-mail: shariefbasha.s@vit.ac.in

B. Rushi Kumar et al. (eds.), *Applied Mathematics and Scientific Computing*,
Trends in Mathematics, https://doi.org/10.1007/978-3-030-01123-9_60

Let di be the degree of ith vertex of G, i = 1, 2, . . . , n. The spectrum of the graph G, consisting of the numbers, is the spectrum of its adjacency matrix [2]. In 1960, the study of domination in graphs was begun. Domination in graphs has applications to several fields. A. Somasundaram and S. Somasundaram [8] introduced domination in fuzzy graphs in terms of effective edges. A. Nagoorgani and V.T. Chandrasekaran [3] introduced domination using strong arcs. R. Parvathi and G. Thamizhendhi [4–6] introduced a dominating set, domination number, independent set, total dominating, and total domination number in intuitionistic fuzzy graphs. Sharief Basha. S and E. Kartheek [9] introduced the new concept Laplacian Energy of an Intuitionistic Fuzzy Graph R. Vijayaragavan, A. Kalimulla, and S. Sharief Basha studied dominating energy in products of intuitionistic fuzzy graphs in [10].

This paper is organized as follows. In Sect. 2, we defined the dominating energy of two products of an intuitionistic fuzzy graphs, and in Sect. 3, we give the conclusion.

2 Dominating Laplacian Energy in Products of Intuitionistic Fuzzy Graphs

2.1 Dominating Laplacian Energy in Cartesian Product of an Intuitionistic Fuzzy Graph $G_1 \square G_2(V, E)$

2.1.1 Now We Find the Dominating Laplacian Energy in Cartesian Product of Intuitionistic Fuzzy Graph $G_1 \square G_2$ (V,E)

According to Fig. 1, Cartesian Product of Intuitionistic Fuzzy Graphs G_1 and G_2, we have

$$\mu_1(v_1u_1) = \max[\mu(v_1u_1, v_1u_2), \mu(v_1u_1, v_2u_1)] = \max[0.1, 0.3] = 0.3$$

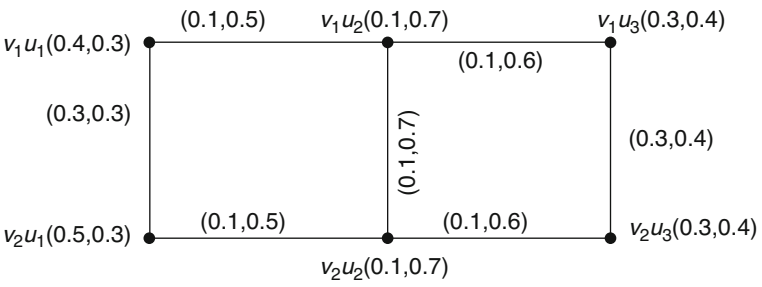

Fig. 1 $G_1 \square G_2$

$$\mu_1(v_1u_2) = \max[\mu(v_1u_2, v_1u_3), \mu(v_1u_2, v_2u_2), \mu(v_1u_2, v_1u_1)]$$
$$= \max[0.1, 0.1, 0.1] = 0.1$$
$$\mu_1(v_1u_3) = \max[\mu(v_1u_3, v_2u_3), \mu(v_1u_3, v_1u_2)] = \max[0.3, 0.1] = 0.3$$
$$\mu_1(v_2u_1) = \max[\mu(v_2u_1, v_1u_1), \mu(v_2u_1, v_2u_2)] = \max[0.3, 0.1] = 0.3$$
$$\mu_1(v_2u_2) = \max[\mu(v_2u_2, v_2u_1), \mu(v_2u_2, v_1u_2), \mu(v_2u_2, v_2u_3)]$$
$$= \max[0.1, 0.1, 0.1] = 0.1$$
$$\mu_1(v_2u_3) = \max[\mu(v_2u_3, v_2u_2), \mu(v_2u_3, v_1u_3)] = \max[0.1, 0.3] = 0.3$$
$$\gamma_1(v_1u_1) = \min[\gamma(v_1u_1, v_1u_2), \gamma(v_1u_1, v_2u_1)] = \min[0.5, 0.3] = 0.3$$
$$\gamma_1(v_1u_2) = \min[\gamma(v_1u_2, v_1u_3), \gamma(v_1u_2, v_2u_2), \gamma(v_1u_2, v_1u_1)]$$
$$= \min[0.6, 0.7, 0.5] = 0.5$$
$$\gamma_1(v_1u_3) = \min[\gamma(v_1u_3, v_2u_3), \gamma(v_1u_3, v_1u_2)] = \min[0.4, 0.6] = 0.4$$
$$\gamma_1(v_2u_1) = \min[\gamma(v_2u_1, v_1u_1), \gamma(v_2u_1, v_2u_2)] = \min[0.3, 0.5] = 0.3$$
$$\gamma_1(v_2u_2) = \min[\gamma(v_2u_2, v_2u_1), \gamma(v_2u_2, v_1u_2), \gamma(v_2u_2, v_2u_3)]$$
$$= \min[0.5, 0.7, 0.6] = 0.5$$
$$\gamma_1(v_2u_3) = \min[\gamma(v_2u_3, v_2u_2), \gamma(v_2u_3, v_1u_3)] = \min[0.6, 0.4] = 0.4$$

Here v_1u_1 dominates v_1u_2 because

$\mu(v_1u_1, v_1u_2) \leq \mu_1(v_1u_1) \wedge \mu_1(v_1u_2)$	$\gamma(v_1u_1, v_1u_2) \leq \gamma_1(v_1u_1) \wedge \gamma_1(v_1u_2)$
$0.1 \leq 0.3 \wedge 0.1$	$0.5 \leq 0.3 \wedge 0.5$

Here v_1u_3 dominates v_2u_3 because

$\mu(v_1u_3, v_2u_3) \leq \mu_1(v_1u_3) \wedge \mu_1(v_2u_3)$	$\gamma(v_1u_3, v_2u_3) \leq \gamma_1(v_1u_3) \wedge \gamma_1(v_2u_3)$
$0.3 \leq 0.3 \wedge 0.3$	$0.4 \leq 0.4 \wedge 0.4$

Here v_2u_1 dominates v_1u_1 because

$\mu(v_2u_1, v_1u_1) \leq \mu_1(v_2u_1) \wedge \mu_1(v_1u_1)$	$\gamma(v_2u_1, v_1u_1) \leq \gamma_1(v_2u_1) \wedge \gamma_1(v_1u_1)$
$0.3 \leq 0.3 \wedge 0.3$	$0.3 \leq 0.3 \wedge 0.3$

Here v_2u_2 dominates v_2u_1 because

$\mu(v_2u_2, v_2u_1) \leq \mu_1(v_2u_2) \wedge \mu_1(v_2u_1)$	$\gamma(v_2u_2, v_2u_1) \leq \gamma_1(v_2u_2) \wedge \gamma_1(v_2u_1)$
$0.1 \leq 0.1 \wedge 0.3$	$0.5 \leq 0.5 \wedge 0.3$

Here V=$\{v_1u_1, v_1u_2, v_1u_3, v_2u_1, v_2u_2, v_2u_3\}$ and D=$\{v_1u_1, v_1u_3, v_2u_1, v_2u_2\}$ V-D=$\{v_1u_2, v_2u_3\}$

$|D|$=4=sum of dominating elements

$$D\,(G_1\square G_2) = \begin{bmatrix} (1,1) & (0.1,0.5) & (0,0) & (0.3,0.3) & (0,0) & (0,0) \\ (0.1,0.5) & (0,0) & (0.1,0.6) & (0,0) & (0.1,0.7) & (0,0) \\ (0,0) & (0.1,0.6) & (1,1) & (0,0) & (0,0) & (0.3,0.4) \\ (0.3,0.3) & (0,0) & (0,0) & (1,1) & (0.1,0.5) & (0,0) \\ (0,0) & (0.1,0.7) & (0,0) & (0.1,0.5) & (1,1) & (0.1,0.6) \\ (0,0) & (0,0) & (0.3,0.4) & (0,0) & (0.1,0.6) & (0,0) \end{bmatrix}$$

$$\mu_D(G_1\square G_2) = \begin{bmatrix} 1 & 0.1 & 0 & 0.3 & 0 & 0 \\ 0.1 & 0 & 0.1 & 0 & 0.1 & 0 \\ 0 & 0.1 & 1 & 0 & 0 & 0.3 \\ 0.3 & 0 & 0 & 1 & 0.1 & 0 \\ 0 & 0.1 & 0 & 0.1 & 1 & 0.1 \\ 0 & 0 & 0.3 & 0 & 0.1 & 0 \end{bmatrix}$$

$$\gamma_D(G_1\square G_2) = \begin{bmatrix} 1 & 0.5 & 0 & 0.3 & 0 & 0 \\ 0.5 & 0 & 0.6 & 0 & 0.7 & 0 \\ 0 & 0.6 & 1 & 0 & 0 & 0.4 \\ 0.3 & 0 & 0 & 1 & 0.5 & 0 \\ 0 & 0.7 & 0 & 0.5 & 1 & 0.6 \\ 0 & 0 & 0.4 & 0 & 0.6 & 0 \end{bmatrix}$$

2.1.2 Cartesian Product of Membership Function

$$d[\mu_D(G_1\square G_2)] = \begin{bmatrix} 0.4 & 0 & 0 & 0 & 0 & 0 \\ 0 & 0.3 & 0 & 0 & 0 & 0 \\ 0 & 0 & 0.4 & 0 & 0 & 0 \\ 0 & 0 & 0 & 0.4 & 0 & 0 \\ 0 & 0 & 0 & 0 & 0.3 & 0 \\ 0 & 0 & 0 & 0 & 0 & 0.4 \end{bmatrix}$$

$$L = d[\mu_D(G_1\square G_2)] - A[\mu_D(G_1\square G_2)]$$

$$L = \begin{bmatrix} -0.6 & -0.1 & 0 & -0.3 & 0 & 0 \\ -0.1 & 0.3 & -0.1 & 0 & -0.1 & 0 \\ 0 & -0.1 & -0.6 & 0 & 0 & -0.3 \\ -0.3 & 0 & 0 & -0.6 & -0.1 & 0 \\ 0 & -0.1 & 0 & -0.1 & -0.7 & -0.1 \\ 0 & 0 & -0.3 & 0 & -0.1 & 0.4 \end{bmatrix}$$

$Eigenvalues = [-0.9327, -0.7251, -0.6651, -0.2988, 0.3237, 0.4980]$

$LE[\mu_D G_1 \square G_2)] = \left|-0.9327 - \frac{2(1.1)}{6}\right| + \left|-0.7251 - \frac{2(1.1)}{6}\right| + \left|-0.6651 - \frac{2(1.1)}{6}\right| + \left|-0.2988 - \frac{2(1.1)}{6}\right|$

$$+ \left|0.3237 - \frac{2(1.1)}{6}\right| + \left|0.4980 - \frac{2(1.1)}{6}\right|$$

$= |-1.2993| + |-1.0917| + |-1.0317| + |-0.6654| + |-0.0429| + |0.1313| = 4.2623.$

2.1.3 Cartesian Product of Nonmembership Function

$$d[\gamma_D(G_1 \square G_2)] = \begin{bmatrix} 0.8 & 0 & 0 & 0 & 0 & 0 \\ 0 & 1.8 & 0 & 0 & 0 & 0 \\ 0 & 0 & 1 & 0 & 0 & 0 \\ 0 & 0 & 0 & 0.8 & 0 & 0 \\ 0 & 0 & 0 & 0 & 1.8 & 0 \\ 0 & 0 & 0 & 0 & 0 & 1 \end{bmatrix}$$

$$L = d[\gamma_D(G_1 \square G_2)] - A[\gamma_D(G_1 \square G_2)]$$

$$L = \begin{bmatrix} -0.2 & -0.5 & 0 & -0.3 & 0 & 0 \\ -0.5 & 1.8 & -0.6 & 0 & -0.7 & 0 \\ 0 & -0.6 & 0 & 0 & 0 & -0.4 \\ -0.3 & 0 & 0 & -0.2 & -0.5 & 0 \\ 0 & -0.7 & 0 & -0.5 & 0.8 & -0.6 \\ 0 & 0 & -0.4 & 0 & -0.6 & 1 \end{bmatrix}$$

$Eigenvalues = [-0.7930, -0.2915, -0.0661, 0.5639, 1.3128, 2.4740]$

$LE[\gamma_D(G_1 \square G_2)] = \left|-0.7930 - \frac{2(3.6)}{6}\right| + \left|-0.2915 - \frac{2(3.6)}{6}\right| + \left|-0.0661 - \frac{2(3.6)}{6}\right| + \left|0.5639 - \frac{2(3.6)}{6}\right|$

$$+ \left|1.3128 - \frac{2(3.6)}{6}\right| + \left|2.4740 - \frac{2(3.6)}{6}\right|$$

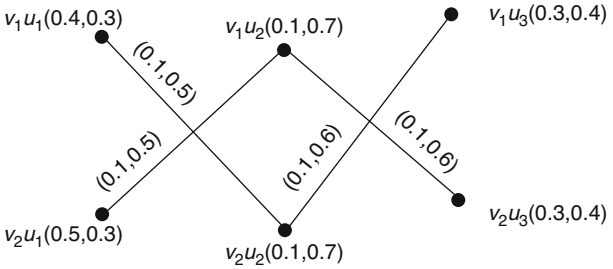

Fig. 2 $G_1 \otimes G_2$

$$= |-1.993| + |-1.4915| + |-1.2661| + |-0.6361| + |0.1128| + |1.274| = 6.7735.$$

2.2 Dominating Laplacian Energy in Tensor Product of an Intuitionistic Fuzzy Graph $G_1 \square G_2(V, E)$

2.2.1 Now We Find the Dominating Laplacian Energy in Tensor Product of Intuitionistic Fuzzy Graph $G_1 \circ G_2$(V,E)

Similarly, by using Fig. 2 -Tensor Product of Intuitionistic Fuzzy Graph G_1 and G_2, then we have

$$\mu_1(v_1u_1) = \max[\mu(v_1u_1, v_2u_2)] = \max[0.1] = 0.1$$

$$\mu_1(v_1u_2) = \max[\mu(v_1u_2, v_2u_1), \mu(v_1u_2, v_2u_3)] = \max[0.1, 0.1] = 0.1$$

$$\mu_1(v_1u_3) = \max[\mu(v_1u_3, v_2u_2)] = \max[0.1] = 0.1$$

$$\mu_1(v_2u_1) = \max[\mu(v_2u_1, v_1u_2)] = \max[0.1] = 0.1$$

$$\mu_1(v_2u_2) = \max[\mu(v_2u_2, v_1u_1), \mu(v_2u_2, v_1u_3)] = \max[0.1, 0.1] = 0.1$$

$$\mu_1(v_2u_3) = \max[\mu(v_2u_3, v_1u_2)] = \max[0.1] = 0.1$$

$$\gamma_1(v_1u_1) = \min[\gamma(v_1u_1, v_2u_2)] = \min[0.5] = 0.5$$

$$\gamma_1(v_1u_2) = \min[\gamma(v_1u_2, v_2u_1), \gamma(v_1u_2, v_2u_3)] = \min[0.5, 0.6] = 0.5$$

$$\gamma_1(v_1u_3) = \min[\gamma(v_1u_3, v_2u_2)] = \min[0.6] = 0.6$$

$$\gamma_1(v_2u_1) = \min[\gamma(v_2u_1, v_1u_2)] = \min[0.5] = 0.5$$

$$\gamma_1(v_2u_2) = \min[\gamma(v_2u_2, v_1u_1), \gamma(v_2u_2, v_1u_3)] = \min[0.5, 0.6] = 0.5$$

$$\gamma_1(v_2u_3) = \min[\gamma(v_2u_3, v_1u_2)] = \min[0.6] = 0.6$$

Here v_1u_1 is dominates v_2u_2 because

$\mu(v_1u_1, v_2u_2) \leq \mu_1(v_1u_1) \wedge \mu_1(v_2u_2)$ $\gamma(v_1u_1, v_2u_2) \leq \gamma_1(v_1u_1) \wedge \gamma_1(v_2u_2)$
$0.1 \leq 0.1 \wedge 0.1$ $0.5 \leq 0.5 \wedge 0.5$

Here v_1u_2 is dominates v_2u_1 because

$\mu(v_1u_2, v_2u_1) \leq \mu_1(v_1u_2) \wedge \mu_1(v_2u_1)$ $\gamma(v_1u_2, v_2u_1) \leq \gamma_1(v_1u_2) \wedge \gamma_1(v_2u_1)$
$0.1 \leq 0.1 \wedge 0.1$ $0.5 \leq 0.5 \wedge 0.5$

Here v_1u_3 is dominates v_2u_2 because

$\mu(v_1u_3, v_2u_2) \leq \mu_1(v_1u_3) \wedge \mu_1(v_2u_2)$ $\gamma(v_1u_3, v_2u_2) \leq \gamma_1(v_1u_3) \wedge \gamma_1(v_2u_2)$
$0.1 \leq 0.1 \wedge 0.1$ $0.6 \leq 0.6 \wedge 0.5$

Here v_2u_3 is dominates v_1u_2 because

$\mu(v_2u_3, v_1u_2) \leq \mu_1(v_2u_3) \wedge \mu_1(v_1u_2)$ $\gamma(v_2u_3, v_1u_2) \leq \gamma_1(v_2u_3) \wedge \gamma_1(v_1u_2)$
$0.1 \leq 0.1 \wedge 0.1$ $0.6 \leq 0.6 \wedge 0.5$

Here V={v_1u_1,v_1u_2,v_1u_3,v_2u_1,v_2u_2,v_2u_3} and D={v_1u_1,v_1u_2,v_1u_3,v_2u_3} V-D= {v_2u_1,v_2u_2}

$|D|$=4=Sum of dominating elements

$$D(G_1 \otimes G_2) = \begin{bmatrix} (1,1) & (0,0) & (0,0) & (0,0) & (0.1,0.5) & (0,0) \\ (0,0) & (1,1) & (0,0) & (0.1,0.5) & (0,0) & (0.1,0.6) \\ (0,0) & (0,0) & (1,1) & (0,0) & (0.1,0.6) & (0,0) \\ (0,0) & (0.1,0.5) & (0,0) & (0,0) & (0,0) & (0,0) \\ (0.1,0.5) & (0,0) & (0.1,0.6) & (0,0) & (0,0) & (0,0) \\ (0,0) & (0.1,0.6) & (0,0) & (0,0) & (0,0) & (1,1) \end{bmatrix}$$

$$\mu_D(G_1 \otimes G_2) = \begin{bmatrix} 1 & 0 & 0 & 0 & 0.1 & 0 \\ 0 & 1 & 0 & 0.1 & 0 & 0.1 \\ 0 & 0 & 1 & 0 & 0.1 & 0 \\ 0 & 0.1 & 0 & 0 & 0 & 0 \\ 0.1 & 0 & 0.1 & 0 & 0 & 0 \\ 0 & 0.1 & 0 & 0 & 0 & 1 \end{bmatrix} \gamma_D(G_1 \otimes G_2) = \begin{bmatrix} 1 & 0 & 0 & 0 & 0.5 & 0 \\ 0 & 1 & 0 & 0.5 & 0 & 0.6 \\ 0 & 0 & 1 & 0 & 0.6 & 0 \\ 0 & 0.5 & 0 & 0 & 0 & 0 \\ 0.5 & 0 & 0.6 & 0 & 0 & 0 \\ 0 & 0.6 & 0 & 0 & 0 & 1 \end{bmatrix}$$

2.2.2 Tensor Product of Membership Function

$$d[\mu_D(G_1 \otimes G_2)] = \begin{bmatrix} 0.1 & 0 & 0 & 0 & 0 & 0 \\ 0 & 0.2 & 0 & 0 & 0 & 0 \\ 0 & 0 & 0.1 & 0 & 0 & 0 \\ 0 & 0 & 0 & 0.1 & 0 & 0 \\ 0 & 0 & 0 & 0 & 0.2 & 0 \\ 0 & 0 & 0 & 0 & 0 & 0.1 \end{bmatrix}$$

$$L = d[\mu_D(G_1 \otimes G_2)] - A[\mu_D(G_1 \otimes G_2)]$$

$$L = \begin{bmatrix} -0.9 & 0 & 0 & 0 & -0.1 & 0 \\ 0 & -0.8 & 0 & -0.1 & 0 & -0.1 \\ 0 & 0 & -0.9 & 0 & -0.1 & 0 \\ 0 & -0.1 & 0 & 0.1 & 0 & 0 \\ -0.1 & 0 & -0.1 & 0 & 0.2 & 0 \\ 0 & -0.1 & 0 & 0 & 0 & -0.9 \end{bmatrix}$$

$Eigenvalues = [-0.9645, -0.9179, -0.9000, -0.7466, 0.1111, 0.2179]$

$L[\mu_D(G_1 \otimes G_2) = \left|-0.9645 - \frac{2(0.4)}{6}\right| + \left|-0.9179 - \frac{2(0.4)}{6}\right| + \left|-0.9000 - \frac{2(0.4)}{6}\right| + \left|-0.7466 - \frac{2(0.4)}{6}\right|$

$$+ \left|0.1111 - \frac{2(0.4)}{6}\right| + \left|0.2179 - \frac{2(0.4)}{6}\right|$$

$= |-1.0978| + |-1.0512| + |-1.0333| + |-0.8799| + |-0.0222| + |0.0845| = 4.1689$

2.2.3 Tensor Product of Nonmembership Function

$$d[\gamma_D(G_1 \otimes G_2)] = \begin{bmatrix} 0.5 & 0 & 0 & 0 & 0 & 0 \\ 0 & 1.1 & 0 & 0 & 0 & 0 \\ 0 & 0 & 0.6 & 0 & 0 & 0 \\ 0 & 0 & 0 & 0.5 & 0 & 0 \\ 0 & 0 & 0 & 0 & 1.1 & 0 \\ 0 & 0 & 0 & 0 & 0 & 0.6 \end{bmatrix}$$

$$L = d[\gamma_D(G_1 \otimes G_2)] - A[\gamma_D(G_1 \otimes G_2)]$$

$$L = \begin{bmatrix} -0.5 & 0 & 0 & 0 & -0.5 & 0 \\ 0 & 0.1 & 0 & -0.5 & 0 & -0.6 \\ 0 & 0 & -0.4 & 0 & -0.6 & 0 \\ 0 & -0.5 & 0 & 0.5 & 0 & 0 \\ -0.5 & 0 & -0.6 & 0 & 1.1 & 0 \\ 0 & -0.6 & 0 & 0 & 0 & -0.4 \end{bmatrix}$$

$$Eigenvalues = [-0.8623, -0.7741, -0.4527, 0.1235, 0.9387, 1.4268]$$

$$LE = \left|-0.8623 - \frac{2(2.2)}{6}\right| + \left|-0.7741 - \frac{2(2.2)}{6}\right| + \left|-0.4527 - \frac{2(2.2)}{6}\right| + |0.1235 - \frac{2(2.2)}{6}|$$

$$+ \left|0.9387 - \frac{2(2.2)}{6}\right| + \left|1.4268 - \frac{2(2.2)}{6}\right|$$

$$= |1.5956| + |1.5074| + |1.1860| + |0.6098| + |0.2053| + |0.6934| = 5.7975$$

3 Conclusion

In this paper we have defined the dominating intuitionistic fuzzy graph $G = (V, E, \mu, \gamma, \mu_1, \gamma_1)$. The dominating Laplacian energy in the two products of two intuitionistic fuzzy graphs is defined, and the results with suitable examples are examined in detail.

References

1. Atanassov, K.: Intuitionistic Fuzzy sets : Theory and Applications, Springer-Verlag, Heidelberg, (1999).
2. Gutman,I.: Gutman,I. The Energy of a Graph, Ber. Math - Statist. Sekt. Forschungsz. Graz, 103, 1–22 , (1978).

3. Nagoorgani.A and Chandrasekaran.V.T, Domination in Fuzzy Graph, Advances in Fuzzy Sets and systems, 1(1),17–26 (2006).
4. Parvathi R, Karumbigai M G. Intutionistic fuzzy graphs. Computational Intelligence, Theory and Applications. 139–150.
5. Parvathi R and G. Thamizhendhi, Domination in intuitionistic fuzzy graphs, Fourteenth Int. Conf. on IFSs, Sofia, 15–16 May 2010 ,NIFS Vol. 16 (2010), 2, 39–49.
6. Parvathi R and G. Thamizhendhi, Some results on domination number in products of intuitionistic fuzzy graphs, , Annals of Fuzzy mathematics and Informatics,September 2014, Vol:10 , SNo:10 , pp:1–20.
7. Rosenfeld.A, Fuzzy Graphs, in Zadeh.L.A, Fu. K.cS, Tanaka.K and Shimura.M (eds.),
8. Somasundaram.A and Somasundaram.S, Domination in Fuzzy Graphs – I, Elsevier Science, 19, 787–791 (1998).
9. Sharief Basha.S and E. Kartheek, Laplacian Energy of an Intuitionistic Fuzzy Graph, Indian Journal of Science and Technology, ,*Vol 8(33),1–7* , (Dec2015).
10. R.Vijayaragavan , A.Kalimulla , S. Sharief Basha, Dominating Energy in Products of intuitionistic Fuzzy Graphs, Journal of Global Pharma Technology, 2017; 06(9):58–71.
11. Zadeh.L.A., Fuzzy sets , Information and Control, 1965;, 8: 338–353.

Power Domination Parameters in Honeycomb-Like Networks

J. Anitha and Indra Rajasingh

Abstract A set S of vertices in a graph G is called a dominating set of G if every vertex in $V(G)\backslash S$ is adjacent to some vertex in S. A set S is said to be a power dominating set of G if every vertex in the system is monitored by the set S following a set of rules for power system monitoring. The power domination number of G is the minimum cardinality of a power dominating set of G. In this paper, we obtain the power domination number for triangular graphs, pyrene networks, circum-pyrene networks, circum-trizene networks, generalized honeycomb torus and honeycomb rectangular torus.

1 Introduction

Definition 1 ([1]) For $v \in V(G)$, the open neighbourhood of v, denoted as $N_G(v)$, is the set of vertices adjacent with v; and the closed neighbourhood of v, denoted by $N_G[v]$, is $N_G(v) \cup \{v\}$. For a set $S \subseteq V(G)$, the open neighbourhood of S is defined as $N_G(S) = \bigcup_{v \in S} N_G(v)$, and the closed neighbourhood of S is defined as $N_G[S] = N_G(S) \cup S$. For brevity, we denote $N_G(S)$ by $N(S)$ and $N_G[S]$ by $N[S]$.

Definition 2 ([1]) For a graph $G(V, E)$, $S \subseteq V$ is a dominating set of G if every vertex in $V\backslash S$ has at least one neighbour in S. The domination number of G, denoted by $\gamma(G)$, is the minimum cardinality of a dominating set of G.

J. Anitha (✉)
Department of Mathematics, Vels Institute of Science Technology, Advanced Studies, Chennai, India
e-mail: anitha.sbs@velsuniv.ac.in

I. Rajasingh (✉)
School of Advanced Sciences, Vellore Institute of Technology, Chennai, India
e-mail: indra.rajasingh@vit.ac.in

B. Rushi Kumar et al. (eds.), *Applied Mathematics and Scientific Computing*, Trends in Mathematics, https://doi.org/10.1007/978-3-030-01123-9_61

Definition 3 ([2]) Let $G(V, E)$ be a graph, and let $S \subseteq V(G)$. We define the sets $M^i(S)$ of vertices monitored by S at level i, $i \geq 0$, inductively as follows:

1. $M^0(S) = N[S]$.
2. $M^{i+1}(S) = M^i(S) \cup \{w : \exists v \in M^i(S), N(v) \cap (V(G) \backslash M^i(S)) = w\}$.

If $M^\infty(S) = V(G)$, then the set S is called a power dominating set of G. The minimum cardinality of a power dominating set in G is called the power domination number of G written $\gamma_p(G)$.

The power domination has been well studied for trees [1], product graphs [4], block graphs [3], interval graphs and so on. In fact, the problem has been shown to be NP-complete even when restricted to bipartite graphs and chordal graphs [1].

2 Main Results

In this section, we solve the power domination problem for triangular graphs, pyrene network, circum-pyrene network, circum-trizene network, generalized honeycomb torus and honeycomb rectangular torus. In 2013 Ferrero et al. [5] proved the following lemma which shows the power domination number for honeycomb mesh network $HM(n)$.

Lemma 1 *If G is the honeycomb mesh network $HM(n)$ of dimension n, then* $\gamma_p(G) \geq \left\lceil \frac{2n}{3} \right\rceil$.

The following lemma establishes a critical subgraph H of G in the sense that H contains at least one vertex of any power dominating set.

Lemma 2 *Let G be a graph and H as shown in Fig. 1a be a subgraph G with $deg_H w_i = deg_G w_i = 2$, $\forall i$, $i = 1, 2, 3, 4, 5, 6, 7, 8$. Then H is a critical subgraph of G.*

Proof Neither u nor v, when monitored, can further monitor any of w_i, $i = 1, 2, 3, 4, 5, 6, 7, 8$, as $deg_H u = deg_H v = 3$.

Definition 4 ([8]) Let n be a non-negative integer. A triangle graph of order n, TG_n, is defined in the following way: TG_1 is a hexagon. When $n \geq 2$, TG_n is built according to the following step:

Draw n rows of regular hexagons of the same size within an equilateral triangle (which is called the framework of TG_n) so that the first row consists of one hexagon, the second row consists of two hexagons and the nth row consists of n hexagons. Set all the vertices of these hexagons to be the vertices of TG_n, and set all the sides of these hexagons to be the edges of TG_n.

Lemma 3 *Let G be a triangle graph TG_n, $n \geq 2$. Then* $\gamma_p(G) \geq \left\lceil \frac{n}{2} \right\rceil$.

Proof In TG_n, there are $\left\lceil \frac{n}{2} \right\rceil$ critical subgraphs, each isomorphic to H as described in Lemma 2.2. Therefore, $\gamma_p(G) \geq \left\lceil \frac{n}{2} \right\rceil$.

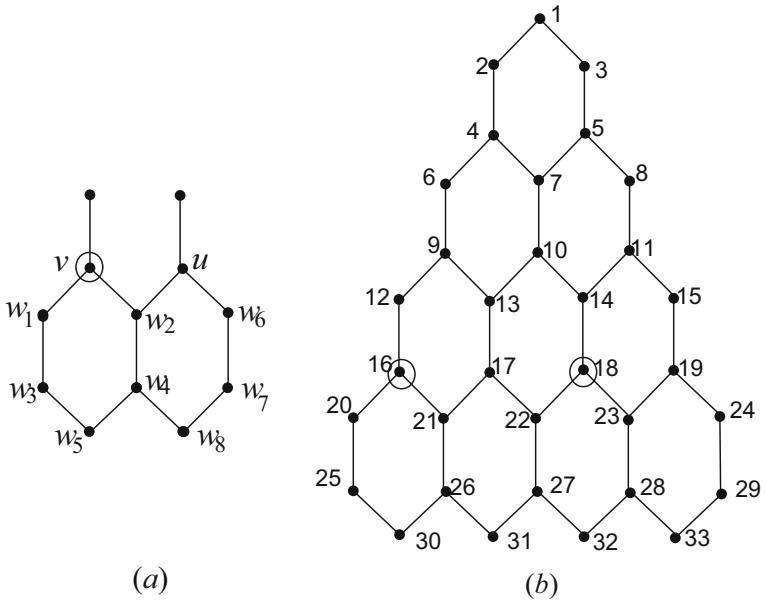

Fig. 1 (**a**) Circled vertices indicate a power dominating set of critical subgraph H induced by G (**b**) power dominating set of TG_4

Power Domination Algorithm in Triangular Graph

Input Triangular graph $TG_n,\ n \geq 2$.

Algorithm Name the vertices of $TG_n,\ n \geq 2$ as 1 to n^2+4n+1 sequentially from left to right, row wise beginning with the top most row.

(i) Select $S_2 = \{4\}$ in TG_2.
(ii) Let $S_3 = \{9, 11\}$ in TG_3.
(iii) Inductively select $S_n = \bigcup_{k=1}^{\lceil \frac{n}{2} \rceil} n^2 + 2(k-1)$ in TG_n.

Output $\gamma_p(TG_n) = \lceil \frac{n}{2} \rceil$.

Proof of Correctness S_4 is a power dominating set of TG_4 with $|S_4| = 2$. Now $M^0(S_4) = N[S_4] = \{16, 20, 21, 12, 18, 22, 23, 14\}$. See Fig. 1b. At least one vertex $v \in M^0(S_4)$ satisfies $|N[v] \backslash M^0(S_4)| = 1$. Proceeding inductively, for every vertex $v \in M^i(S_4),\ |N[v] \backslash M^i(S_4)| = 1,\ i \geq 1$, at every inductive step $i, i \geq 1$. Now $S_n = \bigcup_{k=1}^{\lceil \frac{n}{2} \rceil} n^2 + 2(k-1)$ is a power dominating set of TG_n. This implies that $\gamma_p(TG_n) = \lceil \frac{n}{2} \rceil$, hence the proof.

Theorem 1 *Let G be a triangle graph TG_n. Then $\gamma_p(G) = \lceil \frac{n}{2} \rceil$.*

2.1 Power Domination in Pyrene Network

Pyrene is an alternante polycyclic aromatic hydrocarbon (PAH) and consists of four fused benzene rings, resulting in a large flat aromatic system. It is a colourless or pale yellow solid which forms during incomplete combustion of organic materials and therefore can be isolated from coal tar together with a broad range of related compounds. In the last four decades, a number of research works have been reported on both the theoretical and experimental investigation of pyrene concerning its electronic structure, UV-vis absorption and fluorescence emission spectrum. Indeed, this polycyclic aromatic hydrocarbon exhibits a set of many interesting electrochemical and photophysical attributes, which have resulted in its utilization in a variety of scientific areas. Like most PAHs, pyrene is used to make dyes, plastics and pesticides. Figure 2b depicts the graph of circum-pyrene (1). Circum-pyrene(2) is obtained by adding a layer of hexagons to the boundary of circum-pyrene (1). Inductively, circum-pyrene (n) is obtained from circum-pyrene($n-1$) by adding a layer of hexagons around the boundary of circum-pyrene ($n-1$). Similar construction follows for circum-trizene (n) [6]. See Fig. 3b.

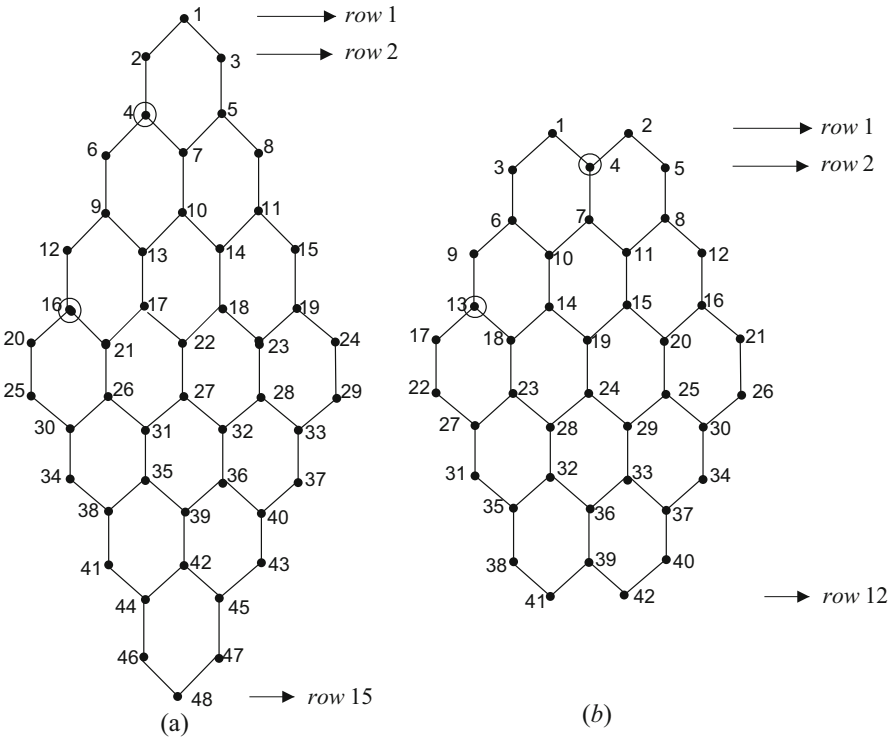

Fig. 2 (**a**) Power dominating set of $PY(4)$, (**b**) power dominating set of circum-pyrene(1)

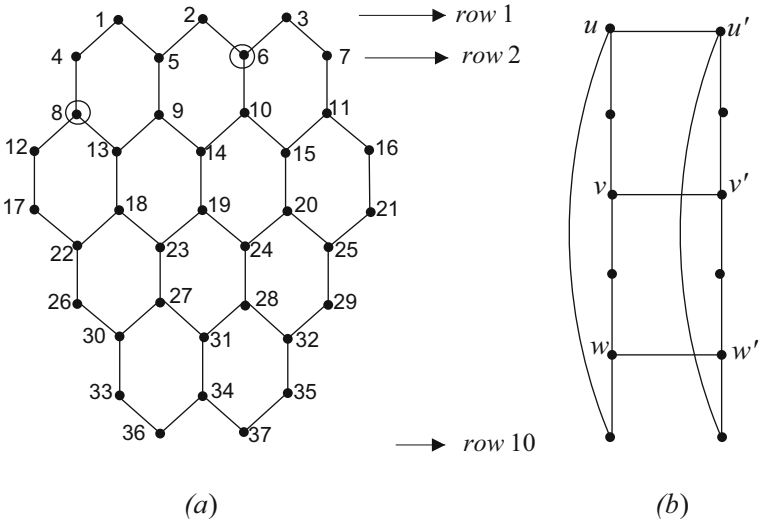

Fig. 3 (**a**) Circled vertices constitute a power dominating set of circum-trizene(1), (**b**) critical subgraph H of G

Lemma 4 *Let G be a pyrene network $PY(n)$, $n \geq 4$. Then $\gamma_p(G) \geq \lceil \frac{n}{2} \rceil$.*

Proof In $PY(n)$, there are $\lceil \frac{n}{2} \rceil$ critical subgraphs, each isomorphic to H as described in Lemma 2.2. Therefore, $\gamma_p(G) \geq \lceil \frac{n}{2} \rceil$.

Power Domination Algorithm in Pyrene Network

Input Pyrene network $PY(n)$, $n \geq 4$.

Algorithm Name the vertices of $PY(n)$, $n \geq 4$ as 1 to $2n^2 + 4n$ sequentially from left to right, row wise beginning with the topmost row. Let P^* denote the path induced by the edges of the hexagons that are not boundary edges of any other hexagon. Select $\lceil \frac{n}{2} \rceil$ vertices of degree 3 in P^*, which are at distance 4 apart on P^*. See Fig. 2a.

Output $\gamma_p(PY(n)) = \lceil \frac{n}{2} \rceil$.

Proof of Correctness S_4 is a power dominating set of $PY(4)$ with $|S_4| = 2$. Now $M^0(S_4) = N[S_4] = \{4, 6, 7, 2, 16, 20, 21, 12\}$. See Fig. 2a. At least one vertex $v \in M^0(S_4)$ satisfies $|N[v] \backslash M^0(S_4)| = 1$. Proceeding inductively, for every vertex $v \in M^i(S_4)$, $|N[v] \backslash M^i(S_4)| = 1$, $i \geq 3$, at every inductive step i, $i \geq 1$. Now $S_n = \bigcup_{i=1}^{\lceil \frac{n}{2} \rceil} (2i)^2$ is a power dominating set of $PY(n)$. This implies that $\gamma_p(PY(n)) = \lceil \frac{n}{2} \rceil$, hence the proof.

Theorem 2 *Let G be a pyrene network $PY(n)$, $n \geq 4$. Then $\gamma_p(G) = \lceil \frac{n}{2} \rceil$.*

Lemma 5 *Let G be a circum-pyrene(n), $n \geq 1$. Then $\gamma_p(G) \geq n+1$.*

Proof In circum-pyrene(n), there are $2n+2$ critical subgraphs, each isomorphic to H as described in Lemma 2.2. Therefore, $\gamma_p(G) \geq \left\lceil \frac{2n+2}{2} \right\rceil = n+1$.

Power Domination Algorithm in Circum-Pyrene

Input Circum-pyrene(n), $n \geq 1$.

Algorithm Name the vertices of circum-pyrene(n), $n \geq 1$ as 1 to $6n^2+20n+16$ sequentially from left to right, row wise beginning with the first row. Consider $2n+2$ hexagons in the outer most layer of the $circum\text{-}pyrene(n)$. Let P^* denote the path induced by the edges of the hexagons that are not boundary edges of any other hexagon. Select $n+1$ vertices of degree 3 in P^*, which are at distance 5 apart on P^*.

Output $\gamma_p(\text{circum}-\text{pyrene}(n)) = n+1$.

Proof of Correctness $S(1)$ is a power dominating set of circum-pyrene(1) with $|S(1)| = 2$. Now $M^0(S(1)) = N[S(1)] = \{1, 2, 4, 7, 13, 17, 18, 9\}$. See Fig. 2b. At least one vertex $v \in M^0(S(1))$ satisfies $|N[v] \backslash M^0(S(1))| = 1$. Proceeding inductively, for every vertex $v \in M^i(S(1))$, $|N[v] \backslash M^i(S(1))| = 1$, $i \geq 1$, at every inductive step $i, i \geq 2$. Now $S(n) = n+1$ is a power dominating set of circum-pyrene(n). This implies that $\gamma_p(G) = n+1$, hence the proof.

Lemma 6 *Let G be a circum-trizene(n), $n \geq 1$. Then $\gamma_p(G) \geq n+1$.*

Proof In circum-trizene(n), there are $2n+2$ critical subgraphs, each isomorphic to H as described in Lemma 2.2. Therefore, $\gamma_p(G) \geq \left\lceil \frac{2n+2}{2} \right\rceil = n+1$.

Power Domination Algorithm in Circum-Trizene

Input Circum-trizene(n), $n \geq 1$.

Algorithm Name the vertices of circum-trizene(n), $n \geq 1$ as 1 to $6n^2+18n+13$ sequentially from left to right, row wise beginning with the first row. Consider $2n+2$ hexagons in the outer most layer of the $circum\text{-}trizene(n)$. Let P^* denote the path induced by the edges of the hexagons that are not boundary edges of any other hexagon. Select $n+1$ vertices of degree 3 in P^*, which are at distance 5 apart on P^*.

Output $\gamma_p(\text{circum}-\text{trizene}(n)) = n+1$.

Proof of Correctness $S(1)$ is a power dominating set of circum-trizene(1) with $|S(1)| = 2$. Now $M^0(S(1)) = N[S(1)] = \{6, 2, 3, 10, 8, 4, 12, 13\}$. See Fig. 3a. At least one vertex $v \in M^0(S(1))$ satisfies $|N[v] \backslash M^0(S(1))| = 1$. Proceeding inductively, for every vertex $v \in M^i(S(1))$, $|N[v] \backslash M^i(S(1))| = 1$, $i \geq 1$, at every inductive step $i, i \geq 2$. Now $S(n) = n+1$ is a power dominating set of circum-trizene(n). This implies that $\gamma_p(G) = n+1$, hence the proof.

Theorem 3 *Let G be a circum-pyrene(n) or a circum-trizene(n), $n \geq 1$. Then $\gamma_p(G) = n + 1$.*

3 Ladderlike Honeycomb Networks

Lemma 7 *Let H be as shown in Fig. 3b. Then $\gamma_p(H) = 1$.*

Proof Let S be a power dominating set of H. We claim that $|S| = 1$. Suppose not, let H be the subgraph that does not contain any member of S. If any vertex of H is monitored, then v is adjacent to two unmonitored vertices of H, a contradiction. See Fig. 3b.

3.1 Honeycomb Rectangular Torus

Definition 5 ([7]) Assume that m and n are positive even integers. The honeycomb rectangular torus $HReT(m, n)$ is the graph with the node set $\{(i, j) \backslash 0 \leq i < m,\ 0 \leq j < n\}$ such that (i, j) and (k, l) are adjacent if they satisfy one of the following conditions:

1. $i = k$ and $j = l \pm 1 (mod\ n)$; and
2. $j = l$ and $k = i - 1 (mod\ m)$ if $i + j$ is even.

Definition 6 ([7]) Assume that m and n are positive integers where n is even. Let d be any integer such that $(m - d)$ is an even number. The generalized honeycomb rectangular torus $GHT(m, n, d)$ is the graph with the node set $\{(i, j) \backslash 0 \leq i < m,\ 0 \leq j < n\}$ such that (i, j) and (k, l) are adjacent if they satisfy one of the following conditions:

1. $i = k$ and $j = l \pm 1 (modn)$
2. $j = l$ and $k = i - 1$ if $i + j$ is even and
3. $i = 0,\ k = m - 1$, and $l = j + d (modn)$ if j is even.

Obviously, any $GHT(m, n, d)$ is a three-regular bipartite graph. We can label those nodes (i, j) white when $i + j$ is even or black otherwise.

Lemma 8 *Let G be a $HReT(m, n)$, m, n are even $m \geq 6,\ n \geq 8$ and $m \leq n$. Then $\gamma_p(G) \geq \frac{n}{2}$.*

Proof In $HReT(m, n)$, there are $\frac{n}{2}$ critical subgraphs, each isomorphic to H as described in Lemma 3.1. Therefore, $\gamma_p(G) \geq \frac{n}{2}$.

Power Domination Algorithm in Honeycomb Rectangular Torus

Input The honeycomb rectangular torus $HReT(m, n)$, m, n is even $m \geq 6,\ n \geq 8$ and $m \leq n$.

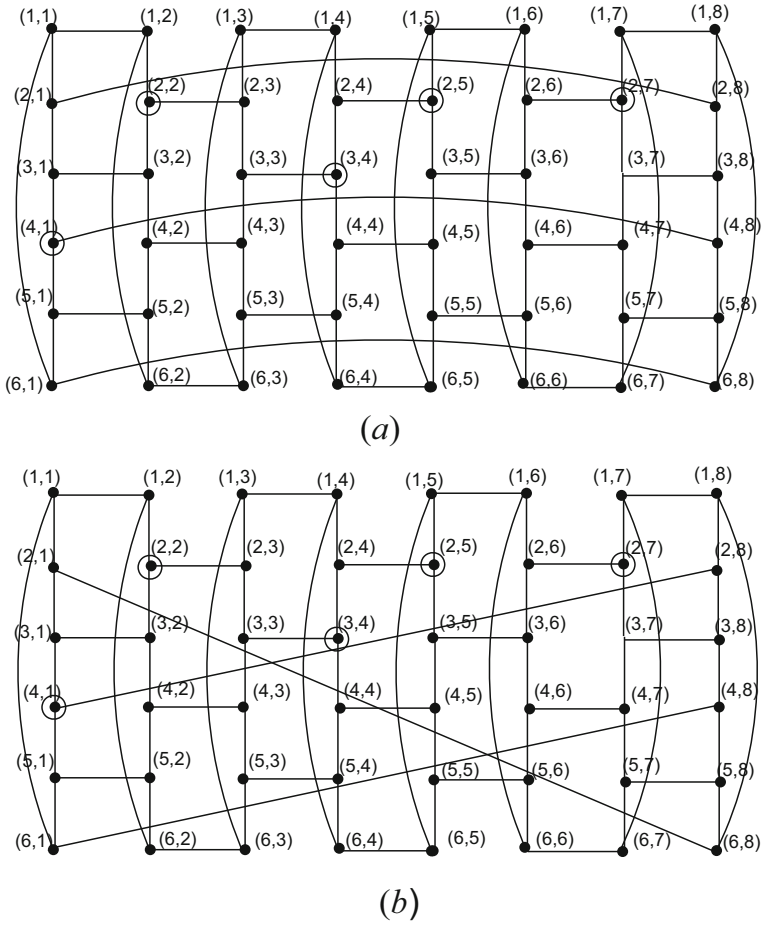

Fig. 4 Circled vertices constitute a power dominating set. (**a**) Honeycomb rectangular torus $HReT(6, 8)$. (**b**) Honeycomb rectangular torus $GHT(6, 8, 2)$

Algorithm Name the vertices in the ith row, jth column position as (i, j), $1 \leq i \leq m$, $1 \leq j \leq n$, and select the vertices $\bigcup_{j=5}^{n-1}(2, j) \cup \{(2, 2), (3, 4), (4, 1)\}$ in S.

Output $\gamma_p(HReT(m, n)) = \frac{n}{2} + 1$.

Proof of Correctness Let S be a power dominating set of $HReT(m, n)$ with $|S| = \frac{n}{2} + 1$. Then $M^0(S) = N[v] = \{(i, j), (2, k), (2, 2), (1, 2), (3, 2), (2, 3), (3, 4), (4, 4), (4, 1), (5, 1), (3, 1), (4, n)\}$, $i = 1, 2, 3, j = 5, 7, \ldots, n-1$, $k = 4, 6, \ldots, n-2$. See Fig. 4a. At least one vertex $v \in M^0(S(1))$ satisfies $|N[v] \backslash M^0(S(1))| = 1$. Proceeding inductively, for every vertex $v \in M^i(S)$, $|N[v] \backslash M^i(S)| = 1$, $i \geq 1$, at every inductive step $i, i \geq 1$.

Now $S = \bigcup_{j=5}^{n-1}(2, j) \cup \{(2, 2), (3, 4), (4, 1)\}$ is a power dominating set of $(HReT(m, n))$. This implies that $\gamma_p(G) = \frac{n}{2} + 1$, hence the proof.

Lemma 9 *Let G be a generalized honeycomb rectangular torus $GHT(m, n, d)$, $m \geq 6,\ n \geq 8,\ m \leq n$. Then $\gamma_p(G) \geq \frac{n}{2}$.*

Proof In $GHT(m, n, d)$, there are $\frac{n}{2}$ vertex-disjoint copies of H as described in lemma 3.1. Therefore, $\gamma_p(G) \geq \frac{n}{2}$.

Theorem 4 *Let G be a honeycomb rectangular torus $HReT(m, n)$ or a generalized honeycomb rectangular torus $GHT(m, n, d)$, $m \geq 6,\ n \geq 8, m \leq n$. Then $\frac{n}{2} \leq \gamma_p(G) \leq \frac{n}{2} + 1$.*

4 Conclusion

In this paper, we have obtained the power domination number for triangular graphs, pyrene networks, circum-pyrene networks, circum-trizene networks, honeycomb rectangular torus and generalized honeycomb torus network.

References

1. Haynes, T.W., Hedetniemi, S.M., Hedetniemi, S.T., Henning, M.A.: Power domination in graphs applied to electrical power networks. SIAM Journal on Discrete Mathematics, **15(4)**, 519–529 (2002).
2. Ferrero, D., Hogben, L., Kenter, F.H.J., Young, M.: Note on Power Propagation Time and Lower Bounds for the Power Domination Number. arXiv:1512.06413v2 [math.CO] 17 (2016).
3. Xu,G.J., Kang, L.Y., Shan, E.F., Zhao,M.: Power domination in block graphs. Theoretical Computer Science, **359** 299–305 (2006).
4. Dorbec, P., Mollard, M., Klavzar, S., Spacapan, S. :Power domination in product graphs. SIAM Journal on Discrete Mathematics, **22(2)** 554–567 (2008).
5. Ferrero, D., Varghese, S., Vijayakumar,A.: Power domination in honeycomb networks, Journal of Discrete Mathematical Science, **14(6)** 521–529 (2011).
6. Quadras, J., Balasubramanian, K., Arputha Christy, K.: Analytical expressions for Wiener indices of n-circumscribed peri-condensed benzenoid graphs. Journal of Mathematical Chemistry (2016), https://doi.org/10.1007/s10910-016-0596-9.
7. Hsu, L.H. , Lin, C.K.: Graph theory and interconnection networks. Taylor and Francies Group, New York, (2009).
8. Yang,X., Megson,G. M., Tang,Y., Evans,D. J.: Diameter of Parallelogramic Honeycomb Torus. An International Journal of Computer and Mathematics with Applications, **50** 1477–1486 (2005).

Improved Bound for Dilation of an Embedding onto Circulant Networks

R. Sundara Rajan, T. M. Rajalaxmi, Joe Ryan, and Mirka Miller

Abstract Implementation of parallel algorithms and simulation of different interconnection networks need an effective tool, that is, graph embedding. This paper focuses on improving a lower bound obtained in Rajan et al. (Comput J 58:3271–3278, 2015) for dilation of an embedding onto circulant networks. In addition, this paper provides algorithms to compute dilation of embedding circulant network into certain trees, for instance, m-rooted complete binary tree, m-rooted sibling tree, and r-dimensional hypertree, proving that the improved bound obtained is sharp.

Keywords Embedding · Dilation · Circulant network · Binary tree · Sibling tree · Hypertree

Mathematics Subject Classification 05C60, 05C85

1 Introduction

Graph embedding is an important technique that traces a guest graph into a host graph, mostly an interconnection network. There are a lot of applications which can be modeled as graph embedding [2]. Few cost criteria are used to measure the quality of an embedding. The criterion *dilation* is significant one. The dilation of an

R. Sundara Rajan (✉)
Department of Mathematics, Hindustan Institute of Technology and Science, Padur, Chennai, India

T. M. Rajalaxmi
Department of Mathematics, SSN College of Engineering, Kalavakkam, Chennai, India

J. Ryan
School of Electrical Engineering and Computer Science, The University of Newcastle, Callaghan, NSW, Australia

M. Miller
School of Mathematical and Physical Sciences, The University of Newcastle, Callaghan, NSW, Australia

B. Rushi Kumar et al. (eds.), *Applied Mathematics and Scientific Computing*, Trends in Mathematics, https://doi.org/10.1007/978-3-030-01123-9_62

embedding f from guest graph G into the host graph H is defined as the maximum distance between a pair of vertices of host graph that are images of adjacent vertices of the guest graph. The dilation of embedding from guest graph G into H is the minimum dilation taken over all embeddings f of G into H. In short, it is a measure of the communication time needed when simulating one network on another [3].

Generally the double-loop network is a circulant network [4]. Circulant graph has been used for decades in the design of computer and telecommunication networks for more than 10 years due to its optimal fault-tolerance and routing capabilities [5]. VLSI design and distributed computations also make use of them [6, 7]. Binary codes are designed by circulant graphs [8].

The rest of the paper is structured as follows: In Sect. 2, we introduce the definitions and other preliminaries. In Sect. 3, we compute the dilation of embedding circulant networks, and we also demonstrate how it can be modeled into certain trees. Finally, we conclude the study with the results of tests performed and with a discussion of future directions in Sect. 4.

2 Basic Concepts

In this section, we describe the basic concepts and preliminaries associated with embedding problems.

Definition 1 ([9, 10]) Let G and H be finite graphs. An embedding *of G into H is a pair (f, P_f) defined as follows:*

1. *f is a one-to-one map from $V(G) \rightarrow V(H)$*
2. *P_f is a one-to-one map from $E(G)$ to $\{P_f(u, v) : P_f(u, v)$ is a path in H between $f(u)$ and $f(v)$ for $(u, v) \in E(G)\}$.*

For brevity, we denote the pair (f, P_f) as f.

Definition 2 ([10]) If $e = (u, v) \in E(G)$, then the length of $P_f(u, v)$ in H is called the *dilation* of the edge e. The maximum dilation over all edges of G is called the dilation of the embedding f. The dilation of embedding G into H, *denoted by $dil(G, H)$, is the minimum dilation taken over all embeddings f of G into H*. The expansion of an embedding f *is the ratio of the number of vertices of H to the number of vertices of G*.

If G illustrates the wiring diagram of an electronic circuit, with the vertices representing components and the edges representing wires connecting them, then the dilation of G into H is the minimum, over all embeddings $f : V(G) \rightarrow V(H)$ (see Fig. 1).

Definition 3 ([7, 11]) The undirected circulant graph $G(n; \pm S)$, $S \subseteq \{1, 2, \ldots, j\}$, $1 \leq j \leq \lfloor n/2 \rfloor$ *is a graph with the vertex set $V = \{0, 1, \ldots, n-1\}$ and the edge set $E = \{(i, k) : |k - i| \equiv s (mod\ n), s \in S\}$.*

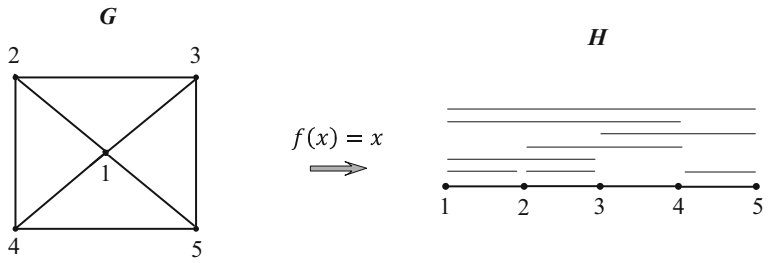

Fig. 1 Wiring diagram of a graph G into path H with $dil_f(G, H) = 4$

Fig. 2 Circulant graph $G(8; \pm\{1, 3, 4\})$

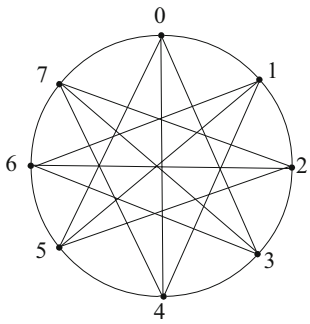

The circulant graph shown in Fig. 2 is $G(8; \pm\{1, 3, 4\})$. It is clear that $G(n; \pm 1)$ is the undirected cycle C_n and $G(n; \pm\{1, 2, \ldots, \lfloor n/2 \rfloor\})$ is the complete graph K_n. The cycle $G(n; \pm 1) \simeq C_n$ contained in $G(n; \pm\{1, 2, \ldots, j\})$, $1 \leq j \leq \lfloor n/2 \rfloor$ is sometimes referred to as the outer cycle C of G.

3 Improved Bound

An embedding stretches edges in the source network (guest) to paths in the target network (host). Computing dilation of an embedding is NP-complete. Harper in 1966 showed that the dilation of embedding the hypercube can be computed into a path graph using vertex isoperimetric problem [12]. However, there is no efficient method to compute exact dilation of graph embeddings in general [11, 13].

Manuel et al. improved this result. In 2012, they obtained a lower bound for dilation of an embedding using optimal wirelength [14]. Moreover, the possibility of obtaining a nontrivial lower bound for dilation without computing the wirelength of an embedding is questioned. Our previous work, the Dilation Lemma [1], provides a partial answer toward this end when the guest graph is regular and has the same number of vertices as the host graph.

Lemma 1 (Dilation Lemma) [1] *Let G be an r-regular graph on n vertices and H be a graph on $m, m \geq n$ vertices with $diam(H) = \delta$. Let $f : G \to H$ be an embedding. Let $D = \{u \in V(H) \mid D_\delta(u) \neq \emptyset\}$, where $D_\alpha(u)$ denotes the set of all vertices in H which are at distance α from u. For $u \in D$, let k_u be the least integer such that $|D_\delta(u)| + |D_{\delta-1}(u)| + \cdots + |D_{\delta-k_u}(u)| > n - r - 1$. Then $dil(G, H) \geq \delta - k$, where $k = \min_{u \in D} k_u$.*

In this section, we improve this lower bound for circulant networks and prove that the improved bound obtained for embedding circulant networks into certain architectures is sharp. Now, we begin with the following definition.

Definition 4 Let $k \geq 0$ be the least positive integer, and for some l, $l \geq 1$, let $D = \{u_1, u_2, \ldots, u_l \in V(H) \mid D_\delta(u_i) \neq \emptyset \text{ and } u_r \notin \bigcup_{t=0}^{k} \bigcup_{i=1}^{l} D_{\delta-t}(u_i), 1 \leq r \leq l, i \neq r\}$, where $D_\alpha(u_i)$ denotes the set of all vertices in H which are at distance α from u_i.

For example, let us consider a path P_6 on 6 vertices and $V(P_6) = \{u_1, u_2, \ldots, u_6\}$. Clearly the vertices u_1 and u_6 satisfy the first condition of Definition 4, but if $u_1 \in D$, then $u_6 \notin D$, since $u_6 \in D_\delta(u_1)$. Let us consider another example, that is, a cycle C_6 on 6 vertices and $V(C_6) = \{u_1, u_2, \ldots, u_6\}$. Clearly all vertices satisfy the first condition of Definition 4, but $D = \{u_1, u_2, u_3\}$ (let us assume that $k = 0$).

Lemma 2 *Let G be an undirected circulant graph $G(n; \pm\{1, 2, \ldots, j\})$, $1 \leq j < \lfloor n/2 \rfloor$ and H be a graph on n vertices with diameter δ. Let $f : G \to H$ be an embedding. For $u_1, u_2, \ldots, u_l \in D$, let $k \geq 0$ be the least integer such that $\left| \bigcup_{t=0}^{k} \bigcup_{i=1}^{l} D_{\delta-t}(u_i) \right| > n - 2j - l$. Then $dil(G, H) \geq \delta - k$.*

Proof Let $v_1, v_2, \ldots, v_l \in V(G)$ such that $D_\delta(f(v_i)) \neq \emptyset$, $1 \leq i \leq l$ and k is minimum. Since G is $2j$ regular, there are at most $n - 2j - l$ vertices in G which has no neighbor in $\{v_1, v_2, \ldots, v_l\}$ in G. Since $\left| \bigcup_{t=0}^{k} \bigcup_{i=1}^{l} D_{\delta-t}(f(v_i)) \right| > n - 2j - l$, there exists at least one vertex w adjacent to some vertex v_p, $1 \leq p \leq l$ in G which is mapped to a vertex in $\bigcup_{t=0}^{k} \bigcup_{i=1}^{l} D_{\delta-t}(f(v_i))$. This implies that $dil(G, H) \geq \delta - k$.

3.1 Circulant Networks into m-Rooted Complete Binary Trees

For any nonnegative integer r, the complete binary tree of height $r - 1$, denoted by T_r, is the binary tree where each internal vertex has exactly two children and all the leaves are at the same level. Clearly, a complete binary tree T_r has r levels. Each level i, $1 \leq i \leq r$, contains 2^{i-1} vertices. Thus, T_r has exactly $2^r - 1$ vertices. The

one-rooted complete binary tree T_r^1 is obtained from a complete binary tree T_r by attaching to its root a pendant edge. The new vertex is called the root of T_r^1 and is considered to be at level 0. The m-rooted complete binary tree T_r^m is obtained by taking m vertex-disjoint one-rooted complete binary trees T_r^1 on 2^r vertices each, with roots $r_1, r_2, \ldots, r_m$ and adding the edges (r_i, r_{i+1}), $1 \leq i \leq m-1$ [15].

Remark 1 The number of vertices and the number of edges of T_r^m are $m \times 2^r$ and $m \times 2^r - 1$, respectively.

Lemma 3 *Let u be a vertex in T_r^m with $D_\delta(u) \neq \emptyset$. Then for any $m \geq 3$, $|D_\delta(u)| = 2^{r-1}$ and $|D_{\delta-1}(u)| = 3 \times 2^{r-2}$, $r \geq 3$.*

Proof We prove this result by induction on r. If $r = 3$, there are exactly four vertices with distance δ from u. Thus the result is true for $r = 3$. Let us assume that the result is true for $r = n$. That is, $|D_\delta(u)| = 2^{n-1}$ in T_n^m. Now consider $r = n + 1$. Since T_{n+1}^m is obtained from a complete binary tree, each vertex in the leaf of the mth copy of T_n^1 in T_n^m has exactly two children. Thus $|D_\delta(u)| = 2 \times 2^{n-1} = 2^n$ in T_{n+1}^m, hence the result. Similarly, we can prove $|D_{\delta-1}(u)| = 3 \times 2^{r-2}$, $r \geq 3$.

Theorem 1 *Let G be the circulant graph $G(m \times 2^r; \pm\{1, 2, \ldots, (4m-7)2^{r-3}+1\})$ and H be an m-rooted complete binary trees T_r^m. Then $dil(G, H) \geq 2r + m - 2$, where $m, r \geq 3$.*

Proof Let $u_1, u_2, \ldots, u_l \in V(G)$ such that $D_\delta(u_i) \neq \emptyset$, for all i. By the definition of circulant graph, there are at most $n - 2j - l = m \times 2^r - 2((4m-7)2^{r-3}+1) - 2^{r-1} = 5 \times 2^{r-2} - 2$ vertices which are not adjacent to the vertices $u_1, u_2, \ldots, u_l$ in G. Since $|D_\delta(f(u_i))| + |D_{\delta-1}(f(u_i))| = 5 \times 2^{r-2} > 5 \times 2^{r-2} - 2$, by Lemma 2, $dil(G, H) \geq 2r + m - 2$.

Dilation Algorithm A

Input The circulant graph $G(m \times 2^r; \pm\{1, 2, \ldots, (4m-7)2^{r-3}+1\})$ and the m-rooted complete binary tree T_r^m, where $m, r \geq 3$.

Algorithm Label the consecutive vertices of $G(m \times 2^r; \pm\{1\})$ in $G(m \times 2^r; \pm\{1, 2, \ldots, (4m-7)2^{r-3}+1\})$ as $0, 1, \ldots, m \times 2^r - 1$ in the clockwise sense. Label the m copies of T_r^1 in T_r^m as follows:

- Label the leaf vertices of the copy of T_r^1 with root r_1 as $0, 1, \ldots, 2^{r-1} - 1$.
- Label the leaf vertices of the copy of T_r^1 with root r_m as $(4m-3)2^{r-3}+1$, $(4m-3)2^{r-3}+2, \ldots, (4m+1)2^{r-3}$.
- Label the remaining vertices in T_r^m arbitrarily (see Fig. 3).

Let $f(x) = x$ for all $x \in V(G)$ and for $(a, b) \in E(G)$; let $P_f(a, b)$ be the shortest path between $f(a)$ and $f(b)$ in T_r^m.

Output An embedding f of $G(m \times 2^r; \pm\{1, 2, \ldots, (4m-7)2^{r-3}+1\})$ into T_r^m with dilation $2r + m - 2$.

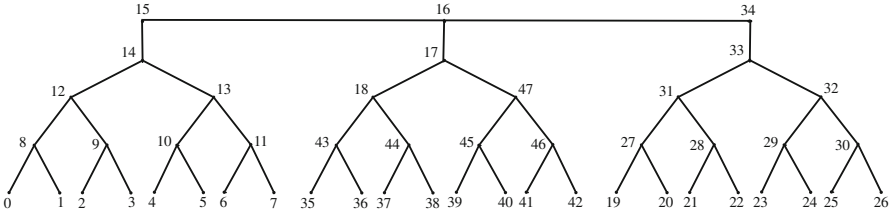

Fig. 3 Labeling of T_4^3

Theorem 2 *Let G be the circulant graph $G(m \times 2^r; \pm\{1, 2, \ldots, (4m-7)2^{r-3}+1\})$ and H be an m-rooted complete binary tree T_r^m. Then $dil(G, H) = 2r + m - 2$, where $m, r \geq 3$.*

Proof Label the vertices of G and H using dilation algorithm A. We assume that the labels represent the vertices to which they are assigned. This labeling implies that there is no edge $e = (u, v)$ of G with $f(u)$ mapped to a leaf node of T_r^1 with root r_1 and $f(v)$ mapped to a leaf node of T_r^1 with root r_m. Thus $dil(G, H) \leq 2r + m - 2$. By Theorem 1, $dil(G, H) \geq 2r + m - 2$. Thus $dil(G, H) = 2r + m - 2$.

Remark 2 If $m = 1$ and $r \geq 3$, then the dilation of embedding circulant graph $G(2^r; \pm\{1, 2, \ldots, 3 \times 2^{r-4}+1\})$ into one-rooted complete binary tree T_r^1 is $2r - 3$.

Remark 3 If $m = 2$ and $r \geq 3$, then the dilation of embedding circulant graph $G(2^{r+1}; \pm\{1, 2, \ldots, 3 \times 2^{r-3} + 1\})$ into two-rooted complete binary tree T_r^2 is $2r - 4$.

3.2 Circulant Networks into m-Rooted Sibling Trees

The one-rooted sibling tree ST_r^1 is obtained from the one-rooted complete binary tree T_r^1 by adding edges (sibling edges) between left and right children of the same parent node. The m-rooted sibling tree ST_r^m is obtained by taking m vertex-disjoint one-rooted sibling trees ST_r^1 on 2^r vertices with roots say $r_1, r_2, \ldots, r_m$ and adding the edges (r_i, r_{i+1}), $1 \leq i \leq m - 1$ [15] (see Fig. 4).

Remark 4 The number of vertices and the edges of ST_r^m is $m \times 2^r$ and $3m \times 2^{r-1} - m - 1$, respectively.

Theorem 3 *Let G be the circulant graph $G(m \times 2^r; \pm\{1, 2, \ldots, (4m-7)2^{r-3}+1\})$ and H be an m-rooted sibling tree ST_r^m. Then $dil(G, H) \geq 2r + m - 2$, where $m, r \geq 3$.*

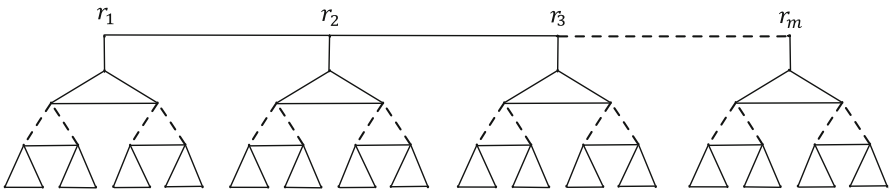

Fig. 4 m-rooted sibling tree ST_r^m

Proof Let $u_1, u_2, \ldots, u_l \in V(G)$ such that $D_\delta(u_i) \neq \emptyset$, for all i. By the definition of a circulant graph, there are at most $n-2j-l = m \times 2^r - 2((4m-7)2^{r-3}+1) - 2^{r-1} = 5 \times 2^{r-2} - 2$ vertices which are not adjacent to the vertices $u_1, u_2, \ldots, u_l$ in G. Since $|D_\delta(f(u_i))| + |D_{\delta-1}(f(u_i))| = 5 \times 2^{r-2} > 5 \times 2^{r-2} - 2$, by Lemma 2, $dil(G, H) \geq 2r + m - 2$.

Dilation Algorithm B

Input The circulant graph $G(m \times 2^r; \pm\{1, 2, \ldots, (4m-7)2^{r-3}+1\})$ and the m-rooted sibling tree ST_r^m, where $m, r \geq 3$.

Algorithm Label the consecutive vertices of $G(m \times 2^r; \pm\{1\})$ in $G(m \times 2^r; \pm\{1, 2, \ldots, (4m-7)2^{r-3}+1\})$ as $0, 1, \ldots, m \times 2^r - 1$ in the clockwise sense. Delete the sibling edges in ST_r^m to obtain T_r^m and label the vertices of T_r^m using Dilation Algorithm A. Let $f(x) = x$ for all $x \in V(G)$ and for $(a, b) \in E(G)$, let $P_f(a, b)$ be a shortest path between $f(a)$ and $f(b)$ in ST_r^m.

Output An embedding f of $G(m \times 2^r; \pm\{1, 2, \ldots, (4m-7)2^{r-3}+1\})$ into ST_r^m with dilation $2r + m - 2$.

The following theorem can be proved in the same way as Theorem 2. So, we omit its proof.

Theorem 4 *Let G be the circulant graph $G(m \times 2^r; \pm\{1, 2, \ldots, (4m-7)2^{r-3}+1\})$ and H be an m-rooted sibling tree ST_r^m. Then $dil(G, H) = 2r + m - 2$, where $m, r \geq 3$.*

Remark 5 If $m = 1$ and $r \geq 3$, then the dilation of embedding circulant graph $G(2^r; \pm\{1, 2, \ldots, 3 \times 2^{r-4}+1\})$ into 1-rooted sibling tree ST_r^1 is $2r - 3$.

Remark 6 If $m = 2$ and $r \geq 3$, then the dilation of embedding circulant graph $G(2^{r+1}; \pm\{1, 2, \ldots, 3 \times 2^{r-3}+1\})$ into 2-rooted sibling tree ST_r^2 is $2r - 4$.

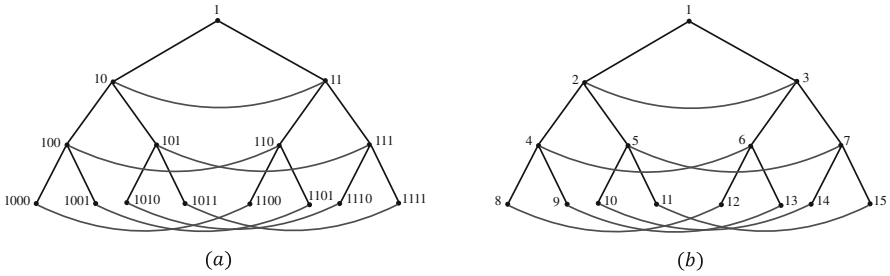

Fig. 5 (**a**) $HT(4)$ with binary labels (**b**) $HT(4)$ with decimal labels

3.3 Circulant Networks into Hypertrees

A hypertree is a hypergraph H if there is a tree T such that the hyperedges of H induce subtrees in T [16]. In the literature, hypertree is also known as subtree hypergraph or arboreal hypergraph [16].

The basic skeleton of a hypertree is a complete binary tree T_r. Here the nodes of the tree are numbered as follows: The root node has label 1. The root is said to be at level 1. Labels of left and right children are formed by appending a 0 and 1, respectively, to the label of the parent node (see Fig. 5a). The decimal labels of the hypertree in Fig. 5a are depicted in Fig. 5b. Here the children of the node x are labeled as $2x$ and $2x + 1$. Additional links in a hypertree are horizontal and two nodes in the same level i of the tree are joined if their label difference is 2^{i-2}. We denote an r level hypertree as $HT(r)$. It has $2^r - 1$ vertices and 3 $(2^{r-1} - 1)$ edges [17].

Theorem 5 *Let G be the circulant graph $G(2^r - 1; \pm\{1, 2, \ldots, 2^{r-4}\})$ and H be the hypertree $HT(r)$. Then $dil(G, H) \geq 2r - 4$, $r \geq 5$.*

Proof Let $u_1, u_2, \ldots, u_l \in V(G)$ such that $D_\delta(u_i) \neq \emptyset$, for all i. By the definition of circulant graph, there are at most $n - 2j - l = 2^r - 1 - 2^{r-3} - 2^{r-2} = 5 \times 2^{r-3} - 1$ vertices which are not adjacent to the vertices $u_1, u_2, \ldots, u_l$ in G. Since $|D_\delta(f(u_i))| + |D_{\delta-1}(f(u_i))| = 5 \times 2^{r-3} > 5 \times 2^{r-3} - 1$, by Lemma 2, $dil(G, H) \geq 2r - 4$.

Dilation Algorithm C

Input The circulant graph $G(2^r - 1; \pm\{1, 2, \ldots, 2^{r-4}\})$ and the hypertree $HT(r)$, $r \geq 5$.

Algorithm Label the consecutive vertices of $G(2^r - 1; \pm\{1\})$ in $G(2^r - 1; \pm\{1, 2, \ldots, 2^{r-4}\})$ as $0, 1, \ldots, 2^r - 2$ in the clockwise sense. Label the vertices in the rth level of $HT(r)$ from left to right as $0, 1, \ldots, 2^{r-2} - 1, 5 \times 2^{r-4}, 5 \times 2^{r-4} + 1, \ldots, 9 \times 2^{r-4} - 1$ and the remaining vertices in $HT(r)$ arbitrarily (see Fig. 6). Let $f(x) = x$ for all $x \in V(G)$ and for $(a, b) \in E(G)$; let $P_f(a, b)$ be a shortest path between $f(a)$ and $f(b)$ in $HT(r)$.

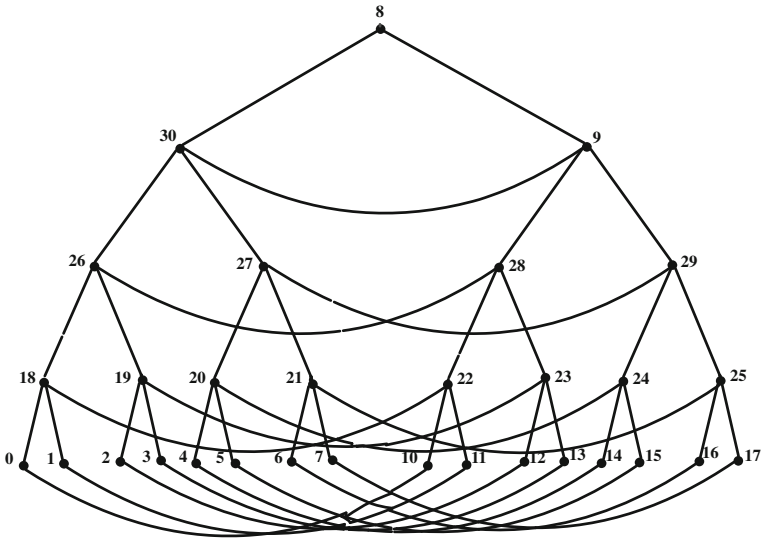

Fig. 6 Labeling of $HT(5)$

Output An embedding f of $G(2^r-1; \pm\{1, 2, \ldots, 2^{r-4}\})$ into $HT(r)$ with dilation $2r-4$.

Theorem 6 *Let G be the circulant graph $G(2^r - 1; \pm\{1, 2, \ldots, 2^{r-4}\})$ and H be the hypertree $HT(r)$. Then $dil(G, H) = 2r - 4$, where $r \geq 5$.*

Proof Label the vertices of G and H using dilation algorithm C. We assume that the labels represent the vertices to which they are assigned. This labeling implies that there is no edge $e = (u, v)$ of G such that $f(u)$ and $f(v)$ are mapped to the rth level vertex of $HT(r)$. Thus $dil(G, H) \leq 2r - 4$. By Theorem 5, $dil(G, H) \geq 2r - 4$. Thus $dil(G, H) = 2r - 4$.

4 Concluding Remarks

In this paper, we have developed a method to improve the lower bound for dilation of an embedding onto circulant networks, and hence it is proved that the improved bound obtained for embedding circulant networks into certain architectures is sharp. Using this technique, finding the dilation of embedding circulant networks into other good candidates of architectures is under investigation.

Acknowledgement The work of R. Sundara Rajan was partially supported by Project No. ECR/2016/1993, Science and Engineering Research Board (SERB), Department of Science and Technology (DST), Government of India.

References

1. Rajan, R.S., Manuel, P., Rajasingh, I., Parthiban, N., Miller, M.: A lower bound for dilation of an embedding. The Computer Journal, **58**, 3271–3278 (2015)
2. Chaudhary, V., Aggarwal, J.K.: Generalized mapping of parallel algorithms onto parallel architectures. Proc. Int'l. Conf. Parallel Process, 137–141, (1990)
3. Dvoŕák, T.: Dense sets and embedding binary trees into hypercubes. Discrete Applied Mathematics, **155**, 506–514 (2007)
4. Wong, G.K., Coppersmith, D.A.: A combinatorial problem related to multimodule memory organization. Journal of the ACM. **21**, 392–401 (1994)
5. Boesch, E.T., Wang, J.: Reliable circulant networks with minimum transmission delay. IEEE Transactions on Circuit and Systems, **32**, 1286–1291 (1985)
6. Wilkov, R.S.: Analysis and design of reliable computer networks. IEEE Transactions on Communications, **20**, 660–678 (1972)
7. Bermond, J.C., Comellas, F., Hsu, D.F.: Distributed loop computer networks. A survey: Journal of Parallel and Distributed Computing, **24**, 2–10 (1995)
8. Karlin, M.: New binary coding results by circulants. IEEE Transactions on Information Theory, **15**, 81–92 (1969)
9. Xu, J.M.: Topological Structure and Analysis of Interconnection Networks. Kluwer Academic Publishers, London (2001)
10. Bezrukov, S.L., Chavez, J.D., Harper, L.H., Röttger, M., Schroeder, U.P.: Embedding of hypercubes into grids. MFCS. **1450** 693–701 (1998)
11. Rajasingh, I., Rajan, B., Rajan, R.S.: Embedding of special classes of circulant networks, hypercubes and generalized Petersen graphs. International Journal of Computer Mathematics, **89**, 1970–1978 (2012).
12. Harper, L.H.: Optimal numberings and isoperimetric problems on graphs. Journal of Combinatorial Theory, **1**, 385–393 (1966)
13. Bezrukov, S.L.: Embedding complete trees into the hypercube. Discrete Applied Mathematics, **110**, 101–119 (2001)
14. Manuel, P., Rajasingh, I., Rajan, R.S.: Embedding variants of hypercubes with dilation 2. Journal of Interconnection Networks, **13**, 1–16 (2012)
15. Rajasingh, I., Manuel, P., Rajan, B., Arockiaraj, M.: Wirelength of hypercubes into certain trees, Discrete Applied Mathematics, **160**, 2778–2786 (2012)
16. Brandstadt, A., Chepoi, V.D., Dragan, F.F.: The algorithmic use of hypertree structure and maximum neighbourhood orderings. Discrete Applied Mathematics, **82**, 43–77 (1998)
17. Goodman, J.R., Sequin, C.H.: A multiprocessor interconnection topology. IEEE Transactions on Computers, **c-30**, 923–933 (1981)